

THIS WEEK

EDITORIALS

ANIMAL RESEARCH Scientists unite to protest against violence **p.158**

WORLD VIEW China's citizens must act against air pollution **p.159**

BEHAVIOUR How archerfish find their targets amid distractions **p.161**



Right to remain silent

The US Supreme Court should overturn the 2003 law that requires federally funded HIV/AIDS programmes abroad to denounce prostitution.

What kind of strings can government funders attach to the money they hand out to organizations? Controlling how the cash is spent is surely a reasonable one. And the US Supreme Court has ruled in the past that it is fair for the government to prohibit recipients of such funding from saying certain things.

But what about compelling funding recipients to make prescribed statements? Given the importance assigned in the United States to the right to free speech, it might surprise some that the US government has tried to force would-be recipients of funds from a high-profile HIV/AIDS programme to denounce prostitution. It certainly surprised many of the groups involved, who in 2005 brought a lawsuit against the government in protest. In 2006, a district court stopped the restrictions from being enforced while the case wound its way through the courts. Last month, the litigation reached the US Supreme Court. The verdict, expected next month, will be important for any scientist funded by a US agency.

The case, *Agency for International Development et al. v. The Alliance for Open Society International, Inc., et al.*, turns on the wording of the United States Leadership Against HIV/AIDS, Tuberculosis and Malaria Act, a 2003 law that authorized a historic disease-directed government programme. The act allowed Congress to spend US\$44 billion between 2004 and 2012 to combat HIV/AIDS through the President's Emergency Plan for AIDS Relief (PEPFAR). At the end of 2012, PEPFAR was providing antiretroviral therapy for more than 5.1 million people globally; the same year, it provided HIV testing and counselling for nearly 47 million people, many of them pregnant women.

For all its virtues, the law that established PEPFAR contains the troubling stipulation that none of its funding may go to "any group or organization that does not have a policy explicitly opposing prostitution and sex trafficking". What is more, it states that any group receiving its funds must refrain from speech that the government judges "inconsistent with" that anti-prostitution policy. The prohibition pertains to all activities by the recipient group, even those funded with private money.

At first, even the US Department of Justice deemed the restrictions unconstitutional and declined to enforce them on groups based in the United States. But officials changed their minds in 2005, prompting many non-governmental organizations to sue. One of the litigants — InterAction, an alliance based in Washington DC — represents more than 190 US-based groups.

Lawyers for the justice department argue that the government has the authority to ensure that its message is "effectively communicated, and not undermined" by recipients of its funds. In the past, the Supreme Court has agreed — up to a point. For instance, in a landmark abortion case, the high court said that the government did not trample on free speech when it forbade groups receiving US family-planning funds to counsel women to have abortions. But to require a group

to remain silent on a certain issue is quite different from compelling the group, as a condition of funding, to proclaim a point of view it disagrees with — a compulsion that justice Samuel Alito called "a dangerous proposition" during last month's oral arguments.

It is not clear how the high court will rule. If it sides with the government, the immediate result would be sobering. Many private organizations receiving PEPFAR funding would face a choice. They could give up that funding. Or they could stop publishing papers, speaking at conferences or preparing training materials about how, for example, to improve sex workers' access to HIV testing or condoms — unless, of course, those speeches or materials explicitly denounce prostitution. Never mind that such proclamations are likely to compromise efforts to educate and deliver health care to sex workers.

More broadly still, a court decision in favour of the government could open the door to making all manner of grants, including awards to scientists, conditional on the broadcasting of whatever point of view a US funding agency happens to deem desirable at a given time. In the past, the Supreme Court has resisted the compelling of behaviour — as when it refused, for instance, to require students in publicly funded schools to salute the US flag. It should now do so again. ■

"The verdict next month will be important for any scientist funded by a US agency."

The cleaner state

Federal regulators could learn much from California's low-carbon fuel programme.

Last week, researchers at the University of California, Davis (UC Davis), released their latest analysis of California's Low Carbon Fuel Standard. The 2009 regulation requires oil companies and refineries to reduce the carbon intensity of transportation fuels — how much carbon dioxide they emit per unit of energy — by 10% by 2020. For 2013, this translates to a reduction of 1%, and the UC Davis researchers found that companies racked up enough gains last year to meet half of their obligations for the current year.

The study confirms what California has reported: a steady shift towards cleaner fuels since the regulations took hold in 2011. The idea is that providers can either document their own cuts in carbon intensity or buy credits from others who have gone beyond their requirements. Advanced biofuels — made from waste products or non-food plant material — still make up less than 1% of the state's fuel, but they represent 10% of the credits that have gone towards meeting the standard.

Despite an ongoing legal challenge brought by industry against the regulations, things seem to be working as they should. Daniel Sperling, director of the UC Davis Institute of Transportation Studies and a member of the California Air Resources Board, which implements the standard, calls the progress “modestly positive”. That stands in stark contrast to the US federal renewable fuels standard, which is in a state of disarray. The difference between the two is illustrative.

The federal standard sets requirements on the volume of biofuels, including ethanol and biodiesel, that must be blended into the US fuel mix, ramping up from roughly 34 billion litres in 2008 to more than 136 billion litres by 2022. But those requirements do not take into account the realities facing the industry. First, cars and petrol stations are equipped for a fuel blend that is 10% ethanol, but not all vehicles and few petrol stations can handle more. As a result, the corn-ethanol industry, which supplies the bulk of US biofuels, has hit what is known as the ‘blend wall’: the 10% fuel blend means that just 49 billion litres of ethanol are required to saturate the US fuel market, which is below what the law requires from this year forward. This discrepancy is made worse by the fact that demand for fuel has fallen off owing to increased prices and the economic slump; consumption is expected to decline even further as new fuel-economy regulations take hold.

The upshot is general confusion. The US Environmental Protection Agency has approved ethanol blends up to 15% for use in most vehicles, but few petrol stations are carrying them. Another way around the blend wall is to use E-85 fuel, which is 85% ethanol. It can be used by many flexible-fuel vehicles, but further expanding its use will take time. Meanwhile, the agency has been forced to waive the requirements for advanced biofuels. By law, the US fuel mix is required to

contain more than 10 billion litres of advanced biofuels this year, but actual commercial production is barely getting off the ground.

California hit the same blend wall in 2010, but it has still made progress since then. By setting a performance standard, the state has required fuel providers to focus on the carbon content of renewable fuels, not on their volume. This applies regardless of the blend wall, and regardless of what happens to the demand for fuel. Rather than setting

“California has required fuel providers to focus on the carbon content of renewables.”

thresholds for the production of different kinds of biofuels, this approach drives innovation by recognizing and rewarding incremental progress. The California programme already covers natural gas and electricity, and it might one day be extended to reward advanced technologies such as carbon capture and sequestration within the refining sector.

The upshot is that fuel providers in California have been finding ways around the blend wall and chalking up small gains, largely by shifting to cleaner processes for producing biofuels. The average carbon intensity of petrol and diesel substitutes dropped by 5% and 6%, respectively, from early 2011 to the end of 2012. Now Sperling and other academics in the National Low Carbon Fuel Standard Project are attempting to put this approach on the national radar. The idea is not entirely new — US President Barack Obama included it in his original energy platform in 2008 — but it has yet to garner political traction in Washington DC. This is unfortunate. As politicians and regulators search for ways to adjust the renewable-fuels mandate in the months and years to come, they would be wise to look west. California might once again be leading the way to smarter environmental policy. ■

Voice of Pro-Test

Confidence is rising among scientists defending animal research. It should be encouraged.

The name Pro-Test is becoming a rallying point for scientists standing up to animal-rights extremists. The term was coined by 16-year-old British school pupil Laurie Pycroft in January 2006, when he stumbled across an animal-rights demonstration in Oxford. The activists were protesting against the construction of a university biomedical building with modern animal facilities. Their violent strategies, including the placing of bombs, had already forced some building contractors to pull out. Important research was being hampered, thought Pycroft. He sprang into action, creating the first Pro-Test committee with university students and teachers, and organizing a rally to coincide with the activists’ next demonstration the following month.

In what was probably the first mass public showing in defence of animal research, about 1,000 scientists and students attended, overshadowing the 200-odd animal-rights protestors. That was a tipping point in Britain. Although the country had some of the world’s strictest animal-experimentation regulations, its scientists felt at risk from militant antivivisectionists. Most kept their heads below the parapet. But under the Pro-Test banner, they lost their fear of speaking out, particularly after politicians including then-prime minister Tony Blair showed support for their cause. The Oxford facility eventually got built.

Fast forward six years, to Italy. Last July, activists broke into the Green Hill beagle-breeding facility near Brescia, claiming that the animals, many of which were used for mandatory toxicity testing of drugs, were treated cruelly. Police allowed the activists to take the dogs away and a court later said that they could keep custody of the animals, pending investigations. Italy’s legal system being notoriously slow, the facility remains shut. Last week, most of the staff were laid off.

Concerned that the police and courts seemed to condone the methods

of the animal activists — and that scientists had no safe platform to explain their animal research — a group of Italian scientists created Pro-Test Italia in September. Just in time, as it unhappily turned out: on 20 April, the same activists (by now calling themselves Fermare Green Hill, or Stop Green Hill), broke into an animal facility at the University of Milan, chaining themselves by the necks to the doors and refusing to leave without the animals, mostly mice. Twelve hours later, after tense negotiations, they left with some of the animals — and with police assurance that they could come back for the rest. Before leaving, the activists mixed up the animals and cage labels to sabotage ongoing experiments.

The next day, scores of scientists and students demonstrated in the streets under the Pro-Test Italia banner. A major pro-research demonstration is planned in Milan’s city centre on 1 June. The university has refused to let the activists come back, and is preparing to bring charges. Scientists there — from students to the rector — have signed open letters condemning the animal-rights activists’ actions and explaining why medical research using animals is important.

The Basel Declaration Society, created in 2010 to encourage scientists to talk openly about their work using animals, has rallied heartening international support for the Milanese scientists. By 7 May, more than 4,000 researchers around the globe had signed its call for solidarity, posted just one week earlier. The call also demands fairer media coverage of research using animals, and zero tolerance from police and policy-makers towards acts of animal-rights extremism.

The use of animal experiments to further medical advances is a delicate issue, and there is no place in the debate for violence. There is, however, a need for scientists to talk openly, and it is encouraging to see their new confidence. Pro-Test Italia is actually the third franchise using Pycroft’s term. Pro-Test for Science was set up at the University of California, Los Angeles, four years ago after attacks on researchers. Meanwhile, UK Pro-Test ended operations in 2011, content that it had

achieved its aim of giving a voice to researchers. It had shown that when it comes to resolving ethical tensions between animal research and medical and veterinary health, we need more scientists prepared to Pro-Test against activist violence. ■

➔ **NATURE.COM**
To comment online,
click on Editorials at:
go.nature.com/xhunqv



China's citizens must act to save their environment

The country's air-pollution crisis offers a lesson in the power of civil society, says Qiang Wang.

Beijing's air pollution is sometimes so bad that citizens walk the streets wearing masks, and new arrivals immediately feel their throats rasping. With record levels of smog enveloping major Chinese cities, air pollution — especially the fine particles with diameters of less than 2.5 micrometres, known as PM_{2.5}, which penetrate deep into the lungs — is replacing food safety and clean drinking water as a key theme for Chinese lawmakers, and the nation has finally laid out a plan to tackle air pollution. By 2015, the government aims to reduce the concentration of PM_{2.5} by 5%, of PM₁₀ by 10% and of other pollutants by up to 10%, in 117 cities in 13 key regions of the country.

But such initiatives, although timely and right, will not make a fundamental difference if practical steps are not taken: China needs to set a national cap on coal use and find a way to limit emissions from cars. So far, Beijing has been the only city to put plans in place to cap coal consumption, at 15 million tonnes a year by 2015. However, even if the other 116 cities named in the government's plan restrict their use of coal, the effects on air quality will be limited — coal-intensive industries will simply move to other areas in China. China should therefore adopt a national plan to cap coal use, and this should be based on the national total energy-use plan it issued in January, which aims to keep total energy use to 4 billion tonnes of coal equivalent per year by 2015.

Even though coal provides 70% of China's energy, a cap need not come at the expense of economic development. For years, inefficient and redundant investments in infrastructure have made China the world's biggest construction site, requiring a vast energy expenditure for steel, cement-making and machinery. In 2011, China consumed 21% of the world's energy and accounted for roughly 10% of the global gross domestic product (GDP). This suggests that China could reach the world average and almost double its GDP without using any more energy by shifting towards a service-oriented model.

Harder to rein in is China's surge in vehicle emissions. With sales that surpassed those of the United States in 2009 and of Europe in 2012, motor vehicles have emerged as the second-largest source of air pollution. As China's economy continues to grow, its car ownership is burgeoning, and top-down measures to limit driving are making little difference. Beijing, for example, requires half of registered vehicles to stay off the roads on any given workday. But the regulation, which states that licence-plate numbers ending in even number can be driven only on certain days, simply led people to buy a second car with an alternate ending number. Car ownership continued to rocket in Shanghai even after the

city raised the cost of a new licence plate to roughly three times the cost of a cheap Chinese car.

Solutions must come from ordinary citizens, who can take responsibility for their environment and express it daily in choices such as riding bicycles or taking public transportation instead of driving. The voice of society is growing, and the government is starting to respond, albeit reluctantly, to the air-pollution crisis. The US Embassy in Beijing posts its air-quality readings on Twitter, and activists have been re-posting the readings on Sina Weibo (China's answer to Twitter, which is blocked in the country). The hashtag "I don't want to be a human vacuum cleaner" attracted more than 1.7 million comments. And when the real-estate titan Pan Shiyi asked his millions of Weibo followers: "Do you agree that PM_{2.5} should be monitored in 2011?

Do you agree that the clean-air act should be stricter?", the replies in favour far outnumbered those against.

In response to this groundswell, the government announced last year that Beijing and 73 other cities would start to monitor and publish PM_{2.5} data in 2013, far ahead of the previously announced 2016 deadline. Meanwhile, public pressure has helped to get a revised clean air act on the way, with the *China Daily* newspaper noting that "more measures to clean up the air are being considered by municipal departments of Chinese cities after netizens began to point the finger at the government over heavy smog".

In recent years, local protests have successfully blocked the construction of individual polluting projects, including plants in Xiamen and Dalian, which would have produced the industrial chemical paraxylene; a trash incinerator in Panyu; and a wastewater treatment plant in Qidong. China is witnessing the beginnings of a civil society in which the Chinese people spontaneously defend their right to a healthy environment, independent of organizers, political goals and commercial interests.

Chinese citizens who want to drink clean water can buy a water purifier; those worried about poisoned milk can buy imported milk. But when the air is polluted, there is no option but to fight. The various stakeholders of China's environment — government, non-government organizations and industry — should seize the opportunity provided by the growing popular involvement, and promote a civil society that stands up for the environment. The air of the people should be protected — by the people, for the people. ■

THE
VOICE
OF SOCIETY IS
GROWING,
AND THE
GOVERNMENT
IS STARTING TO
RESPOND.

➔ **NATURE.COM**
Discuss this article
online at:
go.nature.com/bszi9l

Qiang Wang is director of the Western Research Center for Energy and Eco-Environmental Policy at the Xinjiang Institute of Ecology and Geography, Chinese Academy of Sciences, Urumqi.
e-mail: qiangwang7@gmail.com

RESEARCH HIGHLIGHTS

Selections from the
scientific literature

ORGANIC CHEMISTRY

Iron eases tough synthesis

A new catalyst will help chemists to make complex molecules from simple building blocks.

In drug discovery, chemists first identify a promising organic molecule, but can then end up synthesizing thousands of analogues in the hope of improving the potential drug's properties. One modification that is often desired is swapping a carbon atom for a nitrogen atom in a ring, but standard processes for this are inefficient. Elisabeth Hennessy and Theodore Betley at Harvard University in Cambridge, Massachusetts, designed an iron-containing compound that activates a normally unreactive carbon–hydrogen bond. This speeds up and simplifies the desired chemical synthesis by allowing a greater range of precursors to be used.

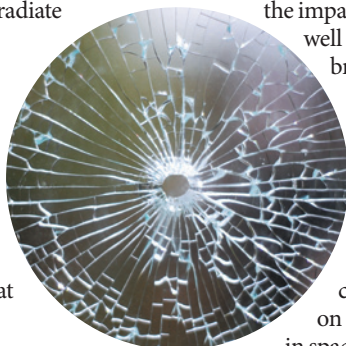
Science 340, 591–595 (2013)

PHYSICS

Clues from shattered glass

The cracks that radiate from a hole in a broken window (pictured) reveal quantitative information about the shattered material and the projectile that smashed it.

Nicolas Vandenberghe and his colleagues at Aix-Marseilles University in France studied such cracks by firing bullet-shaped steel cylinders at sheets of glass and plastic. The team used a high-speed camera to



show how the cracks formed and spread. The number of radial cracks increased with the impact speed, as well as the material's brittleness. The group developed a mathematical model that accounted for these observations. This model could be relevant on Earth and in space — helping forensic investigators to reconstruct crimes, and helping astrophysicists to analyse impact craters on distant planets and moons. *Phys Rev. Lett.* 110, 174302 (2013)

VOLCANOLOGY

Small eruptions get their due

The scale for classifying volcanic eruptions may underplay the danger of weak explosions.

A team led by Bruce Houghton at the University of Hawaii in Honolulu studied material that erupted in 2008 from Kilauea volcano, Hawaii. The largest eruption shot out 310 cubic metres of ash and rock, but ranked only as a category 0 — the lowest possible on the Volcanic Explosivity Index, which is based mainly on how much material is ejected.

Although category 0 is described as

non-explosive, the 2008 Kilauea eruptions were not — they were just low volume. The authors propose splitting the existing category 1 into two, and adding categories down to –6.

Such adjustments could permit more accurate descriptions of small eruptions and allow hazard managers to better communicate the risk to people living near or visiting volcanoes.

Geology <http://dx.doi.org/10.1130/G34146.1> (2013)



BRIGITTE MERZ/LOOK/ROBERT HARDING PICTURE LIBRARY

ECOLOGY

Cheats make yeast unsteady

By fostering freeloaders, charitable yeast cells put their communities at risk.

Alvaro Sanchez and Jeff Gore of the Massachusetts Institute of Technology in Cambridge engineered yeast to be either generous cells, which break down complex sugars to forms that are available to the community; or cheating cells, which rely on others for fuel. When the two strains were mixed in different ratios, the researchers found that — over many generations — large, stable populations formed in which less than 10% of

the yeast population could support an overwhelming majority of freeloaders. However, these mostly mooching communities were prone to extinction: when the researchers simulated environmental disturbance by diluting the populations, they crashed. Such dynamics could help biologists to explain the evolution and variation seen in cooperative communities. *PLoS Biol.* 11, e1001547 (2013)

ASTRONOMY

Baby star wind travels far

What happens in a star-forming galaxy does not stay in a star-forming galaxy.

ISTOCKPHOTO/THINKSTOCK

Powerful outflows from newborn stars can energize space well beyond the main boundaries of a galaxy.

Sanchayeta Borthakur at Johns Hopkins University in Baltimore, Maryland, and her colleagues used the Hubble Space Telescope to probe 20 nearby galaxies. Each galaxy had gone through a burst of star formation within the past few hundred million years.

The authors found that winds flowing from the newborn stars ionize gas particles some 200 kiloparsecs from the galactic centres. This is the first observation of such long-distance changes.

The outflows may modify galactic material in ways that suppress future star growth. *Astrophys. J.* 768, 18 (2013)

ANIMAL BEHAVIOUR

Fish match human search strategy

A small tropical fish seems to scan its surroundings in a similar way to humans.

Archerfish (*Toxotes* spp.) shoot down their prey by spitting jets of water more than 1 metre into the air (pictured). Ingo Rischaw and Stefan Schuster at the University of Bayreuth in Germany trained archerfish to pick out stationary targets amid a distracting background and compared fish performance with that of people throwing tennis balls at a target. Although humans responded faster than the fish, response times for both increased linearly with the number of distracting background objects,

implying that the fish and humans use comparable search strategies.

Humans might share mechanisms for efficient visual search with animals that have much simpler brains, the authors say. *J. Exp. Biol.* <http://dx.doi.org/10.1242/jeb.087734> (2013)

AGRICULTURAL ECOLOGY

Pollen powers honeybee genes

Bees could be dying because they lack a nutrient found in honey.

The western honeybee (*Apis mellifera*) adds billions of dollars to the global economy by pollinating crops, but a mysterious 'colony collapse disorder' has killed off many hives. Agricultural pesticides, overcrowding, frequent transport and bee parasites have all been blamed.

Work by May Berenbaum and her colleagues at the University of Illinois at Urbana-Champaign suggests another contributing factor: honey substitutes, which are often fed to bees by commercial beekeepers. The researchers used liquid chromatography to identify compounds in honey that activate the genes known to be upregulated by the foodstuff, then analysed gene expression in bees that were fed different diets. Those fed *p*-coumaric acid, a compound found in pollen, expressed more detoxification genes than bees given plain sugar syrup. Bees fed the pollen compound also produced higher levels of genes for antimicrobial peptides.

Proc. Natl Acad. Sci. USA <http://dx.doi.org/10.1073/pnas.1303884110> (2013)

ROBOTICS

Tiny, winged machines

Insect-sized robots can mimic the hovering and darting of flies.

COMMUNITY CHOICE

The most viewed papers in science

NEUROSCIENCE

Mechanism for Alzheimer's delay

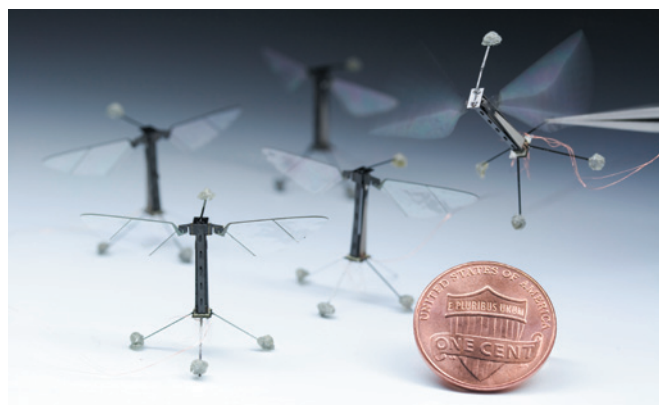
HIGHLY READ
on www.cell.com
in April

Studies suggest that symptoms of Alzheimer's disease can be delayed if people keep their brains active, and researchers have now uncovered a potential underlying mechanism.

Dennis Selkoe, Shaomin Li and their colleagues at Harvard Medical School in Boston, Massachusetts, enhanced the environment of mice by frequently changing their toys. Synaptic plasticity — experience-dependent changes in connectivity between neurons that are associated with learning and memory — increased in mice living in novelty-rich cages for several weeks. The increase came, in part, from activation of β_2 -adrenergic receptors.

The researchers then applied amyloid- β protein, which is known to accumulate in the brains of patients with Alzheimer's disease, to brains from mice that had either been kept in an enriched environment or been given drugs that activate β_2 -adrenergic receptors. Both conditions prevented the synaptic dysfunction that the protein normally causes.

Neuron 77, 929–941 (2013)



Flies have long been admired for their aerial agility, but technical limitations in miniaturization have hindered attempts to replicate this in similar-sized robots. Kevin Ma and his colleagues at Harvard University in Cambridge, Massachusetts, have invented a specialized laser-manufacturing process that allowed them to create tiny composite structures, including mechanical wings and flight muscles. The researchers used

the components to build 80-milligram robotic flies with flapping frequency, wing stroke and energy use similar to that of real flies.

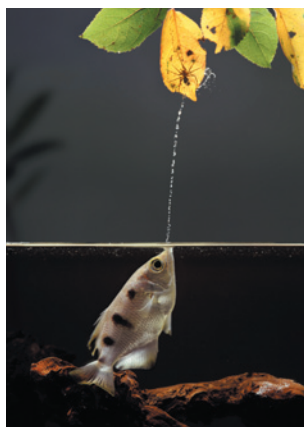
The mechanical flies (pictured) were capable of controlled flight manoeuvres and hovering in place. The work could open the door to additional innovations in miniaturized machines.

Science 340, 603–607 (2013)

NATURE.COM

For the latest research published by Nature visit:

www.nature.com/latestresearch



SEVEN DAYS

The news in brief

EVENTS

Science solidarity

More than 4,000 people from around the world have signed a petition supporting scientists from the University of Milan in Italy, whose animal-research facility was invaded by animal-rights activists on 20 April. The activists took almost 100 animals — mostly mice — and mixed up labels on many of the remaining cages. Researchers say that it will take years to redo their work. The petition was posted online on 29 April by the Basel Declaration Society, based in Switzerland, which encourages openness about the use of animals in research. See page 158 for more.

POLICY

Trial data blocked

A move to release information about industry-sponsored clinical trials has hit a setback. On 30 April, the European General Court ordered the European Medicines Agency (EMA) not to publish documents submitted by two drug companies: AbbVie, headquartered in North Chicago, Illinois, and InterMune, based in Brisbane, California. Both companies had previously filed complaints, stating

NUMBER CRUNCH

\$86 bn

Upper bound on cost of providing electricity and clean-burning cooking fuels and stoves globally by 2030, the International Institute for Applied Systems Analysis in Laxenburg, Austria, said on 2 May.



FEISAL OMAR/REUTERS

Somali famine death toll

Famine in Somalia killed about 258,000 people between October 2010 and April 2012, finds a study released on 2 May. More than half of those who died were under 5 years old (pictured). The report from the Famine Early Warning Systems Network (FEWS NET), funded by the US Agency for International Development in Washington DC, is the first to estimate the

death toll of the crisis, which was triggered by a severe drought. Researchers estimated that nearly 5% of the total population of southern and central Somalia died. "It suggests that what occurred in Somalia was one of the worst famines in the last 25 years," says Chris Hillbruner, decision support adviser for FEWS NET.

that the documents contain confidential data that could cause commercial damage if made public. The injunction is temporary, pending a final ruling on the case, and the EMA is considering an appeal.

Beyond the DSM

The US National Institute of Mental Health (NIMH) will no longer use the *Diagnostic and Statistical Manual of Mental Disorders (DSM)* to guide psychiatric research, NIMH director Thomas Insel announced on 30 April. The manual has long been used as a gold standard for defining mental disorders. Insel described the DSM as ill-suited to scientific studies, and said the NIMH will

now support studies that cut across DSM-defined disease categories. The American Psychiatric Association will release the latest edition of the tome, DSM-5, on 22 May.

Plan B appeal

The US Food and Drug Administration (FDA) made a controversial emergency contraceptive pill available to 15- and 16-year-olds without a doctor's prescription on 30 April. The next day, the government appealed against a decision made last month by New York district court judge Edward Korman, who ordered the FDA to make Plan B One-Step (levonorgestrel) available over the counter without age restrictions within 30 days.

See *Nature* 496, 142 (2013) and go.nature.com/klhp8m for more.

FACILITIES

Autism network

Three US foundations that fund autism research announced on 2 May the launch of Autism BrainNet, a network of facilities to collect and process donated brains from those who have died, including children. The network — which includes centres in New York, California and Texas — will distribute tissue samples to autism researchers, who have struggled to obtain the very young brains needed to study the neurodevelopmental

disorder. Autism BrainNet will actively engage in outreach work to explain the importance of brain donation. See go.nature.com/9bxbphz for more.

PEOPLE

Meningitis lawsuit

The brother of a 25-year-old researcher who died from meningitis last year after getting infected with *Neisseria meningitidis* at a San Francisco laboratory is suing for at least US\$20 million in damages, news reports said last week. The late Richard Din was infected by the bacterium while working on a vaccine for the disease at the Northern California Institute for Research and Education. His brother, Wei-Hsun Din, is suing the US government, the regents of the University of California and the lab's bosses, according to a civil lawsuit filed on 26 April.

RESEARCH

Virus controversy

Chinese researchers have drawn criticism for a study published online on 2 May, which showed that the H5N1 avian influenza virus engineered with genes from the human pandemic H1N1 virus could spread through the air between guinea pigs (Y. Zhang *et al.* *Science* <http://doi.org/mfvf>;



2013). Robert May (pictured), former president of the UK Royal Society in London, called the work “appallingly irresponsible”, citing concerns about laboratory containment and potential human-to-human transmission, according to news reports. The study authors say that the research could help to improve the surveillance of dangerous viruses.

Oil estimates

Underground rock formations in the north-central United States hold more than double the previous estimate of recoverable crude oil, the US Geological Survey said in a report published on 30 April. The Three Forks Formation that underlies parts of North Dakota, South Dakota and Montana was previously thought to hold little oil. New geological data suggest that it holds 3.73 billion barrels

of oil, surpassing the other reserve in the area, the Bakken Formation, where 3.65 billion barrels await recovery.

Coronavirus cases

The novel coronavirus hCoV-EMC, first discovered last year in Saudi Arabia, continues to spread. Saudi Arabia has reported 13 new cases to the World Health Organization since 2 May, including seven deaths. All the cases are linked to a single hospital, suggesting that the virus is spreading from human to human. There have been a total of 30 confirmed cases worldwide, including 18 deaths.

BUSINESS

Hidden emissions

Only 37% of the world's 800 largest companies fully disclose their greenhouse-gas emissions, according to a report released on 1 May by the Environmental Investment Organisation (EIO), a non-profit research group based in Frensham, UK. Italian and Spanish companies were the best disclosers, with more than half providing complete and verified emissions data. The EIO also ranked companies by their environmental impact. “This ought to be a wake-up call for companies,” says Sam Gill, head of the EIO. “Large quantities of emissions are not being accounted for.”

COMING UP

14–17 MAY

In Cancún, Mexico, 14 geophysical societies from North and South America hold a joint Meeting of the Americas, with discussions including megacities and regional climate change.

moa.agu.org

15 MAY

Ministers and scientists from the eight states of the Arctic Council meet in Kiruna, Sweden, to discuss issues including biodiversity and preparedness for marine oil pollution in the Arctic.

go.nature.com/wio3fg

Investment support

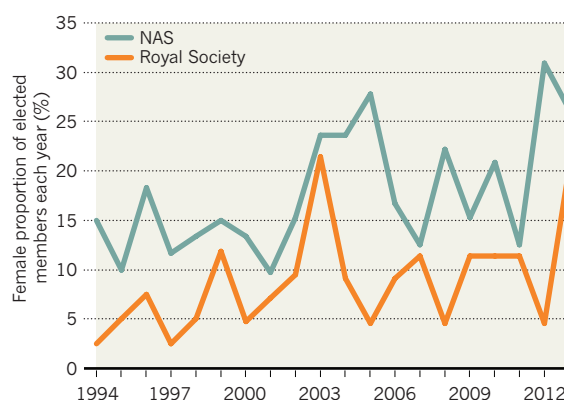
The Academy of Medical Sciences in London announced on 2 May that it will advise a venture-capital firm seeking to invest in biotechnology companies. The effort will give the academy, which has more than 1,000 members, a business role typically taken on by individual scientists. The academy will receive an annual retainer from Park Vale Capital, a London-based investment firm, and a share of its performance fees. Park Vale hopes to invest in up to ten companies over the next two years. See go.nature.com/ybi7th for more.

TREND WATCH

The Royal Society — Britain's national science academy — last week announced 44 new fellows, and the US National Academy of Sciences (NAS) 84 new members. The proportion of women among newly elected members — 20% at the Royal Society and 26% at the NAS — has risen since 1994, but only marginally over the past decade. The Royal Society says that its selection mirrors the proportion of women put forward for membership. (The NAS election process is kept confidential.)

WOMEN IN SCIENCE

The female share of newly elected members of the US National Academy of Sciences is greater than that of new fellows of Britain's Royal Society.



CLARIFICATION

The Trend watch in the 2 May issue (*Nature* **497**, 11; 2013) could be misread to suggest that the Office of Research Integrity is not taking any more cases. We meant to say that the office cannot take on any more cases than usual.

NATURE.COM

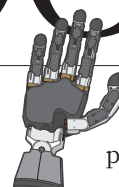
For daily news updates see:
www.nature.com/news

NEWS IN FOCUS

OCEANOGRAPHY Keeping tabs on the oceanic 'conveyor belt' **p.167**

RESOURCES US law would keep supplies of helium flowing **p.168**

MISCONDUCT Controversial dance paper is judged a fraud **p.170**



TECHNOLOGY Adding the human touch to prosthetic limbs **p.176**

ALBUQUERQUE JOURNAL/AP PHOTO



Los Alamos National Laboratory is working on a US\$10-billion project to modify a set of nuclear bombs.

NUCLEAR WEAPONS

US warheads to get a facelift

Obama boosts 'stockpile stewardship' funds at energy labs.

BY JEFF TOLLEFSON

When he took office in 2009, US President Barack Obama bolstered efforts to secure nuclear materials around the globe. That spring, speaking in Prague, he said that he would push Congress to ratify a long-pending treaty to ban nuclear testing. By 2010, he had reached an agreement with Russia to reduce the number of nuclear weapons in both countries' arsenals to historic lows.

Yet the weapons laboratories of the US

Department of Energy continue to be lavished with money. The administration's 2014 budget proposal would boost funding for the weapons programme to US\$7.9 billion, nearly 30% more than when Obama took office. This rising flow of cash contrasts strikingly with a shrinking stockpile (see 'Small stockpile, big expense'). Life-extension programmes for weapons would receive more than \$1 billion of this 'stockpile-stewardship' budget, including \$537

million for a showcase initiative to modify and modernize the B61 line of nuclear gravity bombs.

By keeping weapons scientists busy at top-of-the-line facilities, Obama says that he is maintaining a nuclear deterrent, one based as much on retaining brains as on projecting brawn. "We're going to keep investing in these programmes," he said, during a non-proliferation event in Washington DC in December 2012, "because our national security depends on it."

But the economic toll of doing so has grown increasingly — and, many argue, unnecessarily — steep. "It's been far more expensive than it needs to be," says Richard Garwin, a physicist and one of the designers of the first hydrogen bomb in the 1950s. "There's a real lack of control over budgets and programmes." The most vociferous critics go a step further, arguing that stockpile stewardship is about keeping people employed, and that Obama has used the programme to placate the sprawling nuclear-weapons complex and the politicians that support it while pursuing weapons reductions and non-proliferation goals.

NUCLEAR REMIX

Expensive science facilities and maintenance projects have become commonplace at US weapons labs since the end of the cold war in 1991 and the last US underground weapons test in 1992. Two costly stockpile-stewardship facilities, for example, are housed at Lawrence Livermore National Laboratory in California: the National Ignition Facility, a giant laser that is intended to replicate fusion explosions; and Sequoia, the world's second most powerful supercomputer, which is used to model nuclear explosions. Los Alamos National Laboratory in New Mexico also has a supercomputer and was planning, until recently, to build a major plutonium-research facility.

The latest major stockpile-stewardship initiative is the B61 life-extension programme at Los Alamos. This will merge components from several different versions of the weapon within a new bombshell, which would include updated safety and security features and a new tail.

The consolidation — as well as the improved accuracy that a new tail would provide — would allow the United States to deploy fewer bombs, with lower explosive energy, in places such as Europe, says ►

► **NATURE.COM**
See Nature's special on science and the military:
nature.com/military

► Donald Cook, who heads the weapons programme at the National Nuclear Security Administration (NNSA), a semi-autonomous agency within the energy department. He adds that it would not necessarily be cheaper to simply maintain existing weapons indefinitely.

But observers say the B61 programme is much more expensive than it needs to be. An early analysis by the NNSA showed that a relatively simple refurbishment would have cost around \$1 billion, whereas the current programme is expected to cost about \$10 billion over the length of the project. "Rather than doing the minimum required, they are going for the best possible warheads," says Stephen Young, who tracks nuclear-weapons issues for the Union of Concerned Scientists, a group based in Washington DC that is pushing for nuclear disarmament.

Few doubt the administration's commitment to non-proliferation programmes, which received a boost of more than \$1.1 billion, or 73%, between 2008 and 2012. Much of that extra money was used to secure nuclear materials and reactors in other countries. But Obama's latest budget request would cut non-proliferation programmes by more than \$400 million dollars to pay for weapons activities.

A NEW START

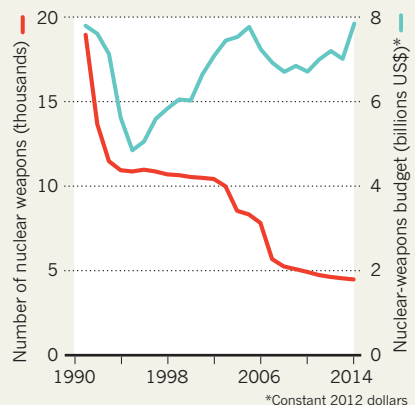
Some of the spending helped to nail down the 2010 agreement with Russia to limit the number of strategic weapons deployed by each country to 1,550 — a reduction of 30% from levels agreed in a 2002 treaty. To get the latest agreement ratified by the Senate, the administration laid out a plan to spend more than \$50 billion on weapons programmes between 2012 and 2017. Many Republican lawmakers now contend that, even with the recent budget boosts for the labs, the president is not keeping his promise.

Senator Bob Corker, a Republican from Tennessee, which is home to the Oak Ridge National Laboratory and the nearby Y-12 National Security Complex, says that Obama's budget requests have come in hundreds of

"This will challenge the core promise that the United States will not build a new warhead."

SMALL STOCKPILE, BIG EXPENSE

The US Department of Energy is spending as much to maintain its nuclear weapons now as it did at the end of the cold war, when it had thousands more warheads.



millions of dollars below the amount promised in 2010 and have delayed the new multi-billion-dollar plutonium-research facility at Los Alamos. "If the Senate believed we would be in this position today, it is unlikely to have approved the treaty in 2010," Corker and Senator James Inhofe (Republican, Oklahoma) wrote last month in *Foreign Policy* magazine.

Other lawmakers think that the requests are excessive. During a budget hearing on 24 April, Senator Diane Feinstein (Democrat, California) pointed out that the amount requested for weapons activities in 2014 would be the same, in real terms, as what was spent in 1985 — when the United States kept 25,000 nuclear weapons and was conducting underground tests and designing new weapons. "None of that is happening today," she said, calling the scope of the NNSA's weapons activities "unsustainable and unrealistic".

Worries about initiatives such as the new B61 bomb extend beyond costs. Nuclear watchdogs say that these projects transgress the spirit, if not the letter, of US commitments to disarmament under the 1968 Treaty on the Non-proliferation of Nuclear Weapons, as well as Obama's promise not to develop new nuclear warheads. A more accurate, lower-yield B61 would constitute a new capability for small nuclear strikes and could be tempting for a president to use, says Hans Kristensen, director of the Nuclear Information Project at the

Federation of American Scientists, a nuclear watchdog group in Washington DC.

A follow-up programme to modify W78 and W88 warheads would edge even closer to creating 'new' weapons than would the B61 project. One option for the programme, which is currently funded only at the conceptual stage, would combine the primary fission starter bomb from one warhead with the secondary fusion device from another. This ensemble would then be encapsulated in a new shell to create a system that would work in ballistic missiles fired from land or sea. "We are moving into completely new territory," Kristensen says. "This will challenge the core promise by the Obama administration that the United States will not build a new warhead." The US Navy has objected to the proposal, saying that it does not want a new warhead, but that has not dissuaded the nuclear labs.

Cook says that trying to merge parts from several weapons into one is a legitimate effort to simplify the arsenal while maintaining robust capabilities. "I wouldn't consider that new," he says of the effort to modify the W78 and W88 warheads. Most importantly, he says, that programme, like the B61 effort, would allow the consolidation of weapons and open the way to further reductions in the arsenal.

The programme would almost surely be more expensive than the B61 project. And cost is the main issue for Garwin. He says that Obama ought to demand that the NNSA lay out a plan for cutting the cost of the stewardship programme by two-thirds, just to get a sense of how effective such a programme might be. That exercise would help the administration and Congress to better understand their options, he says.

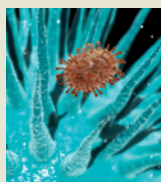
The value of expensive stockpile-stewardship programmes is dubious, says Garwin. US weapons will remain credible, he adds, regardless of the results that come back from high-profile experiments such as the National Ignition Facility. And he points out that the W88, the most advanced weapon in the US arsenal, was designed on a computer that had less processing power than a personal desktop computer has today. He sees no need to capture the interests of an army of bomb designers with powerful lasers and supercomputers. "The training of weapons designers is important, but we only have a couple of dozen of them," he says. "It's not a big deal." ■

SOURCES: US DOE; FEDERATION OF AMERICAN SCIENTISTS; NATURAL RESOURCES DEFENSE COUNCIL



**MORE
ONLINE**

TOP STORY



Artificial hybrid of H5N1 and H1N1 flu viruses can spread through the air between guinea pigs
go.nature.com/e7okru

MORE NEWS

- Plant found in Amazon may be rich in omega-3 fatty acids go.nature.com/oblthg
- Brain-training video game has long-lasting impact on ageing players' cognitive-fitness go.nature.com/uwiitx
- US frees Iranian scientist accused of illegal trade go.nature.com/pcuk45

PODCAST



The driverless cars of the future; making 'green' iron; and oddly shaped atomic nuclei nature.com/nature/podcast

OCEANOGRAPHY

Oceans under surveillance

Three projects seek to track changes in Atlantic overturning circulation currents.

BY QUIRIN SCHIERMEIER

A 'global conveyor belt' stirs the oceans from top to bottom, with surface currents transporting warm water to the poles while cold water in the depths flows back to the tropics. But it operates in fits and starts, with the strength of the currents varying widely. Eager for a better understanding of how the vagaries of the conveyor belt shape weather and climate, oceanographers are planning two new large-scale projects to watch over Atlantic currents.

An array of instruments between Florida and the Canary Islands has been continuously monitoring the strength of the North Atlantic portion of the global conveyor belt since 2004. In December, if all goes well, an international project led by the United States will begin another set of continuous measurements of the Atlantic Meridional Overturning Circulation (AMOC), using an array of sensors strung between South Africa and Argentina. And this month, US and British funding agencies are set to decide whether they will support a new surface-to-bottom monitoring array between Labrador in Canada and Scotland, UK. The United Kingdom will also decide whether to continue operating the existing array.

Expanding such monitoring is crucial if scientists are to improve seasonal weather and climate forecasts, says Harry Bryden, an oceanographer at the University of Southampton, UK. Components of the AMOC, such as the Gulf Stream, ferry vast amounts of heat from the tropics to high latitudes, heating the winds that keep Europe's climate mild. As a result, year-to-year and longer-term changes in the strength of these currents can affect seasonal conditions across much of Europe, Africa, South America and North America.

Observations from the UK-funded Rapid Climate Change monitoring array (RAPID) — the existing line of instrument-equipped moorings that measure current speed and direction, water temperature, salinity and pressure at various depths along the latitude line at 26.5° north — suggest that the strength of the overturning circulation can vary enormously¹.

In April 2009, the array recorded² a 30% drop in average current strength that persisted for a year, reducing the amount of heat transported to the North Atlantic by almost 200 trillion watts — equal to the output of more than

a crucial component of the conveyor belt: the region of the North Atlantic in which surface water heading north from the tropics cools and sinks before it moves back towards the equator. Climate models suggest that the rate of this formation of deep water will decrease

by the end of the century³. That is problematic not only because deep-water formation drives the ocean circulation, but also because it carries vast amounts of carbon dioxide to the depths, sequestering it from the atmosphere.

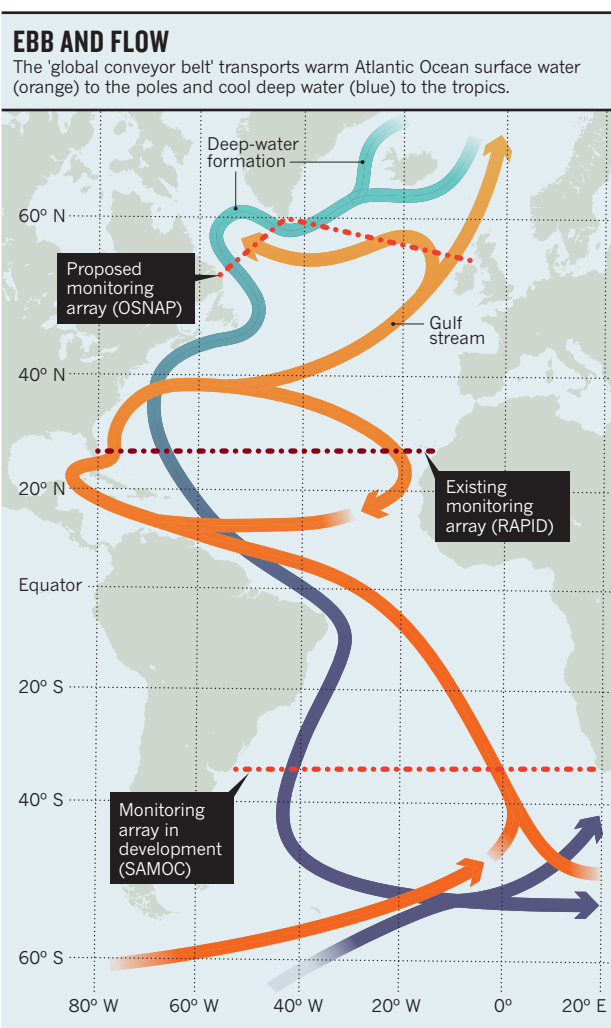
"We need to find out how water masses at high latitudes are tied to the larger Atlantic circulation," says Susan Lozier, a physical oceanographer at Duke University in Durham, North Carolina. "That is not only of interest to oceanographers. The ocean moves such huge amounts of heat and carbon around that most everyone should care."

To understand how deep-water formation works, and why it varies, Lozier and her colleagues have proposed setting up an array of moored instruments and autonomous gliders called the Overturning in the Subpolar North Atlantic Program (OSNAP). This consists of two legs: a western line extending from southern Labrador to the southwest tip of Greenland, and an eastern line from Greenland to Scotland (see 'Ebb and flow'). If the US National Science Foundation and the UK Natural Environment Research Council approve the US\$24-million project, measurements of heat and currents in the deep-water-formation region could start in July 2014. They are expected to give their decision later this month. If the array goes ahead,

Canada, Germany and the Netherlands have all promised to contribute instruments to it.

Scientists are also trying to trace the cold, deep water as it flows into the turbulent South Atlantic, which also receives an influx of warm surface water from the Indian Ocean. South Africa, Brazil, France, Argentina and the United States are all contributing to a monitoring array that is being built at 34.5° south, between South Africa and Argentina, as part of the US\$5-million South Atlantic Meridional Overturning Circulation (SAMOC) programme.

By the end of the year, if all goes well, a ▶



100,000 large power plants.

The anomaly — much bigger than any change that models suggested could happen — was driven by unusual wind patterns, strengthening of warm surface currents and weakening of cold water flows in the deep ocean. It has been linked to the unusually harsh winter in Europe in 2009–10. Bryden wonders whether the anomaly also helped to produce unusually wet weather in the United Kingdom. "We had six lousy summers in a row in Britain," he says. "What's going on?"

To investigate, scientists are now focusing on

► network of bottom-moored instruments will begin to record water temperature and salinity at different levels in the deep, cold currents that run along the edges of the ocean basin. By combining those data with acoustic measurements of current velocity and bottom pressure, and with temperature and salinity data recorded by freely drifting profiling floats in the open ocean, scientists should be able to calculate the strength of the overturning

circulation at that latitude, says Silvia Garzoli, chief scientist at the Atlantic Oceanographic and Meteorological Laboratory in Miami, Florida, and a member of the project's executive committee.

Most scientists regard the idea that global warming will trigger a collapse of ocean circulation — the apocalyptic scenario that inspired the 2004 action film *The Day After Tomorrow* — to be exceedingly unlikely. But Bryden says

that the 2009 Atlantic circulation glitch is an indication of just how surprising ocean behaviour can be. “The next one,” he says, “may be twice as big.” ■

1. Cunningham, S. A. *et al. Science* **317**, 935–938 (2007).
2. McCarthy, G. *et al. Geophys. Res. Lett.* **39**, L19609 (2012).
3. Meehl, G. A. *et al. in Climate Change 2007: The Physical Science Basis* (eds Solomon, S. *et al.*) Ch. 10 (Cambridge Univ. Press, 2007).

SOURCE: USGS/R. CLARKE



MARK HOLM/THE NEW YORK TIMES/REDUX/EYEVINE

The US Federal Helium Reserve was scheduled to end sales of the gas — but they may now continue at higher prices.

GLOBAL RESOURCES

US bill would keep helium store afloat

Russia and Qatar prepare to dominate market as gas price inflation puts researchers under pressure.

BY MARK PELOW

US lawmakers have taken a significant step towards averting a global crisis in helium supply, thanks to a bill passed by the House of Representatives on 26 April. If it passes the Senate and becomes law, the bill would delay the imminent closure of the world's only strategic helium reserve. It would also increase the price of the gas from the reserve, so helium-dependent

researchers and industry could still face ballooning costs. However, the prospect of higher prices is encouraging the development of new helium sources in Qatar and Russia, which may ultimately lead to a more stable helium market.

With a boiling point of 4 kelvin — lower than that of any other element — liquid helium has many uses, including cooling the superconducting magnets in medical imaging scanners. The semiconductor industry also relies

on the inert gas to shield delicate crystals from contaminants during manufacturing.

Demand is on the rise. More than 100 million cubic metres of helium is extracted from natural gas worldwide every year, yet meeting global needs requires a further 60 million cubic metres a year from the US Federal Helium Reserve, a vast geological reservoir near Amarillo, Texas, that stores helium from past gas extraction (see ‘Floating skyward’).

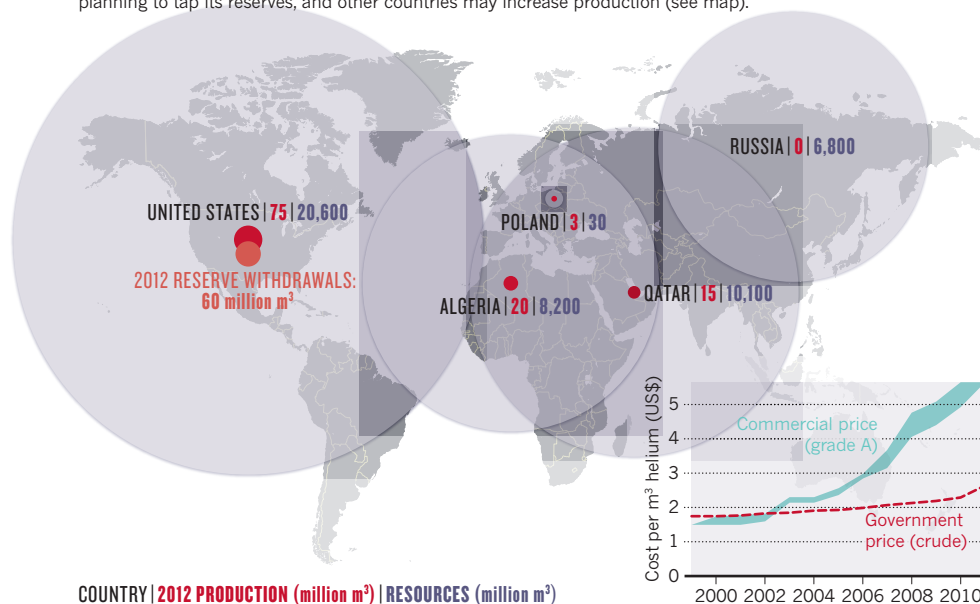
In the mid-1990s, the reserve boasted 1 billion cubic metres of the gas — and a debt of US\$1.3 billion accrued after a large buy-up of helium in the 1960s. Over time, the simple formula used to calculate the price of helium sold from the reserve has failed to keep pace with commercial prices. In 1996, appalled that the government was undercutting a booming commercial gas market, lawmakers passed the Helium Privatization Act. Its goal was to sell

the helium reserve to pay off the debt. Once the debt was gone, no more helium would be sold. “They would literally

► **NATURE.COM**
For more on helium supply, visit:
go.nature.com/fuh4jd

FLOATING SKYWARD

The price of helium from a US government stockpile has not kept pace with commercial prices (see graph). Most helium currently comes from the United States, but with price rises expected to continue, Russia is planning to tap its reserves, and other countries may increase production (see map).



turn off the tap," says Richard Clarke, a process and resources consultant based in Oxford, UK. The shutdown was expected by October this year. And because the reserve's cut-rate prices had dissuaded companies from developing sources elsewhere, a supply shortage was possible. "The Privatization Act has come back to bite them," says Clarke.

Alarmed, researchers and high-tech industries lobbied Congress to keep the helium flowing. Congress responded: the Responsible Helium Administration and Stewardship Act passed by the House maps out a more orderly shutdown. A similar bill has been introduced to the Senate; if it passes this summer, as is expected, and the law takes effect, the stockpile would be sold to the highest bidders in semi-annual auctions, until just 85 million cubic metres are left. Experts say that point might be reached in 2020, and prices could rise by 50% in that time.

The remaining stock would be available only to government users such as NASA. "The United States will have ceased to be the major player in helium production," says William Nuttall, an energy expert at the Open University in Milton Keynes, UK. Users will increasingly depend on helium from gas fields in Qatar, Algeria and Russia.

The Russian energy giant Gazprom aims to capture the lion's share of the market. Last year, the global business consultancy Ernst & Young, based in London, estimated that gas fields in eastern Siberia could produce 250 million cubic metres of crude helium per year by 2030, satisfying at least three-quarters of projected demand. One of the most promising resources is the Chayandinskoye natural-gas field, which contains a relatively

rich bounty of about 0.5% helium. In the past six months, Gazprom has signed cooperation agreements with many of the leading companies that purify and supply helium, including Air Liquide, Linde and Matheson. Helium could start to flow from Chayandinskoye by 2018.

In Qatar, extra helium-production capacity is scheduled to come online this year. The Ras Laffan Helium 2 plant could enable the country to meet up to 25% of global helium demand — although much of its output will head east to serve the growing Asian market, says Clarke.

And private efforts in the United States seem to be ramping up. In March, Flatirons Resources of Denver, Colorado, received approval from the US Bureau of Land Management to develop a small well designed to tap helium from a Utah natural-gas field — the first US well devoted solely to helium.

Helium may not run short, but the price increases will hurt labs, says Jodi Lieberman, senior government-relations specialist at the American Physical Society, headquartered in College Park, Maryland. Some low-temperature physicists already spend up to 70% of their grants on the gas, she adds.

In a 2010 report, *Selling the Nation's Helium Reserve*, the US National Academy of Sciences (NAS) recommended that funding agencies help researchers to buy cooling systems that recycle helium, or reduce its consumption. So far, cash-strapped funders have not had the resources to make the expensive equipment widely available, says James Lancaster, NAS study director for the report.

But as prices float skyward, helium-sparing equipment may start to look like a necessity. ■



A study featured in *Nature* in 2005 has drawn suspicion from university officials and one of its authors.

SEXUAL SELECTION

Symmetry study deemed a fraud

University finds evidence of fakery in Jamaican dance data.

BY EUGENIE SAMUEL REICH

Few researchers have tried harder than Robert Trivers to retract one of their own papers. In 2005, Trivers, an evolutionary biologist at Rutgers University in New Brunswick, New Jersey, published an attention-grabbing finding: Jamaican teenagers with a high degree of body symmetry were more likely to be rated 'good dancers' by their peers than were those with less symmetrical bodies. The study, which suggested that dancing is a signal for sexual selection in humans, was featured on the cover of this journal (W. M. Brown *et al.* *Nature* **438**, 1148–1150; 2005).

But two years later, Trivers began to suspect

that the study data had been faked by one of his co-authors, William Brown, a postdoctoral researcher at the time. In seeking a retraction, Trivers self-published *The Anatomy of a Fraud*, a small book detailing what he saw as evidence of data fabrication. Later, Trivers had a verbal altercation over the matter with a close colleague and was temporarily banned from campus.

An investigation of the case, completed by Rutgers and released publicly last month, now seems to validate Trivers' allegations. Brown disputes the university's finding, but it could help to clear the controversy that has clouded Trivers' reputation as the author of several pioneering papers in the 1970s. For example, Trivers advanced an influential theory of

'reciprocal altruism', in which people behave unselfishly and hope that they will later be rewarded for their good deeds. He also analysed human sexuality in terms of the investments that mothers and fathers each make in child-rearing.

Steven Pinker, a psychologist at Harvard University in Cambridge, Massachusetts, calls the dancing paper "a lark" and "journalist bait" that lacks a firm basis in theory. "It was cute rather than deep," he says. But he describes Trivers' earlier work as "monumental", and says that it would be a travesty if Trivers became known for one controversial study rather than his wider contributions to evolutionary biology. "Trivers is one of the most important thinkers in the history of the biological and social sciences," Pinker says.

SIGNIFICANT MEASURES

Since the publication in the early 1990s of studies showing that birds and insects tend to seek mates with symmetrical features, biologists have been interested in the possibility that physical symmetry is subject to sexual selection and is correlated with health. In 1996, Trivers began a long-term study of asymmetry in Jamaican children. He measured the degree to which elbow width or finger length, for instance, differed between the right side and the left, and worked to correlate it with fitness traits such as running ability. In 2004, he and Lee Cronk, an anthropologist also at Rutgers, began to study symmetry in relation to dancing. (As early as 1871, Charles Darwin speculated that dancing is a courtship ritual meant to display genetic fitness.)

Trivers, Cronk and their collaborators used motion-capture cameras and reflectors to record the movements of Jamaican teenagers as they danced. The researchers then made animations that recapitulated the dancers' movements but not their appearances. Other teenagers watched the animations and rated the dancing. The 2005 paper reported that good dancing correlated with high levels of physical symmetry — even when symmetry was not evident to the viewer. The finding suggested that good dancing might accurately convey a dancer's genetic fitness to spectators, and helped to establish dance as an area worthy of research for evolutionary biologists and psychologists. "This was a paper we based a lot of our work on because it led the field," says Nick Neave, a psychologist who studies dancing at the University of Northumbria in Newcastle, UK.

Trivers began to have doubts in 2007, when a Rutgers graduate student was unable to replicate some of the paper's findings. On investigation, Trivers found inconsistencies in symmetry measurements between a data set kept by his group and one received from Brown in 2007. "Not only were the values changed, they were not even internally consistent," says Trivers.

In 2008, Trivers sought to retract the paper, but found the editors at *Nature* reluctant to do

so. The paper remains unretracted, although a spokeswoman for *Nature* says that the case is under “active consideration”. (Information available to *Nature*’s research-manuscript editors is not generally shared with its reporters.)

In 2009, after Trivers published a book about the dispute, Rutgers convened an investigation in accordance with requirements of the US National Science Foundation (NSF), which had spent US\$25,000 on a grant to Trivers and Cronk to develop the motion-capture technique. Last year, the investigation concluded that there was “clear and convincing” evidence of fabrication by Brown, who it alleged had altered overall asymmetry measures of dancers to support the notion that better dancers were more symmetrical. The report was not published for more than a year, at which point Trivers posted it online. Rutgers has sent a copy to the NSF’s inspector-general, who is reviewing it to determine what action, if any, to take. The university officials who oversaw the investigation declined *Nature*’s interview requests.

Brown, now a psychologist at the University of Bedfordshire, UK, denies fabricating the data. He criticizes the Rutgers investigation for comparing his data set with the one from Trivers’ group rather than the original hard copies of the source data. Trivers says that the paper records of the asymmetry measurements

were reliably entered in his group’s database, but Brown says that it is unclear which data set is the original because many versions exist. Brown says that he will not support retracting the paper unless the original data are re-evaluated by an unbiased party and the results are found to be substantially different.



Robert Trivers.

down the line and nothing of what you said, you punk.” He says that Rutgers then banned him from campus for nearly five months under the university’s anti-violence policy.

Richard Wrangham, an evolutionary biologist at Harvard University, says that Trivers’ vehemence is characteristic. “When Bob Trivers gets hold of something intellectually, he is passionate and honest, and this represents that,” he says. Wrangham adds that Trivers typically does not have “great political

Meanwhile, Trivers accuses the university of penalizing him for an incident that took place in Cronk’s office in March 2012. Trivers says that he said loudly to Cronk, who had disputed Trivers’ allegations against Brown: “Well, [the investigation report] supports my position

sensitivity”. Rutgers says that it cannot comment on personnel matters. Cronk declined an interview request but wrote in an e-mail that, contrary to statements by Trivers and in the investigation report, he had not defended Brown.

As to the paper’s claim of a correlation between body symmetry and dancing skill, there might be something to it, says Steven Gangestad, a psychologist at the University of New Mexico in Albuquerque, who says that he reviewed the 2005 paper for *Nature*. He asked that the authors test the correlation with a more conservative statistical method. When this test robustly reconfirmed the effect, he recommended publication. He says that has always found the magnitude of the correlation surprisingly strong compared with other symmetry studies. “The sad thing is I think there probably really was an effect,” he says, just a much weaker one.

Trivers agrees. He says there is a weak but not very significant effect in the data held by his group. He has no plans to replicate the work on dancing, but his symmetry studies in Jamaica continue and have produced at least ten publications. He has just submitted for publication a study of physical symmetry and running ability that he calls “groundbreaking”. “The project is alive and well, and it wasn’t sunk by this damn thing,” he says. ■

THE GENOME HACKER

*Yaniv Erlich shows
how research
participants can
be identified from
'anonymous' DNA.*

BY ERIKA CHECK HAYDEN



Late at night, a video camera captures a man striding up to the locked door of the information-technology department of a major Israeli bank. At this hour, access can be granted only by a fingerprint reader — but instead of using the machine, the man pushes a button on the intercom to ring the receptionist's phone. As it rings, he holds his mobile phone up to the intercom and presses the number 8. The sound of the keypad tone is enough to unlock the door. As he opens it, the man looks back to the camera with a shrug: that was easy.

Yaniv Erlich — the star of this 2006 video — considers this one of his favourite hacks. Technically a “penetration exercise” conducted to expose the bank's vulnerabilities, it was one of several projects that Erlich worked on during a two-year stint with a security firm based near Tel Aviv. Since then, the 33-year-old computational biologist has been bringing his hacker ethos to biology. Now at the Whitehead Institute for Biomedical Research in Cambridge, Massachusetts, he is using genome data in new ways, and in the process exposing vulnerabilities in databases that hold sensitive information on thousands of individuals around the world.

In a study published in January¹, Erlich's lab showed that it is possible to discover the identities of people who participate in genetic research studies by cross-referencing their data with publicly available information. Previous studies had shown that people listed in anonymous genetic data stores could be unmasked by matching their data to a sample of their DNA. But Erlich showed that all it requires is an Internet connection.

Erlich's work has exposed a pressing ethical quandary. As researchers increasingly combine patient data with other types of information — everything from social-media posts to entries on genealogy websites — protecting anonymity becomes next to impossible. Studying these linked data has its benefits, but it may also reveal genetic and medical information that researchers had promised to keep private — and that, if made public, might hurt people's employability, insurability or even personal relationships.

Such revelations may make the scientific community uncomfortable and undermine the public's trust in medical research. But Erlich and his colleagues see their work as a way to alert the world about flawed systems, keep researchers honest and ultimately strengthen science. In March, for instance, the European Molecular Biology Laboratory (EMBL) in Heidelberg, Germany, claimed that the genome sequence that it had published for the HeLa cell line would not reveal anything about Henrietta Lacks — the source of the cells — or her descendants. Erlich issued a tart response: “Nice lie EMBL!” he tweeted. The sequence was later pulled from public databases, and the EMBL admitted that it would indeed be

possible to glean information about the Lacks family from it, even though much of the HeLa genetic data had already been published as part of other studies.

“Most scientists would not go anywhere close to these questions, out of a sense of what it might mean for the field, or for them personally,” says David Page, director of the Whitehead Institute, who has advised Erlich about his research. “But this is not about publicity-seeking — this is about fearlessness, and a kind of interest in how all the parts of the Universe fit together that mark all of Yaniv's work.”

GAMING THE SYSTEM

Erlich was inspired to teach himself programming as a child in Israel after seeing the 1983 film *WarGames*, in which a teenager accidentally hacks into government computer systems and nearly launches “global thermonuclear war”. Erlich thought that he would study maths and physics at university, but after a friend told him that there was a lot of maths in biology, he decided to major in computational neuroscience. In 2006, following his graduation, Erlich moved to the United States to earn his PhD in genetics at Cold Spring Harbor Laboratory in New York.

Under his adviser, molecular biologist Greg Hannon, Erlich devised what he called “DNA Sudoku”: a sequencing method that could be used on tens of thousands of specimens analysed simultaneously. It allowed scientists to use computational techniques to find a gene carrying a rare mutation from this mixed batch of DNA and assign it to the right specimen². Erlich is now using the technique to find disease-causing mutations in young Ashkenazi Jews to inform their decisions about potential marriage partners.

“PEOPLE WERE CONCERNED THAT THE NIH WOULD SHUT DOWN ITS DATABASES OR THAT THE PUBLIC WOULD STOP DONATING.”

In 2011, as Erlich was setting up his first independent lab as a Whitehead Fellow, he met a Colorado-based woman, Wendy Kramer, whose son had managed to track down his father — an anonymous sperm donor — by searching a consumer-focused genetic-genealogy database for people with DNA similar to his own.

Erlich wondered whether a computer program that he had been working on with an undergraduate student, Melissa Gymrek, might enable a similar trick using de-identified genome data from human research studies. The software, called lobSTR, scours sequences and generates a profile of repetitive genetic markers called short tandem repeats (STRs),

which are often used in genealogy to identify people. Could Erlich extract STRs from the anonymous data, and then hunt through public genealogy databases for a match and a name? “I had my background in security, and I had lobSTR in hand, and I thought, ‘Is this going to affect personal genomes?’”

Erlich and his team tested the idea on a man's full genome that had been published in 2007 (ref. 3). They used lobSTR to determine the STR profile of the man's Y chromosome, and then searched a consumer genealogy database called Ysearch until they had matches with a few likely surnames. Public records on one of these surnames linked it to a man fitting the geographic location and age listed in the paper: the genomics pioneer J. Craig Venter. Venter had, in fact, already revealed himself as the donor — one reason Erlich chose that genome was that he thought he could do no harm in revealing Venter's identity. But there was no reason to believe that this process would not work for others.

PROOF OF PRINCIPLE

When Erlich submitted his paper to *Science*, the reviewers wanted proof that a completely anonymous donor could be identified. So his team extended its analysis to men whose genomes had been sequenced as part of the international 1000 Genomes Project. Extensive information about these men, including their ages and detailed family pedigrees, was available on the website of the Coriell Institute for Medical Research in Camden, New Jersey, which distributes cell lines made from their tissues to researchers.

Erlich's team used lobSTR to infer the men's STRs from their 1000 Genomes data, and then searched Y-chromosome databases

to find linked last names. After that, it was relatively easy to search public records databases to find men with those last names who were the right age, came from the right place and had similar family trees. The team identified nearly 50 people, including DNA donors and their relatives. When he first saw the results, Erlich said later, he was so shocked at how easily the method worked that he had to go outside and take a walk.

Geneticists elsewhere had already revealed security flaws in anonymized genetic data. In 2008, for instance, David Craig, a computational biologist at the Translational Genomics Research Institute in Phoenix, Arizona, reported that he could use information from an

individual's DNA sample to confirm whether that person had contributed to a genome-wide association study (GWAS), even if the study reported only summary statistics on hundreds or thousands of participants⁴.

This and other studies prompted policy-makers at the US National Institutes of Health (NIH) to pull GWAS data from public databases, and to require investigators to obtain permission to access it. Many researchers resent this move, because it makes it difficult to pool data from different studies.

Erlich's study upped the stakes, because it showed that it was possible to identify people from their genetic data by linking not to other sources of research data, but to information freely available on the Internet. He realized that publishing these results might stoke public anger, so he consulted lots of other researchers and ethicists first. "People were concerned that the NIH would shut down its databases or that the public would stop donating their material," says Erlich. He contacted NIH officials about his findings, and met some of them in Bethesda, Maryland, last December. The NIH's National Institute of General Medical Sciences, which funds the Coriell repository, decided to remove the ages of participants from public view.

INFORMATION WITHHELD

When Erlich published the results of his work in January¹, he revealed no research participants' names. Neither did he spell out all the steps he had taken to find their identities: "There is an obvious tension, because as a scientist you want to tell everything about how you did the work. On the other hand, you can't do that, because it will expose people's identities to the world," says Erlich.

The question remains of how to handle privacy in future. Removing information after

say that they are not at risk.

Eric Green, director of the US National Human Genome Research Institute (NHGRI) in Bethesda, says that the NIH is trying to balance access and privacy. "One value is to make the data as widely available and unencumbered as possible, but then you're trading that off against concerns about how data is being used, and maintaining privacy and confidentiality," he says. "We're constantly exploring models that put us between those two extremes."

CAREFUL SCRUTINY

Currently, anyone with an Internet connection can access data from the 1000 Genomes Project. Researchers must apply for access to genetic data from most other studies, and must usually submit a new access request for information from each one. That makes it onerous to analyse data from different sources together.

Many large data-holders around the world take this approach; the EMBL's European Bioinformatics Institute in Hinxton, UK, for instance, relies on data-access committees to determine what uses of data are appropriate given the consent terms of any particular study. "It's difficult to imagine how else one would do it, since most of these studies are built around consent agreements," says Paul Flicek, head of DNA resources at the institute.

Some researchers say that genetic data should be deposited with central data-hosting agencies that then grant broad access to trusted users. This would mean that the data would be off-limits to the public, but researchers would not have to ask for permission to access every data set. Laura Rodriguez, director of the NHGRI's division of policy, communications and education, says that NIH committees on data use have concerns about this idea: "We've seen investigators request access to large swathes of data, and it's clear from their proposed-research

such as encrypting the data before they are deposited, allowing researchers who possess the decryption key to work with them freely without jeopardizing privacy. But Green is concerned that researchers might not be able to work as freely with encrypted data as they can with unencrypted data.

There are no simple answers, but researchers give Erlich credit for forcing these issues onto the public stage. Page warns that this could be a double-edged sword for a young scientist: "This piece of work represents only a slice of Yaniv's broader interests, and the danger could be the risk of being completely consumed by this debate," he says.

Erlich seems happy to be consumed. In a new project that he calls Genetic Epidemiology 2.0, for example, he is working with Daniel MacArthur, a geneticist at Massachusetts General Hospital and Alkes Price, a biostatistician at Harvard School of Public Health, both in Boston, to mine social networks for information that might yield insight into the genetic basis for complex human traits. The project focuses on genealogy-based social networks on which members post extensive family trees — a potentially rich source of information about inherited traits.

Erlich is aware of the ethical complexities of such a study. To start with, he is focusing on public information about deceased people, to minimize the risk that anyone will be harmed by the work. But if the project succeeds, he may go on to ask members of the networks whether they want to upload other types of information — such as medical records, which could yield insight into a wider range of disease traits.

It is a project that plays to Erlich's strengths, says Hannon. "When Yaniv says, 'What data is out there?' he doesn't think, 'What data is out there in the literature?' He thinks about what data is out there holistically." If the technique works, it would use information in the public domain to tackle one of the most difficult problems facing genetic researchers: how to assemble the enormous groups of related individuals needed to illuminate the complex genetic underpinnings of human biology. "Yaniv believes nothing is impossible," says Hannon.

Of course, it could expose all kinds of new vulnerabilities. That may not be such a bad thing, says Erlich, harking back to his penetration testing on banks. "As a client of a US bank, I'm sure you are happy that they undergo these tests. You wouldn't want to say, 'Let's not find something we won't like.'" ■

Erika Check Hayden writes for *Nature* from San Francisco, California.

"YANIV BELIEVES NOTHING IS IMPOSSIBLE."

loopholes are revealed — what some call the whack-a-mole response⁵ — does not seem to satisfy anyone.

Some geneticists argue that the public is becoming more accustomed to sharing personal information, and that no harm has ever been done to anyone identified from genetic studies. But many, including Brad Malin a privacy researcher at Vanderbilt University in Nashville, Tennessee, consider that a weak argument. "A lot of people say that because information flows much more freely today than it did 10 years ago, that privacy is dead, and this is certainly not the case," he says. People still expect some information — especially health and medical data — to be private, says Malin. And so far, none of the people identified from anonymous genetic data sets has been named publicly, so it is perhaps too early to

statement that they haven't read the use limitations of the data they're requesting."

Erlich argues that genetic data should be broadly available, but that scientists should be more honest about the difficulty of guaranteeing anonymity. Amy McGuire, a lawyer and ethicist at Baylor College of Medicine in Houston, Texas, with whom Erlich consulted on his publication, agrees. But she is not sure that informing people of the risk of re-identification is enough. It may be difficult for someone signing up for a research study to understand all the ways in which their data might be used in the future, let alone to weigh the risks when researchers themselves do not necessarily know them. "There are challenges to putting so much weight on informed consent," she says.

Scientists should explore further ways to protect research participants, says Erlich,

1. Gymrek, M., McGuire, A. L., Golan, D., Halperin, E. & Erlich, Y. *Science* **339**, 321–324 (2013).
2. Erlich, Y. *et al. Genome Res.* **19**, 1243–1253 (2009).
3. Levy, S. *et al. PLoS Biol.* **5**, e254 (2007).
4. Homer, N. *et al. PLoS Genet.* **4**, e1000167 (2008).
5. Ohm, P. *UCLA Law Rev.* **57**, 1701 (2010).



Once more, with feeling

Prosthetic arms are getting ever more sophisticated.
Now they just need a sense of touch.

BY ROBERTA KWOK

Sitting motionless in her wheelchair, paralysed from the neck down by a stroke, Cathy Hutchinson seems to take no notice of the cable rising from the top of her head through her curly dark hair. Instead, she stares intently at a bottle sitting on the table in front of her, a straw protruding from the top. Her gaze never wavers as she mentally guides a robot arm beside her to reach across the table, close its grippers around the bottle, then slowly lift the vessel towards her mouth. Only when she finally manages to take a sip does her face relax into a luminous smile.

This video of 58-year-old Hutchinson illustrates the strides being taken in brain-controlled prosthetics¹. Over the past 15 years, researchers have shown that a rat can make a robotic arm push a lever², a monkey can play a video game³ and a person with quadriplegia — Hutchinson — can sip from a bottle of coffee¹, all by simply thinking about the action. Improvements in prosthetic limbs have been equally dramatic, with devices now

able to move individual fingers and bend at more than two dozen joints.

But Hutchinson's focused stare in that video also illustrates the one crucial feature still missing from prosthetics. Her eyes could tell her where the arm was, but she could not feel what it was doing. Nor could she sense when the grippers touched the bottle, or whether it was slipping out of their grasp. Without this type of sensory feedback, even the simplest actions can be slow and clumsy, as Igor Spetic of Madison, Ohio, knows well. Fitted with a prosthetic after his right hand was crushed in an industrial accident in 2010, Spetic describes breaking dishes, grabbing fruit too hard and bruising it and dropping a can when trying to pick it up at the local shop. Having a sense of touch would be "tremendous", he says. "It'd be one step closer to having the hand back."

The Modular Prosthetic Limb will help patients to feel and manipulate objects just as they would with a native hand.

JOHNS HOPKINS UNIV. APPLIED PHYSICS LAB.

Prosthetics researchers are now trying to grant him that wish by creating prosthetics that can 'feel' more like the real thing. It is a daunting task: researchers have managed to read signals from the brain; now they must write information into the nervous system. Touch encompasses a complicated mix of information — everything from the soft prickliness of a woollen top to the slipping of a sweaty soft-drink can. The research is still in its infancy, with approaches that range from stimulating nerves in a stump and re-routing nerves to other parts of the body, to tapping directly into the brain (see 'Closing the loop'). But "it's probably the next big thing that has to happen", says Robert Kirsch, a biomedical engineer at Case Western Reserve University in Cleveland, Ohio.

ALTERNATIVE SENSES

Conventional prosthetics are not devoid of feedback. The widely used 'split-hook' hand replacement, for instance, typically has a harness that lets the user open and close the device by moving another part of the body, such as the opposite shoulder; patients then feel resistance in the harness when they grab something. Likewise, users of motorized prosthetics — which are controlled by electrical signals from muscles in the stump — will feel pressure on the stump when they push something, or may hear subtle changes in the motor's sound when grabbing an object. Researchers have even tried to introduce such feedback deliberately, through vibrations, air pressure and electrical stimulation.

But none of these sensations feels natural — which may be one reason that many people reject prosthetic limbs: the replacement just doesn't seem like part of the body.

Recreating life-like sensation is a tall order. The sensations arise from a host of receptors in the skin, which detect texture, vibration, pain, temperature and shape, as well as from receptors in the muscles, joints and tendons that contribute to 'proprioception' — the sense of where a limb is in space. Prosthetics are being outfitted with sensors that can gather many of these sensations, but the challenge is to get the resulting signals flowing to the correct part of the brain.

For people who, like Spetic, have had limbs amputated, the obvious way to achieve that is to route the signals into the remaining nerves in the limb's stump. Researchers including Ken Horch, a neuro-prosthetics researcher at the University of Utah in Salt Lake City, have done just that by threading electrodes into the nerves in stumps then stimulating them with a tiny current, so that patients felt like their fingers were moving or being touched⁴.

The technique can even allow patients to distinguish basic features of objects: a man who had lost his lower arms was able to determine

the difference between blocks made of wood or foam rubber by using a sensor-equipped prosthetic hand. He correctly identified the objects' size and softness more than twice as often as would have been expected by chance⁵. Information about force and finger position was delivered from the prosthetic to a computer, which prompted stimulation of electrodes implanted in his upper-arm nerves. Researchers at Florida International University in Miami are now working to build an implantable device using the technique.

But some researchers worry that implanting electrodes directly into a nerve could damage it. Dustin Tyler, a biomedical engineer at Case Western Reserve University, and his colleagues have therefore developed a cuff-like electrode that encircles the nerve. "We want to get access to as much of the nerve as we can without actually penetrating into it," says Tyler. The researchers showed that by running current to the cuffs in cats, they could precisely activate nerves and make the animals move their feet in specific directions⁶. They are now trying to stimulate nerves that carry sensory information. Their first patient — Spetic — had the cuffs implanted in his forearm last May, says Tyler, and can feel "very natural sensation" at multiple spots. The team is now testing the electrodes in a second patient.

COMPLEX SENSATION

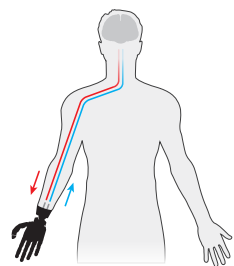
As promising as such results are, researchers will probably need to stimulate hundreds or thousands of nerve fibres to create complex sensations, and they will need to keep the devices working for many years if they are to minimize the number of surgeries required to replace them. So some researchers are instead trying to give patients sensory feedback by touching their skin.

This technique was discovered by accident in 2002, when a group led by Todd Kuiken, director of the Center for Bionic Medicine at the Rehabilitation Institute of Chicago in Illinois, was testing a way to improve patients' control of their prosthetic limbs. The idea was to rewire arm nerves that used to serve the hand, for example, to muscles in other parts of the body. When the patient thought about closing his or her hand, the newly targeted muscle would contract and generate an electric signal, driving movement of the prosthetic.

The first patient to receive this 'targeted reinnervation' therapy was Jesse Sullivan, a power-line engineer who had lost both arms from electrical burns. After his arm nerves were re-routed to his chest muscles, Sullivan could operate a prosthetic hand just by thinking about the actions. But to everyone's surprise, he also began to feel

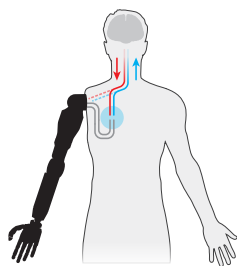
Closing the loop

Prosthetic limbs can be controlled by nerve signals flowing from the brain (→). But fast, fluid motion requires sensory feedback flowing back to the brain (←). Sensor-equipped prosthetics are under development (right), and researchers are exploring several ways to route the output from the sensors into the nervous system (below).



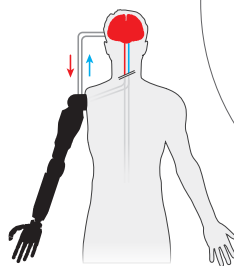
Use the remaining nerves

Electrical leads from the prosthetic's sensors stimulate nerves in the person's stump that once served the real limb.



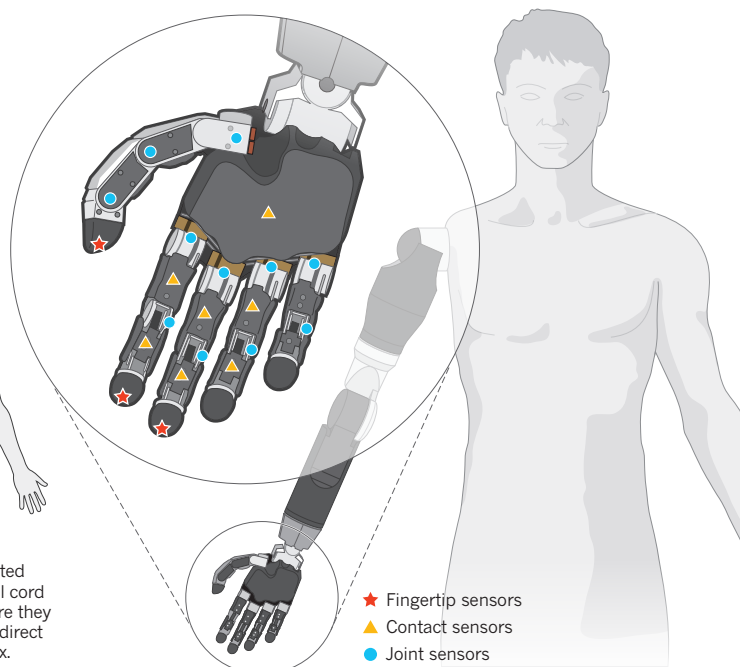
Move the nerves

Re-routed nerves grow new endings into muscle and skin, where external devices translate signals going to and from the prosthesis.



Stimulate the brain

Sensory signals are routed around a severed spinal cord and into the brain, where they produce sensations by direct stimulation of the cortex.



as though his missing hand was being touched when his chest was touched. It turned out that the re-routed nerves had grown into the chest skin, and his brain was interpreting the sensory signals as coming from his hand. Some parts of his chest felt like his palm, whereas others felt like his fingers or forearm⁷.

The results raised the possibility that sensory information from a prosthetic could be delivered to a device that pushes different parts of the skin. For people who have had targeted reinnervation surgery, pressure on the newly wired skin would then trigger sensations of touch in the missing hand. The technique isn't perfect: the parts of the hand don't map neatly onto the reinnervated skin, and each patient has a different map. And delivering detailed sensory information from a prosthetic can be challenging, as the area for stimulation is limited to a small patch of skin. But even so, one of Kuiken's former colleagues is working with the company HDT Robotics in Evanston, Illinois, to make such a device, and Kuiken plans to develop one as well.

DIRECT HIT

None of these techniques will work for people who, like Hutchinson, have had a stroke, or received spinal-cord injuries that severed the nerve pathways from the limbs to the brain. So some researchers are skipping directly to the brain. In principle, this should be straightforward. Because signals from specific parts of the body go to specific parts of the brain, scientists should be able to create sensations of touch or proprioception in the limb by directly activating the neurons that normally receive those signals.

This is immensely difficult to do, however, because scientists still have an incomplete knowledge of which neurons those are. Researchers therefore have two options: identify and mimic the natural signals, or make the brain learn a new set.

A team led by Sliman Bensmaia, a neuroscientist at the University of Chicago, is taking the first approach. In one study, the researchers repeatedly poked monkeys in two spots on the hand and trained the animals to move their eyes left or right, depending on whether the second poke was to the left or right of the first one. They then placed electrodes in the monkeys' brains and mapped which parts of the brain responded as they touched the different spots.

Next, the researchers simulated a poke by sending current to the neurons that had been activated when the monkey was touched on the little finger. The animals moved their eyes as if their finger had actually been poked, says Bensmaia, who reported the results at the Society for Neuroscience's 2012 meeting in New Orleans, Louisiana.

Miguel Nicolelis, a neuroscientist at Duke University School of Medicine in Durham, North Carolina, favours the second approach. He and his colleagues trained monkeys to direct a virtual hand around a computer screen — and to touch on-screen objects — using their thoughts alone⁸. When the hand rubbed a 'rough' object, the team sent low-frequency electrical pulses to the monkey's brain; for a 'smooth' object, it sent a high-frequency signal.

Over time, the monkey learned to pick the right object from the frequency of the signal its brain received, and could essentially 'feel' the objects on screen. Nicolelis hopes that he can use the same tactic in people with prosthetics.

But neither he nor Bensmaia know whether the monkeys they tested felt poking, roughness or some other sensation such as tingling. "They are feeling something for sure," Nicolelis says, "but what exactly they feel is inside their heads."

Irrespective of which signals are used, scientists will need a more

finely tuned technique to deliver them. With electrical stimulation, all neurons close to the electrode's tip are activated indiscriminately, so "even if I had the sharpest needle in the Universe", that could create unintended effects, says Arto Nurmikko, a neuroengineer at Brown University in Providence, Rhode Island. For example, an attempt to create sensation in one finger might produce sensation in other parts of the hand as well, he says.

Nurmikko and other researchers are therefore using light, in place of electricity, to activate highly specific groups of neurons and recreate a sense of touch. They first used a technique called optogenetics to express genes for light-sensitive proteins in parts of a monkey's brain that receive tactile information from the hand. They then trained the monkey to remove its hand from a pad when the device vibrated. When the team then stimulated the brain with a light source implanted in the animal's skull, the monkey lifted its hand off the pad about 90% of the time, according to results reported at the Society for Neuroscience meeting. The use of such techniques in humans is still probably 10–20 years away, says Bensmaia, but it is a promising strategy.

APPROXIMATIONS

Even if such techniques can be made to work, it is unclear how closely they will approximate natural sensations. Tingles, pokes and vibrations are still a far cry from

the complicated sensations that we feel when closing a hand over an apple, or running a finger along a table's edge.

But patients don't need a perfect sense of touch, says Douglas Weber, a bioengineer at the University of Pittsburgh in Pennsylvania. Simply having enough feedback to improve their control of grasp could help people to perform tasks such as picking up a glass of water, he explains. Patients who wear cochlear implants, for example, are often happy to regain enough hearing to hold a phone conversation, even if they are still unable to distinguish musical subtleties.

One of the most sophisticated devices to include sensory feedback is a prosthetic arm developed by researchers at the Johns Hopkins University Applied Physics Laboratory in Laurel, Maryland. Built as part of a US Department of Defense research programme that has spent US\$144 million since 2006 to improve prosthetics for injured soldiers returning from Iraq and Afghanistan, the arm is equipped with more than 100 sensors that detect sensations ranging from pressure to temperature. Scientists at the University of Pittsburgh and the California Institute of Technology in Pasadena are seeking regulatory approval to use brain stimulation to deliver sensory feedback from the prosthetic limb to patients.

Spetic, for one, can hardly wait to get hold of a prosthetic hand with a sense of touch. "I'd probably lay everything on the countertop and just start grabbing stuff," he says. "I'd be so excited I wouldn't even know where to begin." ■

Roberta Kwok is a freelance science writer in Seattle, Washington.

1. Hochberg, L. R. *et al. Nature* **485**, 372–375 (2012).
2. Chapin, J. K. *et al. Nature Neurosci.* **2**, 664–670 (1999).
3. Serruya, M. D. *et al. Nature* **416**, 141–142 (2002).
4. Dhillon, G. S., Lawrence, S. M., Hutchinson, D. T. & Horch, K. W. *J. Hand Surg.* **29**, 605–615 (2004).
5. Horch, K., Meek, S., Taylor, T. G. & Hutchinson, D. T. *IEEE Trans. Neur. Syst. Rehab. Eng.* **19**, 483–489 (2011).
6. Tyler, D. J. & Durand, D. M. *IEEE Trans. Neural Syst. Rehab. Eng.* **10**, 294–303 (2002).
7. Kuiken, T. A., Marasco, P. D., Lock, B. A., Harden, R. N. & Dewald, J. P. A. *Proc. Natl Acad. Sci. USA* **104**, 20061–20066 (2007).
8. O'Doherty, J. E. *et al. Nature* **479**, 228–231 (2011).

COMMENT

TRANSPORT A call for networked fleets of small, shared, driverless cars **p.181**

FOSSILS Digital scans will only revolutionize palaeontology if they're easier to access **p.183**



PHILOSOPHY Daniel Dennett's latest book aims to aid thinking **p.184**

DATA Handsome guide to visualizations should improve science graphics **p.186**

CANDACE FEIT/REUTERS/CORBIS



An African Union peacekeeper patrols after a rebel attack in drought-ridden Darfur, Sudan, in 2006.

A call for peace on climate and conflict

Researchers trying to work out whether global warming will cause more wars need to stop fighting and work together, urges **Andrew R. Solow**.

Among the most worrying of the mooted impacts of climate change is an increase in civil conflict as people compete for diminishing resources, such as arable land and water¹. Recent statistical studies^{2–4} reporting a connection between climate and civil violence have attracted attention from the press and policy-makers, including US President Barack Obama. Doubts about such a connection have not been as widely aired^{5–7}, but a fierce battle has broken out within the research community.

The battle lines are not always clear, but on one side are the 'quants', who use quantitative methods to identify correlations between

conflict and climate in global or regional data sets. On the other side are the 'quals', who study individual conflicts in depth. They argue that the factors that underlie civil conflict are more complex than the quants allow and that the reported correlations are statistical artefacts. In my view, although the concern that climate change could increase conflict is valid, the link remains unproven.

The way forward is for the two factions to work together to make the quants' statistical models reflect the quals' understanding of the factors that affect civil conflict and to strengthen inferences about the impact of climate on human behaviour. The stakes are

too high not to try: civil conflict keeps poor countries poor and, if climate change turns out to be an important contributor to such conflict, it would be costly indeed.

QUANTS AND QUALS

Quants use regression models to identify relationships between measures of civil conflict, such as the number of countries in which deaths exceed some threshold, and climate variables, such as rainfall and temperature. The data sets used typically cover a few decades and tens of countries. Attempts are made to control for non-climate-related factors such as national income and the ►

► strength of civil institutions. A climate effect is identified if the inclusion of climate variables significantly improves the model's fit to the data.

For example, economist Marshall Burke at the University of California, Berkeley, and his colleagues linked the annual incidence of civil conflict resulting in at least 1,000 deaths in sub-Saharan Africa over the period 1981–2002 to warmer temperatures in the same and preceding years³. They found that a 1 °C increase in temperature increased the incidence of civil conflict by 4.5% in the same year and 0.9% in the following year. On the basis of climate-model projections of future warming, the authors predicted an alarming 54% increase in the incidence of civil conflict in this region by 2030, with additional deaths in the hundreds of thousands.

But political scientist Halvard Buhaug of the Peace Research Institute in Oslo argued that this finding was fragile⁵. It could be quashed by using a different threshold for the number of deaths or a different observation period. Burke and his colleagues defended their work⁶ and deserve credit for tackling an important problem. But, in my view, such disagreements indicate that a deeper look behind the statistics is warranted.

Most of these statistical studies, including Burke's, relate the incidence of civil conflict to year-to-year variations in climate variables. In fact, short-term variability corresponds to weather and not to climate, which is average weather over the long run. The overall incidence of civil conflict has actually been declining since the late 1990s, while the signature of climate change has grown stronger⁵.

But the quals' fundamental complaint is that the quants' statistical models are black boxes, reflecting little understanding of the social, economic and political pressures that underlie civil conflict. For example, Buhaug and colleagues pointed out that the six cases

that contributed most to the findings of Burke *et al.* involved foreign intervention⁷.

The most influential case was the outbreak of civil conflict in Guinea-Bissau in 1998, when Senegal demanded that the Guinea-Bissau military stop supporting Senegalese rebels. When President João Bernardo Viera of Guinea-Bissau moved to comply, he was ousted in a coup, and Senegal intervened on his behalf. Quants might respond that these interventions too were associated with high temperatures, and include a variable for foreign intervention in their next model. But this throws up a problem. The quants are not basing their models on an underlying theory of civil conflict, but rather are going where the data take them.

Quants looking for relationships in the data might ask: is conflict correlated with temperature? No? How about temperature last year? Better, but what about precipitation? Of course, this is a caricature of a more thoughtful process. But using the same data to choose a model and to assess its fit is notorious for producing impressive, but spurious, results. As Buhaug showed, models can be so customized that even modest changes can overturn their results.

This is where quals could help, by drawing on individual cases. As political scientist Stathis Kalyvas of Yale University in New Haven, Connecticut, has argued, the dynamics of particular civil conflicts can provide a basis for statistical models⁹. For example, the role of asset inequality in civil conflict has been underscored by economist Klaus Deininger at the World Bank¹⁰ in Washington DC and others.

Studies of single conflicts have their

"Publishing in each other's journals and participating in each other's conferences would be a start."

limits. Those that rely on interviews and the judgements of experts are highly subjective. Most cannot be easily generalized. To paraphrase Leo Tolstoy, every unhappy country is, to some extent, unhappy in its own way. Nevertheless, bringing together all sources of information will be progress.

A WAY FORWARD

I urge quants and quals to talk more to — and less about — each other. The goal of both should be to develop statistical models that better reflect the real drivers of civil conflict. Publishing in each other's journals and participating in each other's conferences, both of which behaviours are sadly rare, would be a start.

It is hard to predict where such a joint effort would go. My guess is that the statistical models would become more complicated — for example, separate ones for the effects of climate on resources and the effects of resources on conflict. Even if it is not possible to translate a qualitative understanding of civil conflict into a quantitative model that can readily be fitted and tested, the effort would still deepen our understanding of the effect of climate on violence.

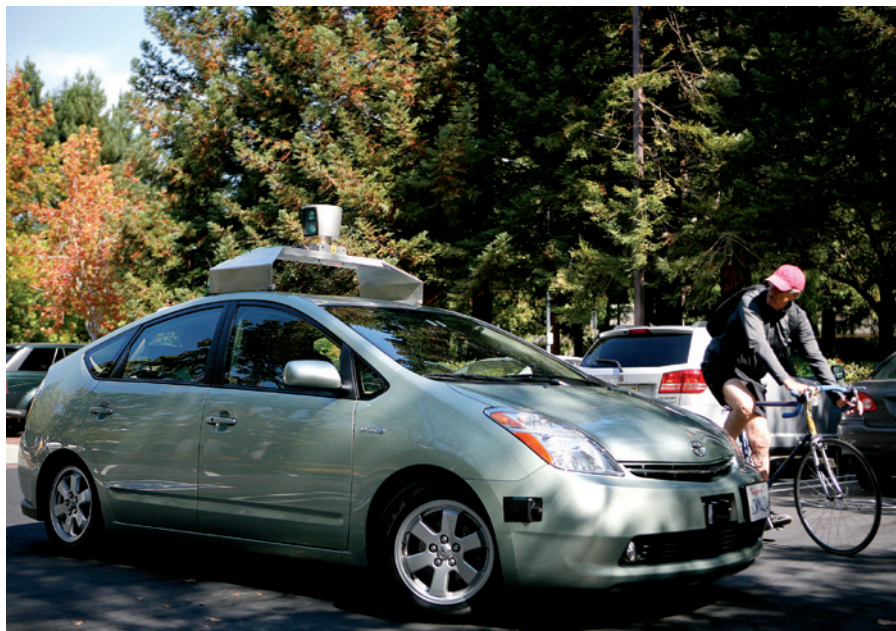
In the meantime, what should policy-makers do? The argument that, in some parts of the world, a nexus exists between climate, resources and civil conflict has too much force to dismiss. However, the relationship is complex and it is too soon to make confident predictions. There is broad agreement on one matter: social, economic and institutional factors are at least as important for driving civil conflict as climate change. The promotion of social justice, balanced economic development and civil society generally must be a priority for policy-makers. ■

Andrew R. Solow is a senior scientist at Woods Hole Oceanographic Institution, Woods Hole, Massachusetts 02543, USA. e-mail: asolow@whoi.edu

1. Homer-Dixon, T. *Environment, Scarcity, and Violence* (Princeton Press, 1999).
2. Miguel, E., Satyanath, S. & Sergenti, E. J. *Polit. Econ.* **112**, 725–753 (2004).
3. Burke, M. B., Miguel, E., Satyanath, S., Dykema, J. A. & Lobell, D. B. *Proc. Natl Acad. Sci. USA* **106**, 20670–20674 (2009).
4. Hsiang, S. M., Meng, K. C. & Cane, M. A. *Nature* **476**, 438–441 (2011).
5. Buhaug, H. *Proc. Natl Acad. Sci. USA* **107**, 16477–16482 (2010).
6. Theisen, O. M., Holtermann, H. & Buhaug, H. *Internat. Secur.* **36**, 79–106 (2011).
7. Buhaug, H., Hegre, H. & Strand, H. *Sensitivity Analysis of Climate Variability and Civil War* (Peace Research Institute of Oslo, 2010).
8. Burke, M. B., Miguel, E., Satyanath, S., Dykema, J. A. & Lobell, D. B. *Proc. Natl Acad. Sci. USA* **107**, E185 (2010).
9. Kalyvas, S. N. in *Order, Conflict and Violence* (eds Kalyvas, S. N., Shapiro, I. & Masoud, T.) 1–14 (Cambridge Univ. Press, 2008).
10. Deininger, K. *Oxf. Econ. Pap.* **55**, 579–606 (2003).



The role of climate change in driving the 1998 Guinea-Bissau conflict is open to debate.



Google's self-driving car senses nearby objects to mimic the decisions of a human driver.

A vision of our transport future

Lawrence D. Burns explains how networks of driverless, shared cars will revolutionize motoring.

When I was named vice-president of research and development at General Motors (GM) in 1998, I was asked: "If we reinvented the automobile, what would be different?" This question has framed my work since.

Today, around a billion cars and trucks move people and goods on the world's roads. Parked end-to-end, this fleet would circle Earth more than 100 times. It is remarkable that such scale has been achieved with little change to the machine that was invented by Karl Benz and popularized by Henry Ford more than a century ago. The basic design of automobiles today is the same as it was in 1900: energized by oil, powered by combustion, driven mechanically by a person and intended for broad purpose.

Yet road transportation as we know it is unsustainable. More than 1.2 million people die on the road each year, equivalent to an epidemic, according to the World Health Organization. Ninety-five per cent of motor vehicles depend on oil for energy, holding car travel hostage to geopolitical issues and volatility in oil prices. Vehicle combustion engines account for more than one-fifth of the world's carbon dioxide emissions, making them a significant contributor to global climate change.

And average speeds in congested cities can be as low as 20 kilometres per hour, causing productivity losses and travel stress.

The road transport system has remained stable because of its complexity. With a mix of public and private elements, the motor industry has strong vested interests and ingrained business models. People and businesses derive value from all parts of the system working together — vehicles, roads, fuel stations, traffic laws, regulations, vehicle standards and trained drivers.

So overcoming the problems requires rethinking the entire system. It is not enough to focus on better batteries or fuel economy or the automobile industry alone. The solution must meet the needs of all users, including business. Fortunately, the technology now exists to build an integrated network of driverless, electrical vehicles that are connected, coordinated and shared.

Consider a typical car owner, Joe, living in a medium-sized city such as Ann Arbor, Michigan. Joe drives his car about 50 kilometres a day at a cost of around US\$0.40 per kilometre, which includes depreciation, insurance, fuel,

maintenance, licence fees, finance charges and taxes. Parking costs more, and he spends more than an hour each day driving to work, shops and schools.

Now imagine a different scenario. Joe requests a car using a smartphone application. A driverless electric vehicle arrives within minutes and transports him to his destination. During the trip, Joe can read, work, eat, talk on the phone, watch a film or send e-mails. There is no need to park — the vehicle zooms off to pick up another rider.

Joe concludes that he no longer needs to own a car. His trips are safe, timely and convenient. He can use his travel time productively. The price and mode of payment are attractive — his account is automatically debited for each journey. And Joe appreciates that electric vehicles create fewer emissions than his petrol-powered car. His enthusiasm stems not from any one technology, but from a combination of satisfactory experiences.

BUILDING BLOCKS

Can this dream be realized? I think so — the building blocks already exist.

Connected vehicles. These communicate with surrounding vehicles and infrastructure through the digital 'cloud' to enable hands-free calling, navigation, emergency response and concierge services. They have matured rapidly since the first Global Positioning System unit appeared in a personal car in 1995: products such as GM's OnStar and Ford's SYNC are already installed in tens of millions of cars. Logistics companies such as FedEx and UPS use vehicle connectivity to enhance fleet operations.

Coordinated vehicles. These choreograph the movement of people and goods just as the Internet manages streams of information. Real-time data optimize traffic flow and parking¹. Most large cities already provide traffic information to help drivers avoid bottlenecks. And California is testing smart parking systems, such as SFpark and LA Express Park, that allow drivers to use mobile apps to check parking availability and pricing.

Shared vehicles. These serve several people throughout a day, in contrast to personally owned vehicles that are parked 90% of the time. More than 25 shared-vehicle companies already exist, such as Zipcar, Uber and RelayRides in the United States, Buzzcar in France and Car2Go in Germany. As of December 2012, there were 1.7 million car-sharing members in 27 countries, according to the Transportation Sustainability Research Center at the University of California, Berkeley. It is estimated that, by 2016, vehicle-sharing revenue will exceed \$3 billion in North America².

Driverless vehicles. The companies developing these — Google, Daimler, Volvo, GM, Toyota, Volkswagen, BMW, Bosch, ►

► NATURE.COM

More on small electric vehicles:
go.nature.com/azklzq

► Continental and Delphi — claim that they will have proven technology by 2020 or sooner. Google, for example, has a fleet of Toyota Prius and Lexus vehicles that has already driven some 800,000 kilometres on public roads. Driverless vehicles respond to others nearby to evade crashes and free up drivers' time. Because these cars are less prone to crashing, they need fewer safety features and can therefore be smaller and lighter than current vehicles, making them better suited to electric power.

Much work remains to be done to convince consumers and regulators that driverless vehicles are safer than human-driven ones in all circumstances, such as mixed traffic, snow-covered roads and construction zones. But the rise in computer processing power, better sensors made possible by nanotechnology and improved algorithms stemming from 'big data' analytics will, in my view, continue to accelerate progress.

Electrical vehicles. These are powered by electric motors and have digital controls to diversify sources of energy, reduce emissions and improve efficiency. They include hybrids, such as the Toyota Prius; plug-in electric or hybrid cars, such as the Nissan Leaf, Chevrolet Volt and Tesla Model S; and fuel-cell vehicles, such as the Hyundai ix35. After 15 years on the market, hybrids are now approaching a 4% share of new car sales in the United States.

Although the use of lithium-ion batteries has improved plug-in electric vehicles, their popularity is still limited by range, recharging time and cost. Further battery breakthroughs and reductions in vehicle weight will be required if plug-in cars are to have as wide appeal as conventional-sized cars. And although Hyundai, Daimler, Ford, Nissan, Toyota and Honda have all announced commercial plans to launch hydrogen fuel-cell electrical vehicles in the next five years, the development of a hydrogen-refuelling infrastructure remains a challenge.

Tailored vehicles. These are designed for specific types of mobility and numbers of occupants, making them more energy-, space- and cost-efficient than most cars, which are often overspecified for their typical use. For example, 90% of US car journeys carry one or two people³, but most vehicles have four or more seats. And whereas cars can travel at speeds of more than 160 kilometres an hour, average speeds in cities are less than 50 kilometres per hour.

In response to growing urbanization, tailored vehicles have become a dominant theme at global car shows. A 2012 report⁴ concluded that 150 varieties of one- and two-passenger vehicles could exist by 2020. At one-third of the weight of typical cars, tailored vehicles can go much farther on smaller batteries, making them better suited to being plug-in cars.

Together, these building blocks can bring radical improvements. How will the costs and benefits compare with the status quo? In 2010, I teamed up with economist Jeffrey Sachs at Columbia University's Earth Institute in New York to establish the Program on Sustainable Mobility and to assess the potential of driverless electrical vehicle systems for various locations.

For a citizen of a city like Ann Arbor, such a service could be more than 70% cheaper and would require residents to invest less than one-fifth of the amount needed to own their cars⁵. About 80% fewer shared, coordinated vehicles would be needed than personally owned vehicles to provide the same level of mobility, with less investment.

And there are other benefits. Lightweight, two-passenger vehicles are ten times more energy efficient than a typical car. Driverless, shared vehicles free up time that people currently spend driving and parking. For example, at the US minimum wage of \$7.25 per hour, travelling costs \$0.15 per kilometre at a speed of 50 kilometres per hour, or \$0.50 per kilometre at the US median income of \$25 per hour. Americans drive almost 5 trillion kilometres per year, so saving even just 1 cent per kilometre by freeing up people's time accrues \$50 billion per year.

Connected and driverless vehicles that avoid crashes mean fewer deaths and injuries and less property damage. Vehicles in shared fleets reduce the need for car parks. Smoother traffic flow and lighter vehicles reduce emissions and congestion.

NEXT STEPS

Not everyone is as excited by my vision as I am. Many people like to drive, and do not like to share their cars. Others think that we should instead invest in public transport, such as trains, trams, buses and cycle-lease systems, which, although heavily subsidized, already impart some of the benefits described above. Still others question whether the reliability and security of computer networks can deliver safe driverless travel. And those with vested interests in today's road-transport system might resist substantial changes. But even though connected, coordinated, shared and driverless vehicles are not the only option, I see them as one mode of travel that should be explored. The market will ultimately determine whether this model can succeed.

Technology is no longer the biggest hurdle. We need to create the collective will to move forward. Prototypes need to be deployed in representative communities so

that we can learn what works. Such learning cycles are essential to prove what is possible, to identify what consumers like and dislike, to determine which business models are attractive and to avoid unintended consequences.

California, Florida and Nevada already allow prototype self-driven vehicles to be used on public roads. In Ann Arbor, the University of Michigan Transportation Research Institute is conducting a connected vehicle safety pilot with more than 3,000 drivers, sponsored by the US Department of Transportation. This is the world's first opportunity to assess the safety benefits and reliability of connected vehicle systems on real roads. The university is launching a mobility transformation centre, to develop and test innovative prototype systems based on connected, coordinated, shared, driverless and tailored vehicles.

Once proven and regulated, prototype systems should scale quickly without public incentives. Policy-makers can allow this innovation to play out safely. As with other new products that converged on a market tipping point — such as mobile phones, electronic books, digital photography and music formats, and flat-screen televisions — economic forces will naturally lead to large-scale deployment when consumers want to use a product because its value exceeds what they pay, and businesses want to supply it because their revenue exceeds their cost.

Sustainable mobility is a team sport. We must bring together technology, systems-design methods and business models to supply better mobility at a low cost to consumers and to societies. After 15 years of striving to reinvent the automobile, the question that now frames my work is: "How do we achieve what is possible?" ■

Lawrence D. Burns is professor of engineering practice at the University of Michigan, Ann Arbor, Michigan, USA, and directs the Program on Sustainable Mobility at the Earth Institute, Columbia University, New York, USA. He was corporate vice-president of research and development and planning at General Motors until 2009. e-mail: lawrencedburns@gmail.com

1. Mitchell, W. J., Borroni-Bird, C. E. & Burns, L. D. *Reinventing the Automobile: Personal Mobility for the 21st Century* (MIT Press, 2010).
2. Sacks, D. 'The Sharing Economy' *Fast Company* (18 April 2011); available at <http://go.nature.com/co6pte>.
3. *Summary of Travel Trends: 2009 National Household Travel Survey* (US Department of Transportation Federal Highway Administration, 2011).
4. Shankar, V. *Strategic Analysis and Benchmarking of Global OEMs Micro-Mobility Solutions* (Frost & Sullivan, 2012).
5. Burns, L. D., Jordan, W. C. & Scarborough, B. A. *Transforming Personal Mobility* (Earth Institute, Columbia University, 2013).

The author declares competing financial interests: see go.nature.com/eb9bu3 for details.

Free digital scans of human fossils

Draconian access requirements are squandering the potential of imaging technology to advance human palaeontology, cautions **Jean-Jacques Hublin**.

Being refused the right to examine a sought-after specimen is a common experience in the professional life of a palaeoanthropologist. Too often I have heard in the back rooms of museums that “nobody can find the key to the Neanderthal’s cabinet”, “the fossil is away on exhibition” or “it is currently being reconstructed”. Human fossils that make international celebrities of their discoverers are difficult to find in geological strata, but they can become unreachable relics when they are in storage.

The spread of micro-computed tomography (microCT) seemed to offer a salve to the frustrations of the field. High-resolution digital avatars of bones and teeth avoid the risks associated with manipulating original fossils. Scans allow endless reconstruction attempts, the exploration of fine internal features and the use of mathematical tools to quantify anatomical variation.

Virtual palaeoanthropology began in the 1980s, but it took decades for microCT scanners to become widely available. Today, researchers routinely bring fossils to synchrotron X-ray facilities. Many large museums have their own scanning equipment, and the transportable devices of the Department of Human Evolution (of which I am director) at the Max Planck Institute for Evolutionary Anthropology (MPI-EVA) in Leipzig, Germany, have made large international CT scanning projects possible. All these efforts have built up digital facsimiles of tangible collections.

Like many others, I believed these advances meant that issues related to consent, scarcity and distance would soon be behind us. Sadly, fluid access to the fossil record, real or virtual, remains a dream. It has become a major bone of contention in palaeoanthropology that digital data, once produced and exploited, are not made available to other researchers.

The release online earlier this week of a large series of palaeoanthropological data — produced by my department from the hominin collection of the Kromdraai B site near Johannesburg, South Africa — is an important new step (<http://paleo.eva.mpg.de>; see also M. M. Skinner *et al.* *J. Hum. Evol.* **64**, 434–447; 2013). This collaboration between the Ditsong National Museum of Natural History in Pretoria and the MPI-EVA makes images and three-dimensional surface models of each Kromdraai specimen freely accessible. Highlights include the type specimen

of *Paranthropus robustus* first described in 1938, as well as some never-published specimens. Researchers can also download the microCT data through a password-protected system controlled by curators of the Ditsong Museum. To move forward, the field requires such offerings to become more widespread.

The reasons that in the past constrained access to fossils — sometimes discovered a century ago — still limit the diffusion of digital substitutes today. In most cases, curating institutions retain copyright to all digital data and demand continuous control over their use. Ten years ago, a simple exchange of letters preceded the scanning of a fossil. Now, the same operation depends on the signing of long and sometimes lawyer-proofed memoranda of understanding. These agreements are primarily designed to limit the dissemination of digital data.

Among other issues, museums are wary of the risk of commercial production of printed 3D models. Especially in developing countries, bench fees for the study of specimens and the sale of casts are a significant source of income for museums.

CONFLICTS OF INTEREST

Importantly, many curating institutions want to manage any research that is based on data derived from their fossil collections. In theory, such control avoids overlap in research efforts. However, it also results in clear conflicts of interest, with most of these institutions hosting their own palaeoanthropological research teams. In these situations, the digital data can become a local resource to protect.

After specialists have processed and studied CT scans, one can — in theory — request copies from curators. But obtaining the data remains difficult, partly because ill-funded institutions cannot easily manage large bodies of digital information. Requests succeed sporadically for isolated and less-prestigious specimens or for low-resolution data.

Nevertheless, I am rather optimistic. The breakthroughs of virtual palaeoanthropology create pressure to allow access

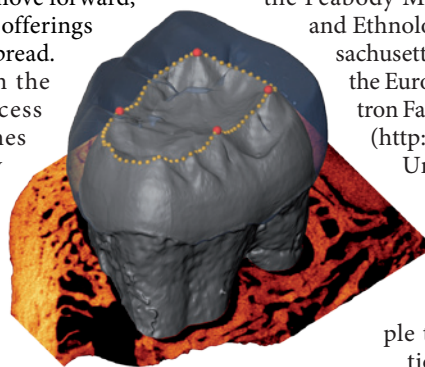
to numerical data, and some kind of sea change is increasingly perceived as vital for the development of the field. Some institutions already offer open or affordable access to small sets of digital data; these include the Peabody Museum of Archaeology and Ethnology in Cambridge, Massachusetts (go.nature.com/lalyis), the European Research Synchrotron Facility in Grenoble, France (<http://paleo.esrf.eu>), and the University of Vienna in Austria (go.nature.com/qakehi). The NESPOS initiative (go.nature.com/ehmkxw) is another positive example that provides information on available sources of CT data and some direct downloads.

The Kromdraai initiative is unique in providing direct access to an entire collection, not just a few iconic fossils. This type of collaboration between museums and producers of digital data might serve as a model for other institutions. Among other benefits, such websites give museums that need to generate income the option to implement a fee-based system for data access. Furthermore, because CT scans cannot address all potential research questions, the availability of CT data and digital avatars will probably increase requests to study the original fossils.

Easier access to digital data also depends on journals. Museums’ desire to control the raw data derived from their collections will probably lead them to resist pressures from funding agencies and editors. But journals should mandate that secondary products such as surface models of hypothetical 3D reconstructions be made freely available at the time of publication.

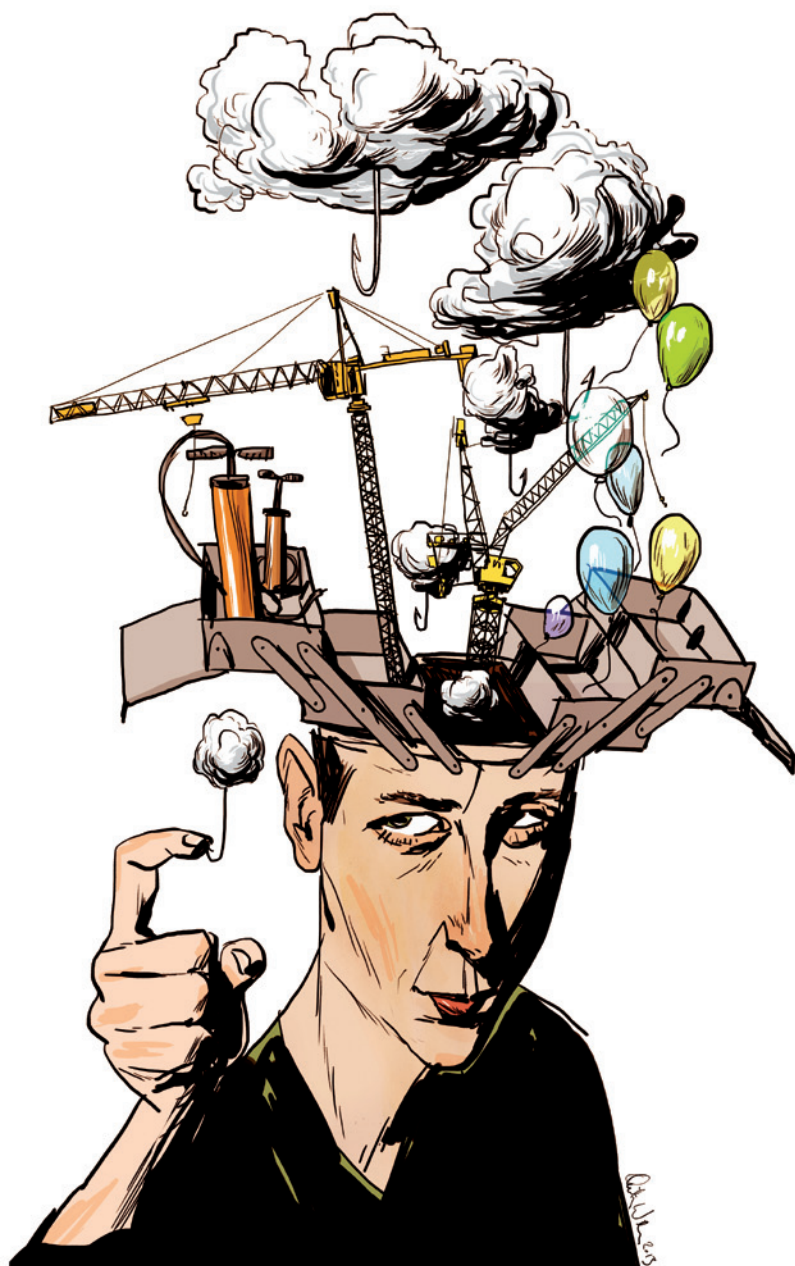
Modern palaeoanthropological studies are driven by questions that are testable on series of specimens, not by the description of isolated fossils. Many answers require high-resolution imaging. These virtual representations are integral to scientific inquiry and should facilitate access to the human fossil record. ■

Jean-Jacques Hublin is director of the Department of Human Evolution at the Max Planck Institute for Evolutionary Anthropology, Leipzig, Germany.
e-mail: hublin@eva.mpg.de



This virtual reconstruction of a hominin tooth reveals internal structures.

MATTHEW SKINNER



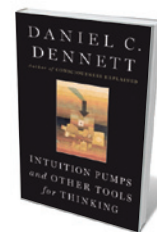
his previous books, he performed a service that is one of philosophy's main contributions: clarification of discourse.

For me, this is not quite achieved in *Intuition Pumps*. The book reads like a collection of short essays — nearly 80 chapters in 440 pages — grouped in sections loosely connected by theme.

One section is a fairly conventional precis of basic ideas in computing; others explain evolution, consciousness and free will. The intuition pumps are, as the title says, tools for thinking: they are thought experiments focused on problem-solving. And although Dennett wants to help us to think with them, he dislikes many and treats them as straw men. For example, skyhooks — thinking-tools that hang an explanation on nothing — are bad. These include intelligent design, for explaining too-intricate bits of biological machinery, and divine inspiration, for too-brilliant works of art. But cranes — concepts built on a solid factual foundation — are good. Take symbiosis or sexual reproduction, which speed up the work of random, blind-designer evolution; these are concepts that give evolution a legitimate boost.

Well, yes. But are skyhooks and cranes comparable kinds of ideas? Symbiosis and sex are evolved processes like respiration or photosynthesis; each began with random mutation and, by gradual natural selection, produced a 'design' that changed the history of life. But what do skyhooks and cranes add to the basic principles of how we think about evolution? The next time I comfort a student struggling between faith and Darwin, it will not help me to say, "What you learned in Sunday school about evolution needing a 'big boost'? That's just a skyhook." Rather, I will do what I do now: help the student to zero in on variation, inheritance, selection and, crucially, how very many generations there have been since evolution began. As Dennett states elsewhere in this book, the word for this is not 'crane' but 'algorithm' — both more and better than a metaphor.

A two-page chapter defines 'deepities', a coinage borrowed from a child, as meaningless statements that seem deep. His main example: "Love is just a word", which Dennett follows with, "Oh wow! Mind-blowing, right? Wrong." The idea of deepities is offered as a thinking tool to protect us from such shallow statements in



Intuition Pumps and Other Tools for Thinking

DANIEL C. DENNETT
W. W. Norton: 2013.
512 pp. \$28.95

ILLUSTRATION BY QUINTON WINTER

PHILOSOPHY

Deepities, cranes and skyhooks

Melvin Konner sorts through a philosopher's box of tools for the musing mind.

Full disclosure: I am no sort of philosopher — I am not even a 'sorta' philosopher, to use one of Daniel Dennett's favourite coinages. But I aspire to being a sorta intelligent general reader, which would make me a fair example of the target audience of Dennett's *Intuition Pumps and Other Tools for Thinking*. I am also more

than a sorta Dennett fan: I reviewed *Freedom Evolves* (Penguin, 2004) favourably in these pages, and I liked *Consciousness Explained* (Penguin, 1993) and *Darwin's Dangerous Idea* (Penguin, 1996). Dennett, a noted philosopher, is one of those who take science seriously, believing that reasoning without facts can be a fool's errand. And in

NATURE.COM

For Melvin Konner on
Dennett's *Freedom
Evolves*, see:
go.nature.com/k24byv

disguise. But are we to find his reply to this deepity deep?

I share many of Dennett's views: a 'designed' nature without a designer; the mechanistic, emergent character of consciousness; the rejection of the homunculus argument, or the idea that an entity (often characterized in discussion as a little person) watches a theatre consisting of the rest of the brain; and the compatibility of free will with determinism. But I do not see the need to repeat arguments made less flippanantly in earlier books. An artfully selected Dennett anthology would overlap considerably with this one, and might be easier to follow.

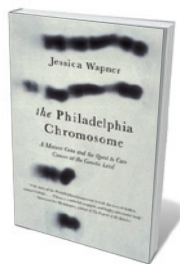
There is quite a bit of score settling. Dennett takes issue with thinkers ranging from Robert Beverley MacKenzie, who in 1868 called Darwin foolish for believing in designs with no designer, to evolutionist Stephen Jay Gould, who died in 2002, and the philosopher John Searle, both of whom Dennett has often censured.

Gould, for instance, found nature full of biological traits that he did not consider were in themselves adaptations, and hated what he called 'Panglossian adaptationism', or what he saw as the overly optimistic explanatory efforts of much recent Darwinian thinking. He used the evidence for punctuated equilibrium — long stretches of stasis in fossil records interrupted by change — to suggest a need for revising Darwin. Yet the 'punctuations' were easily long enough for natural selection. Even so, I fail to see what is gained by Dennett's coining a verb, goulding, to denote certain logical errors. Gould's research is valued; he was also a fine science communicator and a spirited defender of evolution.

Dennett says that although philosophers would rather be clearly right than clearly wrong, many would most like to be confusing, because confusing things endure in reprints and homework. He admits to abetting that process by engaging with the work of those he criticizes. But I fail to see the point of keeping bad ideas famous with reiterated arguments; perhaps that is why I am not a philosopher. I look forward to Dennett's next book, which I hope will be something ambitious: *Evolution and History* perhaps, or *How the Brain Decides*, or maybe *Philosophy as a Science*. But it is not for me to put a title in his laptop. I just hope that it reminds me more of his earlier, grander books, so that I can turn to it on my night table, once again a delighted Dennett fan. ■

Melvin Konner is professor of anthropology and behavioural biology at Emory University in Atlanta, Georgia. His latest book is *The Evolution of Childhood: Relationships, Emotion, Mind*. e-mail: antmk@mindspring.com

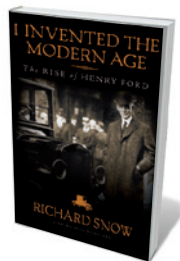
Books in brief



The Philadelphia Chromosome: A Mutant Gene and the Quest to Cure Cancer at the Genetic Level

Jessica Wapner THE EXPERIMENT 320 pp. \$25.95 (2013)

A crucial link between genetics and cancer emerged in a US lab in 1959, as researcher David Hungerford peered down a microscope at an abnormally small chromosome. In 1990, this 'Philadelphia chromosome' was found to cause the swiftly fatal chronic myeloid leukaemia. As science writer Jessica Wapner reveals in this taut, elegant study, a cascade of breakthroughs then led to success with targeted drug Gleevec, a tyrosine kinase inhibitor — and hopes for the cancer-busting potential of rational drug design in general.



I Invented the Modern Age: The Rise of Henry Ford

Richard Snow SCRIBNER 384 pp. \$30 (2013)

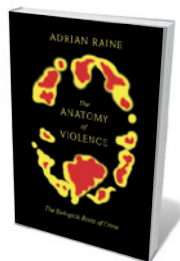
He was as obsessed by the inner workings of a watch as by a locomotive's wheels. His name was synonymous with mass production and the automobile's century-plus reign. Henry Ford's samurai-sword vision simply cut through hurdles, moral or physical. Eventually, as this biography-cum-technical history amply shows, Ford the mechanical genius and innovator was eclipsed by Ford the vindictive anti-Semite. Richard Snow skilfully evokes everything from patenting battles to internal-combustion dramas — and his bullheaded subject, who set out to remake America, and succeeded.



Moving Innovation: A History of Computer Animation

Tom Sito MIT PRESS 336 pp. \$29.95 (2013)

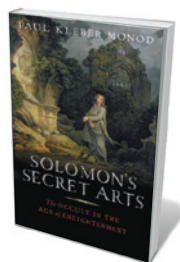
From Buzz Lightyear all the way to Gollum in the film *Lord of the Rings*, computer graphics is techno-art of mind-boggling sophistication. Tom Sito, who helped to set up the Dreamworks Animation Unit in 1995, traces its roots to the modernist era, when James Whitney's abstract films and Ivan Sutherland's Sketchpad program were making waves; he then untangles its evolution in corporations, academia and film. Sito unveils the hard graft, thrills and frustrations behind the digital wizardry, taking us through watersheds such as *Jurassic Park* and beyond.



The Anatomy of Violence: The Biological Roots of Crime

Adrian Raine PANTHEON 496 pp. \$35 (2013)

Are 'criminal tendencies' hard-wired or acquired? In this perturbing study, psychologist Adrian Raine argues the biological case, marshalling swathes of findings and case studies of murderers and rapists. We learn, for instance, of Jeffrey Landrigan, who was adopted into a privileged family as an infant, yet mirrored his biological father's and grandfather's criminal careers; of links between aggression and prefrontal-cortex impairment; and of potentially sticky legal implications. But, although provocative and bristling with data, the book's complexities fail to boil down to a simple answer.



Solomon's Secret Arts: The Occult in the Age of Enlightenment

Paul Kleber Monod YALE UNIVERSITY PRESS 412 pp. £27.50 (2013)

The British Enlightenment, historian Paul Monod avers, was shot through with the esoteric: an undercurrent of occultism persisted as the current of rationality came into full flow. Revelations may not be rife, but Monod conjures up an array of figures who swam in both streams, from secret alchemist Isaac Newton to openly "fervent alchemical adept" Elias Ashmole. Ultimately, Monod argues, occult thinking may even have freed intellectual development by liberating the imagination at this key scientific tipping point. **Barbara Kiser**

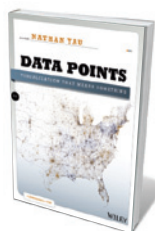
Drawing out the meaning

Felice Frankel relishes an inspired handbook on the art and science of picturing data.

Scientists, probably more than most, are aware of the ever-increasing presence of data visualization in newspapers, television, online shopping, social media and even policy-making sales pitches in the US Congress. I'll bet there's a brand new office building in Washington DC devoted to creating chart-laden poster boards for congressional members. Statistician and visualization expert Nathan Yau's *Data Points: Visualization That Means Something* is a clear and passionate exploration of this burgeoning phenomenon.

A detailed handbook, *Data Points* is especially useful for those working on scientific data visualization, guiding the reader through fascinating examples of data, graphics, context, presentation and analytics. But this is more than a mere how-to manual. Yau reminds us that the real purpose of most visualization work is to communicate data to pragmatic ends. He points to the other end of the spectrum: visualizations created by those so seduced by artful design that meaning becomes inconsequential. As Yau writes of statistics and design knowledge, "having skills in both provides you with the luxury — which is growing into a necessity — to jump back and forth between data exploration and storytelling".

Yau entices us to look and think, study, dissect and judge. As a visualizer himself, he has made intelligent choices of illustrations in this wonderfully varied collection; they are not there as decoration. Lokesh Dhakar's *Coffee Drinks Illustrated* (<http://go.nature.com/tcxs21>), for instance, is accessibly simple, yet rich in information. Yau includes an interactive astronomical visualization by Santiago Ortiz (<http://go.nature.com/hwnsdX>) as an example of how perspective and context are inseparable when zooming and rotating the night sky. The visualization of constellations is both elegant and beautiful, and could become an inspiration for scientists creating interactive molecular configurations. And although there are few



Data Points: Visualization That Means Something

NATHAN YAU
John Wiley & Sons: 2013.
384 pp. \$39.99/£26.99

specifically scientific visualizations on offer, the creative researcher could find much to adapt in these approaches.

Yau illustrates and discusses the fundamental components of visualizations and how small changes can improve readability.

concept or data into a formatted representation — that is, to reduce a visual expression to its fundamental information — is one of the least discussed but most important elements of successful visual representations.

I have some quibbles. You might need a magnifying lens while reading *Data Points*: a number of the figures need considerable enlargement to make sense on the printed page. And ensure you view online his many examples of visualizations intended for online publication, especially those intended for interactivity. I would also have liked to see a more in-depth discussion on representing uncertainty. We are all aware of the

various levels of imprecision in our data, and not to communicate that somehow in our representations can be irresponsible — but that exercise probably warrants a separate book. Finally, I found it annoying that many figures do not appear next to where they are referenced in the text; I sometimes had to turn a page or even two to see what Yau was describing.

But this remains a masterpiece. I can imagine some initial eye-rolling in the visualization community on the first viewing of some of Yau's seemingly 'obvious' examples. But there is much to learn from studying what Yau does here. That is, defining and demonstrating good visualization with clarity and precision as "a representation of data that helps you see what you otherwise would have been blind to if you

looked only at the naked source ... trends, patterns, and outliers that tell you about yourself and what surrounds you".

Thank you, Nathan Yau, for helping us to begin. ■

Felice Frankel is a research scientist in the Massachusetts Institute of Technology's Center for Materials Science and Engineering in Cambridge, Massachusetts, USA. Her latest book is *Visual Strategies: A Practical Guide to Graphics for Scientists and Engineers*, co-authored with Angela DePace. e-mail: felfra@mit.edu

Visual Cues			
	Position	Length	Angle
Patterns			
Increase			
Decrease			
Combination			
Outlier			

Characteristics abstracted into form: each cell combines two properties of data.

He teaches us to think graphically. On one spread (and there are many), he cleverly uses the 'visual cues' described by William Cleveland and Robert McGill in their 1985 study on graphical perception and methods (W. S. Cleveland and R. McGill *Science* **229**, 828–833; 1985) in a table that subtly encourages the reader to think their way into visual abstraction (section **pictured**). The table shows patterns in data — such as an increase or decrease in the population of a species — and how these can be represented graphically through angle, position, area or colour saturation. How to visually abstract a



Mariele Neudecker's *There is Always Something More Important (Iceberg)* is on display in Brighton, UK.

ARTS

Framing change

Daniel Cressey tours scientists and artists who are showcasing elusive environmental shifts.

Imagine opening a door and zipping from the sea floor to Arctic skies in the space of a few minutes. In a Regency townhouse on England's south coast, you can. *Heterotopias and Other Domestic Landscapes*, artist Mariele Neudecker's extraordinary installation in Hove, sets on different storeys of the dwelling artworks sparked, in part, by global environmental issues. The juxtaposition jars the observer into seeing them with a fresh eye.

Neudecker is the lead artist for the HOUSE 2013 festival. This shows contemporary art in domestic contexts and is part of the annual Brighton Festival, which bills itself as "England's biggest arts festival". *Heterotopias* also features the latest product of a series of collaborations set up by Invisible Dust, a London-based organization that brings scientists and artists together to highlight environmental shifts that, curator and founder Alice Sharp says, "are difficult to see or understand"

Heterotopias and Other Domestic Landscapes

HOUSE 2013:
BRIGHTON AND
HOVE'S CURATED AND
PROGRAMMED VISUAL
ARTS FESTIVAL.
Brighton and Hove, UK.
Until 26 May

scapes; the ground floor, an iceberg-inspired sculpture 4.5 metres long; and the first floor, *Recent Futures*, photographs of the Sun in the Arctic sky. This is, Neudecker says, a "slice through my work as much as through geological space".

Alex Rogers, an eminent marine researcher at the University of Oxford, UK, collaborated on the deep-sea videos, which were filmed by remotely operated vehicles in the southwest Indian Ocean and reveal human detritus,

because their triggers and effects are invisible to the naked eye.

Neudecker's domestic 'biosphere' mirrors strata of the living world. The basement features *The Great Day of His Wrath*, videos of deep sea-

such as fishing equipment. For the 'Arctic' upper floors, Neudecker spent weeks in northwestern Greenland taking photographs of the ice sheet and sky with everything from a biscuit-tin pinhole camera to a cutting-edge digital rig. Each environment — sea, ice sheet and atmosphere — is both isolated from and intricately interlinked with the rest, not least in terms of the effects of human activity, from overfishing to climate change.

Neudecker is not forcing a simplistic message about human intrusion into untrammelled spaces. "I don't see it as my role to make linear statements," she says. There are conceptual layers in this work. By confining her landscapes to the bounds of a house, she has created what philosopher Michel Foucault called 'heterotopias' — described by Neudecker as "spaces that are neither here nor there ... they are simultaneously physical and mental". The conscious framing in her work — by the limits of the human eye, the torch beam of a deep-sea vehicle or a doorway — adds to the disquiet generated by the compression of vast landscapes into humdrum domesticity.

Invisible Dust is becoming known for its subtle delivery of powerful messages. Its contemplative handling of environmental damage sprang, Sharp says, from discussions of nineteenth-century artist J. M. W. Turner's paintings of London, in which the vividly coloured skies clearly show the diffraction of sunlight caused by atmospheric pollution.

But some of today's pollutants — such as the minuscule particles discharged by car engines — are not so easily made visible. To draw attention to them, Invisible Dust curated 'Invisible Breath', a series of installations between 2010 and 2012. These included *Breathe* by artist Dryden Goodwin, a 'flickbook' video of drawings of a child breathing that was projected onto a huge screen on the roof of London's St Thomas' Hospital, opposite the Houses of Parliament.

Collaborations with the Tyndall Centre Newcastle and the UK Space Agency are planned. Invisible Dust is also teaming video artist Elizabeth Price — winner of the 2012 Turner Prize — with Hugh Mortimer, a planetary scientist at the Rutherford Appleton Laboratory in Didcot, UK, and a consultant on the science-fiction blockbuster *Prometheus* (Ridley Scott, 2012).

Sharp is developing a reputation for "bringing strong artists together with strong scientists", says Meroë Candy, a senior arts adviser at London's Wellcome Trust, one of the funders of Invisible Dust. And audiences for three of the Invisible Breath projects that it backed have vastly exceeded predictions. Organizers expected 30,000, but 300,000 came to see these visible manifestations of hidden, shifting change. ■

Daniel Cressey is a reporter for Nature.

Correspondence

Overhaul pesticide testing on bees

Political action is needed to address the adverse side effects of systemic pesticides on bees (*Nature* **496**, 408; 2013) by revising procedures for pesticide registration. The current risk-assessment process for these chemicals is outdated and does not incorporate important developments from the past 30 years.

To register a new pesticide in industrialized countries, the substance must be assessed for toxicity to the honeybee (*Apis mellifera*), which was originally chosen as a representative model of the Apoidea superfamily of some 20,000 bee species. However, the life histories of different bee species vary considerably. Unlike honeybees, most bee species are solitary, so individuals killed by pesticides are not easily replaced. There are 42 studies (source: Web of Science) reporting side effects of registered pesticides on other bee species, even though these passed risk assessment for honeybees. Tests need to be much more sensitive if they are to pick up all pesticide-related effects for bees as a whole.

Current risk assessments evaluate the survival of adult honeybees only after a short exposure to pesticide. However, numerous studies have stressed the importance of also testing for chronic toxicity, larval toxicity and sublethal effects of pesticides (N. Desneux *et al.* *Annu. Rev. Entomol.* **52**, 81–106; 2007).

More rigorous pesticide testing therefore needs to include a broader range of exposure scenarios and to take relevant biological traits into account. This will stand to improve insect pollination generally, which is currently worth about €153 billion (US\$202 billion) annually worldwide (N. Gallai *et al.* *Ecol. Econ.* **68**, 810–821; 2009).

Axel Decourtye Association for Technical Coordination in Agriculture (ACTA), Avignon, France.

Mickaël Henry French National Institute for Agricultural Research (INRA), Avignon, France.

Nicolas Desneux French National Institute for Agricultural Research (INRA), Sophia-Antipolis, France. nicolas.desneux@sophia.inra.fr

An open dialogue on solar engineering

We agree with Clive Hamilton that the use of geoengineering to counter climate change is a complex and controversial topic (*Nature* **496**, 139; 2013). This is precisely why it calls for wide-ranging, open, informed and objective discussion. This applies especially to research into solar radiation management (SRM) techniques, which may be quick, cheap, effective and risky.

That is why the SRM Governance Initiative (www.srmgi.org) was created: to ensure that any research undertaken is carefully considered, safe and transparent. It is a non-governmental organization convened by the Royal Society, the Environmental Defense Fund and TWAS, the academy of sciences for the developing world. It involves partner organizations from 16 countries, and has run meetings in Asia and Africa to seek the opinions of local members of the scientific community and others.

In the United States, the Bipartisan Policy Center in Washington DC has issued a report (go.nature.com/13ktv7) recommending that any geoengineering research programme should be supported by research governance that incorporates transparent peer-review and public deliberation.

A growing community of scientists and stakeholders are already taking into consideration

the serious implications of SRM technologies for governance, ethics and politics.

John Shepherd University of Southampton, UK.

jgs@noc.soton.ac.uk

Berhanu Abegaz African Academy of Sciences, Nairobi, Kenya.

Jane Long Bipartisan Policy Center, Washington DC; and Environmental Defense Fund, San Francisco, California, USA.

Oil-palm concerns in Brazilian Amazon

Brazil's Environmental Council of Pará State (COEMA) is debating a resolution to the new Brazilian Forest Code that will help to define 'low-impact' land uses in legally designated areas of permanent protection (APPs). One proposal is that plantations of oil palm (*Elaeis guineensis*), which are rapidly expanding in the eastern Amazon, might offer a sustainable option for restoring permanently protected areas. We have some concerns about this proposal.

Evidence from across the tropics (E. B. Fitzherbert *et al.* *Trends Ecol. Evol.* **23**, 538–545; 2008) shows that oil-palm plantations have a considerable impact on the environment because they require substantial agrochemical inputs and host few native species. Therefore, oil-palm plantations must not be allowed to displace natural forest vegetation and should not count as a component of the legally required forest reserves on private land.

We suggest that any approval from the COEMA that officially designates oil palm as a low-impact crop should await a full investigation into the biological and social effects of oil-palm cultivation in APPs. This will ensure that the biological function of these ecologically sensitive regions is not compromised, as the law demands.

Several other areas in Brazil would be more suitable for oil

palm — particularly degraded land, where the impact on biodiversity would be minimal.

Alexander C. Lees, Ima C. G.

Vieira Emilio Goeldi Museum, Belém, Pará, Brazil.

alexanderlees@btopenworld.com

Non-coding RNA foreseen 48 years ago

The recent enthusiasm for studying non-coding RNAs (*Nature* **496**, 127–129; 2013) brings to mind a largely forgotten review article that I wrote almost half a century ago in *Evolving Genes and Proteins* (V. Bryson and H. J. Vogel (eds) 469; Academic Press, 1965). This review reached a conclusion that was judged to be profoundly heretical at the time.

The article summarized years of work on the turnover of nuclear RNA, carried out during a period when pulse-labelled RNA was almost universally misdiagnosed as messenger RNA. It concluded: "Only a small proportion of the RNA made in the nucleus of animal and higher plant cells serves as a template for the synthesis of protein. This RNA is characterised by its ability to assume a form which protects it from intracellular degradation. Most of the nuclear RNA, however, is made on parts of the DNA which do not contain information for the synthesis of specific proteins. This RNA does not assume the configuration necessary for protection from degradation and is eliminated."

Henry Harris University of Oxford, UK.

henry.harris@path.ox.ac.uk

CORRECTION

The Comment article 'Choose satellites to monitor deforestation' (*Nature* **496**, 293–294, 2013) wrongly stated that more than one billion people in the tropics depend on forests. In fact, it is more than one billion people worldwide.

FORUM Nuclear physics

Exotic pear-shaped nuclei

The elusive pear shapes of certain nuclei, which are challenging to predict theoretically, have at last been measured precisely. Two experts offer their views on what the results mean for nuclear physics and particle physics. [SEE ARTICLE P.199](#)

THE PAPER IN BRIEF

- Atomic nuclei are not only spherical, but can be found in a variety of shapes — for example, squashed or stretched spheres.
- The existence of pear-shaped nuclei has long been predicted, but although some qualitative signatures of this nuclear shape have been found, only sparse quantitative information has been obtained.

- Using accelerated beams of heavy, radioactive ions, Gaffney *et al.*¹ have studied short-lived isotopes of radon and radium that are expected to be pear-shaped, and found a clear pear shape in the radium nucleus.
- The results have ramifications both for the understanding of nuclear structure and for testing the standard model of particle physics.

particles and those that are empty. Excitation of coherent correlated pairs of nucleons between these states drives the whole nucleus into a pear shape. Of all known nuclei, the isotopes of radon, radium, thorium and uranium are predicted to have the strongest octupole correlations of this type, leading to static pear shapes as the most bound configuration.

Although the existence of pear-shaped nuclei has been predicted for a long time², many of those anticipated to be the best candidates do not occur as stable nuclei in nature, so they have to be synthesized in a nuclear reaction before study. Practically, the nuclear charge distribution is a small rotating aerial, or antenna, so it radiates a special pattern of electromagnetic radiation. A pear-shaped antenna should emit enhanced electric-dipole and electric-octupole radiation patterns. In their study, Gaffney *et al.* report a direct measurement of these radiation patterns and their enhancement.

Their experiment is special: instead of using nuclei from the world around us, the authors tailor-made specific isotopes of radon and radium in a preparatory nuclear reaction. These special short-lived isotopes were harvested, prepared for acceleration by tearing off many of their electrons and then accelerated to about 10% of the speed of light as a beam of particles. The beams of heavy radioactive nuclei can then be scattered off thin metal foils to excite the antennas and make them radiate. This is the technique of Coulomb excitation — a purely electromagnetic technique for probing nuclear shapes

Novel nuclear antennas

C. J. (KIM) LISTER

At the centre of every atom lies a dense, highly charged nucleus containing 99.999% of the atom's mass. Although this has been known for 100 years — since Ernest Rutherford's discovery of the nucleus — there is still much that we do not understand about nuclei and nuclear matter. Gaffney *et al.* have improved our knowledge of nuclear structure by quantifying one specific and unusual nuclear shape.

In an atom, the static external electric field generated by the tiny central nuclear charge is spherical, so the cloud of electrons that defines its chemical and mechanical properties is always spherical. The nucleus, however, is very different. It generates its own binding field, driven by the strong force that exists between

all of its constituent nucleons (neutrons and protons). As such, nuclei have a much less well-defined 'centre'. Nuclei are easily polarized away from spherical shapes (Fig. 1) — in fact, more than one-third of all nuclei are bound most tightly if they settle away from sphericity and into elongated, axially symmetrical 'rugby ball' shapes.

Quantum correlations between the nucleons are expected occasionally to favour more exotic shapes, such as pears, bananas or pyramids, although few of these shapes have been proven to exist in nature. These special nuclei represent specific tests of such correlations, so experimental verification of exotic shapes allows a direct comparison of theoretical models to data. Gaffney and colleagues' study was specifically aimed at testing the octupole correlations that are predicted to lead to asymmetrical pear-shaped nuclei. These particular correlations arise only when a certain combination of quantum states straddles the Fermi surface, the boundary between states that are occupied by

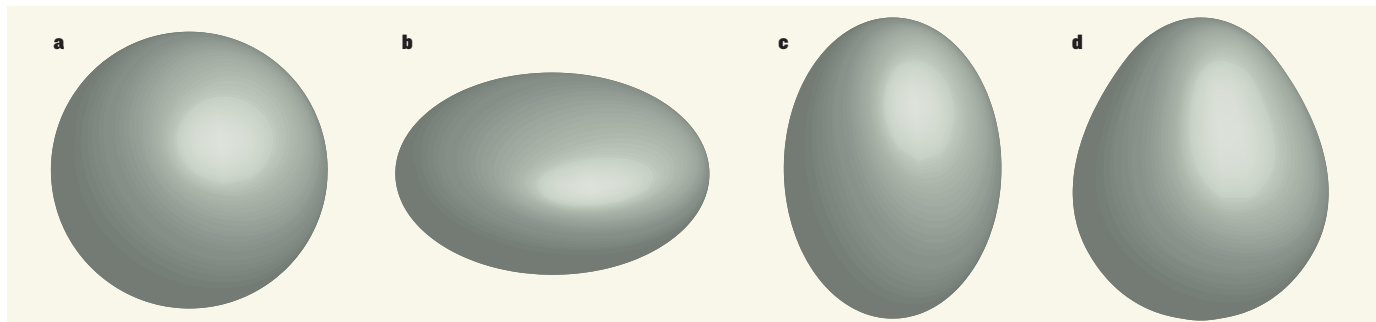


Figure 1 | Nuclear shapes. Nuclei can take several shapes, including a sphere (a), an oblate spheroid (b) and a prolate spheroid (c). Gaffney *et al.*¹ have observed the more exotic pear shape (d).

that is well understood. The authors found a lower boundary beyond which nuclei exhibit enhanced electric-octupole patterns: radon, which has a proton number (Z) of 86, showed only modest enhancement of these patterns, whereas radium ($Z = 88$) showed strong enhancement. The next heavier nuclei, thorium ($Z = 90$) and uranium ($Z = 92$), are expected to exhibit even stronger patterns, but we must await the next generation of accelerators to produce these nuclei in sufficient quantity to measure.

With new accelerators being built around the world with the aim of producing beams of exotic isotopes, and ever more sensitive detectors for measuring electromagnetic radiation patterns, we can expect more of this 'isotope tailoring' followed by Coulomb excitation. By picking out special and interesting features for study, these methods will allow us to gain a more profound understanding of how all nuclei really work. Beyond testing models of nuclear structure, pear-shaped 'drops' of nuclear matter do not have the same centre of mass and centre of charge. This effect is predicted to favour searches for static nuclear electric dipole moments and other new physical phenomena.

C. J. (Kim) Lister is in the Department of Physics and Applied Physics, University of Massachusetts, Lowell, Massachusetts 01854, USA.
e-mail: christopher_lister@uml.edu

Particle–physics laboratory

JONATHAN BUTTERWORTH

Gaffney and colleagues' results on exotic pear-shaped nuclei are of significance to the search for a putative permanent electric-dipole moment (EDM) in particles. Nuclei, like the protons and neutrons that comprise them, are complex objects made up of quarks, bound together by the exchange of gluons — the force carriers of the strong interaction. Because the interaction is strong, the equations that describe it cannot be solved using conventional approaches based on perturbation theory. Numerical techniques, principally lattice approximations in which space-time is broken up into discrete chunks on a lattice, have made much progress, but most of these particles' properties still cannot be calculated from first principles. For nuclei, it is even more complex than for protons and neutrons, and many different approximations are applied to try to understand nuclear structure.

Given all of this, it may come as a surprise that such objects can be excellent laboratories

for studying the standard model — the theory that elegantly encapsulates everything we know about elementary particles and fundamental forces. Perhaps most famously, the smashing together of protons at CERN's Large Hadron Collider near Geneva, Switzerland, led to the discovery of a Higgs boson, and has extended the possible validity of the standard model to a new range of high energies. But on much smaller energy scales, precision experiments use nuclei too. For example, searching for rare nuclear decays is the only way to discover whether the neutrino is its own antiparticle. And searching for an EDM of any particle, including a nucleus, is an indirect probe of physics beyond the standard model³, through one of its key underlying approximate symmetries — time reversal (T). The current limits on the EDM of mercury nuclei⁴ are among the most stringent.

The standard model is approximately invariant under T symmetry. This means that most individual, fundamental interactions between particles work equally well backwards and forwards. There is also a theorem, called CPT invariance, that states that all fundamental interactions are invariant if you swap particles for antiparticles (charge, C), swap left for right (parity, P) and swap forwards in time for backwards (T). Thus, breaking T symmetry, as an EDM would do, implies breaking CP symmetry too, so that CPT symmetry can still hold overall.

The CPT theorem connects the hunt for an EDM to the hunt for matter–antimatter asymmetry. Although there is a small amount of CP -symmetry violation in the standard model, it is not enough to explain why we live in a matter-dominated Universe, with so little antimatter around. Many theories of physics beyond the standard model introduce new

sources of CP violation, in part to deal with this. As a result, they also violate T symmetry, and often give particles a relatively large EDM.

To see why an EDM violates T symmetry, one has to consider the fact that a particle generally has a magnetic dipole moment (MDM), which can be thought of as being due to a tiny current flowing in a circle, or to the particle spinning. And there is a contribution to the particle's energy that depends on the relative alignment of the EDM and the MDM. If T is reversed, the current flows in the opposite direction, so the MDM changes direction. But the EDM remains unchanged. So the alignment between the two has changed, the energy has changed and the symmetry is broken.

The structure of the nucleus cannot itself generate an EDM, at least not in the standard model. However, if a small EDM exists, it can be amplified by distortions in the shape of the nucleus, such as the pear shapes reported by Gaffney and colleagues. This means that, in evaluating how sensitive an EDM search really is to physics beyond the standard model, or indeed to understanding the implications should an EDM be measured, a good understanding of these kinds of exotic nuclear shapes is essential. The authors' results look like a big step forward. ■

Jonathan Butterworth is in the Department of Physics and Astronomy, University College London, London WC1E 6BT, UK.
e-mail: j.butterworth@ucl.ac.uk

1. Gaffney, L. P. *et al.* *Nature* **497**, 199–204 (2013).
2. Leander, G. A. *et al.* *Nucl. Phys. A* **388**, 452–476 (1982).
3. Fukuyama, T. *Int. J. Mod. Phys. A* **27**, 1230015 (2012).
4. Griffith, W. C. *et al.* *Phys. Rev. Lett.* **102**, 101601 (2009).

GALAXY FORMATION

The cosmic web in focus

Detection of the trace neutral fraction of hydrogen gas that stretches between the nearby Andromeda and Triangulum galaxies has allowed resolved spectral imaging of this elusive intergalactic medium. SEE LETTER P.224

ROBERT BRAUN

The historical concept that galaxies are 'island universes' that formed in the distant past and have since evolved in isolation from their surroundings has long been recognized as inadequate. That model was replaced by the hierarchical growth scenario^{1,2}, which highlights the role of galaxy interactions, collisions and mergers in shaping the mature galaxies that we see today. But as Wolfe *et al.*³ report on page 224 of this issue, it could be

argued that another model is now taking precedence, in which a diffuse 'cosmic web' between the discrete galaxies is the dominant reservoir for continued galaxy growth and evolution.

The impetus for looking further than the hierarchical growth scenario to better explain galaxy evolution has come from simple observational evidence. Over the past decade, it has become clear that the rate at which stars are forming in the Universe has varied markedly with time, first increasing to a peak some 10 billion years ago and then declining more

than tenfold to the modest levels of today^{4,5}. At the same time, the total amount of hydrogen in the atomic phase, which forms the basic fuel for star formation, has declined by only about half^{6,7}. How can that be? To compound the mystery, measurements of the capacity of atomic-gas reservoirs and the rates of hydrogen-gas consumption by galaxies have shown that, surprisingly, the timescale for complete gas depletion is typically rather short, only a few billion years⁸. This is true for a wide range of galaxy types⁹, including spiral galaxies such as our own, which seem to have been consuming gas at a relatively constant rate over a large fraction of the Universe's 13.8-billion-year history¹⁰.

The answer to this mystery apparently lies on our Galactic doorstep, having been revealed by observations of our two nearest major galaxies — the Andromeda and Triangulum galaxies. The gas reservoir that fuels star formation through cosmic time may reside not in the galaxies themselves, but rather in their extended surroundings. What is more, in contrast to what has previously been assumed, this reservoir may not be in the form of atomic hydrogen at all, but instead in the form of ionized hydrogen. Numerical simulations of increasing precision^{11,12} suggest that, at the current cosmic epoch, about one-third of all baryonic (ordinary) matter in the Universe has been processed into the condensed form we know as galaxies, with two-thirds still residing in filaments of ionized gas in the intergalactic medium (Fig. 1). It is the gradual condensation of this ionized gas that seems to dominate the process of galactic-mass assembly, rather than the episodic interaction and merger of condensed (proto-) galaxies.

Although this solution to the galaxy-assembly enigma is appealing in its simplicity, it has proved surprisingly difficult to verify experimentally. The difficulty arises because diffuse ionized hydrogen is almost invisible. Regions of ionized hydrogen emit radiation called thermal Bremsstrahlung and recombination radiation, which has a brightness that is proportional to the square of the gas density. Although such emission from the high-density regions of massive star formation in our own and other galaxies is extremely bright, once the density has declined by a factor of 10^5 (the levels that apply to the intergalactic regime) the brightness has fallen by about 10^{10} and become almost undetectable. The first heroic efforts at detecting this medium directly are only beginning to achieve some, albeit limited, success¹³.

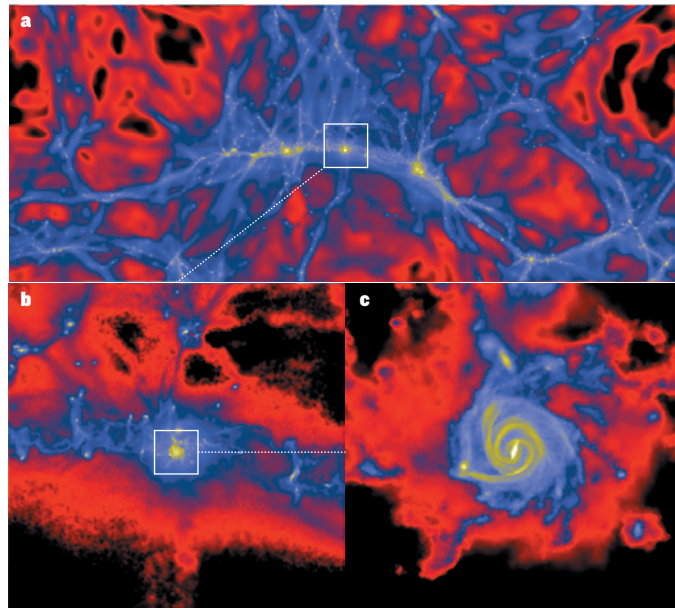


Figure 1 | Galactic-mass assembly. Numerical simulations of galaxy formation and evolution, such as the one shown here¹⁷, suggest that the assembly of mass in galaxies is dominated by the gradual condensation and accretion of ionized gas organized as filaments in the intergalactic environment. In this sequence of zoomed images (a–c), the colour map is different for each zoom level, but in all images green denotes higher gas density and black denotes lower density. A spiral galaxy with a bar-shaped central structure is seen in c. Wolfe *et al.*³ have detected the trace neutral fraction of the intergalactic gas that lies between the nearby Andromeda and Triangulum galaxies.

An alternative strategy, which Wolfe *et al.* employ, makes use of the fact that the amount of hydrogen ionization is never 100% under intergalactic conditions. Even in the case in which the hydrogen gas is smoothly distributed, so that it is illuminated by ionizing radiation from all directions, there will be a small but finite neutral fraction¹⁴ that can be as much as 1%. The neutral fraction would be further enhanced under conditions of gas clumping, which would provide directional shielding against the ionizing radiation. Wolfe and colleagues' strategy consists of mapping the 21-centimetre emission of the trace neutral fraction to allow resolved spectral imaging of this elusive medium between the Andromeda and Triangulum galaxies.

Although 21-cm emission has been used extensively to document the atomic-gas content and kinematics of galaxies in the nearby Universe¹⁵, this has normally been undertaken in the high-density, fully neutral gas regime. Extending such studies to the low-density, highly ionized realm, in which atomic densities are a factor of 10^4 or more lower, is extremely challenging. What makes this approach feasible at all is the fact that the brightness of 21-cm emission varies only linearly with gas density, rather than as the square of it that applies to the ionized emission tracers. Even so, the required precision for its detection is at the very limits of what is possible with current technology.

Wolfe and colleagues' confirmation of the first detection¹⁶ of 21-cm radiation in this regime represents a milestone in the application of this approach to cosmic-web imaging. Their demonstration opens the door for broader application of the method to document the location and kinematics of the densest filaments of ionized gas in the environments of other nearby galaxies. Such imaging should give a clear picture of the evolutionary state of individual galaxies and galaxy groups. It should also provide evidence for feedback processes, such as galactic outflows, that may have shaped the galaxies' broader environment.

However, the pinnacle of this research endeavour — confirmation of the total mass of gas in the intergalactic volume — will require further forms of observation to supplement the 21-cm imaging. Also required is determination of the amount of ionization, so that the total mass can be deduced. Although it is unlikely that high precision would be achieved in such a combined observation, it would still be a major advance in

overcoming our current ignorance about two-thirds of the baryonic matter in the cosmos. ■

Robert Braun is at CSIRO Astronomy and Space Science, Epping, New South Wales 1710, Australia.

e-mail: robert.braun@csiro.au

1. Davis, M. *et al. Astrophys. J.* **292**, 371–394 (1985).
2. Stewart, K. R., Bullock, J. S., Wechsler, R. H., Maller, A. H. & Zentner, A. R. *Astrophys. J.* **683**, 597–610 (2008).
3. Wolfe, S. A., Pisano, D. J., Lockman, F. J., McGaugh, S. S. & Shaya, E. J. *Nature* **497**, 224–226 (2013).
4. Madau, P., Ferguson, H. C. & Dickinson, M. E. *Mon. Not. R. Astron. Soc.* **283**, 1388–1404 (1996).
5. Hopkins, A. M. & Beacom, J. F. *Astrophys. J.* **651**, 142–154 (2006).
6. Noterdaeme, P., Petitjean, P., Ledoux, C. & Srianand, R. *Astron. Astrophys.* **505**, 1087–1098 (2009).
7. Braun, R. *Astrophys. J.* **749**, 87 (2012).
8. Wong, T. & Blitz, L. *Astrophys. J.* **569**, 157–183 (2002).
9. Bigiel, F. *et al. Astrophys. J.* **730**, L13 (2011).
10. Ade, P. A. R. *et al.* Preprint at <http://arxiv.org/abs/1303.5076> (2013).
11. Davé, R. *et al. Astrophys. J.* **552**, 473–483 (2001).
12. Kereš, D., Katz, N., Fardal, M., Davé, R. & Weinberg, D. H. *Mon. Not. R. Astron. Soc.* **395**, 160–179 (2009).
13. Simionescu, A. *et al. Science* **331**, 1576–1579 (2011).
14. Dove, J. B. & Shull, J. M. *Astrophys. J.* **423**, 196–206 (1994).
15. Walter, F. *et al. Astron. J.* **136**, 2563–2647 (2008).
16. Braun, R. & Thilker, D. A. *Astron. Astrophys.* **417**, 421–435 (2004).
17. Vogelsberger, M., Sijacki, D., Kereš, D., Springel, V. & Hernquist, L. *Mon. Not. R. Astron. Soc.* **425**, 3024–3057 (2012).

STRUCTURAL BIOLOGY

Security measures of a master regulator

At last, the crystal structure is revealed for the catalytically active mTOR kinase enzyme, a master regulator of cell growth. The structure indicates a gatekeeper mechanism that controls substrate access to the active site. [SEE ARTICLE P.217](#)

DARIO R. ALESSI & YOGESH KULATHU

Whether or not a cell grows is decided by a remarkable protein kinase enzyme called mTOR. As part of two complexes, mTORC1 and mTORC2, mTOR integrates and interprets all sorts of factors that influence cell growth — including nutrients, stressors and the outputs of signal-transduction networks — by targeting a multitude of substrates that drive processes such as protein translation, metabolism and cell division. Research into mTOR-mediated signalling has taken on added urgency since it was discovered that most cancers contain mutations that inappropriately activate this protein¹. In an eagerly awaited study published in this issue, Yang *et al.*² (page 217) report the crystal structure of the part of mTOR that has enzymatic activity and encompasses many of its crucial domains (the FAT, FRB, catalytic core and FATC domains), in complex with mLST8, a component of both mTORC1 and mTORC2*.

The authors' stunning structure, at 3.2 ångströms resolution, comprises some 1,500 amino-acid residues and reveals how mTOR, an atypical member of the phosphoinositide kinase-related kinase family, is evolutionarily related to a group of lipid phosphoinositide 3-kinases and to other phosphoinositide kinase-related kinases (ATR, ATM, DNA-PKcs, SMG1 and TRRAP). It also shows that the 600-residue FAT domain consists mostly of α -helical repeats, which wind like a twisted telephone wire to form a C-shaped lobe around a kinase domain (Fig. 1a, b). Like all other kinases so far described, at its core mTOR possesses the characteristic N and C bi-lobal architecture. However, the kinase domain is roughly 300 residues larger than those of most kinases.

The immunosuppressant drug rapamycin inhibits mTORC1 — and hence signalling downstream of mTOR — by binding to the protein FKBP12. Yang *et al.* find that the additional residues in the kinase domain of mTOR include a 100-residue FRB region located in the N lobe. And in the C lobe, a 40-residue insertion called LBE interacts with mLST8. This creates a network of

stabilizing interactions that probably explains why mLST8 is indispensable for mTOR activity³. The 35-residue FATC domain at the carboxy terminus forms an integral part of the C lobe and is packed against the activation loop.

Most kinases can readily switch between an inactive 'open' conformation and an active 'closed' conformation in response to various signals. By contrast, the mTOR structure shows that its kinase domain has an intrinsically active conformation, in which the catalytic residues and ATP (the molecule that provides phosphate groups) are poised to phosphorylate substrates. But how is the activity of the always-active mTOR controlled? It seems that the FRB domain operates as a gatekeeper of the active site, perhaps preventing access to all but genuine substrates.

Yang *et al.* also provide evidence that FRB interacts with specific residues (those close to

the threonine residue at position 389) in one of its substrates, S6K1, and that this markedly enhances phosphorylation of S6K1 at this threonine residue. Intriguingly, the substrate-binding region on FRB is also the binding site of the FKBP12–rapamycin complex. Therefore, the mechanism by which the FKBP12–rapamycin complex inhibits mTOR probably involves sequestering the FRB docking site and physically blocking substrate access to the catalytic cleft of mTOR.

The authors' detailed sequence inspection shows that some of the mTOR-related kinases (such as DNA-PKcs, SMG1 kinase and TRRAP) contain an FRB-like insertion. It would be fascinating to learn whether the FRB-like domain in these enzymes also participates in substrate recruitment and whether inhibitors similar to rapamycin can be used to target these domains.

The structure lacks the amino-terminal residues that bind regulatory subunits such as RAPTOR (in mTORC1) and RICTOR (in mTORC2). These subunits might be important for controlling the localization and recruitment of substrates to mTOR complexes¹. For example, most mTORC1 substrates have a docking site termed the TOS motif, and RAPTOR recognizes this motif⁴.

Yang *et al.* present an attractive model (Fig. 1c) for substrate selectivity by mTORC1: initially, RAPTOR recognizes substrates through their TOS motifs and recruits them, and then FRB functions as a secondary, fine-tuning docking site, recognizing residues that

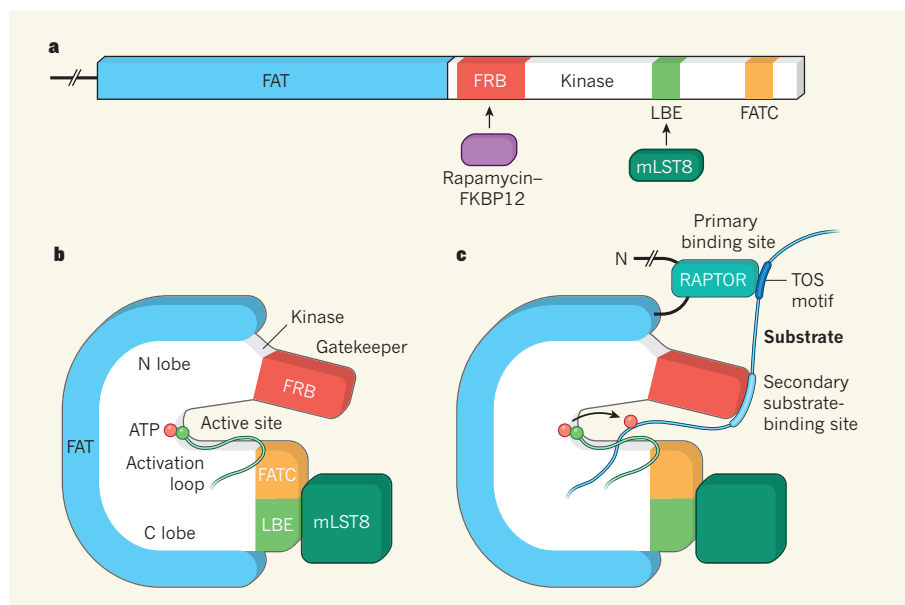


Figure 1 | mTOR simplified. **a**, Domain organization of the C-terminal portion of mTOR, spanning the FAT and kinase domains² (FRB, LBE and FATC). The structure of the mTOR–mLST8 complex shows that the FKBP12–rapamycin binding (FRB) site is an integral part of the kinase domain, and that mLST8 interacts with the LBE region. **b**, In three dimensions, the FAT domain wraps around the kinase domain, and the FRB site and mLST8 locate to opposite ends of the catalytic cleft to restrict substrate access to the active site. ATP binds to the kinase domain, close to the activation loop, and is the source of phosphate groups for substrate phosphorylation. **c**, For substrate binding, the RAPTOR component of the mTORC1 complex binds to the N terminus of mTOR and creates the primary binding site for the TOS motif of substrates. The FRB domain forms a secondary substrate-binding site, acting as a gatekeeper to provide privileged access to bona fide substrates.

*This article and the paper under discussion were published online on 1 May 2013.



50 Years Ago

The emphasis on eugenics as the point of application of molecular biology overlooks the most immediate prospects for the understanding and then control of human development. To dramatize the antinomy, I propose the term 'euphenics' as the counterpart of 'eugenics' in the same sense that 'phenotype' is opposed to 'genotype'... Man's control of his own development, 'euphenics', transmutes the means, and also the ends of eugenics, as have all the precedent cultural revolutions that have shaped the species: language, agriculture, political organization, the physical technologies.

From *Nature* 4 May 1963

100 Years Ago

Practical men are at length beginning to realise that the utilisation of the store of potential energy in coal by more rational methods than have hitherto prevailed is a problem that has to be grappled with seriously if our supremacy in the chief manufactured products of the world is to be maintained... Enormous economies might be effected if more scientific—that is, more common-sense—methods were employed in the consumption of coal... It has been calculated that our annual consumption of coal is from 143 to 168 million tons per annum, of which from 30 to 36 million tons are used for domestic purposes. Of this huge amount it is estimated that from 40 to 60 million tons are practically wasted... The subject, indeed, is admittedly of national importance, but the fear is that this country will only waken up to the full significance of that fact when the pinch of necessity has tightened to a real grip—so tight, indeed, that it will be too late to shake it off.

From *Nature* 1 May 1913

lie close to the substrate phosphorylation site before guiding it into the mTOR active site. The authors suggest that this two-part substrate-recruitment mechanism facilitates substrate selectivity and entry into the otherwise restricted catalytic site. It might also provide an additional layer of regulation to ensure that mTOR does not inappropriately phosphorylate non-physiological substrates that do not possess a TOS motif and an FRB-binding domain.

In cancer cells, several mutations that hyperactivate mTOR have been identified in the FAT domain and its interface with the kinase domain⁵. Yang and colleagues argue that these mutations cluster to regions that control substrate access and loosen the structural skeleton, including the FRB domain, which otherwise restricts substrate admission to the active site.

There are more than 250 clinical trials in progress or planned to evaluate the efficacy of diverse mTOR inhibitors as anticancer agents⁶. Yang *et al.* have crystallized mTOR with a highly specific inhibitor (Torin2), as well as with two other, less selective compounds⁷ (PP242 and PI-103). These compounds bind and inhibit mTOR in markedly different ways, providing a wealth of information on features of the mTOR active site that will undoubtedly be exploited to develop even more potent and selective inhibitors.

Previous work⁸ showed that the complete mTORC1 complex is a dimer with a striking empty central cavity, which was proposed to facilitate substrate access. The same paper also found that rapamycin treatment caused

disassembly of mTORC1 subunits. The current study provides no insight into how kinase activity and substrate phosphorylation would be affected by mTORC1 dimerization, nor does it suggest how rapamycin could induce complex disassembly.

Further work is also required to uncover why rapamycin does not inhibit mTORC2. Also, much remains to be understood about how RAPTOR and RICTOR sense the diverse upstream signals that continuously bombard mTOR complexes, and how this information is coupled to mTOR activation and substrate access to its active site. Fruitful knowledge is to be gained from research in this area, especially from structural analysis of even larger mTOR fragments in complex with other subunits. ■

Dario R. Alessi and Yogesh Kulathu are at the MRC Protein Phosphorylation and Ubiquitylation Unit, College of Life Sciences, University of Dundee, Dundee DD1 5EH, UK. e-mails: d.r.alessi@dundee.ac.uk; y.kulathu@dundee.ac.uk

1. Laplante, M. & Sabatini, D. M. *Cell* **149**, 274–293 (2012).
2. Yang, H. *et al.* *Nature* **497**, 217–223 (2013).
3. Kim, D. H. *et al.* *Mol. Cell* **11**, 895–904 (2003).
4. Schalm, S. S. & Blenis, J. *Curr. Biol.* **12**, 632–639 (2002).
5. Hardt, M., Chantaravissut, N. & Tamanoi, F. *Genes Cells* **16**, 141–151 (2011).
6. Wander, S. A., Hennessy, B. T. & Slingerland, J. M. *J. Clin. Invest.* **121**, 1231–1241 (2011).
7. Liu, Q. *et al.* *J. Biol. Chem.* **287**, 9742–9752 (2012).
8. Yip, C. K., Murata, K., Walz, T., Sabatini, D. M. & Kang, S. A. *Mol. Cell* **38**, 768–774 (2010).

IMMUNOLOGY

Memory cells sound the alarm

In a finding that could have implications for vaccine design, memory immune cells at mucosal surfaces have been shown to respond to encounters with pathogens by issuing signals that recruit other memory cells to the site.

JENNIFER E. SMITH-GARVIN & LUIS J. SIGAL

The immune system clears pathogens it has encountered before more efficiently than those of an initial infection because specialized cells, known as memory cells, can remember and rapidly eliminate them. This process is the bedrock of all vaccines. Writing in *Nature Immunology*, Schenkel *et al.*¹ show that, in mice, a small number of memory cells that reside near sites of pathogen entry sound an alarm that recruits more memory cells from the blood to rapidly boost defences at the front line of a subsequent infection.

Most infections are initiated by pathogens

that breach epithelial surfaces, such as the skin and the mucous membranes that line the genital, respiratory and gastrointestinal tracts. The immune system responds through the orchestrated actions of innate and adaptive immune cells. Innate cells are distributed throughout the body in large numbers; they can immediately identify and respond to pathogens, but they lack specificity and often fail to control an infection on their own. However, the B cells and T cells of the adaptive immune system have surface receptors that allow them to respond in a specific manner; they also have diverse mechanisms to eliminate infections. For example, in the case of CD8⁺

T cells, receptor binding by a specific pathogen activates the cells such that they start producing immunomodulatory cytokine proteins and acquire a killing function. However, adaptive cells that are specific to any one pathogen are exceedingly rare and, to function, they first need to proliferate. This takes time, and so, in the meantime, innate immune cells attempt to control pathogen spread.

An important function of innate cells is to produce chemokines, a subset of cytokines that attracts other immune cells to the site of infection (Fig. 1a). In addition, some innate cells travel through the 'highways' of the lymphatic system to bring pathogens or pathogen debris to nearby lymph nodes and other lymphoid organs, where naive B and T cells (those that have not yet been activated) normally reside. Here, the few B and T cells that recognize the pathogen undergo massive proliferation, become activated and migrate to the site of initial infection. For pathogens that remain at this site, such as papillomaviruses or the influenza virus, this response may be enough to eliminate the infection. However, many pathogens, including the viruses that cause chickenpox, smallpox and measles, can proliferate in the lymph nodes and escape through lymph vessels to access the circulatory system and invade other organs^{2,3}. In such cases, CD8⁺ T cells must enter those organs to eliminate the pathogen.

Although most of the responding CD8⁺ T cells die after an infection subsides, a fraction of pathogen-specific, but deactivated, cells persists at frequencies that are substantially higher than before the infection. Some of these memory cells take up residence in lymphoid organs, others circulate in the blood and yet others remain in non-lymphoid tissues as resident memory T cells (T_{RM} cells)^{4,5}. T_{RM} cells can be found in skin and mucosal tissues, and are able to rapidly secrete cytokines and kill infected cells on recognition of a pathogen⁴ (Fig. 1b). Thus, these memory cells are spatially and temporally poised to be the first line of defence against reinfection. Studies in mice have shown^{6,7} that T_{RM} cells in the skin and vaginal tract can limit viral spread during localized infection. Now, Schenkel *et al.* show how T_{RM} cells communicate with circulating memory cells to swell the cellular army for battle at the site of a recall infection.

Schenkel and colleagues provide strong evidence that, like innate immune cells, T_{RM} cells in the vaginal mucosa have an alarm function — by rapidly producing the cytokine IFN- γ , the T_{RM} cells induce surrounding innate immune cells and vascular cells to express chemokines. One of these chemokines is CXCL9, a molecule that has been shown to attract T cells to the vaginal tract⁶. The authors observed that, by sounding the IFN- γ alarm, T_{RM} cells rapidly recruit large numbers of additional memory CD8⁺ T cells from the blood to the site of infection. Notably,

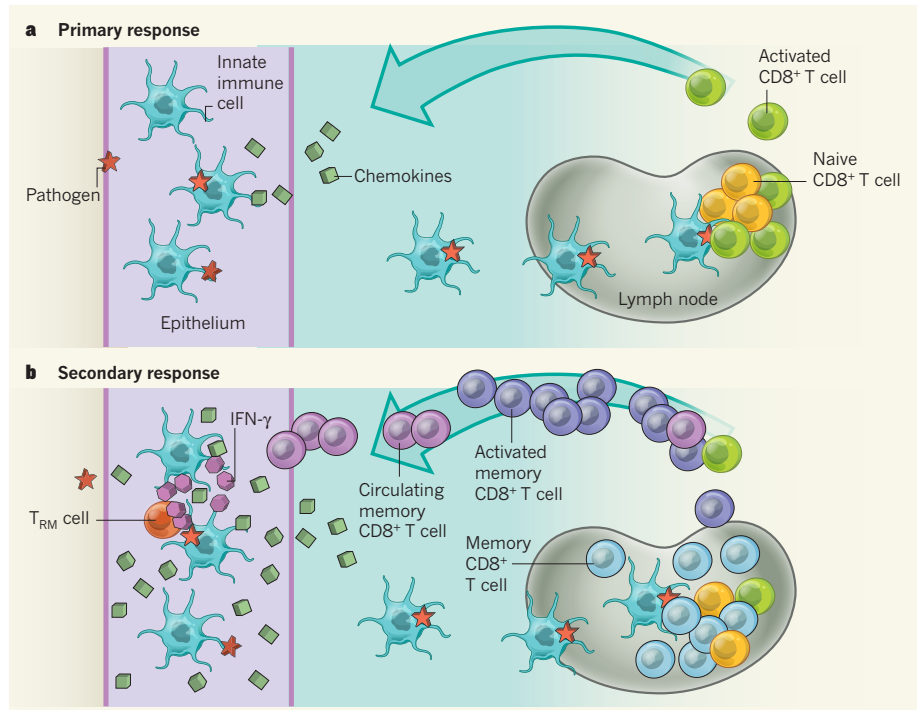


Figure 1 | Cytokine alarms accelerate memory T-cell recruitment. **a**, During a primary immune response, innate immune cells in the body's epithelial surfaces attempt to control the pathogen, and secrete chemokine proteins that sound an alarm to cells of the adaptive immune system. If the pathogen breaches this first line of defence and enters the lymph nodes, it will activate the few naive CD8⁺ T cells that specifically recognize it. These cells proliferate and are attracted to the site of infection by the chemokines. **b**, After infection, some pathogen-specific CD8⁺ T cells survive in lymphoid organs and as circulating or tissue-resident memory (T_{RM}) T cells. During a secondary response, T_{RM} cells act rapidly at the site of infection and, if the pathogen enters the lymph node, resident memory CD8⁺ T cells are activated, and rapidly proliferate to curb further pathogen spread from the lymph node and to migrate to infected tissues. Schenkel *et al.*¹ show that, in addition to their direct function on infected cells, T_{RM} cells send out an alarm. They secrete the cytokine IFN- γ , which induces chemokine production by the surrounding cells to draw circulating memory CD8⁺ T cells into the infected tissue before the response in the lymph node occurs.

the T_{RM} -cell-induced chemokine response was faster and larger than that of an innate response. Furthermore, only memory CD8⁺ T cells, which are poised for a rapid response, were recruited; naive CD8⁺ T cells were not. It should be noted, however, that after immunization and rechallenge of mice with the vaccinia virus, T_{RM} cells in the skin reduce viral proliferation in the absence of circulating T cells⁷; this suggests that the alarm function is absent or dispensable in some infection circumstances. Thus, future studies should determine the relevance of this alarm function in different tissues and disease settings.

By activating their own effector functions and calling additional memory CD8⁺ T cells to the site of infection, it is possible that T_{RM} cells not only directly and indirectly decrease infection at the primary site, but also reduce pathogen spread to the lymph nodes. Memory CD8⁺ T cells in the lymph nodes curb the spread of viruses to the blood and other organs^{8,9}. By reducing spread to lymph nodes, T_{RM} cells might reduce some of their burden. In the end, the more roadblocks the immune system creates to prevent pathogen spread, the fewer chances there are for a

pathogen to cause disease.

Vaccines that induce T_{RM} cells could prove to be effective against pathogens that are resistant to existing vaccine strategies. Indeed, work in mice has shown⁶ that, after vaccination, a population of T_{RM} cells specific for herpes simplex virus 2 can be established in the vaginal mucosa by topical application of CXCL9, and that this results in reduced spread of this virus after subsequent infection. Schenkel and colleagues' findings suggest that, for an optimal front-line response, vaccines should induce both a T_{RM} -cell population and circulating memory T cells that can respond to the T_{RM} cells' alarm. ■

Jennifer E. Smith-Garvin and Luis J. Sigal are at the Research Institute of Fox Chase Cancer Center, Immune Cell Development and Host Defense Program, Philadelphia, Pennsylvania 19111, USA.
e-mail: luis.sigal@fccc.edu

- Schenkel, J. M., Fraser, K. A., Vezys, V. & Masopust, D. *Nature Immunol.* **14**, 509–513 (2013).
- Virgin, H. W. in *Fields' Virology* Vol. 1 (eds Fields, B. N., Knipe, D. M. & Howley, P. M.) 335–336 (Wolters Kluwer/Lippincott Williams & Wilkins, 2007).
- Flint, S. J., Enquist, L. W., Racaniello, V. R. & Skalka, A.

- A. M. *Principles of Virology* 3rd edn (ASM Press, 2009).
4. Gebhardt, T. & Mackay, L. K. *Front. Immunol.* **3**, 340 (2012).
5. Jameson, S. C. & Masopust, D. *Immunity* **31**, 859–871 (2009).

6. Shin, H. & Iwasaki, A. *Nature* **491**, 463–467 (2012).
7. Jiang, X. *et al.* *Nature* **483**, 227–231 (2012).
8. Remakus, S. *et al.* *Cell Host Microbe* (in the press).
9. Xu, R. H., Fang, M., Klein-Szanto, A. & Sigal, L. J. *Proc. Natl Acad. Sci. USA* **104**, 10992–10997 (2007).

contact and adhesion between myoblasts and the developing myofibres called myotubes, with related and novel proteins continuing to be identified^{1,2}. It remains unclear how the different receptors contribute to and coordinate the fusion process.

Previous studies^{6–8} have linked exposure of phosphatidylserine on myoblasts to the enhancement of fusion, yet the receptor mediating this signal has not been identified. Hochreiter-Hufford *et al.* asked whether BAI1 might transduce the phosphatidylserine signal during mammalian myoblast fusion. They find that the levels of this receptor increase during fusion *in vitro*, and that it is expressed in actively fusing myotubes *in vivo*. Moreover, increasing the expression of BAI1 enhanced fusion in an ELMO/Dock180/Rac1-dependent manner *in vitro*, indicating that the signalling pathway downstream of this receptor is intact (Fig. 1).

The authors also report that BAI1 seems to be required for muscle development and repair *in vivo*. The muscles of mice lacking the *Bai1* gene were fully formed but were smaller than those of control animals. And after injury, the regenerating muscles of the mutant mice remained smaller and contained fewer centrally localized nuclei; centrally positioned nuclei are a hallmark of muscle repair⁹. That muscles can still undergo some fusion in the

absence of BAI1 suggests that the BAI1-related proteins BAI2 and/or BAI3, which are also expressed in muscle, may compensate for its loss.

Contact between apoptotic cells and myotubes has been documented^{4,7} during normal muscle development *in vivo*. Hochreiter-Hufford and co-workers show that phosphatidylserine externalization, together with the activity of the caspase enzymes that mediate apoptosis, are necessary to enhance fusion. In agreement with previous work¹⁰, they find that inhibiting caspase activity using a pan-caspase inhibitor blocks fusion *in vitro*. Strikingly, the researchers could overcome this inhibition by adding apoptotic myoblasts, or even apoptotic thymocytes — unrelated cells belonging to the blood lineage. Thus, various types of apoptotic cell can provide a cue to healthy muscle cells to promote fusion.

Hochreiter-Hufford *et al.* did not observe fusion between apoptotic myoblasts and myotubes, whereas earlier work^{7,8} indicated that even non-apoptotic myoblasts show a feature of apoptosis, transiently externalizing phosphatidylserine before fusion. It could be that different cell populations contribute to fusion: fusion-capable myoblasts transiently expose

CELL BIOLOGY

Death brings new life to muscle

Fusion of muscle cells called myoblasts underlies the generation and maintenance of skeletal muscle throughout an animal's life. Emerging data indicate that cell death acts as a signal to enhance these processes in mammals. SEE LETTER P.263

SHANNON F. YU & MARY K. BAYLIES

The multinucleated myofibres that comprise skeletal muscle are generated from the iterative fusion of mononucleated myoblasts. During muscle development, myoblast fusion is mediated by an evolutionarily conserved signalling pathway that alters the actin cytoskeleton^{1,2} — a network of filaments that controls cellular movement and organization. A second, but related, pathway that regulates the actin cytoskeleton drives phagocytosis, the process by which phagocytic cells engulf dead cells³. On page 263 of this issue, Hochreiter-Hufford *et al.*⁴ show that the phagocytic pathway also contributes to myoblast fusion. Specifically, they find that the presence of cells dying by the process of apoptosis, and a receptor that recognizes these dying cells, potentiate myoblast fusion during muscle development, regeneration and repair*.

The phospholipid phosphatidylserine is normally present in the inner leaflet of the cell membrane, but serves as an 'eat me' signal when exposed on the outer leaflet in apoptotic cells (Fig. 1). On phagocytic cells, BAI1, the seven-pass transmembrane receptor for phosphatidylserine, signals through the conserved ELMO/Dock180/Rac1 signalling pathway to regulate the downstream actin cytoskeleton network and promote engulfment of dying cells⁵.

In the fruitfly *Drosophila*, four transmembrane receptors mediate myoblast adhesion, which

subsequently activates the ELMO/Myoblast city/Rac signalling module. (Myoblast city is the *Drosophila* version of Dock180.) At the site of myoblast–myoblast contact, this module remodels the actin cytoskeleton to drive fusion. The ELMO/Dock180/Rac1 module is conserved in zebrafish and mammals. In mammals, however, numerous receptors have been found that mediate myoblast–myoblast

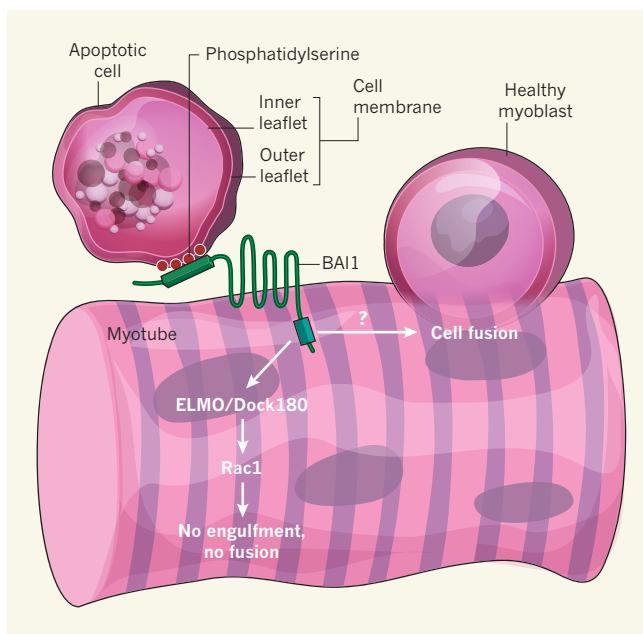


Figure 1 | Helping hand from a dying cell. Exposure of phosphatidylserine on the outer leaflet of the cell membrane, rather than its normal location in the inner leaflet, marks apoptotic cells for engulfment by phagocytic cells (not shown). During phagocytosis, phosphatidylserine is recognized by the membrane receptor BAI1, which normally signals through the ELMO/Dock180/Rac1 pathway to drive actin cytoskeleton rearrangements and engulfment of apoptotic cells³. In muscle cells, however, this pathway does not lead to engulfment of apoptotic cells. But Hochreiter-Hufford *et al.*⁴ report that phosphatidylserine–BAI1 signalling also enhances myoblast fusion — with healthy myoblasts and with the multinucleated myotubes — in an ELMO/Dock180/Rac1-dependent manner. The precise mechanism by which this occurs remains unclear, but it does not require fusion or engulfment of the apoptotic cell.

*This article and the paper under discussion were published online on 24 April 2013.

phosphatidylserine without undergoing apoptosis; and dying myoblasts (and other cell types) enhance the fusion of healthy myoblasts without participating in fusion themselves. Indeed, as noted earlier, apoptotic mouse thymocytes, a cell type that does not fuse, could restore fusion in caspase-inhibited myoblasts. It is not clear how phosphatidylserine is presented by apoptotic cells and non-apoptotic cells so as to allow fusion of the latter but not of the former. Additional phosphatidylserine-binding proteins are required for myoblast fusion *in vitro*¹¹, suggesting that phosphatidylserine may affect parallel, yet different, pathways during myoblast fusion.

If the apoptotic cells are not fusing with myotubes, how is the phosphatidylserine–BAI1 signal integrated with the other elements of the fusion machinery? It is likely that, in this case, BAI1 is not participating in the regulation of actin necessary for cell fusion, despite the fact that its influence on fusion depends on ELMO/Dock180/Rac1 signalling within the myotube. Because signalling by BAI1 can restore fusion capacity in caspase-inhibited myoblasts, which have decreased expression of several regulators of muscle-gene transcription¹⁰, this receptor may target genes essential

for myoblast differentiation.

Transient externalization of phosphatidylserine has been observed in other cell-fusing systems — for instance, in trophoblast cells during placental development¹². So the exposure of this phospholipid may be part of a conserved fusion mechanism. But is phosphatidylserine–BAI1 signalling common to all fusing systems? Moreover, apoptotic epithelial cells have previously been linked to compensatory proliferation and regeneration in a variety of organisms — from *Hydra* and planarians to *Drosophila* and mice¹³. It would be interesting to know whether phosphatidylserine–BAI1 signalling also induces proliferation and differentiation of satellite cells, the resident stem cells of skeletal muscle.

The present work provides a new dimension to the fields of myoblast fusion, muscle differentiation and muscle regeneration. A better understanding of the link between apoptosis, BAI1 signalling and fusion could lead to interventions that aid muscle recovery, be it after intense physical training or under conditions of disease-associated muscle wasting, prolonged bed rest or in the elderly. ■

Shannon F. Yu and Mary K. Baylies are in the Program in Developmental Biology,

Sloan-Kettering Institute, New York, New York 10065, USA. S.F.Y. is also at the Louis V. Gerstner, Jr. Graduate School of Biomedical Sciences, Memorial Sloan-Kettering Cancer Center, New York, New York, USA.
e-mail: m-baylies@ski.mskcc.org

1. Rochlin, K., Yu, S., Roy, S. & Baylies, M. K. *Dev. Biol.* **341**, 66–83 (2010).
2. Abmayr, S. M. & Pavlath, G. K. *Development* **139**, 641–656 (2012).
3. Gumieny, T. L. *et al. Cell* **107**, 27–41 (2001).
4. Hochreiter-Hufford, A. E. *et al. Nature* **497**, 263–267 (2013).
5. Park, D. *et al. Nature* **450**, 430–434 (2007).
6. Sessions, A. & Horwitz, A. F. *FEBS Lett.* **134**, 75–78 (1981).
7. van den Eijnde, S. M. *et al. J. Cell Sci.* **114**, 3631–3642 (2001).
8. Jeong, J. & Conboy, I. M. *Biochem. Biophys. Res. Commun.* **414**, 9–13 (2011).
9. Chargé, S. B. P. & Rudnicki, M. A. *Physiol. Rev.* **84**, 209–238 (2004).
10. Fernando, P., Kelly, J. F., Balazsi, K., Slack, R. S. & Megeney, L. A. *Proc. Natl Acad. Sci. USA* **99**, 11025–11030 (2002).
11. Leikina, E. *et al. J. Cell Biol.* **200**, 109–123 (2013).
12. Gauster, M., Moser, G., Orendi, M. & Huppertz, B. *Placenta* **30**, S49–S54 (2009).
13. Bergmann, A. & Steller, H. *Sci. Signal.* **3**, re8 (2010).

PHYSIOLOGY

Inflammation links ageing to the brain

Inflammation-activated signalling pathways in the brain's hypothalamus control the production of ageing-related hormones. This finding provides a link between inflammation, stress responses and systemic ageing. SEE ARTICLE P.211

DANA GABUZDA & BRUCE A. YANKNER

One of the least-understood aspects of ageing is its coordinated and stereotyped progression in all organ systems. Although researchers have long suspected that the brain orchestrates systemic ageing, compelling evidence of this in mammals has been lacking. Furthermore, we have had no clear understanding of how ageing is affected by inflammation, which is a hallmark of age-related diseases such as diabetes, cardiovascular disease, arthritis and Alzheimer's disease. In this issue, Zhang *et al.*¹ (page 211) help to make this connection by documenting the integration of inflammatory responses with systemic control of ageing by the hypothalamus — a part of the brain that controls growth, reproduction and metabolism*.

Studies in invertebrate models of ageing,

such as the nematode worm *Caenorhabditis elegans*^{2,3} and the fruitfly *Drosophila*⁴, have suggested that nutrient-sensing and environmental-stress-sensing neurons can regulate ageing of the entire organism. Zhang and colleagues now propose that the hypothalamus, which has similar sensing functions in the mammalian brain, could also exert broad control over the physiological changes we call ageing. Their findings show that activity of the signalling molecule NF- κ B increases in many regions of the brain in ageing mice, but that this increase is greatest in the hypothalamus. NF- κ B is an important regulator of gene transcription that mediates immune-cell communication and inflammatory responses, and has been implicated previously in the control of gene expression during ageing⁵. Zhang and colleagues' work indicates that activation of NF- κ B in microglia (cells in the brain that functionally resemble the macrophages of the immune

system) stimulates secretion of the inflammatory cell-signalling molecule TNF- α , which, in turn, stimulates NF- κ B signalling in hypothalamic neurons (Fig. 1).

The authors go on to show that this feed-forward loop leads to epigenetic changes (chemical and structural modifications that alter gene expression without changing the DNA sequence) in the gene that encodes gonadotropin-releasing hormone (GnRH), leading to its reduced expression. Moreover, their studies in mice suggest that reduced hypothalamic release of GnRH could contribute to several systemic attributes of ageing, including declining muscle strength, skin atrophy, bone loss, reduced neurogenesis and memory impairment. If validated, the results could have important implications for our understanding and treatment of age-related diseases, particularly those linked to inflammation.

'Inflammageing' describes the close relationship between low-grade chronic inflammation and ageing that has been linked to a wide spectrum of age-related disorders in various organs, including the brain⁶. Healthy ageing and longevity could relate, in part, to reduced levels of inflammation or strong protective mechanisms that guard against adverse effects of chronic inflammation. Conversely, genetic and environmental factors that promote inflammation or disrupt the mechanisms involved in reducing inflammation seem to confer increased susceptibility to 'accelerated ageing' and age-related disorders such as insulin resistance, metabolic disorders

*This article and the paper under discussion were published online on 1 May 2013.

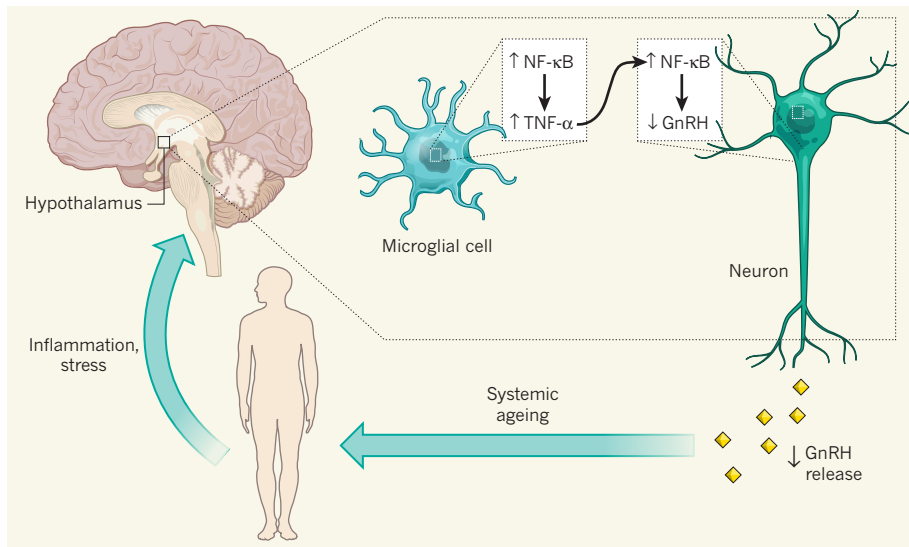


Figure 1 | Hypothalamic inflammation and control of systemic ageing. Zhang *et al.*¹ report that inflammation leads to activation of the signalling molecule NF- κ B in the hypothalamus of the brain, and suggest that this contributes to the control of systemic ageing. They show that NF- κ B activation in hypothalamic cells called microglia results in production of TNF- α , which, in turn, stimulates NF- κ B activity in nearby neurons. This signalling results in epigenetic repression of the gene that encodes gonadotropin-releasing hormone (GnRH), leading to reduced GnRH release from the neurons, which is associated with multiple physiological changes related to ageing, including bone loss, skin atrophy, muscle weakness and memory loss. This pathway might also mediate the effects of a variety of environmental and physiological stressors.

and cardiovascular disease⁷. Accelerated ageing typically involves multiple organ systems, although the effects in some organs might not be seen as clinical symptoms.

At the molecular level, attention has focused on how interplay between several cellular processes — including mitochondrial function, autophagy, the generation of reactive oxygen species and activation of the NLRP3 inflammasome — drives age-dependent inflammatory conditions^{8–10}. Zhang and colleagues' suggestion that inflammageing is driven by the integration of immune and hormonal responses in the hypothalamus is a new paradigm for this process. It is possible that the observed hypothalamic NF- κ B signalling and decline in GnRH production are a response to local inflammatory molecules produced by microglia, as the authors suggest. Alternatively, this response may be due to systemic signals — dendrites of GnRH-producing hypothalamic neurons extend through the blood–brain barrier, so they are able to sense inflammatory and metabolic signals in the blood¹¹.

In addition to the classical activity of GnRH in regulating the release of sex steroids involved in development and reproduction (oestrogens and progesterone in females and androgens in males), the hormone might also mediate other functions¹². Notably, Zhang *et al.* found that when mice were administered GnRH, it abrogated ageing effects and increased the production of new neurons in the hypothalamus and hippocampus (a part of the brain that regulates

memory). By contrast, sex steroids did not have these anti-ageing effects. A decrease in gonadal sex steroids is a well-established marker of ageing, but many other hormonal changes occur as well; and some of these age-regulated hormones (such as dehydroepiandrosterone) also regulate inflammation and other immune responses. Thus, interplay between the hormonal and immune systems occurs at multiple levels.

Zhang and colleagues' model may also be relevant to the suggestion — from several studies — that early-life adversity, such as childhood neglect or nutritional deprivation, can increase the risk of age-related disorders later in life¹³. It is possible that, in addition to responding to inflammation, NF- κ B signalling functions as an integrator of environmental and experience-related stresses to reset the interactions between the hypothalamus and the hormone-producing pituitary gland, and thus systemically alter hormonal responses. This could be mediated by epigenetic reprogramming of important stress-response genes in the brain that persist throughout adult life. One such gene, *NR3C1*, encodes the receptor for hormones called glucocorticoids. This receptor mediates stress responses through a feedback loop whereby its activation in the hippocampus inhibits neuronal activity in the hypothalamus. Early-life deprivation in rats or a history of early-life abuse in humans are both associated with epigenetic silencing of *NR3C1* (ref. 14), resulting in heightened sensitivity of the hypothalamus and elevated release of stress hormones.

Another mechanism might involve direct effects of glucocorticoids on the NF- κ B pathway. Although glucocorticoids are typically anti-inflammatory, it has been suggested¹⁵ that they can have the opposite effect in some brain regions and stimulate NF- κ B signalling. As such, NF- κ B signalling may integrate diverse inputs related to stress and inflammation to regulate ageing through changes in hypothalamic function, as well as other target organ systems.

How might hypothalamic regulation of ageing have evolved? Chronic inflammation arises from many kinds of insult, from acute infection to genomic instability. The concept that the hypothalamus can sense inflammation through immune pathways is a new one; just as the hypothalamus responds to nutrient status, its response to inflammation may enable the organism to rapidly adapt to physiological perturbations. Turning down the hypothalamic release of modulators such as GnRH to prevent reproduction and reduce growth may be evolutionarily advantageous during acute infection, injury or deprivation. Although this would have been adaptive for our shorter-lived ancestors, it may accelerate ageing in older individuals and have become apparent now that we live longer. This idea also raises the intriguing possibility that hypothalamic regulation could be therapeutically manipulated to have broad effects on the ageing process and age-related pathology. ■

Dana Gabuzda is in the Department of Neurology, Dana-Farber Cancer Institute and Harvard Medical School, Boston, Massachusetts 02115, USA. **Bruce A. Yankner** is in the Department of Genetics, Harvard Medical School.
e-mails: dana_gabuzda@dfci.harvard.edu; bruce_yankner@hms.harvard.edu

1. Zhang, G. L. J. *et al.* *Nature* **497**, 211–216 (2013).
2. Alcedo, J. & Kenyon, C. *Neuron* **41**, 45–55 (2004).
3. Bishop, N. A. & Guarente, L. *Nature* **447**, 545–549 (2007).
4. Fridell, Y. W., Sanchez-Blanco, A., Silvia, B. A. & Helfand, S. L. *Cell Metab.* **1**, 145–152 (2005).
5. Adler, A. S. *et al.* *Genes Dev.* **21**, 3244–3257 (2007).
6. Franceschi, C. *et al.* *Mech. Ageing Dev.* **128**, 92–105 (2007).
7. Osborn, O. & Olefsky, J. M. *Nature Med.* **18**, 363–374 (2012).
8. Bishop, N. A., Lu, T. & Yankner, B. A. *Nature* **464**, 529–535 (2010).
9. Green, D. R., Galluzzi, L. & Kroemer, G. *Science* **333**, 1109–1112 (2011).
10. Kepp, O., Galluzzi, L. & Kroemer, G. *Nature Immunol.* **12**, 199–200 (2011).
11. Herde, M. K., Geist, K., Campbell, R. E. & Herbison, A. E. *Endocrinology* **152**, 3832–3841 (2011).
12. Stevenson, T. J., Hahn, T. P., MacDougall-Shackleton, S. A. & Ball, G. F. *Front. Neuroendocrinol.* **33**, 287–300 (2012).
13. Waterland, R. A. & Michels, K. B. *Annu. Rev. Nutr.* **27**, 363–388 (2007).
14. McGowan, P. O. *et al.* *Nature Neurosci.* **12**, 342–348 (2009).
15. Munhoz, C. D., Sorrells, S. F., Caso, J. R., Scavone, C. & Sapolsky, R. M. *J. Neurosci.* **30**, 13690–13698 (2010).

Studies of pear-shaped nuclei using accelerated radioactive beams

L. P. Gaffney¹, P. A. Butler¹, M. Scheck^{1,2}, A. B. Hayes³, F. Wenander⁴, M. Albers⁵, B. Bastin⁶, C. Bauer², A. Blazhev⁵, S. Bönig², N. Bree⁷, J. Cederkäll⁸, T. Chupp⁹, D. Cline³, T. E. Cocolios⁴, T. Davinson¹⁰, H. De Witte⁷, J. Diriken^{7,11}, T. Grahn¹², A. Herzan¹², M. Huyse⁷, D. G. Jenkins¹³, D. T. Joss¹, N. Kesteloot^{7,11}, J. Konki¹², M. Kowalczyk¹⁴, Th. Kröll², E. Kwan¹⁵, R. Lutter¹⁶, K. Moschner⁵, P. Napiorkowski¹⁴, J. Pakarinen^{4,12}, M. Pfeiffer⁵, D. Radeck⁵, P. Reiter⁵, K. Reynders⁷, S. V. Rigby¹, L. M. Robledo¹⁷, M. Rudigier⁵, S. Sambi⁷, M. Seidlitz⁵, B. Siebeck⁵, T. Stora⁴, P. Thoele⁵, P. Van Duppen⁷, M. J. Vermeulen¹³, M. von Schmid², D. Voulot⁴, N. Warr⁵, K. Wimmer¹⁸, K. Wrzosek-Lipska^{7,14}, C. Y. Wu¹⁵ & M. Zielinska^{14,19}

There is strong circumstantial evidence that certain heavy, unstable atomic nuclei are ‘octupole deformed’, that is, distorted into a pear shape. This contrasts with the more prevalent rugby-ball shape of nuclei with reflection-symmetric, quadrupole deformations. The elusive octupole deformed nuclei are of importance for nuclear structure theory, and also in searches for physics beyond the standard model; any measurable electric-dipole moment (a signature of the latter) is expected to be amplified in such nuclei. Here we determine electric octupole transition strengths (a direct measure of octupole correlations) for short-lived isotopes of radon and radium. Coulomb excitation experiments were performed using accelerated beams of heavy, radioactive ions. Our data on ²²⁰Rn and ²²⁴Ra show clear evidence for stronger octupole deformation in the latter. The results enable discrimination between differing theoretical approaches to octupole correlations, and help to constrain suitable candidates for experimental studies of atomic electric-dipole moments that might reveal extensions to the standard model.

The atomic nucleus is a many-body quantum system, and hence its shape is determined by the number of nucleons present in the nucleus and the interactions between them. For example, nuclei in their ground state in which the proton and neutron shells are completely filled (‘doubly magic’ nuclei) are spherical. If this configuration is excited, or if more nucleons are added, the long-range correlations between valence nucleons distort the shape from spherical symmetry and the nucleus becomes deformed. In most of these cases, it is well established that the shape assumed has quadrupole deformation with axial and reflection symmetry; that is, the nucleus is shaped like a rugby ball (prolate deformation) or as a discus (oblate deformation). For certain combinations of protons and neutrons, there is also the theoretical expectation that the shape of nuclei can assume octupole deformation, corresponding to reflection asymmetry or a ‘pear-shape’ in the intrinsic frame, either in a dynamic way (octupole vibrations) or having a static shape (permanent octupole deformation).

Octupole deformation and EDMs

Atoms with octupole-deformed nuclei are very important in the search for permanent atomic electric-dipole moments (EDMs). The observation of a non-zero EDM at the level of contemporary experimental sensitivity would indicate time-reversal (T) or equivalently charge-parity (CP) violation due to physics beyond the standard model. In fact, experimental limits on EDMs provide important constraints on many proposed extensions to the standard model^{1,2}. For a neutral atom in its ground state, the Schiff moment (the electric-dipole

distribution weighted by radius squared³) is the lowest-order observable nuclear moment. Octupole-deformed nuclei with odd nucleon number A ($= Z + N$, see below) will have enhanced nuclear Schiff moments owing to the presence of the large octupole collectivity (spatial correlation between particle states) and the occurrence of nearly degenerate parity doublets that naturally arise if the deformation is static^{3–5}. Because a CP-violating Schiff moment induces a contribution to the atomic EDM, the sensitivity of the EDM measurement to CP violation over non-octupole-enhanced systems such as ¹⁹⁹Hg (ref. 2), currently providing the most stringent limit for atoms, can be improved by a factor of 100–1,000 (ref. 4). Essential in the interpretation of such limits in terms of new physics is a detailed understanding of the structure of these nuclei. Experimental programmes are in place to measure EDMs in atoms of odd- A Rn and Ra isotopes in the octupole region (see for example, ref. 6) but so far there is little direct information on octupole correlations in these nuclei.

Strong octupole correlations leading to pear shapes can arise when nucleons near the Fermi surface occupy states of opposite parity with orbital and total angular momentum differing by $3\hbar$. This condition is met for proton number $Z \approx 34, 56$ and 88 and neutron number $N \approx 34, 56, 88$ and 134 . The largest array of evidence for reflection asymmetry is seen at the values of $Z \approx 88$ and $N \approx 134$, where phenomena such as interleaved positive- and negative-parity rotational bands in even-even nuclei⁷, parity doublets in odd-mass nuclei⁸, and enhanced electric-dipole (E1) transition moments⁹ have been observed. Many theoretical approaches have been developed to describe the observed

¹Oliver Lodge Laboratory, University of Liverpool, Liverpool L69 7ZE, UK. ²Institut für Kernphysik, Technische Universität Darmstadt, Darmstadt D-64289, Germany. ³Department of Physics and Astronomy, University of Rochester, Rochester, New York 14627-0171, USA. ⁴ISOLDE, CERN (Organisation Européenne pour la Recherche Nucléaire), Geneva CH-1211, Switzerland. ⁵Institut für Kernphysik, Universität zu Köln, Köln D-50937, Germany. ⁶GANIL (Grand Accélérateur National d'Ions Lourds), Caen, BP 55027, F-14076, France. ⁷Instituut voor Kern- en Stralingsfysica, KU Leuven, Leuven B-3001, Belgium. ⁸Department of Nuclear Physics, Lund University, Lund, PO Box 118, 221 00, Sweden. ⁹Department of Physics, University of Michigan, Ann Arbor, Michigan 48104, USA. ¹⁰School of Physics & Astronomy, University of Edinburgh, Edinburgh EH9 3JZ, UK. ¹¹SCK-CEN (Studiecentrum voor Kernenergie - Centre d'Etude de l'énergie Nucléaire), Mol B-2400, Belgium. ¹²Department of Physics, University of Jyväskylä, Jyväskylä FI-40014, Finland, and Helsinki Institute of Physics, PO Box 64, FI-00014 Helsinki, Finland. ¹³Department of Physics, University of York, York YO10 5DD, UK. ¹⁴Heavy Ion Laboratory, University of Warsaw, Warsaw 02-093, Poland. ¹⁵Physics Division, Lawrence Livermore National Laboratory, Livermore, California 94551, USA. ¹⁶Maier-Leibnitz-Laboratorium, Ludwig-Maximilians-Universität und Technische Universität München, Garching D-85748, Germany. ¹⁷Departamento de Física Teórica, Universidad Autónoma de Madrid, Madrid 28049, Spain. ¹⁸Physik Department E12, Technische Universität München, Garching D-85748, Germany. ¹⁹DSM/IRFU/SPHn, CEA Saclay, Gif-sur-Yvette F-91191, France.

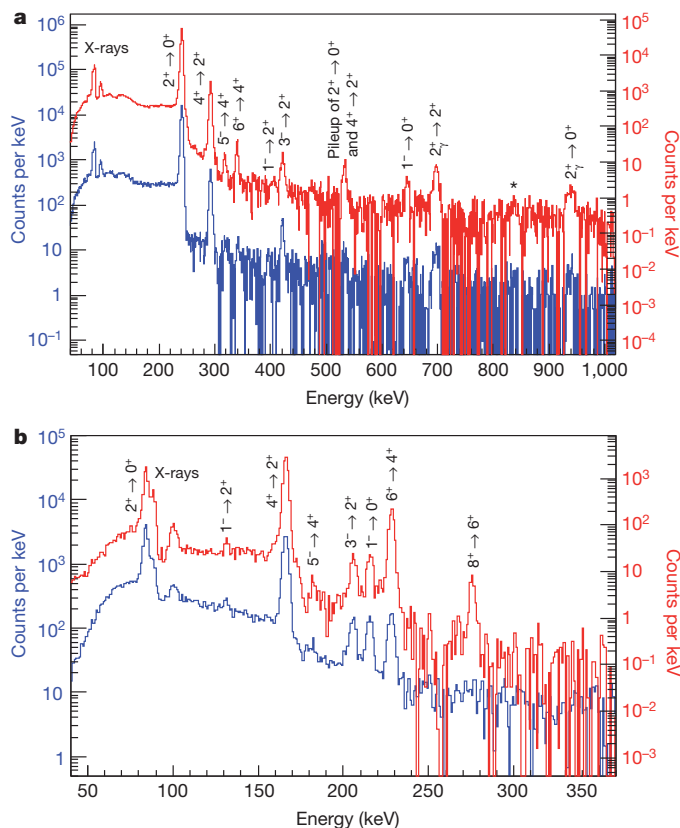


Figure 1 | Representative γ -ray spectra following the bombardment of 2 mg cm⁻² ^{60}Ni and ^{120}Sn targets by ^{220}Rn and ^{224}Ra . **a**, ^{60}Ni (blue) and ^{120}Sn (red) bombarded by ^{220}Rn ; **b**, targets as **a** but with bombardment by ^{224}Ra . The differences in excitation cross-section for the targets with different Z are apparent for the higher spin states. The γ -rays are corrected for Doppler shift assuming that they are emitted from the scattered projectile. The asterisk in **a** marks an unassigned, 836.2 keV transition. A state at 937.8(8) keV is assigned $I^\pi = 2^+$ on the basis of its excitation and decay properties; it is assumed to be the bandhead of the γ -band in ^{220}Rn .

experimental features: shell-corrected liquid-drop models^{10,11}, mean-field approaches using various interactions^{12–16}, models that assume α -particle clustering in the nucleus^{17,18}, algebraic models¹⁹ and other semi-phenomenological approaches²⁰. A broad overview of the experimental and theoretical evidence for octupole correlations is given in ref. 21.

In order to determine the shape of nuclei, the rotational model can be used to connect the intrinsic deformation, which is not directly

observable, to the electric charge moments that arise from the non-spherical charge distribution. For quadrupole deformed nuclei, the typical experimental observables are the electric-quadrupole (E2) transition moments that are related to the matrix elements connecting differing members of rotational bands in these nuclei, and E2 static moments that are related to diagonal matrix elements for a single state. If the nucleus does not change its shape under rotation, both types of moments will vary with angular momentum but can be related to a constant ‘intrinsic’ moment that characterizes the shape of the nucleus. For pear-shaped nuclei, there will be additionally E1 and electric-octupole (E3) transition moments that connect rotational states having opposite parity. The E1 transitions can be enhanced because of the separation of the centre-of-mass and centre-of-charge. The absolute values of the E1 moments are, however, small ($<10^{-2}$ single particle units) and are dominated by single-particle and cancellation effects⁹. In contrast, the E3 transition moment is collective in behaviour (>10 single particle units) and is insensitive to single-particle effects, as it is generated by coherent contributions arising from the quadrupole-octupole shape. The E3 moment is therefore an observable that should provide direct evidence for enhanced octupole correlations and, for deformed nuclei, can be related to the intrinsic octupole deformation parameters²². Until the present measurements, E3 transition moments have been determined for only one nucleus in the $Z \approx 88$, $N \approx 134$ region, ^{226}Ra (ref. 23), so that theoretical calculations of E3 moments in reflection-asymmetric nuclei have not yet been subject to detailed scrutiny.

Experiments and discussion

Coulomb excitation is an important tool for exploring the collective behaviour of deformed nuclei that gives rise to strong enhancement of the probability of transitions between states. Traditionally, this technique has been employed by exciting targets of stable nuclei with accelerated ion beams of stable nuclei at energies below the Coulomb barrier, ensuring that the interaction is purely electromagnetic in character. Whereas E2, E1 and magnetic dipole (M1) transition probabilities dominate in the electromagnetic decay of nuclear states, and hence can be determined from measurements of the lifetimes of the states, E2 and E3 transition moments dominate the Coulomb excitation process allowing these moments to be determined from measurement of the cross-sections of the states, often inferred from the γ -rays that de-excite these levels. In exceptional cases, the Coulomb excitation technique has been applied to radioactive targets like ^{226}Ra , which is sufficiently long-lived (half-life 1,600 yr) to produce a macroscopic sample. It is only comparatively recently that the technique has been extended to the use of accelerated beams of radioactive nuclei such as those from the Radioactive beam EXperimental facility at ISOLDE, CERN (REX-ISOLDE²⁴). In the experiments described here,

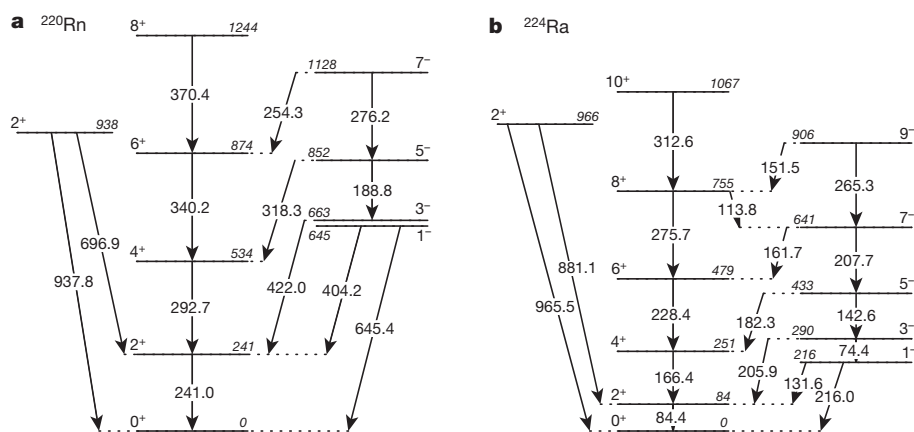


Figure 2 | Partial level-schemes for ^{220}Rn and ^{224}Ra , showing the excited states of interest for this work. **a**, ^{220}Rn ; **b**, ^{224}Ra . Arrows indicate known γ -ray transitions. All energies are in keV (upright font refers to transition energies,

italic font refers to state energies) and spins in units of \hbar . Note that the level at 938 keV in ^{220}Rn is observed for the first time in this work.

Table 1 | Values of matrix elements measured in the present experiment

Matrix element	^{220}Rn		^{224}Ra	
	$\langle I' E\lambda I \rangle$	$ \text{m.e.} $ (e fm^λ)	$ \text{m.e.} $ (e fm^λ)	$B(E\lambda)$ (WU)
$\langle 0^+ E1 1^- \rangle$		<0.10	<0.018	$<5 \times 10^{-5}$
$\langle 2^+ E1 1^- \rangle$		<0.13	<0.03	$<1.3 \times 10^{-4}$
$\langle 2^+ E1 3^- \rangle$		<0.18	0.026 ± 0.005	$3.9^{+1.7}_{-1.4} \times 10^{-5}$
$\langle 4^+ E1 5^- \rangle$		0.028 ± 0.009	0.030 ± 0.010	$4^{+3}_{-2} \times 10^{-5}$
$\langle 6^+ E1 7^- \rangle$		<1.3	<0.10	$<3 \times 10^{-4}$
$\langle 0^+ E2 2^+ \rangle$		137 ± 4	199 ± 3	98 ± 3
$\langle 1^- E2 3^- \rangle$		180 ± 60	230 ± 11	93 ± 9
$\langle 2^+ E2 4^+ \rangle$		212 ± 4	315 ± 6	137 ± 5
$\langle 3^- E2 5^- \rangle$		220 ± 150	410 ± 60	190 ± 60
$\langle 4^+ E2 6^+ \rangle$		274 ± 14	405 ± 15	156 ± 12
$\langle 6^+ E2 8^+ \rangle$			500 ± 60	180 ± 60
$\langle 0^+ E2 2^+_{\gamma} \rangle$		32 ± 7	23 ± 4	1.3 ± 0.5
$\langle 0^+ E3 3^- \rangle$		810 ± 50	940 ± 30	42 ± 3
$\langle 2^+ E3 1^- \rangle$		$<2,600$	$1,370 \pm 140$	210 ± 40
$\langle 2^+ E3 3^- \rangle$		$<5,300$	$<4,000$	<600
$\langle 2^+ E3 5^- \rangle$		$1,700 \pm 400$	$1,410 \pm 190$	61 ± 17

The experimental measurements for the absolute values of the matrix elements, $| \text{m.e.} |$, and the reduced transition probabilities, $B(E\lambda)$, are given here. The values of $B(E\lambda)$ for electromagnetic decay (λ) are derived from the matrix elements and are given in single particle units (Weisskopf units, WU). The uncertainties include the 1σ statistical error from the fit ($\chi^2 + 1$ type) and systematic contributions—beam energy and target thickness uncertainties, deorientation, beam spot effects, and so on. The upper limits correspond to 3σ .

^{220}Rn ($Z = 86$, $N = 134$) and ^{224}Ra ($Z = 88$, $N = 136$) ions were produced by spallation in a thick uranium carbide target bombarded by $\sim 10^{13}$ protons s^{-1} at 1.4 GeV from the CERN PS Booster. The ions were post-accelerated in REX-ISOLDE to an energy of 2.82 or 2.83 MeV per nucleon and bombarded secondary targets of ^{60}Ni , ^{112}Cd or ^{114}Cd , and ^{120}Sn of thickness approximately 2 mg cm^{-2} with an intensity of about 3×10^5 ions s^{-1} and 7×10^5 ions s^{-1} for Rn and Ra, respectively (Methods). The targets were chosen to give differing electromagnetic excitation (Ni, $Z = 28$ versus Sn, $Z = 50$; see Fig. 1) and, in the case of Cd, to provide a cross-check to the excitation of a target whose matrix elements are well known and can be measured in these experiments.

The γ -rays emitted following the excitation of the target and projectile nuclei were detected in MINIBALL²⁵, an array of 24 high-purity germanium detectors, each with six-fold segmentation and arranged in eight triple-clusters. The scattered projectiles and target recoils, distinguished by their differing dependence of energy with angle measured in the laboratory frame-of-reference, were detected in a highly segmented silicon detector²⁶. Representative spectra for ^{220}Rn and ^{224}Ra , for which the γ -ray energy is corrected for Doppler shift assuming emission from the scattered projectile, are shown in Fig. 1. Here events were accumulated only if the target recoil was detected in

coincidence with γ -rays within a 600-ns time window; these data were corrected for random events. The energy level schemes for ^{220}Rn and ^{224}Ra are shown in Fig. 2.

The spectra reveal strong population of the ground-state band of positive-parity states, excited by direct and multiple E2 Coulomb excitation, and substantial population of the octupole band of negative-parity states, excited by E3 excitation. The yields of the observed γ -ray transitions detected in MINIBALL were measured for two ranges of recoil angles of the target nucleus (28° – 38° and 38° – 52° for ^{220}Rn ; 24° – 40° and 40° – 54° for ^{224}Ra) for each of the three targets, and combined with existing spectroscopic data (lifetimes of low-lying states^{27,28} and their γ -ray branching ratios^{7,29,30}) to provide input to the Coulomb-excitation analysis code GOSIA³¹ (Methods). The separation of angular ranges increased sensitivity in the measurement by varying the relative excitation probabilities. For ^{220}Rn , 34 independent data points determined 22 free parameters (16 matrix elements and 1 normalization constant for each combination of target and recoil angle range) whereas for ^{224}Ra , 57 data points determined 23 free parameters (17 matrix elements). The analysis was also carried out for ^{220}Rn independently of the previously measured lifetime of the $I^\pi = 2^+$ state (τ_{2^+})²⁷, and for ^{224}Ra independently of τ_{4^+} (ref. 28); here I is the total angular

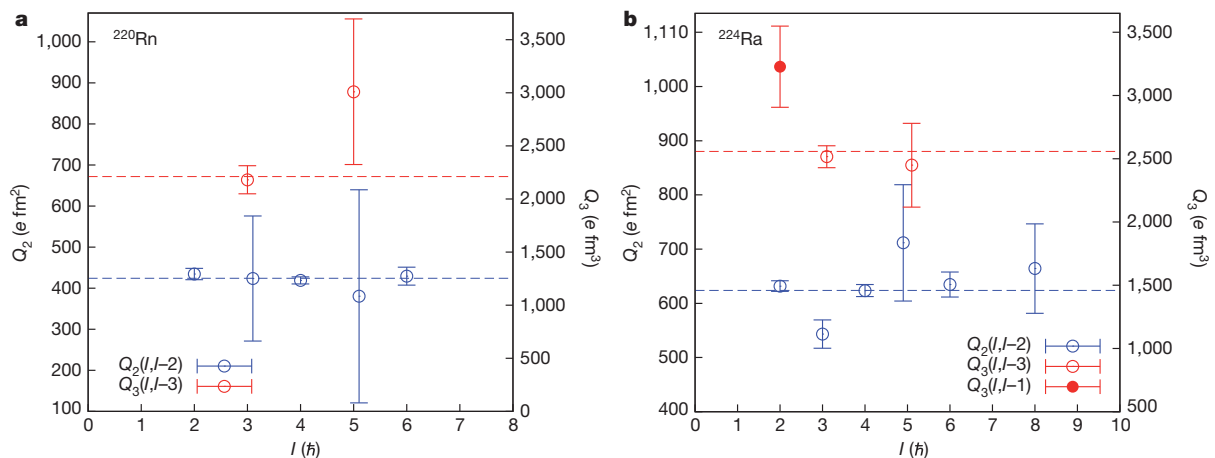


Figure 3 | The values of the E2 and E3 intrinsic moments, $Q_\lambda(I, I')$. **a, b**, These values are derived from the matrix elements using the relation $\langle I' || E\lambda || I \rangle = \sqrt{(2I' + 1)(2\lambda + 1)/16\pi} (I' 0 \lambda 0 | I 0) Q_\lambda$ for ^{220}Rn (**a**) and ^{224}Ra (**b**). Here $\langle I' || E\lambda || I \rangle$ is the matrix element between states of angular momenta

I and I' defined in the text and $(I' 0 \lambda 0 | I 0)$ is a Clebsch-Gordon coefficient. The dashed lines have the value of the weighted mean for each Q_λ , the error bars are $\pm 1\text{s.d.}$

Table 2 | The values of the E2 and E3 intrinsic moments, Q_i

Q_i	Nucleus						
	^{208}Pb	^{220}Rn	^{224}Ra	^{226}Ra	^{230}Th	^{232}Th	^{234}U
Q_2 (e fm ²)	179 ± 4 (ref. 44)	434 ± 14	632 ± 10	717 ± 3 (ref. 23)	900 ± 6 (ref. 45)	932 ± 5 (ref. 46)	$1,047 \pm 5$ (ref. 45)
Q_3 (e fm ³)	$2,100 \pm 20$ (ref. 44)	$2,180 \pm 130$	$2,520 \pm 90$	$2,890 \pm 80$ (ref. 23)	2140 ± 100 (ref. 47)	1970 ± 100 (ref. 48)	$2,060 \pm 120$ (ref. 47)

Values of Q_i given here are derived from the matrix elements (see Fig. 3 legend) connecting the lowest-lying states in nuclei near $Z = 88$ and $N = 134$. The values for ^{220}Rn and ^{224}Ra are taken from the present work.

momentum of the state and π is its parity. (For ^{224}Ra the previously measured value of τ_{2+} cannot be determined independently as the $2^+ \rightarrow 0^+$ transition is contaminated with the Ra X-rays.) In both cases the fitted matrix elements for the $2^+ \rightarrow 0^+$ E2 transition (^{220}Rn) and for the $4^+ \rightarrow 2^+$ E2 transition (^{224}Ra) were found to agree, within the experimental uncertainties, with the values obtained using the lifetime measurements.

The measured E1, E2 and E3 matrix elements for ^{220}Rn and ^{224}Ra are given in Table 1. The values of the intrinsic moments, Q_i , are given in Fig. 3. These are determined from the experimental values of the reduced matrix element between two states having angular momenta I and I' induced to undergo a transition by the electromagnetic operator $E\lambda$, $\langle I' || E\lambda || I \rangle$, assuming the validity of the rotational model²². Here $\lambda = 1, 2, 3$ refers to E1, E2, E3 respectively. For the E2 and E3 matrix elements, the measured values are all consistent with the geometric predictions expected from a rotating, deformed distribution of electric charge, although these data do not distinguish whether the negative-parity states arise from the projection of a quadrupole-octupole deformed shape or from an octupole oscillation of a quadrupole shape³². Table 2 compares the experimental values of Q_i derived from the matrix elements connecting the lowest states for nuclei near $Z = 88$ and $N = 134$ measured by Coulomb excitation. It is striking that while the E2 moment increases by a factor of 6 between ^{208}Pb and ^{234}U , the E3 moment changes by only 50% in the entire mass region. Nevertheless, the larger Q_3 values for ^{224}Ra and ^{226}Ra indicate an enhancement in octupole collectivity that is consistent with an onset of octupole deformation in this mass region. On the other hand, ^{220}Rn has similar octupole strength to ^{208}Pb , $^{230,232}\text{Th}$ and ^{234}U , consistent with it being an octupole vibrator. In the case of a vibrator, the coupling of an octupole phonon to the ground state rotational band will give zero values for matrix elements such as $\langle 1^- || E3 || 4^+ \rangle$, because an aligned octupole phonon would couple the 4^+ state to a 7^- state. Although the present experiment does not have sensitivity to this quantity, this effect has been observed for ^{148}Nd in the $Z \approx 56$, $N \approx 88$ octupole region³³, while for ^{226}Ra the intrinsic moment derived from the measured $\langle 1^- || E3 || 4^+ \rangle$ is similar to that derived from the value of $\langle 0^+ || E3 || 3^- \rangle$ (ref. 23). The deduced shapes of ^{220}Rn and ^{224}Ra are presented in Fig. 4. Here the values of quadrupole and octupole

deformation β_2 and β_3 were extracted from the dependence of the measured Q_2 and Q_3 on the generalized nuclear shape³⁴.

The conclusions drawn from the present measurements are also consistent with suggestions from the systematic studies of energy levels⁷ (relative alignment of the negative-parity band to the positive-parity band) that the even-even isotopes $^{218-222}\text{Rn}$ and ^{220}Ra have vibrational behaviour while $^{222-228}\text{Ra}$ have octupole-deformed character (see figures 12 and 13 in ref. 7). For odd-mass ^{219}Ra there is no evidence³⁵ for parity doubling, whereas for ^{221}Ra a parity doublet of states with $I = 5/2$ separated by 103.6 keV has been observed³⁶. In the Ba–Nd region with $Z \approx 56$ and $N \approx 88$, where the octupole states arise from vibrational coupling to the ground-state band, the evidence for parity doubling of the ground state arising from reflection asymmetry is inconclusive^{37,38}. This suggests that the parity doubling condition that leads to enhancement of the Schiff moment¹⁵ is unlikely to be met in $^{219,221}\text{Rn}$. On the other hand $^{223,225}\text{Ra}$, having parity doublets separated by ~ 50 keV (ref. 21), will have large enhancement of their Schiff moments.

The values of Q_i , deduced from the measured transition matrix elements, are plotted in Fig. 5 as a function of N . The anomalously low value of Q_1 for ^{224}Ra , measured here for the first time, has been noted elsewhere^{9,13,39}. The measured Q_1 and Q_2 values are in good agreement with recent theoretical calculations of the generator-coordinate extension of the Gogny Hartree–Fock–Bogoliubov (HFB) self-consistent mean field theory¹⁶, particularly using the D1M parameterization⁴⁰. However, as remarked earlier, the trend of the experimental data is that the values of Q_3 decrease from a peak near ^{226}Ra with decreasing N (or A), which is in marked contrast to the predictions of the cluster model calculations¹⁷. It is also at variance with the Gogny HFB mean-field predictions of a maximum for ^{224}Ra (ref. 16). It should be noted, however, that relativistic mean field calculations¹⁴ predict that the maximum value of Q_3 occurs for radium isotopes between $A = 226$ and 230, depending on the parameterization, and Skyrme Hartree–Fock calculations¹⁵ predict that ^{226}Ra has the largest octupole deformation. Both predictions are consistent with our data. We cannot completely eliminate the possibility that there are unobserved couplings from the ground state to higher-lying 3^- states that should be added (without energy weighting) to the observed coupling to the

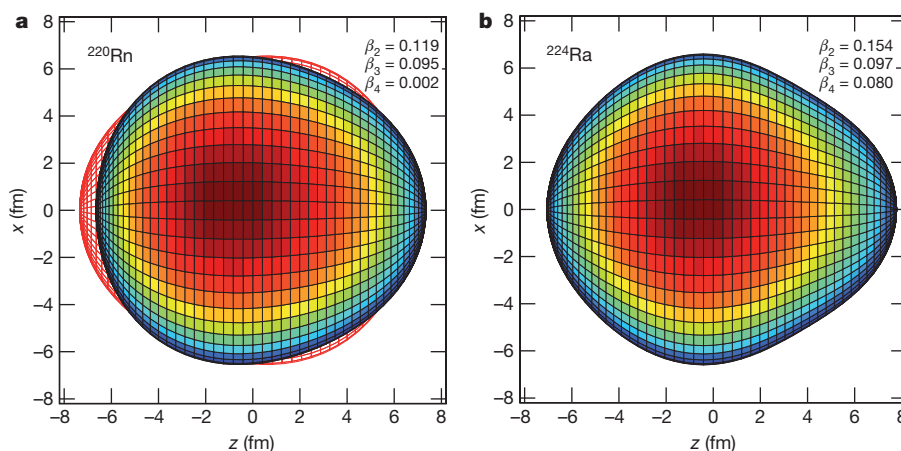


Figure 4 | Graphical representation of the shapes of ^{220}Rn and ^{224}Ra . **a**, ^{220}Rn ; **b**, ^{224}Ra . Panel **a** depicts vibrational motion about symmetry between the surface shown and the red outline, whereas **b** depicts static deformation in

the intrinsic frame. Theoretical values of β_4 are taken from ref. 10. The colour scale, blue to red, represents the y -values of the surface. The nuclear shape does not change under rotation about the z axis.

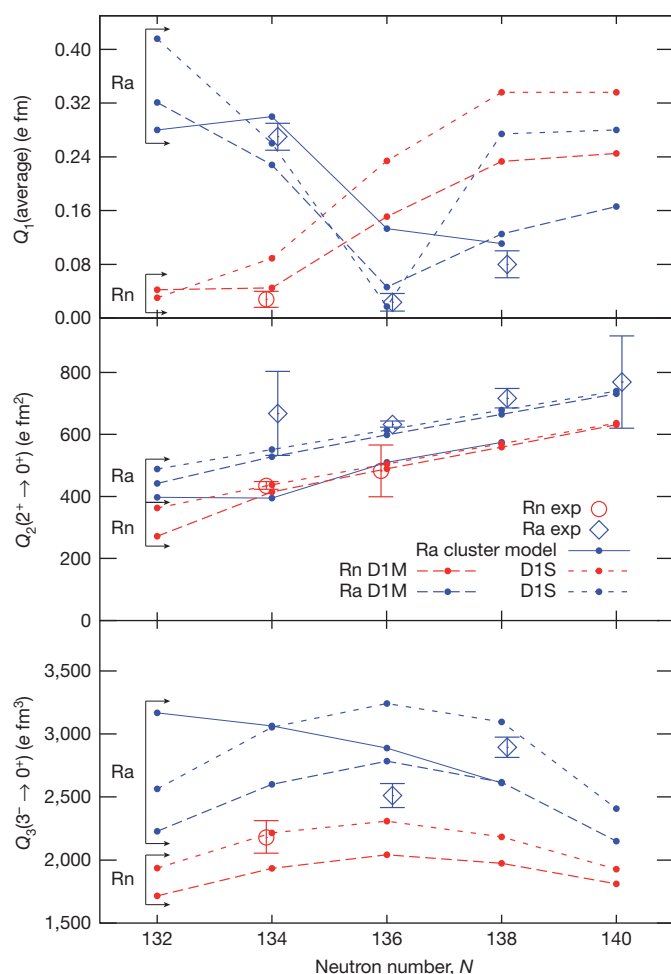


Figure 5 | Values of Q_2 for low-lying transitions in nuclei as a function of N . Measured values for $\lambda \rightarrow 0$ transitions are used for $\lambda = 2, 3$; for $\lambda = 1$ an average value over the measured spin range ($\leq 5h$) is used. Comparisons are made to the theoretical predictions of a cluster model¹⁷ ('Ra cluster model') and mean-field calculations¹⁶ (with two different parameterizations D1M and D1S⁴⁰, 'Rn D1M, D1S' and 'Ra D1M, D1S'). The points are connected by lines as a guide to the eye. The experimental data for Rn and Ra isotopes are denoted 'Rn exp' and 'Ra exp' respectively; the data for ²²⁰Rn ($N = 134$) and ²²⁴Ra ($N = 136$) are from the present work, other data are taken from refs 23, 49 and 50. The error bars are ± 1 s.d.

lowest 3^- state. However, in a detailed study³³ of octupole strength in ¹⁴⁸Nd, where these states lie closer in energy to the lowest state, such couplings were not observed.

Outlook

We have demonstrated that radioactive beams of heavy nuclei with $A \approx 220$ can be successfully accelerated with sufficient intensity to measure both even- and odd-order electric-multipole matrix elements with an accuracy of 10% or better. The extracted electric-quadrupole and electric-octupole moments are consistent with constant values over the range of measured angular momentum. Our data show that ²²⁰Rn has weaker octupole collectivity than ²²⁴Ra. We conclude that ^{219,221}Rn are likely to have smaller octupole-enhanced EDMs than ^{223,225}Ra, though more favourable Rn candidates may emerge from future studies of the low-lying structure of heavier isotopes. Comparing our data with predictions of the E3 strength from recent models, we find that the trend in octupole deformation extracted from the data presented here reveals detailed differences from some mean field predictions¹⁶ and opposes the trend predicted by the cluster model¹⁷. Our findings for the comparisons with models should be confirmed

by extending studies to other radioactive isotopes in the Rn and Ra chain. It is interesting to note that the Gogny HFB calculations¹⁶ predict that Th and U isotopes with $N = 134$ – 136 , already known to exhibit the characteristics of a rigid octupole shape^{7,41}, should have significantly enhanced E3 transition strengths (70 Weisskopf units); however, tests of this prediction await major developments in radioactive beam technology.

METHODS SUMMARY

In our experiments, the ²²⁰Rn and ²²⁴Ra produced by spallation diffused to the primary target surface and were then singly ionized ($q = 1^+$) in either an enhanced plasma ion-source⁴² with a cooled transfer line (Rn) or a tungsten surface ion-source (Ra), accelerated to 30 keV, separated according to A/q , and delivered to a Penning trap, REXTRAP⁴³, at a rate of around 1.25×10^7 ions s^{-1} for ²²⁰Rn and 4.4×10^7 ions s^{-1} for ²²⁴Ra at the entrance. Inside the trap, the singly-charged ions were accumulated and cooled before allowing the ions to escape in bunches at 400 ms intervals into an electron-beam ion source, REXEBIS⁴³. Here, the ions were confined for 400 ms in a high-density electron beam that stripped more electrons to produce a charge state of 52^+ , extracted as 400 μs pulses before being mass-selected again according to A/q , and injected at 2.5 Hz into the REX linear post-accelerator. The level of isobaric impurity (for example, Fr) in the Ra beam was estimated to be below 1% by observing radioactive decays at the end of the beam line. For Rn, observation of contaminant decays was more difficult because of the small α -decay branching ratios to excited states, and only an upper limit of 5% could be obtained.

The GOSIA code performs a least-squares fit to the matrix elements between all known states coupled by electromagnetic operators, which are treated as free parameters. Although the fit is sensitive to the relative E1/E2 decay rates, E1 (and M1) excitation is negligible at the beam energies used and can be ignored. The magnitudes of the values of the starting parameters were chosen to be random, within reasonable limits. The fit was found to be insensitive to many of the matrix elements; these were either fixed or coupled to other matrix elements assuming the validity of the rotational model.

Received 30 January; accepted 13 March 2013.

- Pospelov, M. & Ritz, A. Electric dipole moments as probes of new physics. *Ann. Phys.* **318**, 119–169 (2005).
- Griffith, W. C. *et al.* Improved limit on the permanent electric dipole moment of ¹⁹⁹Hg. *Phys. Rev. Lett.* **102**, 101601 (2009).
- Spevak, V., Auerbach, N. & Flambaum, V. V. Enhanced T-odd, P-odd electromagnetic moments in reflection asymmetric nuclei. *Phys. Rev. C* **56**, 1357–1369 (1997).
- Dobaczewski, J. & Engel, J. Nuclear time-reversal violation and the Schiff moment of ²²⁵Ra. *Phys. Rev. Lett.* **94**, 232502 (2005).
- Ellis, J., Lee, J. & Pilaftsis, A. Maximal electric dipole moments of nuclei with enhanced Schiff moments. *J. High Energy Phys.* **2011**, 045 (2011).
- Guest, J. R. *et al.* Laser trapping of ²²⁵Ra and ²²⁶Ra with repumping by room-temperature blackbody radiation. *Phys. Rev. Lett.* **98**, 093001 (2007).
- Cocks, J. *et al.* Spectroscopy of Rn, Ra and Th isotopes using multi-nucleon transfer reactions. *Nucl. Phys. A* **645**, 61–91 (1999).
- Dahlinger, M. *et al.* Alternating parity bands and octupole effects in ²²¹Th and ²²³Th. *Nucl. Phys. A* **484**, 337–375 (1988).
- Butler, P. A. & Nazarewicz, W. Intrinsic dipole moments in reflection-asymmetric nuclei. *Nucl. Phys. A* **533**, 249–268 (1991).
- Nazarewicz, W. *et al.* Analysis of octupole instability in medium-mass and heavy nuclei. *Nucl. Phys. A* **429**, 269–295 (1984).
- Möller, P. *et al.* Axial and reflection asymmetry of the nuclear ground state. *At. Data Nucl. Data Tables* **94**, 758–780 (2008).
- Bonche, P., Heenen, P. H., Flocard, H. & Vautherin, D. Self-consistent calculation of the quadrupole-octupole deformation energy surface of ²²²Ra. *Phys. Lett. B* **175**, 387–391 (1986).
- Egido, J. & Robledo, L. Microscopic study of the octupole degree of freedom in the radium and thorium isotopes with Gogny forces. *Nucl. Phys. A* **494**, 85–101 (1989).
- Rutz, K., Maruhn, J. A., Reinhard, P.-G. & Greiner, W. Fission barriers and asymmetric ground states in the relativistic mean-field theory. *Nucl. Phys. A* **590**, 680–702 (1995).
- Engel, J., Bender, M., Dobaczewski, J., Jesus, J. H., d. & Olbratowski, P. Time-reversal violating Schiff moment of ²²⁵Ra. *Phys. Rev. C* **68**, 025501 (2003).
- Robledo, L. M. & Bertsch, G. F. Global systematics of octupole excitations in even-even nuclei. *Phys. Rev. C* **84**, 054302 (2011).
- Shneidman, T. M., Adamian, G. G., Antonenko, N. V., Jolos, R. V. & Scheid, W. Cluster interpretation of properties of alternating parity bands in heavy nuclei. *Phys. Rev. C* **67**, 014313 (2003).
- Buck, B., Merchant, A. C. & Perez, S. M. Negative parity bands in even-even isotopes of Ra, Th, U and Pu. *J. Phys. G* **35**, 085101 (2008).
- Zamfir, N. V. & Kusnezov, D. Octupole correlations in the transitional actinides and the spdf interacting boson model. *Phys. Rev. C* **63**, 054306 (2001).

20. Frauendorf, S. Heart-shaped nuclei: condensation of rotational-aligned octupole phonons. *Phys. Rev. C* **77**, 021304 (2008).
21. Butler, P. A. & Nazarewicz, W. Intrinsic reflection asymmetry in atomic nuclei. *Rev. Mod. Phys.* **68**, 349–421 (1996).
22. Robledo, L. M. & Bertsch, G. F. Electromagnetic transition strengths in soft deformed nuclei. *Phys. Rev. C* **86**, 054306 (2012).
23. Wollersheim, H. J. *et al.* Coulomb excitation of ^{226}Ra . *Nucl. Phys. A* **556**, 261–280 (1993).
24. Voulot, D. *et al.* Radioactive beams at REX-ISOLDE: present status and latest developments. *Nucl. Instrum. Methods B* **266**, 4103–4107 (2008).
25. Eberth, J. *et al.* MINIBALL A Ge detector array for radioactive ion beam facilities. *Prog. Part. Nucl. Phys.* **46**, 389–398 (2001).
26. Ostrowski, A. *et al.* CD: A double sided silicon strip detector for radioactive nuclear beam experiments. *Nucl. Instrum. Methods A* **480**, 448–455 (2002).
27. Bell, R. E., Bjornholm, S. & Severiens, J. C. Half lives of first excited states of even nuclei of Fm, Ra, Th, U, and Pu. *Kgl. Danske Vid. Selsk. Mat.-Fys. Medd.* **32**, 1–48 (1960).
28. Neal, W. R. & Krane, H. W. Mean lives of excited rotational states of heavy even-even nuclei. *Phys. Rev.* **137**, B1164–B1174 (1965).
29. Liang, C. F., Paris, P., Ruchowska, E. & Briancon, C. A new isotope $^{85}_{220}\text{At}_{135}$. *J. Phys. G* **15**, L31–L33 (1989).
30. Artna-Cohen, A. Nuclear data sheets for $A = 224$. *Nucl. Data Sheets* **80**, 227–262 (1997).
31. Cline, D. Quadrupole and octupole shapes in nuclei. *Nucl. Phys. A* **557**, 615–634 (1993).
32. Nazarewicz, W. & Tabor, S. L. Octupole shapes and shape changes at high spins in the $Z \sim 58$, $N \sim 88$ nuclei. *Phys. Rev. C* **45**, 2226–2237 (1992).
33. Ibbotson, R. W. *et al.* Quadrupole and octupole collectivity in ^{148}Nd . *Nucl. Phys. A* **619**, 213–240 (1997).
34. Leander, G. A. & Chen, Y. S. Reflection-asymmetric rotor model of odd $A \sim 219$ –229 nuclei. *Phys. Rev. C* **37**, 2744–2778 (1988).
35. Riley, L. A. *et al.* Conversion electron- γ coincidences and intrinsic reflection asymmetry in ^{219}Ra . *Phys. Rev. C* **62**, 021301 (2000).
36. Ackermann, B. *et al.* Level structure of ^{217}Rn and ^{221}Ra investigated in the alpha-decay $^{225}\text{Th} \rightarrow ^{221}\text{Ra} \rightarrow ^{217}\text{Rn}$. *Z. Phys. A* **332**, 375–381 (1989).
37. Nosek, D., Sheline, R. K., Sood, P. C. & Kvasil, J. Microscopic structures of parity doublets in the ^{151}Pm , ^{153}Eu and ^{155}Eu nuclei. *Z. Phys. A* **344**, 277–283 (1993).
38. Rzača-Urban, T. *et al.* Reflection symmetry of the near-yrast excitations in ^{145}Ba . *Phys. Rev. C* **86**, 044324 (2012).
39. Poynter, R. J. *et al.* Observation of unexpectedly small E1 moments in ^{224}Ra . *Phys. Lett. B* **232**, 447–451 (1989).
40. Goriely, S., Hilaire, S., Girod, M. & Péru, S. First Gogny-Hartree-Fock-Bogoliubov nuclear mass model. *Phys. Rev. Lett.* **102**, 242501 (2009).
41. Greenlees, P. T. *et al.* First observation of excited states in ^{226}U . *J. Phys. G* **24**, L63–L70 (1998).
42. Penescu, L., Catherall, R., Lettry, J. & Stora, T. Development of high efficiency versatile arc discharge ion source at CERN ISOLDE. *Rev. Sci. Instrum.* **81**, 02A906 (2010).
43. Wolf, B. H. *et al.* First radioactive ions charge bred in REXEBIS at the REX-ISOLDE accelerator. *Nucl. Instrum. Methods Phys. Res. B* **204**, 428–432 (2003).
44. Martin, M. J. Nuclear data sheets for $A = 208$. *Nucl. Data Sheets* **108**, 1583–1806 (2007).
45. Bemis, C. E. *et al.* E2 and E4 transition moments and equilibrium deformations in the actinide nuclei. *Phys. Rev. C* **8**, 1466–1480 (1973).
46. Baktash, C. & Saladin, J. X. Determination of E2 and E4 transition moments in ^{232}Th . *Phys. Rev. C* **10**, 1136–1139 (1974).
47. McGowan, F. K. *et al.* Coulomb excitation of vibrational-like states in the even- A actinide nuclei. *Phys. Rev. C* **10**, 1146–1155 (1974).
48. McGowan, F. & Milner, W. Coulomb excitation of states in ^{232}Th . *Nucl. Phys. A* **562**, 241–259 (1993).
49. Singh, S., Jain, A. & Tuli, J. K. Nuclear data sheets for $A = 222$. *Nucl. Data Sheets* **112**, 2851–2886 (2011).
50. Artna-Cohen, A. Nuclear data sheets for $A = 228$. *Nucl. Data Sheets* **80**, 723–786 (1997).

Acknowledgements The support of the ISOLDE Collaboration and technical teams is acknowledged. This work was supported by the following Research Councils: STFC (UK), BMBF (Germany; 05P12RDCIA, 06DA9036I, 06KY9136I and 06KY205I), HIC for FAIR (Germany), FWO-Vlaanderen (Belgium), Belgian Science Policy Office (IAP-BriX network P7/12), Academy of Finland (contract no. 131665), DOE (US; DE-AC52-07NA27344 and DE-FG02-04ER41331), NSF (US), MICINN (Spain; FPA2009-08958 and FIS2009-07277), Consolider-Ingenio 2010 Programmes (Spain; CPAN CSD2007-00042 and MULTIDARK CSD2009-00064), Polish Ministry for Science and Higher Education (grant no. 589/N-G-POOL/2009/0), EC via I3-EURONS (FP6 contract no. RII3-CT-2004-506065), MC Fellowship scheme (FP7 contract PIEF-GA-2008-219175) and IA-ENSAR (FP7 contract 262010).

Author Contributions Instrument set-up: M.A., C.B., A.B., T.D., H.D.W., L.P.G., J.K., J.P., P.R., M. Seidlitz, B.S., M.J.V. and N.W. DAQ and on-line analysis: A.B., L.P.G., R.L. and N.W. Data analysis and interpretation: L.P.G., P.A.B., D.C., A.B.H., M. Scheck and M.Z. REX development and set-up: F.W., D.V. and J.C. Primary target: T.S. Preparation of manuscript: P.A.B., L.P.G., T.C., A.B., D.G.J., Th.K., J.P., P.R., M. Scheck, P.V.D. and N.W. Theoretical interpretation: L.M.R. All authors except L.M.R. took part in the experiments.

Author Information Reprints and permissions information is available at www.nature.com/reprints. The authors declare no competing financial interests. Readers are welcome to comment on the online version of the paper. Correspondence and requests for materials should be addressed to P.A.B. (peter.butler@liverpool.ac.uk).

Hierarchy of orofacial rhythms revealed through whisking and breathing

Jeffrey D. Moore^{1*}, Martin Deschênes^{2*}, Takahiro Furuta³, Daniel Huber^{4†}, Matthew C. Smear⁴, Maxime Demers² & David Kleinfeld^{1,5}

Whisking and sniffing are predominant aspects of exploratory behaviour in rodents. Yet the neural mechanisms that generate and coordinate these and other orofacial motor patterns remain largely uncharacterized. Here we use anatomical, behavioural, electrophysiological and pharmacological tools to show that whisking and sniffing are coordinated by respiratory centres in the ventral medulla. We delineate a distinct region in the ventral medulla that provides rhythmic input to the facial motor neurons that drive protraction of the vibrissae. Neuronal output from this region is reset at each inspiration by direct input from the pre-Bötzinger complex, such that high-frequency sniffing has a one-to-one relationship with whisking, whereas basal respiration is accompanied by intervening whisks that occur between breaths. We conjecture that the respiratory nuclei, which project to other premotor regions for oral and facial control, function as a master clock for behaviours that coordinate with breathing.

Active sensing is an essential component of orofacial behaviour. Animals rhythmically sniff to smell, lick to taste, and whisk to touch. The muscles involved in these patterned sensory behaviours overlap with those involved with the ingestive behaviours of chewing, swallowing and suckling. Notably, all of these behaviours share the motor plant involved in respiration and control of the upper airway. Given the essential nature of breathing and the biomechanical constraints that link the different behaviours, the coordination among orofacial behaviours constitutes a computational aspect of homeostatic control with little margin for error^{1–6}.

Here we investigate the coordination of orofacial behaviours in the context of sniffing and whisking in rodents. These closely associated rhythmic behaviours constitute the animals' predominant activities during exploration and social interactions^{7–9}. The cycle of rhythmic breathing is driven by neurons in the pre-Bötzinger complex, which generates the inspiratory rhythm^{10,11}, the Böttinger complex and parafacial respiratory groups, which shape the expiratory rhythm⁵, the ventral respiratory groups, which drive the respiratory pump muscles¹², and several pools of cranial motor neurons that control the upper airway valve muscles¹³. The drive for rhythmic whisking remains to be identified. However, whisking persists after decortication^{7,14} and sensory deafferentation^{7,15,16}, which suggests that it too involves a rhythmic generator in the brainstem. Furthermore, the facial motor neurons that drive the muscles involved in whisking are located immediately rostral to nuclei within the ventral medulla that generate breathing, and activity within these facial motor neurons and muscles is time-locked to breathing^{17,18}. These results reported previously support a common neural circuitry for the rhythmic control of both breathing and whisking.

Obligatory phase-locking of whisking and breathing

Concurrent measurements of breathing and whisking in head-fixed rats reveal key aspects of their coordination (Fig. 1a, b). First, breathing over a wide range of rates can occur without substantial whisking

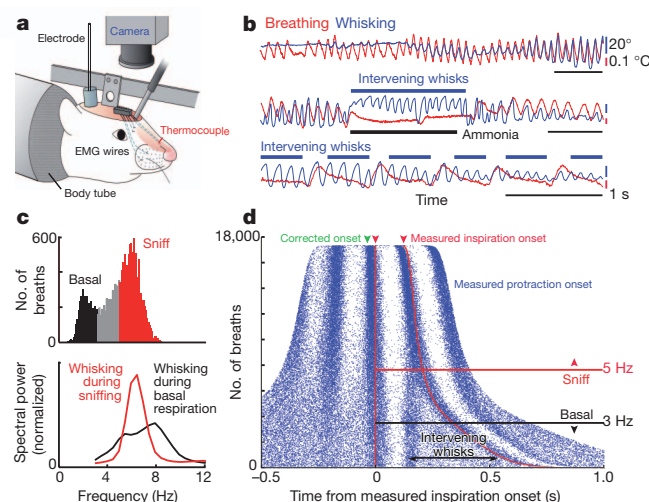


Figure 1 | Coordination of whisking and breathing. **a**, Procedures to measure whisking, breathing and associated electrophysiology in head-restrained rats. **b**, Simultaneous measurement of vibrissa position (blue) and breathing (red). Protraction and inspiration are upwards. **c**, Histogram of instantaneous breathing frequencies (top) delineates the classification of breaths below 3 Hz as basal respiration (black) and those above 5 Hz as sniffs (red); unclassified frequencies are in grey. The spectral power of whisking (bottom) is plotted during periods of basal respiration (black) as well as sniffing (red). **d**, Raster plots of inspiration onset times (red) and protraction onset times (blue) relative to the onset of inspiration for individual breaths are ordered by the duration of the breath; green arrow represents the 30-ms lead of inspiratory drive to facial muscles as opposed to the measured inspiration. Whisks and inspiration onset times are significantly correlated during both sniffing and basal respiration ($P < 0.01$).

¹Department of Physics, University of California at San Diego, 9500 Gilman Drive, La Jolla, California 92093, USA. ²Department of Psychiatry and Neuroscience, Centre de Recherche Université Laval Robert-Giffard, 2601 de la Canardière, Québec City G1J 2G3, Canada. ³Department of Morphological Brain Science, Building C Room 204, Graduate School of Medicine, Kyoto University, Yoshida Konoe-cho, Sakyo-ku, Kyoto 606-8501, Japan. ⁴Howard Hughes Medical Institute, Janelia Farm Research Campus, 19700 Helix Drive, Ashburn, Virginia 20147, USA. ⁵Section on Neurobiology, University of California at San Diego, 9500 Gilman Drive, La Jolla, California 92093, USA. [†]Present address: Department of Neuroscience, 1, rue Michel Street, University of Geneva, 1206 Geneva, Switzerland.

*These authors contributed equally to this work.

(Fig. 1b). To test whether whisking can also occur without breathing, we applied a puff of ammonia to the snout, which inactivates the central inspiratory drive¹⁹ (Supplementary Fig. 1) and temporarily inhibits respiration. Critically, rats can whisk during such a disruption in breathing (Fig. 1b), which implies that the oscillator (or oscillators) for breathing and whisking are separately gated.

Exploratory behaviour typically consists of bouts of simultaneous whisking and fast breathing, or ‘sniffing’²⁷. Under such circumstances, fast breathing has a one-to-one relationship with whisking (that is, each breath is associated with a whisk) (Fig. 1b), which is clearly evident as the rat begins to breathe again after apnea (Fig. 1b). In contrast, basal breathing is accompanied by whisks that are coincident with an inspiration, termed ‘inspiratory whisks’, and with decrementing ‘intervening whisks’ that occur between successive breaths (Fig. 1b). This leads to an incommensurate relationship between whisking and breathing, with multiple whisks between breaths. These data imply that there are separate, or separable, oscillators for breathing and whisking, and that the breathing rhythm may reset the whisking rhythm.

The temporal relationship between whisking and breathing was quantified across the complete data set (five rats) (Fig. 1c, d). We observe that breathing occurs over a broad range of frequencies, but has two modes (Fig. 1c). We define ‘basal respiration’ as epochs with a breathing rate that is below 3 Hz, and ‘sniffing’ as epochs with rates that are higher than 5 Hz (Fig. 1c). Whisking has a broad, high-frequency spectral content during both basal respiration and sniffing (Fig. 1c). The detailed timing between whisking and breathing is revealed through a frequency-ordered plot of the correlation of whisking with breathing (Fig. 1d). Vibrissa protractions are time-locked to the onset of inspiration across the entire range of breathing frequencies; the green arrow in Fig. 1d accounts for the delay between inspiratory drive to diaphragm relative to that of the upper airway²⁰. Basal respiration cycles are accompanied by multiple whisks per breath, with an instantaneous whisking frequency of approximately 8 Hz for the intervening whisks (Figs 1d and Supplementary Fig. 2). Analogous results, but with an instantaneous whisking frequency of approximately 13 Hz for the intervening whisks, are observed with mice ($n = 4$) (Supplementary Fig. 3). Lastly, phase-sensitivity analysis²¹ shows that inspirations late in the whisk cycle elicit a new protraction earlier than expected (Supplementary Fig. 4) and that breathing drives whisking but not vice versa (Supplementary Fig. 5). Collectively, these data imply a unidirectional connection from the breathing oscillator^{5,6,10} to a still hypothetical oscillator that generates whisking.

Facial muscles involved in whisking and breathing

Whisking and breathing-associated nose movements share facial muscle groups^{22–24}. Thus, the difference in the pattern of whisking versus basal respiration (Fig. 1b) raises the issue of which muscle groups follow the sequence of motor commands associated with whisking²⁵ as opposed to those associated with breathing¹. In particular, protraction of the vibrissae is driven primarily by intrinsic papillary muscles that wrap around the individual vibrissa follicles (Fig. 2a), whereas retraction involves viscoelastic forces as well as translation of the mystacial pad¹⁵ that is driven by the ‘extrinsic’ nasolabialis and maxillo-labialis muscles²⁵ (Fig. 2a). This determination of motor control is essential to understand the premotor brainstem circuits that drive different aspects of whisking.

We observe that the activity of the intrinsic muscles, measured from their differential electromyogram (VEMG), leads protraction for both sniffing (Fig. 2b) and basal respiration (Fig. 2c). The nasolabialis muscle, also measured from its VEMG, is active for every whisk during sniffing (Fig. 2b) but is only active for inspiratory whisks during basal breathing (Fig. 2c). The timing and extent of this process was quantified in terms of the population averaged cross-correlations between the different features of whisking and the $|\nabla\text{EMG}|$ of the different muscle groups (3,600 inspiratory and 500 intervening whisks in two rats). This analysis indicates that there is consistent modulation

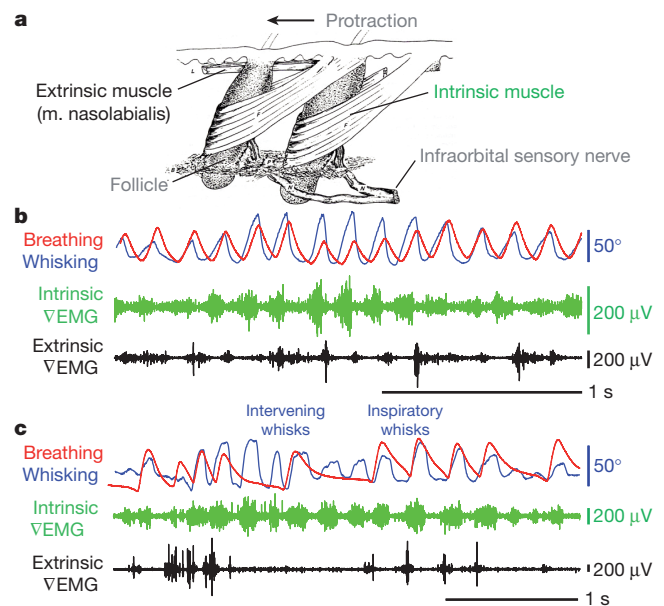


Figure 2 | Facial muscle activity during whisking and breathing. **a**, The musculature responsible for vibrissa and mystacial pad motion (adapted from a study published previously²⁴). **b**, Vibrissa motion, breathing, and intrinsic and extrinsic VEMG activity during whisking and sniffing. **c**, The same activity during whisking and mixed basal respiration and sniffing.

of the intrinsic $|\nabla\text{EMG}|$ during both inspiratory and intervening whisks but that modulation of the extrinsic $|\nabla\text{EMG}|$ activity only occurs during inspiratory whisks (Supplementary Fig. 6), thus providing information that adds to our understanding of the role of extrinsic muscles gained from previous studies^{15,25}. These data imply that protraction is driven by the proposed whisking oscillator, whereas retraction of the mystacial pad is at least partly controlled by respiratory patterning circuitry.

Identification of a region that signals whisking

The coordination of whisking with breathing, and the resetting of whisking by inspiration, suggest that a vibrissa pattern generator is driven by respiratory nuclei, which are known to lie in the ventral medulla¹. Furthermore, the differences in the basal respiration and whisking patterns provides a signature to discriminate between breathing and potential whisking neuronal centres (Fig. 1b). We recorded multi-unit spiking activity in the area of the pre-Bötzinger, Bötzing and adjoining ventral and parafacial respiratory regions (Fig. 3a–c), and identified each recording site by the location of a fiducial in a subsequent reconstruction of the brainstem (Fig. 3d, e). The functional attributes of each multi-unit signal were categorized as inspiratory or protractive (32 units), expiratory or retractive (29 units), or whisking (5 units) based on their patterns of activity during whisking and sniffing (Fig. 3f). We find that units that have a similar phase preference also lie in close spatial proximity (Fig. 3d–f). Specifically, multi-unit activity in the region of the pre-Bötzing complex and the ventral respiratory group occurred in phase with inspiration and protraction of inspiratory whisks (Fig. 3a, d, e). Multi-unit activity in the region of the Bötzing complex and the parafacial respiratory group occurred in approximate phase with expiration and retraction of inspiratory whisks (Fig. 3b, d, e). In both cases the activity did not track the intervening whisks. In contrast, we located a subset of units in the intermediate band of the reticular formation (IRT) whose spiking was tightly phase-locked to the protraction of both inspiratory and intervening whisks (Figs 3c and Supplementary Fig. 7). These units are potential premotor drivers of the intrinsic muscles that serve rhythmic whisking (Fig. 2a) and are henceforth referred to as ‘whisking units’. They are located in the ventral part of the IRT, medial to the ambiguous nucleus

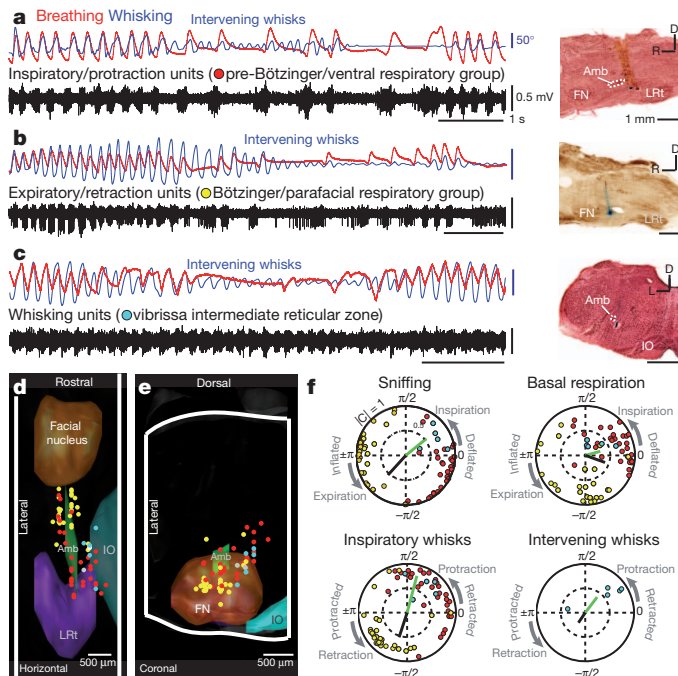


Figure 3 | Activity in medullary respiratory centres during breathing and whisking. **a**, Concurrent recordings of breathing (red), whisking (blue), and multiunit activity (black) in the pre-Bötzinger complex. The location of the recording site is labelled with Chicago sky blue and is shown in a sagittal section counterstained with neutral red. Amb, nucleus ambiguus; D, dorsal; FN, facial nucleus; IO, inferior olive; L, lateral; LRt, lateral reticular nucleus; R, rostral. **b**, Multi-unit spike activity in the Böttinger complex. The section is counterstained for cytochrome oxidase. **c**, Multi-unit spike activity in the vibrissa zone of the intermediate reticular formation. The section is counterstained with neutral red. **d, e**, The recording sites for all data, indicated by coloured dots in panels **a** to **c**, imposed on a three-dimensional reconstruction of the medulla. Whisking units are located dorsomedially to the pre-Bötzinger complex in the IRT. Two units whose spiking had no relation to breathing or whisking are shown in white. White lines are tissue boundaries or limits of the reconstruction. **f**, Polar plots of the magnitude (0 to 1 radial coordinate) and phase (angular coordinate) of the coherence between multiunit spiking activity and measured behaviours at the peak frequency for each behaviour; that is, 2 Hz for basal respiration, 6 Hz for sniffing and inspiratory whisking, and 8 Hz for intervening whisking (Fig. 1c). Only units with significant coherence ($P < 0.01$) are shown and correspond to the points in panels **d** and **e**. The coherence (C), between the measured behaviour and the ∇ EMG of the intrinsic muscles (green bar) and nasolabialis muscle ∇ EMG (black bar) are shown.

pars semicompacta and near the pre-Bötzinger complex (Fig. 3d, e). We denote this new region the vibrissa zone of the IRT (vIRt).

The phase of the neuronal activity of the above three classes of rhythmically spiking units with respect to behaviour was compared with that of the intrinsic and nasolabialis ∇ EMG (Fig. 3f). First, there is a slight phase lead between the majority of whisking units and the intrinsic muscles. Second, the activity of inspiratory or protraction units tends to lead that of the whisking units, which is particularly robust during near synchronous whisking and sniffing (Fig. 3f). These data are consistent with inspiratory or protraction units located in or near the pre-Bötzinger complex resetting a group of rhythmic whisking units in the IRT to initiate protraction. In addition, expiratory or retraction units show a phase shift between sniffing and basal respiration that is paralleled by a concurrent shift in activation of the nasolabialis muscle (Fig. 3f).

Activation of the vIRt induces whisking

The hypothesis that whisking in the vIRt constitutes the oscillator for whisking predicts that activation of this region will lead to prolonged autonomous activity. Indeed, microinjection of the glutamate receptor

agonist kainic acid in the vicinity of the vIRt is a robust means to induce prolonged rhythmic muscular activation (Fig. 4a and Supplementary Fig. 8) and coordinated vibrissa protraction (Supplementary Fig. 9), near 10 Hz, in the lightly anaesthetized head-fixed rat (Fig. 4b and Supplementary Video 1). The frequency of whisking decreases over time, and the amplitude increases, as the effect of anaesthesia declines, whereas the frequency of breathing remains constant (Fig. 4b). This implies that the chemical activation is sufficiently strong to decouple rhythmic protraction from breathing (Supplementary Fig. 10). Quantitatively, the modulation depth of protraction with breathing was less than 0.01 and insignificant for all but one case (11 epochs for three rats), compared with 0.08 for basal respiration and 0.26 for sniffing in awake animals. Finally, consistent with the conclusions from the EMG studies (Supplementary Fig. 6), the mystacial pad moves in synchrony with breathing (Fig. 4a).

Chemical activation of rhythmic whisking, with a frequency incommensurate with that of breathing, provides an opportunity to stably record from units whose firing times were coherent with rhythmic protraction (Fig. 4c). We identified units that spiked in synchrony

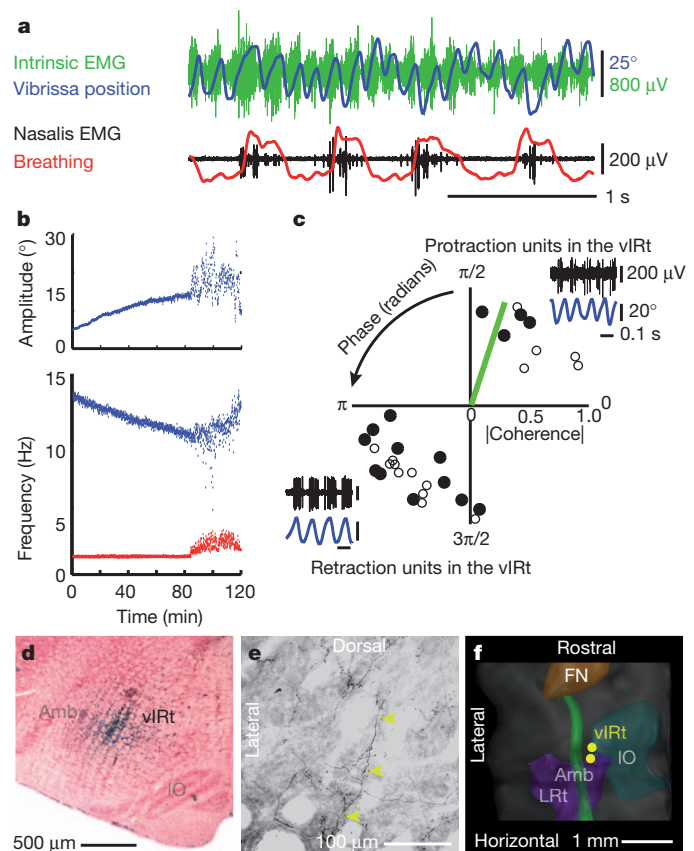


Figure 4 | Injection of kainic acid in the medullary reticular formation induces whisking. **a**, Vibrissa motion, breathing, intrinsic and extrinsic ∇ EMG. **b**, Time-course of kainic-acid-induced whisking. Instantaneous peak-to-peak amplitude (top) and frequency (bottom) of vibrissa motion (blue) and frequency of breathing (red). The animal starts to wake by 100 min. **c**, Polar plots of the coherence between spiking activity and vibrissa motion at the peak frequency of whisking (8.8 Hz median); only units with statistically significant coherence (32 of 33 units, $P < 0.01$) are shown. Open circles represent multi-unit activity and closed circles represent single units. The green bar represents the coherence of the ∇ EMG for the intrinsic muscle (panel **a**) with vibrissa motion. (Inserts) Spiking activity of neuronal units in the vIRt (black) in relation to vibrissa motion (blue). **d**, One of the locations that corresponded to a unit in panel **c**, labelled via iontophoretic injection of neurobiotin through the recording electrode. **e**, Axons (yellow arrowheads) and terminals in the ventral lateral division of the facial nucleus labelled after neurobiotin injection at the recording site in panel **d**. **f**, Three-dimensional reconstruction of the labelled recording locations for the units in panel **c**.

with protraction, as in the case of units identified during intervening whisks in the behaving animal (Fig. 3c–f), as well as units that spiked in anti-phase (32 units for four rats) (Fig. 4c). Microinjection of neurobiotin at the recording site (Fig. 4d) resulted in anterograde labelling of axon terminals in the ventrolateral part of the facial nucleus, where motor neurons that innervate the intrinsic muscles are clustered (Fig. 4e). The recording sites were located medial to the ambiguous nucleus (Fig. 4f), similar to the region localized by recording in behaving animals (Fig. 3d, e).

Lesion of the vIRt abolishes ipsilateral whisking

The above results provide evidence for the sufficiency of neurons in the vIRt to drive rhythmic protraction. We next considered the necessity of the vIRt for rhythmic motion, and tested whether a lesion to this zone suppresses whisking. First, small electrolytic lesions of the IRT medial to the ambiguous nucleus abolish whisking on the side of the lesion, whereas whisking persists on the contralateral side (Fig. 5a–c and Supplementary Video 2). Neither basal respiration nor sniffing is affected by the lesion. Furthermore, the suppression of whisking seemed to be permanent as no recovery was observed up to 10 days after the lesion. Qualitatively similar results were found with ibotenic acid or Sindbis viral lesions (Supplementary Fig. 11), which indicates that the abolition of whisking is not attributable to severed axons of passage.

The spatial specificity of the ablations was assessed by lesioning various regions in the pons and medulla in a number of animals (head-fixed, three electrolytic; free-ranging, 16 electrolytic, 1 ibotenic acid, and 5 Sindbis). Lesions made in the dorsal part of IRT, in the parvocellular reticular formation, in the paragigantocellular reticular formation, or in the caudal part of the medullary reticular formation excluding the pre-Bötzinger complex, only minimally affected whisking (Fig. 5d–f). Critically, lesions within the vIRt that were as small as 200 μm in diameter were sufficient to severely impair whisking on the

ipsilateral side. We conclude that units in the vIRt have an obligatory role in the generation of whisking.

Anatomy of the circuit for rhythmic whisking

The behavioural (Figs 1 and 2) and physiological data (Figs 3–5) suggest that cells in inspiratory nuclei reset an oscillatory network of whisking units in the vIRt that can drive protraction of the vibrissa concurrent with each inspiration. We used tract-tracing methods to assess this proposed connection. Injections of biotinylated dextran amine (BDA) into the pre-Bötzinger complex, identified by the phase relation of units relative to breathing (two rats), led to dense anterograde labelling in the IRT medial to the ambiguous nucleus, including a number of axon terminals (Fig. 6a). This corresponds to the same region in which we observed whisking units (Figs 3d, e and 4d, f) and in which lesions extinguished ipsilateral whisking (Fig. 5e, f). These results support a direct connection from the pre-Bötzinger complex to the vIRt.

We next delineated the projections from neurons in the vIRt to facial motor neurons (Fig. 4d, e). Neurobiotin (three rats) or Fluorogold (two rats) was injected in the lateral aspect of the facial nucleus (Figs 6b and Supplementary Fig. 12). We observed a cluster of retrogradely labelled cells in the IRT that lie medial to the ambiguous nucleus (Fig. 6b). A detailed map of the location of cells that were retrogradely labelled from an injection in the lateral aspect of the facial nucleus (1,300 cells in one rat) reveals a rostrocaudal band of cells in the IRT; we identify this region as vIRt (Fig. 6c and Supplementary Fig. 12). Together, these and previous^{26,27} patterns of neuronal labelling in the IRT support a direct connection from the vIRt to the facial nucleus and substantiate the role of the vIRt as a premotor nucleus.

The neurotransmitter content of neurons in the vIRt that project to the facial motor neurons was assessed by the combination of retrograde labelling and *in situ* hybridization²⁸ (Supplementary Figs 13 and 14). We find a fractional contribution of 0.12 ± 0.02 (mean \pm s.e.m.; 259 cells in 3 rats) glutamatergic, 0.85 ± 0.02 (303 cells) glycinergic, and 0.53 ± 0.03 (237 cells) GABAergic neurons. These data support either monosynaptic excitatory transmission through glutamate receptors and through glycine NR3b receptors²⁹, or monosynaptic inhibitory transmission through glycine and GABA receptors in the presence of a tonic excitatory drive.

The involvement of the nasolabialis muscle during inspiratory whisks, but not intervening whisks, suggests that retraction of the mystacial pad is controlled by units in the Bötzing or parafacial complex (Figs 2c and 3b). These units are phase-locked with expiration (Fig. 3d–f). The Bötzing and parafacial region is in close proximity to the facial nucleus¹ and is reported to modulate the activity of facial motor neurons^{18,30} that drive the nasolabialis muscle³¹. In support of a direct connection from the Bötzing complex to facial motor neurons, we observed that the map of retrogradely labelled projections to the facial nucleus shows strong labelling (Fig. 6c). In addition, small injections of neurobiotin that were made in the parafacial region (three rats) (Fig. 6d) labelled axon terminals specifically in the dorsolateral part of the facial nucleus, where motor neurons that innervate the extrinsic muscles are clustered. This result supports the conclusion that retraction of the vibrissae is at least partly mediated by neurons in the Bötzing or parafacial region.

Discussion

We have identified units in a newly defined zone of the intermediate band of the reticular formation in the medulla, the vIRt, that oscillate in phase with motion of the vibrissae (Fig. 7a). This zone functions as the premotor pattern generator for rhythmic whisking and is part of a larger circuit in which cells in nuclei that are obligatory for inspiration^{11,32,33} reset the phase of vIRt units with each breath (Fig. 7b). Thus, whisking during sniffing is effectively driven on a cycle-by-cycle basis by the inspiratory rhythm generator, whereas intervening whisks between successive inspirations result from oscillations of the

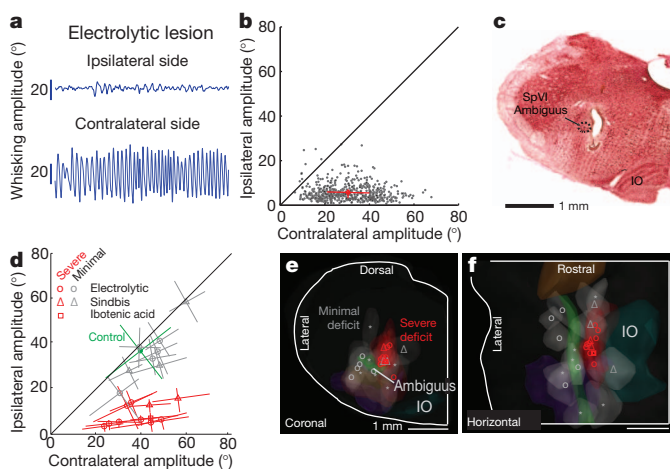


Figure 5 | Lesion of the vIRt impairs ipsilateral whisking. **a**, An example of a whisking bout after an electrolytic lesion. **b**, A scatter plot of ipsilateral versus contralateral whisk amplitudes reveals the functional completeness of the lesion; each dot represents one whisk, the red cross represents the mean, and red lines represent the inter-quartile range. **c**, Histological analysis confirms that the lesion is in the vIRt; coronal section stained with neutral red. SpVI, interparietal division of the spinal trigeminal complex. **d**, Composite results for a subset of lesions (19 rats) for which vibrissa position was tracked; lines are central quartiles. Symbols correspond to the method of lesion. Results were scored by the severity of the ipsilateral whisking deficit: severe, greater than 50% reduction (as in panels **a** and **b**), or minimal, less than 50% reduction. Whisking of a non-lesioned control rat is shown in green. **e, f**, Lesion sites were mapped onto a three-dimensional reconstruction of the medulla and selected anatomical substructures (as in Fig. 4f). The lesion centroids are denoted with the symbols in panel **d** and have a median volume of 0.2 μl . Sites marked with an asterisk (six rats) represent additional lesions (not shown in panel **d**) that resulted in minimal whisking deficits as assessed by visual inspection. White lines are tissue boundaries or limits of the reconstruction.

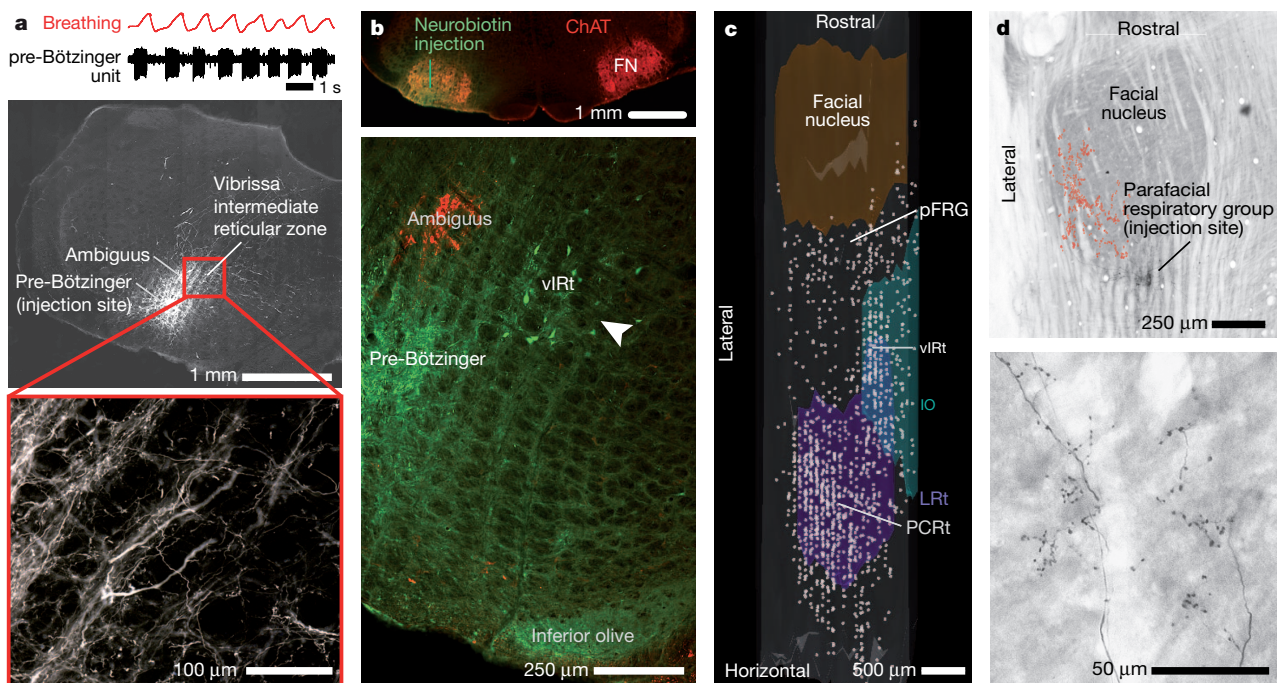


Figure 6 | Anatomical evidence for connections between respiratory and whisking zones. **a**, Recording of a single inspiratory unit in the pre-Bötzinger complex, together with breathing (top). Injection of biotinylated dextran amine through the same pipette (middle) leads to anterograde labelling of axons and terminals in the vIRt (bottom); middle and bottom panels are coronal sections. **b**, Injection of neurobiotin (green) into the facial nucleus (FN) (top) retrogradely labels neurons in the vIRt (bottom; white arrowhead). Labelling with α -choline acetyl-transferase (ChAT) highlights motor neurons in the facial and ambiguus nuclei (red). **c**, The locations of cells that were retrogradely labelled from the facial nucleus with neurobiotin, superimposed on a

three-dimensional reconstruction of the medulla. Note the labelled cells in the vIRt, located between coronal planes -12.5 and -13.0 mm relative to bregma, that span approximately $200\ \mu\text{m}$ along the lateral–medial axis. PCRt, parvocellular reticular nucleus; pFRG, the parafacial respiratory group. **d**, Injection of neurobiotin into the parafacial region labels terminals in the dorsolateral aspect of the facial nucleus (top). Individual axons and terminals are seen in the bottom panel, and a compendium across three consecutive sections is summarized in the top panel (red dots). Horizontal sections were stained for cytochrome oxidase.

whisking units in the vIRt. Retraction of the vibrissae by extrinsic muscles in the mystacial pad is probably controlled by nuclei that lie immediately caudal to the facial nucleus and that are active during expiration.

Our results may be relevant to the generation of other rhythmic orofacial behaviours, for which licking is particularly well described. First, tongue protrusions are coordinated with the respiratory cycle³⁴. Second, the hypoglossal premotor neurons are concentrated in the Irt, dorsomedial to the pre-Bötzinger complex^{3,35}, and are driven by

bursts of spikes that are locked to inspiration³⁶. Third, the output of units in the hypoglossal Irt zone locks to rhythmic licking³⁷. Finally, infusion of an inhibitory agonist into the Irt blocks licking³⁸. These past results are consistent with a model in which pre-Bötzinger units reset the phase of bursting in a network of hypoglossal premotor neurons in the Irt zone, in parallel with our circuit for whisking (Fig. 7b). Serotonergic and other modulatory inputs may serve to gate and accelerate all of these rhythms^{39–43}.

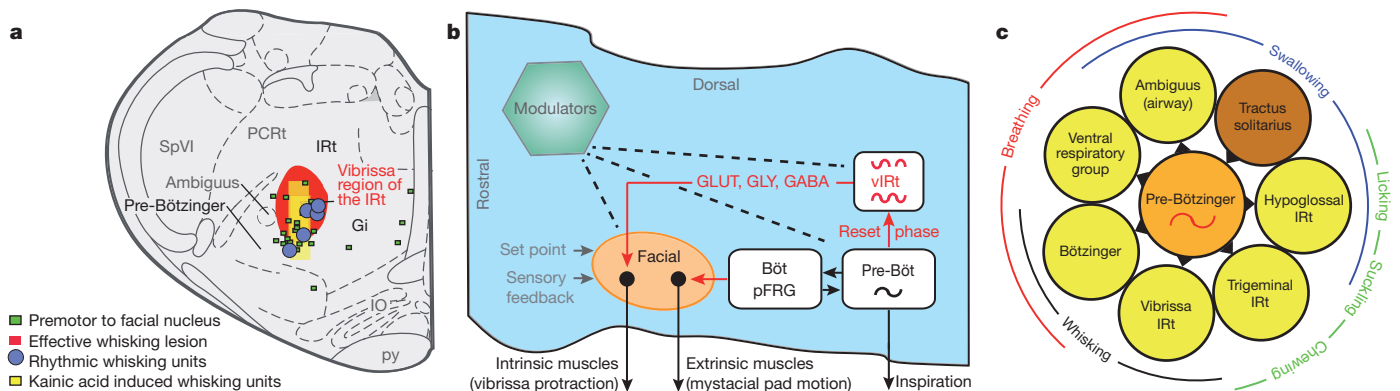


Figure 7 | The whisking rhythm generator circuit in the broader context of orofacial behaviours. **a**, Summary of evidence for a rhythm generator in the vibrissa zone of the intermediate band of the reticular formation (Irt; grey). This region contains units that fire in phase with all whisking events in freely behaving animals as well as when whisking is induced by microinjection of kainic acid. This region also contains cells that project to the facial nucleus, and lesions of this area severely disable whisking on the ipsilateral side. Gi, gigantocellular reticular formation; py, pyramidal tract. **b**, Model of the

medullary circuitry that generates whisking in coordination with breathing. Red lines indicate new findings from this work. Dashed lines indicate diffuse synaptic input from modulatory brain nuclei. GLUT, glutamate; GLY, glycine; GABA, γ -aminobutyric acid. **c**, Summary of all premotor nuclei (yellow) that are known to receive rhythmic drive from the pre-Bötzinger complex (orange), or conjectured to receive input based on anatomical projections, along with a potential resetting circuit (brown). The nuclei serve shared oral facial behaviours, as shown here for whisking (black) and breathing (red).

The common architecture of the control circuits for whisking (Fig. 7b) and licking³ supports the primary role of breathing in the coordination of orofacial behaviours. In the absence of interruptions, such as from swallowing⁴⁴ or aversive stimuli¹⁹, we propose that the inspiratory pattern generator broadcasts a master clock signal to the various patterning circuits throughout the IRT and nearby zones (Fig. 7c). Coordination by this breathing clock can ensure that these rhythmic behaviours, which share muscle groups, do not confound each other. It is also possible that the breathing clock serves as a phase-locking rhythmic signature to bind the perception of olfactory and tactile inputs.

METHODS SUMMARY

All procedures are in accordance with the Institutional Animal Care and Use Committee guidelines of the home institute of each investigator. Thirty-seven female Long Evans rats were used for behavioural and electrophysiological experiments, an additional 25 Long Evans rats of mixed sex were used solely for lesion studies, and 10 female Long Evans and 3 male Sprague Dawley rats were used for anatomical studies. Recording, labelling, anatomy and *in situ* hybridization were carried out using longstanding methods^{25,28,45} but with refinements.

Full Methods and any associated references are available in the online version of the paper.

Received 13 June 2012; accepted 14 March 2013.

Published online 28 April 2013.

- Smith, J. C., Abdala, A. P. L., Rybak, I. A. & Paton, J. F. R. Structural and functional architecture of respiratory networks in the mammalian brainstem. *Phil. Trans. R. Soc. B* **364**, 2577–2587 (2009).
- Nakamura, Y. & Katakura, N. Generation of masticatory rhythm in the brainstem. *Neurosci. Res.* **23**, 1–19 (1995).
- Travers, J. B., Dinardo, L. A. & Karimnamazi, H. Motor and premotor mechanisms of licking. *Neurosci. Biobehav. Rev.* **21**, 631–647 (1997).
- Alheid, G. F. & McCrimmon, D. R. The chemical neuroanatomy of breathing. *Respir. Physiol. Neurobiol.* **164**, 3–11 (2008).
- Feldman, J. L., Del Negro, C. A. & Gray, P. A. Understanding the rhythm of breathing: so near, yet so far. *Annu. Rev. Physiol.* **75**, 423–452 (2013).
- Garcia, A. J., Zanella, S., Koch, H., Doi, A. & Ramirez, J. M. Networks within networks: the neuronal control of breathing. *Prog. Brain Res.* **188**, 31–50 (2011).
- Welker, W. I. Analysis of sniffing of the albino rat. *Behaviour* **22**, 223–244 (1964).
- Brecht, M. & Freiwald, W. A. The many facets of facial interactions in mammals. *Curr. Opin. Neurobiol.* **22**, 259–266 (2011).
- Vincent, S. B. The function of the vibrissae in the behavior of the white rat. *Behavior Monographs* **1**, 7–81 (1912).
- Smith, J. C., Ellenberger, H. H., Ballanyi, K., Richter, D. W. & Feldman, J. L. Pre-Bötzinger complex: a brainstem region that may generate respiratory rhythm in mammals. *Science* **254**, 726–729 (1991).
- Tan, W. *et al.* Silencing preBötzinger complex somatostatin-expressing neurons induces persistent apnea in awake rat. *Nature Neurosci.* **11**, 538–540 (2008).
- Dobbins, E. G. & Feldman, J. L. Brainstem network controlling descending drive to phrenic motoneurons in rat. *J. Comp. Neurol.* **347**, 64–86 (1994).
- Bieger, D. & Hopkins, D. A. Viscerotopic representation of the upper alimentary tract in the medulla oblongata in the rat: the nucleus ambiguus. *J. Comp. Neurol.* **262**, 546–562 (1987).
- Semba, K. & Komisaruk, B. R. Neural substrates of two different rhythmic vibrissal movements in the rat. *Neuroscience* **12**, 761–774 (1984).
- Berg, R. W. & Kleinfeld, D. Rhythmic whisking by rat: retraction as well as protraction of the vibrissae is under active muscular control. *J. Neurophysiol.* **89**, 104–117 (2003).
- Gao, P., Bermejo, R. & Zeigler, H. P. Vibrissa deafferentation and rodent whisking patterns: behavioral evidence for a central pattern generator. *J. Neurosci.* **21**, 5374–5380 (2001).
- Huangfu, D., Koshiya, N. & Guyenet, P. G. Central respiratory modulation of facial motoneurons in rats. *Neurosci. Lett.* **151**, 224–228 (1993).
- Onimaru, H., Kumagawa, Y. & Homma, I. Respiration-related rhythmic activity in the rostral medulla of newborn rats. *J. Neurophysiol.* **96**, 55–61 (2006).
- Lawson, E. E., Richter, D. W., Czyzyk-Krzeska, M. F., Bischoff, A. & Rudesill, R. C. Respiratory neuronal activity during apnea and other breathing patterns induced by laryngeal stimulation. *J. Appl. Physiology* **70**, 2742–2749 (1991).
- Fukuda, Y. & Honda, Y. Differences in respiratory neural activities between vagal (superior laryngeal), hypoglossal, and phrenic nerves in the anesthetized rat. *Jpn. J. Physiol.* **32**, 387–398 (1982).
- Ermentrout, G. B. & Kleinfeld, D. Traveling electrical waves in cortex: insights from phase dynamics and speculation on a computational role. *Neuron* **29**, 33–44 (2001).
- Sherrey, J. H. & Megirian, D. State dependence of upper airway respiratory motoneurons: functions of the cricothyroid and nasolabial muscles of the unanesthetized rat. *Electroencephalogr. Clin. Neurophysiol.* **43**, 218–228 (1977).
- Haidarliu, S., Golomb, D., Kleinfeld, D. & Ahissar, E. Dorsorostral snout muscles in the rat subserve coordinated movement for whisking and sniffing. *Anat. Rec.* **295**, 1181–1191 (2012).
- Dörfel, J. The musculature of the mystacial vibrissae of the white mouse. *J. Anat.* **135**, 147–154 (1982).
- Hill, D. N., Bermejo, R., Zeigler, H. P. & Kleinfeld, D. Biomechanics of the vibrissa motor plant in rat: rhythmic whisking consists of triphasic neuromuscular activity. *J. Neurosci.* **28**, 3438–3455 (2008).
- Takato, J. *et al.* New modules are added to vibrissal premotor circuitry with the emergence of exploratory whisking. *Neuron* **77**, 346–360 (2013).
- Isokawa-Akesson, M. & Komisaruk, B. R. Difference in projections to the lateral and medial facial nucleus: anatomically separate pathways for rhythmic vibrissa movement in rats. *Exp. Brain Res.* **65**, 385–398 (1987).
- Furuta, T. *et al.* Inhibitory gating of vibrissal inputs in the brainstem. *J. Neurosci.* **28**, 1789–1797 (2008).
- Chatterton, J. E. *et al.* Excitatory glycine receptors containing the NR3 family of NMDA receptor subunits. *Nature* **415**, 793–798 (2002).
- Pagliardini, S. *et al.* Active expiration induced by excitation of ventral medulla in adult anesthetized rats. *J. Neurosci.* **31**, 2895–2905 (2011).
- Klein, B. G. & Rhoades, R. The representation of whisker follicle intrinsic musculature in the facial motor nucleus of the rat. *J. Comp. Neurol.* **232**, 55–69 (1985).
- Gray, P. A. *et al.* Developmental origin of preBötzinger complex respiratory neurons. *J. Neurosci.* **30**, 14883–14895 (2010).
- Bouvier, J. *et al.* Hindbrain interneurons and axon guidance signaling critical for breathing. *Nature Neurosci.* **13**, 1066–1074 (2010).
- Welzl, H. & Bures, J. Lick-synchronized breathing in rats. *Physiol. Behav.* **18**, 751–753 (1977).
- Koizumi, H. *et al.* Functional imaging, spatial reconstruction, and biophysical analysis of a respiratory motor circuit isolated *in vitro*. *J. Neurosci.* **28**, 2353–2365 (2008).
- Ono, T., Ishiwata, Y., Inaba, N., Kuroda, T. & Nakamura, Y. Modulation of the inspiratory-related activity of hypoglossal premotor neurons during ingestion and rejection in the decerebrate cat. *J. Neurophysiol.* **80**, 48–58 (1998).
- Travers, J. B., DiNardo, L. A. & Karimnamazi, H. Medullary reticular formation activity during ingestion and rejection in the awake rat. *Exp. Brain Res.* **130**, 78–92 (2000).
- Chen, Z., Travers, S. P. & Travers, J. B. Muscimol infusions in the brain stem reticular formation reversibly block ingestion in the awake rat. *Am. J. Physiol. Regul. Integr. Comp. Physiol.* **280**, R1085–R1094 (2001).
- DePuy, S. D., Kanbar, R., Coates, M. B., Stornetta, R. L. & Guyenet, P. G. Control of breathing by raphe obscurus serotonergic neurons in mice. *J. Neurosci.* **31**, 1981–1990 (2011).
- Doi, A. & Ramirez, J. M. Neuromodulation and the orchestration of the respiratory rhythm. *Respir. Physiol. Neurobiol.* **164**, 96–104 (2008).
- Hattox, A., Li, Y. & Keller, A. Serotonin regulates rhythmic whisking. *Neuron* **39**, 343–352 (2003).
- VanderMaalen, C. P. & Aghajanian, G. K. Intracellular studies showing modulation of facial motoneuron excitability by serotonin. *Nature* **287**, 346–347 (1980).
- Harish, O. & Golomb, D. Control of the firing patterns of vibrissa motoneurons by modulatory and phasic synaptic inputs: a modeling study. *J. Neurophysiol.* **103**, 2684–2699 (2010).
- Saito, Y., Ezure, K., Tanaka, I. & Osawa, M. Activity of neurons in ventrolateral respiratory groups during swallowing in decerebrate rats. *Brain Dev.* **25**, 338–345 (2003).
- Kleinfeld, D., Sachdev, R. N. S., Merchant, L. M., Jarvis, M. R. & Ebner, F. F. Adaptive filtering of vibrissa input in motor cortex of rat. *Neuron* **34**, 1021–1034 (2002).

Supplementary Information is available in the online version of the paper.

Acknowledgements We thank A. Kepecs and F. Wang for sharing unpublished work, and these colleagues as well as M. S. Fee, J. L. Feldman, H. J. Karten, P. M. Knutsen, D. W. Matthews and K. Svoboda for discussions. We also thank K. Svoboda for sponsorship of the mouse experiments, M. Agrochao and B. elJundi for assistance with these experiments, T. Ito and D. L. Oliver for use of their GlyT2 probe, K. K. Baldwin for the gift of the Sindbis viral vector and K. Yang for assistance with behavioural training. We are grateful to the Canadian Institutes of Health Research (grant MT-5877), the Howard Hughes Medical Institute, the Japan Society for the Promotion of Science (KAKENHI grants 23135519 and 24500409), the National Institutes of Health (grants NS058668, NS066664 and NS047101) and the US–Israeli Binational Science Foundation (grant 2003222).

Author Contributions M.D., D.K. and J.D.M. planned the experiments and wrote the manuscript. M.D., T.F. and J.D.M. carried out the rat experiments with assistance from M.D. for the histology and vibrissae tracking. D.H. carried out the mouse experiments with surgical assistance from M.C.S. Data analysis was carried out by J.D.M. with methodological contributions from D.K.

Author Information Reprints and permissions information is available at www.nature.com/reprints. The authors declare no competing financial interests. Readers are welcome to comment on the online version of the paper. Correspondence and requests for materials should be addressed to M.D. (martin.deschenes@cruilg.ulaval.ca) or D.K. (dk@physics.ucsd.edu).

METHODS

Animals. Thirty-seven female Long Evans rats (250 to 350 g, Charles River) were used for behavioural and electrophysiological experiments, an additional 25 Long Evans rats of mixed sex were used solely for lesion studies, and 10 female Long Evans and 3 male Sprague Dawley rats were used for anatomical studies. Four adult mice, two male C57BL/6J and two female Chr2-MBD⁴⁶ mice were used for behavioural studies. Experimental protocols were carried out in accordance with federally prescribed animal care and use guidelines and were approved by the Institutional Animal Care and Use Committees at the University of California in San Diego, Laval University, Kyoto University, and the Janelia Farms Research Center.

Preparation. Head-fixed rats were habituated to body restraint for 5 days, then implanted with a custom-built head restraining mount⁴⁵ and a thermocouple (K-type; Omega Engineering) in the nasal cavity⁴⁷. Surgical procedures were carried out in animals anaesthetized with ketamine (90 mg kg⁻¹) and xylazine (5 mg kg⁻¹). In brief, a craniotomy was performed over the cerebellum, and a plastic chamber was centred over the opening and secured with acrylic cement. The craniotomy was filled with silicone gel (no. 3-4689; Dow Corning). In two animals, Teflon-coated tungsten wires were inserted in the vibrissa pad to record activity of the intrinsic muscles and of the nasolabialis muscle^{15,25}. Rats were allowed to recover for 2 days before the onset of behavioural experiments. During the recording sessions, rats were placed inside a body-restraining cloth sack and rigid tube, and the animals were head-restrained⁴⁵. All vibrissae except C2 or D2 were cut at the base and movement of the intact vibrissa was recorded with videography. Rats were coaxed to whisk by presenting food or bedding from the home cage⁴⁸. Finally, in some experiments, a tube was placed in front of the snout to deliver one or two 2-s puffs of air saturated with ammonia while the animal whisked.

Head-fixed mice were implanted with a titanium bar for head fixation⁴⁹ and with a stainless steel cannula to measure breathing, as described previously⁵⁰. The mice were allowed to recover for 10 days before behavioural experiments.

Recording and analysis. To measure whisking, vibrissa motion in head-fixed rats was monitored in one of several ways with a Basler A602f camera at a spatial resolution of 120 μ m per pixel or an NMOS linear sensor (S3904-2048Q; Hamamatsu). For behavioural measurements, 360 \times 250 pixel planar images were acquired at 250 Hz with a white light emitting diode backlight for trials of 10 s each. Vibrissa angle was tracked by fitting a line to the spatially contiguous pixels comprising the initial 5 mm segment of the vibrissa base. For measurements in conjunction with extracellular recording from brainstem, we used either the Basler A602f camera in line-scan mode with a 1-kHz scan rate or the NMOS linear sensor and imaged motion along a line that was 5 to 10 mm from the edge of the mystacial pad. Pixel intensity along the line was thresholded and the centroid of the detected vibrissa was converted to a voltage proportional to pixel position in real time.

Vibrissa motion in freely moving rats with one or more vibrissae in the C or D row was monitored with a HiSpec 2G Mono camera (Fastec Imaging) at a 250-Hz frame rate, or a Powershot SX260HS camera at a 120-Hz frame rate (Canon). Rats were placed in a raised, clear plastic box with a passageway that allowed them to perch in search of their home cage, located 20 cm away. Trained animals craned across the gap and sniffed and whisked vigorously⁴⁸. Vibrissa motion was tracked with commercial software (ProAnalyst, Xcitex), and previously described algorithms⁵¹.

Vibrissa motion in head-fixed mice with vibrissae in the C row was recorded with a high-speed CMOS camera (EOSENS CL; Mikrotrotron) through a telecentric lens ($\times 0.36$; Edmund Optics). Streampix 3 software (Norpix) was used to acquire the images, 640 \times 352 pixels at a spatial resolution of 24 μ m per pixel. The vibrissae were illuminated from below with collimated infrared light from a high-power light emitting diode (640 nm; Roithner). Vibrissa motion was tracked with automated procedures⁴⁹.

The extracted vibrissa movements for all cases were separated into single whisks by band-pass filtering the position traces between 3 and 25 Hz with a 3-pole Butterworth filter run in forwards and backwards directions, and applying the Hilbert transform⁵². Individual candidate whisks were identified by phase resets of the Hilbert transform, and were accepted only if the minimum-to-maximum amplitude exceeded 5° and the whisk lasted less than 250 ms. The onset time of each whisk was defined as the time at which the vibrissa angle exceeded 10% of the minimum-to-maximum amplitude.

For electromyography, muscular activity was monitored in different muscle groups, and the integrated envelope of the EMG activity, denoted $|\text{VEMG}|$, was computed as described previously^{15,25}. We then computed the cross-correlation between protraction onset times and the $|\text{VEMG}|$. The 95% confidence intervals were obtained by 1,000 re-samples from the set of protraction onset times and computing the cross-correlation with the re-sampled data set.

To measure breathing, respiration-related changes in temperature or pressure sensors were digitized and band-pass filtered between 1 and 15 Hz with a 3-pole Butterworth filter run backwards and forwards in time. Onset times for inspiratory events were defined as described above for whisking.

In rats, respiration-related changes in temperature were verified to be synchronous with chest expansion, which are presumed to track diaphragm movements, as measured with a piezoelectric strap around the abdomen in separate experiments.

To examine neuronal signalling in awake, behaving rats, multi-unit neuronal activity was recorded in the ventral medulla with quartz micropipettes, with a tip diameter of 10 to 25 μ m, filled with 2% (w/v) Chicago sky blue (Sigma) in artificial cerebral spinal saline, or with tungsten microelectrodes (1 M Ω impedance; Microprobes). Electrode position was controlled by a motorized manipulator (model MP-285, Sutter). Units were held for 1 to 20 min. Signals were amplified, band-pass filtered between 300 Hz and 6 kHz and sampled at 20 or 40 kHz. The noise level, σ , was defined as the standard deviation of the voltages recorded over the entire time that the electrode was maintained at a recording site. Multi-unit spike events were defined as voltage fluctuations that exceeded 3.5 times σ .

One or more recording sites in each session were marked with an extracellular deposit of Chicago sky blue by electrophoresis; -10 to -50 μ A with 10-s pulses spaced every 20 s for 5 min, or by electrolytic lesion with 40 to 80 μ A applied for three intervals of 2 to 5 s. Rats were deeply anaesthetized at the end of the session and perfused with phosphate buffered saline (PBS), and then with 4% (w/v) paraformaldehyde in PBS. Brains were post-fixed overnight in 4% paraformaldehyde in PBS, cryoprotected in 30% (w/v) sucrose in PBS, and sectioned along the sagittal or coronal plane at a thickness of 60 μ m with a freezing microtome. Sections were stained with either Neutral red, Neurotrace blue (fluorescent Nissl; Invitrogen) or cytochrome oxidase⁵³.

To investigate kainic acid-induced whisking, microinjections of kainic acid were made through quartz or glass micropipettes, 10 to 15 μ m in diameter, in rats that were anaesthetized with ketamine and xylazine as described above. Injections were targeted to the approximate vibrissa region of the intermediate band of the reticular formation (vIRT) as defined in our anatomical studies (Fig. 6) using stereotaxic coordinates. Kainic acid was prepared as 1% (w/v) in Tris buffer, pH 8.2, and delivered by iontophoresis with -500 nA, 250-ms pulses spaced every 500 ms for 600 s. In several experiments, biotinylated dextran amine (M_r 3000; Invitrogen) prepared as 2% (w/v), was added to the solution to label the injection site.

Rats were secured with a head-fixed mount and their vibrissae were monitored with a camera in linescan mode (Basler A602f). Coordinated, rhythmic vibrissa movements typically began 15 to 30 min after the kainic acid injection, at which point all vibrissae except C2 or D2 were trimmed. Individual whisks were detected, as described above, with the exception that the threshold for detecting a whisk was set to 1°.

Single and multi-unit recordings in the vicinity of the site of the kainic acid injections were made in a subset of rats using glass microelectrodes with 2- to 3- μ m tips back-filled with neurobiotin (Vector Labs), prepared as a 2% (w/v) solution in 500 mM potassium acetate. These pipettes served for both recording and labelling of the recording site. The centroid of injection sites that induced whisking varied by up to 1 mm relative to the actual anatomical location of the vIRT, consistent with variability in stereotaxic coordinates between rats⁵⁴ and the rapid diffusion of kainic acid. We thus made multiple penetrations offset from each other by at most 100 μ m to locate units whose spiking was locked to whisking after the kainic acid injection. The depth of each unit along a penetration was noted, and at the end of a subset of the experiments the recording site was labelled by iontophoresis; +50 to +100 nA, 2-s pulses spaced every 4 s for 1,000 s. The animals were perfused 2 h after the injection.

For coherence and correlation analysis, we assessed the degree and statistical significance of correlation between whisking and breathing events (Fig. 1d) by computing the cross correlation between whisk onset times and breath onset times separately for basal respiration, with rates of less than 3 Hz, and sniffing, with rates of greater than 5 Hz. The maximum lag for the cross correlation computed in each case was bounded by the minimum breathing period. Statistical significance was assessed by performing a one sample Kolmogorov-Smirnov test versus the uniform distribution expected by chance. In accordance with this, we define the modulation depth of the cross correlation as the corresponding Kolmogorov-Smirnov test statistic.

Additional analyses were carried out in the frequency domain to assess the spectral content and synchrony between whisking, breathing and spiking activity. For experiments in awake animals, whose behaviour exhibited interleaved bouts of basal respiration, sniffing and whisking, our data were segmented as follows. First, 'inspiratory' whisks were defined as those whisks whose onset occurred within 100 ms of an inspiration, whereas intervening whisks were defined as whisks that did not occur within 100 ms of the closest onset of inspiration.

Next, behavioural epochs were classified as 'basal respiration' when the instantaneous respiratory frequency was less than 3 Hz, 'sniffing' for periods when the instantaneous respiratory frequency was greater than 5 Hz, 'inspiratory whisking' for periods of successive inspiratory whisks, and 'intervening whisking' for periods of successive intervening whisks during 'basal respiration'. Bouts of these behaviours were divided into non-overlapping segments of a pre-determined length; that is, 1 s for basal respiration, 500 ms for sniffing and inspiratory whisking, and 300 ms for intervening whisking. For each segment, we extracted the relevant behavioural signal; that is, inspiration onset times for basal respiration and sniffing, and vibrissa position for inspiratory and intervening whisking, and the relevant physiological signal (the $|\nabla \text{EMG}|$ or the multi-unit spike times).

The Chronux toolbox (<http://www.chronux.org>) was used to compute the spectral coherence between these respective behavioural and physiological signals, averaged over all segments with a time-bandwidth product of one. We report the magnitude and phase of the coherence at the peak frequency of the behaviour (Fig. 1c); that is, 2 Hz for basal respiration, 6 Hz for sniffing and inspiratory whisking, and 8 Hz for intervening whisking. The whisking and breathing analyses are normalized so that a phase of zero corresponds to the onsets of protraction and inspiration, respectively, as defined above.

For experiments in anaesthetized animals with pharmacologically induced whisking, we computed the spectral coherence between vibrissa position and either spike times or $|\nabla \text{EMG}|$ irrespective of breathing, averaged over all 2-s segments with a time-bandwidth product of two. We report the magnitude and phase of the coherence at the peak frequency whisking, which varied between experiments. The analysis is normalized as above. Phase zero corresponds to the onset of protraction.

Medullary lesions and whisking. Electrolytic lesions were made with metal microelectrodes (0.5 M Ω ; FHC) by passing direct current of +40 to +80 μA for 5 s at multiple nearby spatial locations. In select cases the lesions were performed with glass pipettes in head-fixed animals immediately after unit recordings in the vIRT. Ibotenic acid lesions were made by pressure injection of approximately 300 nl of ibotenic acid, prepared as 1% (w/v) in physiological saline. Sindbis virus lesions were made by pressure injection of approximately 100 to 300 nl of viral vector⁵⁵ (approximately 3×10^3 infectious particles per μl) using glass micropipettes with tips 30 μm in diameter. Two to five days after the animal recovered from surgery, high-speed videography of vibrissa motion was carried out on both sides of the face in both head-fixed and freely moving animals. Vibrissae were tracked and individual whisks were identified based on the motion on the contralateral side, as described above. The mean amplitude of the Hilbert transform over the period of each whisk was calculated for both the ipsilateral and contralateral sides.

Anatomy. For anterograde and retrograde labelling, all tracer injections were made under ketamine and xylazine anaesthesia, as above, with concurrent monitoring of respiration. Cells in the Böttinger–parafacial complex were labelled with neurobiotin (Vector Labs), prepared as a 2% (w/v) solution in 500 mM potassium acetate. Glass microelectrodes with 4- to 5- μm tips served for both recording and injection. Böttinger cells were identified by their expiration-related activity and neurobiotin was delivered by iontophoresis; +50 to +100 nA, 2-s pulses spaced every 4 s for 1,000 s. The animals were perfused after 90 min of recovery.

Cells in the pre-Böttinger complex were similarly identified by their inspiration-related activity and labelled with biotinylated dextran amine (10 kDa molecular mass; Invitrogen), prepared as a 2% (w/v) solution in 500 mM potassium acetate. Biotinylated dextran amine was delivered by iontophoresis using glass microelectrodes with 8- to 10- μm tips; +200 nA, 2-s pulses spaced every 4 s for 1,000 s. The animals were perfused after 2 days of recovery.

Cells that projected to the facial motor nucleus were labelled retrogradely with neurobiotin, prepared as a 2% (w/v) solution in 10 mM sodium citrate buffer at pH 3.0 using glass microelectrodes with 20- μm diameter tips. The location was confirmed by microstimulation, +5- to +10- μA pulses, 100 μs in width, delivered at 100 Hz, that led to movements of approximately 2° of one or more vibrissae. Neurobiotin was delivered by iontophoresis; +300 nA, 2-s pulses spaced every 4 s for 1,000 s. The animals were perfused after 3 h of recovery. Complementary studies involved the use of Fluorogold (Fluorochrome), prepared as a 1% (w/v) in 0.1 M cacodylate buffer at pH 7.0, delivered as above but with the animals perfused after 2 days.

After perfusion, brains were post-fixed for 2 h and cryoprotected in 30% (w/v) sucrose for 12 h. The brainstems were then isolated and cut in the coronal or

sagittal plane at a thickness of 50 μm on a freezing microtome. Neurobiotin and BDA were revealed with ABC Elite and SG kits (Vector Labs) or with streptavidin-Alexa 488 (1:200 dilution; Invitrogen). Fluorogold was revealed by immunohistochemistry (1:5,000 dilution; Millipore). Sections were then counterstained with Neutral red, immunostained for choline acetyltransferase (1:1,000 dilution of α -ChAT; Millipore), or reacted for cytochrome oxidase.

To examine lesion anatomy, animals lesioned with the Sindbis viral vector, for which we observed a severe deficit in whisking, were perfused immediately after video recordings; this corresponded to 50 to 75 h after injection of the virus. Animals that did not exhibit a deficit were perfused after 4 to 6 days. Animals lesioned electrolytically or with ibotenic acid were perfused 2 to 10 days after the procedure. For electrolytic lesions, 60- μm coronal or sagittal sections were stained for neutral red. For ibotenic acid and Sindbis viral lesions, 30 μm coronal or sagittal sections were immunostained for neuronal nuclear protein (1:200 dilution of anti-NeuN; Millipore). For Sindbis viral lesions, alternate sections were stained for myelin (Luxol fast blue; Sigma) and cell bodies (neutral red).

For mapping, histological sections were scanned at 1 μm spatial resolution using a Nanoscope (Hamamatsu) digital slide scanner. The stereotaxic recording sites were superimposed on the scans according to their distance to the nearest labelled site. Sections containing Chicago sky blue deposits and associated recording sites were aligned by manual rotation and translation with an atlas of sagittal Nissl sections (brainmaps.org). The outlines of prominent medullary structures, including the facial nucleus, lateral reticular nucleus, nucleus ambiguus and inferior olive were traced with neuroLucida (MicroBrightfield) software, and sections were aligned based on these anatomical borders to yield a three-dimensional reconstruction of the medulla. The extents of brainstem lesions were similarly mapped onto standard frontal sections⁵⁶.

Combined anatomy and *in situ* hybridization. For retrograde labelling and *in situ* hybridization, tracer injections were made under ketamine and xylazine anaesthesia. Fluorogold, 4% (w/v) in saline, was injected into the lateral part of the facial nucleus by passing 500-nA current pulses, 7 s in duration, every 14 s for 300 s using glass microelectrodes with tips 20 μm in diameter. After a survival period of 48 h, rats were perfused as described above. After fixation, brains were removed, the brainstem isolated, cryoprotected with diethylpyrocarbonate-treated sucrose, and cut into 30- μm -thick sagittal sections on a freezing microtome for *in situ* hybridization⁵⁷.

To count cells, retrogradely labelled cells in sections processed for *in situ* hybridization were counted under confocal microscopy with a $\times 40$ objective, as described²⁸. Approximately ten fields were scanned in a grid-like manner across the vIRT, as defined in our other anatomical tracing experiments (Supplementary Fig. 8). For each field, a stack of 5 to 10 optical sections were acquired, and counts were made from the stacked images.

46. Lewis, T. L. Jr, Mao, T. & Svoboda, K. Myosin-dependent targeting of transmembrane proteins to neuronal dendrites. *Nature Neurosci.* **12**, 568–576 (2009).
47. Uchida, N. & Mainen, Z. F. Speed and accuracy of olfactory discrimination in the rat. *Nature Neurosci.* **6**, 1224–1229 (2003).
48. Ganguly, K. & Kleinfeld, D. Goal-directed whisking behavior increases phase-locking between vibrissa movement and electrical activity in primary sensory cortex in rat. *Proc. Natl Acad. Sci. USA* **101**, 12348–12353 (2004).
49. O'Connor, D. H. et al. Vibrissa-based object localization in head-fixed mice. *J. Neurosci.* **30**, 1947–1967 (2010).
50. Shusterman, R., Smear, M. C., Koulakov, A. A. & Rinberg, D. Precise olfactory responses tile the sniff cycle. *Nature Neurosci.* **14**, 1039–1044 (2011).
51. Knutsen, P. M., Derdikman, D. & Ahissar, E. Tracking whisker and head movements in unrestrained behaving rodents. *J. Neurophysiol.* **93**, 2294–2301 (2005).
52. Hill, D. N., Curtis, J. C., Moore, J. D. & Kleinfeld, D. Primary motor cortex reports efferent control of vibrissa position on multiple time scales. *Neuron* **72**, 344–356 (2011).
53. Deschênes, M., Timofeeva, E. & Lavallee, P. The relay of high frequency sensory signals in the whisker-to-barrel cortex pathway. *J. Neurosci.* **23**, 6778–6787 (2003).
54. Paxinos, G., Watson, C., Pennisi, M. & Topple, A. Bregma, lambda and the interaural midpoint in stereotaxic surgery with rats of different sex, strain and weight. *J. Neurosci. Methods* **13**, 139–143 (1985).
55. Ghosh, S. et al. Sensory maps in the olfactory cortex defined by long-range viral tracing of single neurons. *Nature* **472**, 217–220 (2011).
56. Paxinos, G. & Watson, C. *The Rat Brain in Stereotaxic Coordinates* 6th edn (Academic Press, 2007).
57. Ito, T. & Oliver, D. L. Origins of glutamatergic terminals in the inferior colliculus identified by retrograde transport and expression of VGLUT1 and VGLUT2 genes. *Front. Neuroanat.* **4**, 135 (2010).

Hypothalamic programming of systemic ageing involving IKK- β , NF- κ B and GnRH

Guo Zhang^{1,2,3*}, Juxue Li^{1,2,3*}, Sudarshana Purkayastha^{1,2,3*}, Yizhe Tang^{1,2,3*}, Hai Zhang^{1,2,3*}, Ye Yin^{1,2,3}, Bo Li^{1,2,3}, Gang Liu^{1,2,3} & Dongsheng Cai^{1,2,3}

Ageing is a result of gradual and overall functional deteriorations across the body; however, it is unknown whether an individual tissue primarily works to mediate the ageing progress and control lifespan. Here we show that the hypothalamus is important for the development of whole-body ageing in mice, and that the underlying basis involves hypothalamic immunity mediated by I κ B kinase- β (IKK- β), nuclear factor κ B (NF- κ B) and related microglia-neuron immune crosstalk. Several interventional models were developed showing that ageing retardation and lifespan extension are achieved in mice by preventing ageing-related hypothalamic or brain IKK- β and NF- κ B activation. Mechanistic studies further revealed that IKK- β and NF- κ B inhibit gonadotropin-releasing hormone (GnRH) to mediate ageing-related hypothalamic GnRH decline, and GnRH treatment amends ageing-impaired neurogenesis and decelerates ageing. In conclusion, the hypothalamus has a programmatic role in ageing development via immune-neuroendocrine integration, and immune inhibition or GnRH restoration in the hypothalamus/brain represent two potential strategies for optimizing lifespan and combating ageing-related health problems.

Ageing is characterized by the gradual and overall loss of various physiological functions, leading to the end of lifespan. Although the search for resolution of ageing pathology is continuing^{1–6}, research has shown that certain neurons can mediate environmental influences on ageing in *Caenorhabditis elegans* and *Drosophila*, and neural manipulations of insulin or insulin-like growth factor 1 signalling or uncoupling protein 2 were shown to affect lifespan in animals^{7–11}. In this study, we have focused on the hypothalamus, a key brain region that is crucial for the neuroendocrine interaction between the central nervous system and the periphery. We asked whether the hypothalamus may have a fundamental role in ageing development and lifespan control, in addition to its critical involvement in basic life-supporting functions such as growth, reproduction and metabolism. In tackling this bold question, we increasingly appreciated that an atypical collection of hypothalamic inflammatory changes can broadly and causally underlie the development of metabolic syndrome components including being overweight, glucose intolerance and hypertension^{12–15}, and of note, all of these disorders are often related to ageing. Furthermore, we have noted recent literature showing that microglia are involved in neurodegenerative diseases^{16–24}, which aligns with the appreciated connection between systemic immunity and ageing^{25,26}. Here, through targeting hypothalamic immunity/inflammation, we designed to test whether the hypothalamus is fundamentally important for ageing and lifespan control.

Ageing-dependent hypothalamic NF- κ B activation

In studying the potential role of the hypothalamus in ageing, we developed a strategy of targeting hypothalamic immunity, and as shown in our recent work^{12–15}, infection-unrelated inflammatory changes in the mediobasal hypothalamus (MBH) contribute to the development of various metabolic syndrome components, and the molecular basis is mediated crucially by NF- κ B and its upstream IKK- β . Indeed, using phosphorylation of NF- κ B subunit RelA to report NF- κ B activation, we observed that although hypothalamic NF- κ B was barely active in

mice of young age (3–4 months), it was activated in the hypothalamus of mice at middle-old ages (11–13 months), and the activities further increased as the mice became older (22–24 months) (Fig. 1a, b). Agreeing with this observation, messenger RNA levels of many cytokines and immune regulators increased in the hypothalamus of old mice compared to the young group (data not shown). To visualize NF- κ B activity in the MBH directly, we used an NF- κ B reporter that induces green fluorescent protein (GFP) after the binding of NF- κ B to its transcriptional response element in a lentiviral vector (Fig. 1c). After *in vitro* assessment of this approach (Supplementary Fig. 1a, b), we performed animal experiments by delivering this lentiviral NF- κ B reporter into the MBH of mice at young, middle-old and old ages. A prolonged recovery period was used to minimize the procedure-related nonspecific effects on NF- κ B. We found that GFP was negligible in the MBH of young mice (Fig. 1c), but was evident in the MBH of middle-old mice and became more profound in old mice (Fig. 1c, d), confirming that ageing is associated with hypothalamic NF- κ B activation. We also injected this lentiviral NF- κ B reporter into various other brain regions, and comparatively, the MBH was most sensitive to ageing-related NF- κ B activation (Supplementary Fig. 1c–e). Of interest, immunostaining with the neuronal marker NeuN revealed that NF- κ B activation in neurons was relatively modest under middle-old ageing, but became prominent when age further increased (Fig. 1c, d). Thus, ageing development is characterized by chronic activation of NF- κ B-directed innate immune pathway predominantly in the hypothalamus.

Control of ageing by hypothalamic IKK- β and NF- κ B

We then tested our proposed involvement of IKK- β and NF- κ B in the hypothalamic control of ageing, and our experiments focused on the MBH. Using MBH-directed lentiviral gene delivery as we previously established^{12,13}, we delivered dominant-negative I κ B- α (^{DN}I κ B- α) to inhibit NF- κ B, and constitutively active IKK- β (^{CA}IKK- β) to activate NF- κ B in MBH neurons; MBH delivery of GFP in the same lentiviral

¹Department of Molecular Pharmacology, Albert Einstein College of Medicine, Bronx, New York 10461, USA. ²Diabetes Research Center, Albert Einstein College of Medicine, Bronx, New York 10461, USA.

³Institute of Aging, Albert Einstein College of Medicine, Bronx, New York 10461, USA.

*These authors contributed equally to this work.

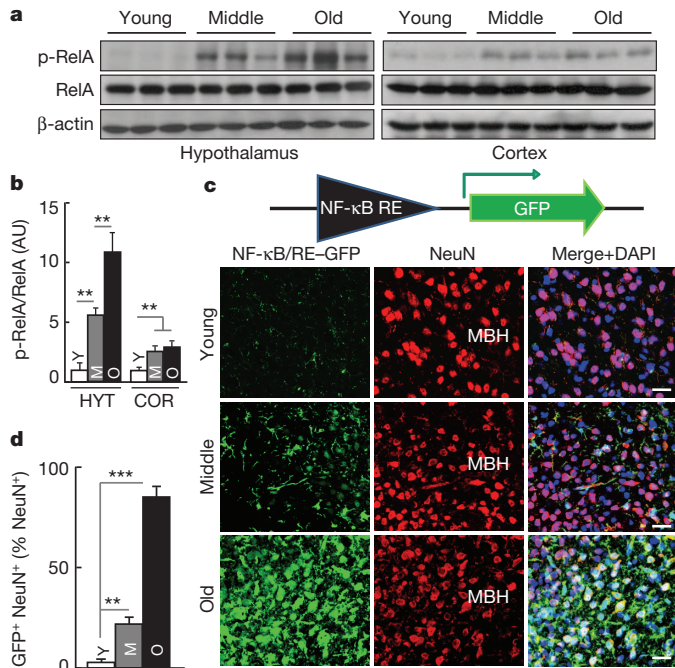


Figure 1 | Ageing-dependent hypothalamic NF- κ B activation. C57BL/6 mice (chow-fed males) were analysed at young (3–4 months) age (Y), middle-old (11–13 months) age (M), and old (22–24 months) age (O). **a**, Hypothalamus and cortex were analysed via western blots. **b**, The intensity of phosphorylated RelA (p-RelA) normalized to RelA in hypothalamus (HYT) and cortex (COR). AU, arbitrary units. **c**, Mice received MBH injections of lentiviral GFP controlled by NF- κ B response element (NF- κ B/RE), and after a ~3-week recovery, brain sections were made to reveal GFP and NeuN staining. 4',6-diamidino-2-phenylindole (DAPI) staining shows entire cell populations. Scale bars, 25 μ m. **d**, Percentages of cells co-expressing GFP and NeuN (GFP⁺ NeuN⁺) among NeuN-expressing cells (NeuN⁺) in the MBH. ** $P < 0.01$; *** $P < 0.001$; $n = 6$ (b) and 3 (d) per group. Error bars reflect mean \pm s.e.m.

system was used as the control (Supplementary Fig. 2a). Middle-old C57BL/6 mice received bilateral MBH lentiviral injections; use of middle-old age mice helped to eliminate developmental concerns, and, indeed, ageing retardation can be achieved through intervention starting at a middle-old age²⁷. These mice with MBH delivery of ^{DN}I κ B- α , ^{CA}I κ B- β and control GFP were named MBH-I κ B- α , MBH-I κ B- β and MBH-ctrl mice, respectively, and all mice were maintained under pair feeding of a normal chow so that they had similar daily food intake. Our longitudinal follow-up revealed that MBH-ctrl mice displayed a typical pattern of lifespan (Fig. 2a), which indicated that our approach of MBH injection was technically suitable. Importantly, we found that lifespan significantly increased in MBH-I κ B- α mice but decreased in MBH-I κ B- β mice compared to controls (Fig. 2a). In parallel with lifespan analysis, separate mice were generated to evaluate ageing-related physiology and histology. We assessed cognition and muscle endurance of mice at ~6 months after gene delivery, at which hypothalamic NF- κ B remained overactivated in MBH-I κ B- β mice but suppressed in MBH-I κ B- α mice (Supplementary Fig. 2b). In cognitive tests, we found that compared to controls, MBH-I κ B- α mice performed better but MBH-I κ B- β mice performed worse (Fig. 2b), and all of these mice were technically eligible for the test (Supplementary Fig. 2c). These mice were also subjected to a grip test, showing that ageing-related muscle weakness was attenuated in MBH-I κ B- α mice but worsened in MBH-I κ B- β mice (Fig. 2c). Furthermore, these mice were examined for a panel of histological biomarkers including muscle size, skin thickness, bone mass, and tail tendon collagen cross-linking. As shown in Fig. 2d–g, ageing-related changes of these biomarkers were dampened in MBH-I κ B- α mice but exacerbated in MBH-I κ B- β mice. Finally,

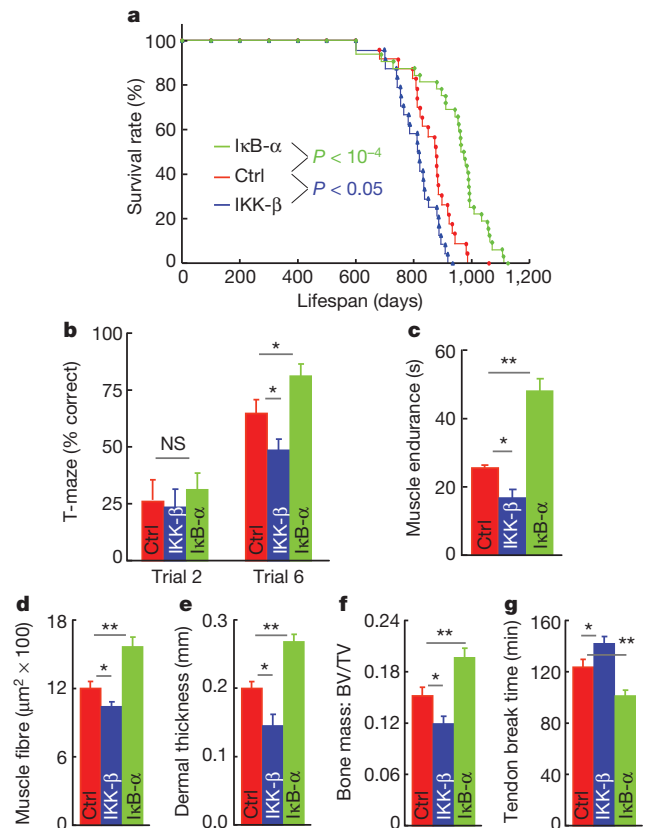


Figure 2 | Ageing manipulations by hypothalamic IKK- β and NF- κ B. MBH-I κ B- β , MBH-I κ B- α and MBH-ctrl mice were generated using ~18-month-old C57BL/6 mice (chow-fed males) via MBH injections of lentiviruses expressing ^{CA}I κ B- β , ^{DN}I κ B- α and control GFP under the control of synapsin promoter. **a**, Lifespan of these mice ($n = 23$ –31 mice per group). **b**, **c**, Mice at ~6 months after gene delivery were assessed for cognition via the T-maze (b) and muscle endurance (c). **d**–**g**, Mice were killed at 8–10 months after gene delivery for measuring muscle (quadriceps) fibre size (d), dermal thickness (e), bone mass (f), and tail tendon breaking time (g). BV, trabecular bone volume; TV, total tissue volume. * $P < 0.05$; ** $P < 0.01$; MBH-ctrl: $n = 23$ (a), 9 (b), 6 (c), 3 (d, e), 4 (f) and 7 (g); MBH-I κ B- β : $n = 24$ (a), 10 (b), 6 (c), 3 (d, e), 4 (f) and 5 (g); MBH-I κ B- α : $n = 31$ (a), 12 (b), 7 (c), 3 (d, e), 6 (f) and 8 (g). Error bars reflect mean \pm s.e.m.

given that these data were based on males, we further generated female mouse models, and results from females agreed with the observations in males (Supplementary Fig. 3). In summary, the hypothalamus has a unique role in the development of systemic ageing, and hypothalamic IKK- β and NF- κ B represents a driving force in this process.

Hypothalamic microglia in ageing development

To understand ageing-related hypothalamic immunity/inflammation further, we profiled microglia in the hypothalamus. Using immunostaining, we found that numbers of microglial cells in the MBH increased in an age-dependent manner (Fig. 3a, b). Overproduction of tumour necrosis factor- α (TNF- α) (Fig. 3a, c) and activation of NF- κ B (Supplementary Fig. 4) were both detected in these microglial cells, indicating that they were inflammatory. We noted that under early ageing, NF- κ B activation was already evident in hypothalamic microglia (Fig. 3a, b); however, this change was still modest in hypothalamic neurons (Fig. 1c, d). Also as observed, TNF- α overproduction was mostly limited to hypothalamic microglia during early ageing, but became prevalent across the MBH, which affected other neural cells (such as neurons) in this region. We additionally measured hypothalamic *Tnfa* mRNA levels in mice of different ages, and data obtained (Supplementary Fig. 5a) well correlated with cell counting of TNF- α immunostaining (Fig. 3c). It should be mentioned that TNF- α is a gene product of NF- κ B and also acts to

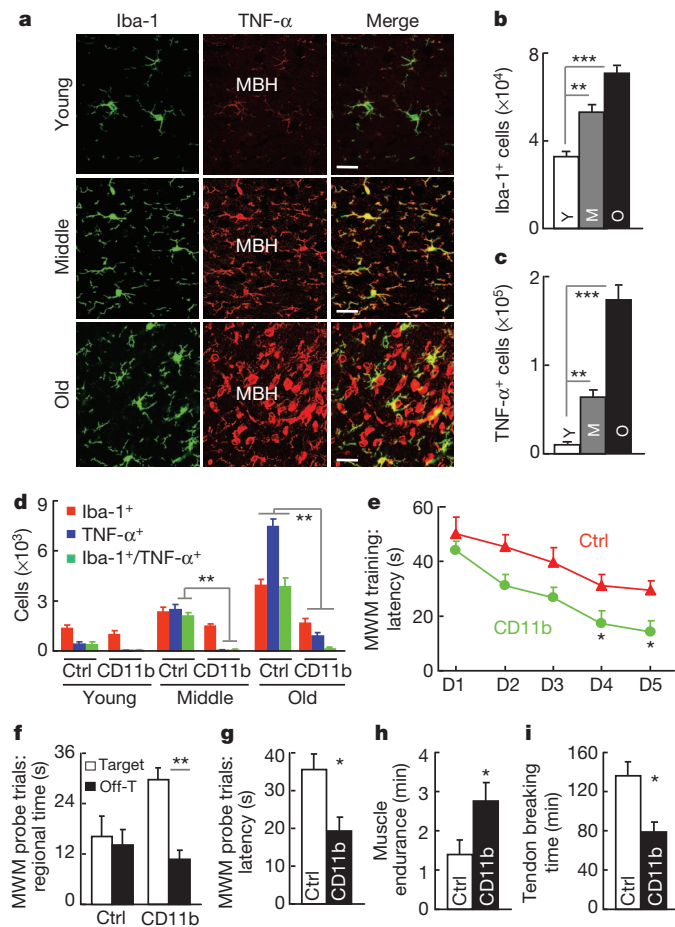


Figure 3 | Role of hypothalamic microglia in ageing. **a–c**, Brain sections of young, middle-old and old C57BL/6 mice were analysed for hypothalamic microglia. **a**, Images of immunostaining in MBH subregion. Scale bars, 25 μm. **b, c**, Numbers of cells expressing Iba-1 (Iba-1⁺) (**b**) or TNF-α (TNF-α⁺) (**c**) in the hypothalamic medial basal region (across the confocal microscopic field of serial sections under ×200 magnification). **d**, Middle-old *Ikkb*^{lox/lox} mice received bilateral MBH injections of lentiviral CD11b promoter-driven Cre (CD11b) versus control (ctrl). At 1 or 8 months after injection, brain sections were made for Iba-1 and TNF-α staining (images in Supplementary Fig. 4c). Mice generated at a young age provided normal references. Data show numbers of cells immunoreactive for Iba-1, TNF-α or both in the arcuate nucleus. **e–i**, Mice were generated via viral injections at a middle-old age and assessed at old ages for cognition (**e–g**), muscle endurance (**h**), and tail tendon breaking time (**i**). Morris water maze (MWM) data included time in target quadrant versus one representative off-target (off-T) quadrant in probe trials. D1–D5, days 1–5. **P* < 0.05; ***P* < 0.01; ****P* < 0.001; *n* = 4 (**b, c**) and 3 (**d**) per group; ctrl: *n* = 6 (**e–g, i**) and 9 (**h**); CD11b: *n* = 5 (**e–g**) and 6 (**h, i**). Error bars reflect mean ± s.e.m.

activate IKK-β and NF-κB. Overall, our data indicate that TNF-α is generated mainly by microglia during early ageing, and the paracrine actions of this cytokine on neighbouring cells is predicted to lead to ageing-associated neuronal IKK-β and NF-κB activation. In the literature, TNF-α is known to be neurotoxic or neuroprotective^{28–30}, which may reflect the differential functions of soluble versus transmembrane TNF-α (ref. 30). In our ageing model, soluble TNF-α seems to be involved in IKK-β and NF-κB-mediated microglia–neuron crosstalk that controls systemic ageing.

Hypothalamic control of ageing by microglial IKK-β

Subsequently, we generated a mouse model with IKK-β knockout in the MBH microglia through bilaterally delivering microglia-specific (CD11b promoter-driven) lentiviral Cre into the MBH of *Ikkb*^{lox/lox} mice, and control mice were *Ikkb*^{lox/lox} mice injected with Cre-deficient

lentiviruses. Our assessment confirmed that Cre was delivered specifically in ionized calcium binding adaptor molecule 1 (Iba-1)-expressing microglia, and most of these cells in the MBH were induced with Cre (Supplementary Fig. 5b). By profiling these IKK-β knockout mice and matched controls, both of which were generated at a middle-old age, we observed that IKK-β ablation in microglia prevented against the increase of microglial cells over ageing (Fig. 3d and Supplementary Fig. 5c). Moreover, IKK-β ablation prevented ageing from inducing TNF-α expression not only in microglia but also in neighbouring cells. Such ageing-related hypothalamic microglia–neuron crosstalk via IKK-β and NF-κB led us to predict that microglia-specific IKK-β ablation might slow down ageing. To test this prediction, we continued to use this IKK-β knockout mouse model generated at a middle-old age, maintained them until old ages, and assessed their ageing manifestations. After technical evaluation (Supplementary Fig. 5d–f), we tested these mice using the Morris water maze, and data showed that microglia-specific IKK-β ablation reduced ageing-related cognitive decline (Fig. 3e–g). Furthermore, IKK-β ablation resulted in improvements in ageing-related muscle weakness (Fig. 3h) and tail collagen cross-linking (Fig. 3i). Altogether, hypothalamic microglia can act via IKK-β and NF-κB to contribute to the role of the hypothalamus in ageing development.

Genetic longevity by suppressing brain IKK-β

We further resorted to a genetic model of brain-specific IKK-β knockout mice, *N/Ikkb*^{lox/lox} mice, which we generated by breeding nestin-Cre with *Ikkb*^{lox/lox} mice as described previously¹³. Compared to wild-type littermates with matched *Ikkb*^{lox/lox} background, these knockout mice were developmentally indistinguishable in terms of brain size and gross morphology (Supplementary Fig. 6). We also compared *Ikkb*^{lox/lox} mice to additional types of control, and confirmed that all these mice were similar across a spectrum of ageing-related physiological and histological changes (Supplementary Fig. 7). In this context, we profiled ageing-related physiology and pathology in *N/Ikkb*^{lox/lox} mice and littermate wild types. At an old age, after technical assessment (Supplementary Fig. 8a–c), we subjected mice to the Morris water maze, and found that *N/Ikkb*^{lox/lox} mice outperformed wild types (Fig. 4a). This cognitive improvement was specific to ageing, because young *N/Ikkb*^{lox/lox} mice and wild types performed similarly (Supplementary Fig. 8d–h). Thus, although NF-κB seems to have a role in the development of hippocampal synaptic plasticity^{31–33}, the net effect from suppressing brain IKK-β and NF-κB under the ageing model is cognitively beneficial. Using a grip test, we further found that compared to wild type, *N/Ikkb*^{lox/lox} mice had a reduced extent of ageing-related muscle weakness (Fig. 4b). Also, as shown in Fig. 4c–h, *N/Ikkb*^{lox/lox} mice were protected against ageing-induced muscle and skin atrophy, bone loss and collagen cross-linking. In addition to males, female *N/Ikkb*^{lox/lox} mice were studied, and the findings were consistent (Supplementary Fig. 9). Notably, we did lifespan analysis by following a cohort of male *N/Ikkb*^{lox/lox} mice and wild-type littermates. As shown in Fig. 4i, wild-type mice had a typical pattern of median and maximal lifespan; by contrast, *N/Ikkb*^{lox/lox} mice showed a pronounced phenotype of longevity, with median lifespan 23% longer (*P* = 0.0002) and maximal lifespan 20% longer (*P* < 0.05) than wild types. We recognize that the longevity phenotype of this genetic model could be a result of IKK-β inhibition jointly in neurons and glia, as nestin-Cre is known to target neural stem/progenitor cells and derived neurons and glia. To summarize, longevity in this genetic model considerably recapitulates ageing retardation from hypothalamic IKK-β and NF-κB inhibition, and technologically, ageing retardation can be achieved via IKK-β and NF-κB inhibition across the brain without evident side effects or compromised efficacy.

Ageing-related NF-κB-induced GnRH decline

To depict the hypothalamic control of ageing better, we focused on neuroendocrine pathways of the hypothalamus, and found that IKK-β and NF-κB negatively regulated GnRH. The classical action of GnRH

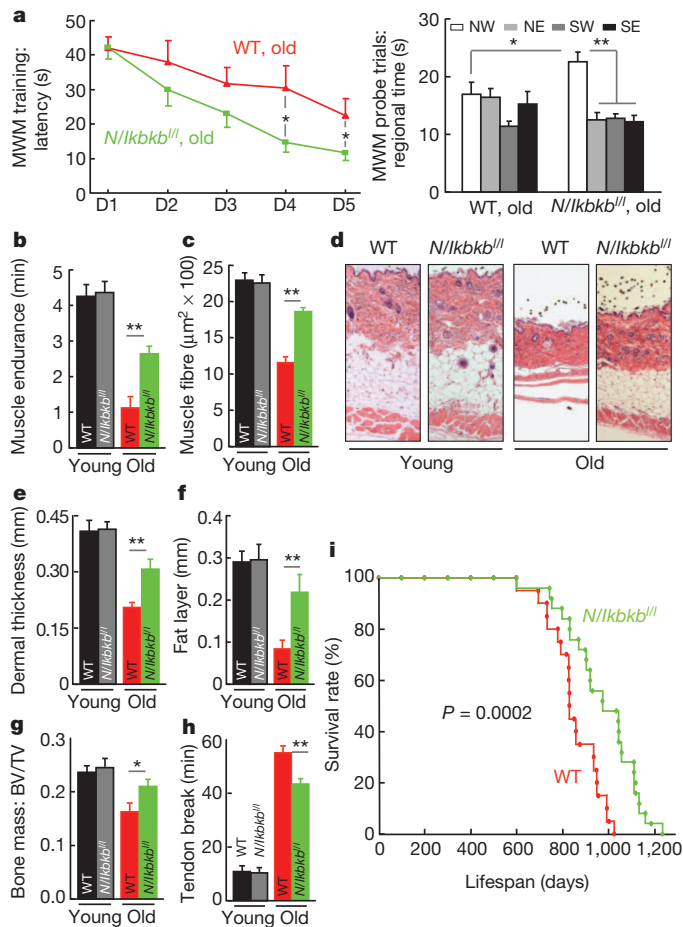


Figure 4 | Genetic longevity by brain-specific IKK- β knockout. *N/Ikkb1^{lox/lox}* mice (*N/Ikkb1^{lox/lox}*) and wild-type (WT) littermates males were maintained on chow since weaning. **a**, **b**, Young (3 months) and old-age (18–20 months) mice were tested for cognition (**a**) and muscle endurance (**b**). Morris water maze data included time in target northwest (NW) versus off-target northeast (NE), southwest (SW) and southeast (SE) quadrants in probe trials. **c**–**h**, Young (3–4 months) and old (20–24 months) mice were killed for assessing muscle (quadriceps) fibre size (**c**), dermal thickness (**d**–**f**), bone mass (**g**), and tail tendon breaking time (**h**). **i**, Lifespan follow-up ($n = 20$ in wild type and $n = 25$ in *N/Ikkb1^{lox/lox}*). * $P < 0.05$; ** $P < 0.01$; young wild type: $n = 10$ (**b**), 3 (**c**), 5 (**f**), 6 (**g**) and 8 (**h**); young *N/Ikkb1^{lox/lox}*: $n = 14$ (**b**), 3 (**c**), 5 (**f**), 6 (**g**) and 8 (**h**); old wild type: $n = 10$ (**a**), 7 (**b**), 3 (**c**), 5 (**f**), 6 (**g**) and 6 (**h**); old *N/Ikkb1^{lox/lox}*: $n = 10$ (**a**), 7 (**b**), 3 (**c**), 5 (**f**) and 6 (**g**, **h**). Error bars reflect mean \pm s.e.m.

is to regulate sex hormones and reproduction, but whether GnRH is important for whole-body ageing has yet to be determined. We found that ageing was associated with reduced hypothalamic *Gnrh1* mRNA, and this change was reversed by IKK- β and NF- κ B inhibition but enhanced by their activation (Fig. 5a–c and Supplementary Fig. 10a). Using GT1-7 cells, a cell line of GnRH neurons, we confirmed that GnRH release from these cells decreased after IKK- β and NF- κ B activation, but increased after IKK- β and NF- κ B inhibition (Fig. 5d). To study whether NF- κ B might inhibit the *Gnrh1* gene, we introduced *Gnrh1* promoter-driven luciferase into GT1-7 cells, and simultaneously activated or inhibited IKK- β and NF- κ B in these cells. Results showed that *Gnrh1* promoter activity reduced $\sim 50\%$ after IKK- β and NF- κ B activation, but increased 4–5-fold by IKK- β and NF- κ B inhibition (Fig. 5e, f). Moreover, IKK- β and NF- κ B activation increased *Fos* (also known as *c-fos*), *Jun* (*c-jun*), *Prkca* (*Pkca*) and *Prkcd* (*PKC δ*) mRNA levels (Fig. 5g), and this finding was relevant because c-Fos and c-Jun overexpression and protein kinase C (PKC) activation were both able to inhibit the *Gnrh1* promoter (Fig. 5h). Furthermore, IKK- β and NF- κ B inhibition of the *Gnrh1* promoter was attenuated by blocking c-Fos

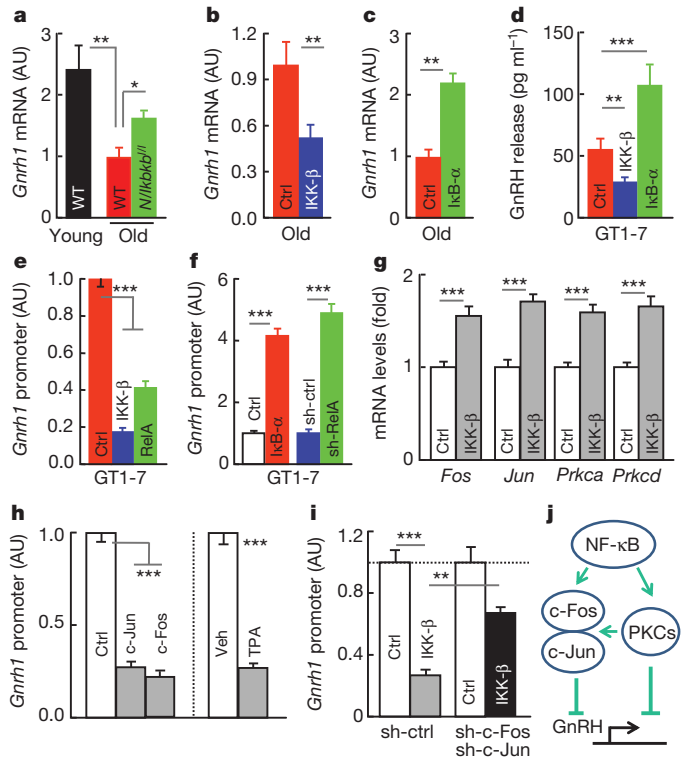


Figure 5 | Inhibition of GnRH by IKK- β and NF- κ B. **a**–**c**, Hypothalamic *Gnrh1* mRNA of mice described in Figs 2 and 3. **d**–**g**, GT1-7 cells were transfected with *CAIKK β* , *RelA* or *DNIKK α* or control plasmid (**d**, **e**, **g**), co-transfected with *Gnrh1*-promoter luciferase plasmid (**e**, **f**), or together with *RelA* short hairpin RNA (shRNA) (sh-*RelA*) or control shRNA (sh-ctrl) plasmid (**f**), and were measured for GnRH release (**d**), *Gnrh1* promoter (**e**, **f**), and *Fos*, *Jun*, *Prkca* and *Prkcd* mRNA levels (**g**). **h**, *Gnrh1* promoter activities were measured for GT1-7 cells transfected with *Gnrh1*-promoter luciferase plasmid, co-transfected with c-Jun or c-Fos plasmid versus control plasmid, or treated with 12-*O*-tetradecanoylphorbol-13-acetate (TPA) or vehicle (veh). **i**, *Gnrh1* promoter activities were measured for GT1-7 cells transfected with *Gnrh1*-promoter luciferase plasmid, co-transfected with *CAIKK β* or control plasmid, and with *Fos* and *Jun* shRNA plasmids (sh-c-Fos and sh-c-Jun) or scramble shRNA control (sh-ctrl). Values in both control groups were normalized as 1. **j**, Summarized schematic model. * $P < 0.05$, ** $P < 0.01$, *** $P < 0.001$; $n = 12$ (**a**, **e**) and 3 (**f**–**i**) per group, and $n = 6$ (**b**), 8 (**c**) and 4 (**d**) in Ctrl, $n = 8$ (**b**) and 6 (**d**) in IKK- β , and $n = 8$ (**c**) and 6 (**d**) in IKK- α . Error bars reflect mean \pm s.e.m.

and c-Jun (Fig. 5i) or by suppressing the PKC pathway (Supplementary Fig. 10b). Altogether, the c-Fos, c-Jun and PKC pathways can work together to mediate the inhibitory effect of IKK- β and NF- κ B on GnRH (Fig. 5j), and in conjunction with relevant literature³⁴, transcriptional integration of NF- κ B and c-Jun seems to account for down-regulation of GnRH in the hypothalamus.

GnRH treatment prevents ageing-impaired neurogenesis

On the basis of the known role of GnRH in regulating sex hormones, GnRH changes in our mouse models might correlate with changes in sex hormones, and this prediction was proved (Supplementary Fig. 10c, d). However, a sex hormone may not be a primary mediator for ageing phenotypes in our models, because hypothalamic IKK- β and NF- κ B are important for ageing in both sexes. This context provoked us to propose that GnRH works as a primary mediator independently of a specific sex hormone. To explore whether GnRH exerts intra-brain actions to affect ageing, we delivered GnRH into the hypothalamic third-ventricle of old mice, and examined ageing-related changes in brain cell biology. A notable observation was that GnRH promoted adult neurogenesis despite ageing. Using BrdU tracking following a

single BrdU injection to report neurogenesis¹², we found that ageing is characterized by diminished neurogenesis, particularly in the hypothalamus and the hippocampus; however, this defect was substantially reversed by GnRH treatment (Fig. 6a–c). Thirty-day BrdU tracking (with seven days of daily BrdU injections) also confirmed that BrdU-labelled cells in GnRH-treated mice significantly survived (Fig. 6d, e). Of note, these effects were seen in not only the hypothalamus but also the hippocampus and other brain regions (data not shown), reflecting the fact that GnRH travels within the brain to promote neurogenesis. Therefore, given the leadership role of the brain in controlling whole-body physiology, the brain-wide neurogenesis induced by hypothalamic GnRH may provide an explanation about how the hypothalamus, a very small structure in the brain, could control systemic ageing.

GnRH therapy decelerates ageing development

Finally, to study whether GnRH could affect ageing, we subjected old MBH-IKK- β mice and MBH-ctrl mice described in Fig. 2 to daily GnRH therapy for a prolonged period, and then examined their ageing physiology and histology. As we were also interested in testing whether GnRH could act peripherally to affect ageing, we treated mice

with GnRH via peripheral injections. Notably, GnRH treatment reduced the magnitude of ageing histology in control mice and abrogated the pro-ageing phenotype in MBH-IKK- β mice (Fig. 6f–h). Interestingly, despite the peripheral administration, GnRH led to an amelioration of ageing-related cognitive decline (Fig. 6i and Supplementary Fig. 11). Thus, a prolonged increase of systemic GnRH can cumulatively yield actions on the brain; despite the mechanism remains to be studied, some GnRH-responsive brain regions outside of the blood–brain barrier, such as the median eminence, subfornical organ and area postrema, can have access to peripheral-delivered GnRH. These effects of GnRH were not specific to a sex, as similar outcomes were shown in males (Fig. 6f–i, Supplementary Fig. 11) and females (Supplementary Fig. 12). For comparison, we treated MBH-IKK- α mice with GnRH, and it turned out that GnRH did not further enhance the anti-ageing phenotype in MBH-IKK- α mice (Supplementary Fig. 13), suggesting that NF- κ B inhibition and GnRH action may work in the same pathway to counteract ageing. Clearly, future studies are still needed to detail the central and peripheral roles of GnRH in hypothalamic control of ageing; regardless, this body of data can lead to the conclusion that the hypothalamus can integrate NF- κ B-directed immunity and GnRH-driven neuroendocrine system to program ageing development.

Discussion

In this work, we conceived that the hypothalamus, which is known to have fundamental roles in growth, development, reproduction and metabolism, is also responsible for systemic ageing and thus lifespan control. Notably, through activating or inhibiting immune pathway IKK- β and NF- κ B in the hypothalamus of mice, we were able to accelerate or decelerate the ageing process, leading to shortened or increased lifespan. Thus, in line with the literature that appreciated the effects of the nervous system on lifespan^{7–11}, our findings provide a proof of principle to the hypothesis that ageing is a life event that is programmed by the hypothalamus. Indeed, brain change is an early ageing manifestation⁴, and we reasoned that some hypothalamic alterations may act to motivate ageing of the rest parts in the body, and this outreaching role of the hypothalamus aligns with the fact that it is the neuroendocrine ‘head-quarters’ in the body. Along this line, we further revealed a direct link between IKK- β and NF- κ B activation and GnRH decline, and also importantly, we discovered that GnRH induces adult neurogenesis broadly in the brain, and GnRH therapy can greatly amend ageing disorders. Thus, whereas the inhibition of GnRH by NF- κ B may lead to the end of reproductive length—which seems necessary for species’ quality—it initiates systemic ageing at the same time. Questions remain about how hypothalamic IKK- β and NF- κ B is activated in this process; speculatively, as deduced from some recent studies about sirtuins and NF- κ B^{35,36}, age increase-induced epigenetic changes might be accountable, which calls for future investigations.

To summarize, our study using several mouse models demonstrates that the hypothalamus is important for systemic ageing and lifespan control. This hypothalamic role is significantly mediated by IKK- β and NF- κ B-directed hypothalamic innate immunity involving microglia–neuron crosstalk. The underlying basis includes integration between immunity and neuroendocrine of the hypothalamus, and immune inhibition and GnRH restoration in the hypothalamus or the brain represent two potential strategies for combating ageing-related health problems.

METHODS SUMMARY

All mice in this study were in C57BL/6 background, and *Ikkb*^{lox/lox} and nestin-Cre mice were described previously¹³. Physiological analyses included open field, visual platform test, Morris water maze, T-maze and grip test. Skin and muscle histology, bone mass via X-ray microtomography, and tail tendon breaking time were examined using standard methods in the literature. Lentiviral DNAs, virus production, MBH injection, immunostaining, western blot, and real-time PCR were similarly used in our recent research¹³, and described in the Methods. The *Gnrh1* promoter was analysed in GT1-7 cells transfected with *Gnrh1* promoter-driven luciferase plasmids. Lifespan analyses were performed as detailed in

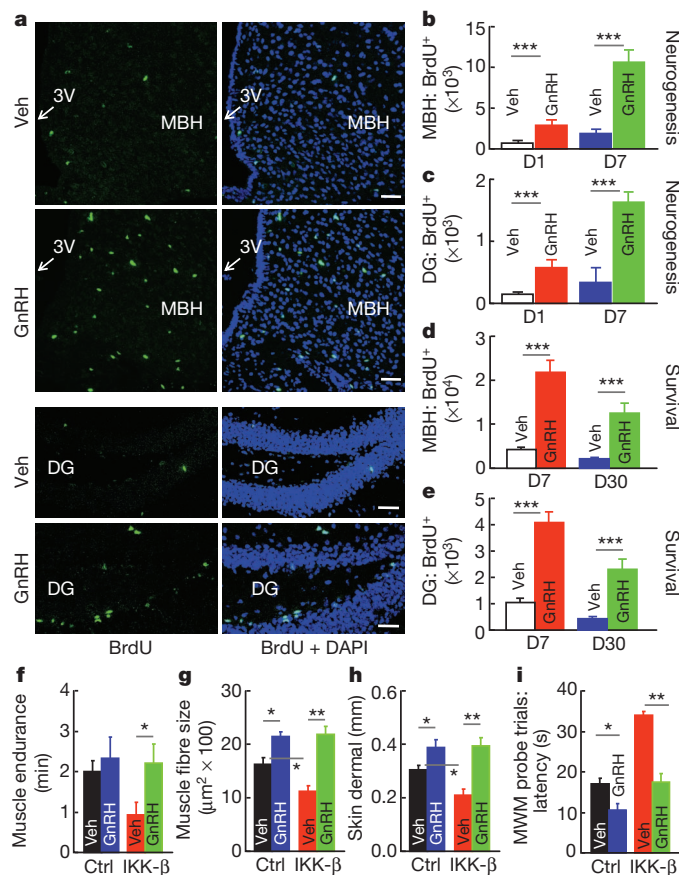


Figure 6 | Central and systemic actions of GnRH in counteracting ageing. a–e, C57BL/6 mice at an old age were subjected to neurogenesis (a–c) and survival (d, e) assays, as detailed in the Methods. a, BrdU staining images of MBH subregion and dentate gyrus (DG) in neurogenesis assay. 3V, third ventricle. Scale bars, 50 μ m. b, c, BrdU-labelled (BrdU⁺) cells in the MBH (b) and dentate gyrus (c) in a neurogenesis assay. d, e, Survival of BrdU-labelled (BrdU⁺) cells in the MBH (d) and dentate gyrus (e) in a survival assay. f–i, MBH-IKK- β and MBH-ctrl mice at an old age were daily injected subcutaneously with GnRH or vehicle for 5 weeks, and analysed for muscle endurance (f), skeletal muscle fibres (g), dermal thickness (h) and cognition (i) (see Supplementary Fig. 10 for additional data). * P < 0.05; ** P < 0.01; *** P < 0.001; n = 4 (b–e), 7 (f) and 3 (g, h) per group, and n = 12 (control, vehicle), 7 (control, GnRH), 7 (IKK- β , vehicle) and 8 (IKK- β , GnRH) (i). Error bars reflect mean \pm s.e.m.

Methods. Statistics included analysis of variance (ANOVA) and appropriate post-hoc analyses for comparisons involving more than two groups and two-tailed Student's *t*-test for comparisons involving only two groups. Data were presented as mean \pm s.e.m. *P* < 0.05 was considered significant.

Full Methods and any associated references are available in the online version of the paper.

Received 5 October 2011; accepted 2 April 2013.

Published online 1 May 2013.

1. Miller, R. A. Genes against aging. *J. Gerontol. A Biol. Sci. Med. Sci.* **67A**, 495–502 (2012).
2. Mattson, M. P. Pathways towards and away from Alzheimer's disease. *Nature* **430**, 631–639 (2004).
3. Masoro, E. J. Overview of caloric restriction and ageing. *Mech. Ageing Dev.* **126**, 913–922 (2005).
4. Finch, C. E. Neurons, glia, and plasticity in normal brain aging. *Adv. Gerontol.* **10**, 35–39 (2002).
5. Zitnik, G. & Martin, G. M. Age-related decline in neurogenesis: old cells or old environment? *J. Neurosci. Res.* **70**, 258–263 (2002).
6. Martin, G. M. Epigenetic gambling and epigenetic drift as an antagonistic pleiotropic mechanism of aging. *Ageing Cell* **8**, 761–764 (2009).
7. Bishop, N. A. & Guarente, L. Two neurons mediate diet-restriction-induced longevity in *C. elegans*. *Nature* **447**, 545–549 (2007).
8. Fridell, Y. W., Sanchez-Blanco, A., Silvia, B. A. & Helfand, S. L. Targeted expression of the human uncoupling protein 2 (hUCP2) to adult neurons extends life span in the fly. *Cell Metab.* **1**, 145–152 (2005).
9. Alcedo, J. & Kenyon, C. Regulation of *C. elegans* longevity by specific gustatory and olfactory neurons. *Neuron* **41**, 45–55 (2004).
10. Wolkow, C. A., Kimura, K. D., Lee, M. S. & Ruvkun, G. Regulation of *C. elegans* lifespan by insulinlike signaling in the nervous system. *Science* **290**, 147–150 (2000).
11. Taguchi, A., Wartschow, L. M. & White, M. F. Brain IRS2 signaling coordinates life span and nutrient homeostasis. *Science* **317**, 369–372 (2007).
12. Li, J., Tang, Y. & Cai, D. IKK β /NF- κ B disrupts adult hypothalamic neural stem cells to mediate a neurodegenerative mechanism of dietary obesity and pre-diabetes. *Nature Cell Biol.* **14**, 999–1012 (2012).
13. Zhang, X. *et al.* Hypothalamic IKK β /NF- κ B and ER stress link overnutrition to energy imbalance and obesity. *Cell* **135**, 61–73 (2008).
14. Purkayastha, S. *et al.* Neural dysregulation of peripheral insulin action and blood pressure by brain endoplasmic reticulum stress. *Proc. Natl Acad. Sci. USA* **108**, 2939–2944 (2011).
15. Purkayastha, S., Zhang, G. & Cai, D. Uncoupling the mechanisms of obesity and hypertension by targeting hypothalamic IKK- β and NF- κ B. *Nature Med.* **17**, 883–887 (2011).
16. Okun, E., Griffioen, K. J. & Mattson, M. P. Toll-like receptor signaling in neural plasticity and disease. *Trends Neurosci.* **34**, 269–281 (2011).
17. Glass, C. K., Saijo, K., Winner, B., Marchetto, M. C. & Gage, F. H. Mechanisms underlying inflammation in neurodegeneration. *Cell* **140**, 918–934 (2010).
18. Saijo, K. *et al.* A Nurr1/CoREST pathway in microglia and astrocytes protects dopaminergic neurons from inflammation-induced death. *Cell* **137**, 47–59 (2009).
19. Saijo, K., Collier, J. G., Li, A. C., Katzenellenbogen, J. A. & Glass, C. K. An ADIOL-ER β -CtBP transrepression pathway negatively regulates microglia-mediated inflammation. *Cell* **145**, 584–595 (2011).
20. Saijo, K. & Glass, C. K. Microglial cell origin and phenotypes in health and disease. *Nature Rev. Immunol.* **11**, 775–787 (2011).
21. Lucin, K. M. & Wyss-Coray, T. Immune activation in brain aging and neurodegeneration: too much or too little? *Neuron* **64**, 110–122 (2009).
22. Villeda, S. & Wyss-Coray, T. Microglia—a wrench in the running wheel? *Neuron* **59**, 527–529 (2008).
23. Villeda, S. A. *et al.* The ageing systemic milieu negatively regulates neurogenesis and cognitive function. *Nature* **477**, 90–94 (2011).
24. Yoshiyama, Y. *et al.* Synapse loss and microglial activation precede tangles in a P301S tauopathy mouse model. *Neuron* **53**, 337–351 (2007).
25. Adler, A. S. *et al.* Motif module map reveals enforcement of aging by continual NF- κ B activity. *Genes Dev.* **21**, 3244–3257 (2007).
26. Peng, B. *et al.* Defective feedback regulation of NF- κ B underlies Sjogren's syndrome in mice with mutated κ B enhancers of the I κ B α promoter. *Proc. Natl Acad. Sci. USA* **107**, 15193–15198 (2010).
27. Harrison, D. E. *et al.* Rapamycin fed late in life extends lifespan in genetically heterogeneous mice. *Nature* **460**, 392–395 (2009).
28. Barger, S. W. *et al.* Tumor necrosis factors α and β protect neurons against amyloid β -peptide toxicity: evidence for involvement of a κ B-binding factor and attenuation of peroxide and Ca²⁺ accumulation. *Proc. Natl Acad. Sci. USA* **92**, 9328–9332 (1995).
29. Bruce, A. J. *et al.* Altered neuronal and microglial responses to excitotoxic and ischemic brain injury in mice lacking TNF receptors. *Nature Med.* **2**, 788–794 (1996).
30. Taoufik, E. *et al.* Transmembrane tumour necrosis factor is neuroprotective and regulates experimental autoimmune encephalomyelitis via neuronal nuclear factor- κ B. *Brain* **134**, 2722–2735 (2011).
31. Kaltschmidt, B. *et al.* NF- κ B regulates spatial memory formation and synaptic plasticity through protein kinase A/CREB signaling. *Mol. Cell Biol.* **26**, 2936–2946 (2006).
32. Meffert, M. K., Chang, J. M., Wiltgen, B. J., Fanselow, M. S. & Baltimore, D. NF- κ B functions in synaptic signaling and behavior. *Nature Neurosci.* **6**, 1072–1078 (2003).
33. O'Mahony, A. *et al.* NF- κ B/Rel regulates inhibitory and excitatory neuronal function and synaptic plasticity. *Mol. Cell Biol.* **26**, 7283–7298 (2006).
34. Huang, W., Ghisletti, S., Perissi, V., Rosenfeld, M. G. & Glass, C. K. Transcriptional integration of TLR2 and TLR4 signaling at the NCoR derepression checkpoint. *Mol. Cell* **35**, 48–57 (2009).
35. Kawahara, T. L. *et al.* SIRT6 links histone H3 lysine 9 deacetylation to NF- κ B-dependent gene expression and organismal life span. *Cell* **136**, 62–74 (2009).
36. Michishita, E. *et al.* SIRT6 is a histone H3 lysine 9 deacetylase that modulates telomeric chromatin. *Nature* **452**, 492–496 (2008).

Supplementary Information is available in the online version of the paper.

Acknowledgements We thank other Cai laboratory members for technical assistance, and L. Farhana, D. Stocco, L. Eckhardt, T. Ohshima, A. Lin and D. Tantin for reagents. This study was supported by National Institutes of Health (NIH) grants R01 AG 031774, R01 DK078750, and American Diabetes Association grant 1-12-B5-20 (all to D.C.). D.C. is a recipient of Irma T. Hirschl Scholarship.

Author Contributions D.C. conceived project and designed the study; G.Z., J.L., S.P., Y.T., H.Z. and Y.Y. performed experiments with assistance from B.L. and G.L. All authors carried out data analyses and interpretations; D.C. organized experimentation and wrote the paper.

Author Information Reprints and permissions information is available at www.nature.com/reprints. The authors declare no competing financial interests. Readers are welcome to comment on the online version of the paper. Correspondence and requests for materials should be addressed to D.C. (dongsheng.cai@einstein.yu.edu).

METHODS

Mouse models and treatments. Nestin-Cre mice and *Ikkb^{lox/lox}* mice were described in our previous publications^{13–15,37}, and maintained on C57BL/6 strain for more than 15 generations. C57BL/6 mice were obtained from Jackson Laboratory or the National Institute of Ageing, NIH. All mice were kept under standard and infection-free housing, with 12-h light/12-h dark cycles and 4–5 mice per cage. Pathogen-free quality was ensured with quarterly serology, quarterly histopathological examinations and routine veterinarian monitoring, and a bacteriological test was additionally included. All mice in this study were maintained on a normal chow from LabDiet (4.07 kcal g⁻¹).

For animal GnRH therapy, mice were subcutaneously injected with GnRH (Sigma) at the dose of 2 ng per mouse on a daily basis for a period of 5–8 weeks. The Institutional Animal Care and Use Committee at the Albert Einstein College of Medicine approved all the procedures. Body weight and food intake were measured regularly using a laboratory scale. We performed the grip test to measure muscle endurance using the method as similarly described in the literature^{38,39}, using a homemade square grid with a small mesh size to allow mice to hang for longer time. In brief, a mouse was lifted by the tail and placed on a homemade square grid (1-cm mesh size). The grid was then inverted 30.5 cm over a soft pad, and the mouse was allowed to hang by paws for a maximum of 5 min. The time that the mouse was able to hang was recorded during a 5-min test period.

Lentiviruses and MBH injection. Synapsin promoter-directed lentiviral vector was used to drive neuron-specific gene delivery as previously established^{13–15,37}. These lentiviral vectors contain the cDNA of ^{CA}IKK- β or ^{DN}IKK- α or only GFP under the control of synapsin promoter. To create lentiviral NF- κ B reporter vector, a target plasmid was constructed to have the GFP open reading frame controlled by a DNA cassette containing five tandem repeats of the NF- κ B transcriptional response element, according to the approach established in the literature⁴⁰. The lentiviruses were produced from HEK293T cells via co-transfecting a target plasmid with two package plasmids (VSVg and delta 8.9) using CaCl₂. Lentiviruses were purified through ultracentrifugation. Intra-MBH viral injections were performed as we previously established^{13–15,37}. In brief, under an ultraprecise stereotactic instrument (resolution: 10 μ m) (Kopf Instruments), lentiviruses were bilaterally injected at the coordinates of 1.5 mm posterior to the bregma, 5.8 mm below the skull, and 0.2 mm lateral to the midline.

Cognitive behavioural tests. All mice were tested for general health, sensorimotor reflexes and motor responses before the onset of all behavioural testing. Mice were maintained on a 12-h light/12-h dark schedule in an isolation unit located inside the behavioural testing room. An AnyMaze video tracking system (Stoelting) equipped with a digital camera connected to a computer was used to videotape the whole course of animal activities in training and experimental sessions of behavioural tests.

Open field test. Locomotor activities were assessed using the open field test. The open field arena consisted of a clear Plexiglas chamber that was 40 cm \times 40 cm, with walls that were 35 cm high. The arena was placed in a brown box to reduce visual cues. Mice were placed in the arena and allowed to explore for 5 min, and measured for distance and time travelled and mean speed.

Morris water maze test. The maze was filled with 22–23 °C water that was made opaque with Crayola non-toxic paint, and was located in the centre of a small square room with numerous extra-maze cues (various black shapes on white background, a cabinet and an experimenter). The diameter of the maze was 90 cm and divided into four quadrants (northwest, northeast, southwest and southeast). A circular platform with a diameter of 10 cm was placed 25 cm from the wall in the centre of the northwest quadrant. Visual platform test: the visual platform test was performed on a single day. There were six trials with 30-min inter-trial intervals. In the test, a visible flag was placed on the top of the platform to increase the visibility, and the platform was placed on a random location for each trial. A mouse was placed on water, at the same starting location for all trials, and was measured for latency, distance and mean speed travelled to the platform. Hidden-platform training: mice were first required to swim to and sit on a circular visible platform at 0.5 cm above water level for 10 s. If mice could not find the platform within 60 s, they were gently guided to the platform using a glass stirring rod. Mice were then subjected to five consecutive days of training, consisting of two trials per entry location (entry locations were north, south, east and west) for a total of eight trials per day. The platform was made invisible by submerging it 1 cm below the surface of the water. Mice were expected to find the location of the invisible platform, and measured for latency to reach the platform, distance travelled to reach the platform, path efficiency, time spent in and distance travelled in each quadrant as well as total distance and mean swim speed. Probe trial: on day 6, mice were subjected to a single probe trial, in which the platform was removed and mice were allowed to swim for 60 s. Mice were measured for the amount of time spent in all quadrants, distance and number of times that mice crossed the location of the former platform, and total distance and mean swim speed.

T-maze. Mice were tested for reward (1:1 water/full-fat sweetened condensed milk) (Nestle) on a forced-choice alternation test in a T-maze with an opaque floor and plastic sides. Mice first received food restriction to reduce body weight by 5–10%, and then a 4-day adaptation to the apparatus with the reward. After that, mice were given six pairs of training per day for 12 days, and tests of every 2 days were designated as a trial block. On the first trial of each pair, a mouse was placed in the start arm, forced to choose one of two goal arms in the T (the other is blocked by a removable door), and received the reward at the end. The mouse was kept in this goal arm for 15–20 s and subsequently returned by the experimenter to the start arm. The animal was then given a free choice between two goal arms, rewarded for choosing the ‘novel’ arm (the one that was not chosen in the first trial of the pair), but punished for choosing the other goal arm (the one that was chosen on the first trial of the pair) using a 20 s-blocking without the reward. The location of the sample arm (left or right) was varied across trials so that mice received equal numbers of left and right presentations, and no more than two consecutive trials with the same sample location. Mice were tested in squads of 4–5 to minimize variations in inter-trial intervals, which was 5–10 min for all animals throughout 12-day training period.

Collagen cross-linking. The method of tail tendon breaking test was used to examine collagen cross-linking, as described⁴¹. In brief, a collagen fibre was teased from a mid-tail section of the lateral tail tendon and tied to a 2-g weight. The fibre was suspended into a bath containing 7 M urea at 45 °C. The fibre breaking time was determined in quadruplicate for each mouse.

Tissue histology. Skeletal muscles (quadriceps) and dorsal skin were dissected from mice, fixed in 10% neutralized formalin at 4 °C overnight, and embedded into paraffin. Paraffin sections were prepared at 5- μ m thickness and subjected to haematoxylin and eosin staining. Images were collected using an Axioskop II light microscope (Zeiss) and analysed using Image J.

Bone volume fraction measurement. We adopted the bone volume fraction procedure established in the literature⁴². In brief, the left intact femurs were removed and analysed via LaTheta LCT-100A X-ray microtomography scanner (Aloka) through mouse physiology core facility at Albert Einstein College of Medicine. The distal part of femur encompassing the cancellous bone was analysed. The trabecular and cortical bone regions were outlined for each tomography slice by the software of the scan system. Bone volume fraction was calculated as the trabecular bone volume divided by the total bone volume. A calibration phantom was used for calibration of each scan.

Immunostaining, histology and western blot. Mice under anaesthesia were perfused with 4% paraformaldehyde, and brains were removed, post-fixed in 4% paraformaldehyde, and infiltrated in 20–30% sucrose. Brain sections were made at 20- μ m thickness via a cryostat, blocked with serum, penetrated with Triton-X 100, treated overnight at 4 °C with primary antibody, followed by reaction with fluorescence-conjugated secondary antibody (Jackson), and imaged under a confocal microscope. For BrdU staining, sections were pre-treated with 1 M HCl for 30 min at 37 °C, followed by 5-min treatment with 0.1 M sodium borate, pH 8.5. Primary antibodies included rabbit anti-Iba-1 (Wako), rabbit anti-GFAP (Millipore), mouse anti-TNF- α (Abcam), mouse anti-NeuN (Millipore), and goat anti-Cre antibody (Santa Cruz). For Nissl staining, freshly isolated mice brains were fixed in 4% paraformaldehyde in PBS for overnight at 4 °C. The fixed whole brains were then subjected to cryosectioning coronally, and frozen sections were stained to detect Nissl body by using the NovaUltra Nissl stain kit (IHCWORLD) according to the manufacturer's instruction.

Serial brain sections across the MBH were made at 20 μ m thickness, and every five sections were represented by one section with staining and cell counting. For western blotting, animal tissues were homogenized, and proteins were dissolved in a lysis buffer, and western blots were conducted as previously described³. Proteins separated by SDS-PAGE were identified by immunoblotting with primary rabbit anti-pRelA, anti-RelA and anti- β -actin antibodies (Cell Signaling) and horseradish peroxidase (HRP)-conjugated anti-rabbit secondary antibody (Pierce).

DNA vectors, cell culture and molecular/biochemical analysis. Promoter sequence of the rat *Gnrh1* gene was PCR amplified (–1934 to +21) from a rat genomic DNA preparation, and subcloned into the pGL3-basic luciferase reporter vector (Promega) using standard cloning strategies. pcDNA expressing ^{CA}IKK- β or ^{DN}IKK- α versus control were previously described^{13–15,37}, or pcDNA expressing RelA-RelA was provided by A. Lin. RelA shRNA and control (GFP) shRNA vectors were obtained from Addgene, as studied in the literature⁴³. RelA shRNA: 5'-GCATGCGATTCC GCTATAA-3'; control shRNA: 5'-ACAGCCACAACGTCTATAT-3'. Expression plasmids for c-Jun or c-Fos were provided by D. Stocco. Vectors expressing c-Jun or c-Fos shRNA or scramble shRNA control were provided by L. Fahana. c-Jun shRNA: 5'-AGTCATGAACCAACGTTAAC-3'; c-Fos shRNA: 5'-TCCGAAGAG AACGGAATAA-3'; scramble shRNA: 5'-GTTATTACTGTTTCGATCGC-3'. 12-O-tetradecanoylphorbol-13-acetate (also known as phorbol 12-myristate 13-acetate or TPA) and calphostin-C were from Sigma-Aldrich. TPA or calphostin-C was

dissolved in dimethylsulphoxide (DMSO) and applied in cell culture medium at a final concentration of 0.2 μM or 0.01 μM , respectively, and DMSO did not exceed 0.1% of cell culture medium. GT1-7 cells were previously described¹³, and cultured in a standard humidified incubator at 37 °C and 5% CO₂ with DMEM cell culture medium supplemented with 10% FBS, 2 mM L-glutamine, and PenStrep (50 U ml⁻¹ penicillin G, 50 μg ml⁻¹ streptomycin). Transfection of cultured cells with luciferase plasmids and expression plasmids was performed through Lipofectamine 2000 (Invitrogen). The dual luciferase reporter assay (Promega) was performed according to the manufacturer's instruction, and co-transfection of the pRL-TK vector expressing *Renilla* luciferase was used to control firefly activity internally. Empty plasmids pGL3 and pcDNA3.1 were used as negative controls. RNA was extracted by TRIzol (Invitrogen) and analysed via SYBR green real-time PCR (StepOnePlus real-time PCR system, Invitrogen). Testosterone and oestradiol were measured using testosterone and oestradiol EIA kits (Cayman Chemical). GnRH was measured using the luteinizing hormone-releasing hormone EIA kit (Phoenix Pharmaceuticals).

BrdU labelling study. Mice were pre-implanted with intracerebroventricular (i.c.v.) cannula in the hypothalamic third ventricle, and after a ~3-week recovery, they were subjected to neurogenesis assay or survival assays. In the neurogenesis assay, mice were daily pre-injected with GnRH or vehicle at the dose of 1 ng per day through cannula for 3 days, subsequently a single i.c.v. injection of BrdU (Sigma) at the dose of 10 μg (defined as day 0), and continued to receive daily i.c.v. injections of GnRH (1 ng per day) or vehicle for 7 days before they were killed for brain sectioning. In the survival assay, mice pre-received daily i.c.v. injections of GnRH (1 ng per day) or vehicle for 3 days, then daily i.c.v. injections of BrdU (10 μg per day) together with daily i.c.v. injections of GnRH (1 ng per day) or vehicle for 7 days (last day was defined as day 7), and followed by continued daily i.c.v. injections of GnRH (1 ng per day) or vehicle until day 30 when mice were killed for brain sectioning.

Statistical analyses. Kolmogorov–Smirnov test was used to determine parametric distribution of data. Analysis of variance (ANOVA) and appropriate post-hoc analyses were used for comparisons involving more than two groups. Two-tailed Student's *t*-tests were used for comparisons involving only two groups. Lifespan analysis was performed using Kaplan–Meier survival analysis; the mutant and control survivorship curves were compared in pairs and *P* values were obtained with log-rank test. Maximal lifespan of mice were statistically analysed using Chi-squared test according to the literature⁴⁴. All data were presented as mean \pm s.e.m. *P* < 0.05 was considered significant.

37. Meng, Q. & Cai, D. Defective hypothalamic autophagy directs the central pathogenesis of obesity via the I κ B kinase β (IKK β)/NF- κ B pathway. *J. Biol. Chem.* **286**, 32324–32332 (2011).
38. Banks, W. A. *et al.* Effects of a growth hormone-releasing hormone antagonist on telomerase activity, oxidative stress, longevity, and aging in mice. *Proc. Natl Acad. Sci. USA* **107**, 22272–22277 (2010).
39. Tillerson, J. L. & Miller, G. W. Grid performance test to measure behavioral impairment in the MPTP-treated-mouse model of parkinsonism. *J. Neurosci. Methods* **123**, 189–200 (2003).
40. Mueller, J. M. & Pahl, H. L. Assaying NF- κ B and AP-1 DNA-binding and transcriptional activity. *Methods Mol. Biol.* **99**, 205–216 (2000).
41. Flurkey, K., Papaconstantinou, J., Miller, R. A. & Harrison, D. E. Lifespan extension and delayed immune and collagen aging in mutant mice with defects in growth hormone production. *Proc. Natl Acad. Sci. USA* **98**, 6736–6741 (2001).
42. Ramanadham, S. *et al.* Age-related changes in bone morphology are accelerated in group VIA phospholipase A2 (iPLA2 β)-null mice. *Am. J. Pathol.* **172**, 868–881 (2008).
43. Meylan, E. *et al.* Requirement for NF- κ B signalling in a mouse model of lung adenocarcinoma. *Nature* **462**, 104–107 (2009).
44. Wang, C., Li, Q., Redden, D. T., Weindruch, R. & Allison, D. B. Statistical methods for testing effects on “maximum lifespan”. *Mech. Ageing Dev.* **125**, 629–632 (2004).

mTOR kinase structure, mechanism and regulation

Haijuan Yang¹, Derek G. Rudge¹, Joseph D. Koos¹, Bhamini Vaidialingam¹, Hyo J. Yang¹ & Nikola P. Pavletich^{1,2}

The mammalian target of rapamycin (mTOR), a phosphoinositide 3-kinase-related protein kinase, controls cell growth in response to nutrients and growth factors and is frequently deregulated in cancer. Here we report co-crystal structures of a complex of truncated mTOR and mammalian lethal with SEC13 protein 8 (mLST8) with an ATP transition state mimic and with ATP-site inhibitors. The structures reveal an intrinsically active kinase conformation, with catalytic residues and a catalytic mechanism remarkably similar to canonical protein kinases. The active site is highly recessed owing to the FKBP12–rapamycin-binding (FRB) domain and an inhibitory helix protruding from the catalytic cleft. mTOR-activating mutations map to the structural framework that holds these elements in place, indicating that the kinase is controlled by restricted access. *In vitro* biochemistry shows that the FRB domain acts as a gatekeeper, with its rapamycin-binding site interacting with substrates to grant them access to the restricted active site. Rapamycin–FKBP12 inhibits the kinase by directly blocking substrate recruitment and by further restricting active-site access. The structures also reveal active-site residues and conformational changes that underlie inhibitor potency and specificity.

The mTOR pathway controls cell growth in response to energy, nutrients, growth factors and other environmental cues, and it figures prominently in cancer^{1,2}. Central to the pathway is the mTOR protein, which belongs to the phosphoinositide 3-kinase (PI3K)-related protein kinase (PIKK) family³. mTOR assembles into two complexes with distinct inputs and downstream effects. mTOR complex 1 (mTORC1) is defined by its RAPTOR subunit^{4–6}, which is replaced by RICTOR in mTOR complex 2^{6,7} (mTORC2). Both complexes also contain the requisite mLST8 subunit^{8,9}, but they differ in a number of other subunits that interact with RAPTOR or RICTOR¹.

mTORC1 regulates cell growth by promoting translation, ribosome biogenesis and autophagy^{1,4,5}. Its activation requires nutrients and amino acids, which result in the RAPTOR-mediated recruitment of mTORC1 to lysosomes and late endosomes^{10,11}, and co-localization with its activator, the small GTPase RHEB^{12,13}. Ways in which RHEB is proposed to act include binding to and activating the mTOR kinase domain¹⁴, and displacing the mTORC1 inhibitor PRAS40 from RAPTOR^{15,16}. RHEB in turn is negatively regulated by the GTPase-activating domain of the TSC2 tumour suppressor, which relays signals from multiple growth factor and stress pathways¹⁷. mTORC1 substrates include the eIF4E-binding protein 1 (4E-BP1) and ribosomal S6 kinases (S6K), which control cap-dependent translation initiation and elongation, respectively¹⁸. Phosphorylation of 4E-BP1 and S6K1 is dependent on their Tor signalling sequence (TOS) motif^{19,20}, which binds to RAPTOR and is also present in the negative regulator PRAS40^{21,22}.

mTORC2 responds primarily to growth factors, promoting cell-cycle entry, cell survival, actin cytoskeleton polarization and anabolic output^{6,7,23}. Its substrates include the Ser/Thr protein kinases AKT, SGK and PKC, which share the hydrophobic motif phosphorylation site with S6K1^{1,2}.

Rapamycin, which forms a ternary complex with the FKBP12-binding protein 12 (FKBP12) and the FRB domain of mTOR, is thought to be an allosteric inhibitor^{24,25}. Rapamycin–FKBP12 inhibits mTORC1 to a variable extent that is substrate and phosphorylation-site dependent²⁵,

and it does not bind to mTORC2²³. To overcome these limitations, ATP-competitive inhibitors that potently and uniformly inhibit both mTORC1 and mTORC2 are being developed as anticancer agents²⁶.

The six mammalian PIKKs regulate diverse cellular processes²⁷. They share three regions of homology consisting of a ~600-residue FAT domain (named after FRAP, ATM and TRRAP), a ~300-residue PIKK catalytic domain and a ~35-residue FATC domain at the carboxy terminus²⁸. In mTOR, the ~100-residue FRB domain is thought to occur between the FAT domain and the catalytic domain, and the region amino terminal to the FAT domain is required for binding to RAPTOR and RICTOR¹.

Here we present the crystal structure at 3.2 Å of a ~1,500-amino-acid mTOR–mLST8 complex containing the FAT, FRB, kinase and FATC domains, as well as the structures of this complex bound to an ATP transition state analogue and, respectively, ATP-competitive inhibitors. We discuss their implications for understanding mTOR function, regulation and inhibition by rapamycin and ATP-competitive compounds.

Overall structure of mTOR^{AN}–mLST8

Crystals were grown using N-terminally truncated human mTOR (residues 1376–2549; hereafter mTOR^{AN}) bound to full-length human mLST8 (Supplementary Table 1). The complex was produced in an HEK293-F cell line that was stably transfected sequentially by Flag-tagged mLST8 and Flag-tagged mTOR^{AN} vectors. The kinase activity of mTOR^{AN}–mLST8 is overall comparable to that of mTORC1 (Supplementary Fig. 1). mTORC1 is more active towards low-micromolar concentrations of S6K1^{ki} (kinase-inactive mutant) and 4E-BP1, consistent with RAPTOR recruiting these substrates through their TOS motifs, whereas mTOR^{AN}–mLST8 is more active at higher substrate concentrations.

The mTOR^{AN}–mLST8 structure has a compact shape (Fig. 1). The FAT domain, which consists of α – α -helical repeats, forms a 'C'-shaped α -solenoid that wraps halfway around the kinase domain and clamps onto it. mLST8 and the FRB domain protrude from the kinase domain,

¹Structural Biology Program, Memorial Sloan-Kettering Cancer Center, New York, New York 10065, USA. ²Howard Hughes Medical Institute, Memorial Sloan-Kettering Cancer Center, New York, New York 10065, USA.

on opposite sides of the catalytic cleft. The FATC domain is integral to the kinase domain structure.

The ~550-residue mTOR kinase domain adopts the two-lobe structure that is characteristic of both the PI3K and canonical protein kinase families²⁹. It consists of an N-terminal lobe (N lobe), a larger C-terminal lobe (C lobe) and a cleft between the two that binds to ATP. The mTOR kinase domain contains the core PI3K kinase domain fold, but with substantial differences. Whereas PI3K kinase domain structures superimpose essentially across their entire ~350 residues, only ~250 residues of the mTOR kinase domain superimpose on PI3Ks (Supplementary Table 2). In addition, the mTOR kinase domain contains ~200 additional residues of insertions that decorate the common fold. The largest of these is the FRB domain (residues 2021–2118), which is inserted within the kinase N lobe (Fig. 1). There is also a ~40-residue insertion in the C lobe that forms the binding site for mLST8 (residues 2258–2296; hereafter LBE).

Kinase domain structure

The mTOR kinase domain structure starts before the FRB domain, with the long $\kappa\alpha 1$ helix ('k' denoting kinase domain) that is present in PI3Ks as well (Fig. 2a and Supplementary Fig. 2a). The $\kappa\alpha 1$ helix is integral to the structure of the N lobe, because it packs in the concave surface of the N-lobe β -sheet in both mTOR and PI3Ks²⁹. The FRB insertion occurs immediately after the $\kappa\alpha 1$ helix. It is followed by a β -strand and two short helices that pack with the base of the FRB and replace the $\kappa\alpha 2$ helix of the PI3K kinase domain fold. Thereafter, the mTOR and PI3K N lobes have similar structures.

The mTOR structure indicates that the $\kappa\alpha 1$ helix is present in all PIKKs (Supplementary Fig. 3a). The SMG1, DNA-PKcs and TRRAP PIKKs also seem to have an FRB-like domain, because they respectively contain insertions of 128, 95 and 128 residues that are predicted to be α -helical. This is supported by the 6.6 Å X-ray diffraction data of DNA-PKcs reported recently³⁰. Although the deposited DNA-PKcs model³⁰, which contains a PI3K-derived kinase domain, lacks the FRB insertion, a reinterpretation of the data using the mTOR structure reveals electron density indicative of an FRB-like four-helix bundle (Supplementary Fig. 3b). ATM and ATR seem to lack a comparable insertion.

In the C lobe, the vicinity of the catalytic cleft contains four structural insertions in the PI3K core structure (LBE, $\kappa\alpha\text{AL}$, $\kappa\alpha 9\text{b}$ and FATC;

Fig. 2a). These form a spine of interactions centred on the activation loop, which is a ~30 residue segment with a central role in the function and regulation of canonical protein kinases. It forms part of the polypeptide-binding site, provides an active-site residue and undergoes a conformational change, typically a disorder-to-order transition, on kinase activation³¹. The activation loop is thought to have an analogous role in PI3Ks, among which it is ordered in only the class III PIK3C3 structures³². In the mTOR structure, the entire activation loop is well ordered (Supplementary Fig. 2b) and its middle portion contains the $\kappa\alpha\text{AL}$ helix insertion. One side of the activation loop packs with the $\kappa\alpha 9\text{b}$ insertion, and the other side packs with the FATC (Fig. 2a). The FATC is not unique to PIKKs in its entirety, because its N-terminal half forms a helix ($\kappa\alpha 11$) that is also present in PI3K structures^{29,32}. Its C-terminal half, which is absent from PI3Ks, forms three short helices that pack with the activation loop on one side and with the LBE on the other (Fig. 2a).

The interactions that the FATC makes with the activation loop suggest that it may have a role in stabilizing the activation loop structure, and the LBE, through its interactions with the FATC, may contribute to this indirectly (Supplementary Fig. 4a). The FATC and activation loop sequences are highly conserved among PIKKs. Although the LBE is not conserved, all PIKK family members contain an LBE-like insertion that may similarly pack with FATC (Supplementary Fig. 3a).

The $\kappa\alpha 9\text{b}$ insertion (residues 2425–2436) plugs one end of the catalytic cleft (Fig. 2a). It partly overlaps with a segment, called the negative regulatory domain (residues 2430–2450), whose deletion activates mTOR *in vitro*³³ and *in vivo*^{34,35}. After $\kappa\alpha 9\text{b}$, there is a 55-residue unstructured segment (residues 2437–2491) that is not conserved and has variable length in mTOR orthologues (Supplementary Fig. 2a).

Active-site conformation

To assess the activation state of the kinase domain structure and investigate the mechanism of phosphotransfer, we co-crystallized mTOR^{AN}–mLST8 with ADP, Mg^{2+} and MgF_3^- , a mimic of the γ -phosphate group of ATP in the transition state³⁶ (Supplementary Table 1). The $F_o - F_c$ map of these crystals at 3.5 Å shows strong electron density extending from the β -phosphate group of ADP, consistent with a bound MgF_3^- group (Fig. 2b). The presence of two additional Mg^{2+} ions is supported by the anomalous dispersion maps of apo-crystals soaked in AMPPNP- Mn^{2+} (Supplementary Fig. 4b).

A superposition with the protein kinase CDK2 bound to the same ATP transition state mimic³⁶ reveals that the arrangement of key active-site residues and MgF_3^- is remarkably conserved in mTOR (Fig. 2c and Supplementary Fig. 4c). These include the C-lobe Asn 2343 and Asp 2357, which in both mTOR and protein kinases serve as metal ligands, and Asp 2338, which in protein kinases has a key catalytic role in orienting and activating the substrate hydroxyl group for nucleophilic attack^{36,37}. The mTOR–CDK2 superposition also reveals a coincidence of the mTOR His 2340 and CDK2 Lys 129 side chains (Fig. 2c). In protein kinases, a basic residue at this position interacts with both the substrate hydroxyl group and the γ -phosphate transition state mimic, and is postulated to stabilize the build-up of charge at the transition state^{36,37}. Consistent with a similar role, we find that the kinase activity of the His2340Ala mTOR^{AN}–mLST8 mutant is barely detectable, and comparable to the Asp2338Ala mutant previously shown to be inactive³⁸ (Supplementary Fig. 4d).

These findings strongly suggest that the crystallized mTOR^{AN}–mLST8 complex is intrinsically active in the absence of any additional regulatory subunits. They also indicate that PIKKs, and most probably PI3Ks, use the same catalytic mechanism as canonical protein kinases, in contrast to a recently proposed PI3K mechanism³² (Supplementary Fig. 4c).

Substrate-binding site

The MgF_3^- γ -phosphate mimic points to an extended C-lobe groove that is highly conserved and is the likely site of substrate binding.

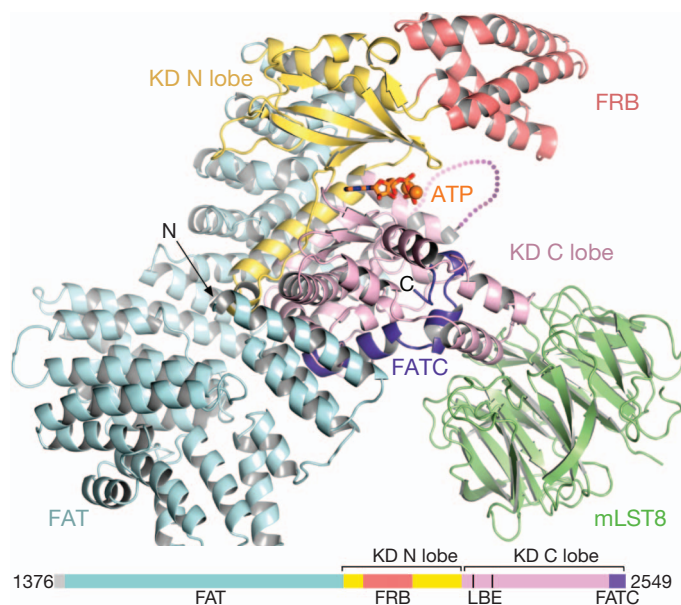


Figure 1 | Structure of the mTOR^{AN}–mLST8–ATP γ S–Mg complex. mTOR is coloured as indicated schematically, mLST8 is coloured green, ATP γ S is shown as sticks and Mg^{2+} ions are shown as spheres. KD, kinase domain.

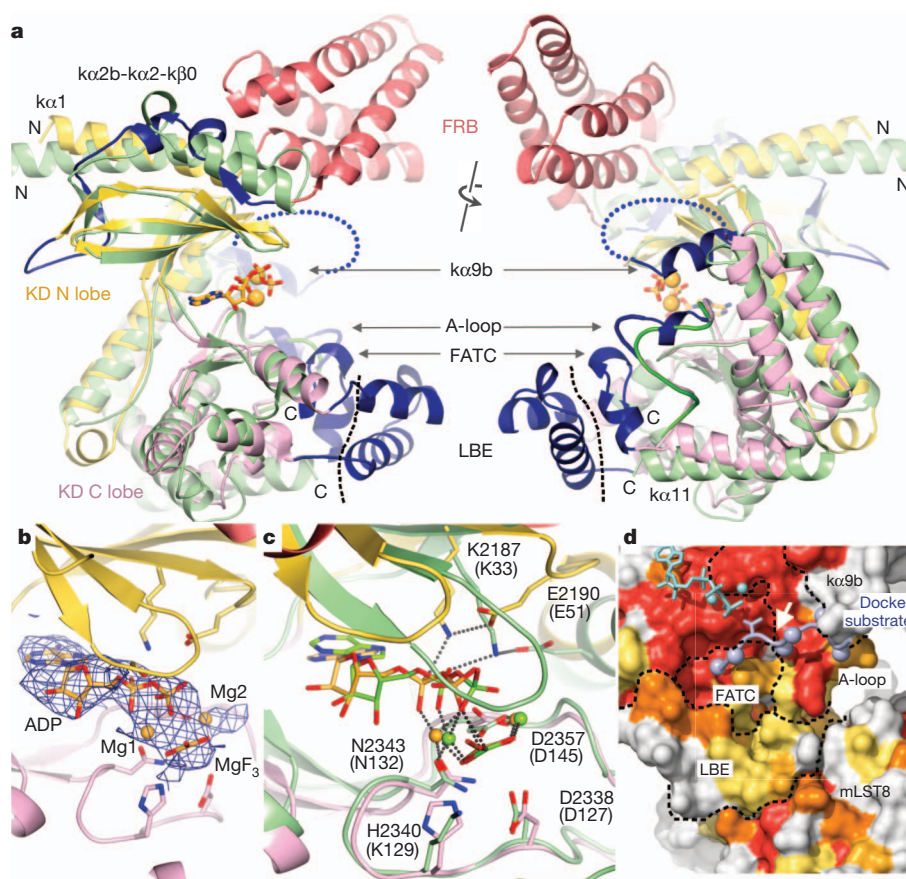


Figure 2 | mTOR kinase domain and active site conformation.

a, Superposition of the kinase domains of mTOR and PIK3C3 (Protein Data Bank (PDB) ID, 3IHV; green) in two views rotated by ~180°. Left view is related to that of Fig. 1. The FRB is coloured red, and the remaining mTOR insertions are coloured dark blue. The α AL helix is in the activation loop (A-loop). The black dashed lines delineate the LBE, and the blue dotted loops indicate the disordered region between α 9b and α 10. **b**, The 3.5 Å $F_o - F_c$ electron density, contoured at 2.5 σ , of the mTOR transition state complex before ADP-MgF₃-Mg₂ was built. ADP-MgF₃ is shown as sticks and Mg²⁺ ions

are shown as spheres. **c**, Superposition of the mTOR and CDK2 transition state (PDB ID, 3QHW) complexes. CDK2 and its nucleotide are coloured green (its residue labels are shown in parentheses). **d**, Molecular surface representation of the C-lobe portion of the mTOR catalytic cleft, coloured according to conservation entropy (red invariant in 22 orthologues, orange in 21, yellow-orange in 20 and yellow in 18 or 19). Dashed lines delineate the boundaries of the labelled structural elements. The docked substrate peptide is coloured light blue, with its threonine phosphorylation site shown as sticks, the remaining side chains as spheres (C β atoms) and its +1 position indicated by a white arrow.

Figure 2d illustrates this with a CDK2-bound substrate peptide docked by superposing the mTOR and CDK2 transition state³⁶ complexes. The groove consists of the activation loop, as in protein kinases, but also of portions of the FATC and LBE.

Carboxy-terminal to the phosphorylation site (the + direction), the groove extends only to the +1 position, abruptly terminating with the α 9b helix that plugs this end of the cleft (Fig. 2d). Thereafter, the peptide can exit along the C-lobe towards mLST8 or along the N-lobe towards the FRB. The +1 portion of the groove has a pronounced pocket lined with three aromatic residues, consistent with the two classes of mTOR substrates—exemplified by 4E-BP1 and S6K1—that have a proline and a tyrosine residue, respectively, at +1 (Supplementary Fig. 5a, b). The groove extends considerably more in the direction N-terminal to the phosphorylation site (the - direction), and it may account for the low-level sequence preference at -4 and -5 suggested by a positional scanning peptide array³⁹.

Restricted access to the active site

The four-helix FRB substantially extends the N-lobe side of the catalytic cleft, whereas the LBE and mLST8 extend the C-lobe side. This gives the cleft a deep, 'V'-shaped cross-section, restricting access to the substrate-binding site at the bottom of the cleft (Fig. 3a). Substrate access is further hindered by one end of the cleft being plugged by α 9b and the 55-residue unstructured segment that follows the helix. Portions of α 9b and the unstructured segment form the negative

regulatory region^{33–35}, suggesting that restricted access to the active site negatively regulates mTOR. Helix α 9b is probably the key element because deleting the bulk of the unstructured segment (residues 2443–2486) does not activate mTOR (Supplementary Fig. 6).

The end of the cleft opposite α 9b is unencumbered in the mTOR^{AN}-mLST8 structure. However, it is near the FAT N terminus, and the region deleted from the crystallized mTOR^{AN} may restrict cleft access directly or through its associated RAPTOR or RICTOR proteins, or by both means. In support, we find that towards TOS mutant 4E-BP1 and S6K1^{ki} substrates, mTOR^{AN}-mLST8 is more active than mTOR-mLST8, which in turn is more active than mTOR-mLST8-RAPTOR (Supplementary Fig. 6). A restricted active site would reduce the probability of substrates hitting the active site by random diffusion, and could thus be important in allowing for the regulation of phosphorylation by substrate recruitment.

Inhibition by rapamycin-FKBP12

In a model constructed by superposing the FRB domains of the FRB-rapamycin-FKBP12²⁴ and mTOR^{AN}-mLST8 structures, FKBP12 extends from the FRB towards mLST8 on the C-lobe, nearly capping the catalytic cleft (Fig. 3b). At their closest approach, FKBP12 and mLST8 are only 8 Å apart, with the catalytic centre recessed by 37 Å. The model suggests that rapamycin-FKBP12 inhibits in part by drastically reducing the accessibility of the already constricted catalytic cleft. This is consistent with the extent of mTORC1 inhibition being

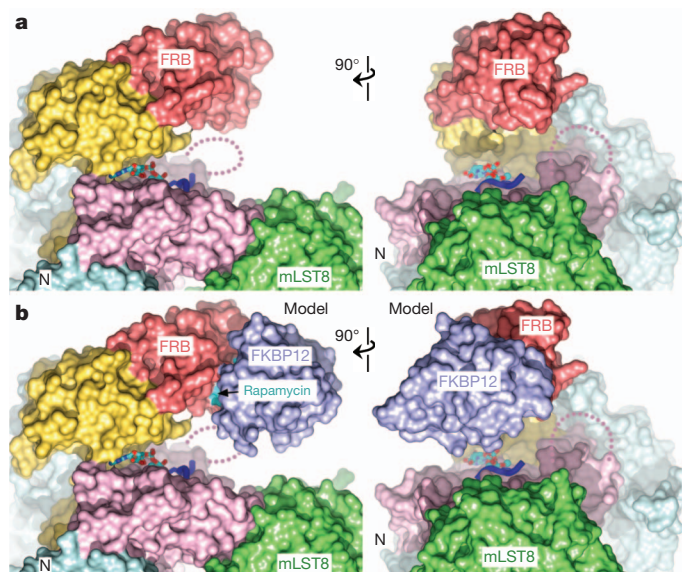


Figure 3 | The kinase active site is recessed at the bottom of a deep cleft. **a**, Surface representation of mTOR^{AN}-mLST8-ADP-MgF₃-Mg₂ in two orthogonal views. Dark blue ribbons indicate the docked substrate peptide (positions -2 to +2) from Fig. 2d. **b**, Surface representation of the mTOR^{AN}-mLST8-rapamycin-FKBP12 model. Rapamycin (cyan) and FKBP12 (blue) are labelled.

substrate and phosphorylation-site dependent²⁵ (additional discussion in Supplementary Fig. 6 legend).

FRB recruits S6K1 to the active site

The rapamycin-binding site maps to the FRB surface closest to the active site, in a region of highly conserved residues (Fig. 4a). Four of these residues are invariant in 22 mTOR orthologues from yeast to human, and another four in 21 orthologues, in stark contrast to the FRB surface opposite the active site (Fig. 4a and Supplementary Fig. 7). This raises the possibility that the rapamycin-binding site interacts with substrates to facilitate their entry to the recessed active site.

This model is supported by the observation that mutation of Ser 235, a rapamycin contact^{38,40} at the centre of the conservation region, reduces phosphorylation of S6K1 and 4E-BP1³³. It can also explain inhibition of mTORC1 and mTORC2 by rapamycin in the absence of FKBP12, albeit at ~100-fold-higher concentrations reflecting the weaker rapamycin-FRB binary interaction⁴¹. However, these observations can also be explained by the rapamycin-binding site interacting with other parts of mTOR, or with associated proteins, especially because rapamycin was thought to be an allosteric inhibitor²⁵. To rule this out, we assayed mTOR^{AN}-mLST8 and found that rapamycin, but not the closely related FK506 macrolide, inhibits S6K1^{ki} overall phosphorylation, as measured by ³²P incorporation (Fig. 4b). Inhibition reaches ~45% at the 20 μM solubility limit of rapamycin, close to the free rapamycin-FRB dissociation constant. Phosphorylation of the key Thr 389 site of the S6K1 hydrophobic motif, measured by a phospho-Thr-389-specific antibody, is inhibited by ~80% (Fig. 4b).

In a complementary approach, we tested whether the isolated FRB domain inhibits phosphorylation *in trans*. Figure 4c shows that wild-type FRB but not the Ser2035Ile FRB mutant^{38,40} inhibits overall S6K1^{ki} phosphorylation by ~50% and Thr 389 phosphorylation by ~75% at the highest concentration tested.

To map the region of S6K1 involved in FRB interactions, we reasoned that its deletion should reduce Thr 389 phosphorylation and also render any residual phosphorylation insensitive to rapamycin. By testing successively truncated polypeptides from the S6K1 tail, we found that both criteria are met by residues 393–398 (Fig. 4d). In addition, residues 399–402 and 403–410 probably contribute to FRB interactions, because

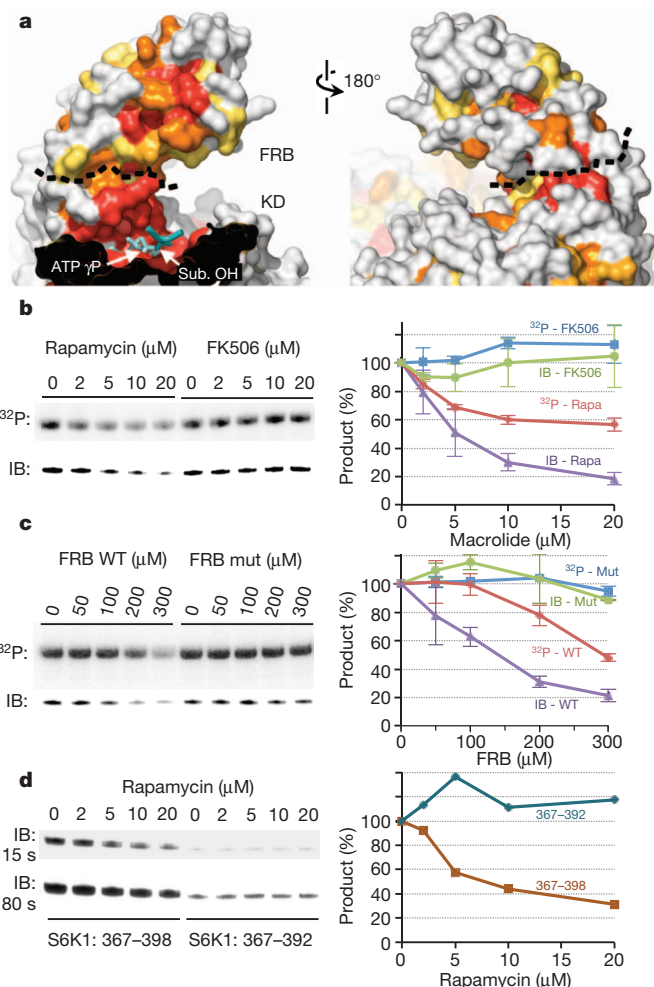


Figure 4 | The rapamycin-binding site of the FRB recruits S6K1 into the catalytic cleft. **a**, Surface representations of the FRB and a portion of the catalytic cleft, coloured by sequence conservation as in Fig. 2d. ADP-MgF₃-Mg₂ is in cyan with the transition state mimic MgF₃ group labelled 'ATP γP'. The black dashed lines delineate the boundary between FRB and the kinase domain. The docked substrate peptide from Fig. 2d is shown in blue (positions -1 to +1), with its phosphorylation site labelled 'Sub. OH'. **b**, Phosphorylation of S6K1^{ki} (10 μM) by mTOR^{AN}-mLST8 (20 nM), measured by ³²P incorporation (top) and by immunoblotting (IB) with a phospho-Thr-389-specific antibody (bottom), in the presence of the indicated concentrations of rapamycin or FK506. The average and standard deviation of three independent repetitions is plotted as a percentage of the 0 μM macrolide reaction of each set. **c**, Phosphorylation of S6K1^{ki} (10 μM) by mTOR^{AN}-mLST8 (20 nM) in the presence of the indicated concentrations of wild-type (WT) or S2035I mutant FRB. Reactions were repeated twice, and results plotted as in **b**. **d**, Phosphorylation of GST-tagged S6K1³⁶⁷⁻³⁹⁸ (10 μM) and S6K1³⁶⁷⁻³⁹² (10 μM) by mTOR^{AN}-mLST8 (20 nM) in the presence of the indicated concentrations of rapamycin. Two different exposures (15 and 180 s) of the phospho-Thr-389-specific immunoblot are shown. The quantification of the 15-s immunoblot is plotted on the right.

their truncation progressively reduces phosphorylation (Supplementary Fig. 8). Amino-terminal truncations up to residue 381 have no significant effect.

Together, these data indicate that the FRB provides a secondary substrate-recruitment site near the entrance of the catalytic cleft. We presume that, although the TOS motif, and possibly others, is the primary means of substrate recruitment, the secondary site may facilitate substrate entry into the otherwise restricted active site and may also provide an additional level of specificity, at least for a subset of substrates.

A bipartite substrate-recruitment mechanism is analogous to what has been proposed for the phosphatase calcineurin, the target of

FK506–FKBP12. Most calcineurin substrates require both a primary and a secondary recruitment motif for efficient dephosphorylation, and FK506–FKBP12 inhibits by binding to the secondary recruitment motif site⁴².

FAT domain

The FAT domain contains 28 α -helices arranged as α - α -helical repeats. Helices $\alpha 1$ to $\alpha 22$ belong to the TPR repeat family and form three discontinuous domains (TRD1, TRD2 and TRD3). Helices $\alpha 23$ to $\alpha 28$ belong to the HEAT family and form a single domain (HRD). The four domains pack sequentially to form a 'C'-shaped α -solenoid that clamps onto the kinase domain (Supplementary Fig. 9a, b). TRD1 interacts with the C lobe on one side of the kinase domain, and after TRD2 and TRD3 traverse to the other side, the HRD interacts with both the N lobe and the C lobe of the kinase domain (Supplementary Fig. 9c, d).

The contacts TRD1 and HRD make to the kinase domain involve conserved residues, consistent with the two interfaces being important for the structure and function of mTOR. For example, three sets of buried hydrogen bond contacts (Glu 1401 to Arg 2317 for TRD1, and Arg 1905 to Glu 2419 and Gln 1941 to Gln 2200 for HRD) involve residues invariant in 22 mTOR orthologues (Supplementary Fig. 9c, d).

The TRD1 and HRD segments correspond to the FAT segments best conserved among PIKK family members²⁸ as well, suggesting that the FAT domain clamping onto the kinase domain is a common feature of this family. In addition, PI3Ks contain a HEAT-repeat domain analogous to the HRD in its structure and interactions with the kinase domain, although they lack the rest of the FAT domain (Supplementary Fig. 9e).

mLST8

mLST8 consists of seven WD40 repeats. At the narrow end of the mLST8 β -propeller structure, a surface that extends across six WD40 repeats binds to both helices and the intervening loop of the LBE helix-loop-helix structure. The interface involves mostly polar LBE residues and polar or aromatic mLST8 residues, and it is dominated by hydrogen bonds (Supplementary Fig. 10).

mLST8 is thought to be a requisite activating subunit of mTOR complexes^{8,9}. The structure suggests that the extended interaction surface of mLST8 may directly stabilize the LBE structure and indirectly influence the organization of the active site through the LBE/FATC/activation-loop spine of interactions (Supplementary Fig. 4a). In support of this, we note that lack of mLST8 results in the association of mTOR with heat shock proteins⁹, and we find that the solubility of overexpressed mTOR is highly dependent on mLST8 co-expression (not shown). In addition, the growth-suppression phenotype of a temperature-sensitive yeast *lst8* allele can be rescued by mutations⁴³ either at the LBE hydrophobic core (Ala2290Val) or at the following $\kappa\alpha 5$ helix (Leu2302Gln), and the structure is consistent with these mutations stabilizing the local LBE structure.

Control of mTOR kinase activity

The proposal that active-site restriction is a negative regulatory mechanism is supported by hyperactivating mutations^{43–45}, most of which map to structural elements involved in limiting active-site access. A large number of mutations cluster at the end of the catalytic cleft that is plugged by $\kappa\alpha 9b$ (Fig. 5 and Supplementary Fig. 11). They map to the $\kappa\alpha 3$, $\kappa\alpha 9$, $\kappa\alpha 9b$ and $\kappa\alpha 10$ helices that pack extensively with each other, and to the FAT HRD portion that packs with $\kappa\alpha 3$ and $\kappa\alpha 9$. These mutations are likely to loosen the $\kappa\alpha 9b$ -centred structural framework that restricts access from this end of the cleft, presumably without destabilizing the entire active-site structure. The role of the FAT clamp is highlighted by the widely studied Glu2419Lys activating mutation, which eliminates the Glu 2419/Arg 1905 salt bridge at the $\kappa\alpha 9$ –HRD interface (Supplementary Figs 9c and 11).

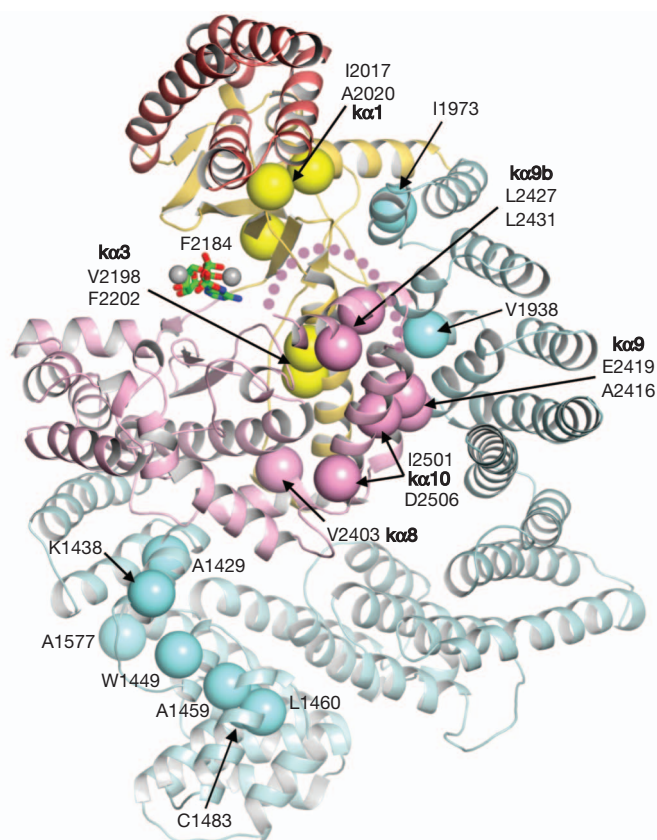


Figure 5 | mTOR-activating mutations map to structural elements involved in restricting active site access. Activating mutations^{43–45} reported for mTOR, yeast Tor2 and Tor1 are shown as large spheres (labelled, with structural elements in bold), coloured as in Fig. 1.

Two other hyperactivating mutations map to a portion of the $\kappa\alpha 1$ helix that is sandwiched between the FRB base and the N-lobe β -sheet^{43,44}. These mutations (Ile2017Val and Ala2020Val) are unlikely to unfold the FRB, because an FRB hydrophobic core mutation (Trp2027Phe) abolishes kinase activity⁴⁰. The structure suggests that these mutations may loosen the rigid coupling of the FRB to the catalytic cleft, increasing access to the active site.

A third cluster of mutations⁴³ maps to the N-terminal portion of the FAT domain and to structural residues of TRD1 and the TRD1-proximal portion of TRD2. These mutations would probably destabilize interactions between TRD1 and the kinase domain through loss of structural integrity. They may also destabilize the interactions between HRD and the kinase domain, because the structural coupling of TRD1 and HRD would thermodynamically couple their kinase domain contacts. In addition, the disposition of the N-terminal mTOR segment and its associated RAPTOR could change or become more flexible relative to the kinase domain.

Inhibitors of the ATP-binding site

To explore the determinants of inhibitor potency and specificity, we determined the structures of mTOR^{AN}–mLST8 bound to Torin2 and PP242, which are highly specific for mTOR, and to PI-103, which has dual specificity for mTOR and class I PI3Ks (Supplementary Table 3).

The overall orientation of Torin2 in the ATP site is as predicted⁴⁶ (Fig. 6a and Supplementary Fig. 12a). The tricyclic benzonaphthridinone ring binds to the adenine site and makes a hydrogen bond with the 'hinge' between the N and C lobes, analogous to one of two backbone hydrogen bonds made by ATP and diverse inhibitors of PI3 or protein kinases. The aminopyridine group reaches into the 'inner hydrophobic pocket', an area at the back of the cleft that many kinase inhibitors

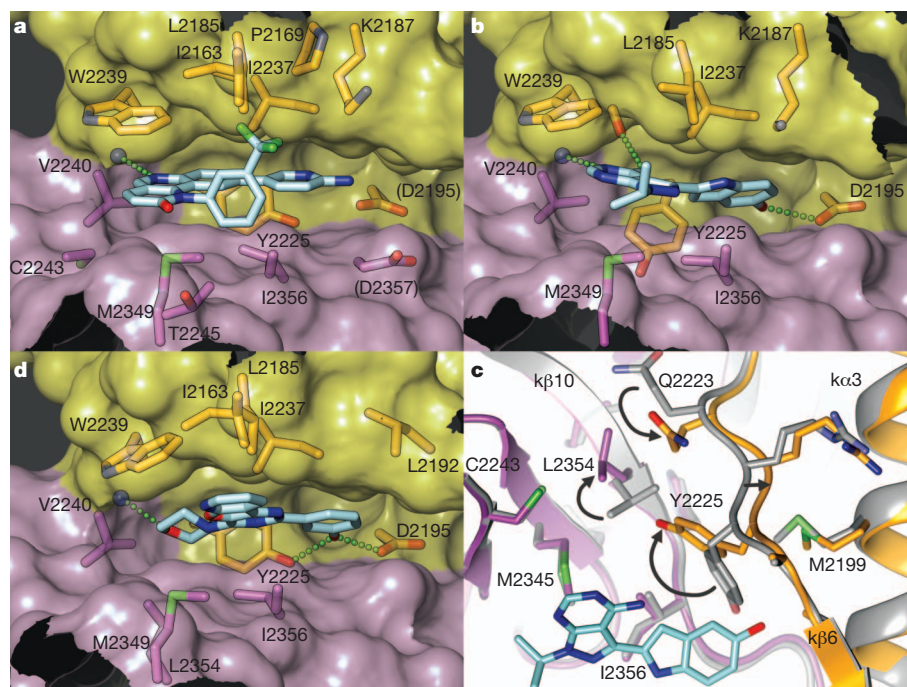


Figure 6 | Structures of the Torin2, PP242 and PI-103 inhibitors bound to the mTOR catalytic cleft. **a**, Stick representation of Torin2 (C, cyan; N, blue; O, red; F, green) and of mTOR residues within 4 Å (except for Asp 2195 and Asp 2357). The mTOR cleft is shown in transparent surface representation, with the N-lobe in yellow and the C-lobe in pink. Green dotted lines indicate

atoms within hydrogen-bonding distance. **b**, PP242–mTOR structure, represented as in **a**. **c**, Conformational change in the inner hydrophobic pocket of mTOR on PP242 (cyan) binding. Arrows indicate side-chain rotations and main-chain shifts compared to ATP γ S-bound mTOR (grey). View looking down the vertical axis of **b**. **d**, PI-103–mTOR structure, represented as in **a**.

contact. However, it does not make the three predicted hydrogen bonds⁴⁶ (to Asp 2195, Asp 2357 and Tyr 2225). Rather, the structure reveals that a key interaction is the extensive stacking of the tricyclic benzonaphthyridinone ring with the indole group of Trp 2239 from the hinge (Fig. 6a). In the ATP γ S complex, Trp 2239 stacks partly with a three-atom portion of the adenine. In the Torin2 complex, by contrast, Trp 2239 stacks with a ten-atom portion of the tricyclic Torin2 ring. This probably makes a substantial contribution to the subnanomolar potency⁴⁶ of Torin2. In addition, because Trp 2239 is not present in canonical protein kinases or in PI3Ks, it would also contribute to the \sim 800-fold specificity of Torin2 for mTOR over PI3Ks⁴⁶. The structure also reveals that the Torin2 trifluoromethyl group packs into an N-lobe pocket (Ile 2163, Pro 2169 and Leu 2185; Fig. 6a). These contacts are less extensive than those made to Trp 2239, and only Leu 2185 is variable across the PIKK and PI3K families. They may contribute to Torin2–mTOR specificity, however, because this portion of the N-lobe β -sheet exhibits considerable variation in its relative orientation in PI3K structures.

PP242 consists of the adenine-mimetic pyrazolopyrimidine scaffold common to PI3 or tyrosine kinase inhibitors, with a hydroxyindole substituent at a position that often points to the inner hydrophobic pocket⁴⁷. In mTOR, this pocket is lined with residues conserved across the PI3K and PIKK families, and the selectivity of PP242 for mTOR was unexpected⁴⁷. The structure reveals that, although these two PP242 groups are generally positioned as predicted⁴⁷, mTOR undergoes a conformational change that expands and deepens the inner hydrophobic pocket, with the PP242 hydroxyindole group reaching deep into the new space (Fig. 6b and Supplementary Fig. 12b). The conformational change involves the Tyr 2225 side chain at the back of the pocket swinging out of the way of the hydroxyindole group (by $\Delta\chi_1 = 108^\circ$; Fig. 6c and Supplementary Fig. 12c). Because Tyr 2225 is part of the local hydrophobic core between the N and Clobes, this necessitates additional concerted changes. The Leu 2354 side chain rotates away from the incoming Tyr 2225 ($\Delta\chi_1 = 166^\circ$), the Gln 2223 side chain moves in to plug a resulting gap and a three-residue main-chain

stretch (residues 2223–2225) shifts by ~ 1 Å. In PI3Ks, Leu 2354 is replaced by a conserved phenylalanine that cannot undergo a similar conformational change, at least not without even more extensive repacking of the local hydrophobic core. Leu 2354 is thus likely to be a major, although indirect, determinant of the selectivity of PP242 for mTOR over PI3Ks and other kinases.

The multi-targeted pyridinylfuranopyrimidine inhibitor PI-103⁴⁸ does not take advantage of any of the aforementioned mTOR-specific features. The morpholine ring binds to the adenine pocket and makes two hydrogen bonds to the hinge, whereas the phenol group binds to the inner pocket and makes two hydrogen bonds to the Tyr 2225 and Asp 2195 side chains at the back of the cleft (Fig. 6d and Supplementary Fig. 12d). These hydrogen bonds are likely to be important for the high affinity of PI-103 for mTOR and, presumably, for class I PI3Ks where the relevant protein groups are similarly positioned. In support of this, we note that the \sim 500-fold-weaker-affinity⁴⁸ class III PI3K/PI-103 complex lacks both phenol hydrogen bonds and one of the hinge hydrogen bonds³².

Conclusions

The mTOR^{AN} structure reveals an intrinsically active but otherwise highly restricted catalytic centre, and, together with activating mutations, points to substrate recruitment as a major mechanism controlling the kinase activity. Our biochemical data on S6K1 indicate that in addition to a primary recruitment motif, a secondary recruitment motif proximal to the phosphorylation site is needed for efficient phosphorylation. The FRB acts as a gatekeeper by restricting access to the active site while also granting privileged substrates access through its binding site for the secondary motif. Co-crystal structures of ATP-competitive inhibitors reveal multiple determinants of mTOR specificity, including a conformational change deep inside the catalytic cleft.

METHODS SUMMARY

Details of protein expression, crystallization, structure determination and enzyme assays are described in Methods.

Full Methods and any associated references are available in the online version of the paper.

Received 2 January; accepted 26 March 2013.

Published online 1 May 2013.

- Zoncu, R., Efeyan, A. & Sabatini, D. M. mTOR: from growth signal integration to cancer, diabetes and ageing. *Nature Rev. Mol. Cell Biol.* **12**, 21–35 (2011).
- Shaw, R. J. & Cantley, L. C. Ras, PI(3)K and mTOR signalling controls tumour cell growth. *Nature* **441**, 424–430 (2006).
- Keith, C. T. & Schreiber, S. L. PIK-related kinases: DNA repair, recombination, and cell cycle checkpoints. *Science* **270**, 50–51 (1995).
- Hara, K. *et al.* Raptor, a binding partner of target of rapamycin (TOR), mediates TOR action. *Cell* **110**, 177–189 (2002).
- Kim, D. H. *et al.* mTOR interacts with raptor to form a nutrient-sensitive complex that signals to the cell growth machinery. *Cell* **110**, 163–175 (2002).
- Loewith, R. *et al.* Two TOR complexes, only one of which is rapamycin sensitive, have distinct roles in cell growth control. *Mol. Cell* **10**, 457–468 (2002).
- Sarbassov, D. D. *et al.* Rictor, a novel binding partner of mTOR, defines a rapamycin-insensitive and raptor-independent pathway that regulates the cytoskeleton. *Curr. Biol.* **14**, 1296–1302 (2004).
- Chen, E. J. & Kaiser, C. A. LST8 negatively regulates amino acid biosynthesis as a component of the TOR pathway. *J. Cell Biol.* **161**, 333–347 (2003).
- Kim, D. H. *et al.* GβL, a positive regulator of the rapamycin-sensitive pathway required for the nutrient-sensitive interaction between raptor and mTOR. *Mol. Cell* **11**, 895–904 (2003).
- Sancak, Y. *et al.* The Rag GTPases bind raptor and mediate amino acid signaling to mTORC1. *Science* **320**, 1496–1501 (2008).
- Kim, E., Goraksha-Hicks, P., Li, L., Neufeld, T. P. & Guan, K. L. Regulation of TORC1 by Rag GTPases in nutrient response. *Nature Cell Biol.* **10**, 935–945 (2008).
- Saucedo, L. J. *et al.* Rheb promotes cell growth as a component of the insulin/TOR signalling network. *Nature Cell Biol.* **5**, 566–571 (2003).
- Stocker, H. *et al.* Rheb is an essential regulator of S6K in controlling cell growth in *Drosophila*. *Nature Cell Biol.* **5**, 559–566 (2003).
- Long, X., Lin, Y., Ortiz-Vega, S., Yonezawa, K. & Avruch, J. Rheb binds and regulates the mTOR kinase. *Curr. Biol.* **15**, 702–713 (2005).
- Sato, T., Nakashima, A., Guo, L. & Tamanoi, F. Specific activation of mTORC1 by Rheb G-protein *in vitro* involves enhanced recruitment of its substrate protein. *J. Biol. Chem.* **284**, 12783–12791 (2009).
- Sancak, Y. *et al.* PRAS40 is an insulin-regulated inhibitor of the mTORC1 protein kinase. *Mol. Cell* **25**, 903–915 (2007).
- Zhang, Y. *et al.* Rheb is a direct target of the tuberous sclerosis tumour suppressor proteins. *Nature Cell Biol.* **5**, 578–581 (2003).
- Ma, X. M. & Blenis, J. Molecular mechanisms of mTOR-mediated translational control. *Nature Rev. Mol. Cell Biol.* **10**, 307–318 (2009).
- Schalm, S. S., Fingar, D. C., Sabatini, D. M. & Blenis, J. TOS motif-mediated raptor binding regulates 4E-BP1 multisite phosphorylation and function. *Curr. Biol.* **13**, 797–806 (2003).
- Nojima, H. *et al.* The mammalian target of rapamycin (mTOR) partner, raptor, binds the mTOR substrates p70 S6 kinase and 4E-BP1 through their TOR signaling (TOS) motif. *J. Biol. Chem.* **278**, 15461–15464 (2003).
- Oshiro, N. *et al.* The proline-rich Akt substrate of 40 kDa (PRAS40) is a physiological substrate of mammalian target of rapamycin complex 1. *J. Biol. Chem.* **282**, 20329–20339 (2007).
- Fonseca, B. D., Smith, E. M., Lee, V. H., MacKintosh, C. & Proud, C. G. PRAS40 is a target for mammalian target of rapamycin complex 1 and is required for signaling downstream of this complex. *J. Biol. Chem.* **282**, 24514–24524 (2007).
- Jacinto, E. *et al.* Mammalian TOR complex 2 controls the actin cytoskeleton and is rapamycin insensitive. *Nature Cell Biol.* **6**, 1122–1128 (2004).
- Choi, J., Chen, J., Schreiber, S. L. & Clardy, J. Structure of the FKBP12-rapamycin complex interacting with the binding domain of human FRAP. *Science* **273**, 239–242 (1996).
- Choo, A. Y. & Blenis, J. Not all substrates are treated equally: implications for mTOR, rapamycin-resistance and cancer therapy. *Cell Cycle* **8**, 567–572 (2009).
- Wander, S. A., Hennessy, B. T. & Slingerland, J. M. Next-generation mTOR inhibitors in clinical oncology: how pathway complexity informs therapeutic strategy. *J. Clin. Invest.* **121**, 1231–1241 (2011).
- Lovejoy, C. A. & Cortez, D. Common mechanisms of PIKK regulation. *DNA Repair (Amst.)* **8**, 1004–1008 (2009).
- Bosotti, R., Isacchi, A. & Sonhammer, E. L. FAT: a novel domain in PIK-related kinases. *Trends Biochem. Sci.* **25**, 225–227 (2000).
- Walker, E. H., Perisic, O., Ried, C., Stephens, L. & Williams, R. L. Structural insights into phosphoinositide 3-kinase catalysis and signalling. *Nature* **402**, 313–320 (1999).
- Sibanda, B. L., Chirgadze, D. Y. & Blundell, T. L. Crystal structure of DNA-PKcs reveals a large open-ring cradle comprised of HEAT repeats. *Nature* **463**, 118–121 (2010).
- Nolen, B., Taylor, S. & Ghosh, G. Regulation of protein kinases; controlling activity through activation segment conformation. *Mol. Cell* **15**, 661–675 (2004).
- Miller, S. *et al.* Shaping development of autophagy inhibitors with the structure of the lipid kinase Vps34. *Science* **327**, 1638–1642 (2010).
- McMahon, L. P., Choi, K. M., Lin, T. A., Abraham, R. T. & Lawrence, J. C. Jr. The rapamycin-binding domain governs substrate selectivity by the mammalian target of rapamycin. *Mol. Cell Biol.* **22**, 7428–7438 (2002).
- Sekulic, A. *et al.* A direct linkage between the phosphoinositide 3-kinase-AKT signaling pathway and the mammalian target of rapamycin in mitogen-stimulated and transformed cells. *Cancer Res.* **60**, 3504–3513 (2000).
- Edinger, A. L. & Thompson, C. B. An activated mTOR mutant supports growth factor-independent, nutrient-dependent cell survival. *Oncogene* **23**, 5654–5663 (2004).
- Bao, Z. Q., Jacobsen, D. M. & Young, M. A. Briefly bound to activate: transient binding of a second catalytic magnesium activates the structure and dynamics of CDK2 kinase for catalysis. *Structure* **19**, 675–690 (2011).
- Madhusudan, A. P., Xuong, N. H. & Taylor, S. S. Crystal structure of a transition state mimic of the catalytic subunit of cAMP-dependent protein kinase. *Nature Struct. Biol.* **9**, 273–277 (2002).
- Brown, E. J. *et al.* Control of p70 S6 kinase by kinase activity of FRAP *in vivo*. *Nature* **377**, 441–446 (1995).
- Hsu, P. P. *et al.* The mTOR-regulated phosphoproteome reveals a mechanism of mTORC1-mediated inhibition of growth factor signaling. *Science* **332**, 1317–1322 (2011).
- Vilella-Bach, M., Nuzzi, P., Fang, Y. & Chen, J. The FKBP12-rapamycin-binding domain is required for FKBP12-rapamycin-associated protein kinase activity and G1 progression. *J. Biol. Chem.* **274**, 4266–4272 (1999).
- Shor, B. *et al.* A new pharmacologic action of CCI-779 involves FKBP12-independent inhibition of mTOR kinase activity and profound repression of global protein synthesis. *Cancer Res.* **68**, 2934–2943 (2008).
- Rodríguez, A. *et al.* A conserved docking surface on calcineurin mediates interaction with substrates and immunosuppressants. *Mol. Cell* **33**, 616–626 (2009).
- Ohne, Y. *et al.* Isolation of hyperactive mutants of mammalian target of rapamycin. *J. Biol. Chem.* **283**, 31861–31870 (2008).
- Reinke, A., Chen, J. C., Aronova, S. & Powers, T. Caffeine targets TOR complex I and provides evidence for a regulatory link between the FRB and kinase domains of Tor1p. *J. Biol. Chem.* **281**, 31616–31626 (2006).
- Urano, J. *et al.* Point mutations in TOR confer Rheb-independent growth in fission yeast and nutrient-independent mammalian TOR signaling in mammalian cells. *Proc. Natl Acad. Sci. USA* **104**, 3514–3519 (2007).
- Liu, Q. *et al.* Discovery of 9-(6-aminopyridin-3-yl)-1-(3-(trifluoromethyl)phenyl)benzo[h][1,6]naphthyridin-2(1H)-one (Torin2) as a potent, selective, and orally available mammalian target of rapamycin (mTOR) inhibitor for treatment of cancer. *J. Med. Chem.* **54**, 1473–1480 (2011).
- Apfel, B. *et al.* Targeted polypharmacology: discovery of dual inhibitors of tyrosine and phosphoinositide kinases. *Nature Chem. Biol.* **4**, 691–699 (2008).
- Knight, Z. A. *et al.* A pharmacological map of the PI3-K family defines a role for p110α in insulin signaling. *Cell* **125**, 733–747 (2006).

Supplementary Information is available in the online version of the paper.

Acknowledgements We thank D. King for mass spectroscopic analysis, H. Erdjument-Bromage for N-terminal sequencing, the staff of the Advanced Photon Source ID24 beamlines for help with data collection and D. Tzvetkova-Robev for help with protein expression in HEK293 cells. This work was supported by the Howard Hughes Medical Institute.

Author Contributions H.Y. and N.P.P. designed the experiments, solved the structures and wrote the manuscript. H.Y., D.G.R., J.D.K., B.M. and H.J.Y. carried out protein production, crystallization and biochemical experiments. H.Y. performed all other experiments.

Author Information The coordinates and structure factors have been deposited in the Protein Data Bank under the accession numbers 4JSN (native structure), 4JSP (ATPγS-Mg complex), 4JSV (ADP-Mg-F complex), 4JSX (Torin2 complex), 4JT5 (PP242 complex) and 4JT6 (PI-103 complex). Reprints and permissions information is available at www.nature.com/reprints. The authors declare no competing financial interests. Readers are welcome to comment on the online version of the paper. Correspondence and requests for materials should be addressed to N.P.P. (pavletin@mskcc.org).

METHODS

Protein expression and purification. The boundary of the crystallized human mTOR^{AN} (residues 1376–2549) was identified by screening successive N-terminal truncations of mTOR, produced by transient transfection in HEK293-F cells, for expression levels, solubility and size exclusion chromatography profile (not shown). For large-scale production of mTOR^{AN}–mLST8, we generated a HEK293-F cell line that was stably transfected sequentially by modified pcDNA3.1 vectors encoding Flag-tagged mLST8 and Flag-tagged mTOR^{AN}. In the absence of mLST8 co-expression, the level of soluble mTOR^{AN} was substantially lower, and it co-purified with endogenous mLST8 (not shown). The mTOR^{AN}Δ2443–2486–mLST8, full-length human mTOR–mLST8 and human mTORC1 (mTOR–mLST8–RAPTOR) complexes were similarly produced in HEK293-F cell lines that were stably transfected with the Flag-tagged versions of the proteins. Cells were grown as monolayers in 15-cm plates. They were lysed in 50 mM Tris-Cl, pH 8.0, 100 mM KCl, 400 mM NaCl, 1 mM EDTA, 1 mM EGTA, 10% (v/v) glycerol, 2 mM dithiothreitol (DTT) and protease inhibitors using French Press. After centrifugation, the Flag-tagged proteins were affinity purified using anti-Flag M2 agarose beads (Sigma). Following cleavage of the Flag tags by tobacco etch virus (TEV) protease, they were purified by ion exchange (MonoQ) and gel-filtration chromatography. The purified complex was concentrated to 5 mg ml^{−1} by ultrafiltration in 20 mM Tris-Cl, 500 mM NaCl, 10 mM DTT, pH 8.0 and was used for crystallization immediately. For kinase assays, 10% (v/v) glycerol was added to protein aliquots for storage at −80 °C.

Human S6K1α^{hi} protein, which contains the kinase-inactivating K100R mutation, was produced by infecting High Five insect cells with a pFastBac1 baculovirus expressing the Flag-tagged protein. It was purified by affinity chromatography with anti-Flag M2 agarose beads. The protein was concentrated to 8 mg ml^{−1} in 50 mM Tris-Cl, 400 mM NaCl, 1 mM EDTA, 1 mM EGTA, 5% (v/v) glycerol, 10 mM DTT and 1 mM Pefabloc, pH 8.0, and was stored at −80 °C.

Human 4E-BP1 was overexpressed in the *Escherichia coli* strain BL21(DE3) from a modified pGEX4T3 vector, and was purified by glutathione affinity chromatography, cleavage of the GST tag with TEV protease, fractionation on a MonoQ column, removal of free GST by glutathione affinity and gel-filtration (Superdex 75) chromatography. The peak fractions were concentrated to 20 mg ml^{−1} in 20 mM Tris-Cl, 200 mM NaCl, 5% (v/v) glycerol and 10 mM DTT, pH 8.0. **Crystallization and data collection.** Crystals were grown by the hanging-drop vapour diffusion method at 4 °C. Apo-crystals of the mTOR^{AN}–mLST8 complex were grown from 100 mM Tris-Cl, 6–8% (w/v) polyethylene glycol (PEG) 8000, 500 mM NaCl, 10% (v/v) glycerol and 10 mM DTT, pH 8.5. Crystals of mTOR^{AN}–mLST8 bound to ADP–MgF₃–Mg₂ were grown similarly, except the well buffer contained 10 mM MgCl₂, 3 mM ADP and 20 mM NaF. The mTOR^{AN}–mLST8–ATPγS–Mg₂ complex was prepared by soaking apo-crystals for one hour in a stabilization buffer of 50 mM Tris-Cl, pH 8.5, 10 mM Tris-Cl, pH 8.0, 10% PEG 8000, 0.1 M NaCl and 6% glycerol, supplemented with 5 mM MgCl₂ and 1 mM ATPγS. The mTOR^{AN}–mLST8–AMPPNP–Mn₂ complex was prepared by soaking apo-crystals similarly, except the stabilization buffer had pH 7.5 and was supplemented with 1 mM AMPPNP and 2 mM MnCl₂, and the data was collected at the manganese absorption edge. Crystals of mTOR^{AN}–mLST8–Torin2 and mTOR^{AN}–mLST8–PI-103 were prepared by mixing 1 mM of the inhibitors with the protein. Co-crystals appeared from the same condition as the apo-crystals. Crystals of mTOR^{AN}–mLST8–PP242 were prepared by soaking apo-crystals for 2.5 h in the stabilization buffer supplemented with 0.2 mM PP242. Apo-crystals were collected in stabilization buffer, transferred to 50 mM Tris-Cl, pH 8.5, 10 mM Tris-Cl,

pH 8.0, 0.1 M NaCl, 14% (w/v) PEG 8000 and 22% (v/v) glycerol, and were flash-frozen in liquid nitrogen. Crystals with ADP–MgF₃–Mg₂, ATPγS–Mg₂, Torin2, PI-103 and PP242 were flash-frozen similarly, except for the presence of the corresponding cofactors or inhibitors (0.1 mM) in the buffers. Diffraction data were collected at −170 °C at the ID24C and ID24E beamlines of the Advanced Photon Source, and they were processed with the HKL suite⁴⁹.

Structure determination and refinement. Initial phases were obtained from isomorphous and anomalous differences of two heavy-atom derivatives, prepared by soaking crystals in stabilization buffer lacking DTT and supplemented with 1 mM uranyl acetate (1 h), or with 0.4 mM potassium gold cyanide (75 min) at 4 °C. Initial phases, calculated with the program SHARP⁵⁰, had a mean figure of merit of 0.35 (35.0 to 4.5 Å). The uranyl derivative had a dispersive phasing power (P_p) of 0.89 and an anomalous P_p of 0.60, with a dispersive R_{Cullis} of 0.79 and anomalous R_{Cullis} of 0.95. The gold derivative had a dispersive P_p of 0.80 and an anomalous P_p of 0.29, with a dispersive R_{Cullis} of 0.66 and an anomalous R_{Cullis} of 0.98. The phases were improved using solvent flattening and twofold NCS averaging with multiple masks in the program DM⁵¹. The model was built using O⁵² and refined first with REFMAC⁵³ and then with PHENIX⁵³, using tight NCS restraints on atom positions. The final model contains residues 1385–2549 of human mTOR and residues 8–324 of human mLST8. mTOR^{AN} residues 1376–1384 at the N terminus, residues 1815–1866 in the FAT domain and residues 2437–2491 between $\alpha 9b$ and $\alpha 10$ in the kinase domain are disordered. mLST8 residues 1–7 and 325–326 from the N and C termini are disordered. The Ramachandran plot, calculated by PROCHECK, has 88.5%, 11.0% and 0.5% of the residues in the most favoured, additionally allowed and generously allowed regions, respectively. There are no residues in disallowed regions. The R_{free} test set of the native data contains 1,699 reflections.

In vitro kinase assays. All kinase assays were performed in a buffer of 25 mM HEPES, pH 7.4, 100 mM NaCl, 10 mM MgCl₂, 2 mM DTT and 3% (v/v) glycerol, for 30 min at 30 °C, in a final volume of 15 μ l. For a typical reaction, the indicated amount of enzymes, substrates and competitors were incubated together for 10 min on ice in the kinase buffer in a final volume of 13.5 μ l. Reactions were started by the addition of 1.5 μ l of cold ATP (final concentration, 0.5 mM) including 2 μ Ci of [γ -³²P] ATP (6000 Ci mmol^{−1}, Perkin-Elmer). In assays with rapamycin, all reactions in a titration contained a constant level of 3.3% DMSO. Reactions were stopped by the addition of 15 μ l of 2× NuPAGE LDS sample buffer and boiling for 3 min, and were resolved in a 4–12% NuPAGE Bis-Tris gel. Where applicable, each reaction was split into two for analysis by phosphorimaging and immunoblotting. All antibodies were obtained from Cell Signaling Technology, except for the anti-Flag antibody, which was obtained from Sigma.

49. Otwinowski, Z. & Minor, W. Processing of X-ray diffraction data collected in oscillation mode. *Methods Enzymol.* **276**, 307–326 (1997).
50. Bricogne, G., Vonrhein, C., Flensburg, C., Schiltz, M. & Paciorek, W. Generation, representation and flow of phase information in structure determination: recent developments in and around SHARP 2.0. *Acta Crystallogr. D* **59**, 2023–2030 (2003).
51. Collaborative Computational Project, Number 4. The CCP4 suite: programs for protein crystallography. *Acta Crystallogr. D* **50**, 760–763 (1994).
52. Jones, T. A., Zou, J. Y., Cowan, S. W. & Kjeldgaard, M. Improved methods for building protein models in electron density maps and the location of errors in these models. *Acta Crystallogr. A* **47**, 110–119 (1991).
53. Adams, P. D. *et al.* PHENIX: a comprehensive Python-based system for macromolecular structure solution. *Acta Crystallogr. D* **66**, 213–221 (2010).

Discrete clouds of neutral gas between the galaxies M31 and M33

Spencer A. Wolfe¹, D. J. Pisano¹, Felix J. Lockman², Stacy S. McGaugh³ & Edward J. Shaya⁴

Spiral galaxies must acquire gas to maintain their observed level of star formation beyond the next few billion years¹. A source of this material may be the gas that resides between galaxies, but our understanding of the state and distribution of this gas is incomplete². Radio observations³ of the Local Group of galaxies have revealed hydrogen gas extending from the disk of the galaxy M31 at least halfway to M33. This feature has been interpreted to be the neutral component of a condensing intergalactic filament⁴, which would be able to fuel star formation in M31 and M33, but simulations suggest that such a feature could also result from an interaction between both galaxies within the past few billion years (ref. 5). Here we report radio observations showing that about 50 per cent of this gas is composed of clouds, with the rest distributed in an extended, diffuse component. The clouds have velocities comparable to those of M31 and M33, and have properties suggesting that they are unrelated to other Local Group objects. We conclude that the clouds are likely to be transient condensations of gas embedded in an intergalactic filament and are therefore a potential source of fuel for future star formation in M31 and M33.

A recent study⁶ of the region between M31 and M33 using the Robert C. Byrd Green Bank Telescope (GBT) at 9' angular resolution has confirmed the presence of neutral hydrogen at levels of a few times 10^{17} cm^{-2} . The study also showed that this neutral gas has a velocity similar to the systemic velocities of M31 and M33, and is thus not the product of confusion with foreground emission from the Milky Way. The sensitivities of the observations were, however, insufficient to provide a detailed understanding of the structure and extent of this gas. Observations were needed with high angular resolution, high velocity resolution and high sensitivity to distinguish clouds from diffuse gas, and an intergalactic filament from tidal debris. Determining the origin of the gas is important, for if it is from an intergalactic filament, it would represent a new source of material to fuel future star formation in M31 and M33.

We have mapped a portion of the hydrogen gas feature between M31 and M33 with improved sensitivity and higher angular and velocity resolution using the GBT. We detect seven clouds (Fig. 1); Table 1 lists their properties. The positions and velocities of the brightest clouds are consistent with previous GBT results⁶. The primary difference between

the results from the Westerbork Synthesis Radio Telescope (WSRT) survey³, which used that array as a collection of single dishes, and our high-resolution data is that here the H I emission is resolved into features approximately the size of a GBT beamwidth or smaller, and at much higher column densities. The GBT data convolved to 49' angular resolution reproduce the same basic morphology as the WSRT data. The total H I mass detected is $(1.2 \pm 0.1) \times 10^9 M_\odot$ above a level of $3.0 \times 10^{17} \text{ cm}^{-2}$, $(1.3 \pm 0.1) \times 10^6 M_\odot$ above $1.0 \times 10^{17} \text{ cm}^{-2}$ and $(1.9 \pm 0.1) \times 10^6 M_\odot$ above $1.0 \times 10^{16} \text{ cm}^{-2}$ (here M_\odot is the solar mass). These values do not appear to be consistent with the relationship between the mass of neutral atomic hydrogen (M_{HI}) and its column density (N_{HI}) predicted by simulations of intergalactic H I at low redshift⁷. The total H I mass measured across the entire map is $(2.6 \pm 0.2) \times 10^6 M_\odot$, identical to the total H I mass from the WSRT data over the same area. There is probably additional mass present in the form of ionized gas, as at such low column densities photoionization of the H I by the extragalactic radiation field becomes significant⁸.

About 50% of the neutral hydrogen is in clouds, whose diameters range from ≤ 2.4 kpc to 6.4 kpc. This is the size range of dwarf galaxies; however, although stellar surveys^{9,10} have detected dwarf galaxies around M31 as well as potential dwarf galaxy remnants, there are no reports of stellar over-densities at the positions of these clouds¹⁰, even though there is no lack of stellar streams in the general vicinity¹¹. The clouds lie much farther from M31 and M33 than each galaxy's respective high-velocity cloud (HVC) population and also lie closer to the systemic velocities of M31 and M33 than the HVCs (Fig. 2). The clouds are also kinematically cooler as a population than the HVCs, with a lower inter-cloud velocity dispersion by a factor of two to five.

We estimate the baryonic mass and circular rotation speed about the cloud centre for the clouds as well as for the HVCs and dwarf galaxies of M31 and M33, and plot them with the baryonic Tully–Fisher relation^{12,13} (Fig. 3). This allows us to compare the clouds to other members of the Local Group. The clouds are offset from the Tully–Fisher relation for rotating disk galaxies; they occupy a similar region in the Tully–Fisher plane as the HVCs and dwarfs, but cluster more tightly.

If the linewidths of the clouds are interpreted as an equilibrium velocity representative of the gravitational potential, then the clouds would be highly dark-matter dominated. The virial mass of every cloud

Table 1 | H I cloud properties

Cloud ...	RA (h min s)	Dec. (° ' ")	LSR velocity (km s ⁻¹)	FWHM (km s ⁻¹)	$T_{\text{B,Peak}}$ (mK)	$\log[N_{\text{HI,Peak}} (\text{cm}^{-2})]$	M_{HI} (M_\odot)	Diameter (kpc)
1	01 24 42	+37 23 02	-297 ± 1	23 ± 3	47 ± 4	17.6 ± 0.04	$(1.2 \pm 0.2) \times 10^5$	$\leq 2.8 \pm 1$
2	01 20 52	+37 16 58	-236 ± 1	28 ± 2	69 ± 4	17.8 ± 0.03	$(3.5 \pm 0.3) \times 10^5$	6.4 ± 1
3	01 19 25	+37 31 12	-226 ± 2	28 ± 4	41 ± 4	17.6 ± 0.04	$(1.1 \pm 0.2) \times 10^5$	$\leq 2.4 \pm 1$
4	01 08 30	+37 44 51	-277 ± 1	34 ± 3	91 ± 4	17.9 ± 0.02	$(4.0 \pm 0.3) \times 10^5$	4.8 ± 1
5	01 05 09	+36 23 28	-209 ± 4	26 ± 3	34 ± 4	17.5 ± 0.05	$(4.2 \pm 1.0) \times 10^4$	$\leq 2.4 \pm 1$
6	01 03 10	+36 01 46	-282 ± 4	29 ± 3	39 ± 4	17.6 ± 0.05	$(1.4 \pm 0.2) \times 10^5$	$\leq 3.2 \pm 1$
7	01 17 02	+36 49 34	-309 ± 2	24 ± 4	10 ± 2	17.0 ± 0.1	$(4.0 \pm 1.0) \times 10^4$	$\leq 3.4 \pm 1$

RA and Dec. are respectively the right ascension and declination of each cloud; LSR, Local Standard of Rest; FWHM, full-width at half-maximum of the H I line; $T_{\text{B,Peak}}$, peak brightness temperature; $N_{\text{HI,Peak}} = 1.82 \times 10^{18} T_{\text{B,Peak}} \Delta v$ is the peak column density, where $\Delta v \approx 5 \text{ km s}^{-1}$; M_{HI} is the H I mass of the cloud, in solar masses, measured to the 3σ column density contour in the maps; diameter is measured to the same contour along the major axis of the cloud, if one is apparent. The ± 1 kpc error in the diameter is due to the pixel size in our maps projected to a distance of ~ 800 kpc. The values for cloud 7 were obtained from the 15' map. Quantities were calculated assuming a distance to the clouds of 800 kpc (ref. 6).

¹Department of Physics, West Virginia University, PO Box 6315, Morgantown, West Virginia 26506, USA. ²National Radio Astronomy Observatory, PO Box 2, Green Bank, West Virginia 24944, USA.

³Department of Astronomy, Case Western Reserve University, Cleveland, Ohio 44106, USA. ⁴Department of Astronomy, University of Maryland, College Park, Maryland 20742, USA.

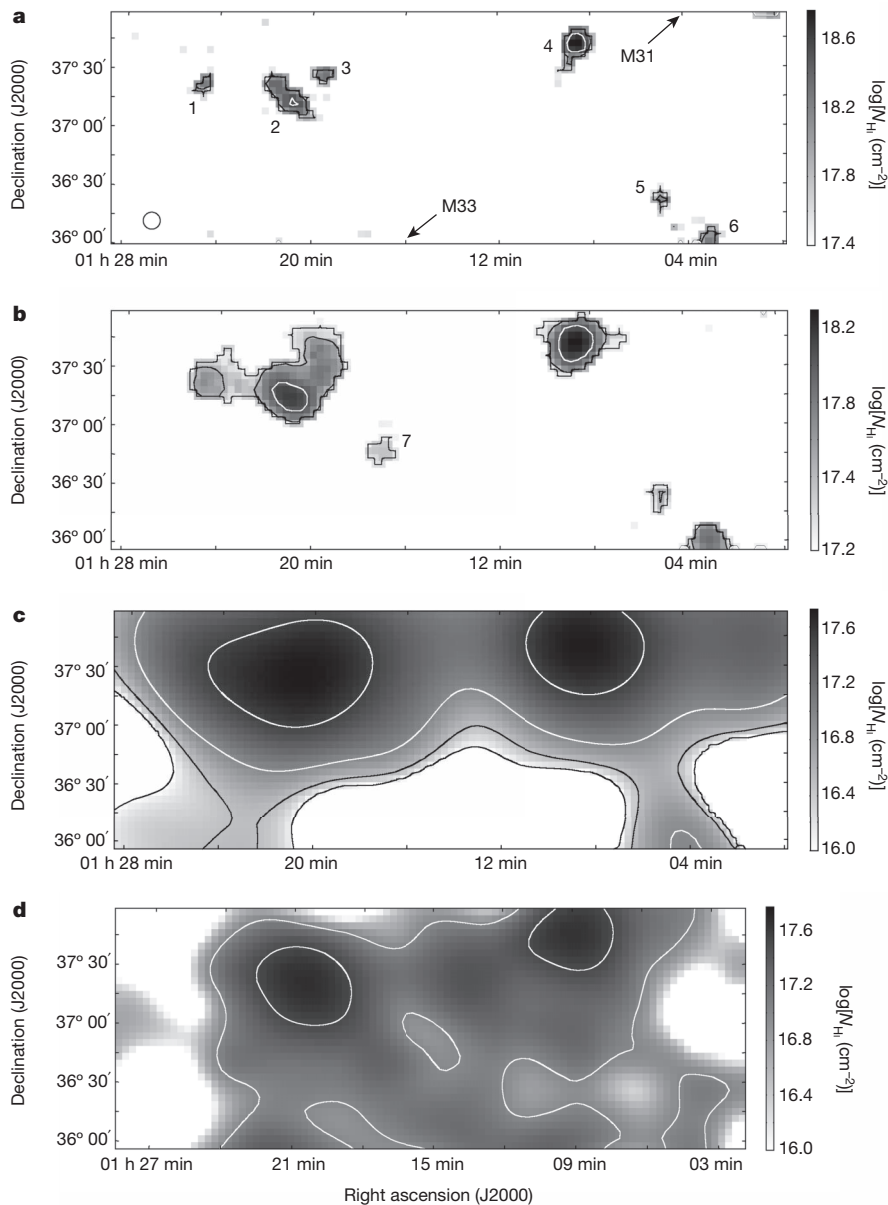


Figure 1 | H I column density maps. Maps of 21-cm emission over a 12 square-degree region between M31 and M33^{18,19}. The data from which these plots were compiled are available in Supplementary Information. **a**, Column density map of H I (in units of cm^{-2}) of the section of the area between M31 and M33 mapped with the GBT. This is a result of nearly 250 h of integration. The 3σ sensitivity limit in N_{HI} is $2.7 \times 10^{17} \text{ cm}^{-2}$ for a linewidth of 25 km s^{-1} at $9'$ angular resolution with a velocity resolution of 5 km s^{-1} . The contours are for $\log(N_{\text{HI}}) = 17.5, 18.0, 18.5$. There are six confirmed H I clouds, labelled in order of decreasing right ascension. M31 is to the northwest and M33 to the southeast, as indicated by the arrows. Both galaxies are about five degrees from the respective edges of the map. **b**, The GBT data, smoothed to a $15'$ resolution to match the sensitivity of the WSRT data ($1 \times 10^{17} \text{ cm}^{-2}$). A seventh cloud is now visible, labelled 7. The contours are for $\log(N_{\text{HI}}) = 17.0, 17.5, 18.0$. **c**, The GBT data, smoothed to a $49'$ resolution to match the angular resolution of the WSRT data. The contours are for $\log(N_{\text{HI}}) = 16.0, 16.5, 17.0, 17.5$. **d**, Part of the WSRT H I survey³ that first detected neutral gas between M31 and M33, at an angular resolution of $49'$ and a velocity resolution of 18 km s^{-1} . H I emission was detected over a wide area at $N_{\text{HI}} \geq 10^{17} \text{ cm}^{-2}$, most of it only 2–3 times the noise level. The contours are for $\log(N_{\text{HI}}) = 17.0, 17.5$.

is two to three orders of magnitude larger than its H I mass. The presence of an ionized component, however, would decrease the amount of dark matter necessary to match the virial mass. The free-fall time for these clouds, or the time it would take for these clouds to freely collapse under their own gravity, is $\sim 400 \text{ Myr}$ and the crossing time, the time it would take for a parcel of gas to cross the length of the cloud, is $\sim 100 \text{ Myr}$. These times are quite short to have resulted from the interaction between M31 and M33 proposed to have occurred a few billion years ago^{5,10} unless confined by an external pressure. The warm-hot intergalactic medium (WHIM)⁴ at a temperature $\sim 10^6 \text{ K}$ and of density $\gtrsim 10^{-7} \text{ cm}^{-3}$ would supply the pressure if the clouds have a temperature of $\sim 10^4 \text{ K}$, consistent with the values inferred from the cloud linewidths. The WHIM densities needed are comparable to those predicted¹⁴ beyond the virialized region of galaxies, therefore these clouds could be in complete pressure equilibrium with the WHIM.

These clouds have several possible origins. First, they may be primordial, gas-rich objects similar to the dwarf spheroidal or dwarf irregular galaxies in the Local Group, but this does not explain why the gas seems to lie along a connecting structure, even when resolved into clouds. Second, the clouds may be gas that is accreting onto sub-haloes. This might occur naturally if the gas is part of a cosmic filament. If instead the gas is tidal in origin, it is likely to be moving at

relative speeds that exceed the escape velocities of sub-haloes, making accretion unlikely. Third, the clouds may be analogous to tidal dwarf galaxies¹⁵. This would account for their spatial and kinematical distribution with respect to M31 and M33. If so, the clouds would need to be in pressure equilibrium with the WHIM, so that they could persist for a few billion years following the interaction between M31 and M33. It is also possible that there may have been a more recent interaction that produced these clouds, such as M31 with IC10 or some other object. These clouds contain no evidence of stars, however, and do not fall on the Tully–Fisher relation, as one system of tidal dwarfs is known to do¹⁵. Last, the clouds could be transient objects condensing from an intergalactic filament, as originally proposed^{3,16}. This could explain their spatial distribution, as well as the lack of stellar overdensities. A recent simulation¹⁷ of a Milky Way sized galaxy has produced analogous material out to $\sim 100 \text{ kpc}$ with H I masses $\sim 10^5 M_{\odot}$, suggesting that the clouds are most probably condensations from an intergalactic filament.

We conclude that the H I clouds between M31 and M33 are a unique population, lacking a clear analogue in other members of the Local Group, such as the dwarf galaxies or HVCs. Although our current results suggest that the clouds may arise in an intergalactic filament, and thus are potential fuel for star formation in M31 and/or M33, the

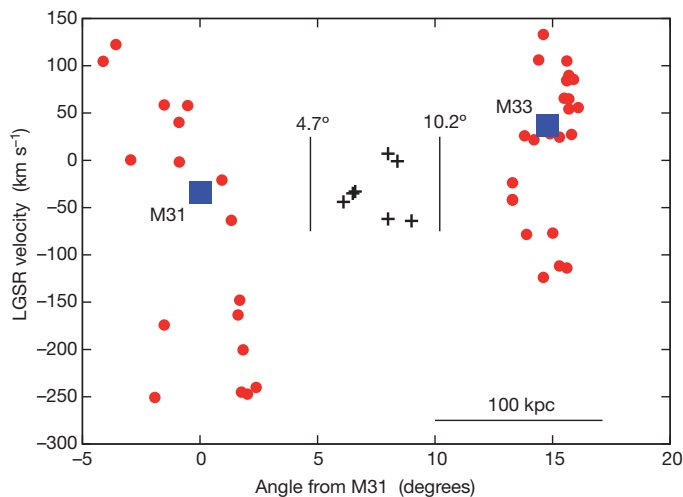


Figure 2 | A position-velocity plot of the H I clouds and selected Local Group objects. The local group standard of rest (LGSr) velocities were calculated using the NASA Extragalactic Database. Large blue squares indicate M31 and M33. Filled red circles are the high-velocity clouds (HVCs) of each galaxy^{20–23}. Crosses show clouds detected in the GBT maps; the vertical bars mark the GBT map boundaries, in terms of angle from M31. The HVCs lie within ~ 50 kpc of each galaxy, whereas the new clouds are found ~ 100 kpc from both galaxies. The new clouds also have an inter-cloud velocity dispersion of 25 km s^{-1} , compared to the $70\text{--}130 \text{ km s}^{-1}$ for the HVCs.

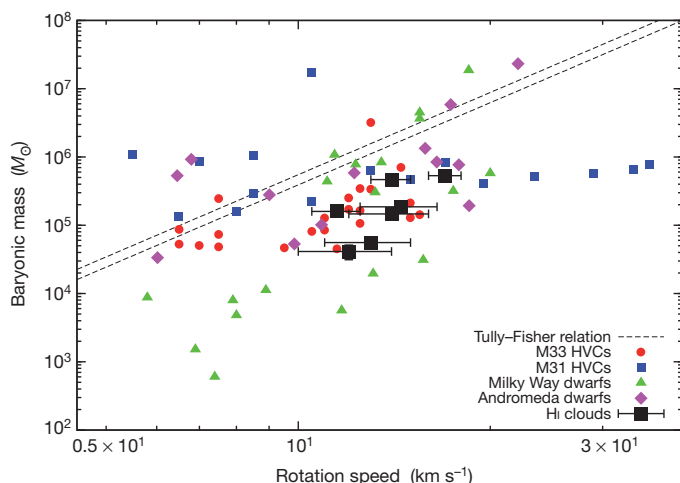


Figure 3 | A plot of baryonic mass versus the equivalent circular rotation speed. This figure compares the newly detected H I clouds (black filled squares with 1σ error bars), the HVCs of M31 and M33 (squares, circles), Milky Way dwarf satellite galaxies²⁴ (triangles) and the Andromeda dwarfs²⁵ (diamonds) to the baryonic Tully-Fisher relation²⁶ with $\pm 1\sigma$ uncertainty (dashed lines). We assume that all of the mass is in the neutral atomic gas and that $M_{\text{baryonic}} = 1.33 \times M_{\text{H I}}$ to account for helium. The masses are plotted in units of solar masses. The presence of an ionized component will increase the baryonic mass and move the clouds closer to the relation, but we have no way at present to estimate its magnitude. The effective circular rotation speed is $v_{\text{rot}} = \text{FWHM}/2$ where FWHM is the full-width at half-maximum of the H I line. This assumption holds in the case where the gas may be in rotation or is a turbulently supported, spherical system with an assumed harmonic radius of $R/2$, where R is the cloud radius, measured to the same column density contour as the diameter in Table 1. The scatter in mass-rotation velocity is 0.5 dex for the clouds, 0.8 dex for the Andromeda dwarfs and M33's HVCs, 1.2 dex for M31's HVCs, and 1.8 dex for the Milky Way dwarfs. The average errors (in dex) for the rotation velocities $\langle \sigma_{v_{\text{rot}}} \rangle$ and masses $\langle \sigma_M \rangle$ are respectively 0.05 and 0.1 for M33's HVCs, 0.05 and 0.06 for M31's HVCs, 0.1 and 0.2 for the Milky Way dwarfs, 0.1 and 0.7 for the Andromeda dwarfs and 0.06 and 0.08 for the H I clouds.

question of their origin needs further consideration. The new clouds we report here were discovered in only about half of our survey time and thus are not at the full sensitivity that we intend to achieve. The region we have studied is only a fraction of the area around M31 reported³ to have diffuse H I, so the clouds measured here may be the first representatives of a much larger population.

Received 13 December 2012; accepted 18 March 2013.

1. Leroy, A. K. *et al.* The star formation efficiency in nearby galaxies: measuring where gas forms stars effectively. *Astron. J.* **136**, 2782–2845 (2008).
2. Shull, J. M., Smith, B. D. & Danforth, C. W. The baryon census in a multiphase intergalactic medium: 30% of the baryons may still be missing. *Astrophys. J.* **759**, 23–37 (2012).
3. Braun, R. & Thilker, D. A. The WSRT wide-field H I survey II. Local Group features. *Astron. Astrophys.* **417**, 421–435 (2004).
4. Davé, R. *et al.* Baryons in the warm-hot intergalactic medium. *Astrophys. J.* **552**, 473–483 (2001).
5. Bekki, K. Formation of a giant H I bridge between M31 and M33 from their tidal interaction. *Mon. Not. R. Astron. Soc.* **390**, L24–L28 (2008).
6. Lockman, F. J., Free, N. L. & Shields, J. C. The neutral hydrogen bridge between M31 and M33. *Astron. J.* **144**, 52–58 (2012).
7. Popping, A., Davé, R., Braun, R. & Oppenheimer, B. D. The simulated H I sky at low redshift. *Astron. Astrophys.* **504**, 15–32 (2009).
8. Maloney, P. Sharp edges to neutral hydrogen disks in galaxies and the extragalactic radiation field. *Astrophys. J.* **414**, 41–56 (1993).
9. Ibata, R. *et al.* The haunted halos of Andromeda and Triangulum: a panorama of galaxy formation in action. *Astrophys. J.* **671**, 1591–1623 (2007).
10. McConnachie, A. W. *et al.* The remnants of galaxy formation from a panoramic survey of the region around M31. *Nature* **461**, 66–69 (2009).
11. Lewis, G. F. *et al.* PAndAS in the mist: the stellar and gaseous mass within the halos of M31 and M33. *Astrophys. J.* **763**, 4–13 (2013).
12. Tully, R. B. & Fisher, J. R. A new method of determining distances to galaxies. *Astron. Astrophys.* **54**, 661–673 (1977).
13. McGaugh, S. S., Schombert, J. M., Bothun, G. D. & de Blok, W. J. G. The baryonic Tully-Fisher relation. *Astrophys. J.* **533**, L99–L102 (2000).
14. Fukugita, M. & Peebles, P. J. E. The cosmic energy inventory. *Astrophys. J.* **616**, 643–668 (2004).
15. Gentile, G. *et al.* Tidal dwarf galaxies as a test of fundamental physics. *Astron. Astrophys.* **472**, L25–L28 (2007).
16. Maller, A. H. & Bullock, J. S. Multiphase galaxy formation: high-velocity clouds and the missing baryon problem. *Mon. Not. R. Astron. Soc.* **355**, 694–712 (2004).
17. Fernández, X., Joung, M. R. & Putman, M. E. The origin and distribution of cold gas in the halo of a Milky-Way-mass galaxy. *Astrophys. J.* **749**, 181–192 (2012).
18. Chynoweth, K. *et al.* Neutral hydrogen clouds in the M81/M82 group. *Astron. J.* **135**, 1983–1992 (2008).
19. Boothroyd, A. I. *et al.* Accurate galactic 21-cm H I measurements with the NRAO Green Bank Telescope. *Astron. Astrophys.* **536**, A81 (2011).
20. Thilker, D. A. *et al.* On the continuing formation of the Andromeda galaxy: detection of H I clouds in the M31 halo. *Astrophys. J.* **601**, L39–L42 (2004).
21. Grossi, M. *et al.* H I clouds in the proximity of M33. *Astron. Astrophys.* **487**, 161–175 (2008).
22. Westmeier, T., Brüns, C. & Kerp, J. Relics of structure formation: extra-planar gas and high velocity clouds around the Andromeda Galaxy. *Mon. Not. R. Astron. Soc.* **390**, 1691–1709 (2008).
23. Putman, M. E. *et al.* The disruption and fueling of M33. *Astrophys. J.* **703**, 1486–1501 (2009).
24. McGaugh, S. S. & Wolf, J. Local Group dwarf spheroidals: correlated deviations from the baryonic Tully-Fisher relation. *Astrophys. J.* **722**, 248–261 (2010).
25. Tollerud, E. J. The SPLASH survey: spectroscopy of 15 M31 dwarf spheroidal satellite galaxies. *Astrophys. J.* **752**, 45–73 (2012).
26. McGaugh, S. S. The baryonic Tully-Fisher relation of gas-rich galaxies as a test of Λ CDM and MOND. *Astron. J.* **143**, 40–54 (2012).

Supplementary Information is available in the online version of the paper.

Acknowledgements D.J.P. is an Adjunct Assistant Astronomer at the National Radio Astronomy Observatory; F.J.L. is an Adjunct Professor in the Department of Physics, West Virginia University. S.A.W. acknowledges the student observing support (GSSP11-012) provided by the NRAO for this project. The NRAO is a facility of the NSF operated under cooperative agreement by Associated Universities, Inc. D.J.P. acknowledges support from NSF CAREER grant AST-1149491. S.S.M. acknowledges support in part by NSF grant AST-0908370.

Author Contributions All authors assisted in the development and writing of this work. S.A.W. is the Principal Investigator, and was responsible for data collection, processing and analysis. D.J.P. and F.J.L. assisted in the experimental design, data collection and analysis. S.S.M. provided the techniques of estimating the baryonic masses. E.J.S. provided necessary insights on potential interactions with M31 and ways of estimating circular rotation speeds. All authors aided in the interpretation of the results and provided comments for revisions to this work.

Author Information Reprints and permissions information is available at www.nature.com/reprints. The authors declare no competing financial interests. Readers are welcome to comment on the online version of the paper. Correspondence and requests for materials should be addressed to S.A.W. (swolfef4@mix.wvu.edu).

Bell violation using entangled photons without the fair-sampling assumption

Marissa Giustina^{1,2*}, Alexandra Mech^{1,2*}, Sven Ramelow^{1,2*}, Bernhard Wittmann^{1,2*}, Johannes Kofler^{1,3}, Jörn Beyer⁴, Adriana Lita⁵, Brice Calkins⁵, Thomas Gerrits⁵, Sae Woo Nam⁵, Rupert Ursin¹ & Anton Zeilinger^{1,2}

The violation of a Bell inequality is an experimental observation that forces the abandonment of a local realistic viewpoint—namely, one in which physical properties are (probabilistically) defined before and independently of measurement, and in which no physical influence can propagate faster than the speed of light^{1,2}. All such experimental violations require additional assumptions depending on their specific construction, making them vulnerable to so-called loopholes. Here we use entangled photons to violate a Bell inequality while closing the fair-sampling loophole, that is, without assuming that the sample of measured photons accurately represents the entire ensemble³. To do this, we use the Eberhard form of Bell's inequality, which is not vulnerable to the fair-sampling assumption and which allows a lower collection efficiency than other forms⁴. Technical improvements of the photon source^{5,6} and high-efficiency transition-edge sensors⁷ were crucial for achieving a sufficiently high collection efficiency. Our experiment makes the photon the first physical system for which each of the main loopholes has been closed, albeit in different experiments.

In 1935, Einstein, Podolsky and Rosen¹ argued that quantum mechanics is incomplete when assuming that no physical influence can be faster than the speed of light and that the properties of physical systems are elements of reality. They considered measurements on spatially separated pairs of entangled particles. Measurement on one particle of an entangled pair instantly projects the other particle onto a well-defined state, independently of their spatial separation. In 1964, Bell² showed that no local realistic theory can reproduce all quantum mechanical predictions for entangled states. His renowned Bell inequality proved that there is an upper limit to the strength of the observed correlations predicted by local realistic theories. Quantum theory's predictions violate this limit.

In a Bell experiment, one prepares pairs of entangled particles and sends them to two observers, Alice and Bob, for measurement and detection. Alice and Bob observe correlations between their results that, for specific choices of their measurement settings, violate the Bell inequality and hence force abandonment of local realism.

It is common that in an experiment, some particles emitted by the source will not be detected^{3,8}. In such a case, the subset of detected particles might display correlations that violate the Bell inequality although the entire ensemble can be described by a local realistic theory. To achieve a conclusive Bell violation without assuming that the detected particles are a 'fair' sample, a highly efficient experimental set-up is necessary. This efficiency need not be perfect³.

Experimental limitations have made it necessary to assume fair sampling in nearly every Bell experiment performed to date, with a few exceptions^{9–13}. In particular, owing to the lack of efficient sources and detectors, this assumption has always been unavoidable in Bell experiments on entangled photon pairs.

Since the first experimental Bell test¹⁴, a satisfactory laboratory realization of the motivating *gedankenexperiment* has remained a challenge^{15,16}. The two other main assumptions include "locality"^{17,18} and "freedom of choice"¹⁹. Invoking any of these three assumptions renders an experiment vulnerable to explanation by a local realistic theory. The realization of an experiment that is free of all three assumptions—a loophole-free Bell test—remains an important goal for the physics community²⁰. An important step has been the realization of quantum steering experiments that have also addressed the issue of loopholes^{21–23}. Our experiment makes photons the first physical system for which all three assumptions have been successfully addressed in a Bell test, albeit in different experiments.

In our experiment, we employ Eberhard's inequality, a Bell inequality that inherently does not rely on the fair-sampling assumption⁴. Our scheme is characterized by a number of technical improvements over previous experiments. Each such improvement contributed crucially to reaching the high collection efficiency and visibility necessary for violating the inequality. Our source of photon pairs uses spontaneous parametric down-conversion in a Sagnac configuration, which has proved to be efficient^{5,6}. For photon detection, we use superconducting transition-edge sensors (TESs), which not only have a high detection efficiency but are also intrinsically free of dark counts⁷. These two characteristics are essential for an experiment in which no correction of count rates can be tolerated.

Eberhard's inequality, which was proposed almost two decades ago⁴, is a Clauser–Horne-type Bell inequality²⁴ that explicitly includes undetected (inconclusive) events. Therefore, its mere violation directly implies that the fair-sampling loophole is closed. Also, the derivation of Eberhard's inequality includes pairs not detected on either side (and can be generalized for those not even produced), which means that no post-selection on the created pairs is necessary to violate the inequality.

Eberhard's inequality requires the lowest known symmetric arm efficiency for non-maximally entangled qubit states, namely $\eta = 2/3 \approx$

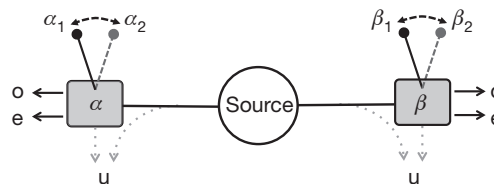


Figure 1 | Principle of the experiment. Violation of an Eberhard inequality involves a source of polarization-entangled pairs as well as polarization measurements. Each measurement device can rotate the photon's polarization according to one of two settings (α_1, α_2 and β_1, β_2) before projecting the photon into the 'ordinary' (o) or 'extraordinary' (e) output of a polarizing beam splitter and detecting it. All lost photons are also included in the derivation of the inequality as 'undetected' (u) events. The different terms of the inequality are photon counts recorded in the different settings.

¹Institute for Quantum Optics and Quantum Information (IQOQI), Austrian Academy of Sciences, Boltzmanngasse 3, Vienna 1090, Austria. ²Quantum Optics, Quantum Nanophysics, Quantum Information, University of Vienna, Faculty of Physics, Boltzmanngasse 5, Vienna 1090, Austria. ³Max Planck Institute of Quantum Optics (MPQ), Hans-Kopfermann-straße 1, 85748 Garching, Germany. ⁴Physikalisch-Technische Bundesanstalt, Abbestraße 1, 10587 Berlin, Germany. ⁵National Institute of Standards and Technology (NIST), 325 Broadway, Boulder, Colorado 80305, USA.

*These authors contributed equally to this work.

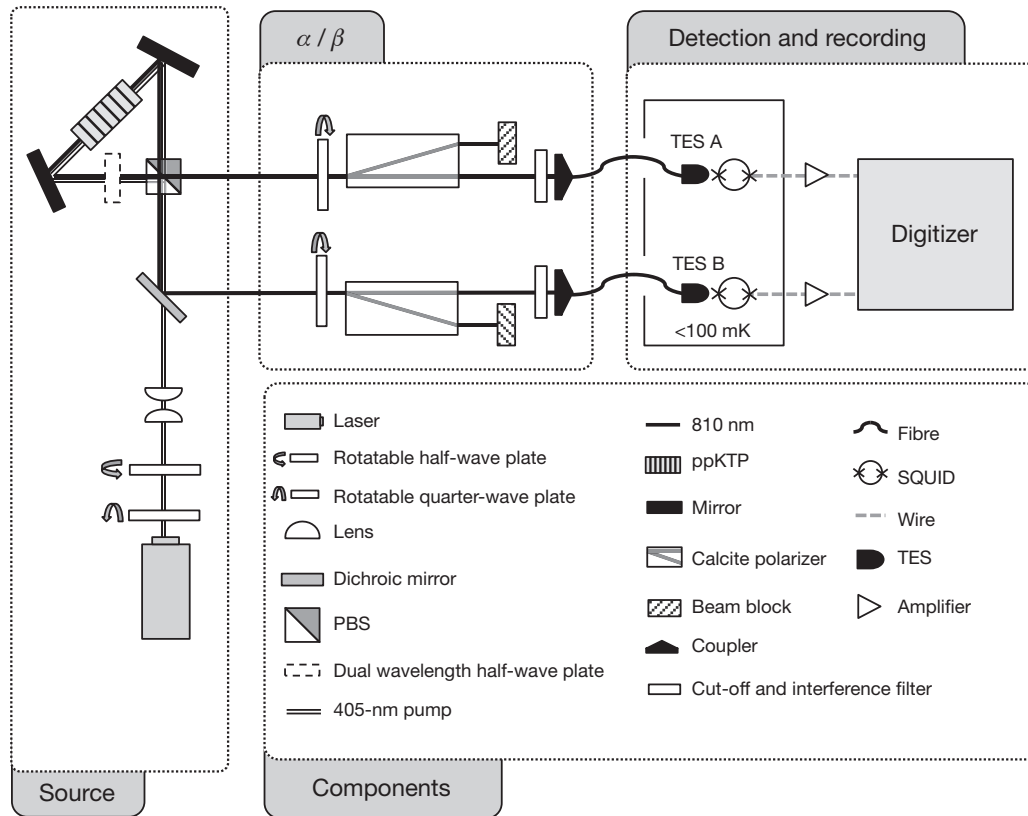


Figure 2 | Measurement set-up. The source, based on spontaneous parametric down-conversion in ppKTP (periodically poled potassium titanyl phosphate) in a Sagnac configuration, produces polarization-entangled photons with a wavelength of 810 nm. A measurement setting is implemented in each arm by rotating a half-wave plate to the desired angle in front of a calcite polarizer.

66.7%. This arm efficiency (that is, the collection efficiency in one arm of the experiment) incorporates all losses, not least those in the source and the measurement set-up (including the detector). Thresholds lower than $2/3$ have been reported for asymmetric efficiencies or higher-dimensionally entangled states^{25,26}. For the most widely used Bell inequality, proposed by Clauser, Horne, Shimony and Holt²⁷, at least $\eta = 2\sqrt{2} - 2 \approx 82.8\%$ is necessary in the symmetric case. For polarization-entangled photon pairs, Eberhard's inequality considers three possible outcomes: o ('ordinary') and e ('extraordinary') for the two recorded outcomes of a polarization measurement, and u ('undetected') if no photon is detected (see Fig. 1). Two different measurement settings are used, (α_1, α_2) on Alice's side and (β_1, β_2) on Bob's side. Let $n_{kl}(\alpha_i, \beta_j)$ denote the number of pairs with the outcome k for Alice's photon and l for Bob's photon, where $k, l \in \{o, e, u\}$, when measured in settings α_i and β_j with $i, j \in \{1, 2\}$. Eberhard's inequality can then be written as:

$$J = -n_{oo}(\alpha_1, \beta_1) + n_{oe}(\alpha_1, \beta_2) + n_{ou}(\alpha_1, \beta_2) + n_{eo}(\alpha_2, \beta_1) + n_{eu}(\alpha_2, \beta_1) + n_{oo}(\alpha_2, \beta_2) \geq 0 \quad (1)$$

Local realism allows J to take only non-negative values. Quantum mechanically, the maximal violation is given by $J/N = (1 - \sqrt{2})/2 \approx -0.207$ (ref. 15), where N denotes the number of entangled particle pairs produced per applied setting combination. This bound is attainable for a symmetric arm efficiency of $\eta = 1$ and maximally entangled states. For the largest possible violation of Eberhard's inequality with $\eta < 1$, non-maximally entangled states must be used. These have the form:

$$|\psi_r\rangle = \frac{1}{\sqrt{1+r^2}}(|HV\rangle + r|VH\rangle) \quad (2)$$

where $0 < r < 1$ and H and V denote horizontal and vertical polarization of Alice's and Bob's photons. Depending on the background count rate,

Photons transmitted through the calcite polarizer (ordinary output beam) are spectrally filtered and coupled into an optical fibre (SMF-28), which leads them to TESs for detection. The output signals from the detectors are amplified by SQUIDs and further electronics before being digitized and processed by an algorithm that identifies photons and time-correlated photon pairs.

efficiencies higher than $\eta = 2/3$ may be needed⁴. Interestingly, for $\eta < 82.8\%$, non-maximally entangled states are not only optimal but even necessary for a violation of Eberhard's inequality.

In an experiment, one records measurements of 'singles counts' S (number of detection events on one side) and 'coincidence counts' C (number of detected pairs) for the four combinations of settings (α_1, β_1) , (α_1, β_2) , (α_2, β_1) and (α_2, β_2) . The number of events for which one of the outcomes is undetected follows directly from the measured rates. For a given measurement length, we denote the measured coincidence counts by $C_{kl}(\alpha_i, \beta_j)$ and the single counts by $S_k^A(\alpha_i)$ for Alice and $S_l^B(\beta_j)$ for Bob ($k, l \in \{o, e\}$). All the terms in Eberhard's inequality are then given by the following measured quantities:

$$n_{oo}(\alpha_1, \beta_1) = C_{oo}(\alpha_1, \beta_1)$$

$$n_{oe}(\alpha_1, \beta_2) = C_{oe}(\alpha_1, \beta_2)$$

$$n_{ou}(\alpha_1, \beta_2) = S_o^A(\alpha_1) - C_{oo}(\alpha_1, \beta_2) - C_{oe}(\alpha_1, \beta_2)$$

$$n_{eo}(\alpha_2, \beta_1) = C_{eo}(\alpha_2, \beta_1)$$

$$n_{eu}(\alpha_2, \beta_1) = S_e^B(\beta_1) - C_{oo}(\alpha_2, \beta_1) - C_{eo}(\alpha_2, \beta_1)$$

$$n_{oo}(\alpha_2, \beta_2) = C_{oo}(\alpha_2, \beta_2) \quad (3)$$

Inserting these expressions into Eberhard's inequality yields:

$$J = -C_{oo}(\alpha_1, \beta_1) + S_o^A(\alpha_1) - C_{oo}(\alpha_1, \beta_2) + S_e^B(\beta_1) - C_{oo}(\alpha_2, \beta_1) + C_{oo}(\alpha_2, \beta_2) \geq 0 \quad (4)$$

where the coincidence counts $C_{oe}(\alpha_1, \beta_2)$ and $C_{eo}(\alpha_2, \beta_1)$ have dropped out. The resulting inequality, which is used in our experiment, now

Table 1 | Measurement results and J value for a total measurement time of 300 s per setting

$C_{00}(\alpha_1, \beta_1)$	$S_0^A(\alpha_1)$	$C_{00}(\alpha_1, \beta_2)$	$S_0^B(\beta_1)$	$C_{00}(\alpha_2, \beta_1)$	$C_{00}(\alpha_2, \beta_2)$	J
1,069,306	1,522,865	1,152,595	1,693,718	1,191,146	69,749	-126,715
(-)	(+)	(-)	(+)	(-)	(+)	

Without background subtraction, the Eberhard J value can be calculated from the measured data according to equation (4). (-) values contribute beneficially to a negative J value (making it more negative). (+) values contribute detrimentally to a negative J value (making it less negative).

contains only directly available detection events related to the ordinary beams of Alice and Bob. Remarkably, this implies that Alice and Bob each need only one detector to test Eberhard's inequality, whereas they each require two detectors for testing a Clauser–Horne–Shimony–Holt inequality. This characteristic can be intuitively understood: consider detectors that monitor 'e' outcomes and whose detection efficiencies decrease gradually to zero. This will just move events from 'e' to 'u': that is, from $n_{oe}(\alpha_1, \beta_2)$ to $n_{ou}(\alpha_1, \beta_2)$ and from $n_{eo}(\alpha_2, \beta_1)$ to $n_{uo}(\alpha_2, \beta_1)$. Only their sum appears in Eberhard's inequality, so the value of J does not change.

The entangled photon pairs at 810 nm are produced in a Sagnac source^{5,28} pumped by a 405-nm-wavelength laser. The source is based on type-II spontaneous parametric down-conversion using a non-linear crystal (periodically poled potassium titanyl phosphate). In each arm, a cut-off filter and a 3-nm interference filter with near 99% transmission are used to suppress counts from the pump laser and reduce the background counts. The source can be tuned to produce non-maximally entangled states with the form expressed by equation (2) for any r by setting the polarization of the pump light with half- and quarter-wave plates.

The measurement set-up (see Fig. 2), containing a rotatable half-wave plate in a high-precision rotation mount and a calcite polarizer, is positioned in front of the fibre coupler on both Alice's and Bob's sides to facilitate measurement of the desired polarization (α and β). The measurements require only one output of the polarizer, so only the transmitted ordinary beam of the polarizer is coupled into the fibre; the extraordinary beam is blocked after transmission. We couple the 810-nm photons into an optical fibre (SMF-28), which guides the photons to the sensitive areas of the detectors. To achieve a high coupling efficiency in both arms, we optimized the focusing of the pump laser and the fibre couplers.

To achieve highly efficient photon detection, we used TES calorimetric detectors that owe their sensitivity to operation at the superconducting transition, a regime characterized by a steep dependence of resistance on temperature⁷. By exploiting a wavelength-optimized optical structure, these detectors have been reported to demonstrate detection efficiencies of up to 98% (including losses from packaging and fibre coupling)^{6,7}. Superconducting quantum interference devices

(SQUIDS)²⁹ amplify the nanoampere-level TES current signal, which is subsequently digitized and stored for later analysis. Without requiring any additional information about the data, algorithms identify photon signatures in the analogue output signal, determine an arrival time for each event, and count two-photon coincidences.

As a guide for the experimental settings needed to observe a violation of local realism, we used numerical simulations and optimization to determine an optimal non-maximally entangled state. For input, the model used the estimated background rate, the observed visibility, and the overall efficiencies η_A and η_B on Alice's and Bob's sides. The model estimated a value for r but also appropriate measurement settings α_1, α_2 on Alice's side and β_1, β_2 on Bob's side.

We set the state with a value of ~ 0.3 for r and measured for a total of 300 s per setting at each of the four settings $\alpha_1\beta_1, \alpha_1\beta_2, \alpha_2\beta_1$ and $\alpha_2\beta_2$, where $\alpha_1 = 85.6^\circ$, $\alpha_2 = 118.0^\circ$, $\beta_1 = -5.4^\circ$ and $\beta_2 = 25.9^\circ$. The relevant single and coincidence counts obtained appear in Table 1 and yield $J = -126,715$.

After recording for a total of 300 s per setting we divided our data into 10-s blocks and calculated the standard deviation of the resulting 30 different J values. This yielded $\sigma = 1,837$ for our aggregate J value of $J = -126,715$, a 69- σ violation (see Fig. 3). Note that this calculation does not assume Poisson counting statistics or any error propagation rules. We estimate the number of produced pairs to $N = 24.2 \times 10^6$ per applied setting, yielding a normalized violation of $J/N = -0.00524$ (± 0.00008).

Under the assumptions of locality and freedom of choice, a negative J value refutes local realism without the fair-sampling assumption or post-selection on created pairs, regardless of the states and angles used for the measurement or any error in their implementation. Nonetheless, additional measurements can provide further insight into the obtained value. The directly measured arm efficiencies (each a ratio of observed coincidence and singles counts without any correction) measured in the HV-basis were $\eta_A = 73.77\%$ ($\pm 0.07\%$) in Alice's arm and $\eta_B = 78.59\%$ ($\pm 0.08\%$) in Bob's arm. We attribute these imperfect coupling efficiencies to various possibly arm-dependent effects including optical losses in the source, coupling, fibre splices, and detectors. We estimate our r value and visibility to be about 0.297 and 97.5%, respectively. Using these values, our numerical model (used for the abovementioned optimization) agrees very well with our measured J value.

Using photons, we have demonstrated an experimental Bell inequality violation that closes the fair-sampling loophole. Without relying on any assumed error distribution, we statistically verify a violation of Eberhard's inequality by nearly 70 standard deviations and thus clearly demonstrate the necessity of abandoning all local realistic theories that take advantage of unfair sampling to explain the observed values. Moreover, because the derivation of Eberhard's Bell inequality even includes events not detected on either side, no post-selection is necessary to violate the inequality. To achieve a loophole-free Bell test as described above, it will be necessary to introduce space-like separation sufficient to prohibit unwanted communication between Alice, Bob, the measurement decisions, and the photon emission event. This will require fast random-number generators, precise timing, and efficiency gains to offset the propagation losses introduced by the increased distance. We do not find this unreasonable.

Received 31 December 2012; accepted 13 February 2013.

Published online 14 April 2013.

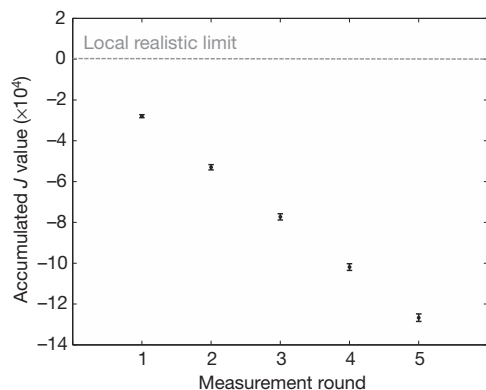


Figure 3 | Eberhard J value computed from up to five measurements of recorded data. Any negative J value violates the inequality and refutes all local realistic models that exploit the fair-sampling loophole. Error bars represent ± 1 standard deviation calculated from the binned raw data.

1. Einstein, A., Podolsky, B. & Rosen, N. Can quantum-mechanical description of physical reality be considered complete? *Phys. Rev.* **47**, 777–780 (1935).
2. Bell, J. S. On the Einstein Podolsky Rosen paradox. *Physics* **1**, 195 (1964).
3. Pearle, P. M. Hidden-variable example based upon data rejection. *Phys. Rev. D* **2**, 1418–1425 (1970).
4. Eberhard, P. H. Background level and counter efficiencies required for a loophole-free Einstein–Podolsky–Rosen experiment. *Phys. Rev. A* **47**, 747–750 (1993).
5. Fedrizzi, A., Herbst, T., Poppe, A., Jennewein, T. & Zeilinger, A. A wavelength-tunable, fiber-coupled source of narrowband entangled photons. *Opt. Express* **15**, 15377–15386 (2007).

6. Ramelow, S. *et al.* Highly efficient heralding of entangled single photons. *Opt. Express* **21**, 6707–6717 (2013).
7. Lita, A. E., Miller, A. J. & Nam, S. W. Counting near-infrared single-photons with 95% efficiency. *Opt. Express* **16**, 3032–3040 (2008).
8. Garg, A. & Mermin, N. D. Detector inefficiencies in the Einstein-Podolsky-Rosen experiment. *Phys. Rev. D* **35**, 3831–3835 (1987).
9. Rowe, M. A. *et al.* Experimental violation of a Bell's inequality with efficient detection. *Nature* **409**, 791–794 (2001).
10. Ansmann, M. *et al.* Violation of Bell's inequality in Josephson phase qubits. *Nature* **461**, 504–506 (2009).
11. Alicki, R. Remarks on the violation of Bell's inequality in Josephson phase qubits. Preprint at <http://arxiv.org/abs/0911.4009> (2009).
12. Matsukevich, D. N., Maunz, P., Moehring, D. L., Olmschenk, S. & Monroe, C. Bell inequality violation with two remote atomic qubits. *Phys. Rev. Lett.* **100**, 150404 (2008).
13. Hofmann, J. *et al.* Heralded entanglement between widely separated atoms. *Science* **337**, 72–75 (2012).
14. Freedman, S. J. & Clauser, J. F. Experimental test of local hidden-variable theories. *Phys. Rev. Lett.* **28**, 938–941 (1972).
15. Kwiat, P. G. & Eberhard, P. H. Steinberg, A. M. & Chiao, R. Y. Proposal for a loophole-free Bell inequality experiment. *Phys. Rev. A* **49**, 3209–3220 (1994).
16. Rosenfeld, W. *et al.* Towards a loophole-free test of Bell's inequality with entangled pairs of neutral atoms. *Adv. Sci. Lett.* **2**, 469–474 (2009).
17. Aspect, A., Dalibard, J. & Roger, G. Experimental test of Bell's inequalities using time-varying analyzers. *Phys. Rev. Lett.* **49**, 1804–1807 (1982).
18. Weihs, G., Jennewein, T., Simon, C., Weinfurter, H. & Zeilinger, A. Violation of Bell's inequality under strict Einstein locality conditions. *Phys. Rev. Lett.* **81**, 5039–5043 (1998).
19. Scheidl, T. *et al.* Violation of local realism with freedom of choice. *Proc. Natl Acad. Sci. USA* **107**, 19708–19713 (2010).
20. Merali, Z. Quantum mechanics braces for the ultimate test. *Science* **331**, 1380–1382 (2011).
21. Smith, D. H. *et al.* Conclusive quantum steering with superconducting transition-edge sensors. *Nature Commun.* **3**, 625–631 (2012).
22. Bennet, A. J. *et al.* Arbitrarily loss-tolerant Einstein-Podolsky-Rosen steering allowing a demonstration over 1 km of optical fiber with no detection loophole. *Phys. Rev. X* **2**(3), 031003 (2012).
23. Wittmann, B. *et al.* Loophole-free Einstein-Podolsky-Rosen experiment via quantum steering. *N. J. Phys.* **14**, 053030 (2012).
24. Clauser, J. F. & Horne, M. A. Experimental consequences of objective local theories. *Phys. Rev. D* **10**, 526–535 (1974).
25. Brunner, N., Gisin, N., Scarani, V. & Simon, C. Detection loophole in asymmetric Bell experiments. *Phys. Rev. Lett.* **98**, 220403 (2007).
26. Vértesi, T., Pironio, S. & Brunner, N. Closing the detection loophole in Bell experiments using qudits. *Phys. Rev. Lett.* **104**, 060401 (2010).
27. Clauser, J. F., Horne, M. A., Shimony, A. & Holt, R. A. Proposed experiment to test local hidden-variable theories. *Phys. Rev. Lett.* **23**, 880–884 (1969).
28. Kim, T., Fiorentino, M. & Wong, F. N. C. Phase-stable source of polarization-entangled photons using a polarization Sagnac interferometer. *Phys. Rev. A* **73**, 012316 (2006).
29. Drung, D. *et al.* Highly sensitive and easy-to-use SQUID sensors. *IEEE Trans. Appl. Supercond.* **17**, 699–704 (2007).

Acknowledgements We acknowledge M. Schmidt of Physikalisch-Technische Bundesanstalt in Berlin, Germany, for assistance with setting up the TES-SQUID system. This work was supported by the ERC (Advanced Grant number QIT4QAD 227844), the Austrian Science Fund (FWF) under projects SFB F4008 and CoQuS, the grant Q-ESSENCE (number 248095), QAP (number 15848), the Marie Curie Research Training Network EMALI (number MRTN-CT-2006-035369) and the John Templeton Foundation. This work was also supported by the NIST Quantum Information Science Initiative (QISI), an agency of the US Government.

Author Contributions M.G. designed and carried out the experiment, and analysed data. A.M. designed and carried out the experiment. S.R. provided theoretical analysis, designed and carried out the experiment, and analysed data. B.W. designed and carried out the experiment. J.K. provided theoretical analysis, and analysed data. J.B., A.L., B.C., T.G. and S.W.N. provided experimental and conceptual assistance. R.U. designed the experiment and provided experimental, organizational and conceptual assistance. A.Z. conceived the research and guided the experiment. All authors wrote the manuscript.

Author Information Reprints and permissions information is available at www.nature.com/reprints. The authors declare no competing financial interests. Readers are welcome to comment on the online version of the paper. Correspondence and requests for materials should be addressed to M.G. (marissa.giustina@univie.ac.at) or A.Z. (anton.zeilinger@univie.ac.at).

Formation of a topological non-Fermi liquid in MnSi

R. Ritz¹, M. Halder¹, M. Wagner¹, C. Franz¹, A. Bauer¹ & C. Pfleiderer¹

Fermi liquid theory provides a remarkably powerful framework for the description of the conduction electrons in metals and their ordering phenomena, such as superconductivity, ferromagnetism, and spin- and charge-density-wave order. A different class of ordering phenomena of great interest concerns spin configurations that are topologically protected, that is, their topology can be destroyed only by forcing the average magnetization locally to zero¹. Examples of such configurations are hedgehogs (points at which all spins are either pointing inwards or outwards) and vortices. A central question concerns the nature of the metallic state in the presence of such topologically distinct spin textures. Here we report a high-pressure study of the metallic state at the border of the skyrmion lattice in MnSi, which represents a new form of magnetic order composed of topologically non-trivial vortices². When long-range magnetic order is suppressed under pressure, the key characteristic of the skyrmion lattice—that is, the topological Hall signal due to the emergent magnetic flux associated with the topological winding—is unaffected in sign or magnitude and becomes an important characteristic of the metallic state. The regime of the topological Hall signal in temperature, pressure and magnetic field coincides thereby with the exceptionally extended regime of a pronounced non-Fermi-liquid resistivity^{3,30}. The observation of this topological Hall signal in the regime of the NFL resistivity suggests empirically that spin correlations with non-trivial topological character may drive a breakdown of Fermi liquid theory in pure metals.

To address the nature of the metallic state at the border of long-range topological order, we have selected the B20 compound MnSi. At zero pressure, $p = 0$, MnSi undergoes a fluctuation-induced first-order transition to helimagnetic order at $T_c = 29.5$ K (ref. 4). The helimagnetism originates in a hierarchy of three energy scales, comprising ferromagnetic exchange on the strongest scale, Dzyaloshinsky–Moriya interactions on an intermediate scale and higher-order spin–orbit coupling on the weakest scale⁵. As a function of magnetic field, B , conical order appears for $B > B_{c1} \approx 0.1$ T, and this is followed by a spin-polarized state for $B > B_{c2} \approx 0.6$ T. A phase pocket in the vicinity of T_c , known as the A-phase, supports the skyrmion lattice². The magnetic phase diagram of MnSi including the skyrmion lattice is thereby generic for all helimagnetic B20 compounds, regardless whether they are high-purity metals^{2,7}, semiconductors^{6,8} or insulators^{9,10}.

As a function of pressure, the helimagnetic transition in MnSi vanishes above $p_c \approx 14.6$ kbar without quantum criticality^{11–13}. Yet the resistivity changes from the T^2 dependence of a Fermi liquid to the $T^{3/2}$ dependence of a non-Fermi liquid (NFL) when p exceeds p_c . The exceptionally wide NFL range^{3,30} and the lack of sample dependence of the $T^{3/2}$ coefficient contrast with the excellent quantitative description of MnSi as a weak itinerant magnet¹⁴, suggesting that the cause of the NFL behaviour may be an intrinsic mechanism mimicking the effects of disorder and glassiness. This notion is supported by neutron scattering, NMR and muon spin resonance measurements, suggesting partial magnetic order on timescales between 10^{-10} s and 10^{-11} s (refs 11, 13). In turn, several theoretical studies^{15–17} have explored a proliferation of topological spin textures as the cause of the partial order, with a possible link to the NFL resistivity¹⁸. However,

until now, evidence for topologically non-trivial spin textures in the NFL regime as well as a link between such textures and the NFL behaviour has not been reported.

A unique experimental probe of the topology of magnetically ordered states is the Hall effect, which reflects the Berry phases developed by the electrons as they follow the spin orientation of the magnetic structure. The consequences of these Berry phases may be viewed in terms of an emergent magnetic field with two limiting types of behaviour¹⁹. For variations on atomic scales, the emergent field acts essentially in reciprocal space, giving rise to dissipationless Hall currents; this is referred to as the intrinsic anomalous Hall effect. In contrast, for smooth variations on length scales much larger than the Fermi wavelength, the emergent field acts similarly to a real magnetic field, giving rise to a topological Hall signal. Experimentally, these two limits may be readily distinguished in terms of their dependence on temperature and magnetization. Namely, the Hall resistivity associated with the intrinsic anomalous Hall contribution scales with the square of the longitudinal resistivity, ρ_{xx} ². Therefore, in ‘good’ metals, where ρ_{xx} rapidly decreases with temperature, the intrinsic anomalous contribution to ρ_{xy} also decreases with decreasing temperature. This is different from the topological contribution to ρ_{xy} , which increases rapidly with decreasing temperature, owing to the increase in the spin polarization and a reduction in spin-flip scattering¹⁹.

At ambient pressure, the Hall effect in MnSi is dominated by the sum of a normal contribution and an intrinsic anomalous contribution²⁰. In addition, a topological Hall signal has been observed in the skyrmion lattice phase^{19,21}. Moreover, a giant topological Hall signal exists for pressures between 6 and 12 kbar (ref. 22). However, that study²² failed to connect the giant topological Hall signal experimentally with the skyrmion lattice phase at ambient pressure and the NFL behaviour at high pressure. In addition, the size and field range of the Hall signal seemed anomalously large and at odds with the behaviour expected at ambient pressure.

To search for a link between the skyrmion lattice and the NFL resistivity, and to resolve the origin of the giant topological Hall signal reported in ref. 22, we performed an extensive high-pressure study exploring the roles of sample purity, pressure transmitter, cooling procedure and sample orientation. To this end, we assembled eight pressure cells covering nearly 40 pressure points (details of the experimental methods are reported in ref. 19 and Supplementary Information). As an important first step in studying the complex phase diagram near p_c , we demonstrated that the giant topological Hall signal at low pressures reported in ref. 22 is connected to the skyrmion lattice phase at $p = 0$. We found that the large size of the signal is intrinsic, and that the large field range is most probably due to low sample purity and inhomogeneous pressure conditions.

Here we report that the topological Hall signal of the skyrmion lattice evolves into a prominent characteristic of the entire NFL regime for pressures up to 18.1 kbar, the highest pressure we investigated, which is much greater than p_c . Our conclusions are based on the sign and size of the topological Hall signal and the observation of clear boundaries of this signal (Fig. 1a, b) that reproduce the boundaries of the NFL behaviour of ρ_{xx} as a function of pressure, magnetic field and temperature^{3,30}. First, for pressures exceeding $p^* \approx 12$ kbar there is

¹Physik Department E21, Technische Universität München, D-85748 Garching, Germany.

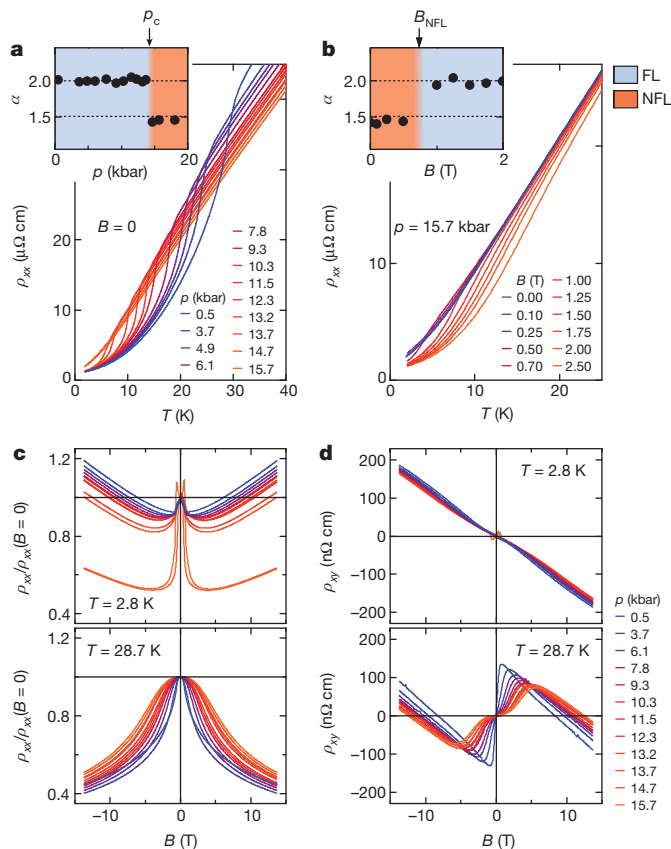


Figure 1 | Temperature and field dependence of the resistivity, ρ_{xx} and Hall resistivity, ρ_{xy} , of MnSi over a wide range. Data shown here were measured in pressure cell pc8 (see also ref. 19 and Supplementary Information). **a**, ρ_{xx} at various pressures (see also ref. 29). Inset, exponent α inferred from ρ_{xx} (see also refs 3, 30). **b**, ρ_{xx} at various fields for $p = 15.7$ kbar. Inset, exponent α at $p = 15.7$ kbar. **c**, ρ_{xx} at 2.8 K and 28.7 K up to 15.7 kbar. **d**, ρ_{xy} up to 15.7 kbar. At 28.7 K a strong knee-shaped intrinsic anomalous Hall contribution emerges; that is, an additional shoulder emerges on top of the intrinsic anomalous Hall contribution that merges with the itinerant metamagnetism above p_c and at low temperatures. FL, Fermi liquid; NFL, non-Fermi liquid.

a clear crossover with decreasing temperature from the regime at high temperatures to a NFL resistivity at $T^* \approx 12$ K, and ρ_{xx} settles into a stable $T^{3/2}$ NFL dependence at temperatures below ~ 8 K. In fact, for what follows below it is essential to emphasize that for $T_c \lesssim T^*$, the crossover and associated NFL behaviour emerges between T_c and $\sim T^*$ (ref. 3; below T_c , Fermi liquid behaviour is observed). Second, as mentioned above, the dependence of ρ_{xx} on T , $\rho_{xx}(T) \propto T^\alpha$, changes abruptly at p_c from a Fermi liquid form ($\alpha = 2$), to the NFL form ($\alpha = 3/2$) (Fig. 1a, inset). Third, for $p > p_c$ the NFL behaviour returns abruptly as a function of field to Fermi liquid behaviour at a value, B_{NFL} , that coincides with the itinerant metamagnetic transition, at B_m (Fig. 1b, inset; we refrain here and in Fig. 2b from showing exponents in the centre of the crossover very close to B_{NFL}).

To be able to present our main observations further below, which requires distinguishing topological contributions to the Hall signal from those that are anomalous, we show in Fig. 1c, d our magnetotransport data over a large field range, -14 to 14 T. At 2.8 K and at low pressures, ρ_{xx} drops by $\sim 10\%$ at B_{c2} , and this is followed by a gradual increase towards high fields (Fig. 1c, upper panel). Above T_c , this decrease in ρ_{xx} broadens and shifts to higher fields (Fig. 1c, lower panel). For $p > p_c$, ρ_{xx} displays a similar decrease at B_m (the itinerant metamagnetic transition) with a temperature dependence for B_m that is empirically similar to what is seen above T_c for low pressures, that is, B_m shifts to higher values. This is consistent with spin scattering processes in the NFL regime that are quenched above B_m . Furthermore,

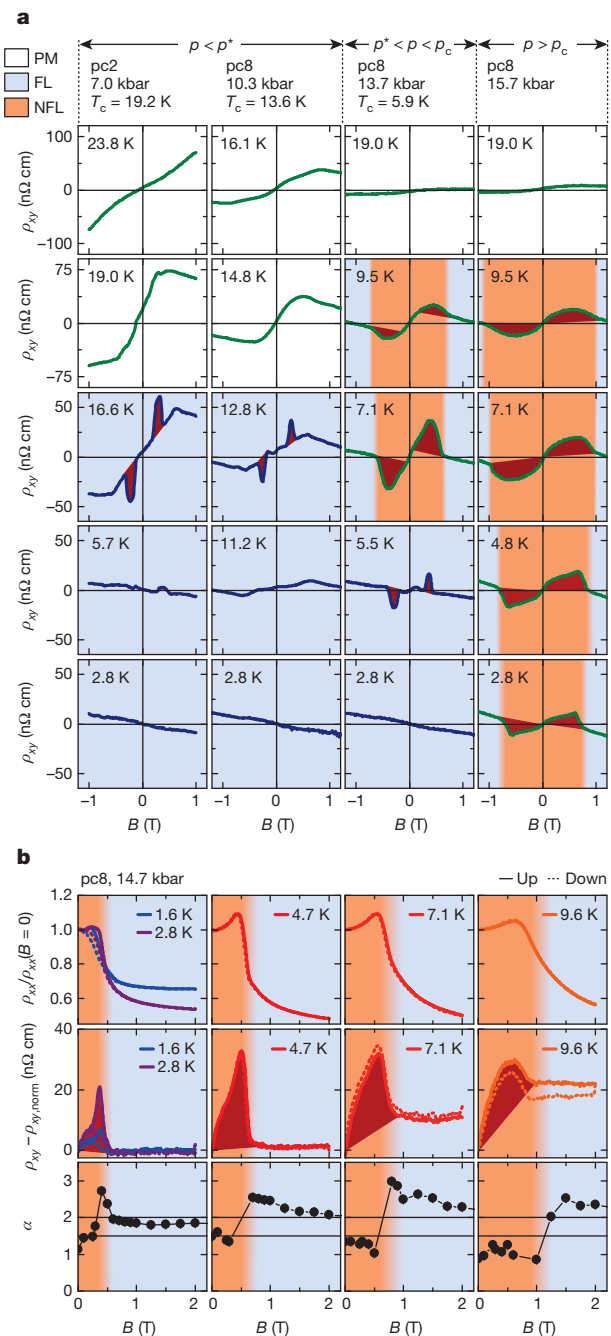


Figure 2 | Hall resistivity, ρ_{xy} , and magnetoresistance, ρ_{xx} , for low fields at various pressures. **a**, ρ_{xy} for a wide range of pressures and temperatures. **b**, Comparison of the magnetoresistance, ρ_{xx} ; the Hall resistivity after subtraction of normal contributions, $\rho_{xy} - \rho_{xy,normal}$; and the exponent of the temperature dependence of the electrical resistivity, α , at various temperatures, for a pressure greater than p_c . With increasing field, α changes from NFL behaviour ($\alpha \approx 3/2$) to Fermi liquid behaviour ($\alpha \approx 2$) at the same field value, above which the topological Hall contribution has vanished. PM, paramagnet; pc2 and pc8 refer to the pressure cells studied¹⁹ (Supplementary Information).

the Hall signal ρ_{xy} at 2.8 K is essentially featureless and linear over the range -14 to 14 T for all pressures studied (Fig. 1d, upper panel), with the exception of the topological contributions at low fields, which we address below. At higher temperatures, a ‘knee-shaped’ anomalous Hall contribution develops in addition to the signal seen at 2.8 K (Fig. 1d, lower panel). This includes, at higher pressures, the emergence of an additional ‘shoulder’ and a related maximum at a field B_s , which reaches several tesla and coincides with the itinerant metamagnetism at B_m at low temperatures and high pressures, as inferred from

the a.c. susceptibility^{19,23}. A discussion of the associated temperature dependences is presented in Supplementary Information. Hence, for large fields ρ_{xy} is dominated by the sum of a normal contribution and an intrinsic anomalous contribution²⁰, of which the latter displays an additional shoulder (see also Fig. 3). The shoulder in ρ_{xy} can therefore be accounted for neither by variations in ρ_{xx} (entering the Hall conductivity $\sigma_{xy} = -\rho_{xy}/(\rho_{xy}^2 + \rho_{xx}^2)$, which is proportional to the

intrinsic anomalous Hall effect) nor by the magnetization, the field dependence of which is qualitatively similar above T_c for all pressures, with no signs of a shoulder^{19,23}. This suggests a more subtle connection between the shoulder in ρ_{xy} and the itinerant metamagnetism, but this connection is not important for the conclusions of our study.

Typical data highlighting the topological contributions to the Hall signal for samples with high residual resistivity ratios (RRRs) are summarized in Fig. 2. Qualitatively similar data for samples with low RRRs are presented in Supplementary Information. To illustrate the relationship between the topological Hall signal and the nature of the metallic state inferred from the temperature dependences of ρ_{xx} , we use the following colour scheme: white for the paramagnetic regime, sky blue for the Fermi liquid and orange for the NFL. For low pressures, a topological Hall signal arises exclusively in the A-phase¹⁹ (red shading). It is important to emphasize that the change in slope of ρ_{xy} in this regime (for example at 0.5 T for 7 kbar and 16.6 K) is due to the conical-to-ferromagnetic transition at B_{c2} and is therefore completely unrelated to the itinerant metamagnetism at B_S at high pressures and above T_c .

As T_c decreases below $T^* \approx 12$ K, the topological signal is also present above T_c up to $\sim T^*$ and over a wide field range where the magnitude and sign of the signal are unchanged compared with the data below T_c (see data for 13.7 kbar in Fig. 2a). Because the shoulder in the itinerant metamagnetism data at these temperatures and pressures is located at a field strength of around several teslas (well outside the field range shown here; see Supplementary Fig. 4), this unambiguously connects the topological Hall signal in the A-phase with the NFL resistivity. At pressures greater than p_c , the topological contribution is observed across the entire NFL regime. We have confirmed this observation in several samples of differing purity, where the topological Hall contribution tends to be larger and broadened for these samples with lower RRRs. We thereby note that, regardless of the RRR, there are no hints of metastable behaviour such as that observed under field cooling at low pressures (see Supplementary Fig. 6 and fig. 7 in ref. 19).

To justify the positioning of regime boundaries in Fig. 2a, we show in Fig. 2b, for $p = 14.7$ kbar $> p_c$, a typical comparison of ρ_{xx} with the Hall resistivity after subtracting the normal Hall contributions, $\rho_{xy} - \rho_{xy, \text{norm}}$ (where $\rho_{xy, \text{norm}}$ was inferred from data above B_{c2}), and with the exponent, α , of the temperature dependence of the resistivity at selected fixed fields. As a function of field, the following characteristic features coincide at B_{NFL} : the onset of the decrease in the magnetoresistance suggestive of a field-induced suppression of a magnetic scattering mechanism, the disappearance of the topological Hall contribution (Fig. 2b, red shading) and the change from Fermi liquid to NFL resistivity. We can therefore confirm that the field dependence of ρ_{xx} neither qualitatively nor quantitatively causes variations in the intrinsic anomalous Hall contribution ($\sigma_{xy} \approx -\rho_{xy}/\rho_{xx}^2$) that may be mistaken for a topological Hall signal. Thus, the topological Hall signal and the NFL resistivity coincide as functions of T , B and p .

In Fig. 3, we show the relevant regions of the pressure–temperature phase diagram and typical magnetic phase diagrams. For zero field, NFL behaviour emerges below T^* and above T_c as well as below T^* for pressures greater than p_c . The NFL behaviour is accompanied by a topological Hall signal that is present even for very low fields, as marked by NFL + TH in each panel. For pressures below $p^* \approx 12$ kbar, the magnetic phase diagram remains qualitatively unchanged as compared with ambient pressure (Fig. 3b), and the topological Hall signal is enhanced as reported in ref. 19. Qualitatively new behaviour emerges for $p > p^*$, where the topological Hall contribution survives above T_c and p_c . This is illustrated in Fig. 3c, d, e, where the boundaries of the regime of the NFL resistivity are shown as a function of T , B and p .

The sign and the magnitude of the topological Hall signal arises from a combination of the strength of the emergent field, given by the topological winding number for the magnetic unit cell; the (local) spin polarization of the conduction electrons; and an average over individual bands taking into account different scattering processes¹⁹. The

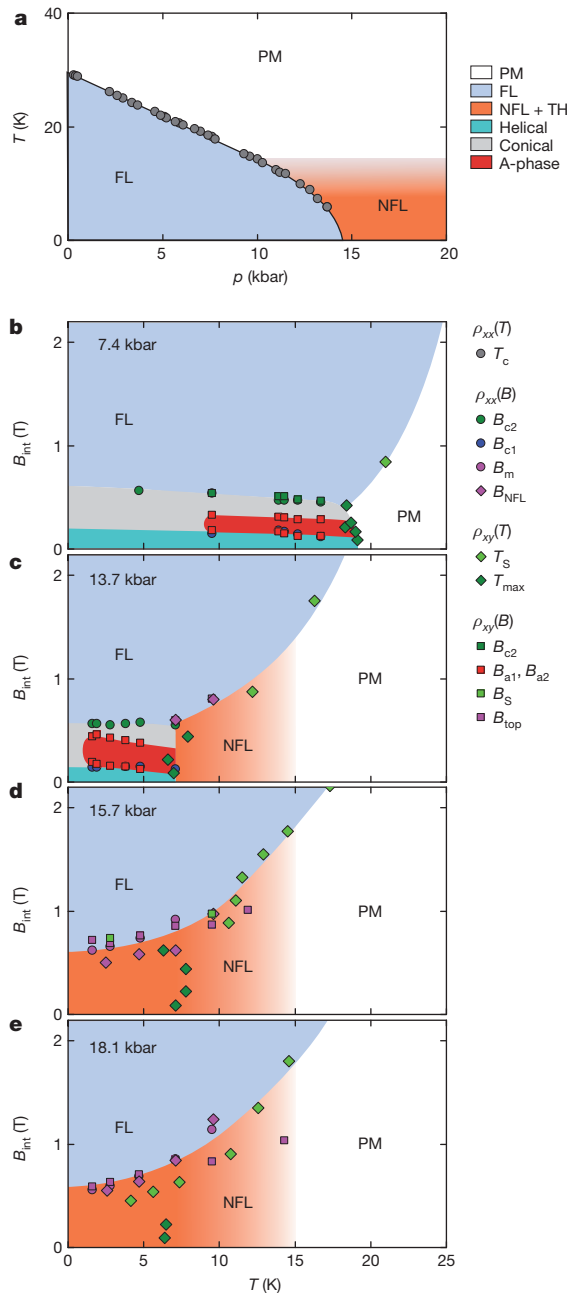


Figure 3 | Phase diagrams of MnSi. **a**, Temperature–pressure phase diagram. NFL + TH refers to the regime of an NFL resistivity in which a small field establishes a topological Hall (TH) signal. **b**, Magnetic phase diagram at $p = 7.4$ kbar, displaying a strongly enhanced topological Hall signal in the A-phase as reported in ref. 19. **c**, Magnetic phase diagram at T_c and $p = 13.7$ kbar. The transition at T_c is first order, and the onset of NFL resistivity occurs at a temperature above T_c . A topological Hall contribution is observed in the A-phase and the NFL regime above T_c . **d**, **e**, Magnetic phase diagrams at $p = 15.7$ and 18.1 kbar, above p_c . The field and temperature range of the topological Hall signal extends over the entire field and temperature range of the $T^{3/2}$ NFL resistivity. See Supplementary Information for illustrated definitions of all characteristic fields and temperatures.

observation of neutron scattering intensity above p_c at a wavelength which corresponds to that of the helical state at low pressures^{11,24} implies that the continuous evolution of the topological Hall signal from the A-phase to the NFL regime must be closely connected to an unchanged topological winding number. As a caveat, neutron intensity is observed only in a small region of the NFL regime, whereas the topological Hall signal we report here is seen everywhere. Thus, the topological winding must be insensitive against fluctuations above p_c , at least on timescales relevant to the Hall effect. As a consequence, any of the following scenarios (or combinations thereof) can arise in the high-pressure state of MnSi: spontaneous formation of randomly oriented skyrmions at $B = 0$ that are stratified in a magnetic field; formation of skyrmions even at very low fields; strong fluctuations between helical modulations and skyrmionic textures. It therefore seems likely that strong quantum fluctuations promote this state.

Our study identifies a topological Hall signal as a prominent characteristic of the NFL regime of MnSi. The sign and magnitude of the Hall signal indicate that the topological winding of skyrmions as seen at $p = 0$ is the long-sought intrinsic mechanism causing the $T^{3/2}$ NFL dependence. This dependence is characteristic of a strong divergence of the quasiparticle self-energy as $T \rightarrow 0$, which suggests a generic breakdown of Fermi liquid theory due to spin correlations with topologically non-trivial character. Notably, several theoretical studies suggest various mechanisms leading to the formation of non-trivial spin textures at the zero-temperature border of itinerant ferromagnetism for different reasons^{25,26}. In fact, experimentally a $T^{3/2}$ NFL resistivity has also been observed near putative ferromagnetic quantum phase transitions, for example in ZrZn_2 ²⁷ and Ni_3Al . However, if this is related to complex spin textures, their average topological winding would be degenerate and no topological Hall effect would therefore be expected. Hence, the topological character of the NFL regime we report here for MnSi may turn out to be the first example of a more general phenomenon, in which the full suppression of the magnetization is generically preceded by the formation of complex spin textures. For the case of MnSi, the peculiar stability of the NFL behaviour may thereby be inherited from the chiral character of the Dzyaloshinsky–Moriya spin–orbit interaction.

METHODS SUMMARY

Sample preparation. Single crystals of MnSi were grown by optical float zoning under ultrahigh-vacuum-compatible conditions²⁸. The specific heat, susceptibility and resistivity of small pieces taken from these single crystals were in excellent agreement with established results. Samples with different RRRs were studied as summarized in Supplementary Information. Samples for the measurements reported here were oriented by Laue X-ray diffraction, cut with a wire saw and carefully polished to size. Current leads were soldered to the small faces of the sample, and platinum wires for the voltage pick-up were spot-welded onto the surface of the sample.

Magnetotransport under pressure. The Hall resistivity and longitudinal resistivity were measured simultaneously using a standard six-terminal phase-sensitive detection system. The voltage signals were amplified with impedance-matching transformers to optimize the signal-to-noise ratio. Low excitation frequencies and excitation currents were applied to minimize parasitic signal pick-up. High hydrostatic pressures were generated with a Cu:Be clamp cell using various different pressure transmitters as described in detail in ref. 19 and Supplementary Information. The sample was suspended by the current and voltage leads, using a Teflon platform to fix the location of the wires and thereby the sample orientation. Data were recorded at temperatures down to 1.5 K under magnetic fields in the range -14 to 14 T, using a conventional superconducting magnet system. Further details may be found in ref. 19 and Supplementary Information.

Received 3 December 2012; accepted 15 February 2013.

Published online 1 May 2013.

1. Chaikin, P. & Lubensky, T. *Principles of Condensed Matter Physics* Chs 9, 10 (Cambridge Univ. Press, 1995).
2. Mühlbauer, S. *et al.* Skyrmion lattice in a chiral magnet. *Science* **323**, 915–919 (2009).

3. Pfleiderer, C., Julian, S. R. & Lonzarich, G. G. Non-Fermi liquid nature of the normal state of itinerant-electron ferromagnets. *Nature* **414**, 427–430 (2001).
4. Janoschek, M. *et al.* Fluctuation-induced first-order phase transition in Dzyaloshinskii–Moriya helimagnets. *Phys. Rev. B* (in the press); preprint available at <http://arxiv.org/abs/1205.4780> (2012).
5. Landau, L. D. & Lifshitz, E. M. *Course of Theoretical Physics* Vol. 8, Sec. 52 (Pergamon, 1980).
6. Yu, X. Z. *et al.* Real-space observation of a two-dimensional skyrmion crystal. *Nature* **465**, 901–904 (2010).
7. Yu, X. Z. *et al.* Near room-temperature formation of a skyrmion crystal in thin-films of the helimagnet FeGe. *Nature Mater.* **10**, 106–109 (2011).
8. Münzer, W. *et al.* Skyrmion lattice in the doped semiconductor $\text{Fe}_{1-x}\text{Co}_x\text{Si}$. *Phys. Rev. B* **81**, 041203 (2010).
9. Seki, S., Yu, X., Ishiwata, S. & Tokura, Y. Observation of skyrmions in a multiferroic material. *Science* **336**, 198–201 (2012).
10. Adams, T. *et al.* Long-wavelength helimagnetic order and skyrmion lattice phase in Cu_2OSeO_3 . *Phys. Rev. Lett.* **108**, 237204 (2012).
11. Pfleiderer, C. *et al.* Partial order in the non-Fermi liquid phase of MnSi. *Nature* **427**, 227–231 (2004).
12. Pfleiderer, C., Böni, P., Keller, T., Rößler, U. K. & Rosch, A. Non-Fermi liquid metal without quantum criticality. *Science* **316**, 1871–1874 (2007).
13. Uemura, Y. J. *et al.* Phase separation and suppression of critical dynamics at quantum transitions of itinerant magnets: MnSi and $(\text{Sr}_{1-x}\text{Ca}_x)\text{RuO}_3$. *Nature Phys.* **3**, 29–35 (2007).
14. Lonzarich, G. G. & Taillefer, L. Effect of spin fluctuations on the magnetic equation of state of ferromagnetic or nearly ferromagnetic metals. *J. Phys. C* **18**, 4339–4371 (1985).
15. Tewari, S., Belitz, D. & Kirkpatrick, T. R. Blue quantum fog: chiral condensation in quantum helimagnets. *Phys. Rev. Lett.* **96**, 047207 (2006).
16. Binz, B., Vishwanath, A. & Aji, V. Theory of the helical spin crystal: a candidate for the partially ordered state of MnSi. *Phys. Rev. Lett.* **96**, 207202 (2006).
17. Rößler, U. K., Bogdanov, A. N. & Pfleiderer, C. Spontaneous skyrmion ground states in magnetic metals. *Nature* **442**, 797–801 (2006).
18. Kirkpatrick, T. R. & Belitz, D. Columnar fluctuations as a source of non-Fermi-liquid behavior in weak metallic magnets. *Phys. Rev. Lett.* **104**, 256404 (2010).
19. Ritz, R. *et al.* Giant generic topological Hall resistivity in MnSi under pressure. *Phys. Rev. B* (submitted).
20. Lee, M., Onose, Y., Tokura, Y. & Ong, N. P. Hidden constant in the anomalous hall effect of high-purity magnet MnSi. *Phys. Rev. B* **75**, 172403 (2007).
21. Neubauer, A. *et al.* Topological Hall effect in the A phase of MnSi. *Phys. Rev. Lett.* **102**, 186602 (2009).
22. Lee, M., Kang, W., Onose, Y., Tokura, Y. & Ong, N. Unusual Hall effect anomaly in MnSi under pressure. *Phys. Rev. Lett.* **102**, 186601 (2009).
23. Thessieu, C., Pfleiderer, C., Stepanov, A. N. & Flouquet, J. Field dependence of the magnetic quantum phase transition in MnSi. *J. Phys. Condens. Matter* **9**, 6677–6687 (1997).
24. Pfleiderer, C., Reznik, D., Pintschovius, L. & Haug, J. Magnetic field and pressure dependence of small angle neutron scattering in MnSi. *Phys. Rev. Lett.* **99**, 156406 (2007).
25. Belitz, D. & Kirkpatrick, T. R. Fluctuation-driven quantum phase transitions in clean itinerant ferromagnets. *Phys. Rev. Lett.* **89**, 247202 (2002).
26. Conduit, G. J., Green, A. G. & Simons, B. D. Inhomogeneous phase formation on the border of itinerant ferromagnetism. *Phys. Rev. Lett.* **103**, 207201 (2009).
27. Smith, R. P. *et al.* Marginal breakdown of the Fermi-liquid state on the border of metallic ferromagnetism. *Nature* **455**, 1220–1223 (2008).
28. Neubauer, A. *et al.* Ultra-high vacuum compatible image furnace. *Rev. Sci. Instrum.* **82**, 013902 (2011).
29. Pfleiderer, C., McMullan, G. J., Julian, S. R. & Lonzarich, G. G. Magnetic quantum phase transition in MnSi under hydrostatic pressure. *Phys. Rev. B* **55**, 8330–8338 (1997).
30. Doiron-Leyraud, N. *et al.* Fermi-liquid breakdown in the paramagnetic phase of a pure metal. *Nature* **425**, 595–599 (2003).

Supplementary Information is available in the online version of the paper.

Acknowledgements We wish to thank P. Böni, K. Everschor, M. Garst, M. Janoschek, S. Mayr and A. Rosch for discussions and support. R.R., M.H., A.B., M.W. and C.F. acknowledge financial support through the TUM Graduate School. Financial support through DFG TRR80 and DFG FOR960 as well as ERC-AdG (291079 TOPFIT) are gratefully acknowledged.

Author Contributions R.R. and C.P. developed the experimental set-up; R.R. performed the transport measurements; M.H. and M.W. performed magnetization measurements; C.F. wrote the software for analysing the data; A.B. grew the single-crystal samples and characterized them; R.R. and C.P. analysed the experimental data; C.P. supervised the experimental work; C.P. proposed this study and wrote the manuscript; all authors discussed the data and commented on the manuscript.

Author Information Reprints and permissions information is available at www.nature.com/reprints. The authors declare no competing financial interests. Readers are welcome to comment on the online version of the paper. Correspondence and requests for materials should be addressed to R.R. (robert.ritz@frm2.tum.de) or C.P. (christian.pfleiderer@frm2.tum.de).

Future sea-level rise from Greenland's main outlet glaciers in a warming climate

Faezeh M. Nick^{1,2,3}, Andreas Vieli^{4,5}, Morten Langer Andersen⁶, Ian Joughin⁷, Antony Payne⁸, Tamsin L. Edwards⁸, Frank Pattyn¹ & Roderik S. W. van de Wal²

Over the past decade, ice loss from the Greenland Ice Sheet increased as a result of both increased surface melting and ice discharge to the ocean^{1,2}. The latter is controlled by the acceleration of ice flow and subsequent thinning of fast-flowing marine-terminating outlet glaciers³. Quantifying the future dynamic contribution of such glaciers to sea-level rise (SLR) remains a major challenge because outlet glacier dynamics are poorly understood⁴. Here we present a glacier flow model that includes a fully dynamic treatment of marine termini. We use this model to simulate behaviour of four major marine-terminating outlet glaciers, which collectively drain about 22 per cent of the Greenland Ice Sheet. Using atmospheric and oceanic forcing from a mid-range future warming scenario that predicts warming by 2.8 degrees Celsius by 2100, we project a contribution of 19 to 30 millimetres to SLR from these glaciers by 2200. This contribution is largely (80 per cent) dynamic in origin and is caused by several episodic retreats past overdeepenings in outlet glacier troughs. After initial increases, however, dynamic losses from these four outlets remain relatively constant and contribute to SLR individually at rates of about 0.01 to 0.06 millimetres per year. These rates correspond to ice fluxes that are less than twice those of the late 1990s, well below previous upper bounds⁵. For a more extreme future warming scenario (warming by 4.5 degrees Celsius by 2100), the projected losses increase by more than 50 per cent, producing a cumulative SLR of 29 to 49 millimetres by 2200.

Greenland's fast-flowing outlet glaciers respond sensitively and rapidly to atmospheric and oceanic perturbations^{3,6,7}. Such responses include ice-flow acceleration, glacier thinning and rapid retreat of outlet glacier termini in the west and east⁸, coincident with increases in air and regional ocean temperatures⁶. One of the largest retreats was observed on Jakobshavn Isbræ, an outlet glacier in west Greenland, and was followed by more than a doubling in flow speed and continued thinning⁹. The Helheim and Kangerdlugssuaq glaciers in southeast Greenland sped up and thinned substantially¹⁰, but both subsequently slowed modestly as their termini slightly re-advanced⁷. Collectively, these observations indicate a complex pattern with rapid changes that may be transient and not necessarily indicative of long-term trends or continued contributions to SLR. Petermann Glacier in north Greenland has been flowing steadily¹¹ and terminates in a relatively long (~50 km) and wide (~20 km) floating ice tongue, under which submarine melt occurs at a high rate¹². The break off of two substantial icebergs in August 2010 (~270 km²) and July 2012 (~120 km²) raised concerns about this glacier's stability but did not cause major flow acceleration¹³.

Various mechanisms related to atmospheric and oceanic forcing have been proposed to explain the recent behaviour of the major outlet glaciers, but large uncertainties in their relative importance remain^{14,15}. A warmer ocean can melt submarine ice and thereby cause the grounding

line to retreat, especially when subglacial melt water produces more vigorous buoyancy-driven circulation¹⁶. Persistent sea ice or ice mélange may exert a small resistive force that stabilizes retreat⁹ by limiting the calving and subsequent rotation of icebergs¹⁷. Higher air temperatures increase surface meltwater production; this melt water may accumulate in surface crevasses causing hydrofracturing, and thereby increase calving¹⁸ and reduce resistance at the lateral margins¹⁹, and may reach the glacier bed to increase basal lubrication²⁰. All these factors may lead to acceleration and subsequent thinning.

The complicated behaviour of narrow outlet glaciers, however, has not yet been fully captured by the ice-sheet models used to predict Greenland's contribution to future sea level. Most such models have insufficient spatial resolution to resolve the narrow outlet glacier channels and inadequately represent processes acting at the marine

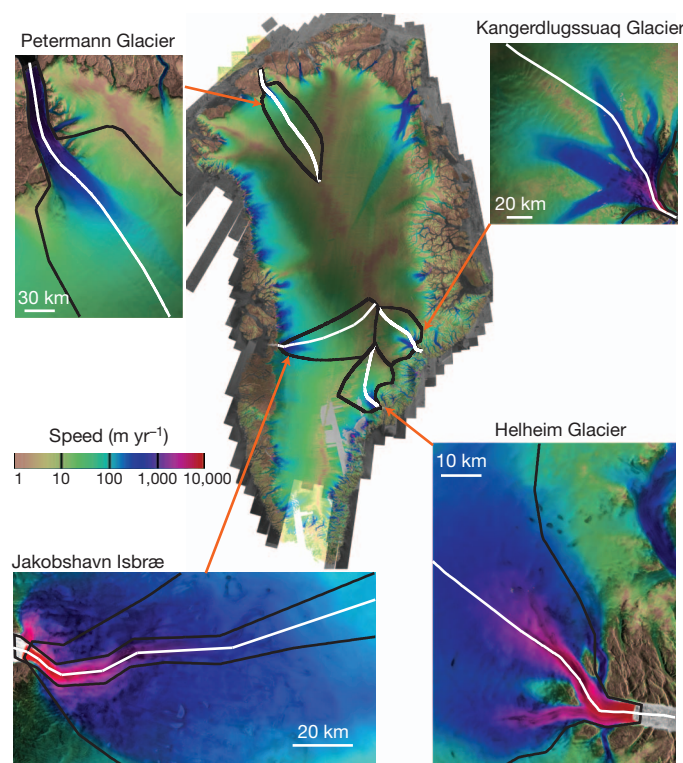


Figure 1 | Major Greenland outlet glaciers examined in this study. Catchments for glaciers in this study are highlighted on the velocity map of Greenland⁸. Jakobshavn Isbræ in the west, drains ~7.5% of the Greenland Ice Sheet area. Helheim and Kangerdlugssuaq Glacier in the southeast, drain about 3.9% and 4.2%, respectively. Petermann Glacier, in the north, drains ~6% of the ice sheet area.

¹Laboratoire de Glaciologie, Université Libre de Bruxelles, B-1050 Brussels, Belgium. ²Institute for Marine and Atmospheric research, Utrecht University, 3508 TA Utrecht, The Netherlands. ³Department of Geology, The University Centre in Svalbard, PO Box 156, NO-9171 Longyearbyen, Norway. ⁴Department of Geography, Durham University, Durham DH1 3LE, UK. ⁵Department of Geography, University of Zürich, CH-8057 Zürich, Switzerland. ⁶Geological Survey of Denmark and Greenland, DK-1350 Copenhagen, Denmark. ⁷Polar Science Center, Applied Physics Laboratory, University of Washington, Seattle, Washington 98108, USA. ⁸Bristol Glaciology Centre, University of Bristol, Bristol BS8 1SS, UK.

boundary, such as submarine melt and calving. Moreover, the basal topography for most outlet channels remains poorly resolved.

To overcome these obstacles and to help assess the impact of Greenland ice-sheet dynamics on SLR, we use a state-of-the-art ice-flow model designed for single outlet glaciers (Supplementary Information, section 2). Importantly, it includes a fully dynamic treatment of the marine boundary and allows the application of oceanic and atmospheric forcing processes, such as surface melt, ocean melt, sea-ice reduction and basal lubrication. We apply the model to four major outlet glaciers in Greenland: the Jakobshavn, Helheim, Kangerdlugssuaq and Petermann glaciers (Fig. 1).

In general, the model reasonably reproduces the observed changes such as terminus positions and velocities over the last decade (Supplementary Figs 3–6), and confirms the sensitivities to different forcing mechanisms indicated by observations. We find that Helheim and Kangerdlugssuaq largely respond to a reduction in sea ice and enhanced hydrofracturing due to surface melt, with little response to submarine melt or basal and lateral lubrication²¹. The dynamics of Jakobshavn, additional to reduction in sea ice and enhanced hydrofracturing, are also sensitive to forcing by submarine melt, owing to the high submarine melt rate²² and a more extensive ice–ocean interface when an ice tongue is present. As a result of weak lateral resistance from its thin, wide, floating ice tongue, the flow of Petermann at present seems insensitive to changes at the terminus. Instead, its dynamics tends to be dominated by submarine melt concentrated near the grounding line¹³.

Using a selection of tuning parameter sets that best reproduce the current observations, we ran the model to determine future behaviour until the year 2200 for a mid-range future warming scenario (A1B). The atmospheric and oceanic forcing for these runs were derived from the regional climate models, MAR and ECHAM5 GCM (Supplementary Information, section 1). For each glacier, we ran simulations with 50 parameter sets. Of these results, we present five parameterizations that sample the full range of retreat (Supplementary Table 2). To further examine the sensitivity of our sea-level projection to the chosen climate scenarios, we perform an additional set of runs for an upper-end future warming scenario²³ (RCP8.5).

Focusing first on the mid-range climate-warming scenario (A1B), our modelling predicts that under all parameter choices, all four glaciers will continue to retreat, thin and thereby lose mass (Fig. 2), albeit at variable rates. They collectively lose 30–47 Gt yr^{−1}, averaged over the twenty-first century, increasing slightly to 34–54 Gt yr^{−1} during

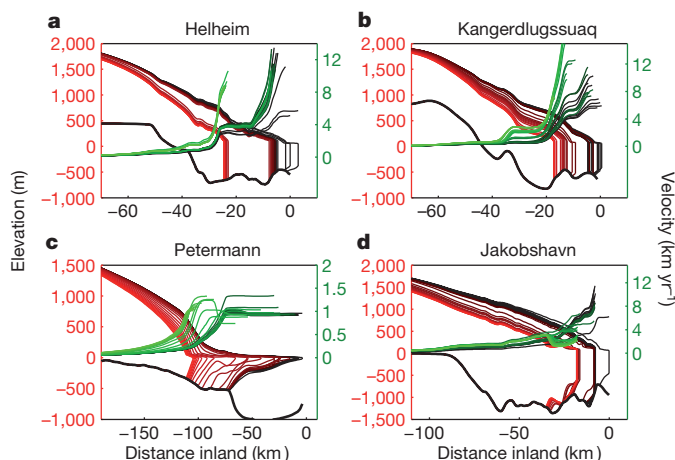


Figure 2 | Modelled evolution of surface elevation and velocity. Along-flow profiles of surface elevation (red lines) and velocity (green lines) of Helheim (a), Kangerdlugssuaq (b), Petermann (c) and Jakobshavn (d) glaciers for one of the high-mass-loss sets. The profiles are shown at 1-yr intervals during 2000–2010 and at 10-yr intervals during 2010–2200. The profiles are colour coded and range from black (2000) to red and green (2200), as appropriate.

the twenty-second century (Table 1). This is equivalent to a cumulative SLR of 8.5–13.1 mm by 2100, and 18.6–30.0 mm by 2200 (Fig. 3e).

Partitioning the mass loss into different components shows that most of the total mass loss (80%) from the four glaciers arises from dynamic effects that are related to retreat and increased discharge. The surface mass balance (SMB) accounts for the remaining 20% of the loss. Helheim and Kangerdlugssuaq gain in SMB owing to enhanced accumulation, relative to the average 2000-to-2010 SMB, implying that mass loss is entirely of dynamic origin (Fig. 3a, b). Because Jakobshavn and Petermann have larger ablation areas, their mass loss by melt is larger, especially in the twenty-second century. Whereas dynamically driven discharge dominates Jakobshavn's mass loss, Petermann loses mass almost entirely by surface melt from 2000 to 2100, and dynamic losses reach a similar magnitude only at the end of the twenty-second century when submarine melt is high (Fig. 3c, d), forcing substantial grounding line retreat (Supplementary Fig. 7c). We note that for all our model runs, the SMB does not include the secondary contributions from enhanced ablation due to surface lowering induced by dynamic thinning; including this effect would further enhance melt contributions to SLR, especially in the twenty-second century.

Dynamic losses are caused by outlet glacier terminus retreat and the related enhanced discharge (Fig. 2 and Supplementary Fig. 12), which take place as an episodic series of rapid retreats. These step changes are closely related to channel geometry and occur, in particular, after an ice front retreats from a basal high through an overdeepening²¹. Our results indicate that for different parameter choices, episodes of rapid retreat occur at different times but at the same locations (Supplementary Fig. 7). Such geometry-controlled retreat behaviour is well known from tidewater glaciers and is related to the strong increase in ice flux with water depth²⁴. In these cases, retreat into deeper water and the accompanying acceleration produce pulses of mass loss of several tens of gigatonnes per year, but such pulses are often short lived. Subsequent decelerations in retreat and mass loss mostly coincide with a decrease in water depth as the glacier retreats or re-advances to a new or, respectively, previous bathymetric high. In late stages of retreat on Helheim and Kangerdlugssuaq, channel narrowing (Supplementary Fig. 8) can temporarily slow down the terminus on an upward

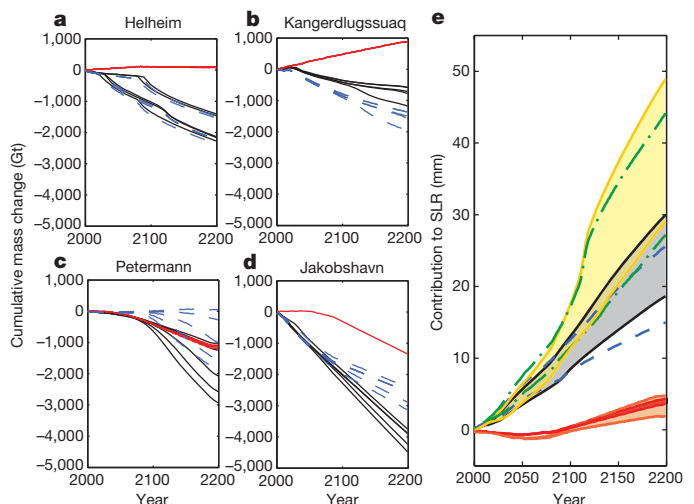


Figure 3 | Projected SLR from the four major outlet glaciers. Modelled cumulative total mass change (black), cumulative SMB anomalies (red) and dynamic mass change anomalies (dashed blue) at Helheim (a), Kangerdlugssuaq (b), Petermann (c) and Jakobshavn (d) glaciers for selected forcing parameter sets. e, Predicted cumulative minimum and maximum total SLR contributions from four major outlet glaciers forced by A1B (black) and RCP8.5 (yellow) future warming scenarios. Also, shown are the contributions from SMB for A1B (red) and RCP8.5 (orange) and from dynamic retreat and thinning for A1B (dashed blue) and RCP8.5 (dash-dot green). Shaded areas cover the range of projected SLR for all selected forcing parameter sets.

Table 1 | Total mass loss and SLR by the end of the twenty-first and twenty-second centuries for two climate scenarios

	Initial flux (km ³ yr ⁻¹)	Scenario	2000–2100				2000–2200			
			ML (Gt)	ML_rate (Gt yr ⁻¹)	SLR (mm)	Flux (km ³ yr ⁻¹)	ML (Gt)	ML_rate (Gt yr ⁻¹)	SLR (mm)	Flux (km ³ yr ⁻¹)
Helheim	25	A1B	476–1,348	4.8–13.5	1.3–3.7	28.5–38	1,403–2,269	7.0–11.4	3.9–6.3	30.5–36
		RCP8.5	442–1,142	4.4–11.4	1.2–3.2	31–38	1,667–2,900	8.4–14.6	4.6–8.0	34–38
Kangerdlugssuaq	28	A1B	351–470	3.5–4.7	1.0–1.3	36–36.5	575–1,178	2.9–5.9	1.6–3.3	34.5–35.5
		RCP8.5	572–832	5.7–8.3	1.6–2.3	34–35.5	1,321–4,028	6.6–20.2	3.6–11.1	33–46.5
Petermann	12	A1B	368–639	3.7–6.4	1.0–1.8	11.5–14	1,022–2,927	5.1–14.7	2.8–8.1	11–22
		RCP8.5	615–968	6.1–9.7	1.7–2.7	11.5–15.5	2,394–3,551	12–17.8	6.6–9.8	16–23
Jakobshavn	22	A1B	1,870–2,281	18.7–22.8	5.2–6.3	49–52.5	3,750–4,476	18.8–22.5	10.4–12.4	48–52
		RCP8.5	2,471–3,407	24.7–34.1	6.8–9.4	48.5–58.5	5,131–7,227	25.8–36.3	14.2–20	49.5–61
Total	87	A1B	3,065–4,739	30.6–47.4	8.5–13.1	125–141	6,750–10,850	33.9–54.5	18.6–30	124–145.5
		RCP8.5	4,100–6,349	41–63.5	11.3–17.5	125–147.5	10,513–17,706	52.8–89	29–49	132–168.5

Initial flux, initial pre-acceleration ice discharge; ML, estimated range of mass loss in gigatonnes (10¹² kg); ML_rate, average mass loss rate per year; Flux, average ice discharge from the grounding line.

bed slope (Fig. 2a, b), similar to modelled past ice-stream behaviour²⁵. Our results show that over the full range of parameters used for each glacier, and despite episodic and short-lived peaks in discharge, century-averaged ice discharge does not exceed 1.7 times the pre-acceleration values of the late 1990s (Table 1). Indeed, the positive trend in dynamic mass loss plateaus after an initial increase in the early twenty-first century. The subsequent slight increase in the twenty-second century is mainly due to the delayed flux response to warming contributed from Petermann (Fig. 3c).

This apparent upper limit in long-term ice flux is crucial to the interpretation of the recent drastic acceleration of outlet glaciers in Greenland. It implies that ice fluxes do not continue to increase indefinitely even after the modelled glaciers have undergone multiple episodic retreats. This indicates that current short-term acceleration trends cannot be extrapolated into the future.

For the more extreme warming scenario (RCP8.5), mass loss increases by more than 50% (Table 1), which is equivalent to a cumulative SLR of 11.3–17.5 mm by 2100, and 29–49 mm by 2200 (Fig. 3e). Although all four glaciers retreat faster and farther inland compared with the A1B scenario, the general dynamic behaviour, responsible processes and partitioning between SMB and dynamic mass loss are similar (Supplementary Information, section 6). Helheim and Kangerdlugssuaq retreat behind the narrow parts of their respective valleys and into deeper, wider areas (Supplementary Figs 8 and 10), resulting in faster flow. This retreat continues until their glacier termini reach shallow water, leading to a reduction in discharge and calving rate. The Jakobshavn grounding line retreats farther back into its deep trough and forms a longer ice shelf, slowing down its retreat. Petermann, however, does not show much higher mass loss and retreat, because its grounding line reaches the shallow region also in the A1B scenario simulations. Therefore, the sensitivity of our projection to a warmer climate is largely controlled by the fjord geometry, width and depth, which tend to be unique to each glacier, perhaps explaining the large degree of observed variability occurring under similar climate forcings⁸.

The only other comprehensive modelling assessment of dynamic mass loss from the three major outlet glaciers Jakobshavn, Helheim and Kangerdlugssuaq suggested an equivalent of ~1.1 mm of increased sea level by 2100²⁶. That study, however, applied a single dynamic perturbation at the beginning of the twenty-first century that produced mass losses similar to present, but the model did not have the ability to simulate retreat. When including dynamic perturbations and feedbacks induced by glacier retreat, we produce a substantially larger estimate of SLR of 7.5–15 mm due to dynamic mass loss from these glaciers by 2100. The four glaciers studied here drain 22% of the entire ice sheet. A linear extrapolation of their dynamic mass loss to the whole of Greenland, by multiplying by a factor five, results in SLR of 40–85 mm by 2100 from dynamic changes. The SMB-only contribution from different climate models has previously been estimated to be between 25–98 mm of SLR by 2100²³. Combined with our dynamic extrapolation, this would produce a total SLR contribution from

Greenland of 65–183 mm by the year 2100. We stress, however, that such an estimate has large uncertainties and ignores important variations in the geometry of individual outlet glacier systems.

We have produced a first estimate of the contribution to SLR from four of Greenland's major marine outlet glaciers that fully accounts for effects of dynamic retreat and is driven by specific emission scenarios (A1B and RCP8.5). The estimate, of a 19–50-mm contribution to SLR by the year 2200, is consistent with the upper-bound estimate of a recent semi-empirical model study²⁶, but is lower than previous estimates based on the extrapolation of current trends^{5,26,27}. Further model development and application to other marine-terminating outlet glaciers are essential to improve these projections.

METHODS SUMMARY

Our model incorporates realistic and fully dynamic marine boundary conditions (for example processes of calving, grounding line retreat and submarine melting), has a robust treatment of grounding line migration²⁸ and calving²⁹, and well reproduces the present observed dynamical behaviour of several narrow marine outlet glaciers^{13,14,21}. The model is applied to four major outlet glaciers in Greenland: the Jakobshavn, Helheim, Kangerdlugssuaq and Petermann glaciers. For each of these glaciers, we have detailed basal topography³⁰, velocity, surface elevation and terminus position records^{3,8}.

We simulate the future behaviour of each glacier by running suites of model experiments with different relative weightings applied to forcing processes, which include variations in (1) water level in surface crevasses, (2) submarine melt rate, (3) seasonal duration and magnitude of sea-ice-induced modulation of longitudinal stress at the calving front, and (4) basal and lateral resistance. We use simple parameterizations to link each of these processes to atmospheric and oceanic variables such as air temperature, deep-ocean temperature, sea surface temperature and glacier surface meltwater run-off, which are provided by regional climate models (see Supplementary Information, sections 1 and 3).

Before simulating future behaviour, we adjust the model to match observed behaviour. Specifically, we perform a series of 50 runs for each glacier to tune various parameters so that the model accurately reproduces the observed (2000–2010) velocity changes and retreat or advance rates for each glacier^{8,11} (Supplementary Information, section 4). This tuning exercise also allows us to determine the sensitivity of each glacier to the different parameters and processes involved (Supplementary Information, section 5).

Received 24 January; accepted 12 March 2013.

- Rignot, E., Velicogna, I., van den Broeke, M. R., Monaghan, A. & Lenaerts, J. Acceleration of the contribution of the Greenland and Antarctic ice sheets to sea level rise. *Geophys. Res. Lett.* **38**, L05503 (2011).
- van den Broeke, M. *et al.* Partitioning recent Greenland mass loss. *Science* **326**, 984–986 (2009).
- Howat, I. M., Joughin, I. & Scambos, T. A. Rapid changes in ice discharge from Greenland outlet glaciers. *Science* **315**, 1559–1561 (2007).
- Solomon, S., *et al.* *Climate Change 2007: The Physical Science Basis* (Cambridge Univ. Press, 2007).
- Pfeffer, W. T., Harper, J. T. & O'Neel, S. Kinematic constraints on glacier contributions to 21st-century sea-level rise. *Science* **321**, 1340–1343 (2008).
- Holland, D. M., Thomas, R. H., de Young, B., Ribergaard, M. H. & Lyberth, B. Acceleration of Jakobshavn Isbræ triggered by warm subsurface ocean waters. *Nature Geosci.* **1**, 659–664 (2008).
- Murray, T. *et al.* Ocean regulation hypothesis for glacier dynamics in southeast Greenland and implications for ice sheet mass changes. *J. Geophys. Res.* **115**, F03026 (2010).

8. Moon, T., Joughin, I., Smith, B. & Howat, I. 21st-century evolution of Greenland outlet glacier velocities. *Science* **336**, 576–578 (2012).
9. Joughin, I. *et al.* Continued evolution of Jakobshavn Isbrae following its rapid speedup. *J. Geophys. Res.* **113**, F04006 (2008).
10. Howat, I. M. *et al.* Mass balance of Greenland's three largest outlet glaciers, 2000–2010. *Geophys. Res. Lett.* **38**, L12501 (2011).
11. Joughin, I., Smith, B. E., Howat, I. M., Scambos, T. & Moon, T. Greenland flow variability from ice-sheet-wide velocity mapping. *J. Glaciol.* **56**, 415–430 (2010).
12. Rignot, E. & Steffen, K. Channelized bottom melting and stability of floating ice shelves. *Geophys. Res. Lett.* **35**, L02503 (2008).
13. Nick, F. M. *et al.* The response of Petermann Glacier, Greenland, to large calving events, and its future stability in the context of atmospheric and oceanic warming. *J. Glaciol.* **58**, 229–239 (2012).
14. Vieli, A. & Nick, F. M. Understanding and modelling rapid dynamic changes of tidewater outlet glaciers: issues and implications. *Surv. Geophys.* **32**, 437–458 (2011).
15. Joughin, I., Alley, R. B. & Holland, D. M. Ice-sheet response to oceanic forcing. *Science* **338**, 1172–1176 (2012).
16. Jenkins, A. Convection-driven melting near the grounding lines of ice shelves and tidewater glaciers. *J. Phys. Oceanogr.* **41**, 2279–2294 (2011).
17. Amundson, J. M. *et al.* Ice mélange dynamics and implications for terminus stability, Jakobshavn Isbræ, Greenland. *J. Geophys. Res.* **115**, F01005 (2010).
18. van der Veen, C. J. Fracture mechanics approach to penetration of surface crevasses on glaciers. *Cold Reg. Sci. Technol.* **27**, 31–47 (1998).
19. Van Der Veen, C. J., Plummer, J. C. & Stearns, L. A. Controls on the recent speed-up of Jakobshavn Isbræ, West Greenland. *J. Glaciol.* **57**, 770–782 (2011).
20. Zwally, H. J. *et al.* Surface melt-induced acceleration of Greenland ice-sheet flow. *Science* **297**, 218–222 (2002).
21. Nick, F. M., Vieli, A., Howat, I. M. & Joughin, I. Large-scale changes in Greenland outlet glacier dynamics triggered at the terminus. *Nature Geosci.* **394**, 110–114 (2009).
22. Motyka, R. J. *et al.* Submarine melting of the 1985 Jakobshavn Isbræ floating tongue and the triggering of the current retreat. *J. Geophys. Res.* **116**, F01007 (2011).
23. Fettweis, X. *et al.* Estimating the Greenland ice sheet surface mass balance contribution to future sea level rise using the regional atmospheric climate model MAR. *Cryosphere* **7**, 469–489 (2013).
24. Joughin, I. *et al.* Ice-front variation and tidewater behavior on Helheim and Kangerdlugssuaq Glaciers, Greenland. *J. Geophys. Res.* **113**, F01004 (2008).
25. Jamieson, S. S. R. *et al.* Ice-stream stability on a reverse bed slope. *Nat. Geosci.* **5**, 799–802 (2012).
26. Price, S. F., Payne, A. J., Howat, I. M. & Smith, B. E. Committed sea-level rise for the next century from Greenland ice sheet dynamics during the past decade. *Proc. Natl Acad. Sci. USA* **108**, 8978–8983 (2011).
27. Cuffey, K. M. & Paterson, W. S. B. *The Physics of Glaciers* 4th edn, 575–610 (Elsevier, 2010).
28. Pattyn, F. *et al.* Results of the Marine Ice Sheet Model Intercomparison Project, MISMP. *Cryosphere* **6**, 573–588 (2012).
29. Nick, F. M., Van Der Veen, C. J., Vieli, A. & Benn, D. I. A physically based calving model applied to marine outlet glaciers and implications for the glacier dynamics. *J. Glaciol.* **56**, 781–794 (2010).
30. Gogineni, P. CReSIS Radar Depth Sounder Data, Lawrence, Kansas USA. <http://data.cresis.ku.edu/> (2012).

Supplementary Information is available in the online version of the paper.

Acknowledgements This research was financially supported by the ice2sea programme of the European Union 7th Framework Programme, grant number 226375 (ice2sea publication 118), and the Netherlands Polar Programme (NPP), and contributes to the Knowledge for Climate (KvK) programme in the Netherlands. The ENSEMBLES data used in this work was funded by the European Union 6th Framework Programme Integrated Project ENSEMBLES (contract number 505539). Support for I.J. was provided by US NSF grant ANT-0424589.

Author Contributions F.M.N., A.V. and M.L.A. were responsible for the numerical modelling. A.P., T.L.E. and I.J. provided the climate and observational data. F.P. and R.S.W.v.d.W. are the principal investigators of the projects of which this research is part. F.P. contributed to the model refinement. F.M.N. wrote the manuscript with substantial contributions from A.V., M.L.A. and I.J.

Author Information Reprints and permissions information is available at www.nature.com/reprints. The authors declare no competing financial interests. Readers are welcome to comment on the online version of the paper. Correspondence and requests for materials should be addressed to F.N. (faezeh.nick@unis.no).

M-CSF instructs myeloid lineage fate in single haematopoietic stem cells

Noushine Mossadegh-Keller^{1,2,3*}, Sandrine Sarrazin^{1,2,3*}, Prashanth K. Kandalla^{1,2,3}, Leon Espinosa⁴, E. Richard Stanley⁵, Stephen L. Nutt⁶, Jordan Moore⁷ & Michael H. Sieweke^{1,2,3,8}

Under stress conditions such as infection or inflammation the body rapidly needs to generate new blood cells that are adapted to the challenge. Haematopoietic cytokines are known to increase output of specific mature cells by affecting survival, expansion and differentiation of lineage-committed progenitors^{1,2}, but it has been debated whether long-term haematopoietic stem cells (HSCs) are susceptible to direct lineage-specifying effects of cytokines. Although genetic changes in transcription factor balance can sensitize HSCs to cytokine instruction³, the initiation of HSC commitment is generally thought to be triggered by stochastic fluctuation in cell-intrinsic regulators such as lineage-specific transcription factors^{4–7}, leaving cytokines to ensure survival and proliferation of the progeny cells^{8,9}. Here we show that macrophage colony-stimulating factor (M-CSF, also called CSF1), a myeloid cytokine released during infection and inflammation, can directly induce the myeloid master regulator PU.1 and instruct myeloid cell-fate change in mouse HSCs, independently of selective survival or proliferation. Video imaging and single-cell gene expression analysis revealed that stimulation of highly purified HSCs with M-CSF in culture resulted in activation of the *PU.1* promoter and an increased number of *PU.1*⁺ cells with myeloid gene signature and differentiation potential. *In vivo*, high systemic levels of M-CSF directly stimulated M-CSF-receptor-dependent activation of endogenous PU.1 protein in single HSCs and induced a PU.1-dependent myeloid differentiation preference. Our data demonstrate that lineage-specific cytokines can act directly on HSCs *in vitro* and *in vivo* to instruct a change of cell identity. This fundamentally changes the current view of how HSCs respond to environmental challenge and implicates stress-induced cytokines as direct instructors of HSC fate.

Lineage-specific cytokines such as M-CSF can be strongly induced during physiological stress or infection^{10,11} and potentially increase the production of mature cells from lineage-committed progenitors^{1,2}. According to the prevailing model, however, they are generally not believed to influence differentiation decisions of HSCs directly^{9,12,13}. Cell fate choice of HSCs has traditionally been explained by stochastic models¹⁴. In this view transcriptional noise¹⁵ and random variations in competing lineage-determining transcription factors lead to cross-antagonistic switches that initiate lineage choice^{4–7}, whereas cytokines are thought to only act on the resulting progeny cells by stimulating their survival and proliferation^{8,9}. A key example of such a master regulator is the transcription factor PU.1 that induces myelo-monocytic differentiation^{16,17}. It is generally unknown whether external signals could drive the initial activation of such intrinsic master regulators. Because HSCs deficient for the transcription factor MAFB are sensitized to PU.1 activation in response to M-CSF³, we have investigated whether high systemic M-CSF levels could induce PU.1 and instruct

myelo-monocytic fate in wild-type HSCs without previous modification of transcription factor balance.

We observed that lipopolysaccharide (LPS), a strong mimetic of bacterial infection stimulating high systemic levels of M-CSF¹¹ (Supplementary Fig. 1a), induced an upregulation of GFP in long-term HSCs (CD117⁺Sca⁺Lin[−]CD135[−]CD34[−]CD150⁺) of *PU.1-GFP* reporter mice¹⁸ (Supplementary Fig. 1b, c). Consistent with the expression of the M-CSF receptor (*M-CSFR*; also called *Csf1r*) in HSCs (Supplementary Fig. 2)^{3,19}, direct intravenous injection of recombinant M-CSF also induced significantly increased *PU.1* activation in HSCs after 16 h (Fig. 1a, b). The treatment caused no significant change in *M-CSFR* or *Maifb* expression (Supplementary Fig. 3), arguing against selection of myeloid primed HSCs with high M-CSFR or low MAFB levels. M-CSF also induced no change in the proportion of CD150^{hi} HSCs, reported to have myeloid lineage bias²⁰, in GFP-positive or GFP-negative HSCs (Supplementary Fig. 4a–c) and activated *PU.1* to a similar extent in CD150^{hi} HSCs (Fig. 1c) as in total HSCs (Fig. 1a, b). Finally, cultured CD150^{hi} HSCs revealed no proliferation or survival advantage in the presence of M-CSF (Supplementary Fig. 5a). Together, these data argued against selective amplification or survival of a pre-existing HSC sub-population and indicated that M-CSF could newly induce PU.1 expression in HSCs.

As shown in Fig. 1d, the effect of M-CSF on stem cells was direct and specific, as fluorescence-activated cell sorting (FACS)-purified HSCs

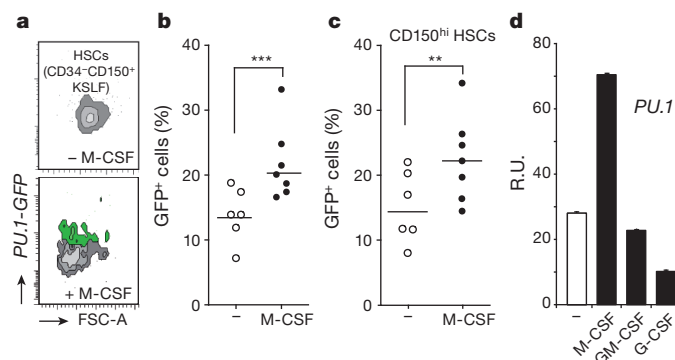


Figure 1 | M-CSF activates the myeloid master regulator PU.1 in HSCs. **a–c**, Representative FACS profile (**a**) and quantification of GFP expression in HSCs (**b**) or CD150^{hi} HSCs (**c**) of *PU.1-GFP* reporter mice 16 h after control (PBS) or M-CSF injection. Horizontal bars show median. ***P* = 0.03; ****P* = 0.009, calculated by a two-tailed non-parametric Mann–Whitney *U*-test. **d**, Quantitative RT–PCR analysis of *PU.1* expression normalized to *Gapdh* expression (R.U.) in sorted HSCs after 16 h culture in the absence or presence of M-CSF, GM-CSF or G-CSF. Error bars show standard deviation of duplicates. G-CSF, granulocyte CSF; GM-CSF, granulocyte–macrophage CSF.

¹Centre d'Immunologie de Marseille-Luminy, Aix-Marseille Université, UMR 7280, Campus de Luminy, Case 906, 13288 Marseille Cedex 09, France. ²Institut National de la Santé et de la Recherche Médicale, U1104, Campus de Luminy, Case 906, 13288 Marseille Cedex 09, France. ³Centre National de la Recherche Scientifique, UMR 7280, Campus de Luminy, Case 906, 13288 Marseille Cedex 09, France. ⁴Laboratoire de Chimie Bactérienne, Centre National de la Recherche Scientifique, UMR 7283, 31 Chemin Joseph Aiguier, 13009 Marseille, France. ⁵Department of Developmental and Molecular Biology, Albert Einstein College of Medicine, Bronx, New York 10461, USA. ⁶Walter and Eliza Hall Institute, 1G Royal Parade, Parkville, Victoria 3052, Australia. ⁷Fluidigm Corporation, South San Francisco, California 94080, USA. ⁸Max-Delbrück-Centrum für Molekulare Medizin, Robert-Rössle-Str. 10, 13125 Berlin, Germany.

*These authors contributed equally to this work.

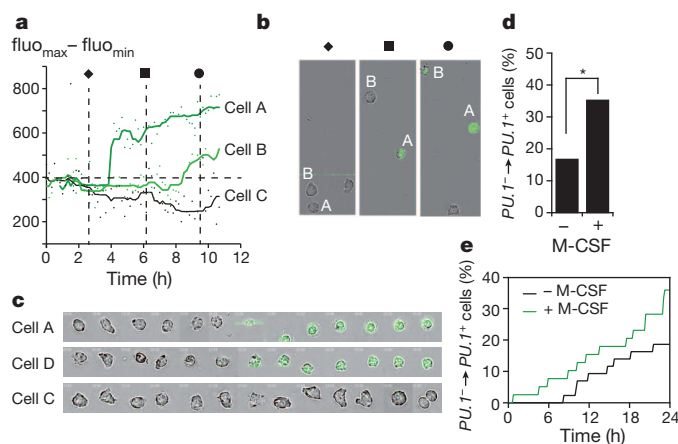


Figure 2 | Continuous video imaging of $PU.1^+$ cell generation from individual $PU.1^-$ HSCs. **a**, GFP fluorescence intensity at 10-min intervals (dots) and sliding median (lines) over 12-h observation time of three individual GFP-negative sorted HSCs from $PU.1$ -GFP reporter mice after 18 h in M-CSF culture, representative of cells quantified in **e** ($n = 39$). Green, cells activating GFP; black, cell remaining GFP negative. **b**, Still photos taken at times indicated by symbols in **a** of fields with two representative HSCs (cells A, B) showing activation of $PU.1$ at different time points. Cell C was outside of the shown field. **c**, Still photos taken at 40-min intervals over 8 h of three representative HSCs in M-CSF culture without (cell C) or with activation of $PU.1$ (cells A, D), representative of cells quantified in **e** ($n = 39$). Complete videos are shown in Supplementary Videos 1–3. **d**, Quantification of $PU.1^+$ cells derived from $PU.1^-$ HSCs (committed cells) with ($n = 39$) or without M-CSF ($n = 42$) as percentage of total cells after 24-h observation period. * $P \leq 0.1$, calculated by a two-tailed non-parametric Mann–Whitney U -test. **e**, Timing of $PU.1$ activation in $PU.1^-$ HSCs of cells shown in **d** over 24-h observation period.

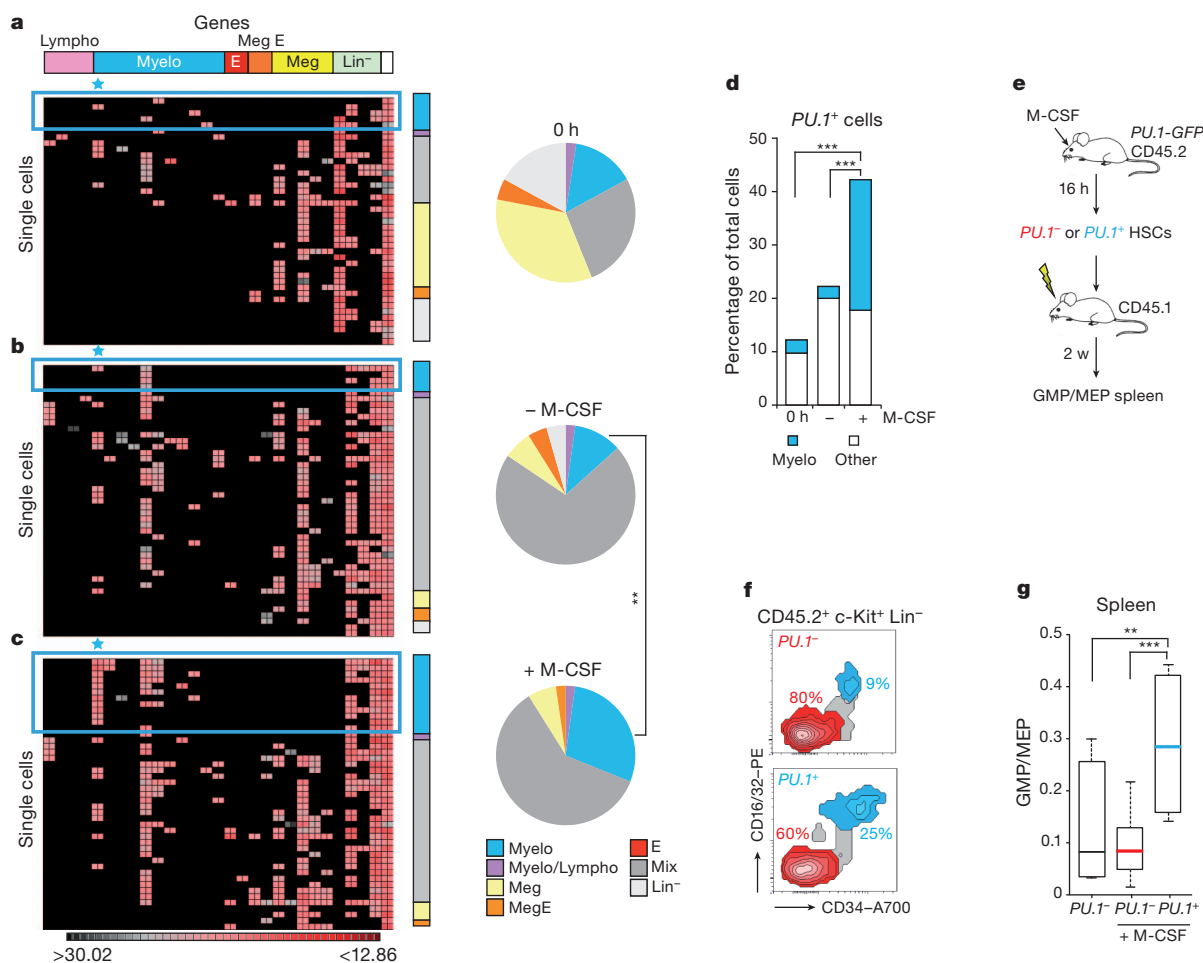


Figure 3 | M-CSF activates $PU.1$ and instructs myeloid identity in single HSCs. **a–c**, Gene expression analysis of single cells (rows) for lineage or stem-cell representative genes (columns) using duplicate nano-fluidic real-time PCR on Fluidigm array for freshly isolated HSCs (**a**) or after 16 h of culture in the absence (**b**) or the presence of M-CSF (**c**). Genes are grouped by lineage (indicated on top) and individual cells were clustered according to lineage-specific, mixed or lineage-negative gene expression profiles shown in bar and pie diagrams on the right. A full gene list and expanded view is shown in Supplementary Figs 7–9. ** $P = 0.04$ calculated by a Pearson's χ^2 test, $n = 41$, 45, 45. Blue star highlights expression of $PU.1$ gene expression. Colour scale on the bottom shows correspondence between colour code and Ct values. E, erythroid; Lympho, lymphoid; Meg, megakaryocytic; MegE, megakaryocytic-erythroid; Myelo, myeloid. **d**, Individual $PU.1^+$ cells with a myeloid gene

expression profile (blue) or expressing other lineage genes (white) as a percentage of total cells. *** $P = 0.009$ (0 h) and $P = 0.005$ (–M-CSF), calculated by a two-tailed non-parametric Mann–Whitney U -test. **e**, Experimental design for transplantation of sorted $PU.1^-$ and $PU.1^+$ HSCs from *in vivo* M-CSF-primed $CD45.2$ $PU.1$ -GFP mice into sub-lethally irradiated $CD45.1$ recipients and analysis of progeny cells after 2 weeks in the spleen (Supplementary Fig. 14). **f**, **g**, Representative FACS profiles (**f**) and quantification of the ratio (**g**) of donor GMP and MEP progenitors derived from transplanted $PU.1^-$ or $PU.1^+$ HSCs before or after M-CSF stimulation *in vivo*. ** $P = 0.05$; *** $P = 0.01$, calculated by a two-tailed non-parametric Mann–Whitney U -test; $n = 4, 8, 4$. Whisker plots show median (lines), upper and lower quartiles (boxes) and extreme outliers (dotted whiskers).

showed increased *PU.1* expression after 16 h in culture with M-CSF but not with GM-CSF or G-CSF, cytokines that may also be released during infection²¹. The observed changes in gene expression cannot be explained by M-CSF-dependent selection of *PU.1*-reporter positive (*PU.1*⁺) cells, as video microscopy of cultured HSCs showed no proliferation or survival advantage in M-CSF and *PU.1* was induced before the onset of cell division (Supplementary Figs 5 and 6). Continuous observation of individual GFP-negative sorted HSCs from *PU.1*-GFP mice by video imaging confirmed that M-CSF could induce *PU.1* expression in previously *PU.1*-negative cells (Fig. 2a–c and Supplementary Videos 1–3). We recorded the fate of HSCs between 18 h and 42 h of culture, when both the induction of *PU.1* in previously negative cells and the division of *PU.1*⁺ cells could theoretically occur. At the end of the 24-h observation period, over twofold more *PU.1*⁺ cells had developed in M-CSF than under control conditions (Fig. 2d); backtracking the origin of these cells revealed that all *PU.1*⁺ cells were derived from previously *PU.1*[−] cells, but none from divisions of *PU.1*⁺ cells. Although the absence of *PU.1*⁺ cell division may be partially due to the phototoxic effects of GFP excitement^{22,23}, we could conclude that the observed increase in *PU.1*⁺ cells was entirely due to M-CSF-induced activation of the *PU.1* reporter. These commitment events of *PU.1* activation occurred 8 h earlier and at a higher rate over the whole observation period in the presence of M-CSF (Fig. 2e). Our results indicated that M-CSF could directly increase *PU.1* promoter activation in single, previously *PU.1*-negative HSCs.

To investigate further whether M-CSF-induced *PU.1* activation changed the cell identity of individual HSCs we analysed the messenger RNA expression profile of single cells by nanofluidic real-time PCR

on Fluidigm dynamic arrays. Consistent with their stem-cell identity, almost all freshly isolated HSCs expressed stem- and progenitor-cell-associated genes and about half expressed either no (*Lin*[−]) or multiple lineage-specific genes (mix). The remainder showed mainly megakaryocytic, megakaryocytic-erythroid or myeloid lineage priming (Fig. 3a and Supplementary Fig. 7). Culture for 16 h without M-CSF led to an increased number of cells with a mixed lineage profile at the expense of megakaryocytic and *Lin*[−] profiles (Fig. 3b and Supplementary Fig. 8). By contrast, culture in the presence of M-CSF induced a strong increase of cells with a myeloid gene expression signature (Fig. 3c, Supplementary Fig. 9 and Supplementary Table 1). Consistent with the video microscopy results, the increase in myeloid gene expression was associated with a doubling of the number of *PU.1*⁺ cells (Fig. 3d). Interestingly, this increase was entirely due to *PU.1*⁺ cells with a myeloid signature that did not express genes from any other lineage. By contrast, the number of *PU.1*⁺ cells that also expressed non-myeloid genes remained approximately constant (Fig. 3d). Together, this indicated that M-CSF-induced *PU.1*⁺ cells had assumed a myeloid cell identity. To evaluate whether this change in gene expression reflected a functional myeloid lineage choice *in vivo*, we compared the differentiation potential of unstimulated *PU.1*[−] HSCs to *PU.1*[−] and *PU.1*⁺ HSCs after *in vivo* priming with M-CSF (Fig. 3e). Progenitor analysis in the spleen 2 weeks after transplantation of these populations revealed a higher ratio of granulocyte/macrophage progenitors (GMP) to megakaryocytic/erythroid progenitors (MEP) developing from *PU.1*⁺ HSCs than from *PU.1*[−] HSCs (Fig. 3f, g). We observed a similar increase in myeloid differentiation potential for *PU.1*⁺ cells derived from M-CSF-stimulated *PU.1*[−] HSCs in culture (Supplementary Fig. 10a–d). Together, these data showed that M-CSF-induced *PU.1* activation led to a myeloid cell fate change in single HSCs.

To investigate further whether M-CSF could also induce a cell fate change of individual HSCs *in vivo*, we transplanted carboxy fluorescein diacetate, succinimidyl ester (CFSE)-labelled HSCs into the spleen, a site of extra-medullary haematopoiesis with adapted stem-cell niches^{3,24}, and analysed the expression of endogenous *PU.1* protein by immunofluorescence in single HSCs after 24 h (Fig. 4a). Whereas

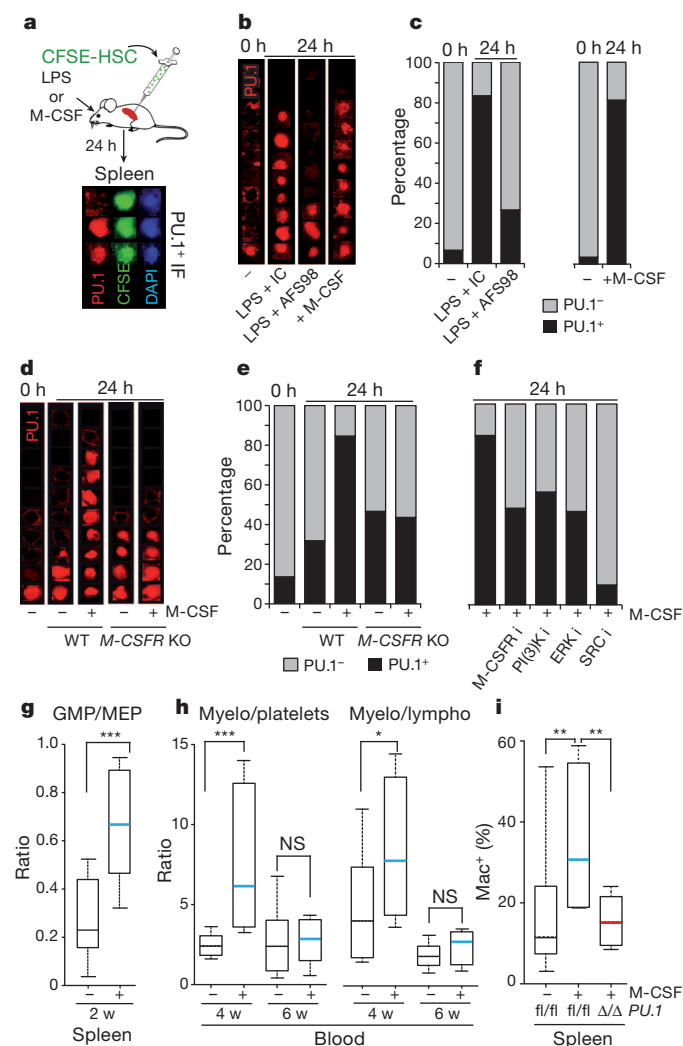


Figure 4 | M-CSF directly induces endogenous *PU.1* protein in single HSCs *in vivo* and stimulates a reversible, *PU.1*-dependent myeloid differentiation preference. **a**, Experimental design of HSC transplantation into spleens of LPS-stimulated or M-CSF-stimulated hosts and typical immunofluorescence detection of *PU.1* in CFSE-labelled HSCs 24 h after transplantation for two representative *PU.1*⁺ and one *PU.1*[−] cell. DAPI, nuclear stain. **b, c**, Representative immunofluorescence images (**b**) and percentage (**c**) of *PU.1*⁺ HSCs immediately (0 h) or 24 h after transplantation into LPS-stimulated host with isotype control (IC) or anti-M-CSF receptor blocking antibody (AFS98), or into M-CSF-injected hosts. ($n \geq 30$). **d, e**, Representative immunofluorescence images (**d**) and percentage (**e**) of *PU.1*⁺ cells immediately (0 h) or 24 h after transplantation of wild-type or *M-CSFR*^{−/−} HSCs into mock or M-CSF-stimulated hosts ($n \geq 50$). **f**, Percentage of *PU.1*⁺ cells 24 h after transplantation of HSCs into M-CSF-stimulated hosts in the absence or presence of kinase inhibitors for M-CSFR (GW2580), PI(3)K (LY294002), ERK/MAPK (PD98059) and SRC (SU6656) ($n = 50$). **g**, Ratio of donor GMP to MEP progenitors in the spleens of sub-lethally irradiated recipients 2 weeks after transplantation of *in vivo* M-CSF-primed or control HSCs. Experimental design is shown in Supplementary Fig. 11. *** $P = 0.003$, calculated by a two-tailed non-parametric Mann–Whitney *U*-test; $n = 8, 9$. **h**, Donor contribution to blood of competitively reconstituted mice 4 weeks and 6 weeks after transplantation of M-CSF-primed or control HSCs, expressed as a ratio of CD11b⁺ myeloid cells to platelets or CD19⁺ lymphoid cells. Experimental design, representative FACS profiles and quantification of contribution to individual lineages are shown in Supplementary Fig. 12. * $P = 0.07$, calculated by a two-tailed non-parametric Mann–Whitney *U*-test, $n = 6, 4$; *** $P = 0.01$, $n = 10, 6$. **i**, Donor contribution to Mac⁺ myeloid cells in the spleen of sub-lethally irradiated recipients 2 weeks after transplantation of control or M-CSF-primed HSCs with control (fl/fl) or deleted (Δ/Δ) *PU.1* alleles. *** $P = 0.05$, calculated by a two-tailed non-parametric Mann–Whitney *U*-test, $n = 6, 4, 5$. NS, not significant. Whisker plots show median (lines), upper and lower quartiles (boxes) and extreme outliers (dotted whiskers).

the vast majority of HSCs were PU.1-negative immediately after transplantation, nearly all had activated PU.1 after transfer into spleens of LPS-challenged hosts (Fig. 4b, c). This effect was principally dependent on M-CSF signalling, as a blocking antibody against the M-CSF receptor²⁵ strongly inhibited PU.1 activation. Furthermore, direct injection of recombinant M-CSF resulted in a similar strong induction of PU.1 in the transplanted HSCs (Fig. 4b, c). This effect appeared to be entirely cell autonomous, as M-CSF-receptor-deficient (*M-CSFR*^{-/-})²⁶ HSCs showed no higher activation of PU.1 in M-CSF-stimulated compared with control recipients (Fig. 4d, e). Similarly, small-molecule inhibitors of the M-CSFR or phosphatidylinositol-3-OH kinase (PI(3)K), ERK and SRC kinases, which signal downstream of the receptor²⁷, also prevented induction of *PU.1* (Fig. 4f), consistent with the stimulation of transcriptional activators of the *PU.1* gene by these pathways (Supplementary Discussion). Furthermore, transplantation of *in vivo* M-CSF-primed CD45.2 HSCs into sub-lethally irradiated CD45.1 recipients revealed an increased ratio of GMP to MEP progenitors in the spleen after 2 weeks (Fig. 4g and Supplementary Fig. 11a, b) and an increased myeloid to lymphoid cell ratio in peripheral blood after 4 weeks (Supplementary Fig. 11c). In competitive transplantation assays, M-CSF-primed HSCs also showed a myeloid advantage compared to platelet and lymphoid contribution at 4 weeks in the blood that re-equilibrated after 6 weeks and did not compromise long-term multi-lineage contribution (Fig. 4h and Supplementary Fig. 12). Finally, this myeloid differentiation preference of M-CSF-primed HSCs could be abolished by deletion of *PU.1* (Fig. 4i and Supplementary Fig. 13). Together, these results indicated that M-CSF could directly instruct a change in cell identity of single HSCs *in vivo* that resulted in a reversible, PU.1-dependent myeloid differentiation preference.

Our results show that under haematopoietic stress conditions of infection, high systemic levels of M-CSF can directly instruct myeloid gene expression and differentiation preference of HSCs. This challenges both the current view of cytokine action and how HSCs make differentiation decisions. Whereas cytokines are commonly thought to act on lineage-committed progenitors, we show here that stem cells are direct targets of lineage instruction by cytokines. HSCs have been shown to proliferate in response to signals characteristic of bacterial²⁸ or viral infections²⁹ but without changing lineage-specific gene expression or differentiation potential. In line with the prevailing paradigm of selective cytokine action it has been proposed that distinct stem-cell subtypes could have a selective advantage in response to different stimuli³⁰. Such a mechanism is difficult to distinguish from instructive mechanisms on a population basis. We have therefore used multiple assays of single-cell analysis in culture and *in vivo* in a time window before the onset of cell division to distinguish induced changes of lineage specification from selective mechanisms. These data indicate that M-CSF can directly change stem-cell identity by activation of the myeloid master regulator PU.1 on the promoter, message and protein level, independently of selective survival or proliferation. The multi-lineage priming of gene expression in HSCs has generally been interpreted as an indication that initial cell-fate decisions are driven solely by stochastic fluctuations in the balance of lineage-specific transcription factors^{4–6,12,13}. Our data now indicate that cytokines can not only amplify random choices but also directly activate key regulators of lineage specification, such as PU.1, to instruct lineage fate of HSCs to induce an insult-tailored output of progeny. As M-CSF can transiently increase the production of myeloid progeny without compromising stem-cell activity, it may be useful to ameliorate myeloid cytopenias, particularly to protect patients from infection after stem-cell transplantation.

METHODS SUMMARY

Flow cytometry, bone-marrow transplantation and *in vivo* immunofluorescence of HSCs were performed essentially as described³. Single-cell nano-fluidics-based real-time PCR was performed using a BioMark HD system and 96.96 dynamic

arrays (Fluidigm) and video microscopy analysis followed proposed standards³³. Details of procedures and reagents are described in Methods.

Full Methods and any associated references are available in the online version of the paper.

Received 13 June 2012; accepted 20 February 2013.

Published online 10 April 2013.

1. Metcalf, D. Hematopoietic cytokines. *Blood* **111**, 485–491 (2008).
2. Rieger, M. A., Hoppe, P. S., Smejkal, B. M., Eitelhuber, A. C. & Schroeder, T. Hematopoietic cytokines can instruct lineage choice. *Science* **325**, 217–218 (2009).
3. Sarrazin, S. *et al.* MafB restricts M-CSF dependent myeloid commitment divisions of hematopoietic stem cells. *Cell* **138**, 300–313 (2009).
4. Orkin, S. H. Diversification of haematopoietic stem cells to specific lineages. *Nature Rev. Genet.* **1**, 57–64 (2000).
5. Cantor, A. B. & Orkin, S. H. Hematopoietic development: a balancing act. *Curr. Opin. Genet. Dev.* **11**, 513–519 (2001).
6. Enver, T., Pera, M., Peterson, C. & Andrews, P. W. Stem cell states, fates, and the rules of attraction. *Cell Stem Cell* **4**, 387–397 (2009).
7. Graf, T. & Enver, T. Forcing cells to change lineages. *Nature* **462**, 587–594 (2009).
8. Socolovsky, M., Lodish, H. F. & Daley, G. Q. Control of hematopoietic differentiation: lack of specificity in signaling by cytokine receptors. *Proc. Natl Acad. Sci. USA* **95**, 6573–6575 (1998).
9. Metcalf, D. On hematopoietic stem cell fate. *Immunity* **26**, 669–673 (2007).
10. Cheers, C. & Stanley, E. R. Macrophage production during murine listeriosis: colony-stimulating factor 1 (CSF-1) and CSF-1-binding cells in genetically resistant and susceptible mice. *Infect. Immun.* **56**, 2972–2978 (1988).
11. Roth, P., Bartocci, A. & Stanley, E. R. Lipopolysaccharide induces synthesis of mouse colony-stimulating factor-1 *in vivo*. *J. Immunol.* **158**, 3874–3880 (1997).
12. Cross, M. A. & Enver, T. The lineage commitment of haematopoietic progenitor cells. *Curr. Opin. Genet. Dev.* **7**, 609–613 (1997).
13. Enver, T., Heyworth, C. M. & Dexter, T. M. Do stem cells play dice? *Blood* **92**, 348–351 (1998).
14. Till, J. E., McCulloch, E. A. & Siminovitch, L. A stochastic model of stem cell proliferation, based on the growth of spleen colony-forming cells. *Proc. Natl Acad. Sci. USA* **51**, 29–36 (1964).
15. Chang, H. H., Hemberg, M., Barahona, M., Ingber, D. E. & Huang, S. Transcriptome-wide noise controls lineage choice in mammalian progenitor cells. *Nature* **453**, 544–547 (2008).
16. Laïosa, C. V., Stadtfeld, M. & Graf, T. Determinants of lymphoid-myeloid lineage diversification. *Annu. Rev. Immunol.* **24**, 705–738 (2006).
17. Orkin, S. H. & Zon, L. I. Hematopoiesis: an evolving paradigm for stem cell biology. *Cell* **132**, 631–644 (2008).
18. Back, J., Allman, D., Chan, S. & Kastner, P. Visualizing PU.1 activity during hematopoiesis. *Exp. Hematol.* **33**, 395–402 (2005).
19. Miyamoto, T. *et al.* Myeloid or lymphoid promiscuity as a critical step in hematopoietic lineage commitment. *Dev. Cell* **3**, 137–147 (2002).
20. Morita, Y., Ema, H. & Nakauchi, H. Heterogeneity and hierarchy within the most primitive hematopoietic stem cell compartment. *J. Exp. Med.* **207**, 1173–1182 (2010).
21. Cheers, C. *et al.* Production of colony-stimulating factors (CSFs) during infection: separate determinations of macrophage-, granulocyte-, granulocyte-macrophage-, and multi-CSFs. *Infect. Immun.* **56**, 247–251 (1988).
22. Hoebe, R. A. *et al.* Controlled light-exposure microscopy reduces photobleaching and phototoxicity in fluorescence live-cell imaging. *Nature Biotechnol.* **25**, 249–253 (2007).
23. Schroeder, T. Long-term single-cell imaging of mammalian stem cells. *Nature Methods* **8**, S30–S35 (2011).
24. Kiel, M. J. & Morrison, S. J. Uncertainty in the niches that maintain haematopoietic stem cells. *Nature Rev. Immunol.* **8**, 290–301 (2008).
25. Sudo, T. *et al.* Functional hierarchy of c-kit and c-fms in intramarrow production of CFU-M. *Oncogene* **11**, 2469–2476 (1995).
26. Dai, X. M. *et al.* Targeted disruption of the mouse colony-stimulating factor 1 receptor gene results in osteopetrosis, mononuclear phagocyte deficiency, increased primitive progenitor cell frequencies, and reproductive defects. *Blood* **99**, 111–120 (2002).
27. Pixley, F. J. & Stanley, E. R. CSF-1 regulation of the wandering macrophage: complexity in action. *Trends Cell Biol.* **14**, 628–638 (2004).
28. Baldrige, M. T., King, K. Y., Boles, N. C., Weksberg, D. C. & Goodell, M. A. Quiescent haematopoietic stem cells are activated by IFN- γ in response to chronic infection. *Nature* **465**, 793–797 (2010).
29. Essers, M. A. *et al.* IFN α activates dormant haematopoietic stem cells *in vivo*. *Nature* **458**, 904–908 (2009).
30. King, K. Y. & Goodell, M. A. Inflammatory modulation of HSCs: viewing the HSC as a foundation for the immune response. *Nature Rev. Immunol.* **11**, 685–692 (2011).

Supplementary Information is available in the online version of the paper.

Acknowledgements We acknowledge grants from the 'Association pour la recherche sur le Cancer' (3422) and the 'Agence nationale de la Recherche' (BLAN07-1_205752). We thank P. Kastner and S. Chan for *PU.1-GFP* reporter mice; T. P. Vu Manh and J. Maurizio for bioinformatics; M. Barad, A. Zouine and M.-L. Thibault for flow cytometry support; L. Razafindramana for animal handling; and J. Favret, P. Perrin and L. Chasson for tissue sectioning. E.R.S. is supported by NIH grant CA

32551. S.L.N. is an Australian Research Council Future Fellow and received Victorian State Government Operational and Australian Government NHMRC Independent Research Institute Infrastructure Support. M.H.S. is a 'Fondation pour la Recherche Médicale' (DEQ20071210559; DEQ20110421320) and INSERM-Helmholtz group leader.

Author Contributions M.H.S. conceived the study, analysed and interpreted data and wrote the paper; S.S. performed experiments, analysed and interpreted data and contributed to the preparation of the manuscript; N.M.-K. performed most experiments and analysed data; P.K.K. performed and analysed video microscopy and contributed to other experiments; L.E. analysed and interpreted video microscopy data; J.M.

provided expertise and service on Fluidigm experiments; E.R.S. and S.L.N. provided essential M-CSFR and PU.1-deficient haematopoietic cells. N.M.-K. and S.S. contributed equally to the study. N.M.-K., S.S., P.K.K., L.E. and M.H.S. jointly designed experiments and S.S. and M.H.S. coordinated the project.

Author Information Reprints and permissions information is available at www.nature.com/reprints. The authors declare no competing financial interests. Readers are welcome to comment on the online version of the paper. Correspondence and requests for materials should be addressed to M.H.S. (sieweke@ciml.univ-mrs.fr) or S.S. (sarrazin@ciml.univ-mrs.fr).

METHODS

Mice. CD45.1 and C57BL/6 mice were obtained from Charles River. *PU.1-GFP* (ref. 31), *M-CSFR^{-/-}* (ref. 27) and *PU.1^{fl/fl}* (ref. 32) mice have been described. Age- and sex-matched CD45.1 recipients that were reconstituted as described³ with CD45.2 fetal liver from wild-type or *M-CSFR^{-/-}* embryos²⁷ and *PU.1^{fl/fl}* or *PU.1^{fl/fl}::Mx-cre* bone marrow was used to isolate CD150⁺CD34⁻ KSLF HSCs not earlier than 8 weeks after reconstitution. For *in vivo* injections, the 10 µg per mouse M-CSF, 5 mg kg⁻¹ LPS (055:B5 *Escherichia coli*) or sorted cells were injected in 100 µl of PBS into the retro-orbital sinus. For HSC transplantation, 400 CD150⁺CD34⁻ KSLF HSCs were sorted from CD45.2 mice and mixed with 100,000 Lin⁺Sca⁻ CD45.1 carrier cells before injection into sub-lethally irradiated (4.5 Gy) CD45.1 recipient mice. For competitive transplantations, 1,300 CD150⁺CD34⁻ KSLF HSCs were isolated 16 h after control or 10 µg M-CSF injection from actin-GFP CD45.2 mice³³, mixed with equal numbers of CD45.2 competitor HSCs and injected with 300,000 Lin⁺Sca⁻ RC-lysed CD45.1 carrier cells into sub-lethally irradiated (4.5 Gy) CD45.1 recipients. Contribution to platelets, CD19⁺ B cells and CD11b⁺ myeloid cells was analysed after 4 and 6 weeks in the blood from mice with at least 5% GFP⁺ donor cells. For *PU.1* deletion, *PU.1^{fl/fl}* or *PU.1^{fl/fl}::Mx-cre* reconstituted mice were intraperitoneally injected with 5 µg g⁻¹ polyinosinic:polycytidylic acid 7 and 9 days before control (PBS) or 10 µg M-CSF injection. All mouse experiments were performed under specific pathogen-free conditions in accordance with institutional guidelines.

FACS analysis. For FACS sorting and analysis we used described staining protocols³ and published stem and progenitor cell definitions³⁴. FACSanto, LSRII and FACSARIAIII equipment and DIVA software (Becton Dickinson), analysing only populations with at least 200 events. For HSC analysis we used antibodies anti-CD34-FITC (clone RAM34, BD Biosciences), anti-CD135-PE (clone A2F10.1, BD Biosciences), anti-CD150-PE-Cy7 (clone TC15-12F12.2, Biolegend), anti-CD117-APC-H7 (clone 2B8, BD Biosciences), anti-Sca-1-PE-Cy5 (clone D7, Biolegend) and anti-CD48-APC (clone HM48-1, Biolegend). Diverging from this or in addition we used antibodies anti-CD34 Alexa 700 (clone RAM34, BD Biosciences), anti-CD16/32 PE (clone 2.4G2, BD biosciences), anti-CD11b PE-CF594 (clone M1/70, BD biosciences), anti-CD19-PE-Cy7 (clone 1D3, BD biosciences), anti-CD45.2 APC (clone 104, BD biosciences) and anti-CD45.1 Pacific blue (clone A20, BD biosciences) for progenitor and blood cell analysis. LIVE/DEAD Fixable Violet Dead cell dye (Invitrogen) was used as viability marker.

Intra-splenic injection of sorted HSCs and fluorescence microscopy. For analysis of HSCs *in vivo*, 1,500 to 7,000 FACS-sorted CD150⁺CD34⁻ KSLF HSCs were stained 10 min at 37 °C with 3 µM CFSE (Invitrogen) in PBS/0.5% BSA, washed 3× in PBS/0.5% BSA and injected in 30 µl PBS (containing or not 1 µg of isotype control or AFS98 anti-M-CSFR antibody²⁶ or 2 µM GW2580, 10 µM Ly29400, 10 µM PD98059 or 2 µM SU6656 inhibitors in 0.9% DMSO) into the spleen of anaesthetized mice. After 24 h spleens were embedded in OCT (Tissue-Tek, Sakura) and frozen at -80 °C. Cryostat sections (5 µm) were prepared from the entire organ, dried and fixed 10 min in 4% PFA/PBS at room temperature and every tenth section was further processed. After washes in PBS, slides were blocked for 1 h at room temperature in PBS/2% BSA/1% donkey serum/1% FCS/0.1% saponin, incubated for 36 h at 4 °C with anti-PU.1 polyclonal antibody (Santa Cruz) in PBS/0.05% saponin (1:50), washed and incubated with secondary Alexa 546-donkey-anti-rabbit antibody (Molecular probes) in PBS/0.05% saponin (1:500). All immunofluorescence samples were mounted with ProLong Gold DAPI antifade (Molecular probes) and analysed by multicolour fluorescence microscopy on a Zeiss AxioPlan 2. All CFSE⁺ cells were analysed for PU.1 expression up to ≥30 or ≥50 cells as indicated. Cell counts and staining were verified by a second trained microscope specialist blinded to sample identity. High-resolution photographs were obtained by confocal microscopy on a Leica SP5X.

In vitro culture of HSCs. CD150⁺CD34⁻ KSLF HSCs or CD150⁺CD34⁻CD48⁻ KSLF HSCs (single cells) were sorted into S-clone SF-03 medium (Sanko Jyunkaku) with 10% FBS supplemented with 100 U ml⁻¹ penicillin and 100 mg ml⁻¹ streptomycin (both Invitrogen) and cultivated in uncoated U-Shape 96-well plates (Greiner) in 100 µl SCM, 20 ng ml⁻¹ rSCF, 50 ng ml⁻¹ rTPO with or without 100 ng ml⁻¹ rM-CSF or 100 ng ml⁻¹ rGM-CSF or 100 ng ml⁻¹ rG-CSF. All cytokines were murine and from PeproTech. Cell viability was analysed by AnnexinV and Propidium iodide FACS staining³⁵.

Quantitative real-time PCR. Total RNA was isolated and reverse transcribed with µMACS One-step T7 template kit (Miltenyi Biotec) and analysed by quantitative real-time PCR using TaqMan Universal PCR Master Mix and a 7500 Fast Real Time PCR System sequence detection system (both Applied Biosystem), following the manufacturers' instructions.

Single-cell gene expression profiling. Single cells were sorted using the autoclone module on an AriaIII sorter (Becton Dickinson) directly into 96-well plates in the CellsDirect Reaction Mix (Invitrogen). Individual cell lysis, cDNA synthesis and amplification were performed according to Fluidigm Advanced Development Protocol, and single-cell microfluidic real-time PCR using Dynamic Array IFCs (Biomark Fluidigm) was performed by a technical support specialist of Fluidigm Inc. Pre-amplified products (22 cycles) were diluted fivefold before analysis with Universal PCR Master Mix and inventoried TaqMan gene expression assays (ABI) in 96.96 Dynamic Arrays on a BioMark System (Fluidigm). Ct values were calculated from the system's software (BioMark Real-time PCR Analysis; Fluidigm) and filtered according to a set of quality control rules outlined below.

Gene filter: (1) for each gene, including controls, data with CtCall = FAILED and CtQuality < threshold were removed. (2) For each gene, including controls, CtValues ≥ 32.0 were removed to filter out very low expression genes. (3) For each gene, including controls, genes with a difference of duplicate CtValues ≥ 2.0 were considered inconsistent and removed.

Sample filter: (1) if the control gene (*Gapdh*) was not expressed or was removed according to gene filters (1–3), the whole sample was removed. (2) If the mean of the Ct values of all genes in a row was ≥ 27.0 the whole sample row was removed.

Time-lapse imaging and analysis. Wherever possible our video microscopy protocols followed proposed guidelines²⁴. In detail, FACS-sorted CD150⁺CD34⁻ KSLF HSCs from wild-type C57BL/6 or GFP-negative CD150⁺CD34⁻ KSLF HSCs from *PU.1-GFP* reporter mouse³¹ bone marrow were suspended in SCM supplemented with 100 U ml⁻¹ penicillin and 100 mg ml⁻¹ streptomycin, 20 ng ml⁻¹ rSCF, 50 ng ml⁻¹ rTPO with or without 100 ng ml⁻¹ rM-CSF and plated in Ibidi µ-slidesVI(0.4) (Biovalley SA). Time-lapse microscopy was performed using a Cell Observer system (Carl Zeiss Microscopy) at 37 °C and 5% CO₂. Images were acquired every 10 min using 10× (A-plan 10x/0.45 Ph1) or 40× (Plan-Apochromat 40x/0.95 Korr M27) objectives in bright-field and fluorescence (GFP filters: EX BP 470/40; at 350 ms) with a CoolSNAP_{HQ2} monochrome camera (Photometrics) with a 2 × 2 binning and a metal halide 120 W source for fluorescence illumination. For image analysis a matrix of 4 × 4 images was acquired for each time point. Images were stitched with AxioVision software (Carl Zeiss Microscopy) and processed with Fiji software (<http://fiji.sc>) using a slight rolling ball subtraction of background and 1-pixel Gaussian blur. For background subtraction of bright-field images, the median of z-projection was subtracted from the time-lapse stack. Single-cell tracking was performed with basic commands of ImageJ (<http://imagej.nih.gov/ij/>) and Fiji (<http://fiji.sc>) software and with specific tracking plugin MTrackJ³⁶ in manual mode. Each cell was tracked manually frame-by-frame in the bright-field channel and cross-controlled by two microscope specialists. Cells with non-standard morphology or size were rejected. The fluorescence signal was measured as the difference of maximum minus minimum intensity within a defined region of interest (ROI) around each cell. Cell properties and behaviour (cell division, cell death, position, fluorescence increase) were manually documented to build cumulated curves. R³⁷ and Excel (Microsoft Corporation) software was used to manage data and build graphics.

- Back, J., Dierich, A., Bronn, C., Kastner, P. & Chan, S. PU.1 determines the self-renewal capacity of erythroid progenitor cells. *Blood* **103**, 3615–3623 (2004).
- Dakic, A. *et al.* PU.1 regulates the commitment of adult hematopoietic progenitors and restricts granulopoiesis. *J. Exp. Med.* **201**, 1487–1502 (2005).
- Okabe, M., Ikawa, M., Kominami, K., Nakanishi, T. & Nishimune, Y. 'Green mice' as a source of ubiquitous green cells. *FEBS Lett.* **407**, 313–319 (1997).
- Bryder, D., Rossi, D. J. & Weissman, I. L. Hematopoietic stem cells: the paradigmatic tissue-specific stem cell. *Am. J. Pathol.* **169**, 338–346 (2006).
- Niu, C. *et al.* c-Myc is a target of RNA-binding motif protein 15 in the regulation of adult hematopoietic stem cell and megakaryocyte development. *Blood* **114**, 2087–2096 (2009).
- Meijering, E., Dzyubachyk, O. & Smal, I. Methods for cell and particle tracking. *Methods Enzymol.* **504**, 183–200 (2012).
- R Development Core Team. *R: A Language and Environment for Statistical Computing* (R Foundation for Statistical Computing, 2012).

A role for the Perlman syndrome exonuclease Dis3l2 in the Lin28–let–7 pathway

Hao-Ming Chang^{1,2,3}, Robinson Triboulet^{1,2,3}, James E. Thornton^{1,2,3} & Richard I. Gregory^{1,2,3}

The pluripotency factor Lin28 blocks the expression of let-7 microRNAs in undifferentiated cells during development, and functions as an oncogene in a subset of cancers¹. Lin28 binds to let-7 precursor (pre-let-7) RNAs and recruits 3' terminal uridylyl transferases to selectively inhibit let-7 biogenesis^{2–4}. Uridylated pre-let-7 is refractory to processing by Dicer, and is rapidly degraded by an unknown RNase⁵. Here we identify Dis3l2 as the 3'–5' exonuclease responsible for the decay of uridylated pre-let-7 in mouse embryonic stem cells. Biochemical reconstitution assays show that 3' oligouridylation stimulates Dis3l2 activity *in vitro*, and knock-down of Dis3l2 in mouse embryonic stem cells leads to the stabilization of pre-let-7. Our study establishes 3' oligouridylation as an RNA decay signal for Dis3l2, and identifies the first physiological RNA substrate of this new exonuclease, which is mutated in the Perlman syndrome of fetal overgrowth and causes a predisposition to Wilms' tumour development⁶.

Post-transcriptional gene regulation by microRNAs (miRNAs) affects many developmental and physiological processes. Functioning by base-pairing with target messenger RNAs of complementary sequence, these ~22-nucleotide RNAs recruit the miRNA-induced silencing complex for translational repression and mRNA decay. Of particular relevance is the ancient let-7 family of miRNAs that is essential for normal development of *Caenorhabditis elegans*. Loss of the tumour suppressor function of the let-7 family affects various human cancers⁷. Expression of let-7 is dynamically regulated during development by the paralogous RNA-binding proteins Lin28A and Lin28B (refs 5, 8–10). Lin28 was identified as a regulator of developmental timing in worms, and has more recently been linked in mammals with controlling developmental timing and growth, as well as maintaining glucose homeostasis^{1,11–13}. Lin28 is a pluripotency factor in stem cells, in which its expression helps to maintain an undifferentiated and proliferative state by blocking let-7 expression^{14,15}. The Lin28–let-7 pathway is normally silenced in adult somatic cells, yet the expression of LIN28A or LIN28B is associated with a wide variety of human cancers^{16,17}. Inhibition of this oncogenic pathway blocks the tumorigenicity of cancer cells¹⁶.

Recent work has provided insight into the mechanisms underlying the Lin28-mediated selective regulation of let-7 (ref. 18). Lin28A functions in the cell cytoplasm, where it recruits the 3' terminal uridylyl transferase (TUTase) Zcchc11 (also known as TUT4) or Zcchc6 (TUT7), which adds an oligouridine tail to pre-let-7 to inhibit Dicer processing and serves as a signal for the rapid decay of the uridylated RNA by an unknown nuclease^{2–5,16}. We sought to identify the downstream nuclease(s), and used a biochemical approach to isolate factors that specifically associate with uridylated pre-let-7 (Fig. 1a, Supplementary Fig. 1 and Supplementary Table 1). This analysis showed that Lin28A and Zcchc11 were associated with both pre-let-7a-1 and uridylated pre-let-7a-1 (pre-let-7+14U), whereas Dis3l2, a 3'–5' exonuclease, was specifically detected in the pre-let-7a-1+14U purification⁶ (Fig. 1b). These mass spectrometry data were confirmed by western blot (Fig. 1c). Co-immunoprecipitation assays using a mouse embryonic stem-cell (ESC) line expressing a doxycycline (Dox)-inducible

Flag–Lin28A transgene showed that Zcchc11, Zcchc6 and Dis3l2 are detectable by western blot in the Flag–Lin28A affinity eluate (Fig. 1d). Additional co-immunoprecipitation with Flag–TRBP, a cytoplasmic miRNA-binding protein highly expressed in ESCs, confirmed the specificity of the Dis3l2 association with Lin28A (refs 15, 19) (Fig. 1e). To address whether this association is mediated through RNA, we performed further co-immunoprecipitation assays using either wild-type Lin28A or a mutant Lin28A (Lin28A(Trp46Ala)) that exhibits compromised RNA-binding activity towards pre-let-7 (ref. 18). We found less Dis3l2 associated with mutant Lin28A, and this association is strongly reduced after RNase A treatment (Fig. 1f). Overall, these results indicate that Lin28A associates with Dis3l2 in an RNA-dependent manner, and implicate Dis3l2 as a possible nuclease in the Lin28–let-7 pathway.

We next cloned and sequenced *Dis3l2* complementary DNA from mouse V6.5 ESCs. *Dis3l2.2* was confirmed as the major transcript variant expressed in V6.5 mouse ESCs that encodes an 870-amino-acid protein (Fig. 1b and Supplementary Fig. 2). Because pre-let-7 degradation occurs in the cell cytoplasm, we next examined the sub-cellular localization of Dis3l2 in ESCs (Supplementary Fig. 3). Dis3l2 was found to localize primarily to the cytoplasm of V6.5 ESCs, consistent with other cell types⁶.

We carried out RNA degradation assays using affinity-purified Flag–Dis3l2. Dis3l2 was found to degrade pre-let-7+14U preferentially compared with pre-let-7 or an unrelated pre-miR-21 (Fig. 2a). To rule out the possibility that this observed activity was due to a co-purifying nuclease in the Flag–Dis3l2 immunoprecipitate, we generated a mutant Dis3l2-expressing construct by replacing a conserved residue in the catalytic domain (Asp389Asn) (Fig. 1b). Mutation of the equivalent aspartic acid in yeast Dis3(Asp551Asn) abolishes exonuclease activity without interfering with RNA binding²⁰. Indeed, Dis3l2(Asp389Asn) displayed no activity, whereas wild-type Dis3l2 displayed preferential activity towards pre-let-7+14U (Fig. 2b, c).

Next, to determine whether Dis3l2 is sufficient for the selective degradation of uridylated pre-let-7, we generated recombinant Dis3l2 (rDis3l2) protein in *Escherichia coli* (Fig. 2d). Although the activity of rDis3l2 was lower than that of the affinity-purified Flag–Dis3l2 complexes, we observed a similar preference for pre-let-7+14U compared with pre-let-7 using the rDis3l2 protein (Fig. 2e, f). To rule out the possibility that this observed activity was due to a bacterial nuclease that might co-purify with histidine-tagged Dis3l2 (His–Dis3l2), we generated a mutant (Asp389Asn) rDis3l2 and confirmed that this catalytic mutant displayed no RNase activity in these assays (Supplementary Fig. 4a). Considering that uridylated pre-let-7 was previously found to be associated with isolated Flag–Lin28A complexes, together with our co-immunoprecipitation data, we next explored whether Lin28A protein influenced Dis3l2 activity *in vitro*⁵. This analysis showed that Lin28A had no effect on Dis3l2 activity (Supplementary Fig. 5). Next, to measure the substrate preference of Dis3l2 for uridylated pre-let-7 quantitatively, we performed time course experiments with rDis3l2. These showed a strong preference for the

¹Stem Cell Program, Boston Children's Hospital, Massachusetts 02115, USA. ²Department of Biological Chemistry and Molecular Pharmacology, Harvard Medical School, Boston, Massachusetts 02115, USA. ³Harvard Stem Cell Institute, Boston, Massachusetts 02115, USA.

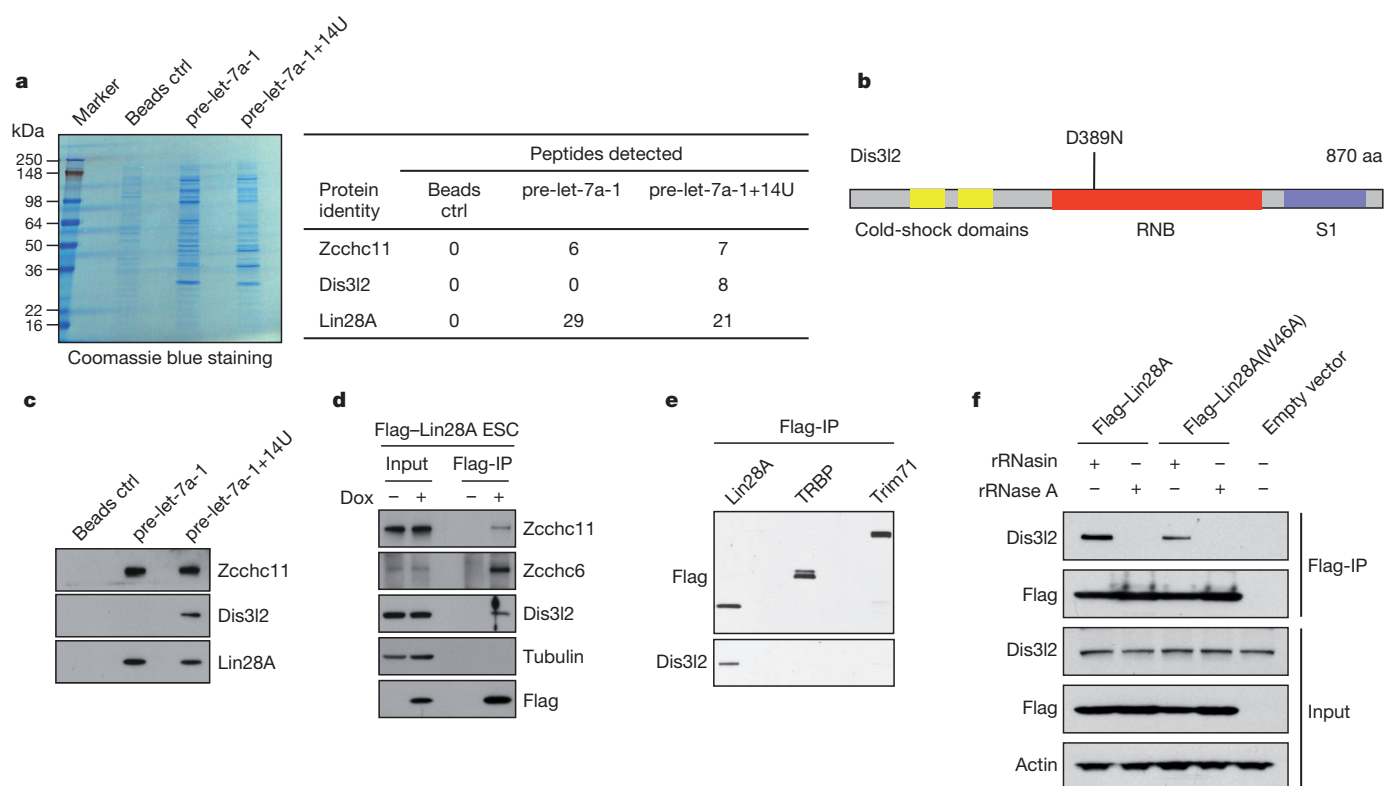


Figure 1 | Dis3l2 is associated with uridylated pre-let-7. **a**, Affinity-purified proteins analysed by Coomassie blue staining and mass spectrometry. Ctrl, control. **b**, Diagrammatic representation of Dis3l2 protein (NCBI accession number NP_705758.1). Cold-shock domains, ribonuclease II domain (RNB)

and S1 RNA-binding domain are indicated. The mutated catalytic Asp is indicated. aa, amino acids. **c**, Western blotting analysis of samples in **a** with indicated antibodies. **d–f**, Co-immunoprecipitation (IP) and western blot analyses. rRNasin, RNase inhibitor.

degradation of uridylated pre-let-7 compared to pre-let-7, with a more than tenfold difference in the relative RNA stability in these assays (Fig. 2g, h). Altogether, these results show that purified rDis3l2 preferentially degrades uridylated pre-let-7 *in vitro*, and that the oligouridine tail serves as a decay signal for this RNase.

To explore further the functional relationship between Lin28A, TUTase and Dis3l2-mediated RNA degradation, we next performed *in vitro* reconstitution assays. We showed previously that Lin28A enhances the uridylation activity of Zcchc11 towards pre-let-7. In these assays TUTase activity was measured by the incorporation of radiolabelled UTP^{3,4,16}. However, owing to a limiting UTP concentration, the oligouridine tails added in these reactions are short, comprising only a few nucleotides. Supplementing such reactions with additional (non-radiolabelled) UTP leads to the generation of longer uridine tails (Fig. 3a, compare lanes 1, 2 and 3). Notably, the addition of Dis3l2 leads to the selective degradation of the pre-let-7 with longer uridine tails (Fig. 3a). These data define the minimal set of proteins and enzymes required to recapitulate the selective degradation of pre-let-7 observed *in vivo*, and raise questions about uridine tail-length requirements to stimulate Dis3l2-mediated degradation. To address this we prepared a panel of pre-let-7 RNA substrates with varying uridine tail lengths and monitored Dis3l2 degradation activity. Tails of at least 10 uridines were found to stimulate Dis3l2 activity, with maximal stimulation observed with uridine tails of 14 or greater (Fig. 3b). This result is consistent with the average length of the uridine tail found on pre-let-7 RNAs cloned and sequenced from Lin28-expressing cells⁵.

To examine the Dis3l2 domain requirements, we generated three deletion mutants lacking the amino terminus, the carboxy terminus, or both the N- and C-terminal regions (Fig. 3c). RNA degradation assays and electromobility shift assays (EMSAs) revealed that truncation of either the N- or the C-terminal region abrogated both Dis3l2 binding and nuclease activities on uridylated pre-let-7 RNA (Fig. 3d, e). This suggests that both the cold-shock domains and the S1 domain are

required for binding to uridylated pre-let-7. Although the catalytic mutant (Asp389Asn) Dis3l2 was inactive in RNA degradation assays, it retained the ability to bind to uridylated pre-let-7 selectively (Fig. 3e and Supplementary Fig. 4b). RNA degradation and binding assays using an unrelated RNA, pre-miR-21 with or without 14 uridines, established the sufficiency of an oligouridine tail to serve as a signal to trigger Dis3l2-mediated decay (Supplementary Fig. 4c, d).

To examine the role of Dis3l2 in the let-7 pathway, we used short interfering RNAs (siRNAs) to deplete Lin28A, Zcchc11 or Dis3l2 expression in mouse ESCs. We also included siRNAs that target the related family member Dis3l1 (Fig. 4a, b). We monitored the effects of gene knockdown on mature miRNA expression by quantitative reverse transcriptase PCR (qRT-PCR) and northern blot (Fig. 4c, d). Whereas Lin28A knockdown caused the expected accumulation of multiple let-7 miRNAs, knockdown of Dis3l2 or Dis3l1 had no effect. We did, however, observe a modest increase in let-7 expression in the Zcchc11-depleted samples, as previously reported^{3–5}. Uridylated pre-let-7 has been previously shown to be resistant to cleavage by affinity-purified Dicer complexes, and consistently we found pre-let-7+14U to be a poor substrate for recombinant Dicer in processing assays. By comparison, pre-let-7 was processed by Dicer to ~22-nucleotide duplexes (Fig. 4e). Because pre-let-7+14U is inefficiently processed by Dicer, we postulated that knockdown of Dis3l2 in cells could lead to accumulation of uridylated pre-let-7 without affecting levels of mature let-7. To test this we developed a sensitive qRT-PCR-based assay for the specific detection of uridylated pre-let-7. We used an oligo(dA) primer for the reverse transcriptase first-strand cDNA synthesis step, and used primers complementary to pre-let-7 for the detection of uridylated pre-let-7 by quantitative PCR. This approach allowed us to detect uridylated pre-let-7 specifically (Supplementary Fig. 6a). RNA from the knockdown samples was size fractionated to measure relative levels of uridylated pre-let-7 in the <200-nucleotide fraction and the corresponding primary let-7 (pri-let-7) transcripts in the large

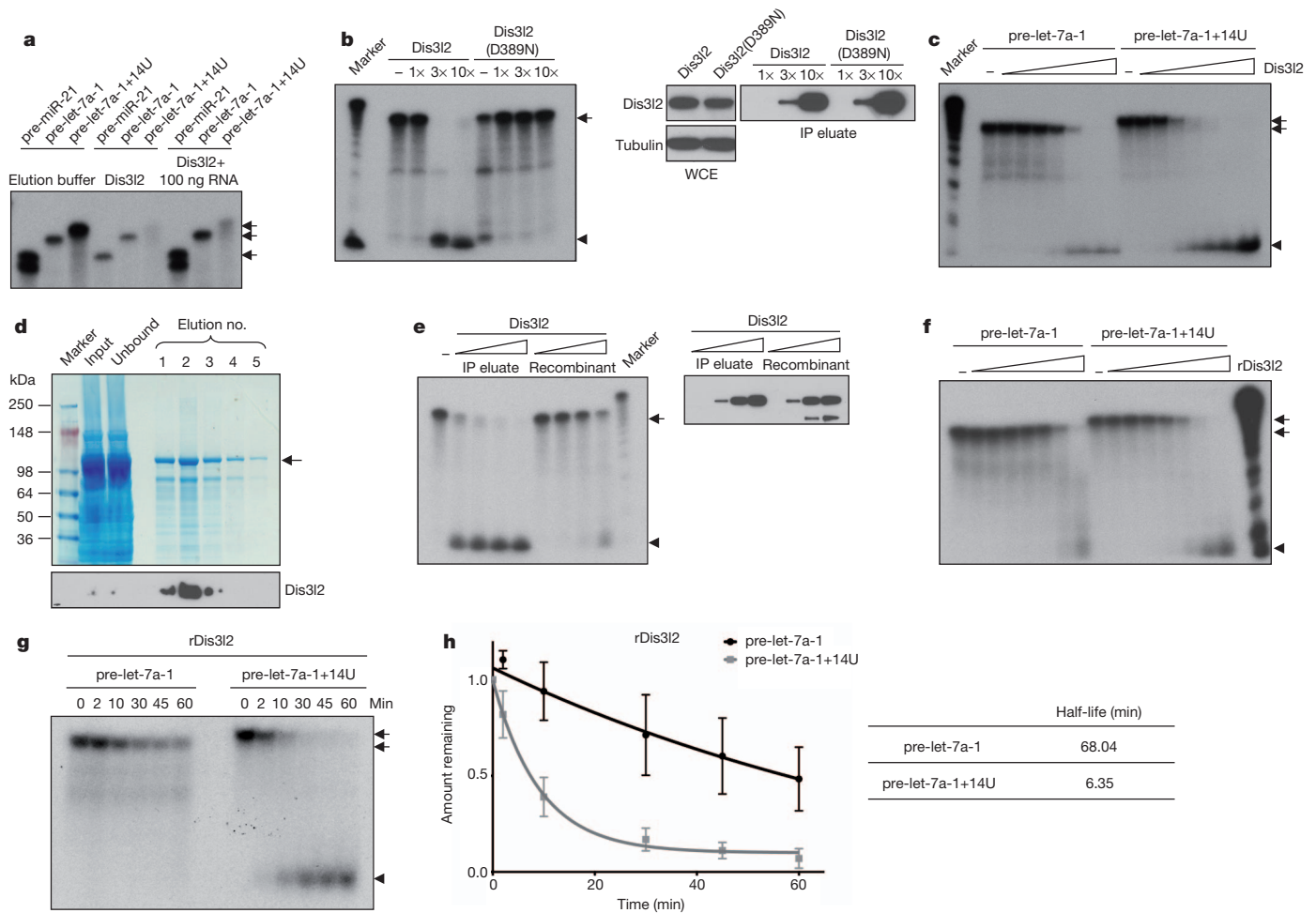


Figure 2 | Dis3l2 preferentially degrades uridylated pre-let-7. **a**, RNA degradation assay with Flag-Dis3l2 incubated with different radiolabelled pre-miRNAs. Where indicated, 100 ng competitor RNA was added to reduce background activity. **b**, RNA degradation assay with Flag-tagged Dis3l2 or mutant Dis3l2 (Dis3l2(D389N)) incubated with pre-let-7a-1+14U. WCE, whole-cell extract. **c**, RNA degradation assay with a titration of Flag-Dis3l2. **d**, His-Dis3l2 examined by Coomassie blue staining and western blot.

e, Flag-Dis3l2 and His-Dis3l2 analysed by western blot and examined for activity. **f**, RNA degradation assay with a titration of His-Dis3l2. **g**, Representative time course assay. **h**, Quantification of three independent experiments as in **g** with the corresponding calculated RNA half-lives. $P < 0.01$ (two-way analysis of variance (ANOVA) test). The error bars represent the s.d. calculated from three independent experiments. In all relevant panels, arrows indicate radiolabelled pre-miRNA, arrowheads indicate degradation products.

>200-nucleotide fraction. This revealed the specific accumulation of uridylated pre-let-7a-1 and pre-let-7g after Dis3l2 knockdown (Fig. 4f), whereas levels of the corresponding pri-let-7 transcripts were unchanged (Fig. 4g). PCR products were cloned and sequenced to confirm the specificity of this assay (Supplementary Fig. 6b, c). Similar results were found using stable Dis3l2 knockdown ESCs (Supplementary Fig. 7a–e). To confirm further the role of Dis3l2 in the regulation of uridylated pre-let-7 levels, we performed northern blot assays using a probe complementary to the terminal loop region of let-7g. This revealed a slower-migrating pre-let-7 band after Dis3l2 depletion that probably corresponds to oligouridylated pre-let-7 (Fig. 4h, i). Finally, we individually depleted two additional 3′–5′ exonucleases, Exosc10 (also known as RRP6) and Rps44 (Dis3), from ESCs and measured the relative uridylated pre-let-7 levels by qRT-PCR. Knockdown of these exosome-associated nucleases did not affect uridylated pre-let-7 levels (Supplementary Fig. 8). These results provide strong support that Dis3l2 is the downstream nuclease that mediates the decay of uridylated pre-let-7 in the Lin28 pathway.

Our results identify Dis3l2 as a new component of the Lin28–let-7 pathway, and as the downstream nuclease responsible for the decay of uridylated pre-let-7 (Supplementary Fig. 9). This contention is based on the following. First, Dis3l2 specifically associates with uridylated pre-let-7 in RNA affinity purifications and is detected as a component

of a Lin28A-containing ribonucleoprotein complex(es). Second, purified Dis3l2 (but not catalytically inactive mutant Dis3l2) complexes display substrate preference for uridylated pre-let-7 in RNA degradation assays *in vitro*. Third, *in vitro* reconstitution experiments with recombinant Dis3l2 reveal the sufficiency of this enzyme for the preferential degradation of uridylated pre-let-7. Last, knockdown of Dis3l2 causes the accumulation of uridylated pre-let-7 in mouse ESCs.

Dis3l2 belongs to a family of related 3′–5′ exonucleases with similar domain organization to bacterial RNase II (refs 6, 21–23). Notably, germline mutations in the human *DIS3L2* gene were recently found to be responsible for Perlman syndrome, a rare, autosomal recessive, fetal overgrowth syndrome⁶. In addition to being large, affected individuals are hypotonic, have organomegaly, characteristic facial dysmorphism, renal abnormalities, neurodevelopmental problems, and a markedly high susceptibility to Wilms' tumours (nephroblastoma), with >60% of surviving children developing Wilms' tumours. Moreover, *DIS3L2* was found to be mutated in ~30% of sporadic Wilms' tumours analysed⁶. It will be important to explain the role of *DIS3L2* in the genesis and development of Perlman syndrome and Wilms' tumours, and future experiments with knockout mouse models will shed light on this question. Our work uncovers the first, to our knowledge, physiological RNA substrate of Dis3l2. Considering the similarities between the disease phenotypes associated with Dis3l2 deletion and those caused

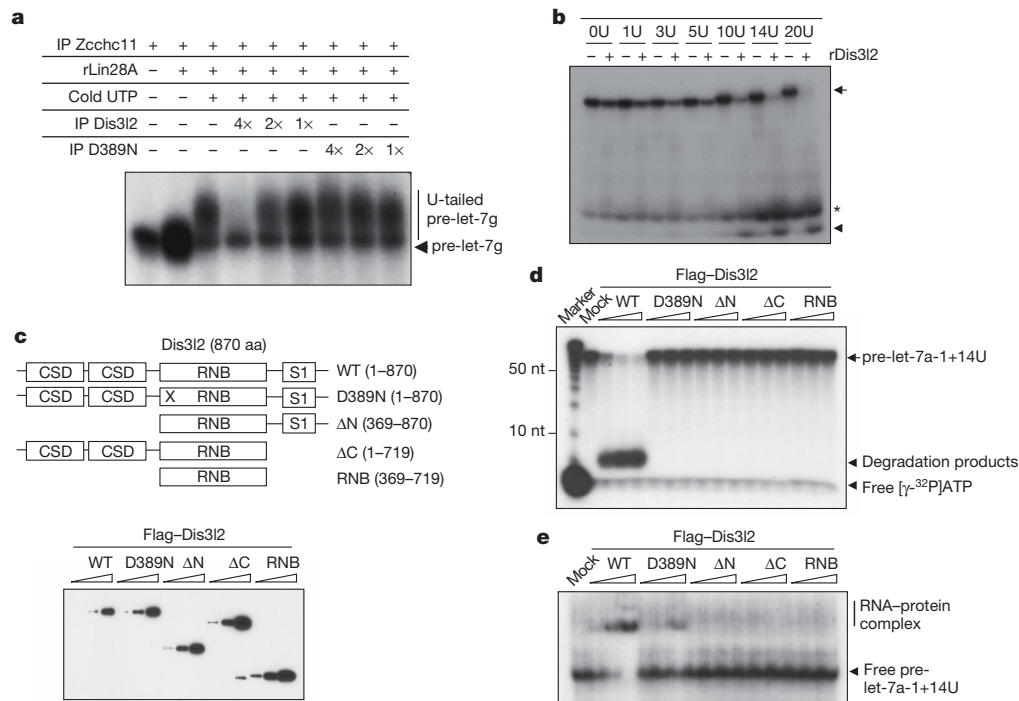


Figure 3 | Molecular determinants of Dis3l2 activity. **a**, Reconstitution assays reveal longer uridine tails are preferred substrates for Dis3l2. **b**, RNA degradation assays using *in vitro* transcribed pre-let-7 RNAs with indicated 3' uridine (U) tail. Asterisk denotes nonspecific background RNA. **c–e**, Schematic representation and western blot of different Dis3l2 truncations (**c**) used for RNA degradation assays (**d**) and EMSAs (**e**). CSD, cold-shock domain; nt, nucleotide. Arrows and arrowheads are as in Fig. 2.

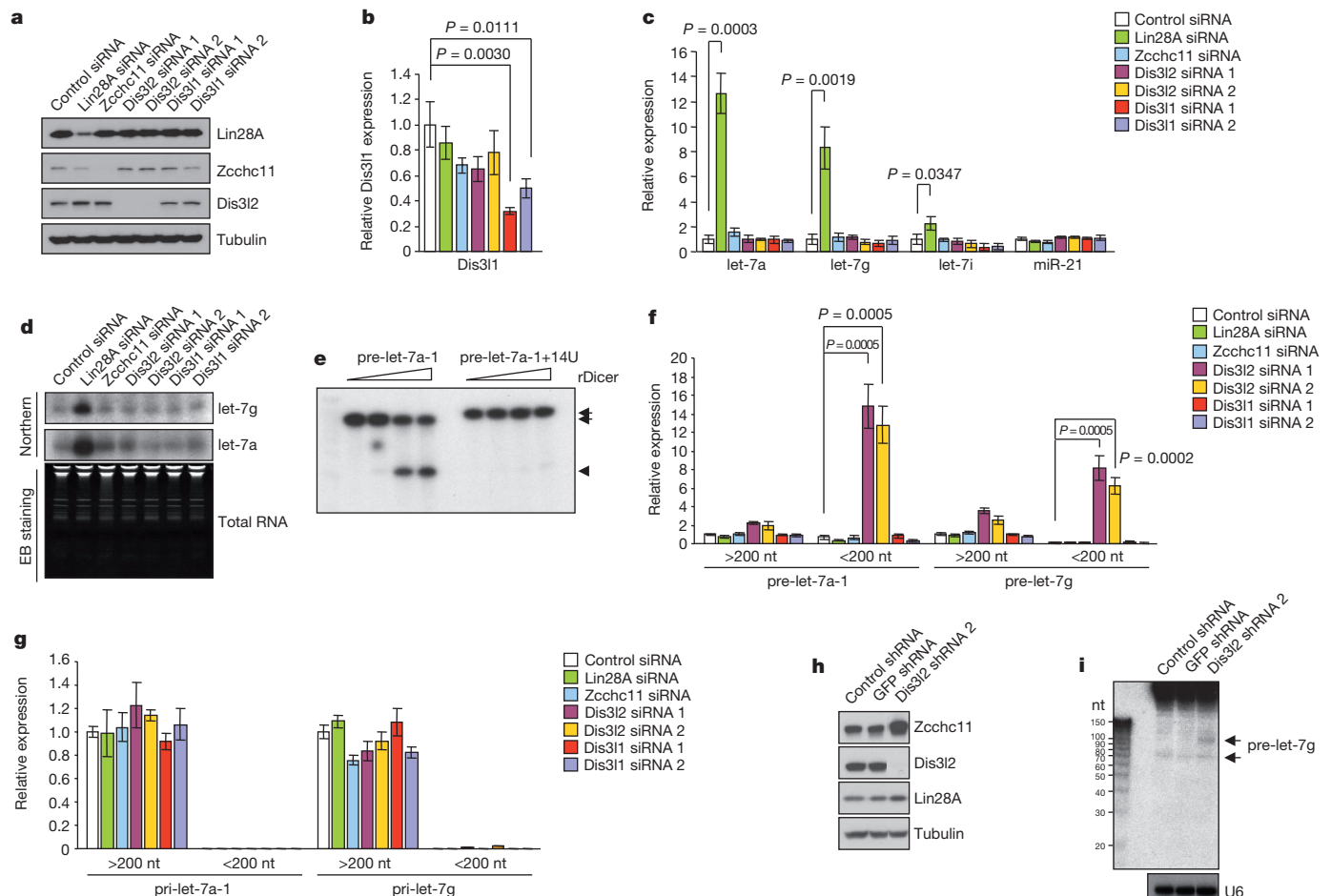


Figure 4 | Dis3l2 is required for degradation of uridylated pre-let-7 in ESCs. **a**, Western blot analysis of siRNA knockdowns. **b**, qRT-PCR analysis of Dis3l1 knockdown. Error bars denote s.d. ($n = 3$). **c**, Mature miRNA levels measured by qRT-PCR. Error bars denote s.d. ($n = 3$). **d**, Northern blot. EB, ethidium bromide. **e**, Dicer processing assay, with arrows indicating pre-miRNA and

arrowhead indicating Dicer products. **f**, **g**, Total RNA from the samples in **a** was fractionated into >200-nucleotide- and <200-nucleotide-long RNA, and relative levels of uridylated pre-let-7 (**f**) or pri-let-7 (**g**) RNA were quantified by qRT-PCR. Error bars denote s.d. ($n = 3$). **h**, Western blot analysis of Dis3l2 cells. **i**, Northern blot analysis of pre-let-7g.

by Lin28 gain of function (that is, overgrowth and tumorigenesis), it is tempting to speculate that this new role of Dis3l2 in the Lin28–let-7 pathway is relevant to Perlman syndrome and cancer.

Our identification of a decay pathway for uridylated RNAs raises questions about how widespread this type of regulation might be on a transcriptome scale, as well as the mechanism by which oligouridylation promotes Dis3l2 ribonucleolytic activity. So far, there are few known examples in which 3' uridylation can serve as a decay signal; these include histone mRNA regulation during the mammalian cell cycle, and the widespread uridylation-dependent mRNA decapping and decay in *Schizosaccharomyces pombe*^{24–26}. Similarly, in *Saccharomyces cerevisiae*, the Trf4/Air2/Mtr4 polyadenylation (TRAMP) complex catalyses the addition of an oligoadenine tail that promotes 3'–5' RNA decay by the exosome as part of a nuclear RNA surveillance mechanism^{27,28}. In the case of pre-let-7, the 3' oligouridylation has two consequences: to block Dicer processing, and to stimulate decay by Dis3l2. This two-step mechanism safeguards against the production of mature let-7 miRNA.

Note added in proof: Notably, the *S. pombe* Dis3l2 homologue displays preference for degradation of uridylated RNAs *in vitro*, and its deletion leads to accumulation of uridylated mRNAs, indicating that this regulatory pathway is more widespread (ref. 29).

METHODS SUMMARY

Affinity pull-down assays. Synthetic pre-let-7a-1 or pre-let-7a-1+14U was conjugated to agarose beads and incubated with whole-cell extract from P19 cells. Affinity eluate was subjected to SDS–PAGE and Coomassie blue staining. Bands were excised and subjected to mass spectrometric sequencing. Protein complexes were affinity-purified using anti-Flag M2 agarose beads (Sigma).

Plasmids and cDNA cloning. Dis3l2 cDNA was cloned into pFlag-CMV2 (Sigma). Dis3l2(Asp389Asn) was generated by site-directed mutagenesis. cDNA was subcloned into pETDuet-1 for His-tagged Dis3l2 expression.

Recombinant Dis3l2 protein purification. Ni-NTA beads were used for the purification of His–Dis3l2 from IPTG (isopropyl-β-D-thiogalactoside)-induced BL21–CodonPlus competent bacteria (Stratagene).

RNA degradation assays. RNA degradation assays were performed using either 5'-end-labelled synthetic pre-miRNA or internally labelled *in vitro* transcribed pre-miRNA, together with Dis3l2 in RNA degradation buffer, and incubated at 37 °C.

RNA EMSAs. EMSA experiments were performed as described previously¹⁶. Nucleoprotein complexes were resolved by 4–20% non-denaturing TBE gel electrophoresis and visualized by autoradiography.

Transfections and siRNA/short hairpin RNA knockdowns. All transfections were performed with Lipofectamine 2000 (Invitrogen) as per manufacturer's instructions. Lentivirus production, infection and stable cell selection are as described¹⁷.

qRT–PCR. RNA was isolated using TRIzol reagent (Invitrogen) and size fractionated using mirVana miRNA isolation kit (Ambion). For detection of uridylated pre-miRNA, size-fractionated RNA (<200-nucleotide RNA fraction) was treated with DNase then reverse transcribed using oligo(dA)₁₂ primer and SuperScript III (Invitrogen). qPCR was performed using iQ SYBR Green Supermix (Bio-Rad).

Northern blotting. Ten micrograms of total RNA from each sample was used for northern blotting, as previously described¹⁹.

Dicer assays. Recombinant Flag–Dicer protein was purified from insect cells as previously described¹⁹.

Full Methods and any associated references are available in the online version of the paper.

Received 17 October 2012; accepted 26 March 2013.

Published online 17 April 2013.

1. Thornton, J. E. & Gregory, R. I. How does Lin28 let-7 control development and disease? *Trends Cell Biol.* **22**, 474–482 (2012).
2. Heo, I. *et al.* TUT4 in concert with Lin28 suppresses microRNA biogenesis through pre-microRNA uridylation. *Cell* **138**, 696–708 (2009).
3. Hagan, J. P., Piskounova, E. & Gregory, R. I. Lin28 recruits the TUTase Zcchc11 to inhibit let-7 maturation in mouse embryonic stem cells. *Nature Struct. Mol. Biol.* **16**, 1021–1025 (2009).

4. Thornton, J. E., Chang, H. M., Piskounova, E. & Gregory, R. I. Lin28-mediated control of let-7 microRNA expression by alternative TUTases Zcchc11 (TUT4) and Zcchc6 (TUT7). *RNA* **18**, 1875–1885 (2012).
5. Heo, I. *et al.* Lin28 mediates the terminal uridylation of let-7 precursor microRNA. *Mol. Cell* **32**, 276–284 (2008).
6. Astuti, D. *et al.* Germline mutations in *DIS3L2* cause the Perlman syndrome of overgrowth and Wilms tumor susceptibility. *Nature Genet.* **44**, 277–284 (2012).
7. Roush, S. & Slack, F. J. The let-7 family of microRNAs. *Trends Cell Biol.* **18**, 505–516 (2008).
8. Viswanathan, S. R., Daley, G. Q. & Gregory, R. I. Selective blockade of microRNA processing by Lin28. *Science* **320**, 97–100 (2008).
9. Newman, M. A., Thomson, J. M. & Hammond, S. M. Lin-28 interaction with the Let-7 precursor loop mediates regulated microRNA processing. *RNA* **14**, 1539–1549 (2008).
10. Rybak, A. *et al.* A feedback loop comprising *lin-28* and *let-7* controls pre-let-7 maturation during neural stem-cell commitment. *Nature Cell Biol.* **10**, 987–993 (2008).
11. Ambros, V. & Horvitz, H. R. Heterochronic mutants of the nematode *Caenorhabditis elegans*. *Science* **226**, 409–416 (1984).
12. Zhu, H. *et al.* *Lin28a* transgenic mice manifest size and puberty phenotypes identified in human genetic association studies. *Nature Genet.* **42**, 626–630 (2010).
13. Zhu, H. *et al.* The *Lin28/let-7* axis regulates glucose metabolism. *Cell* **147**, 81–94 (2011).
14. Yu, J. *et al.* Induced pluripotent stem cell lines derived from human somatic cells. *Science* **318**, 1917–1920 (2007).
15. Chang, H. M. *et al.* Trim71 cooperates with microRNAs to repress *Cdkn1a* expression and promote embryonic stem cell proliferation. *Nature Commun.* **3**, 923 (2012).
16. Piskounova, E. *et al.* Lin28A and Lin28B inhibit let-7 microRNA biogenesis by distinct mechanisms. *Cell* **147**, 1066–1079 (2011).
17. Viswanathan, S. R. *et al.* Lin28 promotes transformation and is associated with advanced human malignancies. *Nature Genet.* **41**, 843–848 (2009).
18. Nam, Y., Chen, C., Gregory, R. I., Chou, J. J. & Sliz, P. Molecular basis for interaction of let-7 microRNAs with Lin28. *Cell* **147**, 1080–1091 (2011).
19. Chendrimada, T. P. *et al.* TRBP recruits the Dicer complex to Ago2 for microRNA processing and gene silencing. *Nature* **436**, 740–744 (2005).
20. Dziembowski, A., Lorentzen, E., Conti, E. & Seraphin, B. A single subunit, Dis3, is essentially responsible for yeast exosome core activity. *Nature Struct. Mol. Biol.* **14**, 15–22 (2007).
21. Tomecki, R. *et al.* The human core exosome interacts with differentially localized processive RNases: hDIS3 and hDIS3L. *EMBO J.* **29**, 2342–2357 (2010).
22. Staals, R. H. *et al.* Dis3-like 1: a novel exoribonuclease associated with the human exosome. *EMBO J.* **29**, 2358–2367 (2010).
23. Frazão, C. *et al.* Unravelling the dynamics of RNA degradation by ribonuclease II and its RNA-bound complex. *Nature* **443**, 110–114 (2006).
24. Mullen, T. E. & Marzluff, W. F. Degradation of histone mRNA requires oligouridylation followed by decapping and simultaneous degradation of the mRNA both 5' to 3' and 3' to 5'. *Genes Dev.* **22**, 50–65 (2008).
25. Norbury, C. J. 3' Uridylation and the regulation of RNA function in the cytoplasm. *Biochem. Soc. Trans.* **38**, 1150–1153 (2010).
26. Rissland, O. S. & Norbury, C. J. Decapping is preceded by 3' uridylation in a novel pathway of bulk mRNA turnover. *Nature Struct. Mol. Biol.* **16**, 616–623 (2009).
27. LaCava, J. *et al.* RNA degradation by the exosome is promoted by a nuclear polyadenylation complex. *Cell* **121**, 713–724 (2005).
28. Wyers, F. *et al.* Cryptic pol II transcripts are degraded by a nuclear quality control pathway involving a new poly(A) polymerase. *Cell* **121**, 725–737 (2005).
29. Malecki, M. *et al.* The exoribonuclease Dis3L2 defines a novel eukaryotic RNA degradation pathway. *EMBO J.* <http://dx.doi.org/10.1038/emboj.2013.63> (15 Mar, 2013).

Supplementary Information is available in the online version of the paper.

Acknowledgements We thank R. LaPierre for technical assistance and F.-L. Meng for Rrp44 and Exosc10 shRNA. Thanks to the Children's Hospital Boston/IDRC Proteomics Core for mass spectrometry. R.I.G. was supported by grants from the US National Institute of General Medical Sciences (NIGMS) (R01GM086386) and The American Cancer Society (121635-RSG-11-175-01-RMC). J.E.T. was supported by a pre-doctoral fellowship from the National Science Foundation. R.T. was supported by the Wolbach fellowship from Boston Children's Hospital.

Author Contributions H.-M.C. designed and performed most of the experiments in Figs 1 and 2, and all of the experiments in Fig. 4. H.-M.C., R.T. and J.E.T. designed and performed experiments in Figs 1–3, as well as the Supplementary Figs. R.I.G. and H.-M.C. wrote the paper with input from R.T. and J.E.T.

Author Information Reprints and permissions information is available at www.nature.com/reprints. The authors declare no competing financial interests. Readers are welcome to comment on the online version of the paper. Correspondence and requests for materials should be addressed to R.I.G. (rgregory@enders.tch.harvard.edu).

METHODS

Cell culture. HEK293 cells were maintained in DMEM, P19 cells in MEM α plus GlutaMax-1, and V6.5 and KH2 ESCs in DMEM with ESGRO (1,000 U ml⁻¹), supplemented with antibiotics, and 10% (for HEK293, P19) or 15% (for ESCs) FBS. A Dox-inducible Flag–Lin28A ESC line was used^{3,12}. The MISSION short hairpin RNA (shRNA) plasmid DNA (Sigma; TRCN0000120760 for Dis3l2 shRNA 1, TRCN0000120761 for Dis3l2 shRNA 2, TRCN0000120745 for Dis3 shRNA, and TRCN0000123544 for Exosc10 shRNA) together with pLP1, pLP2 and VSVG were transfected into 293T cells to produce lentiviral particles that were used to infect V6.5 ESCs. The Dis3l2 shRNA stable cells were then created by puromycin (2.5 μ g ml⁻¹) selection.

Affinity pull-down assays. For RNA affinity pull-down, synthetic mmu-pre-let-7a-1 or mmu-pre-let-7a-1+14U was conjugated to adipic acid dihydrazide agarose beads and incubated with whole-cell extract from P19 cells⁸. The affinity eluate was subjected to SDS–PAGE followed by Coomassie blue staining using the colloidal blue staining kit (Life Technologies). Bands were excised, and subjected to mass spectrometric sequencing. The sequencing results were further confirmed by western blotting. For co-immunoprecipitation assays using mouse KH2 ESCs expressing the Dox-inducible Flag–Lin28A transgene, cells were treated with Dox at 6 μ g ml⁻¹ for 48 h and then collected in lysis buffer (20 mM Tris–HCl, pH 8.0, 137 mM NaCl, 1 mM EDTA, 1% (v/v) Triton X-100, 10% (v/v) glycerol, 1.5 mM MgCl₂, 1 mM dithiothreitol (DTT) and 0.2 mM PMSF (phenylmethylsulfonyl fluoride)) supplemented with 40 U ml⁻¹ of RNase inhibitor (RNASin, Promega). Protein complexes were affinity-purified using anti-Flag M2 agarose beads (Sigma). Beads were washed with lysis buffer seven times before elution with 0.5 mg ml⁻¹ Flag peptide. The eluates were analysed by SDS–PAGE and western blotting. For co-immunoprecipitation assays using ectopically expressed Flag–Lin28A, Flag–Lin28A(Trp46Ala), Flag–TRBP and Flag–Trim71, V6.5 ESCs were transfected using Lipofectamine 2000 (Invitrogen) and collected 48 h later. Cells were lysed as described above, except for the addition of RNase A (20 mg ml⁻¹ final; QIAGEN) where indicated.

Mass spectrometry. The mass spectrometric protein analysis was performed at the Proteomics Center at Boston Children's Hospital. Bands of interest were excised from the Coomassie-stained SDS–PAGE gel, washed with a 2:1 ratio of 100 mM ammonium bicarbonate/acetonitrile, reduced with 10 mM DTT at 56 °C for 45 min, and alkylated for 30 min at room temperature, in the dark, with 55 mM iodoacetamide. Samples were digested with sequencing grade trypsin (Promega) at a concentration of 12.5 ng μ l⁻¹ in 100 mM ammonium bicarbonate at 37 °C overnight. Peptides were extracted with 100 mM ammonium bicarbonate and acetonitrile, and then dried in a speedvac. Samples were resuspended in 5% acetonitrile and 5% formic acid before direct injection into the liquid chromatography–mass spectrometry (LC–MS) system comprising of a nanoLC AS-2 autosampler, a nanoLC 2D HPLC pump (both Eksigent), and an LTQ mass spectrometer (Thermo Scientific). The liquid chromatography system for the mass spectrometer featured a reversed-phase column in-house packed into PicoTip Emitters (New Objective) using Magic C18 (3 μ m, 200 Å; Michrom Bioresource) packing material. The peptides were eluted with a 30-min linear gradient, and data were acquired in a data-dependent fashion, that is, the six most abundant species were selected for fragmentation by collision induced dissociation. The raw files were converted into .mgf files using in-house written scripts³⁰. For each fragment ion spectrum, only the 200 most intense fragment ions were exported into the .mgf file. The mass spectrometric data were searched against the Uniprot Mouse database using the protein identification software Protein Pilot. The results were then filtered to include only proteins with a global false discovery rate of 1%.

Plasmids and DNA cloning. Mouse *Dis3l2* cDNA was generated by PCR using the forward (5'-AAGCTTGC GGCGCGAACCATCCTGACTACAAGCTGAA CCTTCGG-3') and reverse (5'-AGACCTAGTCTGACTCAGTCTCAGGCTC CTCATCAGACGCC-3') primers, and was cloned into the NotI and SalI sites of pFLAG-CMV2 (Sigma). To generate the Dis3l2(Asp389Asn) mutant, site-directed mutagenesis was performed using the forward (5'-CTGCTCGGACCTTA ATGATGCCCTCGC-3') and reverse (5'-GCGAGGGCATCATTAAGGTCTG CGAGCAG-3') primers. For generating His-tagged Dis3l2, the forward (5'-ACTAGGAATTCGAACCATCTGACTACAAGCTGAACCTTCGG-3') and reverse (5'-AAGCTTGC GGCGCGCTCAGTCTCAGGCTCCTCATCAGAGC CC-3') primers were used to amplify *Dis3l2* cDNA that was cloned into the EcoRI and NotI sites of pETDuet-1. For C- and N-terminal green fluorescent protein fusions (CT-GFP and NT-GFP, respectively), the GFP fusion TOPO TA expression kits (Invitrogen) were used. For CT-GFP fusions, the forward (5'-ACCATGAACCATCTGACTACAAGCTGAAC-3') and reverse (5'-CGTCCT CAGGCTCCTCATCAG-3') primers were used. For NT-GFP fusions, the forward (5'-AACCATCCTGACTACAAGCTGAAC-3') and reverse (5'-TCAGTC CTCAGGCTCCTCATCAG-3') primers were used. For deletion mutants, Dis3l2-truncated cDNA was amplified by PCR, with the forward (5'-AACAAGCGG

CCGCGAACCATCCTGACTACAAGCTGAACC-3') and reverse (5'-AACAAG AATTGAGTAGCCAGAGCAGCAGC-3') primers to generate the C-terminal deletion mutant; with the forward (5'-AACAAGCGGCGCGAGAAGAGAGA CCTAAGGAAAGACTGTATCTTCAC-3') and reverse (5'-AACAAGAATTCA GTCCTCAGGCTCCTCATC-3') primers to generate the N-terminal deletion mutant; and with the forward (5'-AACAAGCGGCGCGAGAAGAGACCTAA GGAAAGACTGTATCTTCAC-3') and reverse (5'-AACAAGAATTGAGTA GCCCAGAGCAGCAGC-3') primers to generate the N and C terminus deletion. These PCR products were cloned into NotI and EcoRI sites of the pFLAG-CMV2 vector (Sigma). Flag–TRBP and Flag–Trim71 constructs were as described^{15,19}.

Recombinant Dis3l2 protein purification. Transformed BL21-CodonPlus competent bacteria (Stratagene) were grown to an attenuation (*D*) at 600 nm of 0.4–0.6. Expression was induced with 100 μ M IPTG (isopropyl- β -D-thiogalactoside) for 2–3 h. Cell pellets were resuspended in cold lysis buffer (20 mM imidazole in PBS, pH 8.0, and 0.1% PMSF) and sonicated. Cleared lysates were incubated with Ni-NTA beads and after 90 min incubation at 4 °C the beads were washed with 8 column volumes wash buffer (10 mM Tris, pH 7.8, 50 mM imidazole, pH 8.0, 500 mM NaCl and 0.1% PMSF). Bound His-tagged proteins were eluted from the column with 1 volume elution buffer (10 mM Tris, pH 7.8, 500 mM imidazole, pH 8.0, 500 mM NaCl and 0.1% fresh PMSF), and dialysed overnight against BC100 (20 mM Tris–HCl, pH 7.8, 100 mM KCl, 0.2 mM EDTA, 10% glycerol). Purified protein was dialysed against RNA degradation buffer (see below) and supplemented with 20% glycerol before storage at –80 °C.

RNA degradation assays. RNA degradation assays were performed in a total of 20 μ l reaction using 6.25 nM 5' end-labelled pre-miR-21, pre-let-7a-1 or pre-let-7a-1+14U RNA together with Dis3l2 and/or Lin28A. The reactions were set up in the RNA degradation buffer (20 mM HEPES–KOH, pH 7.5, 50 mM KCl, 0.05 mM MgCl₂ and 1 mM DTT), and incubated at 37 °C for 60 min. For time course assays, recombinant His–Dis3l2 was incubated with radiolabelled pre-let-7a-1 or pre-let-7a-1+14U. Bands from three independent experiments were quantified using ImageJ (NIH) and plotted using Prism (Graphpad). Values were fitted to one-phase decay curves with error bars representing s.d. (*n* = 3). *In vitro* uridylation assays were performed as described previously^{3,4,16} with the addition of 10 μ M cold uridine triphosphate and immunopurified Dis3l2 where indicated. The following synthetic RNA sequences were used (all from Dharmacon): mmu-pre-let-7a-1, 5'-UGAGGUAGUAGGUUGUAUAGUUUAGGGUCACACCCACCACUGGGA GAUAACUAUACAAUCUACUGUCUUUCC-3'; mmu-pre-let-7a-1+14U, 5'-UGAGGUAGUAGGUUGUAUAGUUUAGGGUCACACCCACCACUGGG AGAUAACUAUACAAUCUACUGUCUUUCCUUUUUUUUUUUUUUUU-3'; mmu-pre-miR-21, 5'-UAGCUUAUCAGACUGAUGUUGACUGUUGAAUCUCAU GGCAACAGCAGUCGAUGGGCUGUC-3'.

***In vitro* transcription of pre-miRNAs.** *In vitro* transcribed pre-let-7g RNAs were generated as substrates for RNA degradation assays (in Fig. 3b). DNA templates for *in vitro* transcription of pre-let-7 with different 3' ends by PCR amplification were generated using a universal 5' primer (ACGGTTCAGCTAATACGA CTCACTATAGGGTGAGGTAGTGTGTACAGTTGAGG) (T7 promoter sequence underlined) and a 3' primer (listed below) to amplify from a plasmid DNA template containing pri-let-7g (ref. 8). PCR products were cloned and sequence verified. DNA templates (PCR products) were gel-purified and *in vitro* transcription was performed according to Riboprobe *In-Vitro* Transcription Systems using [α -³²P]rGTP and T7 RNA polymerase (Promega). The labelled pre-miRNAs were treated with RQ1 DNase and cleaned by illustra MicroSpin G-25 Column (GE Healthcare Life Sciences).

The following 3' primers for pre-let-7g-(U)_n were used: pre-let-7g-0U, GCAAGGCAGTGGCCTGTACAGTTATC; pre-let-7g-1U, AGCAAGGCAGT GGCCTGTACAGTTATC; pre-let-7g-3U, AAAGCAAGGCAGTGGCCTGTACAGTTATC; pre-let-7g-5U, AAAAAAGCAAGGCAGTGGCCTGTACAGTTATC; pre-let-7g-10U, AAAAAAGCAAGGCAGTGGCCTGTACAGTTATC; pre-let-7g-10U, AAAAAAGCAAGGCAGTGGCCTGTACAGTTATC; pre-let-7g-14U, AAAAAAGCAAGGCAGTGGCCTGTACAGTTATC; pre-let-7g-20U, AAAAAAGCAAGGCAGTGGCCTGTACAGTTATC; pre-miR-21 forward, ACGGTCAGCTAATACGACTCAT ATAGGGTAGCTTATCAGACTGATGTTGACTG; pre-miR-21 reverse, GACA GCCCATCGACTGCTGTTG; pre-miR-21-14U reverse, AAAAAAGCAAGGCAGTGGCCTGTACAGTTATC.

RNA EMSAs. EMSA experiments were performed as described previously¹⁶. In brief, 1 nM of the indicated radiolabelled synthetic RNA was incubated in the binding buffer (50 mM Tris, pH 7.6, 100 mM NaCl, 10 mM β -mercaptoethanol and 1 U μ l⁻¹ rRNasin (Promega) with varying concentrations of catalytically inert recombinant His–Dis3l2 or recombinant His–Lin28 in the absence of competitor RNA. Nucleoprotein complexes were resolved by 4–20% non-denaturing TBE gel electrophoresis (Bio-Rad) and visualized by autoradiography.

Antibodies and synthetic RNA. The following antibodies and the working concentrations were used: anti-Dis3l2 (0.4 $\mu\text{g ml}^{-1}$; Novus Biologicals, NBP1-84740), anti-Zcchc11 (1:1,000; ProteinTech Group, 18980-1-AP), anti-Zcchc6 (1:500; Open Biosystems, custom-made), anti-Rrp44 (1:1,000; ProteinTech Group, 14689-1-AP), anti-Exosc10 (1 $\mu\text{g ml}^{-1}$; Abcam, ab50558), anti-Lin28A (A177) (1:1,000; Cell Signaling, 3978), anti-Flag (1:5,000; Sigma, A8592), and anti-tubulin (1:10,000; Abcam, ab6046).

Transfections and siRNA/shRNA knockdowns. All transfections were performed with Lipofectamine 2000 (Invitrogen) per manufacturer's instructions. The sequences of the shRNAs and siRNAs are listed below. Lentivirus production, infection and stable cell selection are as described¹⁷. The following synthetic RNA sequences were used (all from Dharmacon): control siRNA 1, 5'-UGGUUUUACAUGUUGUGUGA-3'; control siRNA 2, 5'-UGGUUUUACAUGUUGUGUGA-3'; Lin28A siRNA, 5'-GGGUUGUGAUGACAGGCAA-3'; Zcchc11 siRNA, 5'-GGGCUAAGCUGUGCUAUUAU-3'; mouse Dis3l2 siRNA 1, 5'-CCGCUUUGCUGACGUAUA-3'; mouse Dis3l2 siRNA 2, 5'-GAAUUUACGUACCUCUCAA-3'; mouse Dis3l1 siRNA 1, 5'-AGGAACUACUGGACGGAAA-3'; mouse Dis3l1 siRNA 2, 5'-UGAAACAGAAGGCGUAUUU-3'.

mRNA and miRNA qRT-PCR. Total RNA was isolated using TRIzol reagent (Invitrogen). For fractionation, total RNA was processed by mirVana miRNA isolation kit according to the manufacturer's instructions (Ambion). For mRNA, 100 ng of total RNA was reverse transcribed using random hexamers and SuperScript III (Invitrogen). For mature miRNA, 10 ng of total RNA was reverse transcribed using gene-specific stem-loop reverse transcriptase primers and MultiScribe Reverse Transcriptase (Applied Biosystems). For pre-miRNA, <200-nucleotide fractionated RNA was first treated with 0.66 U RNase-free DNase (Promega) (60 min at 37 °C), stopped with 1 mM of EDTA (10 min at 65 °C), and reverse transcribed by oligo(dA)₁₂ (60 min at 50 °C) using SuperScript III (Invitrogen). The resulting cDNA was further digested with RNase H (30 min at 37 °C). For mRNA and pre-miRNA, iQ SYBR Green Supermix (Bio-Rad) was used for quantifying the cDNA. For mature miRNA, TaqMan universal PCR master mix, no AmpErase UNG (Applied Biosystems) was used for cDNA

detection. All qPCR reactions were performed using iCycler iQ multicolor real-time PCR detection system (Bio-Rad). Normalization controls include mouse *Actb* for mRNAs as well as for pri-miRNAs, *U6* for pre-miRNA, and snoRNA142 for mature miRNAs. For all RT-PCRs, minus reverse transcriptase and water control samples were included, and in all cases the signals were undetectable (data not shown). The following primer sequences were used for qPCR: pre-let-7a-1, forward, 5'-TGAGGTTAGTGGTTGTATAGTTTATAGGG-3'; reverse, 5'-GGAAAGACAGTAGATTGTATAGTTATC-3'; pri-let-7a-1, forward, 5'-CTTCAACATTCACCTGGATGTTTC-3'; reverse, 5'-GAGACCCCATGAATGCAGAC TTT-3'; pre-let-7g, forward, 5'-TGAGGTTAGTGGTTGTACAGTTTGAGG-3'; reverse, 5'-GCAAGGCAGTGGCCTGTACAGTTATC-3'; pri-let-7g, forward, 5'-GTTCTCTTTTGCTGATTCCAGG-3'; reverse, 5'-CATTTGGTAGCTGTGCACTG-3'; *U6*, forward, 5'-CTCGCTTCGGCAGCACA-3'; reverse, 5'-AACGCTTCACGAATTTGCGT-3'; *Actb*, forward, 5'-CAGAAGGAGATTACTGCTCTGGCT-3'; reverse, 5'-TACTCCTGCTTGCTGATCCACATC-3'; *Dis3l1*, forward, 5'-AGTTGACAGACATAGCTCGCCACA-3'; reverse, 5'-TGGTTGGCTAGGATCATGCACTCA-3'.

Northern blotting. Ten micrograms of total RNA from each sample was used for northern blotting as previously described¹⁹. Probe sequences for detecting precursor and mature miRNA are as follows: pre-let-7g, 5'-TATCTCCTGTACCGGGTGGTATCATAGACCCTCA-3'; let-7a, 5'-AACTATACAACCTACTACTCA-3'; let-7g, 5'-AACTGTACAAACTACTACCTCA-3'.

Dicer assays. Recombinant Flag-Dicer protein was purified from insect cells as previously described¹⁹. Dicer processing of pre-let-7 or pre-let-7+14U was performed by incubating recombinant Dicer with gel-purified 5' end-labelled synthetic pre-miRNA in a buffer containing 3.2 mM MgCl₂, 20 mM Tris-HCl, pH 7.9, 0.1 M KCl, 10% glycerol, 5 mM DTT, 0.2 mM PMSF and 40 U ml⁻¹ RNase inhibitor (RNasin, Promega) for 1 h at 37 °C. Samples were resolved by 15% denaturing polyacrylamide gel.

- Renard, B. Y. *et al.* When less can yield more — computational preprocessing of MS/MS spectra for peptide identification. *Proteomics* **9**, 4978–4984 (2009).

Meis1 regulates postnatal cardiomyocyte cell cycle arrest

Ahmed I. Mahmoud^{1*}, Fatih Kocabas^{1*}, Shalini A. Muralidhar^{1*}, Wataru Kimura¹, Ahmed S. Koura², Suwannee Thet¹, Enzo R. Porrello³ & Hesham A. Sadek¹

The neonatal mammalian heart is capable of substantial regeneration following injury through cardiomyocyte proliferation^{1,2}. However, this regenerative capacity is lost by postnatal day 7 and the mechanisms of cardiomyocyte cell cycle arrest remain unclear. The homeodomain transcription factor Meis1 is required for normal cardiac development but its role in cardiomyocytes is unknown^{3,4}. Here we identify Meis1 as a critical regulator of the cardiomyocyte cell cycle. Meis1 deletion in mouse cardiomyocytes was sufficient for extension of the postnatal proliferative window of cardiomyocytes, and for re-activation of cardiomyocyte mitosis in the adult heart with no deleterious effect on cardiac function. In contrast, overexpression of Meis1 in cardiomyocytes decreased neonatal myocyte proliferation and inhibited neonatal heart regeneration. Finally, we show that Meis1 is required for transcriptional activation of the synergistic CDK inhibitors p15, p16 and p21. These results identify Meis1 as a critical transcriptional regulator of cardiomyocyte proliferation and a potential therapeutic target for heart regeneration.

The hallmark of heart failure is the progressive nature of the disease, and the inability of the adult heart to regenerate after injury. Nonetheless, limited myocyte turnover does in fact occur in the adult mammalian heart; however, this is insufficient to restore contractile function following injury^{5,6}. In contrast, the neonatal heart has a proliferative capacity reminiscent of lower vertebrates^{1,2,7}. These findings indicate that the key to unlocking the regenerative potential of the adult mammalian heart may lie within the developmental transitions occurring during neonatal life. Given that cardiac regeneration in neonatal mice, as well as in adult zebrafish^{1,2,8,9}, is primarily mediated by cardiomyocyte proliferation, it is crucial to identify the molecular mechanisms responsible for postnatal cardiac cell cycle arrest.

The transcriptional networks that govern embryonic heart development have been extensively studied. In contrast, little is known about transcriptional regulation of postnatal cardiomyocyte cell cycle arrest. Recent evidence suggests that Meis transcription factors, which belong to the TALE (three amino acid loop extension) family of homeodomain transcription factors, are central regulators of cardiac differentiation during embryonic development^{3,4}. While global deletion shows that *Meis1* is required for normal embryonic haematopoiesis and heart development^{10–12}, the role of *Meis1* in the postnatal heart remains unclear. We recently demonstrated that *Meis1* is an important regulator of haematopoietic stem cells (HSCs) quiescence¹³. Moreover, our initial screens identified *Meis1* as a potential transcriptional regulator of neonatal heart regeneration. Therefore, we conducted this study to determine the role of *Meis1* in regulation of cardiomyocyte cell cycle. We first examined the expression pattern of *Meis1* during neonatal heart development and regeneration. Quantitative PCR with reverse transcription (qRT–PCR) showed a modest increase in *Meis1* expression between postnatal day 1 (P1) and P7 (Fig. 1a). Moreover, immunostaining revealed that *Meis1* is expressed in the heart as early

as P4, and throughout adulthood (Supplementary Fig. 1a). *Meis1* was localized to perinuclear regions in neonatal cardiomyocytes at P1, but became nuclear localized by P4–P7 (Fig. 1c and Supplementary Fig. 1b). Myocardial infarction (MI) at P1, which is associated with an induction of robust cardiomyocyte proliferation at day 7 post-MI², was associated with a modest decrease in the expression of *Meis1*, whereas *Meis1* mRNA expression levels were significantly increased following MI at P7, a time point coinciding with lack of mitotic induction of cardiomyocytes (Fig. 1b).

We also examined the expression of *Meis1* isoforms in the heart postnatally, and we found that isoform *Meis1B* is the predominant isoform (Supplementary Fig. 1c, d). Finally, given that *Meis1* transcriptional activity is known to be tightly linked to other *Hox* genes, we profiled the entire *Hox* family by qRT–PCR (Supplementary Fig. 1e). Intriguingly, we found that the three most upregulated genes were *Hoxa10*, *Hoxa11*, and *Hoxd12* (all belonging to the AbdB-like paralogue of *Hox* genes), which along with *Hoxa9*, and *Hoxb13* are the only *Hox* proteins (out of 37 known mammalian *Hox* genes) known to interact with *Meis1*¹⁴. These *Hox* proteins stabilize *Meis1* DNA binding and enhance its transcriptional activity.

To elucidate a potential role for *Meis1* in cardiomyocyte proliferation, we performed *in vitro* siRNA knockdown using rat neonatal cardiomyocytes, and found that *Meis1* knockdown (Fig. 1d) resulted in a threefold increase in cardiomyocyte proliferation (Fig. 1e). Next, we generated cardiomyocyte-specific *Meis1* knockout (KO) mice by crossing *Meis1*^{fl/fl} mice with α MHC-Cre mice (Fig. 2a). qRT–PCR (Fig. 2b) using isolated cardiomyocytes from *Meis1*^{fl/fl} α MHC-Cre (*Meis1* KO) compared to *Meis1*^{+/+} α MHC-Cre (control) mouse hearts confirmed a change in gene expression consistent with *Meis1* deletion in cardiomyocytes. Phenotypic characterization of *Meis1* KO mice at P14 (1 week beyond the normal window of postnatal cardiomyocyte cell cycle arrest) demonstrated that heart size (Fig. 2c, d) and cardiac function (Fig. 2e) were unaffected by *Meis1* deletion. However, *Meis1* KO cardiomyocytes were smaller compared to control cardiomyocytes (Fig. 2f), which may imply that the cardiomyocyte number is increased in *Meis1* KO (smaller cardiomyocyte size, with no change in heart to body weight ratio). Therefore, we examined the *Meis1* KO hearts for myocyte proliferation using the mitosis marker pH3 (phosphorylated histone H3) and the cytokinesis marker Aurora B kinase. *Meis1* deletion resulted in induction of cardiomyocyte proliferation as quantified by an increase in the number of pH3⁺ TnnT2⁺ (troponin T2) cells (>9 fold) (Fig. 2g, top row of images and bar graph). Moreover, we show that sarcomere disassembly, a hallmark for cardiomyocyte proliferation, was evident in the *Meis1* KO heart sections (Fig. 2g, bottom left image), whereas neighbouring myocardium had normal sarcomeric structure (Fig. 2g, bottom right image). In addition, we found that the cytokinesis marker Aurora B kinase was markedly expressed in the cleavage furrow between proliferating myocytes in the KO hearts (>5 fold) (Fig. 2h). We also found a significant increase in

¹Department of Internal Medicine, Division of Cardiology, The University of Texas Southwestern Medical Center, Dallas, Texas 75390, USA. ²School of Medicine, Ain Shams University, Cairo, 1156, Egypt.

³School of Biomedical Sciences, The University of Queensland, St Lucia, Queensland 4072, Australia.

*These authors contributed equally to this work.

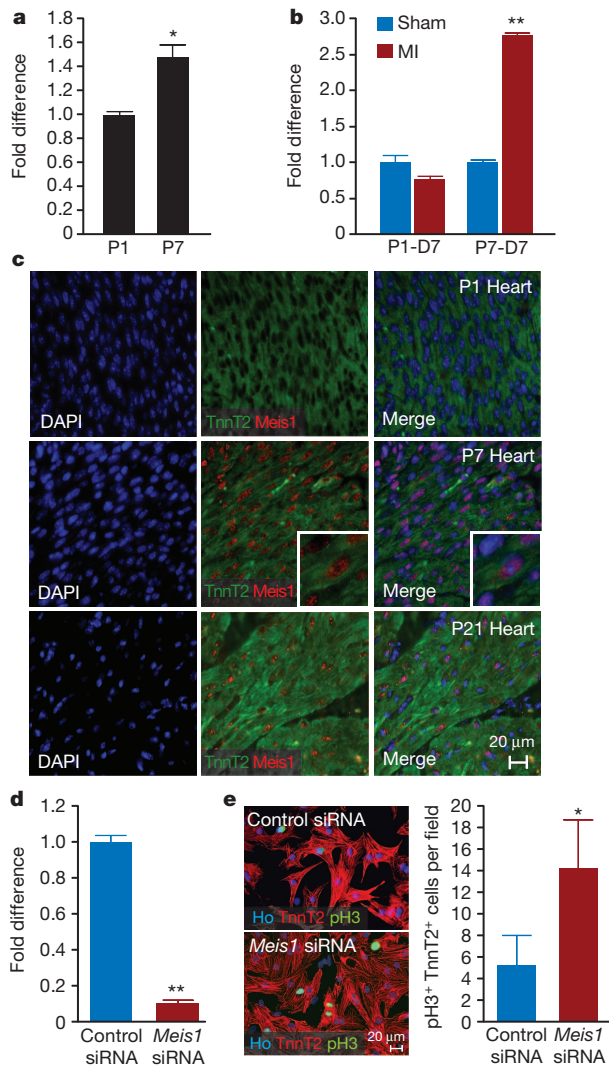


Figure 1 | Expression profile of *Meis1* in the heart. **a**, qRT-PCR showing increased expression of *Meis1* at postnatal day 7 (P7), a time point that coincides with cell cycle arrest of cardiomyocytes. **b**, qRT-PCR showing expression levels of *Meis1* following Sham or MI at P1 or P7. Samples were collected 7 days after the injury was performed (D7). **c**, Expression profile of *Meis1* in cardiomyocytes. Top row, *Meis1* expression is absent at P1. Middle and bottom rows, nuclear localization of *Meis1* in cardiomyocytes at P7 and P21, respectively. **d**, qRT-PCR showing knockdown of *Meis1* in rat neonatal cardiomyocytes using *Meis1* siRNA. **e**, Cardiomyocyte mitosis following *Meis1* knockdown. Left panel, immunostaining showing co-localization of pH3, TnnT2 and Hoechst (Ho) in rat neonatal cardiomyocytes. Right panel, quantification of the pH3⁺ TnnT2⁺ nuclei in control and *Meis1* siRNA treated cardiomyocytes. Quantitative analysis represents counting of multiple fields from three independent samples per group; **P* < 0.05, ***P* < 0.01; error bars represent mean ± s.e.m.

the number of 5-bromodeoxyuridine (BrdU) positive cardiomyocytes in the *Meis1* KO hearts (Fig. 2i).

To determine whether deletion of *Meis1* increases the total number of cardiomyocytes, we isolated adult cardiomyocytes from wild-type and KO hearts by collagenase digestion and found a significant increase in the total number of cardiomyocytes in *Meis1* KO hearts (Fig. 2j, left graph). This was accompanied by an increase in the percentage of mononucleated cardiomyocytes, and a decrease in the percentage of binucleated cardiomyocytes (Fig. 2j, right graph), possibly indicative of proliferation of a mononuclear myocyte population¹⁵, or reflecting the nucleation status of mitotic cardiomyocytes^{16,17}. These results demonstrate that *Meis1* deletion affects both cell cycle activity and nucleation of cardiomyocytes postnatally. Finally, *Meis1* deletion

did not result in an increase in myocyte apoptosis by TdT-mediated dUTP nick end labelling (TUNEL) staining (Fig. 2k).

Next, we examined the effect of *Meis1* deletion on the adult heart. Heart size (Supplementary Fig. 2a) and cardiac function were normal in adult mice at the postnatal stages of 28 days and 7 months (Supplementary Fig. 2b, c). There was no difference in the size of cardiomyocytes in the adult heart following *Meis1* deletion in late gestation (Supplementary Fig. 2d). Similarly, we examined cardiomyocyte mitosis in adult hearts and found that *Meis1* KO hearts continued to show increased mitosis indices even in adulthood, although cardiomyocyte proliferation appeared to decrease with age (Supplementary Fig. 2e, f), with no increase in cardiomyocyte apoptosis (Supplementary Fig. 2g). In addition, there was no change in the expression pattern of hypertrophy markers except for a modest reduction in ANP (also known as natriuretic peptide type A) (Supplementary Fig. 2h).

Although sustained induction of cardiomyocyte cell cycle from birth by overexpression of cell cycle regulators has been previously achieved^{16,17}, cell cycle re-entry in adult cardiomyocytes appears to be limited to a subpopulation of mononucleated myocytes in one report¹⁵, and another study suggested that cell cycle re-entry is associated with contractile dysfunction¹⁸. Therefore, we examined whether conditional deletion of *Meis1* in the adult heart could induce cardiomyocyte cell cycle re-entry. We crossed *Meis1*^{fl/fl} mice with α MHC-MerCreMer mice, which allowed for specific deletion of *Meis1* in cardiomyocytes following tamoxifen administration, these inducible *Meis1* knockout mice are hereafter referred to as *Meis1* iKO. We then confirmed *Meis1* deletion in the majority of cardiomyocytes (Fig. 3a, b), and we found that *Meis1* deletion did not affect cardiac morphology or fibrosis (Fig. 3c); however, the heart to body weight ratio was increased 6 weeks after *Meis1* deletion (Fig. 3d). Further characterization of the *Meis1* iKO mice demonstrated normal cardiac function (Fig. 3e) and cardiomyocyte size (Fig. 3f). Intriguingly, the number of mitotic cardiomyocytes, detected by pH3 staining, increased by more than tenfold (Fig. 3g), with a significant increase in cytokinesis (Fig. 3h) 1 week after tamoxifen administration. In addition, we found that the *Meis1* iKO hearts had increased number of cardiomyocytes (Fig. 3i, left), and a higher number of mononucleated cardiomyocytes (Fig. 3i, right). Finally, we did not detect any significant differences in apoptosis in the *Meis1* iKO hearts (Fig. 3j). Collectively, these results demonstrate that deletion of *Meis1* in adult cardiomyocytes is sufficient for induction of cell cycle re-entry.

To determine whether forced *Meis1* expression can inhibit neonatal cardiomyocyte proliferation, we generated a cardiac-specific *Meis1* overexpressing mouse (*Meis1* OE) by crossing pTRE-*Meis1* mice with α MHC-tTA mice to allow for specific overexpression of *Meis1* in cardiomyocytes (Fig. 4a) around birth in the absence of tetracyclin. We used a *Meis1* line that overexpressed *Meis1* by approximately 2.5-fold (Fig. 4b). Overexpression of *Meis1* did not result in a significant increase in heart to body weight ratio (Fig. 4c, d), normal systolic function (Fig. 4e) and increased cardiomyocyte size (Fig. 4f). This was associated with a modest increase in the hypertrophy marker ANP (Fig. 4g). Despite the increase in cardiomyocyte size in *Meis1* (OE) hearts, the lack of decrease in heart to body weight ratio most probably reflects a decrease in the number of cardiomyocytes. This is supported by a decrease in the number of mitotic cardiomyocytes in the neonatal *Meis1* (OE) hearts (Fig. 4h). More notably, *Meis1* overexpression inhibited neonatal heart regeneration following induction of MI at P1 (Fig. 4i–k), whereas the wild-type hearts regenerated normally. Finally, *Meis1* overexpression in cardiomyocytes resulted in upregulation of CDK inhibitors, most significantly p21 (also known as Cdkn1a) (Fig. 4l). These results indicate that *Meis1* overexpression in the neonatal heart results in premature cardiomyocyte cell cycle arrest.

In order to determine the mechanism by which *Meis1* regulates cardiomyocyte proliferation, we performed a cell cycle PCR array. We found that *Meis1* deletion resulted in downregulation of cyclin-dependent kinase inhibitors in isolated cardiomyocytes, including

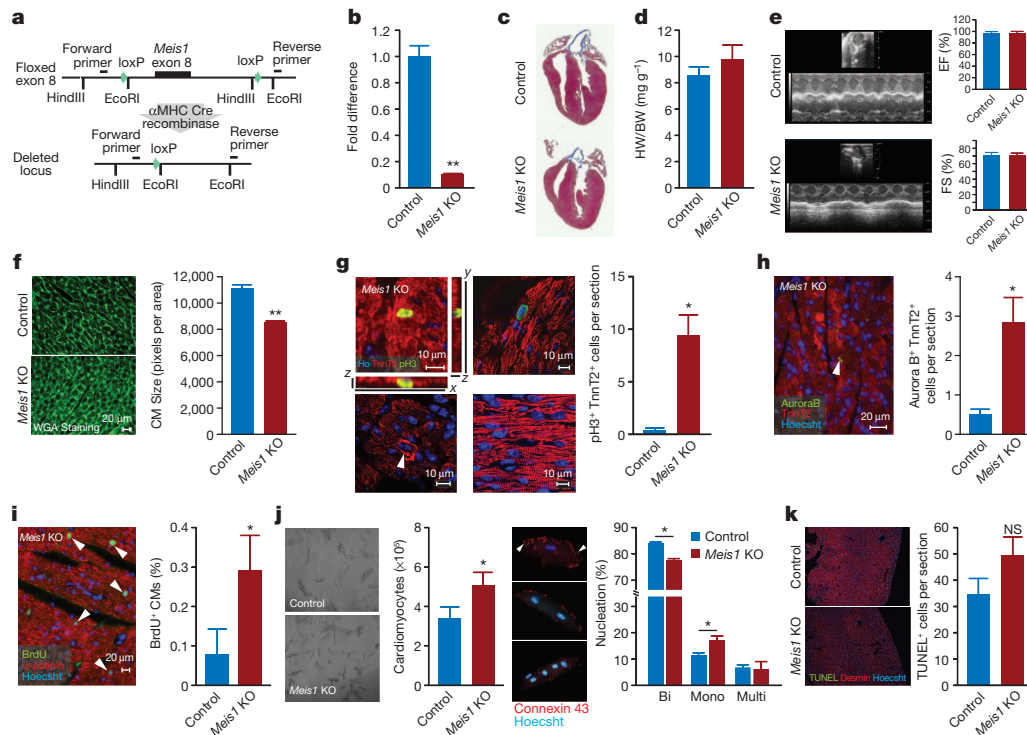


Figure 2 | Cardiomyocyte proliferation at P14 following *Meis1* deletion.

a, Schematic of *Meis1* floxed allele. Control mice were α MHC-Cre, *Meis1* KO mice were *Meis1*^{fl/fl} α MHC-Cre. **b**, qRT-PCR demonstrates deletion of *Meis1* in isolated cardiomyocytes at P14 ($n = 3$). **c**, Trichrome staining of wild-type and *Meis1* KO hearts at P14. **d**, Heart weight (HW) to body weight (BW) ratio in wild-type and *Meis1* KO hearts ($n = 4-7$ per group). **e**, Left ventricular systolic function quantified by ejection fraction and fractional shortening ($n = 4-7$ per group). **f**, Wheat germ agglutinin (WGA) staining and cell size quantification. Quantitative analyses represent counting of multiple fields from three independent samples per group (~ 50 cells per field assessed, total ~ 250 cells per group). **g**, Confocal image with z-stacking showing co-localization of pH3, TnnT2 and Hoechst in a *Meis1* KO heart at P14 (top left). Confocal image of a pH3⁺ cardiomyocyte in a *Meis1* KO heart (top right). Immunostaining showing sarcomere disassembly in *Meis1* KO hearts (arrowhead, bottom left). Normal sarcomeric structure of *Meis1* KO myocardium (bottom right). Graph shows quantification of the number of pH3⁺ TnnT2⁺ nuclei. **h**, Immunostaining showing expression of Aurora B in *Meis1* KO cardiomyocytes at P14 and quantification of the number of Aurora B⁺ TnnT2⁺ cardiomyocytes.

Quantitative analysis of pH3 and Aurora B⁺ cardiomyocytes represents counting of multiple sections from three independent samples per group (~ 3 sections per heart) (**g**, **h**). **i**, Immunostaining showing co-localization of BrdU, α -actinin and Hoechst in *Meis1* KO heart at P14 and quantification of the number of BrdU⁺ cardiomyocytes. Quantification represents counting of several sections from (3–6) independent samples per group. Total number of cardiomyocytes counted for proliferation indices was $2 \times 10^3 - 2.5 \times 10^3$ myocytes per section. **j**, Representative images of control and *Meis1* KO isolated cardiomyocytes, and quantification of the number of myocytes from control and *Meis1* KO hearts. Approximately $1 \times 10^3 - 1.5 \times 10^3$ cardiomyocytes were counted using a haemocytometer per group, using 3 independent samples (left). Immunostaining of isolated cardiomyocytes with Connexin 43, and quantification of the number of nuclei in control and *Meis1* KO hearts. For nucleation, approximately 1×10^3 cardiomyocytes were counted per sample, using 3 independent samples per group (right). **k**, Apoptosis analysis. Image showing co-localization of TUNEL, Desmin, and Hoechst in a control and *Meis1* KO heart. Quantification of TUNEL-positive cells. ($n = 3$). Values presented as mean \pm s.e.m., * $P < 0.05$, ** $P < 0.01$.

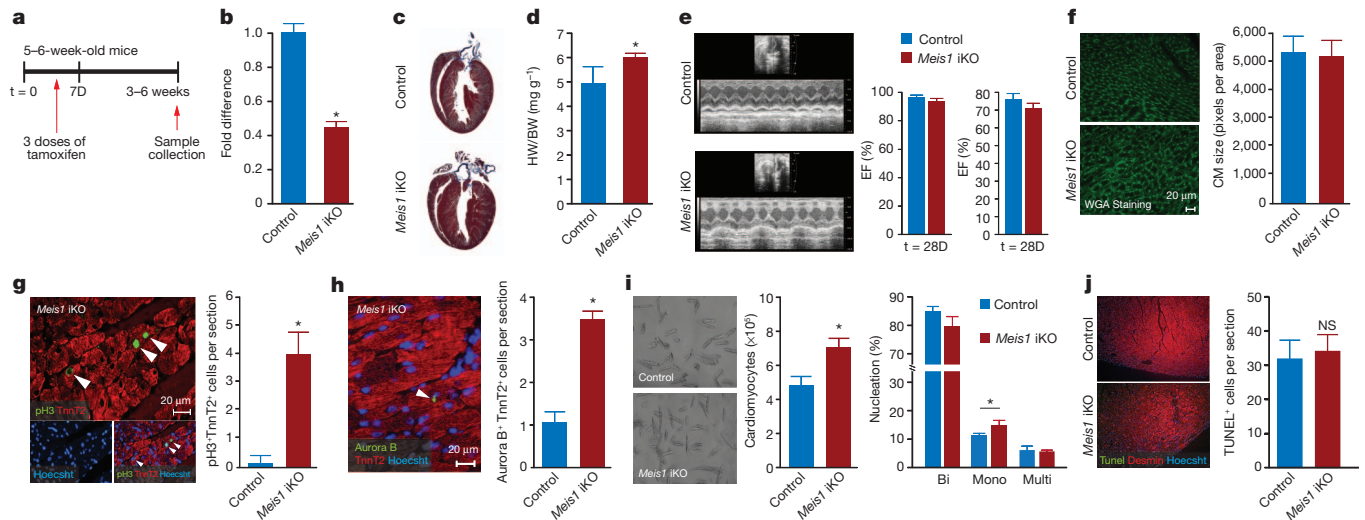


Figure 3 | Inducible deletion of *Meis1* in cardiomyocytes. **a**, Schematic of inducible *Meis1* deletion (*Meis1* iKO). Control mice were α MHC-Cre MerCreMer, *Meis1* iKO mice were α MHC-Cre MerCreMer *Meis1*^{fl/fl}. **b**, qRT-PCR demonstrating deletion of *Meis1* in isolated cardiomyocytes ($n = 3$). **c**, Trichrome stained sections at day 28 following tamoxifen injections. **d**, Heart weight to body weight ratio in wild-type and *Meis1* iKO mice ($n = 4$ per group). **e**, Left ventricular systolic function quantified by ejection fraction and fractional shortening ($n = 4$ per group). **f**, Wheat germ agglutinin staining (WGA) and cell size quantification. Quantitative analyses represent counting of multiple fields from three independent samples per group (~ 50 cells per field assessed, total ~ 250 cells per group). **g**, Immunostaining image for pH3, TnnT2 and Hoechst, 7 days post tamoxifen induction. Arrows mark pH3⁺ myocyte nuclei. Graph shows the number of pH3⁺ TnnT2⁺ nuclei 7 days post tamoxifen treatment in control and *Meis1* iKO hearts ($n = 6$).

h, Immunostaining for Aurora B in *Meis1* iKO heart. Graph shows the number of Aurora B⁺ cardiomyocytes. Quantitative analysis of pH3⁺ and Aurora B⁺ myocytes represents counting of multiple sections from three independent samples per group (~ 3 sections per heart). **i**, Representative images of control and *Meis1* iKO isolated cardiomyocytes and quantification of the number of cardiomyocytes. Approximately $1 \times 10^3 - 1.5 \times 10^3$ cardiomyocytes were counted using a haemocytometer per group, using 3 independent samples. Graph shows quantification of the nucleation of cardiomyocyte nuclei. For nucleation, approximately 1×10^3 cardiomyocytes were counted per sample, using 3 independent samples per group. **j**, Apoptosis following inducible *Meis1* deletion in cardiomyocytes. Immunostaining for TUNEL, Desmin, and Hoechst in control and *Meis1* iKO hearts and quantification of TUNEL positive cells. Values presented as mean \pm s.e.m., * $P < 0.05$.

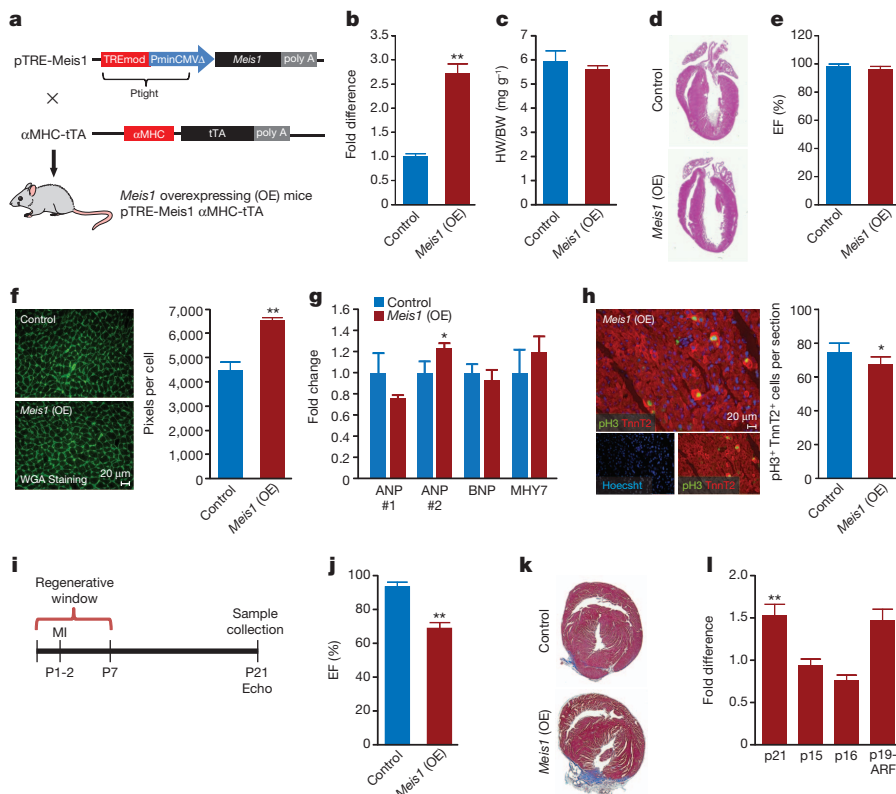


Figure 4 | *Meis1* overexpression in the heart limits neonatal heart regeneration following myocardial infarction. **a**, Schematic of *Meis1* overexpression (OE) in the heart. Control mice were α MHC-tTA, *Meis1* (OE) mice were pTRE-*Meis1* α MHC-tTA. **b**, qRT-PCR demonstrates overexpression of *Meis1* ($n = 3$). **c**, Heart weight to body weight ratio in control and *Meis1* (OE) mice ($n = 11$). **d**, Haematoxylin and eosin stained sections of wild-type and *Meis1* (OE) hearts. **e**, Left ventricular systolic function quantified by ejection fraction ($n = 4-5$ per group). **f**, Wheat germ agglutinin staining and cell size quantification. Quantitative analyses represent counting of multiple fields from three independent samples per group (~ 50 cells per field assessed, total ~ 250 cells per group). **g**, Gene expression of hypertrophy markers in P3 control and *Meis1* (OE) hearts. ANP #1 and #2 represent two different primer sets for the same gene. **h**, Immunostaining image showing co-localization of pH3, TnnT2 and Hoechst in *Meis1* (OE) heart at P3. Graph shows quantification of the number of pH3⁺ TnnT2⁺ nuclei. Quantitative analysis represents counting of multiple sections from three independent samples per group (~ 3 sections per heart). **i**, Schematic of neonatal MI during the regenerative window at P1. **j**, Left ventricular systolic function of wild-type and *Meis1* (OE) hearts at 21 days post-MI. **k**, Masson's trichrome staining at day 21 post-MI. **l**, qRT-PCR of cyclin dependent kinase inhibitors (CDKIs) in hearts of *Meis1* (OE) compared to control. Values presented as mean \pm s.e.m.; * $P < 0.05$, ** $P < 0.01$.

for future studies to define the transcriptional network involved in mediating the effect of *Meis1* on postnatal cardiomyocytes.

The diverse functions of *Meis1* in different organs have begun to emerge. We recently identified *Meis1* as an important regulator of anaerobic glycolysis in the HSC hypoxic niche through regulation of *Hif-1 α* and *Hif-2 α* , in which conditional *Meis1* deletion resulted in a metabolic switch from glycolysis to oxidative phosphorylation resulting in apoptosis of HSCs²³. In contrast, *Meis1* deletion in cardiomyocytes is not associated with increased apoptosis, probably owing to the dependence of cardiomyocytes on oxidative metabolism compared to the glycolytic HSCs.

Although it was previously thought that the heart is a post-mitotic organ, it is now clear that measurable myocyte turnover can occur in the adult mouse^{6,24} and human^{25,26} hearts. Recent reports indicate that cardiomyocyte proliferation is the main source of myocyte turnover in the adult heart²⁷, and can even mediate adult heart regeneration²⁸. Our results indicate that reversal of adult cardiomyocyte cell cycle arrest may be conceivable through careful analysis of early postnatal events, and identifies *Meis1* as a key regulator of postnatal cardiomyocyte proliferation.

METHODS SUMMARY

Neonatal mice were subjected to myocardial infarction surgeries as previously described². Experimental animal protocols were approved by the Institutional Animal Care and Use Committee of the University of Texas Southwestern Medical Center. All experiments were performed on age and sex matched mice, with an equal ratio of male to female mice. Results are expressed as mean \pm s.e.m. An unpaired Student's *t* test was used to determine statistical significance of all samples. **P* < 0.05, ***P* < 0.01 were considered statistically significant.

Received 18 November 2012; accepted 4 March 2013.

Published online 17 April 2013.

- Porrello, E. R. *et al.* Transient regenerative potential of the neonatal mouse heart. *Science* **331**, 1078–1080 (2011).
- Porrello, E. R. *et al.* Regulation of neonatal and adult mammalian heart regeneration by the miR-15 family. *Proc. Natl Acad. Sci. USA* **110**, 187–192 (2013).
- Paige, S. L. *et al.* A temporal chromatin signature in human embryonic stem cells identifies regulators of cardiac development. *Cell* **151**, 221–232 (2012).
- Wamstad, J. A. *et al.* Dynamic and coordinated epigenetic regulation of developmental transitions in the cardiac lineage. *Cell* **151**, 206–220 (2012).
- Bergmann, O. *et al.* Evidence for cardiomyocyte renewal in humans. *Science* **324**, 98–102 (2009).
- Hsieh, P. C. *et al.* Evidence from a genetic fate-mapping study that stem cells refresh adult mammalian cardiomyocytes after injury. *Nature Med.* **13**, 970–974 (2007).
- Heallen, T. *et al.* Hippo pathway inhibits Wnt signaling to restrain cardiomyocyte proliferation and heart size. *Science* **332**, 458–461 (2011).
- Kikuchi, K. *et al.* Primary contribution to zebrafish heart regeneration by *gata4*⁺ cardiomyocytes. *Nature* **464**, 601–605 (2010).
- Jopling, C. *et al.* Zebrafish heart regeneration occurs by cardiomyocyte dedifferentiation and proliferation. *Nature* **464**, 606–609 (2010).
- Azcoitia, V., Aracil, M., Martinez, A. C. & Torres, M. The homeodomain protein *Meis1* is essential for definitive hematopoiesis and vascular patterning in the mouse embryo. *Dev Biol* **280**, 307–320 (2005).
- Hisa, T. *et al.* Hematopoietic, angiogenic and eye defects in *Meis1* mutant animals. *EMBO J.* **23**, 450–459 (2004).
- Imamura, T. *et al.* Frequent co-expression of *HoxA9* and *Meis1* genes in infant acute lymphoblastic leukaemia with *MLL* rearrangement. *Br. J. Haematol.* **119**, 119–121 (2002).
- Kocabas, F. *et al.* *Meis1* regulates the metabolic phenotype and oxidant defense of hematopoietic stem cells. *Blood* **120**, 4963–4972 (2012).
- Shen, W. F. *et al.* AbdB-like Hox proteins stabilize DNA binding by the *Meis1* homeodomain proteins. *Mol. Cell Biol.* **17**, 6448–6458 (1997).
- Bersell, K., Arab, S., Haring, B. & Kuhn, B. Neuregulin1/ErbB4 signaling induces cardiomyocyte proliferation and repair of heart injury. *Cell* **138**, 257–270 (2009).
- Pasumarthi, K. B., Nakajima, H., Nakajima, H. O., Soonpaa, M. H. & Field, L. J. Targeted expression of cyclin D2 results in cardiomyocyte DNA synthesis and infarct regression in transgenic mice. *Circ. Res.* **96**, 110–118 (2005).
- Gude, N. *et al.* Akt promotes increased cardiomyocyte cycling and expansion of the cardiac progenitor cell population. *Circ. Res.* **99**, 381–388 (2006).
- Sdek, P. *et al.* Rb and p130 control cell cycle gene silencing to maintain the postmitotic phenotype in cardiac myocytes. *J. Cell Biol.* **194**, 407–423 (2011).
- Pasumarthi, K. B. & Field, L. J. Cardiomyocyte cell cycle regulation. *Circ. Res.* **90**, 1044–1054 (2002).
- Walsh, S., Ponten, A., Fleischmann, B. K. & Jovinge, S. Cardiomyocyte cell cycle control and growth estimation *in vivo*—an analysis based on cardiomyocyte nuclei. *Cardiovasc. Res.* **86**, 365–373 (2010).
- Poolman, R. A., Gilchrist, R. & Brooks, G. Cell cycle profiles and expressions of p21^{CIP1} AND P27^{KIP1} during myocyte development. *Int. J. Cardiol.* **67**, 133–142 (1998).
- MacLellan, W. R. *et al.* Overlapping roles of pocket proteins in the myocardium are unmasked by germ line deletion of p130 plus heart-specific deletion of Rb. *Mol. Cell Biol.* **25**, 2486–2497 (2005).
- Simsek, T. *et al.* The distinct metabolic profile of hematopoietic stem cells reflects their location in a hypoxic niche. *Cell Stem Cell* **7**, 380–390 (2010).
- Smart, N. *et al.* De novo cardiomyocytes from within the activated adult heart after injury. *Nature* **474**, 640–644 (2011).
- Beltrami, A. P. *et al.* Evidence that human cardiac myocytes divide after myocardial infarction. *N. Engl. J. Med.* **344**, 1750–1757 (2001).
- Mollova, M. *et al.* Cardiomyocyte proliferation contributes to heart growth in young humans. *Proc. Natl Acad. Sci. USA* **110**, 1446–1451 (2013).
- Senyo, S. E. *et al.* Mammalian heart renewal by pre-existing cardiomyocytes. *Nature* **493**, 433–436 (2013).
- Eulalia, A. *et al.* Functional screening identifies miRNAs inducing cardiac regeneration. *Nature* **492**, 376–381 (2012).

Supplementary Information is available in the online version of the paper.

Acknowledgements We thank J. Shelton for help with histology, J. Cabrera for help with figures, N. Copeland and N. Jenkins for providing the *Meis1* KO mice, S. Das for statistics consultation, K. Luby-Phelps for help with microscopy, A. Bugde for confocal assistance, D. Farrar for discussions, H. Nguyen for help with echocardiography, as well as K. Sheth, A. Mercadel and Z. Sadek for technical assistance. This work is supported by grants from the American Heart Association (Grant in Aid) (H.A.S.), the Gilead Research Scholars Program in Cardiovascular Disease (H.A.S.), the Foundation for Heart Failure Research, NY, and the National Institutes of Health (1R01HL115275-01) (H.A.S.).

Author Contributions A.I.M., F.K., S.A.M., E.R.P. and H.A.S. designed the experiments. A.I.M., F.K., S.A.M., W.K. and S.T. performed the experiments. A.I.M., F.K., S.A.M., A.S.K., E.R.P. and H.A.S. analysed the data. A.I.M., F.K., S.A.M. and H.A.S. made the figures. A.I.M. and H.A.S. wrote the manuscript. All authors approved the manuscript.

Author Information Reprints and permissions information is available at www.nature.com/reprints. The authors declare no competing financial interests. Readers are welcome to comment on the online version of the paper. Correspondence and requests for materials should be addressed to H.A.S. (hesham.sadek@utsouthwestern.edu).

A CRISPR/Cas system mediates bacterial innate immune evasion and virulence

Timothy R. Sampson^{1,2,3}, Sunil D. Saroj⁴, Anna C. Llewellyn^{1,2,3}, Yih-Ling Tzeng⁴ & David S. Weiss^{2,3,4}

CRISPR/Cas (clustered regularly interspaced palindromic repeats/CRISPR-associated) systems are a bacterial defence against invading foreign nucleic acids derived from bacteriophages or exogenous plasmids^{1–4}. These systems use an array of small CRISPR RNAs (crRNAs) consisting of repetitive sequences flanking unique spacers to recognize their targets, and conserved Cas proteins to mediate target degradation^{5–8}. Recent studies have suggested that these systems may have broader functions in bacterial physiology, and it is unknown if they regulate expression of endogenous genes^{9,10}. Here we demonstrate that the Cas protein Cas9 of *Francisella novicida* uses a unique, small, CRISPR/Cas-associated RNA (scaRNA) to repress an endogenous transcript encoding a bacterial lipoprotein. As bacterial lipoproteins trigger a proinflammatory innate immune response aimed at combating pathogens^{11,12}, CRISPR/Cas-mediated repression of bacterial lipoprotein expression is critical for *F. novicida* to dampen this host response and promote virulence. Because Cas9 proteins are highly enriched in pathogenic and commensal bacteria, our work indicates that CRISPR/Cas-mediated gene regulation may broadly contribute to the regulation of endogenous bacterial genes, particularly during the interaction of such bacteria with eukaryotic hosts.

F. novicida is a model intracellular pathogen that evades host defences as it traffics through the phagosome of eukaryotic cells to replicate to high numbers within the cytosol. Specifically, it has developed mechanisms to prevent recognition by a variety of pattern recognition receptors (PRRs) that detect bacteria and localize to the surface and phagosomes of host phagocytic cells¹³. One PRR, Toll-like receptor 2 (TLR2), recognizes bacterial lipoproteins (BLPs) and is critical for defence against *F. novicida*^{11–15}. By dampening TLR2 activation, *F. novicida* reaches its replicative niche in the cytosol without inducing significant inflammatory signalling, promoting its pathogenesis¹³.

We demonstrated that *F. novicida* gene *FTN_0757* is involved in the repression of a BLP (*FTN_1103*), although its mechanism of action was unclear¹⁶. Unexpectedly, bioinformatic analysis revealed that *FTN_0757* has significant protein sequence similarity to the CRISPR/Cas system protein Cas9 (15–65% across conserved regions) (Supplementary Fig. 1), typically known to degrade foreign DNA^{6,7}, and not known to regulate endogenous bacterial gene expression. Furthermore, *FTN_0757* is present in a complete type II CRISPR/Cas locus, similar to those in the genomes of pathogens and commensals such as *Streptococcus* spp., *Neisseria* spp., *Campylobacter* spp. and *Lactobacillus* spp. (Supplementary Fig. 2 and Supplementary Table 1). The locus contains Cas1, Cas2 and Cas4, all predicted to be involved in acquisition of new targeting crRNAs^{18,17}, as well as a predicted *trans*-activating crRNA (*tracrRNA*), an accessory small RNA necessary for crRNA activity¹⁸. It also contains a unique small RNA¹⁹ not previously described in a CRISPR/Cas locus, distinct from the crRNAs and *tracrRNA*, which we term small CRISPR/Cas-associated RNA (*scaRNA*) (Fig. 1a).

Because *FTN_0757* (*cas9*) is in a CRISPR/Cas locus (Fig. 1a), we tested whether its ability to repress the bacterial lipoprotein *FTN_1103*

required the canonical CRISPR/Cas system or if an alternative mechanism was involved. Deletion of *cas9*, but not other *cas* genes, led to 100-fold increased levels of *FTN_1103* transcript (Fig. 1b). Because Cas9 degrades DNA targeted by crRNAs, we tested whether the crRNA array or the *tracrRNA* were necessary for *FTN_1103* repression. Deletion of the crRNA array did not alter *FTN_1103* transcript levels (Fig. 1c); however, deletion of the *tracrRNA* resulted in increased *FTN_1103* transcript, similar to the *cas9* mutant (Fig. 1c). Additionally, deletion of the *scaRNA* resulted in increased *FTN_1103* transcript, indicating that it is also critical for *FTN_1103* repression. Complementation of the *cas9*, *tracrRNA* and *scaRNA* mutants restored *FTN_1103* expression to near wild-type levels, and levels of *FTN_1103* transcript in the mutants correlated with an increase in protein production (Supplementary Figs 3 and 4). Furthermore, a triple mutant lacking *cas9*, *tracrRNA* and *scaRNA* expressed levels of *FTN_1103* similar to the single mutants, providing genetic evidence that these components may act together within the same regulatory pathway.

CRISPR/Cas systems mediate degradation of their nucleic acid targets, so we tested whether Cas9, *tracrRNA* and *scaRNA* mediated repression of *FTN_1103* via degradation. Following treatment with rifampicin to prevent messenger RNA production, *FTN_1103* transcript was rapidly depleted in wild-type cells (Fig. 2a). In contrast, *FTN_1103* transcript was not degraded in *cas9*, *tracrRNA* or *scaRNA* mutants (Fig. 2a), indicating that each of these components is required for its degradation. Cas9 proteins contain four RuvC endonuclease domains (RuvC-I to RuvC-IV) and an HNH endonuclease domain¹⁷ (Fig. 2b and Supplementary Fig. 1). RuvC-I and the HNH are necessary for degradation of target DNA^{6,7}. We constructed point mutant strains lacking conserved residues¹⁷ in each endonuclease domain to determine if they were necessary for repression of *FTN_1103* (Fig. 2b). These strains maintained wild-type levels of *FTN_1103* (as well as *cas9*), indicating that none of these domains were required for this activity (Fig. 2c and Supplementary Fig. 5). Additionally, we found no role for known RNases in *FTN_1103* repression (Supplementary Fig. 6). Cas9 proteins also contain a previously uncharacterized, conserved, arginine-rich motif (ARM)¹⁷ (Fig. 2b and Supplementary Fig. 1), a type of motif known to mediate protein–RNA interactions²⁰. A point mutation in the ARM(R59A) completely abrogated the ability of Cas9 to repress *FTN_1103* (Fig. 2c), implicating the potential importance of Cas9–RNA interactions.

We therefore analysed the sequences of the *tracrRNA* and *scaRNA* and predicted that the *tracrRNA* could hybridize to a degenerate repeat region in the *scaRNA* (Fig. 2d and Supplementary Fig. 7), similar to the interaction between the *tracrRNA* and the repeat region of a crRNA, which is necessary for targeting DNA¹⁸. We also predicted that a region of the *scaRNA* could hybridize to a portion of the *FTN_1103* transcript encompassing the start codon and ribosomal binding site (Fig. 2d and Supplementary Fig. 7). To determine whether Cas9 and the RNAs associated, we immunoprecipitated Cas9 from a strain expressing a

¹Microbiology and Molecular Genetics Program, Department of Microbiology and Immunology, Emory University, Atlanta, Georgia 30329, USA. ²Emory Vaccine Center, Emory University, Atlanta, Georgia 30329, USA. ³Yerkes National Primate Research Center, Emory University, Atlanta, Georgia 30329, USA. ⁴Division of Infectious Diseases, Department of Medicine, Emory University School of Medicine, Atlanta, Georgia 30329, USA.

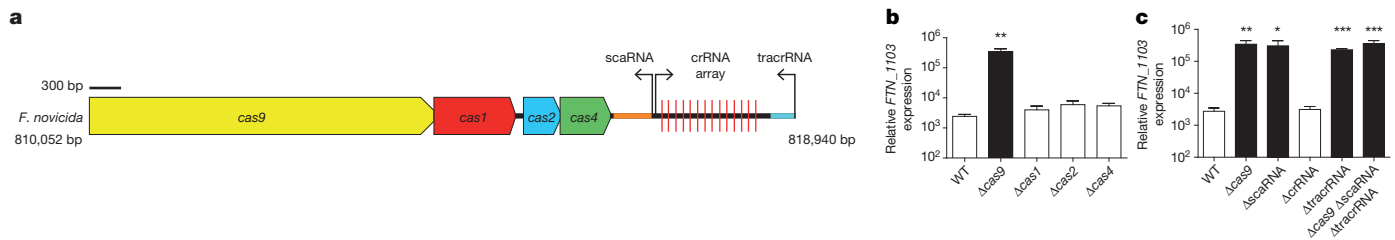


Figure 1 | Cas9, tracrRNA and scaRNA are necessary for *FTN_1103* repression. **a**, Schematic of the *F. novicida* type II CRISPR/Cas locus, containing *cas9*, *cas1*, *cas2* and *cas4*, as well as the crRNA array (repeats indicated by vertical red lines), tracrRNA (blue), scaRNA (orange), and

predicted promoters (black arrows). bp, base pairs. **b**, **c**, Relative expression of *FTN_1103* in wild-type (WT), $\Delta cas9$, $\Delta cas1$, $\Delta cas2$ and $\Delta cas4$ strains (**b**) and in wild-type, $\Delta cas9$, $\Delta scaRNA$, $\Delta crRNA$ and $\Delta tracrRNA$ strains (**c**) ($n = 4$, error bars represent s.d.). * $P \leq 0.05$; ** $P \leq 0.005$; *** $P \leq 0.001$.

Flag-tagged version of this protein. tracrRNA, scaRNA and *FTN_1103* mRNA were significantly enriched in association with Cas9 (Fig. 2e–g). However, these associations were abrogated in the Cas9 ARM(R59A) mutant, suggesting this motif is necessary for Cas9 interaction with these RNAs. We then generated reverse complement mutations in the tracrRNA region (bases 13–17) predicted to interact with the scaRNA, as well as the scaRNA regions predicted to interact with the tracrRNA (bases 4–8) or *FTN_1103* mRNA (bases 48–54). Any of the three mutations resulted in the inability to repress *FTN_1103* (Fig. 2h), whereas a strain that expressed the altered but complementary versions of both the tracrRNA and scaRNA significantly restored *FTN_1103* repression (Supplementary Fig. 8a). Additionally, the mutations predicted to disrupt the interaction between scaRNA and tracrRNA significantly dampened the ability of either small RNA to associate with Cas9, which was immunoprecipitated with equal efficiency in all strains (Supplementary Figs 8b, c and 9). Thus, the sequence-specific association of Cas9, tracrRNA and scaRNA is necessary for the repression of *FTN_1103*.

Because Cas9, tracrRNA and scaRNA repress the expression of the *FTN_1103* BLP, and BLPs are ligands for host TLR2, we tested whether these CRISPR/Cas components were involved in evasion of TLR2

recognition. Membrane protein fractions of the tracrRNA and scaRNA mutants stimulated increased TLR2-dependent secretion of the proinflammatory cytokine IL-6, similar to those from the *cas9* mutant as shown previously¹⁶ (Fig. 3a). This response was rescued in double mutants lacking *FTN_1103*, indicating that overexpression of *FTN_1103* in these strains was largely responsible for the increased TLR2 signalling (Fig. 3a). Mutants lacking *cas9*, tracrRNA or the scaRNA also elicited enhanced TLR2-dependent IL-6 secretion during macrophage infection compared to wild-type *F. novicida*, which was dependent on *FTN_1103* (Fig. 3b). This is in contrast to mutants in other *cas* genes or the crRNA array, which did not alter TLR2 signalling (Supplementary Fig. 10). As a control, a mutant lacking only *FTN_1103* did not have observable differences in membrane protein content nor did it induce altered host signalling (Supplementary Fig. 11). Together these data indicate that CRISPR/Cas component mediated suppression of BLP facilitates evasion of TLR2.

To determine whether repression of *FTN_1103* was an active evasion process, we analysed the temporal expression of CRISPR/Cas components during intracellular infection. We found that *FTN_1103* expression decreased when the bacteria were in the phagosome, as shown previously¹⁶ (Fig. 3c), directly correlating with the approximately

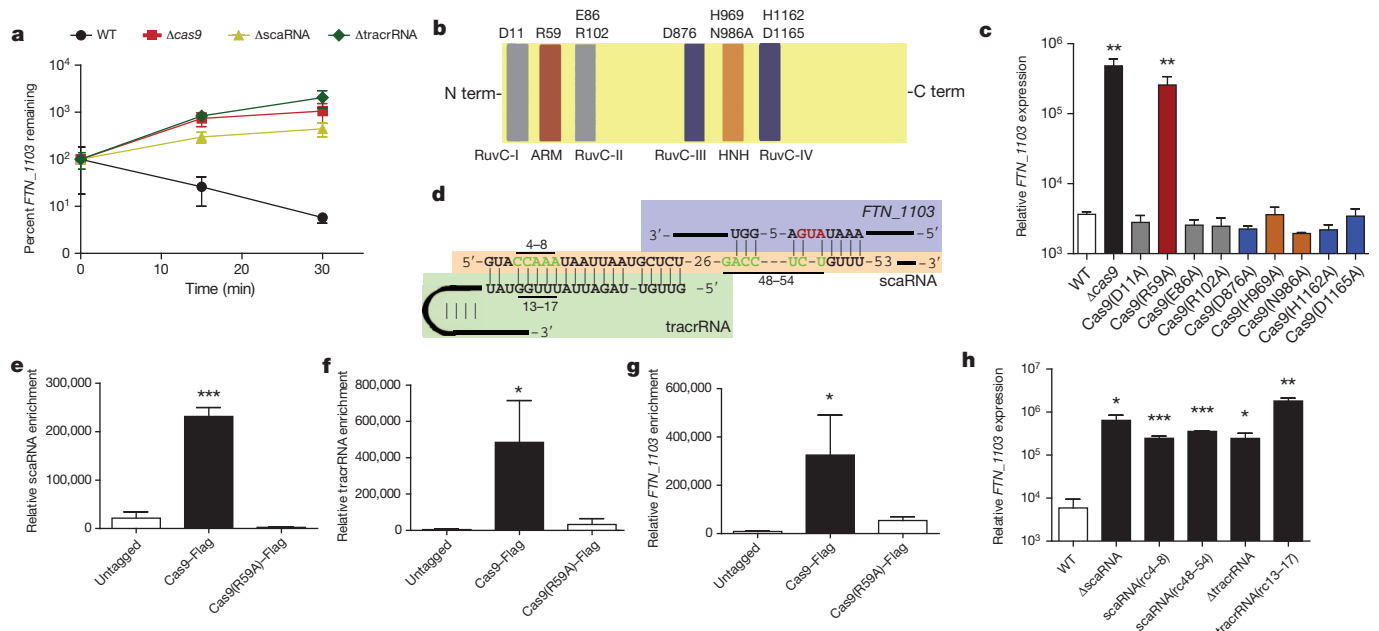


Figure 2 | Cas9, tracrRNA and scaRNA associate and mediate *FTN_1103* degradation. **a**, *FTN_1103* stability in the indicated strains ($n = 3$). **b**, Schematic of Cas9 indicating five endonuclease domains (RuvC-I to RuvC-IV and HNH) and the ARM. C term, carboxy terminus; N term, amino terminus. **c**, Relative expression of *FTN_1103* in the indicated strains ($n = 4$). **d**, Schematic of predicted hybridization between tracrRNA, scaRNA and *FTN_1103*. Bars highlight mutated bases (green) and red indicates the

FTN_1103 start codon. **e–g**, Immunoprecipitation from wild type, Cas9-Flag or Cas9(R59A)-Flag, and quantitative PCR (qPCR) for scaRNA (**e**), tracrRNA (**f**) or *FTN_1103* (**g**) ($n = 4$). **h**, Relative expression of *FTN_1103* in wild type, $\Delta scaRNA$, $\Delta scaRNA(rc4-8)$, $\Delta scaRNA(rc48-54)$, $\Delta tracrRNA$ and $\Delta tracrRNA(rc13-17)$ strains ($n = 4$, error bars represent s.d.). * $P \leq 0.05$; ** $P \leq 0.005$; *** $P \leq 0.001$.

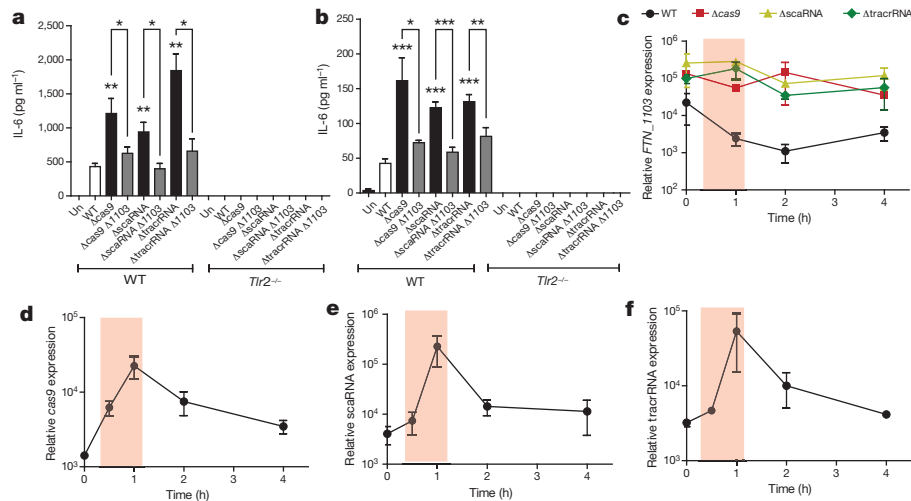


Figure 3 | Cas9, tracrRNA and scaRNA facilitate evasion of TLR2 signalling by temporal repression of *FTN_1103*. a, b, IL-6 secretion from wild-type and *Tlr2*^{-/-} bone marrow-derived macrophages (BMDM) following 5 h exposure to the indicated samples including single mutants or double-deletion strains also lacking *FTN_1103*. Isolated bacterial membranes (a, n = 3) or intact live bacteria (b, n = 6) were both tested using an amount corresponding to a

multiplicity of infection (MOI) of 20:1. Un, unstimulated. Probability brackets indicate the samples being compared, probability values without brackets indicate comparisons made to wild type. c–f, During infection of BMDM with the indicated strains, the graphs show measurements of the relative expression of *FTN_1103* (c), *cas9* (d), *scaRNA* (e) and *tracrRNA* (f) (n = 3, error bars represent s.d.) **P* ≤ 0.05; ***P* ≤ 0.005; ****P* ≤ 0.001.

100-fold induction of *cas9*, *tracrRNA* and *scaRNA* (Fig. 3d–f). In the absence of Cas9, *tracrRNA* or *scaRNA*, the temporal repression of *FTN_1103* was completely abrogated (Fig. 3c). These data indicate that *cas9*, *tracrRNA* and *scaRNA* are induced during intracellular infection, allowing temporal repression of *FTN_1103* when the bacteria are in the proximity of TLR2 in the phagosome, thus facilitating evasion of this innate immune pathway. Although *cas1*, *cas4* and the crRNA array are not required for *FTN_1103* repression, they were similarly expressed during infection (Supplementary Fig. 12). However, their expression differed during *in vitro* growth (Supplementary Fig. 13), possibly indicating specific co-regulation of these CRISPR/Cas components during intracellular infection.

We tested the consequences of the inability to repress *FTN_1103* on fitness during murine infection. We performed competitive infections with wild-type *F. novicida*, and the *cas9*, *tracrRNA* or *scaRNA* deletion mutants, and measured bacterial burden in the spleen 48 h post-infection. All three mutants were highly attenuated (1,000- to 10,000-fold) compared to wild type (Fig. 4a), demonstrating that all three components are critical for *F. novicida* virulence. This attenuation was rescued by deletion of *FTN_1103* from the mutants. Notably, mutants lacking the crRNA array or other *cas* genes were not attenuated (Supplementary Fig. 14). The *cas9*, *tracrRNA* and *scaRNA* mutants were also highly attenuated when inoculated individually; they were non-lethal even at 100 times the LD₅₀ (the dose lethal to

50% of animals tested), whereas mice infected with wild-type or *cis*-complemented strains (which restored repression of *FTN_1103*, Supplementary Fig. 15) rapidly succumbed to disease (Fig. 4b). We conjectured that the mice surviving an initial infection might be protected against subsequent lethal challenge with *F. novicida*. Naive mice rapidly succumbed to a challenge, but mice immunized with *cas9*, *tracrRNA* or *scaRNA* mutants were completely protected (Fig. 4c), demonstrating that mutants lacking these CRISPR/Cas components can efficiently vaccinate mice. Given that CRISPR/Cas systems of other bacteria may also contribute to virulence, mutants of these genes may represent attractive vaccine strains for other pathogens.

Our results demonstrate that the Cas9 system has a non-canonical function in acting with a non-crRNA (*scaRNA*) to regulate gene expression via the degradation of an endogenous mRNA, leading to innate immune evasion and promoting virulence (Supplementary Fig. 16). This surprising observation shows that CRISPR/Cas components have been co-opted to perform functions distinct from foreign nucleic acid defence. Notably, they have also been implicated in DNA repair¹⁰ and biofilm formation⁹. Our work further indicates that predicted self-targeting crRNAs²¹ may have natural roles in endogenous gene regulation, functioning with the Cas9 machinery.

Of the 109 bacteria shown to encode Cas9 (by our and others work)²², 85 are known pathogens or commensals, making it interesting to speculate that the regulatory mechanism we describe may function

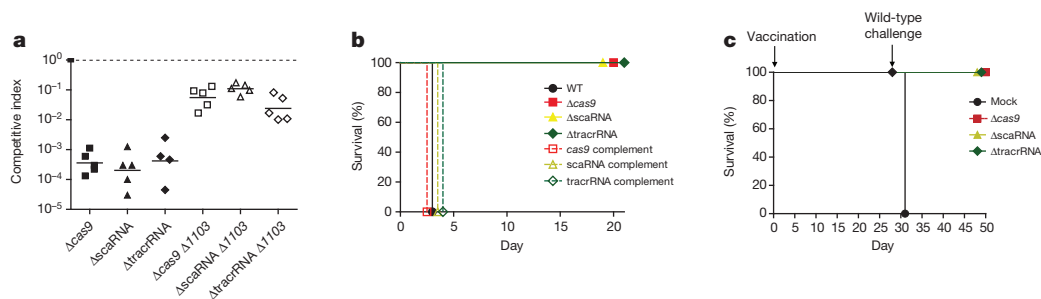


Figure 4 | Cas9, tracrRNA and scaRNA are necessary for virulence.

a, Competitive indices of wild-type and the indicated mutant or double-mutant strains from mouse spleens, 48 h post-infection. Bars represent the geometric mean. b, Mice were infected with 10⁷ colony-forming units (c.f.u.) of wild-type (black circle), *Δcas9* (red square), *ΔscaRNA* (yellow triangle), *ΔtracrRNA*

(green diamond) or the corresponding *cis*-complemented strains (open symbols), and survival monitored over time. c, Mice were vaccinated with 10⁴ c.f.u. of *Δcas9*, *ΔscaRNA* or *ΔtracrRNA* strains, or treated with PBS. Twenty-eight days later, mice were challenged with 10⁷ c.f.u. wild-type *F. novicida*.

in numerous other organisms that interact with eukaryotic cells (Supplementary Table 1). To explore the breadth of this phenomenon further, we generated a *cas9* deletion mutant in *Neisseria meningitidis* str. 92045 and assayed virulence traits. We observed a significant decrease in the ability of the *cas9* mutant to adhere to, invade and replicate in human epithelial cells, leading to an overall defect in survival (Supplementary Fig. 17), indicating that Cas9 plays an important role in *N. meningitidis* pathogenesis. Additionally, a recent study identified *Campylobacter jejuni* Cas9 as critical for interactions with host cells²³. Bioinformatic analysis predicted that *N. meningitidis*, *C. jejuni* and other pathogens may encode a scaRNA, which is critical for Cas9 targeting of endogenous mRNA (Supplementary Table 2). Together, these results clearly show that Cas9 controls virulence traits of several bacteria. It is interesting to note, however, that the whole CRISPR/Cas locus in the highly virulent *Francisella tularensis* is probably non-functional, as it lacks the tracrRNA and contains an internal deletion within Cas9. *F. tularensis* is known to potently inhibit TLR signalling¹³ and may therefore not limit, or use distinct mechanisms to limit, BLP expression. Although its role in different species may therefore vary, the enrichment of Cas9 within the genomes of pathogens and commensals and its demonstrated role in controlling virulence traits in *F. novicida*, *N. meningitidis* and *C. jejuni*, strongly indicate that it is involved in regulating the interaction of bacteria with eukaryotic hosts. Our data support a model whereby type II CRISPR/Cas systems can function in endogenous bacterial gene regulation, ultimately promoting both pathogenesis and commensalism.

METHODS SUMMARY

Bacteria and macrophage infections. *Francisella novicida* U112, *Neisseria meningitidis* str. 92045 and mutant strains constructed by allelic replacement^{24,25} (using primers in Supplementary Table 3) were grown as described^{26,27}. *F. novicida* mutant strains grew similarly to wild type in broth (Supplementary Fig. 18). Macrophages were prepared from wild-type and *Thr2*^{-/-} C57BL/6 mice and cultured and infected at a ratio of 20:1 bacteria per macrophage as described^{26,28}. IL-6 in culture supernatants was quantified by enzyme-linked immunosorbent assay (ELISA) (BD Biosciences). Membrane protein fractions were added to cells at a relative MOI of 20:1.

Mouse infections. Female C57BL/6 mice were infected subcutaneously with 2×10^5 c.f.u. of a 1:1 ratio of wild-type and mutant *F. novicida*. Spleens were collected (48 h) and bacteria enumerated. For survival experiments, mice were infected subcutaneously with 1×10^7 c.f.u. and euthanized when they appeared moribund. After infection with 1×10^4 c.f.u., surviving mice were challenged subcutaneously with 1×10^7 c.f.u. wild-type *F. novicida* 28 days later.

qPCR, RNA degradation assay and immunoprecipitation. RNA was isolated from mid-log broth cultures or macrophage infections (MOI 20:1) at the time points indicated. qPCR was performed using the Power SYBR Green RNA-to-Ct 1-Step kit (Applied Biosystems). Relative transcript levels were calculated by normalizing C_T values to DNA helicase II (*uvrD*, *FTN_1594*) and plotted as $2^{-\Delta\Delta C_T}$. RNA degradation assays were performed as previously described²⁹. Bacteria were treated with rifampicin (USB Corporation) and RNA isolated at given time points. Immunoprecipitation was performed on bacterial lysates using the Flag immunoprecipitation kit (Sigma) according to the manufacturer's instructions and the addition of 0.05% NP-40 during wash steps. RNA was isolated from the precipitate and qPCR performed, normalizing enrichment to *uvrD*.

Statistical analysis. *P* values represent analysis from unpaired, two-tailed, Student's *t*-tests, or Mantel-Cox tests for analysis of survival curves. **P* ≤ 0.05; ***P* ≤ 0.005; ****P* ≤ 0.001.

Full Methods and any associated references are available in the online version of the paper.

Received 19 October 2012; accepted 27 February 2013.

Published online 14 April 2013.

1. Barrangou, R. *et al.* CRISPR provides acquired resistance against viruses in prokaryotes. *Science* **315**, 1709–1712 (2007).
2. Marraffini, L. A. & Sontheimer, E. J. CRISPR interference limits horizontal gene transfer in staphylococci by targeting DNA. *Science* **322**, 1843–1845 (2008).

3. Bhaya, D., Davison, M. & Barrangou, R. CRISPR-Cas systems in bacteria and archaea: versatile small RNAs for adaptive defense and regulation. *Annu. Rev. Genet.* **45**, 273–297 (2011).
4. Garneau, J. E. *et al.* The CRISPR/Cas bacterial immune system cleaves bacteriophage and plasmid DNA. *Nature* **468**, 67–71 (2010).
5. Hale, C. R. *et al.* RNA-guided RNA cleavage by a CRISPR RNA-Cas protein complex. *Cell* **139**, 945–956 (2009).
6. Gasiunas, G., Barrangou, R., Horvath, P. & Siksnys, V. Cas9-crRNA ribonucleoprotein complex mediates specific DNA cleavage for adaptive immunity in bacteria. *Proc. Natl Acad. Sci. USA* **109**, E2579–E2586 (2012).
7. Jinek, M. *et al.* A programmable dual-RNA-guided DNA endonuclease in adaptive bacterial immunity. *Science* **337**, 816–821 (2012).
8. Datsenko, K. A. *et al.* Molecular memory of prior infections activates the CRISPR/Cas adaptive bacterial immunity system. *Nature Commun.* **3**, 945 (2012).
9. Zegans, M. E. *et al.* Interaction between bacteriophage DMS3 and host CRISPR region inhibits group behaviors of *Pseudomonas aeruginosa*. *J. Bacteriol.* **191**, 210–219 (2009).
10. Babu, M. *et al.* A dual function of the CRISPR-Cas system in bacterial antiviral immunity and DNA repair. *Mol. Microbiol.* **79**, 484–502 (2011).
11. Aliprantis, A. O. *et al.* Cell activation and apoptosis by bacterial lipoproteins through toll-like receptor-2. *Science* **285**, 736–739 (1999).
12. Brightbill, H. D. *et al.* Host defense mechanisms triggered by microbial lipoproteins through Toll-like receptors. *Science* **285**, 732–736 (1999).
13. Jones, C. L. *et al.* Subversion of host recognition and defense systems by *Francisella* spp. *Microbiol. Mol. Biol. Rev.* **76**, 383–404 (2012).
14. Malik, M. *et al.* Toll-like receptor 2 is required for control of pulmonary infection with *Francisella tularensis*. *Infect. Immun.* **74**, 3657–3662 (2006).
15. Abplanalp, A. L., Morris, I. R., Parida, B. K., Teale, J. M. & Berton, M. T. TLR-dependent control of *Francisella tularensis* infection and host inflammatory responses. *PLoS ONE* **4**, e7920 (2009).
16. Jones, C. L., Sampson, T. R., Nakaya, H. I., Pulendran, B. & Weiss, D. S. Repression of bacterial lipoprotein production by *Francisella novicida* facilitates evasion of innate immune recognition. *Cell. Microbiol.* **14**, 1531–1543 (2012).
17. Makarova, K. S., Aravind, L., Wolf, Y. I. & Koonin, E. V. Unification of Cas protein families and a simple scenario for the origin and evolution of CRISPR-Cas systems. *Biol. Direct* **6**, 38 (2011).
18. Deltcheva, E. *et al.* CRISPR RNA maturation by trans-encoded small RNA and host factor RNase III. *Nature* **471**, 602–607 (2011).
19. Postic, G. *et al.* Identification of small RNAs in *Francisella tularensis*. *BMC Genomics* **11**, 625 (2010).
20. Bayer, T. S., Booth, L. N., Knudsen, S. M. & Ellington, A. D. Arginine-rich motifs present multiple interfaces for specific binding by RNA. *RNA* **11**, 1848–1857 (2005).
21. Stern, A., Keren, L., Wurtzel, O., Amitai, G. & Sorek, R. Self-targeting by CRISPR: gene regulation or autoimmunity? *Trends Genet.* **26**, 335–340 (2010).
22. Makarova, K. S. *et al.* Evolution and classification of the CRISPR-Cas systems. *Nature Rev. Microbiol.* **9**, 467–477 (2011).
23. Louwen, R. *et al.* A novel link between *Campylobacter jejuni* bacteriophage defence, virulence and Guillain-Barre syndrome. *Eur. J. Clin. Microbiol. Infect. Dis.* **32**, 207–226 (2013).
24. Brotcke, A. *et al.* Identification of MglA-regulated genes reveals novel virulence factors in *Francisella tularensis*. *Infect. Immun.* **74**, 6642–6655 (2006).
25. Janik, A., Juni, E. & Heym, G. A. Genetic transformation as a tool for detection of *Neisseria gonorrhoeae*. *J. Clin. Microbiol.* **4**, 71–81 (1976).
26. Llewellyn, A. C., Jones, C. L., Napier, B. A., Bina, J. E. & Weiss, D. S. Macrophage replication screen identifies a novel *Francisella* hydrogen peroxide resistance protein involved in virulence. *PLoS ONE* **6**, e24201 (2011).
27. Kumar, P., Sannigrahi, S., Scoullar, J., Kahler, C. M. & Tzeng, Y. L. Characterization of DsbD in *Neisseria meningitidis*. *Mol. Microbiol.* **79**, 1557–1573 (2011).
28. Schaible, U. E. & Kaufmann, S. H. E. Studying trafficking of intracellular pathogens in antigen-presenting cells. *Methods Microbiol.* **31**, 343–360 (2002).
29. Postic, G. *et al.* Identification of a novel small RNA modulating *Francisella tularensis* pathogenicity. *PLoS ONE* **7**, e41999 (2012).

Supplementary Information is available in the online version of the paper.

Acknowledgements We would like to thank R. Ahmed, G. Conn, C. Dunham, C. Moran, B. Napier, D. S. Stephens and the Stephens laboratory, and M. Swanson for discussions and critical reading of this manuscript. The project described was supported by National Institutes of Health (NIH) grant U54-AI057157 from the Southeastern Regional Center of Excellence for Emerging Infections and Biodefense and R56-AI87673 to D.S.W., and R56-AI061031 to Y.-L.T. Its contents are solely the responsibility of the authors and do not necessarily represent the official views of the NIH. T.R.S. was supported by the NSF Graduate Research Fellowship, as well as the ARCS Foundation. T.R.S. and D.S.W. have filed a related provisional patent.

Author Contributions T.R.S. performed the experiments; S.D.S. and Y.-L.T. generated the *N. meningitidis* *cas9* deletion mutant and performed associated experiments; A.C.L. generated the Cas9-Flag expressing strain; T.R.S. and D.S.W. conceived and designed experiments, interpreted data and wrote the manuscript.

Author Information Reprints and permissions information is available at www.nature.com/reprints. The authors declare no competing financial interests. Readers are welcome to comment on the online version of the paper. Correspondence and requests for materials should be addressed to D.S.W. (david.weiss@emory.edu).

METHODS

Bacterial growth. *Francisella novicida* U112 was a gift from D. Monack. Cultures were grown overnight at 37 °C with aeration in tryptic soy broth supplemented with 0.2% L-cysteine (BD Biosciences) or on tryptic soy agar (BD Biosciences)²⁶. When necessary, media was supplemented with kanamycin (30 µg ml⁻¹) or tetracycline (20 µg ml⁻¹). Meningococcal strains were grown with 5% CO₂ at 37 °C on GC base (Difco) agar containing supplements of 0.4% glucose and 0.68 mM Fe(NO₃)₃, or GC broth with the same supplements and 0.043% NaHCO₃ (ref. 27). Brain heart infusion medium with 1.25% fetal bovine serum was used when kanamycin selection was required. *N. meningitidis* was transformed as described previously³⁰. To measure growth rate, overnight cultures of wild-type and the indicated *F. novicida* mutant strains were diluted to an attenuation (*D*) at 600 nm of 0.03, incubated at 37 °C with aeration and *D*_{600 nm} was measured hourly in a BioTek Synergy MX plate reader (BioTek) for 20 h.

Mutagenesis. *Francisella* deletion mutant and point mutant strains were constructed by allelic replacement as described previously²⁴ using primers listed in Supplementary Table 3. Double-deletion strains were created using Flp-recombinase, as previously described³¹, and transforming unmarked strains with the second targeting construct. *scarNA* and *tracrNA* were complemented *in trans* by ligation into the broad host range vector, pBAV1K-T5-GFP³² at the EcoRI and BamHI sites, and transformed into unmarked Δ *scarNA* or Δ *tracrNA* strains. The *N. meningitidis cas9* mutant was generated using a targeting construct generated by overlapping PCR²⁵, using primers listed in Supplementary Table 3, that created a 2,615-bp deletion in the *cas9* (3,246 bp) coding sequence. The final PCR product with the expected size was gel-purified and used directly for transformation of a meningococcal serogroup W135 strain Nm92045. Colonies were selected on brain heart infusion agar plates with 80 µg ml⁻¹ of kanamycin. Removal of the *cas9* internal sequence was confirmed by PCR.

Membrane protein fractionation and SDS-PAGE analysis. Membrane protein fractions were prepared as previously described¹⁶. Membrane proteins were normalized to 10⁸ c.f.u., separated via 12–20% SDS-PAGE (Bio-Rad) and stained with Coomassie blue G-250 (Teknova).

RNA isolation and qPCR. RNA was isolated from bacterial cultures or macrophage infections at the given time points using TRI Reagent (Molecular Research Center) and purified using the RNeasy mini kit (Qiagen) and on-column DNase treatment (Qiagen) according to the manufacturer's instructions. qPCR was performed with 40 ng total RNA using the Power SYBR Green RNA-to-CT 1-Step kit (Applied Biosystems) and gene-specific primers (Supplementary Table 3) using an Applied Biosystems StepOne cycler. Relative transcript levels were calculated by normalizing *C_T* values to DNA helicase II (*uvrD*, *FTN_1594*) and plotted as 2^{-ΔΔC_T}.

RNA degradation assay. RNA degradation assays were performed as previously described²⁹. Overnight cultures of bacteria were subcultured 1:10 into 10 ml of tryptic soy broth with 0.2% cysteine and grown to *D*_{600 nm} of ~0.4. Rifampicin (USB Corporation) was added to a final concentration of 500 µg ml⁻¹, cultures were incubated at 37 °C with aeration, and aliquots were taken at the indicated time points for RNA isolation.

Immunoprecipitation. Immunoprecipitation was performed on bacterial lysates using the Flag immunoprecipitation kit (Sigma) according to the manufacturer's instructions and the addition of 0.05% NP-40 during wash steps. Total RNA was isolated from the precipitate and qPCR performed, normalizing to *uvrD*.

Macrophage infections and stimulations. Mouse BMDM were prepared from 6- to 8-week-old wild-type and *Tlr2*^{-/-} C57BL/6 mice and cultured as described²⁸. Macrophages were seeded into 96-well plates (~5 × 10⁴ cells per well) for cytokine analysis, or 24-well plates (~3.2 × 10⁵ cells per well) for RNA isolation, in high

glucose DMEM (Lonza) supplemented with 10% heat-inactivated FBS (HyClone) and 10% L929-conditioned media (conditioned DMEM)²⁶ containing macrophage colony-stimulating factor (M-CSF) overnight. Bacteria were added at a MOI of 20:1 bacteria per macrophage and centrifuged for 15 min at 335g at room temperature to facilitate bacterial uptake. Infected macrophages were incubated for 30 min at 37 °C and washed twice before adding warm conditioned DMEM. The concentrations of IL-6 in culture supernatants at the indicated time points after infection were quantified by enzyme-linked immunosorbent assay (ELISA) (BD Biosciences). For stimulation with bacterial membrane protein fractions, cells were washed gently and media containing membrane fractions at a relative MOI of 20:1 were added. Macrophages were stimulated for the indicated duration of time, before the cell culture supernatant was collected and assayed for IL-6 by ELISA.

***N. meningitidis* intracellular survival assay.** The A549 human lung adenocarcinoma cell line was cultured in DMEM supplemented with heat-inactivated FBS (10%) at 37 °C and 5% CO₂. For the bacterial adherence and invasion assay, A549 cells were seeded at a density of 10⁵ cells per ml in 24-well plates (Corning) two days before the experiment. To prepare the bacterial inoculum, meningococcal strains were grown in GC broth to mid-log phase, collected by centrifugation and resuspended in cell culture media. Bacterial cells were added to cell cultures at a MOI of 100, and serial dilutions of the inoculum were plated to determine the input c.f.u. After a 3-h infection, the monolayers were washed three times with sterile phosphate-buffered saline to remove free bacteria and the c.f.u. of attached bacteria determined. Separately infected cells were washed and then incubated in cell culture media containing 100 µg ml⁻¹ of gentamicin for 1 h to kill extracellular bacteria. A549 cells were lysed by incubation with 1% saponin (Sigma) for 10 min to release intracellular bacteria at 4 h and 6 h post infection. Serial dilutions of lysates in PBS were plated on GC plates for c.f.u. counts of invasion efficiency. Each assay was conducted with 2–3 independently infected monolayers and repeated three times.

***In vivo* experiments.** Female C57BL/6 mice aged 7 to 10 weeks were kept under specific-pathogen free conditions in filter-top cages at Yerkes National Primate Center, and provided food and water *ad libitum*. All experimental procedures were approved by the Emory University Institutional Animal Care and Use Committee (protocol #YER-2000573-061314BN). For competitive infections, groups of five mice were infected subcutaneously with 2 × 10⁵ c.f.u. of wild type and the indicated mutant strain of *F. novicida* at a 1:1 ratio in sterile PBS. At 48 h post-infection, spleens were collected and homogenized in PBS. Appropriate dilutions were plated with or without kanamycin for enumeration of bacterial burden. The competitive index was calculated using the following formula: competitive index = (mutant c.f.u. output/wild-type c.f.u. output)/(mutant c.f.u. input/wild-type c.f.u. input). For vaccination experiments, groups of five mice were infected subcutaneously with 1 × 10⁴ c.f.u. of the indicated mutant strain of *F. novicida* in sterile PBS, or PBS alone. Twenty-eight days later, mice were challenged subcutaneously with 1 × 10⁷ c.f.u. wild-type *F. novicida* in sterile PBS and euthanized when they appeared moribund.

30. Janik, A., Juni, E. & Heym, G. A. Genetic transformation as a tool for detection of *Neisseria gonorrhoeae*. *J. Clin. Microbiol.* **4**, 71–81 (1976).
31. Gallagher, L. A., McKevitt, M., Ramage, E. R. & Manoil, C. Genetic dissection of the *Francisella novicida* restriction barrier. *J. Bacteriol.* **190**, 7830–7837 (2008).
32. Bryksin, A. V. & Matsumura, I. Rational design of a plasmid origin that replicates efficiently in both gram-positive and gram-negative bacteria. *PLoS ONE* **5**, e13244 (2010).
33. Ménard, R., Sansonetti, P. J. & Parsot, C. Nonpolar mutagenesis of the *ipa* genes defines *lpaB*, *lpaC*, and *lpaD* as effectors of *Shigella flexneri* entry into epithelial cells. *J. Bacteriol.* **175**, 5899–5906 (1993).

Thymus-derived regulatory T cells contribute to tolerance to commensal microbiota

Anna Cebula¹, Michal Seweryn^{2,3}, Grzegorz A. Rempala², Simarjot Singh Pabla¹, Richard A. McIndoe¹, Timothy L. Denning⁴, Lynn Bry⁵, Piotr Kraj¹, Pawel Kisielow⁶ & Leszek Ignatowicz¹

Peripheral mechanisms preventing autoimmunity and maintaining tolerance to commensal microbiota involve CD4⁺ Foxp3⁺ regulatory T (T_{reg}) cells^{1,2} generated in the thymus or extrathymically by induction of naive CD4⁺ Foxp3⁻ T cells. Previous studies suggested that the T-cell receptor repertoires of thymic T_{reg} cells and induced T_{reg} cells are biased towards self and non-self antigens, respectively³⁻⁶, but their relative contribution in controlling immunopathology, such as colitis and other untoward inflammatory responses triggered by different types of antigens, remains unresolved⁷. The intestine, and especially the colon, is a particularly suitable organ to study this question, given the variety of self-, microbiota- and food-derived antigens to which T_{reg} cells and other T-cell populations are exposed. Intestinal environments can enhance conversion to a regulatory lineage^{8,9} and favour tolerogenic presentation of antigens to naive CD4⁺ T cells^{10,11}, suggesting that intestinal homeostasis depends on microbiota-specific induced T_{reg} cells¹²⁻¹⁵. Here, to identify the origin and antigen-specificity of intestinal T_{reg} cells, we performed single-cell and high-throughput sequencing of the T-cell receptor repertoires of CD4⁺ Foxp3⁺ and CD4⁺ Foxp3⁻ T cells, and analysed their reactivity against specific commensal species. We show that thymus-derived T_{reg} cells constitute most T_{reg} cells in all lymphoid and

intestinal organs, including the colon, where their repertoire is heavily influenced by the composition of the microbiota. Our results suggest that thymic T_{reg} cells, and not induced T_{reg} cells, dominantly mediate tolerance to antigens produced by intestinal commensals.

We used TCR^{mini} mice¹⁶, whose limited but diversified repertoire allows for a comprehensive comparison of T-cell receptors (TCRs) in various organs and subpopulations¹⁶. In these mice, thymocytes differentiate naturally as CD4⁺ Foxp3⁺ and CD4⁺ Foxp3⁻ T cells, and efficiently repopulate peripheral lymphoid organs¹⁶. Furthermore, the TCR-β chain is identical in all TCR^{mini} T cells, enabling detection of TCR diversity through specific analysis of the TCR-α chain¹⁶. To identify Foxp3⁺ cells, we crossed TCR^{mini} mice with Foxp3^{GFP} reporter mice, which express green fluorescent protein (GFP) under the control of Foxp3 regulatory sequences¹⁷. The TCR^{mini} Foxp3^{GFP} and B6Foxp3^{GFP} mice had very similar numbers of Foxp3^{GFP} cells in different intestinal organs (Supplementary Fig. 1), and CD4⁺ cells in both types of mice expressed comparable levels of α₄β₇ and CCR9 molecules that regulate homing to the intestine (Supplementary Fig. 2). We also found that adoptive transfer of naive CD4⁺ T cells from TCR^{mini} Foxp3^{GFP} mice to lymphopenic, RAG-deficient mice caused inflammation in the colon and wasting disease. The disease could

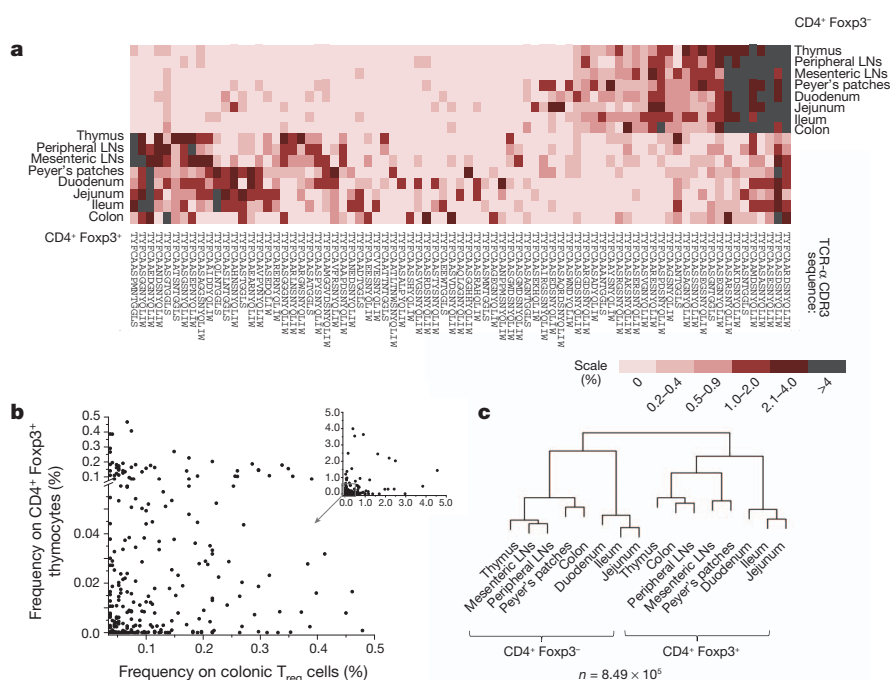


Figure 1 | TCR repertoires of intestinal T_{reg} cells are similar to the TCR repertoire of CD4⁺ Foxp3⁺ thymocytes. **a**, The frequencies of 15 dominant TCRs selected for each population from indicated organs in all organs (based on single-cell TCR sequencing; see Supplementary Table 1 for the number of TCR CDR3 sequences analysed). Colour shades reflect the relative frequency with which a given TCR was found in each organ. LNs, lymph nodes. **b**, The frequencies of dominant TCRs from colonic T_{reg} cells in the population of CD4⁺ Foxp3⁺ thymocytes. **c**, The hierarchical diagrams depict similarity indices (MI) for TCR repertoires from CD4⁺ Foxp3⁻ and CD4⁺ Foxp3⁺ populations (**b** and **c** are based on high-throughput sequencing; see Supplementary Table 1 for the number of TCR CDR3 sequences analysed).

¹Center for Biotechnology and Genomic Medicine, Georgia Regents University, Augusta, Georgia 30912, USA. ²Mathematical Biosciences Institute, College of Public Health, Ohio State University, Columbus, Ohio 43210, USA. ³Faculty of Mathematics and Computer Science, University of Lodz, 90-238 Lodz, Poland. ⁴Department of Pediatrics, Emory University, Atlanta, Georgia 30329, USA. ⁵Department of Pathology, Brigham and Women's Hospital, Harvard Medical School, Boston, Massachusetts 02115, USA. ⁶Department of Tumor Immunology, Ludwig Hirsfeld Institute of Immunology and Experimental Therapy, 53-114 Wrocław, Poland.

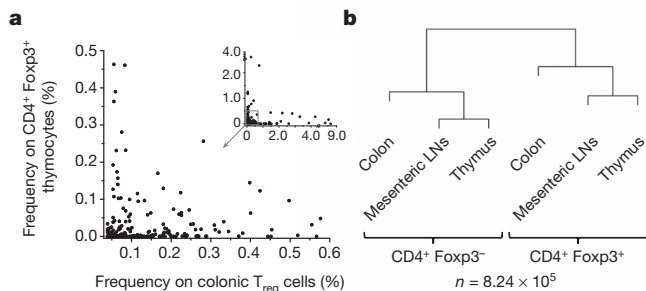


Figure 2 | In TCR- β Foxp3^{GFP} transgenic mice most colonic CD4⁺ Foxp3⁺ T cells share TCRs with CD4⁺ Foxp3⁺ thymocytes. **a**, Dominant TCRs from colonic T_{reg} cells and their frequencies on CD4⁺ Foxp3⁺ thymocytes. **b**, The hierarchical dendrogram depicts MII indices between TCR repertoires from CD4⁺ Foxp3⁺ and CD4⁺ Foxp3⁺ populations from the indicated organs. For calculation of MII, the data set from CD4⁺ Foxp3⁺ thymocytes was limited, as described in the Methods.

be prevented by the co-transfer of TCR^{mini} CD4⁺ Foxp3⁺ thymocytes without affecting the colonization of the colon by CD4⁺ Foxp3⁺ T cells, indicating that thymus-derived T_{reg} cells can control intestinal inflammation at least in these experimental settings (Supplementary Fig. 3).

Thymic T_{reg} cells and induced T_{reg} cells have similar phenotypes, and overlapping but distinct TCR repertoires relative to their thymic or peripheral origin^{16,18,19}. To compare dominant TCRs on CD4⁺ Foxp3⁺ and T_{reg} cells in lymphoid organs and in the intestine, we sorted individual cells, amplified the TCR- α chains by reverse transcriptase PCR (RT-PCR) and sequenced their complementarity determining region 3 (CDR3) (the numbers of sequences analysed by single-cell and high-throughput sequencing, pertaining to Figs 1–3, are shown in Supplementary Tables 1–3). As shown in Fig. 1a, the distribution of

dominant TCRs from CD4⁺ Foxp3⁺ and T_{reg} cells in all analysed organs was asymmetrically skewed, and only a few TCRs were over-represented in both CD4⁺ populations. Dissimilar allocation of abundant TCRs was previously observed in lymphoid organs and was attributed to a separate thymic differentiation pathway for thymic T_{reg} cells and limited conversion of CD4⁺ Foxp3⁺ cells²⁰. In addition, approximately half of the dominant TCRs found on intestinal T_{reg} cells (including colonic T_{reg} cells) were also found on CD4⁺ Foxp3⁺ thymocytes, suggesting that the intestinal T_{reg} cell repertoire includes a considerable proportion of dominant clones of thymic origin (Fig. 1a).

To compare TCR repertoires comprehensively on thymic, peripheral and intestinal CD4⁺ Foxp3⁺ and T_{reg} cell clones, we used high-throughput sequencing (Fig. 1b, c), which also minimized the proportion of unique TCRs identified, that is, found only in one organ. In the colon, unique T_{reg} cell TCRs comprised just 9% of all TCR sequences retrieved from this organ, with overall 5% of TCRs found on CD4⁺ Foxp3⁺ T cells but not on CD4⁺ Foxp3⁺ thymocytes, suggesting that the colonic population of induced T_{reg} cells expressing TCRs specific for the CD4⁺ Foxp3⁺ lineage is limited (data not shown). Accordingly, the remaining 86% of TCRs from colonic T_{reg} cells were expressed on CD4⁺ Foxp3⁺ thymocytes, and Fig. 1b shows that a vast majority of dominant TCRs from colonic T_{reg} cells (found at least ten times) were shared between both populations. These TCRs accounted for approximately half of all TCRs retrieved from CD4⁺ Foxp3⁺ thymocytes, indicating that these thymocytes are not rare, recirculating mature induced T_{reg} cells (Fig. 1c and data not shown). As shown in Fig. 1c, the similarity indices (mutual information index (MII), depicted by the distance between branches of the dendrogram) calculated for the TCR repertoires from various intestinal T_{reg} cell and CD4⁺ Foxp3⁺ populations did not reveal higher similarity, which would be expected if a dominant portion of intestinal T_{reg} cells, including those from the colon, was represented by induced

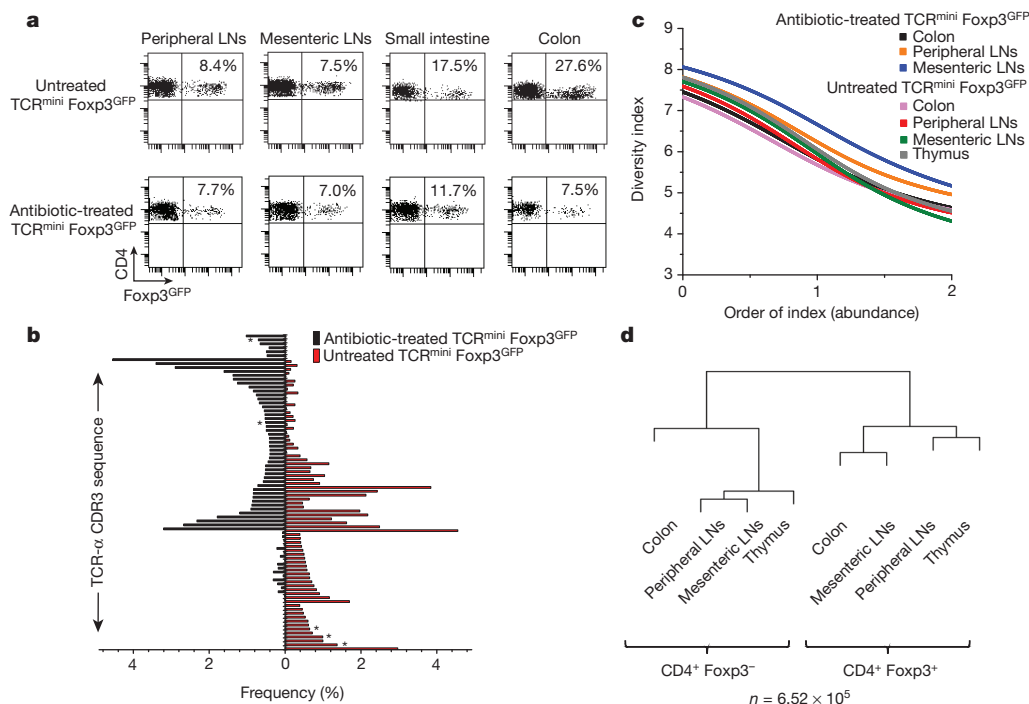


Figure 3 | Antibiotic-induced changes in colonic flora have profound influence on the TCR repertoire of colonic thymic T_{reg} cells. **a**, The effect of antibiotic treatment on the proportion of T_{reg} cells in indicated organs. Three mice per group were analysed. **b**, Fifty dominant TCRs (Supplementary Table 4) of colonic T_{reg} cells from untreated (red bars) or antibiotic-treated (black bars) mice and their frequencies in analysed repertoires. Asterisks denote TCRs

not found on CD4⁺ Foxp3⁺ thymocytes. **c**, Diversity index (Rényi entropy function) of T_{reg} cells from indicated organs of untreated and antibiotic-treated mice. Frequencies close to '0' corresponds to diversity of low-abundant TCRs, and values close to '2' denote high-abundant TCRs. **d**, MII indices for TCR repertoires of CD4⁺ Foxp3⁺ and T_{reg} cell populations from antibiotic-treated mice.

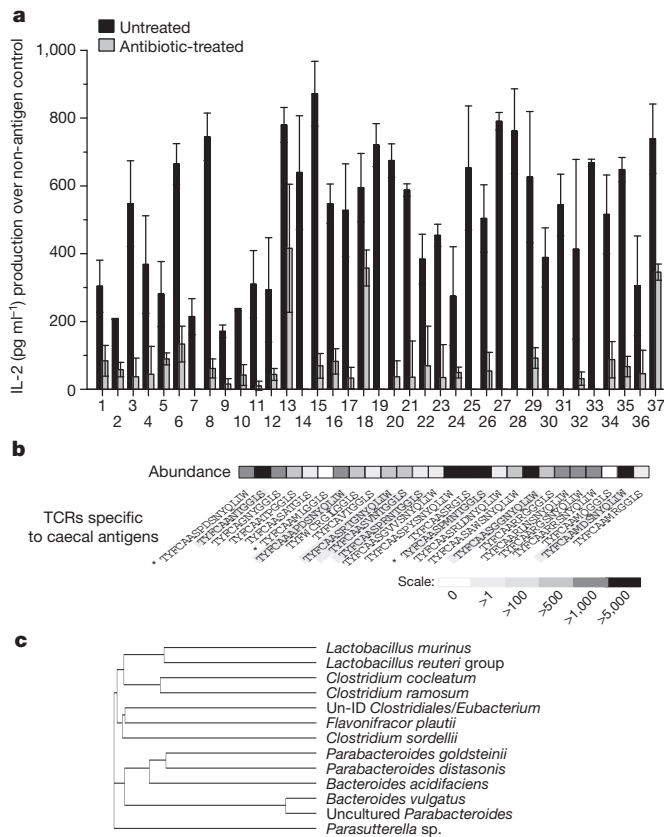
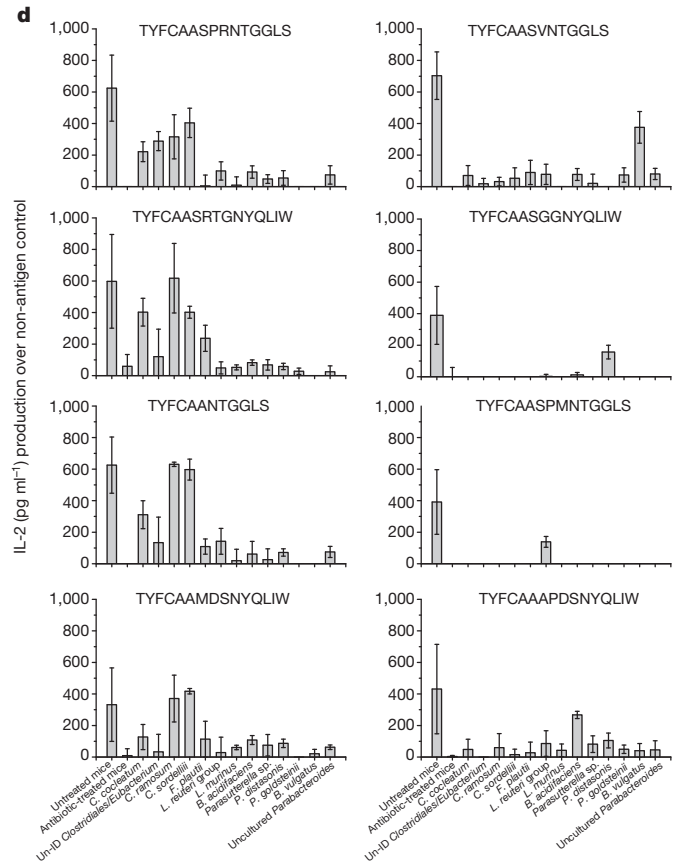


Figure 4 | TCRs from colonic thymic T_{reg} cells recognize microbial antigens. **a**, The response of cloned colonic T_{reg} cell hybridomas, which responded to caecal lysate from untreated TCR^{mini} Foxp3^{GFP} mice (Supplementary Fig. 6), to re-stimulation with caecal lysate from untreated or antibiotic-treated mice. IL-2, interleukin 2. Data are mean ± s.e.m. from three experiments. **b**, The abundance of T_{reg} TCRs from hybridomas that responded

to caecal lysates from untreated mice (shown in **a**) on CD4⁺ Foxp3⁺ thymocytes. Asterisks denote hybridomas that also responded to caecal lysate from antibiotic-treated mice. **c**, Phylogenetic distance of bacterial strains tested here. **d**, The response of hybridomas highlighted in **b** to indicated bacterial sonicates.

T_{reg} cells. In fact, not a single repertoire of T_{reg} cells clustered on the same branch of the dendrogram with CD4⁺ Foxp3⁺ repertoire(s), suggesting that these repertoires remained mostly dissimilar (as also shown for dominant TCRs in Fig. 1a and Supplementary Fig. 4). Limited conversion in the mesenteric lymph nodes or colon of TCR^{mini} Foxp3^{GFP} mice was not a result of impaired recruitment of CD4⁺ Foxp3⁺ cells in this model because the conversion was apparent in the tumour environment, after adoptive transfer of CD4⁺ Foxp3⁺ cells to lymphopenic hosts and *in vitro* (ref. 21 and data not shown).

In view of reports analysing mice with broader repertoire of TCRs than that of TCR^{mini} mice¹⁴, which suggested that induced T_{reg} cells are overwhelmingly abundant in the colon, we also examined whether the extent of TCR diversity could have a role in determining the relative involvement of thymic and induced T_{reg} cells in maintaining tolerance to colonic antigens. To address this question, we analysed TCR-β Foxp3^{GFP} transgenic mice in which the repertoire of TCRs is much larger than that of TCR^{mini} mice owing to the natural diversity of the TCR-α chain. The high-throughput sequencing of the TCRVα2⁺ chains of thymic, peripheral and colonic CD4⁺ Foxp3⁺ and CD4⁺ Foxp3⁺ subpopulations from TCR-β transgenic mice revealed a similar pattern to the respective repertoires collected from TCR^{mini} mice. Approximately 75% of all Vα2⁺ TCRs retrieved from colonic T_{reg} cells from TCR-β Foxp3^{GFP} transgenics were also expressed by CD4⁺ Foxp3⁺ thymocytes, including many abundant colonic TCRs (found in the colonic T_{reg} cell repertoire more than 20 times; Fig. 2a), which accounted for approximately 20% of all TCRs retrieved from CD4⁺



to caecal lysates from untreated mice (shown in **a**) on CD4⁺ Foxp3⁺ thymocytes. Asterisks denote hybridomas that also responded to caecal lysate from antibiotic-treated mice. **c**, Phylogenetic distance of bacterial strains tested here. **d**, The response of hybridomas highlighted in **b** to indicated bacterial sonicates.

Foxp3⁺ thymocytes (data not shown). Furthermore, the MII indices calculated for the TCR repertoires from colonic, mesenteric and thymic CD4⁺ Foxp3⁺ and CD4⁺ Foxp3⁺ cells retained the same hierarchical clustering as originally observed in TCR^{mini} mice (Fig. 2b). Thus, we concluded that the extent of TCR diversity does not have important influence on the predominance of thymic T_{reg} cells in the colon.

To investigate whether changes in the composition of colonic microflora influence the repertoire of thymic T_{reg} cells, we treated the TCR^{mini} Foxp3^{GFP} mice with a cocktail of antibiotics. This treatment considerably altered the composition of the colonic microbiota and reduced the proportion of intestinal T_{reg} cells, particularly in the colon (Fig. 3a). As shown in Supplementary Fig. 5, six out of ten dominant commensal species cultured from the caecum of untreated mice, including members of *Clostridiales*, an abundant anaerobe known to induce colonic induced T_{reg} cells¹³, fell to undetectable levels in cultures from treated mice. Of the remaining four species cultured from the caecum, two markedly increased in biomass with antibiotic treatment and two remained unaffected. Antibiotic treatment also broadly altered the frequency of dominant TCRs identified in colonic T_{reg} cells, as some clones became undetectable, whereas others expanded, probably in response to the rebound growth of more antibiotic-resistant species (Fig. 3b). Most TCRs expressed by dominant T_{reg} cell clones that contracted or expanded in antibiotic-treated mice were also found on CD4⁺ Foxp3⁺ thymocytes, indicating that changes in the intestinal flora influence the repertoire of colonic thymic T_{reg}

cells (Fig. 3b). As shown in Fig. 3c, the diversity of the TCRs on colonic T_{reg} cells from antibiotic-treated and untreated mice (calculated from high-throughput sequencing) was not significantly affected, despite their strong numerical reduction (Fig. 3a). Calculation of the MII index between T_{reg} cells and $CD4^{+}$ Foxp3 $^{-}$ populations from different organs of antibiotic-treated mice (Fig. 3d) showed that the repertoire of colonic T_{reg} cells remained similar (see Fig. 1c) to the rest of the $CD4^{+}$ Foxp3 $^{+}$ repertoires, which argues against the significant recruitment of induced T_{reg} cells in response to the changing composition of bacterial antigens.

To identify T_{reg} cell clones specific to antigens produced by commensal species, we created hybridomas from colonic T_{reg} cells²², and sorted hybridomas that responded to sterile filtrates of caecal contents from untreated TCR mini Foxp3 GFP mice (Supplementary Fig. 6). Of these sub-cloned hybridomas, most that responded to caecal filtrates from untreated mice did not respond to filtrates from antibiotic-treated mice, suggesting that most responding hybridomas expressed TCRs specific for microbial antigens present in untreated mice (Fig. 4a). We then identified 26 TCRs from hybridomas that responded to caecal filtrates from untreated mice, and examined their expression on $CD4^{+}$ Foxp3 $^{+}$ thymocytes. Figure 4b shows that more than 90% of sequenced TCRs derived from colonic T_{reg} cells were also expressed by $CD4^{+}$ Foxp3 $^{+}$ thymocytes. Next, we tested the reactivity of hybridomas, against bacterial sonicates prepared from 13 cultures of individual species identified in the caeca of TCR mini Foxp3 GFP mice (Fig. 4c). Figure 4d (left column) shows that four hybridomas responded to isolates from *Clostridiales* (one of these also responded to phylogenetically related *Flavonifractor*), and another four hybridomas (Fig. 4d, right column) responded to sonicates from *Bacteroides* or *Lactobacillus*, suggesting that these responses were elicited by unidentified bacterial antigen(s). Overall, these results demonstrate that colonic T_{reg} cells and $CD4^{+}$ Foxp3 $^{+}$ thymocytes share different TCRs that recognize microbial antigens.

Our study provides evidence for interactions between the host thymic T_{reg} cell population and the complex communities of microbes present in the gut lumen. In-depth analysis of the TCR repertoire of colonic thymic T_{reg} cells demonstrated that it is sufficiently broad to recognize microflora-derived antigens and that conversion of naive $CD4^{+}$ Foxp3 $^{-}$ cells does not appreciably modify its diversity. These conclusions challenge the recent report suggesting that induced T_{reg} cells constitute the vast majority of colonic T_{reg} cells¹⁴. In that study, the authors sampled TCR repertoires of colonic and peripheral $CD4^{+}$ cells from a TCR- β transgenic line, and used retrogenic mice to determine whether TCRs derived from dominant colonic T_{reg} cell clones support thymic selection of thymus-derived T_{reg} cells. None of the colonic TCRs examined supported thymic T_{reg} cell development, but constitutive expression of TCR in retrogenic mice can compromise thymic T_{reg} cell selection and skew thymocyte commitment to the Foxp3 $^{-}$ lineage, irrespective of the TCR origin²³. The number of TCRs examined in that study was about one order of magnitude smaller than that sequenced here, which would preclude detection of colonic TCRs on low-abundant clones in other organs. Nevertheless, half of the most abundant colonic TCRs were found on T_{reg} cells in lymphoid organs¹⁴, in which 93% of these clones were estimated to represent thymic T_{reg} cells²⁰. Therefore, in both TCR- β transgenic lines^{14,16}, a large proportion of colonic T_{reg} cells can be of thymic origin.

The results of our study are consistent with the findings that thymic T_{reg} cells recognize non-self antigens^{22,24}, become activated after colonization of germ-free mice with standardized microbial flora (Schaedler flora)²⁵, and prevent colitis in CNS1- deficient mice exclusively lacking induced T_{reg} cells²⁶ or in lymphopenic mice that received wild-type, naive $CD4^{+}$ cells²⁷. We conclude that induced T_{reg} cells can participate in maintaining tolerance to intestinal antigens, but that thymic T_{reg} cells play the dominant part in this process.

METHODS SUMMARY

Mice. The TCR mini , TCR mini Foxp3 GFP and TCR- β Foxp3 GFP mice were described previously^{16,17}. C57BL/6 (B6), TCR- α -deficient, and RAG-deficient mice were purchased from Jackson Laboratories. All animals were 8–12 weeks old.

Flow cytometry, single-cell sorting and single-cell RT-PCR. Cell-surface staining with monoclonal antibodies was done by standard procedures. Complementary DNAs from single $CD4^{+}$ Foxp3 $^{GFP+}$ and $CD4^{+}$ Foxp3 $^{GFP-}$ T cells were synthesized followed by two rounds of PCR, and CDR3 V α chains were sequenced as previously described¹⁶. The relative frequency with which a given TCR was found in a particular organ was calculated by dividing its number by the sum of all sequences from this organ.

CDR3 high-throughput sequencing. Analysis of the TCR mini Foxp3 GFP V α 2J α 26J α 2 or V α 2J α CDR3 regions (from TCR- β Foxp3 GFP transgenic mice) was performed from flow-cytometer-purified $CD4^{+}$ Foxp3 $^{GFP-}$ and Foxp3 $^{GFP+}$ T cells (purity >99%). RNA was isolated (RNeasy Mini Kit, Qiagen) and converted to cDNA (SuperScript III, Invitrogen) with a C α -specific primer. TCR- α CDR3 regions were amplified using primers with incorporated barcodes, and the PCR product was sequenced by EdgeBio/BioServ. The results obtained by this procedure may not precisely reflect the original frequency of different templates present in a given preparation because preferential amplification of some templates could occur. This could affect the accuracy of the frequency estimates of some individual sequences but not our conclusion emerging from high-throughput sequencing, corroborated by the results of single-cell sequencing.

Statistics. MII similarity index measures pairwise similarities between populations by considering the overlap and relative abundances of TCRs²⁸. For calculation of MII, the data set from $CD4^{+}$ Foxp3 $^{+}$ thymocytes was limited to 2.4×10^5 randomly selected TCRs to match approximately the number of TCRs retrieved from $CD4^{+}$ Foxp3 $^{-}$ thymocytes.

Antibiotic treatment. TCR mini Foxp3 GFP mice were given metronidazole (2.5 mg ml $^{-1}$), vancomycin (0.5 mg ml $^{-1}$) and ciprofloxacin (0.66 mg ml $^{-1}$) (all from Sigma) in drinking water for 6 weeks.

Hybridoma assays. Polyclonal hybridomas responding to caecal lysates were sorted based on expression of a nuclear factor of activated T cells (NFAT)–GFP reporter. Response of cloned hybridomas was measured using the HT-2 assay²².

Full Methods and any associated references are available in the online version of the paper.

Received 6 March 2012; accepted 15 March 2013.

Published online 28 April 2013.

- Belkaid, Y. & Rouse, B. T. Natural regulatory T cells in infectious disease. *Nature Immunol.* **6**, 353–360 (2005).
- Sakaguchi, S., Powrie, F. & Ransohoff, R. M. Re-establishing immunological self-tolerance in autoimmune disease. *Nature Med.* **18**, 54–58 (2012).
- Jordan, M. S. *et al.* Thymic selection of $CD4^{+}$ CD25 $^{+}$ regulatory T cells induced by an agonist self-peptide. *Nature Immunol.* **2**, 301–306 (2001).
- Ribot, J., Romagnoli, P. & van Meerwijk, J. P. Agonist ligands expressed by thymic epithelium enhance positive selection of regulatory T lymphocytes from precursors with a normally diverse TCR repertoire. *J. Immunol.* **177**, 1101–1107 (2006).
- Coutinho, A. *et al.* Thymic commitment of regulatory T cells is a pathway of TCR-dependent selection that isolates repertoires undergoing positive or negative selection. *Curr. Top. Microbiol. Immunol.* **293**, 43–71 (2005).
- Hsieh, C. S. *et al.* An intersection between the self-reactive regulatory and nonregulatory T cell receptor repertoires. *Nature Immunol.* **7**, 401–410 (2006).
- Curto de Lafaille, M. A. & Lafaille, J. J. Natural and adaptive Foxp3 $^{+}$ regulatory T cells: more of the same or a division of labor? *Immunity* **30**, 626–635 (2009).
- Barnes, M. J. & Powrie, F. Regulatory T cells reinforce intestinal homeostasis. *Immunity* **31**, 401–411 (2009).
- Mucida, D. *et al.* Reciprocal T_H17 and regulatory T cell differentiation mediated by retinoic acid. *Science* **317**, 256–260 (2007).
- Coomes, J. L. *et al.* A functionally specialized population of mucosal CD103 $^{+}$ DCs induces Foxp3 $^{+}$ regulatory T cells via a TGF- β and retinoic acid-dependent mechanism. *J. Exp. Med.* **204**, 1757–1764 (2007).
- Denning, T. L. *et al.* Lamina propria macrophages and dendritic cells differentially induce regulatory and interleukin 17-producing T cell responses. *Nature Immunol.* **8**, 1086–1094 (2007).
- Round, J. L. & Mazmanian, S. K. Inducible Foxp3 $^{+}$ regulatory T-cell development by a commensal bacterium of the intestinal microbiota. *Proc. Natl Acad. Sci. USA* **107**, 12204–12209 (2010).
- Atarashi, K. *et al.* Induction of colonic regulatory T cells by indigenous *Clostridium* species. *Science* **331**, 337–341 (2011).
- Lathrop, S. K. *et al.* Peripheral education of the immune system by colonic commensal microbiota. *Nature* **478**, 250–254 (2011).
- Haribhai, D. *et al.* A requisite role for induced regulatory T cells in tolerance based on expanding antigen receptor diversity. *Immunity* **35**, 109–122 (2011).

16. Pacholczyk, R. *et al.* Origin and T cell receptor diversity of Foxp3⁺CD4⁺CD25⁺ T cells. *Immunity* **25**, 249–259 (2006).
17. Kuczma, M. *et al.* Foxp3-deficient regulatory T cells do not revert into conventional effector CD4⁺ T cells but constitute a unique cell subset. *J. Immunol.* **183**, 3731–3741 (2009).
18. Hsieh, C. S. *et al.* Recognition of the peripheral self by naturally arising CD25⁺CD4⁺ T cell receptors. *Immunity* **21**, 267–277 (2004).
19. Wong, J., Mathis, D. & Benoist, C. TCR-based lineage tracing: no evidence for conversion of conventional into regulatory T cells in response to a natural self-antigen in pancreatic islets. *J. Exp. Med.* **204**, 2039–2045 (2007).
20. Lathrop, S. K. *et al.* Antigen-specific peripheral shaping of the natural regulatory T cell population. *J. Exp. Med.* **205**, 3105–3117 (2008).
21. Kuczma, M. *et al.* Intratumoral convergence of the TCR repertoires of effector and Foxp3⁺CD4⁺ T cells. *PLoS ONE* **5**, e13623 (2010).
22. Pacholczyk, R. *et al.* Nonself-antigens are the cognate specificities of Foxp3⁺ regulatory T cells. *Immunity* **27**, 493–504 (2007).
23. Bautista, J. L. *et al.* Intracloonal competition limits the fate determination of regulatory T cells in the thymus. *Nature Immunol.* **10**, 610–617 (2009).
24. Suffia, I. J. *et al.* Infected site-restricted Foxp3⁺ natural regulatory T cells are specific for microbial antigens. *J. Exp. Med.* **203**, 777–788 (2006).
25. Geuking, M. B. *et al.* Intestinal bacterial colonization induces mutualistic regulatory T cell responses. *Immunity* **34**, 794–806 (2011).
26. Josefowicz, S. Z. *et al.* Extrathymically generated regulatory T cells control mucosal T_H2 inflammation. *Nature* **482**, 395–399 (2012).
27. Fahlén, L. *et al.* T cells that cannot respond to TGF- β escape control by CD4⁺CD25⁺ regulatory T cells. *J. Exp. Med.* **201**, 737–746 (2005).
28. Rempala, G. A. & Seweryn, M. Methods for diversity and overlap analysis in T-cell receptor populations. *J. Math. Biol.* <http://dx.doi.org/10.1007/s00285-012-0589-7> (25 September 2012).

Supplementary Information is available in the online version of the paper.

Acknowledgements This work was supported by basic research grants from the National Institutes of Health (NIH; AI 5R01AI079277 to L.I., and DMS1106485 and R01CA152158 to G.A.R.). The Harvard Digestive Disease Center (HDDC) Microbiome Core facility is supported by P30-DK034854 and Brigham and Women's Hospital in Boston, Massachusetts. Microbiological analyses were performed by M. Delaney, A. Dubois and Q. Liu in the HDDC Microbiome Core, with additional review of findings by A. B. Onderdonk. We thank J. Pihkala and H. Ignatowicz for technical assistance, M. Kuczma, L. Wojciech, E. Szurek, A. Miazek and P. Muranski for discussion and R. Markowitz for editing the manuscript.

Author Contributions A.C. performed most experiments and analysed the data; M.S. and G.A.R. performed statistical analyses; S.S.P. and R.A.M. designed the PACE program; T.L.D. provided expertise in colonic T-cell isolation; L.B. performed the microbiological study; P.Kr. established TCR^{mini} and Foxp3^{GFP} mice models; P.Ki. and L.I. designed the study, analysed the data and wrote the paper.

Author Information Reprints and permissions information is available at www.nature.com/reprints. The authors declare no competing financial interests. Readers are welcome to comment on the online version of the paper. Correspondence and requests for materials should be addressed to L.I. (ignatowicz@gru.edu).

METHODS

Mice. TCR^{mini} Foxp3^{GFP} and TCR-β Foxp3^{GFP} (Vβ14Dβ2Jβ2.6) mice were obtained by mating B6Foxp3^{GFP} (ref. 17) with TCR^{mini} (ref. 16) and TCR-β (ref. 16) mice, respectively. The progeny was screened for the co-expression of the Foxp3^{GFP} reporter, plus the TCR^{mini} Vα2Vβ14⁺ dimer or TCR-β Vβ14⁺ chain, respectively. To eliminate expression of endogenous TCR-α chains, all TCR^{mini} mice were crossed with mice deficient in endogenous TCR-α loci and were heterozygous for TCR-α Vα2Jα26Jα2 mini-locus to ensure expression of a single TCR-α chain per T cell. All animals were housed in Georgia Regents University animal facility in accordance to the Institutional regulations.

Purification of intestinal lamina propria T cells. Intestinal regions were opened longitudinally and contents were flushed with ice-cold HBSS (Cellgro). Each region was cut into small pieces and washed with HBSS supplemented with 5% FCS (HyClone) and 2 mM EDTA at 37 °C. A single-cell suspension was obtained after treatment with collagenase D (1.0 mg ml⁻¹) and DNase I (0.1 mg ml⁻¹) (both from Roche). A purified and concentrated suspension of lamina propria lymphocytes was obtained after centrifugation on Percoll (GE Healthcare) gradient (45% and 70%). The interface, enriched in leukocytes, was collected and used for experiments.

Isolation of thymocytes and T cells from lymphoid organs. Single-cell suspensions were prepared from the thymus, inguinal and mesenteric lymph nodes by mechanical disruption. Peyer's patches were excised from the small intestine wall, and lymphocytes were isolated by enzymatic digestion for 20 min, using collagenase D (1.0 mg ml⁻¹) and DNase I (0.1 mg ml⁻¹) at 37 °C.

Flow cytometry, single-cell sorting and single-cell RT-PCR. Thymocytes and T cells were stained with antibodies against CD4, CD8, Vα2, Vβ14, CCR9 and αβ₇ (BD Biosciences or eBioscience), and analysed using a BD FACS Canto (BD Biosciences). Single cells were sorted (MoFlo cell sorter, Beckman Coulter) into 96-well plates from a sorted (purity >99%) population of CD4⁺ Foxp3^{GFP+} and CD4⁺ Foxp3^{GFP-} T cells. cDNA was synthesized using MMLV reverse transcriptase (Promega) and random hexamers (IDT), followed by two rounds of PCR via Perfect Taq Polymerase (5 PRIME)¹⁶. Products of the CDR3 Vα chain obtained in the second PCR reaction were sequenced in the Genomic Core Facility at the University of Illinois. All necessary precautions were taken to prevent PCR contamination, as previously described¹⁶.

High-throughput CDR3 sequencing. The following Cα-specific primer was used for cDNA synthesis: 5'-TCGGCACATTGATTGGGAGTC-3'. The following primers with incorporated tags for Ion Torrent high-throughput sequencer were used: Vα2IT, 5'-CCATCTCATCCCTGGTGTCTCCGACTCAGTCTCAGCC TGGAGACTCAGC-3'; CαIT, 5'-CCTCTCTATGGGCAGTCGGTGATTGGTA CACAGCAGTTCTGGGT-3'.

CDR3 regions sequenced on the same chip and derived from different subsets were discriminated based on barcodes, which were validated for optimal performance with the Ion Torrent PGM. Data was analysed using the Parallel Algorithm for CDR3 Extraction (PACE) program, and evaluated with statistical methods as described below and in ref 28.

Hybridoma assays. Colonic CD4⁺ Foxp3^{GFP+} T cells were expanded *in vitro* for 7 days as described²⁹ and fused with BW5147 thymoma stably transfected with the nuclear factor of activated T cells (NFAT)-GFP reporter. It should be noted that as a result of fusion, T_{reg} cells lose expression of Foxp3^{GFP}, and therefore expression of NFAT-GFP in hybridomas can be used as a marker of their activation. After 10 days, the heterogeneous pool of hybrids was incubated overnight with splenocytes or bone-marrow-derived dendritic cells from TCR-α-deficient mice preincubated overnight with sterile lysate obtained from the caecum of TCR^{mini} Foxp3^{GFP} mice. Responding hybridomas were sorted based on NFAT-GFP expression (Supplementary Fig. 6), cloned into 96-well plates, and were restimulated 2 weeks later with sterile caecum lysates from untreated or antibiotic-treated TCR^{mini} Foxp3^{GFP} mice in the presence of autologous antigen-presenting cells.

The response of cloned hybridomas towards caecal lysates and microbial sonicates was measured using the HT-2 assay²². In brief, 10⁵ hybridoma cells were incubated with 10⁵ bone-marrow-derived dendritic cells (or splenocytes from TCR-α-deficient mice) alone (no antigen control), and lysate or the indicated bacterial sonicates each in the non-toxic range of different concentrations. After 24 h, the amount of secreted IL-2 was measured with the detector HT-2 cell line and compared to values from a standard curve derived from recombinant IL-2 (Peprotech). The proliferation of HT-2 cells in response to IL-2 was measured with the MTT (Sigma) assay²², and the response at optimal concentration of bacterial sonicate is shown in Fig. 4. The TCR-α CDR3 regions from responding hybridomas were amplified, sequenced and cross-referenced to our database of TCR-α CDR3 collected from various subpopulations of CD4⁺ T cells.

Adoptive transfer. RAG-2-deficient mice were injected intravenously with sorted CD4⁺ subpopulations from TCR^{mini} Foxp3^{GFP} mice. Recipients received naive, pLN CD4⁺ cells, or in addition received thymic or peripheral CD4⁺ Foxp3^{GFP+}

cells. After adoptive transfer, mice weight was monitored on a weekly basis. After 5 weeks all recipients were killed and their colons were examined for the signs of inflammation. The proportions of Foxp3^{GFP-} to Foxp3^{GFP+} of CD4⁺ T cells in the colon were similar in all recipients (data not shown).

PACE. PACE is an application to obtain sequences of TCR CDR3 regions generated by high-throughput sequencers. This algorithm uses BLAST as a core component for sequence comparison to locate known V and J regions in high volumes of sequencing data. Extracted sequences were managed in a centralized SQL database and reported in FASTA format.

Accuracy of CDR3 sequencing. To control for possible contaminations during sorting or PCR, cells from several sorts from different CD4⁺ cell subsets were individually processed, sequenced and data from respective subsets were compared. In addition, it was verified that TCR repertoires obtained from the same cell populations by single-cell and high-throughput TCR sequencing were similar, demonstrating that both sequencing approaches yield comparable data (Fig. 1c and Supplementary Fig. 4a, b). To ensure that dominant CDR3 regions are not contaminants, it was checked whether in each data set these regions were encoded by multiple different nucleotide sequences (indicative of selection at the protein level and not the amplification of a single clonotype due to artificial contamination). Examples of this analysis are shown in Supplementary Fig. 7 and Supplementary Table 5.

The accuracy of the high-throughput CDR3 sequencing was ensured by the use of high-fidelity DNA polymerase with a low intrinsic error rate (AccuPrime Taq DNA Polymerase High Fidelity; Invitrogen). In addition, Ion Torrent Suite software filters were used during data processing to exclude low-quality reads and erroneous sequences derived from mixed DNA templates. Most common Ion Torrent sequencer errors are base insertions and deletions occurring in homopolymers, which result in frameshifts and stop codons. To identify errors within Vα2 and Jα2 (or Jα26) segments, all sequences were aligned to constant regions. To estimate the application-specific error within the CDR3 region, two monoclonal CDR3 regions from TCR^{mini} mice were amplified (approximately 1 × 10⁵ reads were collected), and the reads that differed from the original template were counted. This approach estimated that less than 3% of CDR3 regions may contain errors (Supplementary Table 6), which is significantly below the threshold adversely affecting the statistical similarity and overlap analysis²⁸.

Microbiology. Caeca with content were dissected under sterile conditions, placed in cryovials and immediately snap frozen in liquid nitrogen. Samples were further processed and analysed in the Harvard Digestive Disease Center Microbiome Core facility. Phylogenetic identification and subtyping was based on 16S ribosomal RNA classification. Molecular speciation of bacteria was performed with 16S rRNA gene analyses. Assembled sequences were loaded into the Ribosomal Database Project's SEQMATCH tool to identify the taxonomic assignment (<http://rdp.cme.msu.edu/>).

Statistical analysis. The comparison of various TCR repertoires was conducted by means of the assessment of their respective diversities as well as overlap between populations (Figs 1c, 2b, 3c, d and Supplementary Fig. 4a). In the current context, under the term 'diversity' we understand both the richness and the abundance patterns of the repertoires.

For the sake of quantifying the TCR diversity for a single repertoire, we have adopted the information-theoretic approach based on the notion of the Renyi entropy function of order α denoted H_α (ref. 30). This function quantifies diversity by means of the formula:

$$H_\alpha = \frac{1}{1-\alpha} \log \left(\sum_i p_i^\alpha \right)$$

in which p_i is the observed frequency of the i -th species, and the order α is a non-negative exponential weight parameter. The value of α below unity gives more weight to the less abundant (and thus possibly under-sampled) species, whereas the values above unity give more weight to the more abundant species. For $\alpha = 1$, the above formula is not well-defined but may be obtained by taking the limiting expression as α approaches unity. In this case:

$$H_1 = - \sum_i p_i \log p_i$$

is the usual Shannon entropy function known in the information theory, which weights equally the contributions of all observed species to the repertoire diversity.

By plotting the values of the Renyi entropy H_α against its index, we are able to analyse diversity of TCR populations graphically in terms of their diversity, weighted towards rare ($\alpha < 1$) and abundant ($\alpha > 1$) species (Fig. 3c). Because the p_i quantities are the empirical counts of the observed species, for the sake of obtaining bounds on the sampling error in the values H_α we apply the computational methods based on

the non-parametric bootstrap as described previously²⁸. To improve the robustness of H_x against unseen species (that is, the possible under-sampling of the species richness) we have also considered a version of the analysis in which the 'Chao-Shen' correction was applied to compute the Shannon entropy, as described²⁸. In our particular case, it turned out that the results of this alternative analysis differed only marginally from the original ones.

The pairwise overlap analysis as described in Figs 1c, 2b, 3d and Supplementary Fig. 4a was conducted on the basis of the hierarchical clustering of the repertoires with an appropriately chosen dissimilarity function. Similarly, as for the analysis of the single repertoire diversity, we have adopted an information theoretical approach to pairwise compare TCR repertoires. Because the pairs of observed frequencies of different TCR species may be arranged in a two-way contingency table, the entropy-based index, known as the mutual information index (MII), can be applied to measure the association between observed TCR frequencies and the corresponding class (repertoire) labels. If MI is the usual mutual information statistic in a two-way contingency table, and n_1 and n_2 are the proportions of species observed in different TCR populations (that is, $n_1 + n_2 = 1$), the MII is given by the formula:

$$MII = \frac{MI}{-n_1 \log n_1 - n_2 \log n_2}$$

The MII may be shown to take values between 0 and unity, with the 0 value admitted only for repertoires with linearly dependent vectors of TCR frequencies. This property makes MII an appropriate measure of dissimilarity for the current purpose of TCR populations clustering. For the practical purpose of computing the sampling errors in values of MII for all pairs of repertoires, the statistical computational bootstrap methods were applied as explained above. With the MII as the dissimilarity measure we used a canonical clustering procedure based on agglomerative clustering with Ward linkage method. The outcome of the algorithm is presented as a dendrogram or a tree diagram with its leaves representing TCR populations. The leaves are located at the tree distances from each other computed according to their MII values.

29. Singh, N. *et al.* Generation of T cell hybridomas from naturally occurring FoxP3⁺ regulatory T cells. *Methods Mol. Biol.* **707**, 39–44 (2011).
30. Renyi, A. On measures of information and entropy. *Proc. 4th Berkley Symp. Math. Stat. Prob.* **1**, 547–561 (1961).

Phosphatidylserine receptor BAI1 and apoptotic cells as new promoters of myoblast fusion

Amelia E. Hochreiter-Hufford^{1,2,3}, Chang Sup Lee^{1,2,3}, Jason M. Kinchen^{1,2,3}, Jennifer D. Sokolowski^{3,4}, Sanja Arandjelovic^{1,2,3}, Jarrod A. Call^{5,6}, Alexander L. Klibanov^{5,6}, Zhen Yan^{5,6}, James W. Mandell^{3,4} & Kodi S. Ravichandran^{1,2,3}

Skeletal muscle arises from the fusion of precursor myoblasts into multinucleated myofibres^{1,2}. Although conserved transcription factors and signalling proteins involved in myogenesis have been identified, upstream regulators are less well understood. Here we report an unexpected discovery that the membrane protein BAI1, previously linked to recognition of apoptotic cells by phagocytes³, promotes myoblast fusion. Endogenous BAI1 expression increased during myoblast fusion, and BAI1 overexpression enhanced myoblast fusion by means of signalling through ELMO/Dock180/Rac1 proteins⁴. During myoblast fusion, a fraction of myoblasts within the population underwent apoptosis and exposed phosphatidylserine, an established ligand for BAI1 (ref. 3). Blocking apoptosis potentially impaired myoblast fusion, and adding back apoptotic myoblasts restored fusion. Furthermore, primary human myoblasts could be induced to form myotubes by adding apoptotic myoblasts, even under normal growth conditions. Mechanistically, apoptotic cells did not directly fuse with the healthy myoblasts, rather the apoptotic cells induced a contact-dependent signalling with neighbours to promote fusion among the healthy myoblasts. *In vivo*, myofibres from *Bai1*^{-/-} mice are smaller than those from wild-type littermates. Muscle regeneration after injury was also impaired in *Bai1*^{-/-} mice, highlighting a role for BAI1 in mammalian myogenesis. Collectively, these data identify apoptotic cells as a new type of cue that induces signalling via the phosphatidylserine receptor BAI1 to promote fusion of healthy myoblasts, with important implications for muscle development and repair.

Mammalian skeletal muscle is formed by the proliferation, differentiation and fusion of myogenic precursor cells (myoblasts) into multinucleated myofibres. The Dock180 protein⁵ and its partner ELMO⁴ function as the guanine nucleotide exchange factor to activate the GTPase Rac⁶ and all three have been linked to myoblast fusion^{7–12}. The seven-transmembrane protein BAI1 (a member of the adhesion-type G-protein-coupled receptor family) mediates recognition of phosphatidylserine on apoptotic cells (Fig. 1a), and signals through the ELMO/Dock180/Rac1 pathway³. We asked whether BAI1 might also play a role in myoblast fusion.

We readily detected endogenous BAI1 expression in developing embryonic day 14.5 (E14.5) mouse myofibres (Fig. 1b). Shifting mouse C2C12 myoblasts from growth medium to low-serum fusion medium induces formation of multinucleated, myosin-expressing myotubes¹³, and provides a quantifiable *in vitro* model of myogenesis^{14,15}. BAI1 was expressed in undifferentiated C2C12 myoblasts and a reproducible fourfold increase in BAI1 protein was observed in fusing cultures (Fig. 1c). Because siRNA-mediated knockdown of BAI1 in C2C12 myoblasts was variable and inefficient, we asked whether BAI1 overexpression could provide a 'gain-of-function'. C2C12 myoblast clones stably overexpressing BAI1–green fluorescent protein (BAI1–GFP) showed enhanced myoblast fusion (Fig. 1d, e), and the increased fusion was seen with several independent BAI1–GFP clones. Lentivirus-based

overexpression of BAI1 in C2C12 cells (maintained as heterogeneous populations) also displayed greater fusion, with a 73% increase in the fusion index (the fraction of total nuclei that are contained within the fused myotubes, see Methods) ($P < 0.001$, Fig. 1h). Moreover, myotubes in cultures overexpressing BAI1 appeared longer with more nuclei compared to control cultures. Counting the number of myotubes with 2–4 nuclei (small myotubes) and ≥ 5 (large myotubes) confirmed that BAI1 overexpression increases the total number of myotubes and the number of nuclei per myotube ($P < 0.01$, Fig. 1h).

We next tested whether BAI1-mediated C2C12 fusion was dependent on the ELMO/Dock180/Rac1 signalling module³. C2C12 myoblasts with knockdown of ELMO2 (the predominant isoform in myoblasts, Fig. 1f), formed fewer myotubes and were reduced in size and nuclei content (Fig. 1g). To test the requirement for ELMO in BAI1-mediated enhanced fusion, we transduced a BAI1(AAA) cytoplasmic tail mutant (with the amino acids RKR changed to AAA) unable to engage the ELMO/Dock180/Rac1 module³. BAI1(AAA) overexpression did not increase the fusion index, total number of myotubes or nuclei per myotube (Fig. 1h). The fusion-promoting effect of BAI1 also depends on Rac activity, as the Rac inhibitor EHT1864 (ref. 16) effectively inhibited myoblast fusion in BAI1 overexpressing cells ($P < 0.01$, $P < 0.001$; Fig. 1i). These data indicate that the membrane protein BAI1, signalling through the ELMO/Dock180/Rac1 module, can enhance mammalian myoblast fusion.

During phagocytosis, BAI1 on phagocytes recognizes phosphatidylserine, a near-universal marker exposed on the surface of apoptotic cells; previous studies have indicated that transient externalization of phosphatidylserine is necessary for myoblast fusion^{17,18}. Myoblast fusion was strikingly inhibited by masking phosphatidylserine in fusing cultures, using either a phosphatidylserine binding domain of BAI1 (GST–TSR)³ or a phosphatidylserine-specific antibody fragment (Supplementary Fig. 1a, b). We also found that a significant fraction of C2C12 myoblasts underwent cell death within 24 h after switching to fusion medium (associated with rounding up and detachment from the plate). Such cells displayed several known features of apoptosis, with 17% of cells positive for annexin V, 9% positive for the apoptosis indicator stain TO-PRO-3 (which enters apoptotic cells through caspase-activated channels¹⁹), and 9% positive for active caspase-3 ($P < 0.01$, $P < 0.05$; Fig. 2a). These percentages may be an underestimation due to the unavoidable loss of apoptotic cells during the staining protocols. We also analysed paraspinous muscle tissue at different stages of embryogenesis, and could readily detect apoptotic cells labelled with cleaved caspase 3 (73.8 ± 32.0 per mm²) that were in contact with E14.5 myofibres (Fig. 2b, left panel). Several of these apoptotic cells also displayed blebbing (Fig. 2b, right panel). Of note, E14.5 is also the stage when we observed a strong BAI1 staining of developing myofibres (Fig. 1b).

We next tested whether apoptosis was required for myoblast fusion. Adding z-VAD-FMK (zVAD), a pan-caspase inhibitor that blocks apoptosis, potentially inhibited myoblast fusion (51% decrease in fusion

¹Department of Microbiology, Immunology, and Cancer Biology, University of Virginia, Charlottesville, Virginia 22908, USA. ²Beirne B. Carter Immunology Center, University of Virginia, Charlottesville, Virginia 22908, USA. ³Center for Cell Clearance, University of Virginia, Charlottesville, Virginia 22908, USA. ⁴Department of Pathology, University of Virginia, Charlottesville, Virginia 22908, USA. ⁵Robert M. Berne Cardiovascular Research Center, University of Virginia, Charlottesville, Virginia 22908, USA. ⁶Department of Medicine, University of Virginia, Charlottesville, Virginia 22908, USA.

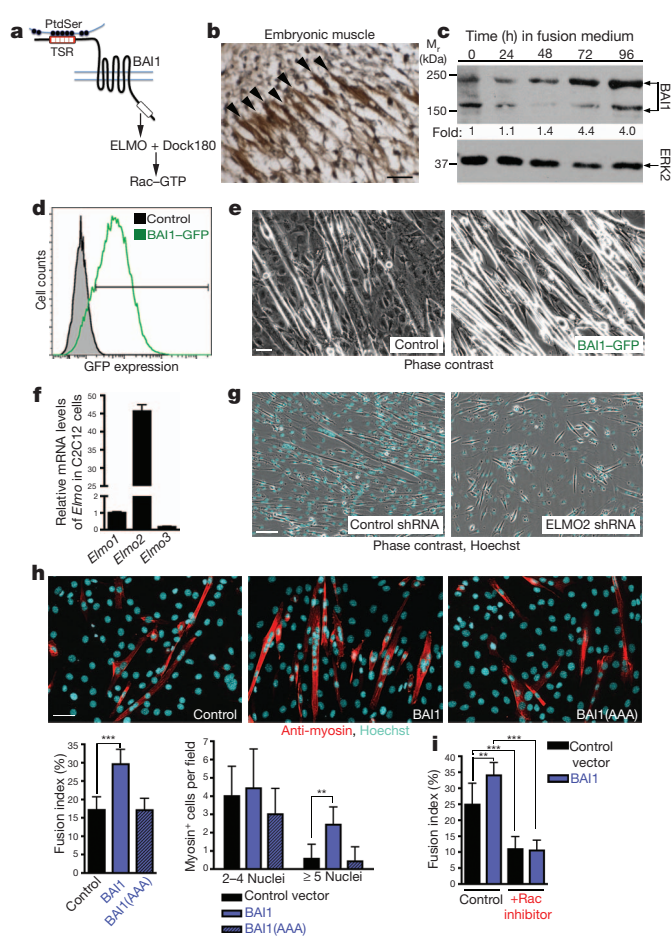


Figure 1 | The phosphatidylserine receptor BAI1 promotes myoblast fusion. **a**, Schematic of BAI1 depicting TSR repeats that bind phosphatidylserine on apoptotic cells and the ELMO1-binding site in its cytoplasmic tail. **b**, Endogenous BAI1 protein (brown) detected within developing E14.5 mouse paraspinal muscle. **c**, BAI1 protein expression in fusing C2C12 myoblast cultures (170-kDa monomer and 220-kDa dimer³). BAI1 expression fold changes are relative to time 0 h. **d**, BAI1-GFP expression in stable C2C12 clones analysed by flow cytometry. **e**, Myoblast fusion in control or BAI1-GFP stable clones. **f**, Quantitative PCR with reverse transcription (qRT-PCR) analysis of *Elmo1*, *Elmo2* and *Elmo3* messenger RNA (normalized to *Hprt*) in C2C12 myoblasts (expression compared to *Elmo1*). **g**, Fewer myotubes and fewer nuclei within myotubes of ELMO2 shRNA stable cells. Scale bar, 100 μ m. **h**, Myoblast fusion in C2C12 cultures transduced with lentivirus encoding wild-type BAI1, mutant BAI1(AAA) or control vector. For fusion index determination (see Methods), nuclei (Hoechst, cyan) and myotubes (anti-myosin antibody, red) were labelled, and six fields analysed per sample for each experiment (** $P < 0.001$, ** $P < 0.01$). **i**, BAI1-mediated increased myoblast fusion is blocked by Rac inhibitor (EHT1864) (** $P < 0.01$, *** $P < 0.001$). All data represent at least three independent experiments. Error bars indicate s.d., and scale bars represent 50 μ m unless otherwise stated.

Concerns that the caspase-inhibitor-mediated block of myoblast fusion could have arisen due to unintended, non-specific effects were overcome when the removal of zVAD from myoblast cultures, even after treatment for 5 days, re-initiated fusion (data not shown). Moreover, zVAD inhibition of myoblast fusion depended on the time when the myoblasts were exposed to the drug; zVAD was far less effective when added to C2C12 cells already switched to fusion medium and after the appearance of floating/apoptotic cells (Fig. 2e). These observations suggest that the emergence of apoptotic myoblasts in fusing cultures is essential for normal myoblast fusion.

Myogenin (MyoG) is an essential basic-helix-loop-helix myogenic transcription factor involved in the development of skeletal muscle *in vivo*²⁰. Caspase inhibition did not block the approximate 60-fold upregulation of the *Myog* transcript (Supplementary Fig. 2), even though both zVAD and Q-VD effectively blocked expression of myosin, another well-known differentiation marker (Fig. 2c and Supplementary Fig. 1c). This suggests that caspase inhibition does not block all differentiation steps, and that caspase-mediated apoptosis during myoblast fusion is required either downstream or parallel to MyoG.

We investigated whether adding apoptotic myoblasts could rescue fusion in zVAD-treated cultures. We collected the floating/apoptotic myoblasts from fusing cultures without zVAD, gently resuspended them in fresh fusion medium containing zVAD, and added them to zVAD-treated fusing cultures (see schematic in Fig. 3a). Adding apoptotic myoblasts effectively rescued zVAD-inhibited myoblast fusion,

index, $P = 0.0002$; Fig. 2c). Similar results were observed with another pan-caspase inhibitor, Q-VD-OPH (Q-VD). Supplementing insulin-transferrin-selenium to fusion medium enhances myoblast fusion, yielding large, sheet-like myotubes within 24–48 h (Supplementary Fig. 1c). Caspase inhibition also potentially inhibited insulin-transferrin-selenium-enhanced fusion (67% decrease, $P < 0.0001$; Supplementary Fig. 1c). zVAD blocked fusion of BAI1-GFP-overexpressing cells, indicating that the fusion-promoting effect of BAI1 also depends on cell death within fusing cultures (Fig. 2d).

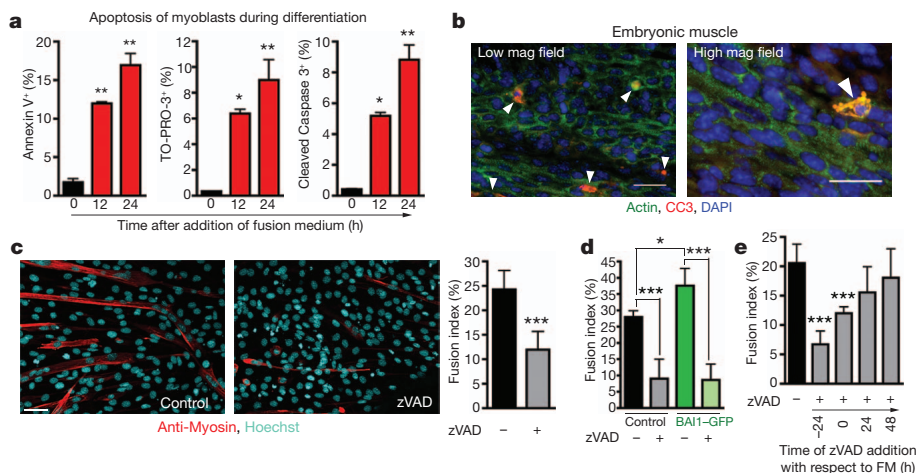


Figure 2 | Apoptosis of myoblasts is necessary cue for fusion. **a**, Apoptosis of C2C12 myoblasts at indicated time points during fusion was assessed by annexin V, TO-PRO-3 (permeable to apoptotic cells) or anti-cleaved caspase 3 (CC3) after permeabilization (* $P < 0.05$, ** $P < 0.01$). **b**, Dying cells (white arrowheads) were detected in developing E14.5 mouse skeletal muscle tissue with CC3 antibody (red); striated muscle fibres detected with anti-actin (green). Higher magnification image displays characteristic blebbing of CC3-positive apoptotic cells. Scale bars represent 25 μ m. **c**, C2C12 cultures were treated with the pan-caspase inhibitor zVAD and analysed for nuclei (Hoechst, cyan), myotubes (anti-myosin, red). Six fields were analysed per treatment for each experiment (** $P = 0.0002$). **d**, BAI1-mediated enhancement of myoblast fusion is also blocked by zVAD (* $P < 0.05$, *** $P < 0.001$). **e**, Myoblast fusion is inhibited by zVAD, only if added before cell death occurs (** $P < 0.001$). All data represent at least three independent experiments. Error bars indicate s.d. and scale bars represent 50 μ m unless otherwise stated. FM, fusion medium.

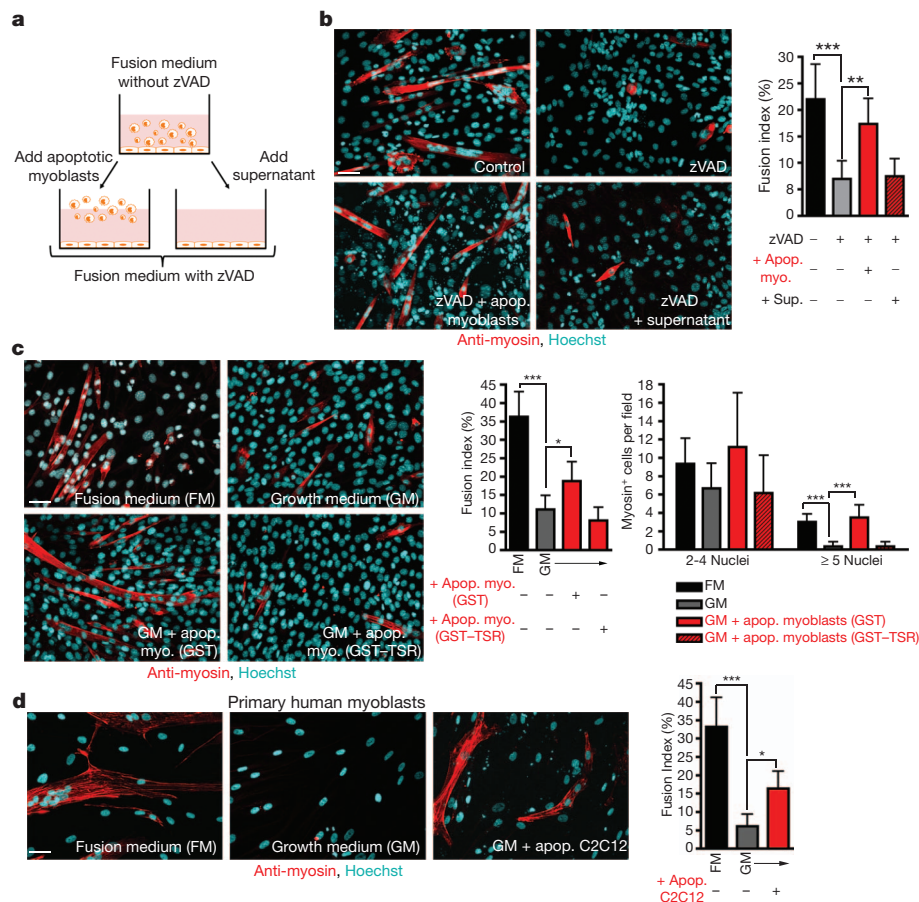


Figure 3 | Cell-cell contact through apoptotic myoblasts promotes healthy myoblast fusion.

a, Schematic depicting the adding back of apoptotic myoblasts. **b**, Apoptotic myoblasts or cell-free supernatants were added to C2C12 cells treated with zVAD in fusion medium. Nuclei (Hoechst, cyan) and myotubes (anti-myosin antibody, red) were labelled, and six fields analysed per treatment group for each experiment (** $P < 0.01$, *** $P < 0.001$). **c**, C2C12 cultures were maintained in fusion medium (FM), growth medium (GM), or GM plus apoptotic C2C12 cells pre-incubated with either control GST protein or GST-TSR (to mask phosphatidylserine) and analysed as above (* $P < 0.05$, *** $P < 0.001$). Note the increase in myotubes with ≥ 5 nuclei (large myotubes) (** $P < 0.01$, *** $P < 0.001$). **d**, Human primary skeletal myoblast cultures were maintained in FM, GM, or GM with apoptotic C2C12 myoblasts and analysed as above (* $P < 0.05$, *** $P < 0.001$). All data represent at least three independent experiments. Error bars indicate s.d. and scale bars represent 50 μm .

with a 149% increase in the fusion index ($P < 0.01$, Fig. 3b). The added apoptotic myoblasts exposed phosphatidylserine (Supplementary Fig. 3a), but did not attach to the tissue culture plate, nor was there fusion between the apoptotic cells (Supplementary Fig. 3b); thus, the simple increase in cell density or adherence could not explain the fusion-promoting effect. Notably, supernatants from fusing myoblast cultures (passed through a 0.2- μm filter) failed to rescue zVAD-inhibited fusion (Fig. 3b). Adding one apoptotic myoblast per two viable myoblasts could maximally rescue the zVAD-inhibited fusion (Supplementary Fig. 3c), whereas adding too many dying myoblasts was less effective.

Consistent with the observation that phosphatidylserine exposure is necessary for myoblast fusion, masking phosphatidylserine on apoptotic myoblasts (with GST-TSR, ref. 3) failed to rescue fusion ($P < 0.001$, Supplementary Fig. 3d). When we tested whether apoptotic myoblasts delivered a unique signal or if any apoptotic-cell type could stimulate fusion, apoptotic primary mouse thymocytes also rescued zVAD-inhibited myoblast fusion ($P < 0.001$, Supplementary Fig. 4c). These data further indicated that caspase inhibition itself does not have a non-specific effect, and that myoblasts can fuse in the presence of zVAD if provided with apoptotic cells. Collectively, these observations suggest that apoptotic myoblasts are necessary to promote myoblast fusion, requiring phosphatidylserine-dependent cell-cell contact between apoptotic and viable myoblasts.

Normally, fusion is deficient or absent in C2C12 myoblasts cultured in growth medium (Fig. 3c). Strikingly, adding apoptotic myoblasts to the myoblast cultures in growth medium stimulated fusion (70% increase in the fusion index, $P < 0.05$; Fig. 3c). This effect of apoptotic myoblasts was again dependent on phosphatidylserine exposure (Fig. 3c). Because myoblasts in growth medium continue to divide with no apparent cell death, these cultures had more nuclei at the end of the assay, artificially lowering the fusion index values. However, counting

the number of myotubes containing 2–4 nuclei (small myotubes) and ≥ 5 nuclei (large myotubes) revealed that apoptotic myoblasts significantly promoted myotubes with ≥ 5 nuclei ($P < 0.001$, Fig. 3c). This fusion-promoting effect of apoptotic cells in growth medium was not caused by lowering nutrients in the culture medium (mimicking low mitogen fusion medium conditions); adding 'viable' T lymphocytes, which proliferated and consumed nutrients from the culture medium did not promote fusion, whereas apoptotic lymphocytes triggered fusion ($P < 0.001$, $P < 0.01$; Supplementary Fig. 4b). We then asked whether these observations might extend to primary human myoblasts. Primary human myoblasts readily fused and formed myotubes when cultured in fusion medium but not in growth medium (Fig. 3d, left). Adding apoptotic C2C12 myoblasts stimulated fusion of primary human myoblasts in growth medium, with a 170% increase in the fusion index ($P < 0.05$, Fig. 3d). Thus, dying cells could stimulate mouse and human myoblasts to fuse and form myotubes.

To address the function of BAI1 in myoblast fusion *in vivo*, we generated *Bai1*^{-/-} mice using embryonic stem cells with an exon trap mutation of exon 2. We compared myofibres from the tibialis anterior (TA) muscle of 12-week-old male *Bai1*^{+/+} versus *Bai1*^{-/-} littermate mice (Fig. 4a). Although *Bai1*^{-/-} muscles did contain fully formed myofibres, they contained smaller-sized fibres as well as clusters of very small fibres (Fig. 4b, arrowheads). We took an unbiased approach to quantitate the cross-sectional areas (CSA) of each myofibre using the CellProfiler software tool²¹, and plotted the frequency distribution of the myofibres (Fig. 4c). The TA muscles of the *Bai1*^{-/-} mice were skewed towards smaller myofibres compared to control littermates. Classifying the myofibres as either small (<1,500 μm^2) or large (>1,500 μm^2), the *Bai1*^{-/-} TA muscle had a greater proportion of small myofibres and significantly fewer large myofibres, suggesting a need for BAI1 in larger myofibre formation ($P < 0.05$, $n = 5$ –8 mice; Fig. 4c, right). Additionally, the average myofibre CSA of *Bai1*^{-/-} mice

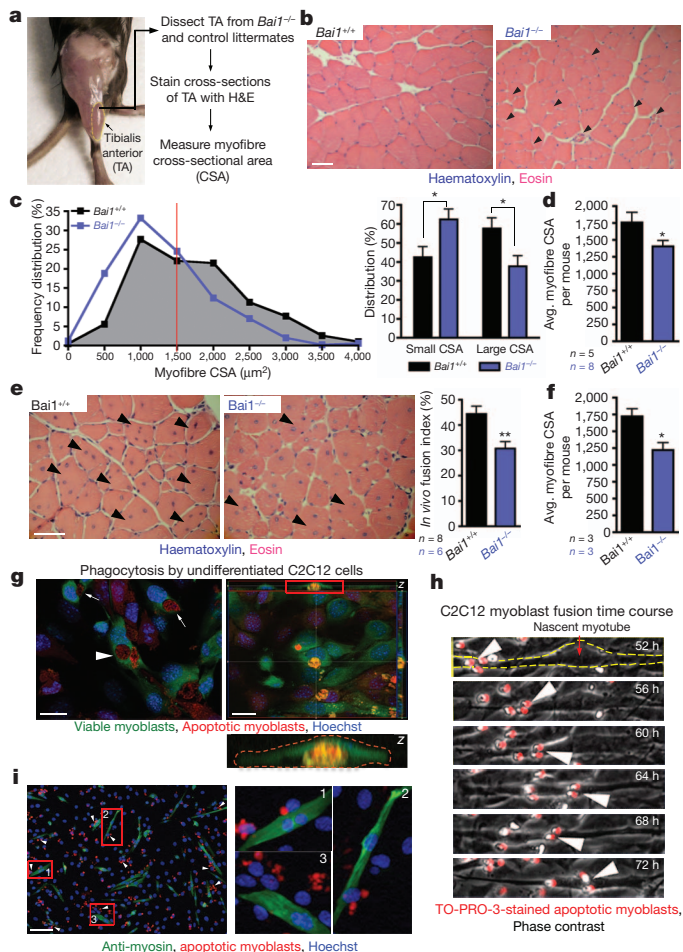


Figure 4 | Defective development of myofibres in *Bcl1*^{-/-} mice.

a, Schematic of TA muscle analysis. **b**, TA muscles from *Bcl1*^{-/-} mice display smaller myofibres (by haematoxylin and eosin (H&E) staining. Arrowheads show smaller myofibres in the *Bcl1*^{-/-} mice. **c**, The per cent distribution of myofibres by CSA (μm²), with the red line demarcating 'small' and 'large' myofibres based on a CSA of 1,500 μm²; the distribution of small and large myofibres is shown on the right. **d**, Average myofibre area (in μm²) per mouse (**P* < 0.05; *n* = 5 or *n* = 8 male mice for *Bcl1*^{+/+} and *Bcl1*^{-/-}, respectively). **e**, Regenerated TA muscles from *Bcl1*^{-/-} mice (14 days after cardiotoxin-induced injury) show fewer regenerating myofibres with central nuclei (arrowhead). Graph shows *in vivo* fusion index for regenerating myofibres in control and *Bcl1*^{-/-} mice (see Methods) (***P* < 0.01; *n* = 8 mice for *Bcl1*^{+/+} and *n* = 6 mice for *Bcl1*^{-/-}). **f**, Regenerated *Bcl1*^{-/-} myofibres display smaller average myofibre area (in μm²) per mouse (**P* < 0.05; *n* = 3 male mice each for *Bcl1*^{+/+} and *Bcl1*^{-/-}). **e** and **f** are representative of two independent injury experiments. **g**, Image of viable myoblasts (green) engulfing apoptotic myoblasts (red). Arrowhead, engulfed cells; arrows, phagocytic cups around partially engulfed targets. The magnified Z dimension within the red box (bottom) outlines the green signal from the viable myoblast completely surrounding the orange dying target. Scale bars, 20 μm. **h**, Time-lapse images monitoring apoptotic myoblasts becoming TO-PRO-3 labelled (red) as they emerge. See Supplementary Fig. 6 and Supplementary Video 1 for additional frames. **i**, Apoptotic myoblasts (viability dye, red) are often in proximity but not within the fusing myoblasts or myotubes (anti-myosin, green). Nuclei are stained blue (Hoechst). Red boxes are shown in higher magnification (right). Scale bar, 100 μm. Error bars indicate s.e.m., and scale bars represent 50 μm, unless otherwise indicated.

(per mouse) was again significantly reduced compared to *Bcl1*^{+/+} littermates (*P* < 0.05, *n* = 5–8 mice; Fig. 4d). It is notable that *Bcl1*^{-/-} mice did develop major skeletal muscle tissues, possibly due to the continued expression of the *Bcl1* homologues *Bai2* and *Bai3* (as seen in the TA muscle, *P* < 0.05, *n* = 5 mice per genotype;

Supplementary Fig. 5a). These data indicated a requirement for BAI1 in optimal myofibre development *in vivo*.

To test whether BAI1 might influence muscle repair and regeneration, we used the cardiotoxin (cdx)-induced muscle injury and repair model²² (Supplementary Fig. 5b). After cardiotoxin injection into TA muscles of control and *Bcl1*^{-/-} mice, we analysed regenerating fibres after 14 days (shown in images of Fig. 4e). Focusing our analysis on the regenerated fibres, the average myofibre cross-sectional areas of the *Bcl1*^{-/-} mice were reduced compared to the *Bcl1*^{+/+} littermates (*P* < 0.05, *n* = 3 mice; Fig. 4f and Supplementary Fig. 5c). Using centralized nuclei number per myofibre to calculate the *in vivo* fusion index (see Methods²³), the *Bcl1*^{-/-} mice displayed a 31% reduction compared to littermate controls (*P* < 0.01, *n* = 6–8 mice; Fig. 4e, right). These results demonstrated a requirement for BAI1 in the optimal fusion and regeneration of myofibres after muscle injury.

Because BAI1 is a phagocytic receptor for apoptotic cells³ and apoptotic cells influence myoblast fusion, an interesting possibility was that engulfment of dying myoblasts by healthy myoblasts contributed to myoblast fusion. Alternatively, engagement by the dying myoblasts with the healthy myoblasts might have provided signalling cues (not contingent on phagocytosis) that contributed to fusion. We found that the healthy myoblasts could engulf apoptotic myoblasts *in vitro*, an observation not reported previously (Fig. 4g). We next used time-lapse microscopy to investigate the fate of apoptotic myoblasts emerging during fusion and what might happen to the nuclei of apoptotic cells (although nuclei of apoptotic cells are damaged and unlikely to directly contribute to the multinucleated myotubes). The apoptotic myoblasts, which were labelled by adding the viability dye TO-PRO-3 to the fusion medium, appeared to not be engulfed by nascent myotubes; rather, TO-PRO-3-stained cells remained in close contact with the newly forming myotubes (Fig. 4h, Supplementary Fig. 6 and Supplementary Video 1). This close association (without obvious phagocytosis) was confirmed with a second viability dye eFluor; 62% of dying myoblasts were in close proximity (but not within) myosin-positive myotubes, and 94% of myotubes were in close proximity to dying myoblasts (Fig. 4i). However, these data do not rule out additional roles for phagocytosis during myoblast fusion (perhaps for acquiring energy). Notably, we could detect actin polymerization at some of the contacts between apoptotic cells and fusing myotubes (Supplementary Fig. 7).

The data presented here identify a new and unexpected positive role for the phosphatidylserine receptor BAI1 in promoting fusion of skeletal myoblasts to form myotubes. Lowered expression of *Bcl1* was observed in transcriptome analyses of muscles from Duchenne muscular dystrophy patients²⁴. Additionally, expression levels of the genes that encode ELMO2 and Dock180 are altered in skeletal muscle disorders^{24–27}. Thus, identification of BAI1 as a novel promoter of myoblast fusion, and the link between ELMO/Dock180/Rac1 signalling pathway and myoblast fusion^{7–12} has relevance for mammalian skeletal muscle development and muscle disorders.

These data also identify the interaction between apoptotic and healthy myoblasts as a new type of fusion cue that in turn promotes fusion between healthy myoblasts. Apoptotic cells appear to contact the viable fusing myoblasts/myotubes without fusing with them, suggesting an interaction distinct from the one between a fusion competent myoblast and a founder cell seen in *Drosophila melanogaster*¹. Interestingly, *Casp3*^{-/-} mice have been reported to be smaller in size with reduction of total skeletal muscle mass compared to their control littermates, and this phenotype was linked to cleavage of MST1 kinase in fusing cells, suggesting additional promyogenic roles for caspase 3 (ref. 28). Because cell death within the muscle is often associated with weight training and strength conditioning exercises that promote muscle mass²⁹, further studies targeting the triggering of BAI1 or other phosphatidylserine receptors in stimulating muscle growth could be beneficial for promoting recovery after muscle injuries.

Although apoptosis and cell clearance have been studied for many years, dying cells are generally considered a nuisance that need to be

removed quickly. The concept that the body may use cell death not only to rid itself of unwanted cells, but also to use them to beneficially regulate differentiation adds an important dimension to considering cell turnover within tissues and organisms. Activated lymphocytes and other cell types are known to transiently expose phosphatidylserine in non-apoptotic contexts³⁰. An intriguing possibility is that these transient phosphatidylserine exposures, through cell–cell contact (for example, in germinal centres of lymph nodes during immune responses), might be involved in differentiation events in other tissues.

METHODS SUMMARY

Cell culture and myoblast fusion assay. C2C12 murine skeletal muscle myoblasts were maintained at sub-confluent densities in DMEM with 20% FBS. Normal human primary skeletal muscle myoblasts (Clonetics) were maintained at sub-confluent densities in defined SkGM-2 medium (Clonetics). Confluent myoblasts on LabTek II Permanox 2-chamber slides (Nunc) were induced to undergo fusion by switching to fusion medium (DMEM with 2% heat-inactivated horse serum). Myoblasts/myotubes were washed, fixed and stained with anti-myosin antibody (see Methods). ImageJ cell counter plugin software was used to quantitate nuclei number. The fusion index (see Methods) was calculated for each of six random fields that were analysed for each sample per experiment.

In vivo myofibre analysis. Embryonic stems cells carrying the exon trap mutation of exon 2 of *Bai1* locus were used to generate *Bai1*^{−/−} null mice. TA muscles from *Bai1*^{−/−} and wild-type littermates (gender matched) were dissected and processed into paraffin blocks. 5-µm sections were stained with H&E and at least five fields were captured for each mouse section. The CSA of each myofibre per field was quantitated using CellProfiler²¹; output files were then screened for accuracy in a blinded fashion. To quantitate myofibre fusion after injury, the *in vivo* fusion index (the percentage of TA myofibres containing multiple central nuclei versus the total number of myofibres) was calculated for each field²³.

Full Methods and any associated references are available in the online version of the paper.

Received 2 September 2012; accepted 25 March 2013.

Published online 24 April 2013.

- Abmayr, S. M. & Pavlath, G. K. Myoblast fusion: lessons from flies and mice. *Development* **139**, 641–656 (2012).
- Chen, E. H. & Olson, E. N. Towards a molecular pathway for myoblast fusion in *Drosophila*. *Trends Cell Biol.* **14**, 452–460 (2004).
- Park, D. *et al.* BAI1 is an engulfment receptor for apoptotic cells upstream of the ELMO/Dock180/Rac module. *Nature* **450**, 430–434 (2007).
- Gumienny, T. L. *et al.* CED-12/ELMO, a novel member of the Crkl/Dock180/Rac pathway, is required for phagocytosis and cell migration. *Cell* **107**, 27–41 (2001).
- Hasegawa, H. *et al.* DOCK180, a major CRK-binding protein, alters cell morphology upon translocation to the cell membrane. *Mol. Cell Biol.* **16**, 1770–1776 (1996).
- Brugnera, E. *et al.* Unconventional Rac-GEF activity is mediated through the Dock180-ELMO complex. *Nature Cell Biol.* **4**, 574–582 (2002).
- Erickson, M. R., Galletta, B. J. & Abmayr, S. M. *Drosophila* myoblast city encodes a conserved protein that is essential for myoblast fusion, dorsal closure, and cytoskeletal organization. *J. Cell Biol.* **138**, 589–603 (1997).
- Hakeda-Suzuki, S. *et al.* Rac function and regulation during *Drosophila* development. *Nature* **416**, 438–442 (2002).
- Moore, C. A., Parkin, C. A., Bidet, Y. & Ingham, P. W. A role for the Myoblast city homologues Dock1 and Dock5 and the adaptor proteins Crk and Crk-like in zebrafish myoblast fusion. *Development* **134**, 3145–3153 (2007).
- Laurin, M. *et al.* The atypical Rac activator Dock180 (Dock1) regulates myoblast fusion *in vivo*. *Proc. Natl Acad. Sci. USA* **105**, 15446–15451 (2008).
- Vasyutina, E., Martarelli, B., Brakebusch, C., Wende, H. & Birchmeier, C. The small G-proteins Rac1 and Cdc42 are essential for myoblast fusion in the mouse. *Proc. Natl Acad. Sci. USA* **106**, 8935–8940 (2009).
- Geisbrecht, E. R. *et al.* *Drosophila* ELMO/CED-12 interacts with Myoblast city to direct myoblast fusion and ommatidial organization. *Dev. Biol.* **314**, 137–149 (2008).

- Yaffe, D. & Saxel, O. Serial passaging and differentiation of myogenic cells isolated from dystrophic mouse muscle. *Nature* **270**, 725–727 (1977).
- Cornelison, D. D. Context matters: *in vivo* and *in vitro* influences on muscle satellite cell activity. *J. Cell. Biochem.* **105**, 663–669 (2008).
- Pajcini, K. V., Pomerantz, J. H., Alkan, O., Doyonnas, R. & Blau, H. M. Myoblasts and macrophages share molecular components that contribute to cell–cell fusion. *J. Cell Biol.* **180**, 1005–1019 (2008).
- Shutes, A. *et al.* Specificity and mechanism of action of EHT 1864, a novel small molecule inhibitor of Rac family small GTPases. *J. Biol. Chem.* **282**, 35666–35678 (2007).
- van den Eijnde, S. M. *et al.* Transient expression of phosphatidylserine at cell–cell contact areas is required for myotube formation. *J. Cell Sci.* **114**, 3631–3642 (2001).
- Jeong, J. & Conboy, I. M. Phosphatidylserine directly and positively regulates fusion of myoblasts into myotubes. *Biochem. Biophys. Res. Commun.* **414**, 9–13 (2011).
- Chekeni, F. B. *et al.* Pannexin 1 channels mediate ‘find-me’ signal release and membrane permeability during apoptosis. *Nature* **467**, 863–867 (2010).
- Hasty, P. *et al.* Muscle deficiency and neonatal death in mice with a targeted mutation in the myogenin gene. *Nature* **364**, 501–506 (1993).
- Kamentsky, L. *et al.* Improved structure, function and compatibility for CellProfiler: modular high-throughput image analysis software. *Bioinformatics* **27**, 1179–1180 (2011).
- Yan, Z. *et al.* Highly coordinated gene regulation in mouse skeletal muscle regeneration. *J. Biol. Chem.* **278**, 8826–8836 (2003).
- Grounds, M. D., Radley, H. G., Lynch, G. S., Nagaraju, K. & De Luca, A. Towards developing standard operating procedures for pre-clinical testing in the mdx mouse model of Duchenne muscular dystrophy. *Neurobiol. Dis.* **31**, 1–19 (2008).
- Chen, Y. W., Zhao, P., Borup, R. & Hoffman, E. P. Expression profiling in the muscular dystrophies: identification of novel aspects of molecular pathophysiology. *J. Cell Biol.* **151**, 1321–1336 (2000).
- Haslett, J. N. *et al.* Gene expression comparison of biopsies from Duchenne muscular dystrophy (DMD) and normal skeletal muscle. *Proc. Natl Acad. Sci. USA* **99**, 15000–15005 (2002).
- Bakay, M. *et al.* Nuclear envelope dystrophies show a transcriptional fingerprint suggesting disruption of Rb-MyoD pathways in muscle regeneration. *Brain* **129**, 996–1013 (2006).
- Bialek, P. *et al.* Distinct protein degradation profiles are induced by different disuse models of skeletal muscle atrophy. *Physiol. Genomics* **43**, 1075–1086 (2011).
- Fernando, P., Kelly, J. F., Balazsi, K., Slack, R. S. & Megeney, L. A. Caspase 3 activity is required for skeletal muscle differentiation. *Proc. Natl Acad. Sci. USA* **99**, 11025–11030 (2002).
- Phaneuf, S. & Leeuwenburgh, C. Apoptosis and exercise. *Med. Sci. Sports Exerc.* **33**, 393–396 (2001).
- Ravichandran, K. S. Find-me and eat-me signals in apoptotic cell clearance: progress and conundrums. *J. Exp. Med.* **207**, 1807–1817 (2010).

Supplementary Information is available in the online version of the paper.

Acknowledgements We thank members of the Ravichandran laboratory for their valuable suggestions at many stages of this work. We also thank L. Haney, A. Bruce and A. Dutta for technical suggestions and assistance and M. Hufford and A. Fond for help with statistical analysis. We thank members of the University of Virginia Flow Cytometry Core, Research Histology Core, and Gene Targeting and Transgenic Facility for cell sorting, histological services and transgenic mouse generation. This work was supported by a grant from the National Institute of General Medical Sciences/National Institutes of Health and the Center for Cell Clearance at the University of Virginia.

Author Contributions A.E.H.-H. designed, performed and analysed most of the experiments in this study with input from K.S.R. C.S.L. generated and supplied the *Bai1*^{−/−} mice, and provided GST-tagged BAI1 TSR. J.M.K. assisted with time-lapse and shRNA studies, and myofibre cross-sectional area analyses. S.A. helped with the *in vivo* muscle regeneration and *ex vivo* primary myoblast cultures. J.D.S. processed, stained and analysed the mouse embryonic tissues. A.L.K. provided phosphatidylserine liposomes for these studies. J.A.C. and Z.Y. assisted with the cardiotoxin injury model. J.W.M. provided intellectual input on the *in vivo* BAI1 studies. A.E.H.-H. and K.S.R. wrote the manuscript with comments from co-authors.

Author Information Reprints and permissions information is available at www.nature.com/reprints. The authors declare no competing financial interests. Readers are welcome to comment on the online version of the paper. Correspondence and requests for materials should be addressed to K.S.R. (Ravi@virginia.edu).

METHODS

Cell culture and myoblast fusion assay. C2C12 murine skeletal muscle myoblasts (American Type Culture collection) were maintained at sub-confluent densities in growth medium (DMEM buffer supplemented with 20% heat-inactivated FBS) at 8.5% CO₂ at 37 °C. Normal human primary skeletal muscle myoblasts (Clonetics) were maintained at sub-confluent densities in defined SkGM-2 medium (Clonetics) at 5% CO₂ at 37 °C. Myoblast fusion (of both C2C12 and primary human myoblasts) was induced by rinsing 70–80% confluent cultures once with PBS and switching them to fusion medium (DMEM supplemented with 2% heat-inactivated horse serum). Fusion medium was replaced every 24 h for a total of 72 h, unless specified otherwise. Where indicated, zVAD-FMK (100 µM, Enzo Life Sciences), Q-VD-OPH (100–150 µM, SM Biochemicals), Dead-Cert imab6 fragment (100 µg ml⁻¹, Immunosolv), or GST-tagged BAI1 TSR (100 µg ml⁻¹)³ was added to cultures 24 h before switching to fusion medium and maintained throughout the experiment. When indicated, EHT 1864 (10 µM, Sigma-Aldrich) or insulin-transferrin-selenium (1×, Gibco) was added at the same time as fusion medium and maintained throughout the experiment.

Fluorescence microscopy and quantitative analysis of fusion. To measure fusion, myoblasts were plated in growth medium on 2-chamber LabTek II Permax chamber slides (Nunc) at 1 × 10⁵ cells per well (C2C12) or 7.5 × 10⁴ cells per well (Human primary skeletal muscle myoblasts and C2C12 in GM in adding-back experiments). Myoblasts were induced to undergo myogenic differentiation as described above. Myoblasts/myotubes were washed and fixed with 4% paraformaldehyde in PBS for 20 min at room temperature and permeabilized in 0.2% Triton X-100, 0.1% citrate in PBS for 5 min at room temperature. After blocking with 2% BSA/PBS, cells were stained with anti-myosin antibody (Skeletal, Fast; Sigma-Aldrich) at 1:1,000 dilution overnight at 4 °C. After washing with PBS, cells were incubated with Alexa Fluor 647-labelled secondary antibody (Invitrogen) at 1:400 for 1 h at room temperature, stained with Hoechst 33342 (1 µg ml⁻¹, Invitrogen) for 2 min at room temperature, washed and then mounted with ProLong Gold (Invitrogen). Microscopy was performed using the Axio Imager 2 with Apotome (Carl Zeiss) and AxioVision software for analysis.

To quantitate *in vitro* myoblast fusion, the fusion index was determined as described previously¹⁵. Briefly, fluorescent images of six random fields were captured for each sample per experiment. ImageJ cell counter plugin software was used to quantitate nuclei number. The fusion index (the percentage of nuclei within myosin positive cells versus the total number of nuclei) was calculated for each field. Fusion indices from each field per sample were compiled and are depicted as the mean plus the standard deviation (s.d.). In addition, the number of myosin positive myotubes per field with 2–4 nuclei (small myotubes) and 5 or more nuclei (large myotubes) were recorded as another means to quantify myoblast fusion.

Flow cytometric analysis for apoptosis. To measure phosphatidylserine exposure, floating and adherent C2C12 myoblasts or thymocytes were stained with APC-conjugated annexin V diluted 1:20 in annexin V-binding buffer (eBioscience) for 10 min at room temperature. Cells were washed, resuspended in annexin V-binding buffer and assessed by flow cytometry. To measure selective membrane permeability during apoptosis, C2C12 cultures at the indicated time points after addition of fusion medium were treated with TO-PRO-3 (1 µM, Molecular Probes) for 20 min at 37 °C. Cells were washed in PBS, resuspended in PBS with 0.5% BSA and assessed by flow cytometry. To measure caspase-3 activation, floating and adherent C2C12 myoblasts were fixed and permeabilized with Cytotfix/Cytoperm solution (BD Biosciences) and stained with Alexa Fluor 488-conjugated cleaved caspase-3 antibody diluted 1:20 in Cytoperm solution (Cell Signaling) for 20 min on ice. Cells were washed in Cytoperm solution, resuspended in PBS with 0.5% BSA and assessed by flow cytometry.

Rescue of myoblast fusion. C2C12 cells were grown to 80% confluence in 15-cm tissue culture plates, after which they were induced to undergo myogenic differentiation as described previously. After 24 h in fusion medium, the floating/dying myoblasts were collected at 115 g for 5 min and resuspended gently into fresh fusion medium or growth medium. Unless specified otherwise, dying C2C12 myoblasts were added at a 1:1 ratio to plated, viable myoblasts at the time of the initial switch to fusion medium, or the myoblasts were <80% confluent if maintained in growth medium. The apoptotic myoblasts were spun down onto the viable myoblasts for 2 min at 30 g. This treatment was repeated each following day for 3 days in total. Where indicated, dying myoblasts were pre-treated with GST-tagged BAI1 TSR (100 µg ml⁻¹) for 1 h at 37 °C before adding them to fusing cultures.

Thymuses were isolated from 4–5 week old mice and crushed through a 70-µm strainer to achieve single cell suspensions. Thymocytes were induced to undergo apoptosis by anti-Fas antibody treatment as described previously¹⁹. Briefly, 10 × 10⁶ thymocytes were collected and resuspended in C2C12 fusion medium with Protein-G (2 µg ml⁻¹, Sigma) and anti-CD95 (Fas) antibody (5 µg ml⁻¹, BD Biosciences). Two hours after treatment with anti-Fas, 5 × 10⁶ apoptotic thymocytes were added

to confluent, zVAD treated C2C12 myoblasts and spun down for 2 min at 30g. This treatment was repeated each following day for 3 days total.

Jurkat T cells (E6.1) were induced to undergo apoptosis by ultraviolet irradiation as described previously¹⁹. Briefly, Jurkat cells were collected at 115 g for 5 min, resuspended in C2C12 growth medium and irradiated with 1,500 mJoules of ultraviolet irradiation. Four hours after irradiation (recovery period), 4 × 10⁶ ultraviolet-treated or viable Jurkat cells were added to <80% confluent plated, viable C2C12 myoblasts and spun down for 2 min at 30g. This treatment was repeated each following day for 3 days in total.

Immunoblotting. C2C12 myoblasts were induced to fuse as described above and were collected at indicated time points after the switch to fusion medium. Cells were lysed and total protein was quantified for each sample lysate using the D_c Protein Assay (Bio-Rad). Samples were analysed by SDS-PAGE and immunoblotted. To detect BAI1 expression, a custom polyclonal rabbit antisera against a conserved carboxy-terminal epitope was generated by injecting rabbits with a KLH-linked peptide (Novus Biologicals). Antibodies were used after one round of affinity purification on peptide columns. Peptide competition experiments and immunoblotting demonstrating antibody specificity were previously reported³¹. BAI1 antibody was used at a concentration of 1 µg ml⁻¹ in 5% milk/TBS-T for immunoblotting in these studies.

Processing and immunostaining of mouse embryonic tissue. C57BL/6 mice were obtained from the Jackson Laboratories. All animal procedures were performed as per protocols approved by the University of Virginia Animal Care and Use Committee.

For the detection of BAI1 *in vivo*, E14.5 mouse tissues were fixed by immersion in 4% paraformaldehyde in PBS and processed into paraffin blocks. 5-µm sections were processed for immunohistochemistry using standard techniques. Immunoperoxidase detection was performed using the ImPress polymeric peroxidase reagent (Vector), according to the supplier's instructions. The chromogen used was diaminobenzidine (Dako S3000) 1 mg ml⁻¹ in PBS plus 0.02% hydrogen peroxide applied for 5 min and sections were counterstained with haematoxylin.

For the detection of apoptotic cells *in vivo*, embryos were collected in PBS and subsequently fixed in 4% paraformaldehyde in PBS for 24 h at 4 °C. Whole embryos were processed for paraffin infiltration by standard methods. Immunohistochemistry was performed on 8-µm-thick paraffin sections using standard techniques. Primary antibodies used were: rabbit polyclonal anti-cleaved caspase 3 (1:100, Cell Signaling Technology), mouse monoclonal anti-actin (1:100, Sigma-Aldrich, clone AC-15). Immunofluorescence detection was performed using Alexa Fluor 488 and Alexa Fluor 546-conjugated secondary antibodies, diluted 1:2,000 (Invitrogen). Images were acquired with an Olympus BX40 upright microscope and a Scion Firewire charge-coupled device (CCD) camera (Scion). The entire paraspinal muscles of four sample sections were analysed for the presence of cleaved caspase 3⁺ bodies.

Stable transfections. For the generation of BAI1-GFP myoblasts, low-passage C2C12 myoblasts grown to 20–40% confluency in a 6-well dish were transfected with 20 µg of plasmid (pEBB-BAI1-GFP) plus 5 µg of selection plasmid (pA-Puro) or selection plasmid alone using Lipofectamine 2000 (Invitrogen). Two days after transfection, the wells were replated into 10-cm² tissue culture plates and puromycin dihydrochloride (5 µg ml⁻¹, Sigma-Aldrich) was added to cultures. GFP-positive puromycin-resistant, or puromycin-resistant only control single-colony clones were isolated. Clones were analysed for BAI1-GFP expression via flow cytometry and epifluorescence microscopy.

For the generation of ELMO2-knockdown shRNA, a 19-mer target sequence was identified using Dharmacon siDESIGN Center (AGCGCAAGGCCATG TATAC), and antisense oligos were generated using the pSicoOligomaker 1.5 program. The oligos were annealed and ligated into the pSicoR-GFP plasmid (Addgene), which co-expresses GFP for detection of expression. Low-passage C2C12 myoblasts grown to 30–40% confluency in a 6-well dish were transfected with 4 µg of ELMO2 or control shRNA plasmid along with 1 µg of selection plasmid (pA-Puro) using Lipofectamine 2000 (Invitrogen). The next day, the cells were replated into 10-cm² tissue culture plates and puromycin (5 µg ml⁻¹, Sigma-Aldrich) was added to cultures. The puromycin-resistant cells were maintained as a heterogenous population. To achieve a pure culture of ELMO2 or control shRNA-expressing myoblasts, the populations were cell-sorted on the basis of GFP expression using an iCyt Reflection cell sorter (Sony Biotechnology).

Lentiviral-mediated transduction. High-titre lentivirus containing wild-type human BAI1, a mutant BAI1(AAA) or empty vector complementary DNA was generated using ViraPower HiPerform lentiviral expression system (Invitrogen) with several modifications. The *attB* sites and *lacZ* in pLenti6.3/V5-GW/*lacZ* were replaced with a multi-cloning site, and wild type or mutant BAI1 cDNA was inserted. In place of 293FT cells, lentivirus was produced in Lenti-X 293T cells (Clontech) transfected using calcium phosphate (Promega), and supernatants containing live virus were concentrated with Lenti-X Concentrator (Clontech)

to better achieve high titre virus. Supernatants collected from two 10-cm² plates of virus-producing Lenti-X cells over 3 days were concentrated and applied to one 6-cm² dish of low-passage C2C12 myoblasts with polybrene (10 µg ml⁻¹, Sigma-Aldrich). Growth medium was replaced every 24 h with the addition of blasticidin (2.5 µg ml⁻¹, Invitrogen) to growth medium 48 h post-transduction. Transduced myoblasts were maintained as heterogeneous populations (no clones selected), and blasticidin selection was complete after 10 days. To specifically detect human BAI1 (wild-type or mutant), expression was measured through qRT-PCR using a human-specific BAI1 TaqMan probe (Hs00181777_m1) that did not cross-react with the mouse endogenous BAI1 from C2C12 myoblasts. We performed rescue of myoblast fusion with these cells. Because apoptotic myoblasts taken from control or BAI1-overexpressing myoblast cultures had a similar effect in the rescue of zVAD-inhibited myoblast fusion, this established that BAI1 signalling within the healthy myoblasts rather than the dying myoblasts was more important in promoting fusion.

qRT-PCR. For the determination of *Elmo1*, *Elmo2* and *Elmo3* in C2C12 myoblasts and the determination of myogenin (*Myog*) mRNA in fusing C2C12 myoblasts, DNase I-treated total RNA was isolated using RNeasy kit (Qiagen). Superscript III SuperMix (Invitrogen), the provided random hexamer oligo, and 0.5 µg of total RNA as template were used to generate cDNA. qRT-PCR was performed using gene-specific TaqMan probes on a StepOne Plus Real-Time PCR instrument (Applied Biosystems). TaqMan probes used were: mouse *Elmo1* (Mm00519109_m1), mouse *Elmo2* (Mm01248046_m1), mouse *Elmo3* (Mm00555221_m1), mouse *Myog* (Mm00446194_m1) and mouse *Hprt* (Mm00446968_m1). For determination of *Bai1*, *Bai2* and *Bai3* mRNA in mouse muscle, total RNA was isolated from the tibialis anterior muscle of 5 individual mice using a TriPure kit (Roche Molecular Biochemicals) as previously described²². Superscript III SuperMix (Invitrogen), the provided random hexamer oligo, and 2 µg of total RNA as template were used to generate cDNA. qRT-PCR was performed using gene-specific TaqMan probes on a StepOne Plus Real-Time PCR instrument. TaqMan probes used were: mouse *Bai1* (Mm00558144_m1), mouse *Bai2* (Mm00557365_m1), mouse *Bai3* (Mm00657451_m1) and mouse *Hprt* (same as above).

Mice. Embryonic stem cells carrying the exon trap mutation of *Bai1* locus (specifically losing exon 2 coding sequence) were purchased from Texas Institutes of Genomic Medicine. These embryonic stem cells (originally in the 129/Sv background) were used to generate chimaeric mice via blastocyst injections. The chimaeric progeny were crossed to C57BL/6 and progeny between the second and fourth backcrosses were used in these studies. TA muscles from 12-week-old mice of the *Bai1*^{-/-} genotype, along with appropriate control littermates (gender matched), were used in the analysis as detailed.

Muscle injury model. All animal procedures were approved by the University of Virginia Animal Care and Use Committee. Muscle injury was performed as previously described²². Briefly, 0.1 ml of cardiotoxin (*Naja nigricollis*) (0.071 mg ml⁻¹, Calbiochem) was injected into the left TA muscles of 12-week-old *Bai1*^{-/-} and control littermate mice, and 0.1 ml saline was injected into the right TA muscle for control injury. The TA muscles were collected at 14 days after injection and processed and analysed as detailed.

In vivo myofibre analysis. The TA muscles of *Bai1*^{-/-} and control littermate mice were dissected and fixed by immersion in 4% paraformaldehyde in PBS and processed into paraffin blocks. 5-µm sections were processed for immunohistochemistry using standard techniques. Sections were stained with H&E and at least five fields were captured for each mouse section using the Axiovert 40 CFL (Carl Zeiss) and AxioVision software for analysis. The CSA of each myofibre per field was quantified using CellProfiler²¹; output files were then screened for accuracy (to exclude mis-identified tubes) in a blinded fashion.

To quantitate myofibre fusion after injury, the *in vivo* fusion index was determined as described previously²³. Briefly, at least five fields of H&E-stained myofibre cross-sections were captured for each mouse as above. ImageJ cell counter plugin software was used to quantitate the number of myofibres with single or multiple central nuclei. The *in vivo* fusion index (the percentage of TA myofibres containing multiple central nuclei versus the total number of myofibres) was calculated for each field. Fusion indices from each field per mouse were compiled and are depicted as the mean plus the standard error of the mean (s.e.m.).

Myoblast engulfment assay. To determine the phagocytic capacity of myoblasts, four 15-cm² plates of C2C12 cells were serum-starved for 72 h to induce apoptosis. The floating and adherent cells were collected and stained with TAMRA-SE (25 µM, Invitrogen). Then 5 × 10⁵ TAMRA-SE-stained dying myoblasts were added to viable, CFDA-SE (7.2 µM, Invitrogen)-stained C2C12 cells on 2-chamber LabTek II Permanox chamber slides (Nunc) seeded 24 h before at a density of 5 × 10⁴ cells per chamber. The two C2C12 populations were incubated together for 5 h at 8.5% CO₂ at 37 °C, after which they were washed with PBS, fixed with 4% paraformaldehyde in PBS for 20 min at room temperature, stained with Hoechst 33342 (1 µg ml⁻¹, Invitrogen) for 2 min at room temperature and then washed and mounted with ProLong Gold (Invitrogen). Microscopy was performed using the Axio Imager 2 with Apotome (Carl Zeiss) and AxioVision software to analyse Z-stack images for three-dimensional analysis.

Analysis of apoptotic cell-contact during myoblast fusion. C2C12 cells were plated in growth medium on 2-chamber LabTek II Permanox chamber slides (Nunc) at 1 × 10⁵ cells per well and were induced to undergo myogenic differentiation as described with or without 100 µM zVAD-FMK. Fixable viability dye eFluor 660 (1 µl ml⁻¹, eBioscience) was added to the fusion medium, for the course of the experiment, to label the myoblasts undergoing fusion medium-induced death. After 3 days, the myoblasts/myotubes were washed and fixed with 4% paraformaldehyde in PBS for 20 min at room temperature and permeabilized in 0.2% Triton X-100, 0.1% citrate in PBS for 5 min at room temperature. After blocking with PBS with 2% BSA, cells were stained with anti-myosin (Skeletal, Fast; Sigma) at 1:1,000 overnight at 4 °C. After washing with PBS, cells were incubated with Alexa Fluor 488-labelled secondary antibody (Invitrogen) at 1:400 for 1 h at room temperature, stained with Hoechst 33342 (1 µg ml⁻¹, Invitrogen) for 2 min at room temperature, washed and mounted with ProLong Gold (Invitrogen).

To analyse the effect of apoptotic cells on the actin cytoskeleton of fusing myoblasts in a time course, C2C12 cells were plated in growth medium on 2-chamber LabTek II Permanox chamber slides (Nunc) at 1 × 10⁵ cells per well and were induced to undergo differentiation. Fixable viability dye eFluor 660 (1 µl ml⁻¹, eBioscience) was added to the fusion medium during the course of the experiment to label the myoblasts undergoing death as part of the fusion process. For a total of 3 days, at 24-h intervals, a slide containing myoblasts/myotubes was washed and fixed with 4% paraformaldehyde in PBS for 20 min at room temperature and then stored at 4 °C in 1% BSA in PBS until the conclusion of the time course. After the fixation of the last time point, all slides were permeabilized in 0.2% Triton X-100, 0.1% citrate in PBS for 5 min at room temperature and then blocked with PBS with 2% BSA. Each slide was stained with 0.5 ml of Alexa Fluor 555 phalloidin (0.005 units per µl, Life Technologies) in PBS with 1% BSA for 20 min at room temperature, Hoechst 33342 (1 µg ml⁻¹, Invitrogen) for 2 min at room temperature, then washed and mounted with ProLong Gold (Invitrogen). Microscopy was performed using the Axio Imager 2 with Apotome (Carl Zeiss) and AxioVision software for analysis.

Time-lapse microscopy of myoblast fusion. C2C12 myoblasts were plated on Poly-L-lysine (Sigma) coated glass coverslips. Once 80–100% cell confluency was achieved, coverslips were inserted into a POC-R2 chamber (Pecon) and fusion medium pre-equilibrated with 8.5% CO₂ including 1 µM TO-PRO-3 was added. Time-lapse images were captured every 20 min for 72 h on a 37 °C heated stage using the Axio Imager 2 with Apotome (Carl Zeiss) and AxioVision software for analysis.

Statistical analysis. Unless otherwise described, the data are representative of at least three independent experiments and are shown as mean ± the standard deviation (s.d.). For analysis of statistical difference between two groups, a Student's two-tailed unpaired *t*-test was applied. For analysis of statistical difference between three or more groups, a one-way analysis of variance with Bonferroni's multiple comparison test was applied. Significance was defined when *P* values were <0.05.

31. Sokolowski, J. D. et al. Brain-specific angiogenesis inhibitor-1 expression in astrocytes and neurons: implications for its dual function as an apoptotic engulfment receptor. *Brain Behav. Immun.* **25**, 915–921 (2011).

Crystal structure of a folate energy-coupling factor transporter from *Lactobacillus brevis*

Ke Xu^{1*}, Minhua Zhang^{1*}, Qin Zhao^{1*}, Fang Yu^{2*}, Hui Guo¹, Chengyuan Wang¹, Fangyuan He¹, Jianping Ding² & Peng Zhang^{1,3}

ATP-binding cassette (ABC) transporters, composed of importers and exporters, form one of the biggest protein superfamilies that transport a variety of substrates across the membrane, powered by ATP hydrolysis. Most ABC transporters are composed of two transmembrane domains and two cytoplasmic nucleotide-binding domains. Also, importers from prokaryotes usually have extra solute-binding proteins in the periplasm that are responsible for the binding of substrates^{1,2}. Structures of importers have been reported that suggested a two-state model for the transport mechanism^{3–11}. Energy-coupling factor (ECF) transporters belong to a new class of ATP-binding cassette importers. Each ECF transporter comprises an energy-coupling module consisting of a transmembrane T protein (EcT), two nucleotide-binding proteins (EcA and EcA'), and another transmembrane substrate-specific binding S protein^{12–14} (EcS). Despite the similarities with ABC transporters, ECF transporters have different organizational and functional properties. The lack of solute-binding proteins in ECF transporters differentiates them clearly from the canonical ABC importers¹⁵. Previously reported structures of the EcS proteins RibU and ThiT clearly demonstrated the binding site of substrate riboflavin and thiamine, respectively^{16,17}. However, the organization of the four different components and the transport mechanism of ECF transporters remain unknown. Here we present the structure of an intact folate ECF transporter from *Lactobacillus brevis* at a resolution of 3 Å. This structure was captured in an inward-facing, nucleotide-free conformation with no bound substrate. The folate-binding protein FolT is nearly parallel to the membrane and is bound almost entirely by EcT, which adopts an L shape and connects to EcA and EcA' through two coupling helices. Two conserved XRX motifs from the coupling helices of EcT have a vital role in energy coupling by docking into EcA–EcA'. We propose a transport model that involves a substantial conformational change of FolT.

We purified the recombinant folate ECF transporter complex that is able to transport folate *in vitro* (Supplementary Fig. 1) and determined its structure at a resolution of 3.0 Å (Supplementary Fig. 2). The overall structure has dimensions of 110 Å × 65 Å × 50 Å and contains one molecule each of FolT, EcT, EcA and EcA', which confirms a stoichiometry of 1:1:1:1. EcA and EcA', which are both nucleotide free, form a heterodimer and are structurally similar to the nucleotide-binding domain (NBD) proteins of other ABC transporters. EcT and FolT form another heterodimer crossing the membrane and are structurally different from the transmembrane domain proteins of the canonical ABC transporters (Fig. 1a, b). A possible folate-binding pocket was found in FolT near the EcT–FolT dimer interface through structure superimposition with RibU and ThiT, in which equivalent pockets were previously identified as the riboflavin- and thiamine-binding sites, respectively^{16,17}. However, there is no electron density for folate in this pocket according to liquid chromatography mass

spectroscopy (data not shown), indicating that this structure represents a substrate-free form. Unlike the transmembrane domain in the ABC transporters, the long axis of which is perpendicular to the membrane, the long axis of FolT is inclined at an angle of about 20° to the membrane plane, such that the substrate-binding pocket faces towards the cytoplasm. There is a large surface cleft at the interface of the two heterodimers, which is connected to the substrate-binding pocket and thus might be the substrate's exit to the cytoplasm (Fig. 1b, c). Furthermore, superposition of the EcA–EcA' heterodimer with the NBD dimer of the maltose transporter indicates that the structure of EcA–EcA' is more similar to the open conformation⁷ (Supplementary Fig. 3). Thus, we conclude that the structure we obtained is in the resting state with an inward-facing conformation.

In contrast to the other three components of the ECF transporters, the structure of EcT has not been previously determined. It is mainly composed of eight helices (Fig. 2a and Supplementary Fig. 4): three cytoplasmic coupling helices, CH1–3, are inserted between the amino-terminal transmembrane helices 1 to 4 (TM1–4) and the carboxy-terminal TM5; TM3 is divided into two short helices owing to the intervention of Pro71; and two long loops, R1 and R2, connect CH2 and CH3 and, respectively, CH3 and TM5. The overall structure of EcT adopts an L shape and the five transmembrane helices are nearly perpendicular to the three coupling helices. The N terminus is located in the cytoplasm and the C terminus faces towards the periplasm.

FolT forms a six-helix bundle (SM1–6, each of which is an EcS protein transmembrane helix) that is similar to the bundles previously reported in RibU (root mean squared deviation, 2.8 Å) and ThiT (root mean squared deviation, 2.5 Å) (Fig. 2b and Supplementary Fig. 5). A potential substrate-binding pocket is found in the middle of the helices (Fig. 1b). Of the six helices, SM2 is a short helix 20 Å in length, whereas SM6 is a long, bent helix consisting of three parts. Three long loops, L1, L3 and L5, connect SM1 and SM2, SM3 and SM4, and SM5 and SM6, respectively. Unlike the T proteins from different species, which share very low sequence identity (<20%) in the transmembrane helices (supplementary Fig. 6), a large number of the residues forming the transmembrane helices of the S proteins from varied species are strictly or highly conserved. Among them, the strictly conserved residues Asp 66, Phe 81, Ala 85, Trp 125 and Arg 141 protrude into the potential substrate-binding pocket and the highly conserved residues Ala 22, Val 26, Arg 29, Phe 77 and Tyr 130 are located at the interface of FolT and EcT (Fig. 2b and Supplementary Fig. 7).

Among the four components of the ECF transporters, EcA and EcA' are very similar (60%) in amino-acid sequence to the NBD proteins of the ABC transporters. The structures of EcA and EcA' are composed of three domains or subdomains: the helical subdomain, the RecA-like subdomain and the C-terminal domain. EcA and EcA' form a heterodimer and the dimer interface involves the C-terminal domains and the RecA-like subdomains of both proteins. The previously identified motifs that are involved in ATP binding and hydrolysis,

¹National Key Laboratory of Plant Molecular Genetics, Institute of Plant Physiology and Ecology, Shanghai Institutes for Biological Sciences, Chinese Academy of Sciences, 300 Fenglin Road, Shanghai 200032, China. ²State Key Laboratory of Molecular Biology, Institute of Biochemistry and Cell Biology, Shanghai Institutes for Biological Sciences, Chinese Academy of Sciences, 320 Yueyang Road, Shanghai 200031, China. ³CAS Key Laboratory of Synthetic Biology, Institute of Plant Physiology and Ecology, Shanghai Institutes for Biological Sciences, Chinese Academy of Sciences, 300 Fenglin Road, Shanghai 200032, China.

*These authors contributed equally to this work.

including Walker A and B motifs, the Q and D loops, the LSGGQ motif and the His switch are also conserved in EcA–EcA' (Fig. 2c and Supplementary Fig. 8).

The structure of the folate ECF transporter shows extensive interactions between FolT and EcT in the current conformation. FolT sits in the L-shaped cleft formed by the five transmembrane helices and the three coupling helices of EcT (Fig. 1). SM1–3, SM6c, and the L3 and L5 loops of FolT are involved in the interactions with TM1, TM3–4 and CH2–3 of EcT. The dimer interface buries about one third of the surface area of each protein and consists of three regions. The main interaction region is formed between SM1–3 and SM6c of FolT and CH2–3 of EcT. Specifically, the conserved residues Ala 22 and Val 26 from SM1, Phe 41 from SM2, Val 64 and Ile 68 from SM3, and Val 164, Ile 168 and Leu 172 from SM6c make extensive hydrophobic interactions with residues Leu 157, Leu 161, Ile 163, Leu 165, Phe 167, Leu 171, Met 172, Leu 201, Met 205, Leu 208, Phe 209, Phe 213, Ala 216 and Leu 219 from CH2–3 (Fig. 3a). In addition, the conserved residue Phe 77 from the L3 loop of FolT forms hydrophobic interactions with a number of residues from TM1 and TM4 of EcT, and the conserved residues Tyr 130 and Gln 131 from the L5 loop of FolT form several hydrogen-bonding and hydrophobic interactions with residues from TM3–4 of EcT (Fig. 3b). It is noteworthy that in this structure the bent TM3 of EcT covers the top of FolT, whereas the L1 loop of FolT, which was previously found to cover the substrate-binding pocket in RibU and ThiT, does not do so here, leaving the pocket open to the cytoplasm (Fig. 1b and Supplementary Fig. 5).

Unlike for the known ABC transporters, the interactions of the transmembrane proteins (EcT and FolT) with the ATP-binding proteins (EcA and EcA') in the inward-facing folate ECF transporter mainly involve EcT. The cytoplasmic coupling helices (CH2–3) of EcT constitute the main interaction surface with EcA and EcA'. Despite the low sequence similarity of EcTs from different species, the three coupling helices, especially CH2–3, show high sequence conservation, suggesting that the ECF transporters might share a common energy-coupling mechanism (Supplementary Fig. 6).

Of the three coupling helices, CH2–3 form an X-shaped bundle via extensive hydrophobic contacts (Figs 1a and 4). In addition, there are several hydrogen-bonding interactions between the conserved residue Asp 173 of CH2 and the conserved residues Ser 211 and Arg 215 of CH3. Helices CH2–3 dock into the surface groove formed by the helical and RecA-like subdomains of EcA–EcA', and the interactions between them are mainly hydrophobic (Fig. 4a). The R1 loop is partly embedded into the groove of EcA, and the R2 loop is partly inserted into that of EcA'. In particular, the side chains of Arg 185 of the R1 loop and Arg 226 of the R2 loop insert into two small cavities of the groove and form hydrogen bonds and salt bridges with Asp 106 of EcA and Asp 102 of EcA', respectively (Fig. 4b, c). The two Arg residues are strictly conserved among different EcT proteins, and are preceded and followed by residues with small side chains (XRX), probably allowing them to insert deeply into the cavities (Supplementary Fig. 6). Previously, it was reported that these two Arg residues are essential for the assembly and transport activity of ECF transporters¹⁸. Our results suggest that the two Arg residues might function as anchors to fix CH2 and CH3 and translate the conformational changes of EcA–EcA' to FolT through EcT, and hence have an important role in the energy coupling of the folate ECF transporter. Therefore, we refer to them as the XRX motifs.

It was reported previously that S proteins of the ECF transporters have very high substrate-binding affinities^{19,20}. This is further confirmed by the RibU, ThiT and BioY structures complexed with their substrates, although no substrates were added in the crystallization experiments^{16,17,21}. Additionally, FolT alone can also bind folate tightly²². However, we failed to obtain a structure of the folate ECF transporter in complex with the substrate even though an excessive amount of folate was added in the crystallization solution. These results, together with the transporting activity of the transporter reconstituted in the proteoliposome, imply that there is at least one other conformation, representing the outward-facing state, which would enable tight binding of folate to the transporter. To achieve the outward-facing conformation, the substrate-binding pocket of FolT observed in the current structure needs to undergo a substantial

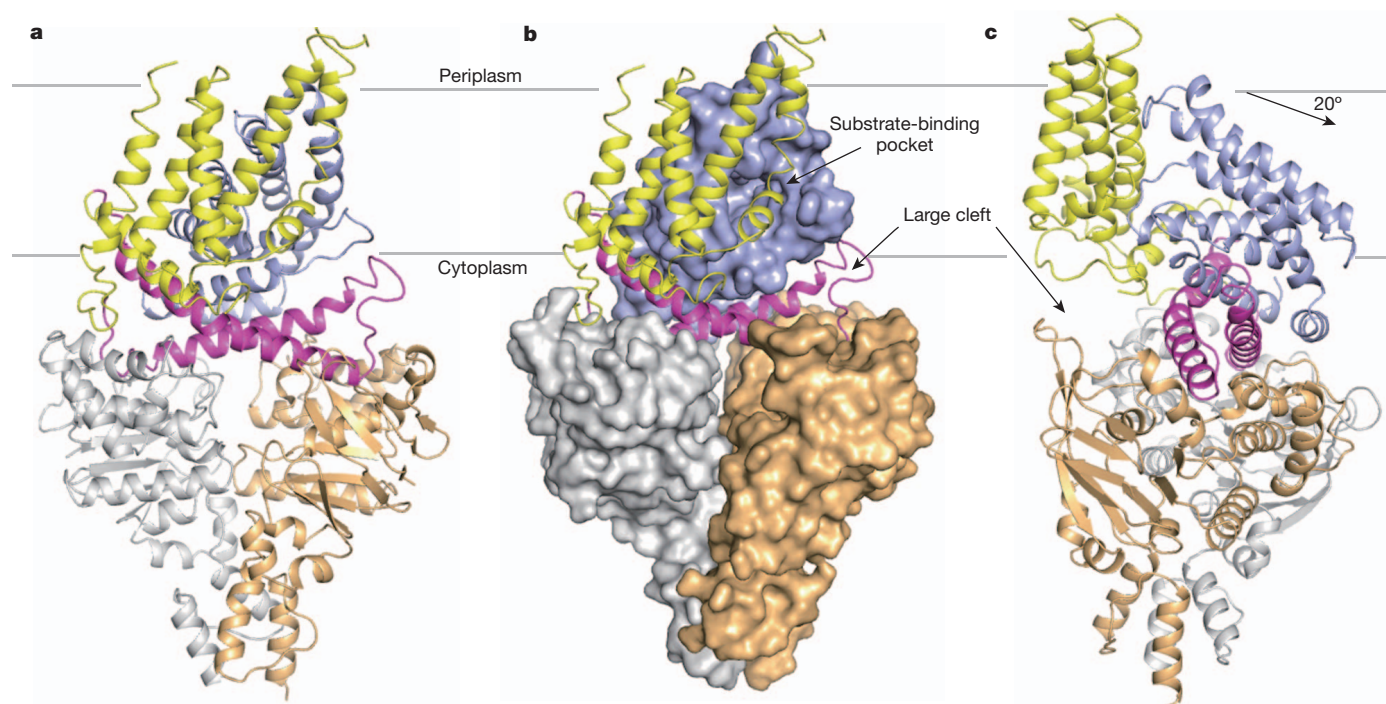


Figure 1 | Architecture of the folate ECF transporter. **a**, A ribbon representation of the structure of the folate ECF transporter viewed in parallel to the membrane. FolT, EcT, EcA and EcA' are coloured light blue, yellow (CH2 and CH3 are magenta), gold and grey, respectively. **b**, FolT, EcA and

EcA' shown as a surface model in the same orientation as in **a**. The potential substrate-binding pocket and a large cleft at the interface of the heterodimers are indicated. **c**, A ribbon representation of the structure rotated clockwise around the vertical axis by 90° relative to **a**.

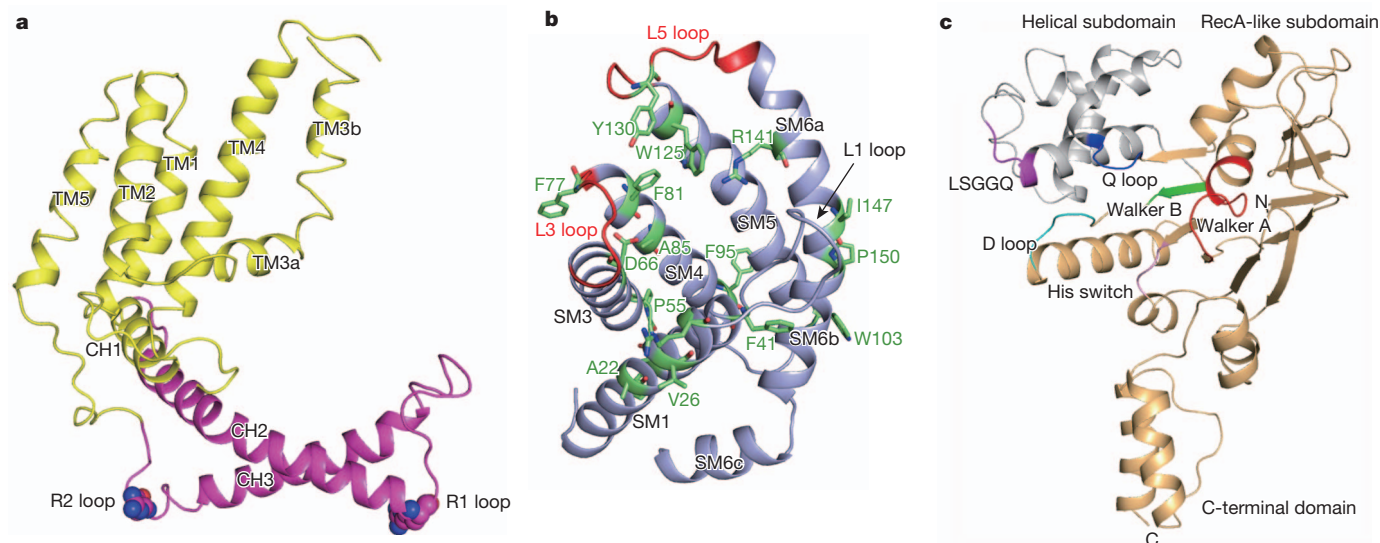


Figure 2 | Overall structures of different components. **a**, Structure of EcfT. Colour coding is same as in Fig. 1a. Arg 185 and Arg 226 in the R1 and R2 loops are marked with spheres. **b**, Ribbon diagram of FolT. The L3 and L5 loops are coloured red, and the conserved residues are shown with a green stick model.

c, Ribbon diagram of EcfA. The conserved Walker A and B motifs, the Q and D loops, the LSGGQ motif and the His switch are coloured red, green, blue, cyan, magenta and pink, respectively.

conformational change to bind the substrate. In addition, EcfA and EcfA' of the heterodimer in its open conformation need to approach each other to assume a closed conformation to allow the ATP hydrolysis to take place. The movements of EcfA and EcfA' towards each other would probably lead to the conformational change of CH2 and CH3 and thus may cause substantial conformational changes to or reorientations of FolT, or both, and may cause the substrate-binding pocket to face to the periplasm as the R1 and R2 loops are anchored into the deep cavities of EcfA and EcfA'.

On the basis of this assumption, we propose a working model for substrate translocation of this folate ECF transporter (Supplementary Fig. 9): in the outward-facing conformation, the six helices of FolT might adopt a conformation perpendicular to the membrane to facilitate substrate capture or binding; following the ATP hydrolysis, the conformational changes occurring in EcfA–EcfA' could be transferred via the coupling helices of EcfT to FolT, which may result in a substantial conformational change to or reorientation of FolT, or both,

and the release of folate to the cytoplasm, leading to the inward-facing conformation represented by our structure. Following the binding or hydrolysis of ATP, the inward-facing conformation may transform back to the outward-facing conformation. However, we cannot exclude other processes by which ECF transporters may switch from the inward-facing conformation to the outward-facing conformation. For instance, substrate-bound S proteins might be replaced through dissociation. In a further experiment, we found that a mutant lacking the ATPase activity (Glu171Gln Glu166Gln) can facilitate the dissociation of the complex in the presence or absence of folate and ATP (Supplementary Figs 10 and 11). A similar mutant enables the ABC transporters to adopt the outward-facing conformation⁶. This implies that the outward-facing conformation of the folate ECF transporter is unstable compared with the inward-facing conformation. The instability of the outward-facing conformation might help different S proteins to bind to or dissociate from the same energy-coupling

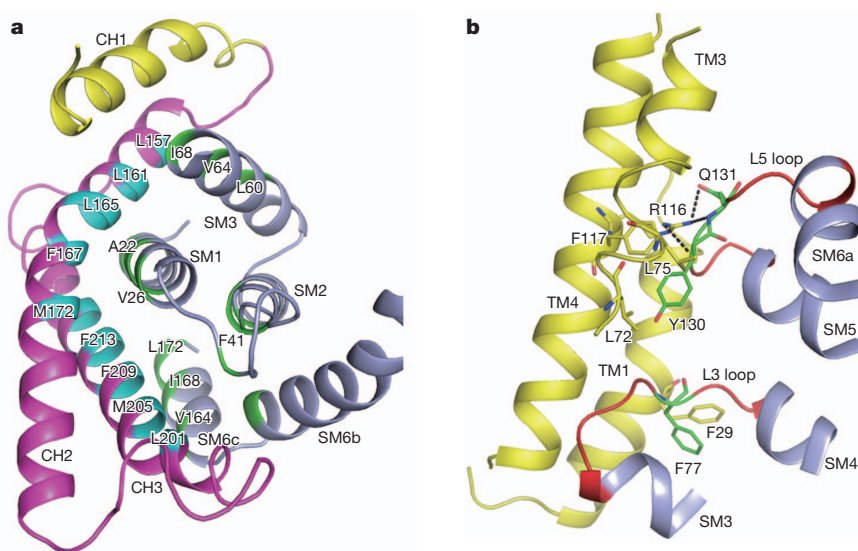


Figure 3 | The interactions between EcfT and FolT. **a**, Hydrophobic interactions formed between helices of FolT and EcfT. The involved conserved residues of FolT and EcfT are coloured green and cyan, respectively. **b**, Two

interaction regions formed between the L3 and L5 loops of FolT and EcfT. The involved residues of FolT and EcfT are shown with green and yellow stick models, respectively, and the hydrogen bonds are indicated with black dashed lines.

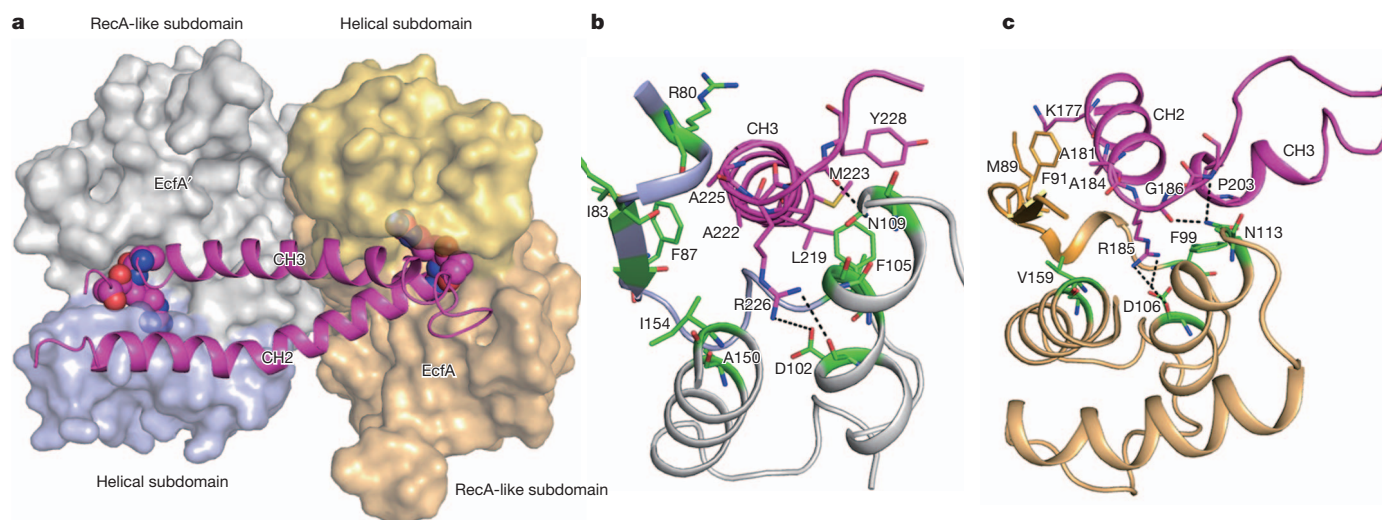


Figure 4 | Structural basis for energy coupling. **a**, Top view of the interaction of CH2 and CH3 (magenta ribbon) of EcfT with EcfA–EcfA' (gold and grey surface models). Two strictly conserved Arg residues, Arg 185 and Arg 226, are shown with spheres. **b**, **c**, Close-up views of the interactions between CH3

EcfA' (**b**) and between CH2 and EcfA (**c**). Residues of EcfT are shown with green stick models, and those of CH2–3 are shown with magenta stick models. Salt bridges and hydrogen bonds are indicated with black dashed lines.

module. This may explain how the class II ECF transporters share the usage of the energy-coupling module. Because the ECF transporters exist mainly in Firmicutes, which include many notable pathogens and probiotic microorganisms, the structure presented here may open a new path to the design of antibiotics and probiotics.

METHODS SUMMARY

FolT, EcfT, EcfA and EcfA' constituting the folate ECF transporter were co-expressed in *Escherichia coli*, purified to homogeneity and crystallized using the hanging-drop vapour diffusion method. All diffraction data were collected at the BL17U beamline of the Shanghai Synchrotron Radiation Facility (SSRF) and processed with HKL2000²³. The crystals belong to space group $P2_12_12_1$ with unit-cell dimensions of $a = 80.6$ Å, $b = 149.0$ Å and $c = 170.9$ Å. Single-wavelength anomalous dispersion phasing was performed using SHLEX²⁴. The initial model was built using PHENIX²⁵. Model building was carried out using COOT²⁶. The structure refinement was done using PHENIX.

Full Methods and any associated references are available in the online version of the paper.

Received 15 August 2012; accepted 27 February 2013.

Published online 14 April 2013.

- Higgins, C. F. ABC transporters: from microorganisms to man. *Annu. Rev. Cell Biol.* **8**, 67–113 (1992).
- Rees, D. C., Johnson, E., & Lewinson, O. ABC transporters: the power to change. *Nature Rev. Mol. Cell Biol.* **10**, 218–227 (2009).
- Locher, K. P., Lee, A. T. & Rees, D. C. The *E. coli* BtuCD structure: a framework for ABC transporter architecture and mechanism. *Science* **296**, 1091–1098 (2002).
- Hvorup, R. N. *et al.* Asymmetry in the structure of the ABC transporter-binding protein complex BtuCD–BtuF. *Science* **317**, 1387–1390 (2007).
- Hollenstein, K., Frei, D. C. & Locher, K. P. Structure of an ABC transporter in complex with its binding protein. *Nature* **446**, 213–216 (2007).
- Oldham, M. L., Khare, D., Quiocho, F. A., Davidson, A. L. & Chen, J. Crystal structure of a catalytic intermediate of the maltose transporter. *Nature* **450**, 515–521 (2007).
- Oldham, M. L. & Chen, J. Crystal structure of the maltose transporter in a pretranslocation intermediate state. *Science* **332**, 1202–1205 (2011).
- Khare, D., Oldham, M. L., Orelle, C., Davidson, A. L. & Chen, J. Alternating access in maltose transporter mediated by rigid-body rotations. *Mol. Cell* **33**, 528–536 (2009).
- Oldham, M. L., Davidson, A. L. & Chen, J. Structural insights into ABC transporter mechanism. *Curr. Opin. Struct. Biol.* **18**, 726–733 (2008).
- Kadaba, N. S., Kaiser, J. T., Johnson, E., Lee, A. & Rees, D. C. The high-affinity *E. coli* methionine ABC transporter: structure and allosteric regulation. *Science* **321**, 250–253 (2008).
- Gerber, S., Comellas-Bigler, M., Goetz, B. A. & Locher, K. P. Structural basis of trans-inhibition in a molybdate/tungstate ABC transporter. *Science* **321**, 246–250 (2008).
- Rodionov, D. A. *et al.* A novel class of modular transporters for vitamins in prokaryotes. *J. Bacteriol.* **191**, 42–51 (2009).
- ter Beek, J., Duurkens, R. H., Erkens, G. B. & Slotboom, D. J. Quaternary structure and functional unit of energy coupling factor (ECF)-type transporters. *J. Biol. Chem.* **286**, 5471–5475 (2011).
- Erkens, G. B., Majasnerowska, M., Ter Beek, J. & Slotboom, D. J. Energy coupling factor-type ABC transporters for vitamin uptake in prokaryotes. *Biochemistry* **51**, 4390–4396 (2012).
- Eitinger, T., Rodionov, D. A., Grote, M. & Schneider, E. Canonical and ECF-type ATP-binding cassette importers in prokaryotes: diversity in modular organization and cellular functions. *FEMS Microbiol. Rev.* **35**, 3–67 (2011).
- Zhang, P., Wang, J. & Shi, Y. Structure and mechanism of the S component of a bacterial ECF transporter. *Nature* **468**, 717–720 (2010).
- Erkens, G. B. *et al.* The structural basis of modularity in ECF-type ABC transporters. *Nature Struct. Mol. Biol.* **18**, 755–760 (2011).
- Neubauer, O. *et al.* Two essential arginine residues in the T components of energy-coupling factor transporters. *J. Bacteriol.* **191**, 6482–6488 (2009).
- Hebbeln, P., Rodionov, D. A., Alfandega, A. & Eitinger, T. Biotin uptake in prokaryotes by solute transporters with an optional ATP-binding cassette-containing module. *Proc. Natl Acad. Sci. USA* **104**, 2909–2914 (2007).
- Duurkens, R. H., Tol, M. B., Geertsma, E. R., Permentier, H. P. & Slotboom, D. J. Flavin binding to the high affinity riboflavin transporter RibU. *J. Biol. Chem.* **282**, 10380–10386 (2007).
- Berntsson, R. P. *et al.* Structural divergence of paralogous S components from ECF-type ABC transporters. *Proc. Natl Acad. Sci. USA* **109**, 13990–13995 (2012).
- Eudes, A. *et al.* Identification of genes encoding the folate- and thiamine-binding membrane proteins in Firmicutes. *J. Bacteriol.* **190**, 7591–7594 (2008).
- Otwowski, Z. & Minor, W. Processing of X-ray diffraction data collected in oscillation mode. *Methods Enzymol.* **A 276**, 307–326 (1997).
- Sheldrick, G. M. Experimental phasing with SHELXC/D/E: combining chain tracing with density modification. *Acta Crystallogr. D* **66**, 479–485 (2010).
- Adams, P. D. *et al.* PHENIX: building new software for automated crystallographic structure determination. *Acta Crystallogr. D* **58**, 1948–1954 (2002).
- Emsley, P. & Cowtan, K. Coot: model-building tools for molecular graphics. *Acta Crystallogr. D* **60**, 2126–2132 (2004).

Supplementary Information is available in the online version of the paper.

Acknowledgements We thank X. Chen and G. Zhao for reading the manuscript and the staff members of Shanghai Synchrotron Radiation Facility for technical assistance in data collection. This work was supported by grants from the Ministry of Science and Technology of China (2013CB127000), the Shanghai Institutes for Biological Sciences, the Chinese Academy of Sciences (2012OHTP, 2009CSP001, 2011KIP101, KSCX2-EW-J-12) and the Shanghai 'Pujiang Talent' programme (11PJ1411300).

Author Contributions P.Z. initiated the project and designed the experiments; K.X., M.Z., Q.Z., F.Y., H.G. and P.Z. performed the bulk of the experiments; C.W. and F.H. contributed to some experiments and discussions; K.X., M.Z., Q.Z., F.Y. and J.D. contributed to data analysis and manuscript preparation; P.Z. wrote the manuscript.

Author Information The structure of the folate transporter has been deposited in the Protein Data Bank under the accession code 4HUQ. Reprints and permissions information is available at www.nature.com/reprints. The authors declare no competing financial interests. Readers are welcome to comment on the online version of the paper. Correspondence and requests for materials should be addressed to P.Z. (pengzhang01@sibs.ac.cn).

METHODS

Protein preparation. Genes encoding the four components of the folate ECF transporter in *L. brevis*, that is, FolT, EcfT, EcfA and EcfA', were subcloned into pRSFDuet and pETDuet vectors to obtain two expression plasmids: pRSFDuet-FolT-EcfT and pETDuet-EcfA-EcfA'. The gene identity and predicted molecular masses are as follows: FolT, GI:116333470, 20.8 kDa; EcfT, GI:122269079, 30.4 kDa; EcfA, GI:122269078, 32.2 kDa; EcfA', GI:122269077, 30.6 kDa. A tag of six histidine residues was added at the N terminus of EcfT. These two plasmids were co-transformed into *E. coli* BL21 (DE3) and induced using 0.25 mM β -D-thiogalactopyranoside at $A_{600\text{ nm}} \sim 1.2$. After 14 h at 37 °C, the cells were collected, homogenized in buffer containing 20 mM Tris-HCl (pH 8.0) and 100 mM NaCl, and lysed using a French press with two passes at 15,000 p.s.i. Cell debris was removed by centrifugation. The supernatant was collected and ultracentrifuged at 150,000g for 1 h. Membrane fraction was incubated with 1% (w/v) n-dodecyl- β -D-maltopyranoside (DDM, Anagrade) for 2 h at 4 °C. After another centrifugation step at 20,000g for 45 min, the supernatant was loaded onto a Ni^{2+} -NTA affinity column (Qiagen). After competitive wash with 20 mM Tris-HCl (pH 8.0), 25 mM imidazole and 0.018% DDM, the protein was eluted from the column using 20 mM Tris-HCl (pH 8.0), 250 mM imidazole and 0.018% DDM and concentrated to around 10 mg ml⁻¹ before further purification by gel filtration (Superdex-200, GE Healthcare). The buffer for gel filtration contained 20 mM Tris-HCl (pH 8.0), 100 mM NaCl and 0.18% DM. The peak fraction was collected and concentrated to approximately 8 mg ml⁻¹ for crystallization.

Crystallization, data collection and structure determination. Crystals were grown at 20 °C by the hanging-drop vapour diffusion method. Large crystals were obtained in many conditions containing polyethylene glycol. However, none of the crystals diffracted X-rays beyond 4 Å at the synchrotron. Addition of 0.3 M MgCl₂ was later found to result in crystals with better diffraction properties. The best crystals, which diffracted X-rays to 3 Å, were grown in 20% polyethylene glycol 2000, 15% glycerol and 0.1 M Tris-HCl (pH 8.4). Crystals used for data collection were directly flash frozen in a nitrogen stream at 100 K. All data sets were collected at the BL17U beamline of the Shanghai Synchrotron Radiation Facility (SSRF) and processed with HKL2000²³. The native crystals belong to the space group $P2_12_12_1$ with unit-cell dimensions of $a = 80.6 \text{ Å}$, $b = 149.0 \text{ Å}$, $c = 170.9 \text{ Å}$. Cell dimensions of other crystals for phasing were slightly different (Supplementary Table 1).

To solve the structure, we tried to use the NBD structures in the PDB database to run molecular replacement, but the resulting density shows only the contours of EcfA and EcfA'; those of FolT and EcfT are not obvious. We then used several heavy atoms to soak the native crystals. Soaking of crystals with 10 mM Pt²⁺ for 3 h produced significant signal and the data were collected to 4 Å. The phases were

solved and optimized with SHELX²⁴ and used to draw a density map for automatic main-chain tracing with PHENIX²⁵. Additional missing residues in the auto-built model were manually added in COOT²⁶. To confirm the topology and connectivity, selenium methionine crystals were obtained in a similar manner and single-wavelength anomalous dispersion data were collected. The final model was refined using PHENIX, and the atomic coordinates contain EcfT (residues 6–87, 100–262), EcfS (residues 10–173), EcfA (residues 2–285) and EcfA' (residues 3–277). The Ramachandran statistics are 87.1% in the most favoured region and 12.9% in the allowed region. Refinement statistics are summarized in Supplementary Table 1. An independent study of a related ECF transporter by Y. Shi and co-workers yields similar results (T. Wang *et al.*, personal communication).

ATPase activity assay. Folate ECF transporter complex and a mutant (containing Glu171Gln in EcfA and Glu166Gln in EcfA') were purified as mentioned above. The assay mixture contained 0.3 μM protein and 1 mM MgCl₂ in a total reaction volume of 25 μl ; 0.5 mM ATP was added to start the reaction at 37 °C. For ATP analogue, 0.5 mM ATP- γ -S was used to replace ATP. To stop the reaction, reagent from the QuantiChrom ATPase assay kit was added to the reaction mixture. After incubation for 30 min at room temperature, the activity was measured by monitoring the increase of absorbance at $A_{620\text{ nm}}$. Phosphate was used as standard.

Proteoliposome-based folate uptake assay. The proteoliposome was prepared according to the published protocol, with minor modifications²⁷. The polar lipids extracted from *E. coli* (Avanti) were used to prepare the liposome. After flash-freezing and thawing for 10 cycles, the liposome was extruded through a 400-nm membrane (Waterman) 11 times. The folate transporter protein complex was inserted in the presence of 0.3% (w/v) Triton X-100 and 20% glycerol at 4 °C for 2 h, with a protein-to-lipid ratio of 1:50 (wt/wt). The proteoliposome was collected by centrifugation at 4 °C at 267,000g for 20 min. After inclusion of Mg-ATP, the proteoliposome was ready for folate uptake assay.

For the time-course experiment, [3,5,7,9-³H] folic acid sodium salt (40 Ci mmol⁻¹, American Radiolabelled Chemical) was added. All the reactions were performed at 37 °C. At the indicated reaction time, an aliquot of proteoliposome was taken for filtration through 0.22 μm cellulose acetate filter (Sartorius). The filter membrane was washed immediately with 2 ml ice-cold isotonic buffer (80 mM KPi, pH 7.0), and then was dried at 37 °C overnight and taken for liquid scintillation counting. Control experiments were performed with proteoliposome included with Mg-ADP and with liposome included with Mg-ATP, but no protein combined. All experiments were repeated three times.

27. Geertsma, E. R., Nik Mahmood, N. A., Schuurman-Wolters, G. K. & Poolman, B. Membrane reconstitution of ABC transporters and assays of translocator function. *Nature Protocols* **3**, 256–266 (2008).

Structure of a bacterial energy-coupling factor transporter

Tingliang Wang^{1,2*}, Guobin Fu^{1,2*}, Xiaojing Pan^{1,2}, Jianping Wu^{1,2}, Xinqi Gong^{1,2}, Jiawei Wang³ & Yigong Shi^{1,2}

The energy-coupling factor (ECF) transporters constitute a novel family of conserved membrane transporters in prokaryotes that have a similar domain organization to the ATP-binding cassette transporters^{1–3}. Each ECF transporter comprises a pair of cytosolic ATPases (the A and A' components, or EcfA and EcfA'), a membrane-embedded substrate-binding protein (the S component, or EcfS) and a transmembrane energy-coupling component (the T component, or EcfT) that links the EcfA–EcfA' subcomplex to EcfS. The structure and transport mechanism of the quaternary ECF transporter remain largely unknown. Here we report the crystal structure of a nucleotide-free ECF transporter from *Lactobacillus brevis* at a resolution of 3.5 Å. The T component has a horseshoe-shaped open architecture, with five α -helices as transmembrane segments and two cytoplasmic α -helices as coupling modules connecting to the A and A' components. Strikingly, the S component, thought to be specific for hydroxymethyl pyrimidine, lies horizontally along the lipid membrane and is bound exclusively by the five transmembrane segments and the two cytoplasmic helices of the T component. These structural features suggest a plausible working model for the transport cycle of the ECF transporters.

The ATP-binding cassette (ABC) transporters harness the energy of ATP binding and hydrolysis for substrate transport across the cell membrane. Mechanistic understanding of the ABC transporters has been greatly facilitated by structural biology⁴, exemplified by the studies on the maltose transporter^{5–7}, the BtuCD importer^{8–10} and the Sav1866 exporter^{11,12}. In contrast to the ABC importer, the membrane-embedded EcfS of the ECF transporter is responsible for substrate binding, with binding affinity typically in the nanomolar range^{13–15}. The energy-coupling component, EcfT, shares no detectable sequence homology with any protein of known structure. Although the EcfS structure has been determined^{16–18}, the structures of EcfT and the quaternary ECF transporter remain unknown, precluding mechanistic understanding of substrate transport.

We cloned the shared *ecfA–ecfA'–ecfT* module and four to six different *ecfS* genes from each of six Gram-positive bacteria. In total, we generated complete clones for 28 distinct ECF transporter complexes, each of which was overexpressed, extracted from membrane using detergents, purified and assessed for stoichiometry and complex stability. Eight of the 28 complexes yielded high expression levels, seemed to be stable in detergent micelles and showed approximate 1:1:1:1 stoichiometry among the four components. These eight complexes were individually purified to homogeneity (Supplementary Fig. 1a) and subjected to crystallization screening.

Two ECF complexes, thought to be specific for hydroxymethyl pyrimidine (HMP) and pantothenate¹, were crystallized. Crystals of the putative HMP transporter from *Lactobacillus brevis* had space group P2₁2₁2₁ (Supplementary Fig. 1b) and were studied further because they were more amenable to X-ray diffraction than were crystals of the pantothenate transporter. This ECF transporter contains four full-length proteins: EcfA (residues 1–279), EcfA' (1–290), EcfS

(1–166) and EcfT (1–266). The purified transporter complex seems, on the basis of mass spectrometric analysis, to be substrate free. After numerous trials, we improved the crystal diffraction limit to a resolution of approximately 3.5–3.7 Å (Supplementary Fig. 1c). Heavy-atom derivatives were generated by soaking the crystals in potassium tetranioplatinate (Supplementary Fig. 2). The structure was determined by platinum-based, single-wavelength anomalous dispersion and refined at a resolution of 3.5 Å (Supplementary Table 1 and Supplementary Figs 3 and 4). There is one complete ECF transporter in each asymmetric unit.

The structure of the quaternary ECF transporter is shaped like a twisted ellipsoid (Fig. 1a), with EcfA–EcfA' constituting the bottom half and the EcfT–EcfS subcomplex comprising the twisted top half. The surface boundary between the EcfA–EcfA' subcomplex and the EcfT–EcfS subcomplex is demarcated by a positively charged strip that encircles the ellipsoidal transporter complex (Fig. 1a, b). The substrate-binding component, EcfS, is bound almost exclusively by the energy-coupling component, EcfT, involving a large buried surface area, of about 5,520 Å². EcfS is separated from the ATPases EcfA and EcfA' by two consecutive, extended α -helices in EcfT (Fig. 1a). These two helices (α 6 and α 7) and the loop sequence following helix α 7 directly interact with EcfA' and EcfA, resulting in a buried surface area of about 4,190 Å² between EcfT and the EcfA–EcfA' subcomplex.

In contrast to most membrane proteins, in which the transmembrane segments are roughly perpendicular to the membrane surface, EcfS lies horizontally along the lipid membrane and its transmembrane segments are approximately parallel to the membrane surface (Fig. 1c). This remarkable structural feature places the opening of the EcfS substrate-binding pocket at the interface between lipid membrane and the cytoplasm (Fig. 1c). Notably, the opening of the EcfS substrate-binding pocket, measuring 10 Å in length and 6 Å in width (Fig. 1d), is large enough to allow passage of the putative substrate HMP.

EcfT contains eight α -helices, of which five (α 1 to α 4 and α 8) constitute the membrane-spanning core and two (α 6 and α 7) are responsible for binding to EcfA–EcfA' in the cytoplasm (Fig. 2a and Supplementary Fig. 5). The horizontally placed helix α 5 connects the membrane-spanning core with the cytoplasmic helices, α 6 and α 7, yielding a horseshoe-shaped overall architecture for EcfT. The coupling module for EcfA' consists of the carboxy-terminal portion of α 6 and the middle section of α 7, whereas the coupling module for EcfA comprises the C terminus of α 7 and the ensuing loop as well as the middle section of α 6 (Fig. 2a). Each coupling module contains a conserved sequence motif Ala-Arg-Gly, located in the C terminus of α 6 or α 7.

An exhaustive search of the Protein Data Bank (PDB) using the Dali server¹⁹ failed to uncover any entry similar to EcfT. The closest entries, with respective similarity Z scores of 4.3 and 4.1, are the structures of IpaH9.8 E3 ubiquitin ligase²⁰ and the N-BAR domain (PDB ID, 4AVM), which have 103 and 109 C α atoms aligned to EcfT with root mean squared deviations of 17.8 and 13.9 Å, respectively. This analysis suggests that EcfT probably represents a previously unreported protein

¹Ministry of Education Key Laboratory of Protein Science, Tsinghua University, Beijing 100084, China. ²Tsinghua-Peking Joint Center for Life Sciences, Center for Structural Biology, School of Life Sciences and School of Medicine, Tsinghua University, Beijing 100084, China. ³State Key Laboratory of Bio-membrane and Membrane Biotechnology, Tsinghua University, Beijing 100084, China.

*These authors contributed equally to this work.

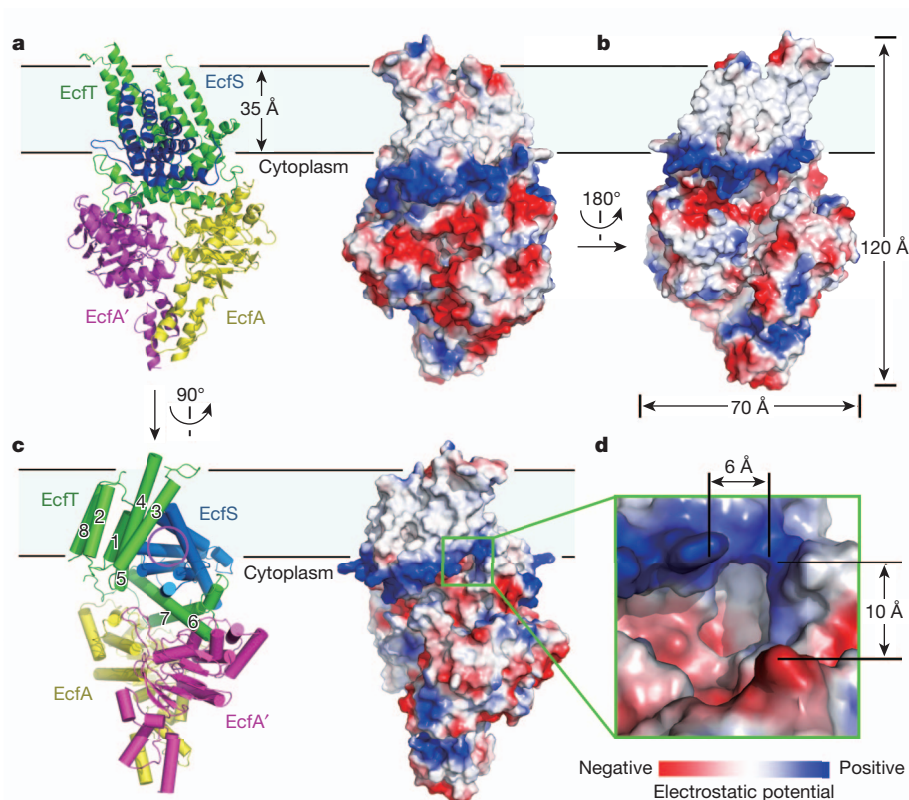


Figure 1 | Overall structure of a quaternary ECF transporter. **a**, Structure of a quaternary ECF transporter shown in ribbon representation (left) and in terms of surface potential (right). The S component (EcS), with its transmembrane segments nearly parallel to the plane of lipid membrane, is mostly bound by the T component (EcT). EcT, on the other hand, uses two consecutive helices to contact the A and A' components (EcA and EcA'). **b**, The electrostatic surface potential of the ECF transporter is viewed after a 180° rotation relative to that in **a**. The strip of positive charge probably marks

the boundary between lipid membrane and cytoplasm. **c**, The putative substrate-binding pocket in EcS (indicated by a magenta circle in the left panel and a green box in the right panel) opens just below the lipid membrane on the cytoplasmic side. **d**, A close-up view of the location of the putative substrate-binding pocket. The opening of the pocket measures approximately 10 Å in length, 6 Å in width and more than 10 Å in depth. All structural figures were prepared using PyMol³⁰.

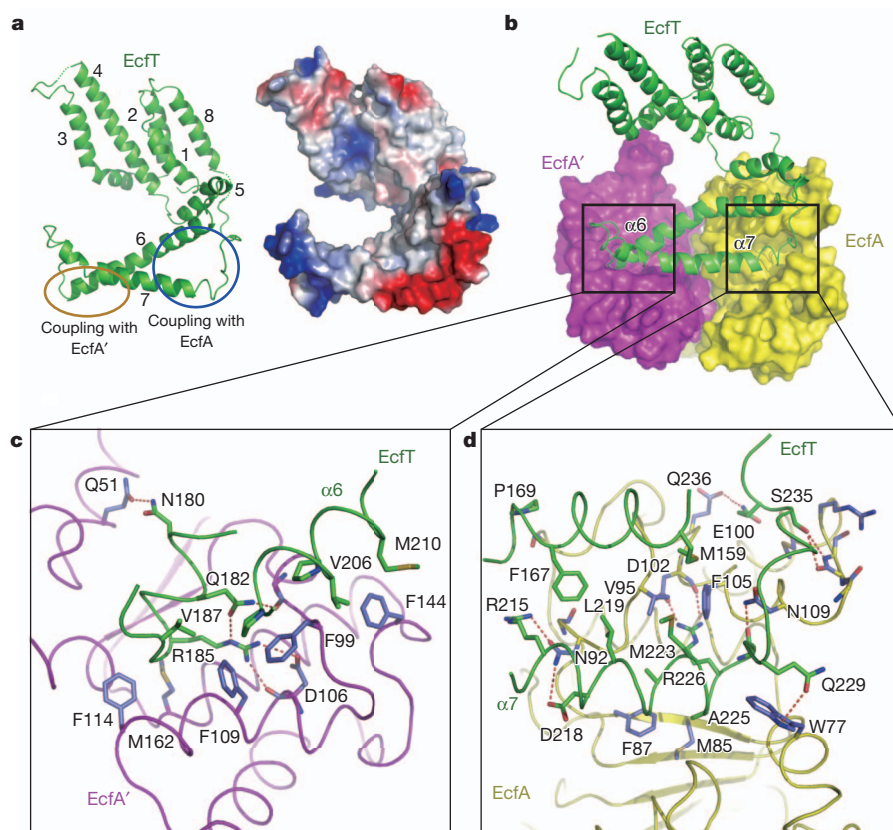
fold, which we refer to here as the ECF fold (Supplementary Fig. 6a). The strong sequence homology of EcT among the ECF transporters (Supplementary Fig. 5) suggests conservation of the ECF fold.

EcA and EcA' have similar structures, with a root mean squared deviation of 2.83 Å for 249 aligned Cα atoms. EcA–EcA' from *L. brevis* and the orthologous subcomplexes from other bacterial species conform to the canonical sequences of nucleotide-binding domains (NBDs) of the ABC transporters (Supplementary Fig. 7). Similar to other ATPases exemplified by MalK of the maltose importer⁵ (Supplementary Fig. 8a), each molecule of EcA–EcA' comprises a RecA-like subdomain, a helical subdomain and a C-terminal subdomain. The key amino acids that coordinate ATP binding and hydrolysis are the same in EcA–EcA' and MalK, including Lys 46–Ser 47 of the phosphate-binding (P) loop, Gln 88 of the Q-loop, Asp 165 of the Walker B motif, and His 199 of the H-loop (Supplementary Fig. 7). These residues are positioned around the putative ATP-binding site (Supplementary Fig. 8b).

The two NBDs of an ABC transporter are known to dimerize. Similarly, EcA and EcA' dimerize mainly through their respective C-terminal subdomains, particularly through the two α-helices at the C terminus of each ATPase (Supplementary Fig. 9). Dimerization results in the burial of approximately 3,004 Å² of surface area between EcA and EcA'. The RecA-like and helical subdomains in EcA are spatially separated from the corresponding subdomains in EcA'. Such a gap is also observed in the structure of nucleotide-free ABC transporters. We speculate that, similar to the NBDs of the ABC transporters, binding to two molecules of ATP at the dimeric interface of EcA–EcA' may lead to interactions between their corresponding subdomains and subsequent closure of the gap.

There are two coupling modules in EcT, one for each ATPase component. In the EcA'–coupling module, the C terminus of helix α6 is placed in a surface groove on EcA' and the middle section of α7 packs against a bulged surface patch on EcA' (Fig. 2b). An identical feature is observed in the EcA–coupling module. Notably, these two coupling modules and their interacting elements in EcA–EcA' can be reasonably superimposed with each other (Supplementary Fig. 6b). In the ABC transporter, the transmembrane domain also interacts with the NBD through a coupling α-helix⁴. Thus, despite a lack of sequence conservation between EcT and the transmembrane domain, both the ECF and the ABC transporter use a similar strategy—a coupling helix—for energy transduction.

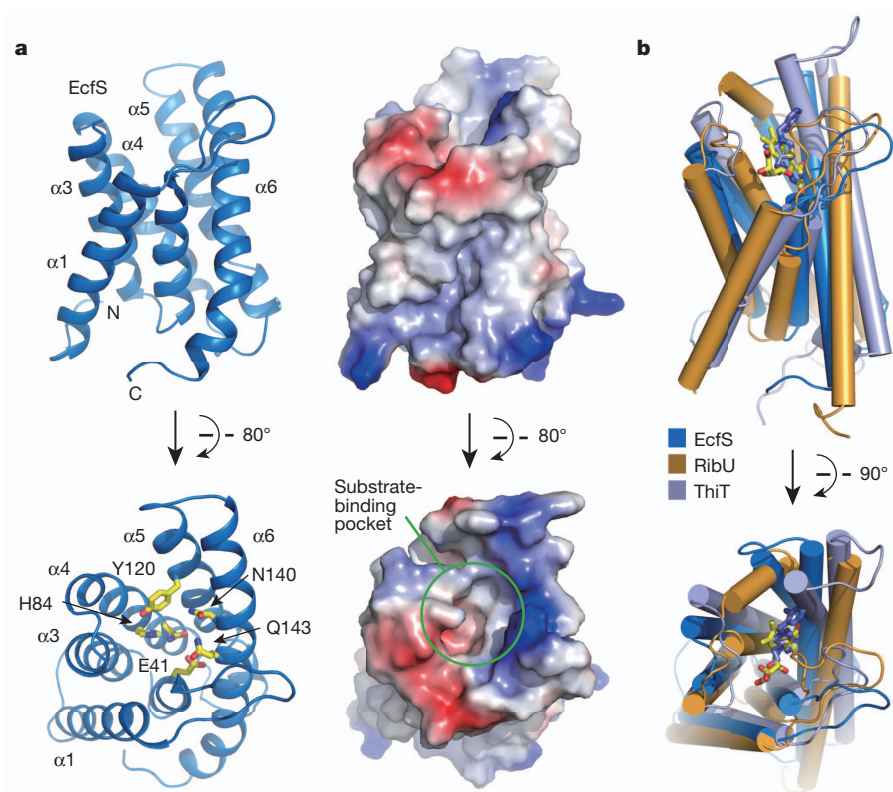
At the interface between EcT and EcA' (Fig. 2c), Arg 185 of the highly conserved ARG motif (Ala 184–Arg 185–Gly 186) in EcT may donate a pair of charge-stabilized hydrogen bonds to Asp 106 in EcA', and the invariant residue Gln 182 in EcT stabilizes Arg 185 while making an additional hydrogen bond to Gln 97 in EcA'. These hydrogen bonds are supported by van der Waals contacts between nonpolar amino acids in helix α7 of EcT and an aromatic surface patch on EcA' comprising Phe 99, Phe 109, Phe 114 and Phe 144. At the EcT–EcA interface, Arg 226 of the Arg motif (Ala 225–Arg 226–Gly 227) in EcT may contact Asp 102 in EcA though a pair of charge-stabilized hydrogen bonds (Fig. 2d). In both coupling modules, the conserved Arg motif is located at the C terminus of the coupling helix, suggesting that it has an important function. Supporting this analysis, the Arg residues in the Arg motif of EcT were shown to be essential for substrate transport in *Leuconostoc mesenteroides*²¹; a single Arg-to-Glu mutation in EcT abrogated vitamin uptake²¹. In addition to the coupling helix,



each coupling module in EcfT also contains a second structural element—a portion of the other α -helix—for van der Waals interactions with a hydrophobic surface bulge on EcfA–EcfA'.

EcfS comprises six α -helices (Fig. 3a). The putative substrate-binding pocket contains six polar or charged amino acids, Glu 41, His 84,

Gln 87, Tyr 120, Asn 140 and Gln 143, which are either invariant or highly conserved among the EcfS homologues from other bacterial species (Supplementary Fig. 10). These amino acids are probably important for substrate binding. As anticipated, the structure of the substrate-free EcfS is similar to that of riboflavin-binding RibU¹⁶ or



thiamine-binding ThiT¹⁷, with root mean squared deviations of 3.45 and 2.35 Å, respectively, for 150 and 137 aligned C α atoms between Ecfs and RibU and between Ecfs and ThiT (Fig. 3b).

Apart from helix α 5, all five other α -helices of Ecfs interact with residues in EctT, with helices α 1 and α 6 having a central role (Supplementary Fig. 11a). A significant proportion of the total interactions are mediated by the α 1 helix of Ecfs, which sits on top of α 6 and α 7 of EctT (Supplementary Fig. 11b). Notably, all interactions between Ecfs and EctT are hydrophobic in nature, with no hydrogen bond. This remarkable structural feature may be essential for the transport activity of Ecfs, because the 'greasy' van der Waals interactions, but not hydrogen bonds, may facilitate movement of Ecfs relative to EctT during substrate transport.

As seen in MalK of the maltose importer⁶ (Fig. 4a, left panel), the two NBDs of the nucleotide-free ABC transporter are separated by a gap at the nucleotide-binding site. On binding to ATP and subsequent hydrolysis, the two NBDs move closer to each other, closing the gap⁷ (Fig. 4a, middle and right panels). The conformation of the complex of the ATPases Ecfa and Ecfa' in our crystal structure is closely related to

that of the nucleotide-free MalK⁶; both have a sizable gap (Fig. 4a, left panel). This structural comparison, together with prior knowledge of the various states of ABC transporters, allows us to propose a working model for the ECF transporters.

In this model (Fig. 4b), the ECF transporter is proposed to exist in two major conformational states: a resting state and a substrate-binding state. In the default, nucleotide-free, resting state (as observed in our crystal structure), the substrate-binding component, Ecfs, is positioned horizontally in the lipid membrane, and the two ATPases Ecfa and Ecfa' exist in an open conformation. ATP binding is proposed to switch Ecfa–Ecfa' to a closed conformation, pushing the substrate entry point of Ecfs towards the extracellular side through the two coupling modules of EctT and allowing the outward-open Ecfs to bind substrate. In this substrate-binding state, hydrolysis of ATP and subsequent release of ADP and phosphate may trigger the conformational switch back to the resting state, where substrate is released into the cytoplasm. The key element of this model is a rigid-body rotation of Ecfs, which allows alternating access of substrate to Ecfs from the extracellular and intracellular sides. Ecfs rotation is probably propelled

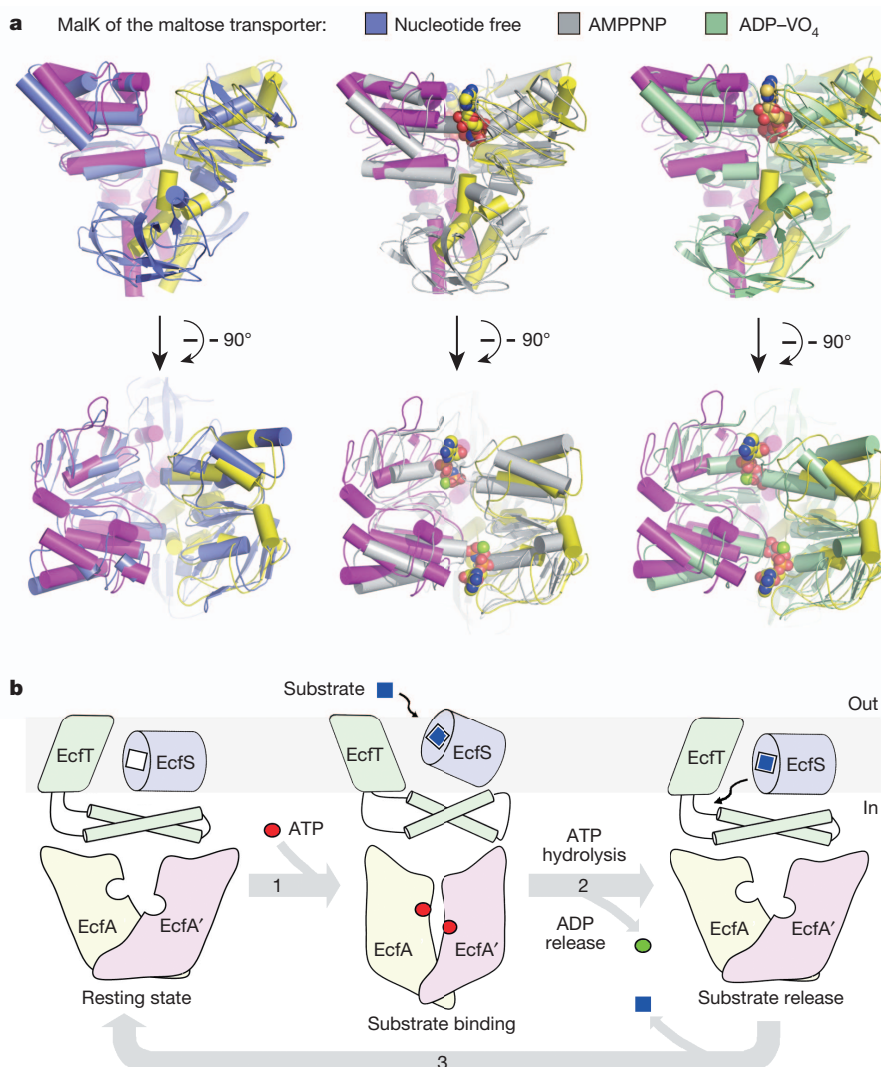


Figure 4 | A working model for the ECF transporter. **a**, Structural comparison between ECF and maltose transporters. The nucleotide-free ATPase components of ECF transporter are compared to the NBDs of maltose transporter in three states: nucleotide free (PDB ID, 3PV0⁶), AMPPNP bound (PDB ID, 3RLF⁷) and ADP-VO₄ bound (PDB ID, 3PUV⁷). **b**, A working model for the ECF transporter. In this model, the default, resting state of the ECF transporter is proposed to be similar to our crystal structure. Ecfa and Ecfa' form

an open dimer, with the nucleotide-binding site unoccupied. On binding to ATP, Ecfa and Ecfa' probably switch to a closed dimer (step 1). The conformational changes in Ecfa–Ecfa' are transferred to Ecfs through the two coupling modules in EctT, pushing the inward-open Ecfs to rotate towards the extracellular space and thus allowing Ecfs to upload extracellular substrate (step 1). Subsequent ATP hydrolysis and release of ADP and phosphate may reset the transporter to the resting state, allowing substrate release (steps 2 and 3).

by movement of the two coupling modules of EcT, which may be further driven by EcA–EcA'-mediated ATP binding and hydrolysis. The proposed substrate transport cycle of ECF transporters mimics filling and decanting a wine glass.

Our proposed transport mechanism of the ECF transporter is highly speculative and requires lengthy experimental verification. To scrutinize the model, we performed functional motion simulation of the quaternary ECF transporter within the lipid bilayer using the coarse-grained anisotropic network model²². This simulation allows determination of the direction of possible movement for a given protein or protein complex. The result shows that EcS rotates upwards and downwards within the membrane, changing the opening of the substrate-binding site relative to EcT and the membrane (Supplementary Video 1). These movements allow EcS to adopt a horizontal position (Supplementary Fig. 12a), where the substrate entry point opens to the cytoplasm, and a tilted position (Supplementary Fig. 12b), where the substrate entry point opens to the extracellular side.

The structure of the ECF transporter provides a satisfactory explanation in relation to published observations. For example, mutation of two Ala residues (Ala15Trp and Ala19Trp) in the thiamine-binding EcS was shown to result in complete loss of transport activity and abrogation of the interaction between EcS and EcT¹⁷. In our structure the two corresponding Ala residues (Ala 17 and Ala 21) are positioned in helix $\alpha 1$ and both mediate interactions with EcT (Supplementary Fig. 11b); replacement of Ala by the bulky Trp residues is predicted to disrupt the interface between EcS and EcT.

Structural elucidation of the resting state of ECF transporter is a necessary step towards understanding the transport mechanism. It should be followed up by structural analysis of the ECF transporter bound to ATP or its analogue. These investigations will not only reveal mechanistic insights but also shed light on potential strategies for the design of novel antibiotics, because many of the Gram-positive bacteria are disease pathogens. The unusually high binding affinity for substrate by the S component, together with the fact that these S components have no mammalian homologues, may facilitate antibiotic design.

METHODS SUMMARY

The quaternary ECF transporter for hydroxymethyl pyrimidine was co-expressed in *Escherichia coli*, purified to homogeneity and crystallized by the hanging-drop vapour diffusion method. Heavy-atom derivatives were obtained by soaking crystals for 4 h in mother liquor containing 10 mg ml⁻¹ potassium tetrakisplatinate (II) (K₂Pt(NO₃)₄). Diffraction data were collected at Shanghai Synchrotron Radiation Facility beamline BL17U and Spring-8 beamline BL41XU and processed with HKL2000 (ref. 23). The crystals belong to the space group *P*2₁2₁2₁. There is one complete quaternary transporter in each asymmetric unit. Ten platinum atoms were determined using the program SHELXD²⁴. The identified platinum sites were then refined and the initial phases were calculated using the program PHASER²⁵. This was followed by density modification using DM²⁶. The resulting phases were then extended to the high-resolution native data with DMMULT²⁶. An initial model was built using COOT²⁷. Sequence docking was aided with the B-factor-sharpened experimental electron density map²⁸. The structure was refined with PHENIX²⁹, using the restraints of stereochemistry and secondary structures.

Full Methods and any associated references are available in the online version of the paper.

Received 15 August 2012; accepted 26 February 2013.

Published online 14 April 2013.

1. Rodionov, D. A. *et al.* A novel class of modular transporters for vitamins in prokaryotes. *J. Bacteriol.* **191**, 42–51 (2009).
2. Eitinger, T., Rodionov, D. A., Grote, M. & Schneider, E. Canonical and ECF-type ATP-binding cassette importers in prokaryotes: diversity in modular organization and cellular functions. *FEMS Microbiol. Rev.* **35**, 3–67 (2011).
3. Erkens, G. B., Majsnierowska, M., Ter Beek, J. & Slotboom, D. J. Energy coupling factor-type ABC transporters for vitamin uptake in prokaryotes. *Biochemistry* **51**, 4390–4396 (2012).

4. Rees, D. C., Johnson, E. & Lewinson, O. ABC transporters: the power to change. *Nature Rev. Mol. Cell Biol.* **10**, 218–227 (2009).
5. Oldham, M. L., Khare, D., Quiocho, F. A., Davidson, A. L. & Chen, J. Crystal structure of a catalytic intermediate of the maltose transporter. *Nature* **450**, 515–521 (2007).
6. Oldham, M. L. & Chen, J. Crystal structure of the maltose transporter in a pretranslocation intermediate state. *Science* **332**, 1202–1205 (2011).
7. Oldham, M. L. & Chen, J. Snapshots of the maltose transporter during ATP hydrolysis. *Proc. Natl Acad. Sci. USA* **108**, 15152–15156 (2011).
8. Locher, K. P., Lee, A. T. & Rees, D. C. The *E. coli* BtuCD structure: a framework for ABC transporter architecture and mechanism. *Science* **296**, 1091–1098 (2002).
9. Pinkett, H. W., Lee, A. T., Lum, P., Locher, K. P. & Rees, D. C. An inward-facing conformation of a putative metal-chelate-type ABC transporter. *Science* **315**, 373–377 (2007).
10. Hvorup, R. N. *et al.* Asymmetry in the structure of the ABC transporter-binding protein complex BtuCD-BtuF. *Science* **317**, 1387–1390 (2007).
11. Dawson, R. J. & Locher, K. P. Structure of a bacterial multidrug ABC transporter. *Nature* **443**, 180–185 (2006).
12. Dawson, R. J. & Locher, K. P. Structure of the multidrug ABC transporter Sav1866 from *Staphylococcus aureus* in complex with AMP-PNP. *FEBS Lett.* **581**, 935–938 (2007).
13. Duurkens, R. H., Tol, M. B., Geertsma, E. R., Permentier, H. P. & Slotboom, D. J. Flavin binding to the high affinity riboflavin transporter RibU. *J. Biol. Chem.* **282**, 10380–10386 (2007).
14. Hebbeln, P., Rodionov, D. A., Alfandega, A. & Eitinger, T. Biotin uptake in prokaryotes by solute transporters with an optional ATP-binding cassette-containing module. *Proc. Natl Acad. Sci. USA* **104**, 2909–2914 (2007).
15. Erkens, G. B. & Slotboom, D. J. Biochemical characterization of ThiT from *Lactococcus lactis*: a thiamin transporter with picomolar substrate binding affinity. *Biochemistry* **49**, 3203–3212 (2010).
16. Zhang, P., Wang, J. & Shi, Y. Structure and mechanism of the S component of a bacterial ECF transporter. *Nature* **468**, 717–720 (2010).
17. Erkens, G. B. *et al.* The structural basis of modularity in ECF-type ABC transporters. *Nature Struct. Mol. Biol.* **18**, 755–760 (2011).
18. Bernstson, R. P. *et al.* Structural divergence of paralogous S components from ECF-type ABC transporters. *Proc. Natl Acad. Sci. USA* **109**, 13990–13995 (2012).
19. Holm, L. & Sander, C. Protein structure comparison by alignment of distance matrices. *J. Mol. Biol.* **233**, 123–138 (1993).
20. Seyedarabi, A., Sullivan, J. A., Sasakawa, C. & Pickersgill, R. W. A disulfide driven domain swap switches off the activity of Shigella IpaH9.8 E3 ligase. *FEBS Lett.* **584**, 4163–4168 (2010).
21. Neubauer, O. *et al.* Two essential arginine residues in the T components of energy-coupling factor transporters. *J. Bacteriol.* **191**, 6482–6488 (2009).
22. Lezon, T. R. & Bahar, I. Constraints imposed by the membrane selectively guide the alternating access dynamics of the glutamate transporter GltPh. *Biophys. J.* **102**, 1331–1340 (2012).
23. Otwinowski, Z. & Minor, W. Processing of X-ray diffraction data collected in oscillation mode. *Methods Enzymol.* **276**, 307–326 (1997).
24. Schneider, T. R. & Sheldrick, G. M. Substructure solution with SHELXD. *Acta Crystallogr. D* **58**, 1772–1779 (2002).
25. McCoy, A. *et al.* Phaser crystallographic software. *J. Appl. Crystallogr.* **40**, 658–674 (2007).
26. Cowtan, K. & DM: an automated procedure for phase improvement by density modification. *CCP4 Newsl.* **31**, 34–38 (1994).
27. Emsley, P. & Cowtan, K. Coot: model-building tools for molecular graphics. *Acta Crystallogr. D* **60**, 2126–2132 (2004).
28. DeLaBarre, B. & Brunger, A. T. Considerations for the refinement of low-resolution crystal structures. *Acta Crystallogr. D* **62**, 923–932 (2006).
29. Adams, P. D. *et al.* PHENIX: building new software for automated crystallographic structure determination. *Acta Crystallogr. D* **58**, 1948–1954 (2002).
30. DeLano, W. L. The PyMOL Molecular Graphics System. <http://www.pymol.org> (2002).

Supplementary Information is available in the online version of the paper.

Acknowledgements We thank S. Huang and J. He at SSRF beamline BL17U for on-site assistance. This work was supported by funds from the Ministry of Science and Technology (973 Programs 2009CB918801 and 2013CB910602) and the National Natural Science Foundation of China (31021002 and 31130002).

Author Contributions T.W., G.F., X.G. and Y.S. designed all experiments. T.W., G.F., X.P., J. Wu, X.G. and J. Wa. performed the experiments. All authors contributed to data analysis. T.W., G.F., X.G., J. Wa. and Y.S. contributed to manuscript preparation. Y.S. wrote the manuscript.

Author Information The atomic coordinates of the quaternary ECF transporter have been deposited in the Protein Data Bank under the accession code 4HZU. Reprints and permissions information is available at www.nature.com/reprints. The authors declare no competing financial interests. Readers are welcome to comment on the online version of the paper. Correspondence and requests for materials should be addressed to Y.S. (shi-lab@tsinghua.edu.cn).

METHODS

Clones and protein preparation. There is only one known gene for EcTf (*ecfT*, GI:116099586), EcA (*ecfA*, GI:116099588) and EcA' (*ecfA'*, GI:116099587) in *L. brevis* ATCC 367, and six known genes for EcS share the same set of energy coupling module. Of these six genes, we focused our attention on the one (GI:116100053) for hydroxymethyl pyrimidine (HMP). The four genes of the HMP transporter (HmpT), *ecfT*, *ecfS*, *ecfA*, and *ecfA'*, were amplified from the *L. brevis* ATCC 367 genomic DNA by PCR. The open reading frames of *ecfT*–*ecfS* and *ecfA*–*ecfA'* were cloned into the co-expression vectors pRSF-Duet-1 and pACYC-Duet-1 (Novagen), respectively. The N terminus of EcTf was fused to a dodecahistidine affinity tag to facilitate the purification. The resulting clones were verified by DNA sequencing. The co-expression vectors were co-transformed into *E. coli* strain C43(DE3) cells (Avidis). Cells were grown to an attenuance at 600 nm ($D_{600\text{nm}}$) of 1.2–1.5 at 37 °C, and the expression of recombinant proteins was induced by 0.25 mM isopropyl- β -D-thiogalactopyranoside for 3 h. Cells were collected by centrifugation, resuspended in 25 mM Tris-HCl (pH 8.0) and 150 mM NaCl, and disrupted by sonication. Cell debris was removed by low-speed centrifugation for 10 min and cell membranes were pelleted by ultracentrifugation at 100,000g for 1 h. The membrane fraction was solubilized in 25 mM Tris-HCl (pH 8.0), 150 mM NaCl, 1% (w/v) n-dodecyl- β -D-maltopyranoside (DDM, Anatrace) for 1.5 h at 4 °C. After another ultracentrifugation step at 100,000g for 30 min, the supernatant was collected and loaded onto Ni²⁺-nitrilotriacetate affinity resin (Ni-NTA, Qiagen) and washed with 25 mM Tris-HCl (pH 8.0), 150 mM NaCl, 20 mM imidazole and 0.02% DDM. The bound protein was eluted from the affinity resin with 25 mM Tris-HCl (pH 8.0), 150 mM NaCl, 250 mM imidazole and 0.02% DDM. All four components of the ECF transporter were clearly visible in the eluent, and their identities were further confirmed by mass spectrometry. The ECF quaternary complex was concentrated to about 10 mg ml^{−1} before further purification by gel filtration (Superdex-200 10/30, GE Healthcare). The buffer for gel filtration contained 25 mM Tris-HCl (pH 8.0), 150 mM NaCl and 0.2% (w/v) n-decyl- β -D-maltopyranoside (DM, Anatrace). The peak fractions were collected for crystallization.

Crystallization. The quaternary ECF transporter complex, purified in 0.2% (w/v) DM (Anatrace), was crystallized by the hanging-drop vapour diffusion method at 18 °C. Protein (1 μ l) was mixed with an equal volume of reservoir solution containing 24% (w/v) polyethylene glycol 1500, 15% (v/v) glycerol, 100 mM Tris buffer (pH 8.4) and 200 mM magnesium chloride. Hexagonal plate-shaped crystals appeared in 2 d and grew to full size within about 5 d. These crystals belong to the space group *P*6₁22 with unit-cell dimensions of $a = 72.528$ Å, $b = 72.528$ Å, $c = 926.071$ Å, $\alpha = 90^\circ$, $\beta = 90^\circ$ and $\gamma = 120^\circ$. Despite their relatively large size (0.3 mm \times 0.3 mm \times 0.1 mm), these crystals diffract X-rays weakly. The best data set collected at beamline BL17U of the Shanghai Synchrotron Radiation Facility (SSRF) had a nominal resolution of 4.5 Å. Further optimization of the crystallization condition led to the generation of rod-shaped crystals, which appeared after 5 d in the well buffer containing 17% (w/v) polyethylene glycol 2000, 16% (v/v) glycerol, 100 mM Tris (pH 8.2) and 100 mM magnesium chloride and grew to full size in 4 weeks. The rod-shaped crystals from space group *P*2₁2₁2₁ diffracted to approximately 3.5 Å at SSRF beamline BL17U. There is one complete transporter in each asymmetric unit. Derivative crystals were obtained by soaking crystals for 4 h in mother liquor containing 10 mg ml^{−1} potassium tetranitroplatinate (II) (K₂Pt(NO₂)₄). Both native and platinum-derived crystals were directly flash-frozen in a cold nitrogen stream at 100 K.

Data collection. The highest-resolution native data (to a resolution of 3.5 Å) was collected on SSRF beamline BL17U. The single-wavelength anomalous dispersion (SAD) data set of the platinum derivative was collected at the peak wavelength (1.07171 Å) on SPring-8 beamline BL41XU. The redundancy for the Pt SAD data was 10.8, which helped improve the phasing power. All data were processed with

the package HKL2000 (ref. 23). Further processing was carried out using programs from the CCP4 suites³¹. Data collection statistics are summarized in Supplementary Table 1.

Structure determination. Ten platinum atoms were identified using the program SHELXD²⁴. These platinum sites were then refined and the initial phases were calculated using the program PHASER²⁵ with the experimental phasing module. The figure of merit right after SAD phasing was measurable only up to 0.278 for the resolution range of 50–4.2 Å. The real-space constraints were then applied to the electron density map using DM²⁶ from the CCP4 program suite, which increased the figure of merit to 0.688. The resulting phases were then extended to the high-resolution native data using DMULTI²⁶. The final map was of sufficient quality for model building.

An initial model was built into the experimental electron density map using COOT²⁷. The electron density for EcA and EcA' was slightly better than that for the EcTf and EcS components. The presence of a large number of aromatic residues in the ECF transporter (12 in EcS, 30 in EcTf, 35 in EcA–EcA') helped the model-building process. Importantly, sequence docking was aided by the B-factor-sharpened experimental electron density map. The best B_{sharp} value, of -212.5 Å², was obtained by determining the minimum absolute B_{sharp} value where the Wilson plot produces all-positive values²⁸. The structure was refined with PHENIX²⁹, using the restraints of stereochemistry and secondary structures. In the final round of refinement, the weights between X-ray target and stereochemistry or atomic displacement parameter restraints were optimized to result in the lowest R_{free} factor. The final structure of the ECF transporter contains 97% of all amino acids in the four components: EcS (residues 1–164), EcA (residues 3–277), EcA' (residues 2–283) and EcTf (residues 17–96, 100–241 and 244–266). Towards the end of structural refinement, we learned about an independent effort by P. Zhang and colleagues to determine the crystal structure of a similar ECF transporter. A brief communication with that group indicates that they came to a similar conclusion.

Functional motion simulation. The functional motion of the ECF transporter system was computed using the coarse-grained anisotropic network model²². In this approach, the whole protein system, including all four components (EcTf, EcS, EcA and EcA'), is treated as an elastic network in which every residue is treated as one bead, with a spring connecting each pair of beads positioned within a distance limit of 11 Å. The implicit membrane anisotropic network model²² was used to model the anisotropic constraints from the membrane on the intrinsic dynamics of the ECF transporter. The spring constants were modified from the traditional anisotropic network model method preferentially to restrain radial motions, thus mimicking the constraining effects of the surrounding lipid molecules. The uniform spring constant, γ , was replaced by the direction-dependent spring constants γ_x , γ_y and γ_z allowing us independently to alter the force constants along each Cartesian coordinate: $\gamma_x = \gamma_y = s\gamma_z$, where s is a scaling factor for radial motions. The x and y directions are within the membrane and the z direction is perpendicular to the membrane. The bigger the value of s , the smaller the radial motion. Radial motions of the protein are suppressed when $s > 1$ and are enhanced when $s < 1$. In our study, an s value of 16 gives the most stable result and the default spring constant was used according to reference 22. The first functional motion mode obtained from this computation was chosen and shown in the movie generated using VMD³². EcS rotates upward and downward within the membrane, changing its substrate entry opening relative to the T component and the membrane.

31. Collaborative Computational Project, Number 4. The CCP4 suite: programs for protein crystallography. *Acta Crystallogr. D* **50**, 760–763 (1994).
32. Humphrey, W., Dalke, A. & Schulten, K. VMD: visual molecular dynamics. *J. Mol. Graph.* **14**, 33–38 (1996).

CAREERS

CANADA Faculty association wants government support for scientists **p.278**

TURNING POINT Geneticist's zeal for research undimmed by lack of PhD **p.279**

NATUREJOBS For the latest career listings and advice www.naturejobs.com

BERTOLD WERKMANN / SHUTTERSTOCK



COLUMN

On my way to being a scientist

Thomas M. Schofield details the stages on his path to a career in research.

I knew I wanted to be a scientist when I realized that science was not about the truth. I know that this statement requires some clarification; it might help if I told you how I came to this realization. There is nothing particularly special about my story except, perhaps, for how it began.

In the early 2000s, I was at work at a recruitment company in London when I got a phone call. It was my mother: she told me that my sister had had a brain haemorrhage, and was critically ill. I ran home, packed a bag and took a train to the hospital, arriving just as my sister came out of surgery. She was in a bad way, the doctors said. The operation had been complicated and there was no way of knowing if she would ever wake up. She did not

regain consciousness for many days.

I stayed at the hospital for the entire time, and sat by her bed through the days and nights. I knew that I wasn't doing anything useful, but I couldn't sleep and the hospital room seemed to be as good a place to be awake as any. I spent most of that time thinking. I was upset. Why could no one tell us what was going on? I assumed that some people, somewhere, knew a great deal about the brain and how it worked. I thought that the problem must have to do with the distribution of the relevant information — if there were more neurologists and psychologists, then more could be done for people who were ill. It seemed to me that the job that I had been doing for five years was not as important as this sort of aspiration. I was earning good

money, but I had started to feel that the job was repetitive and boring. And now I began to feel that it was rather a pointless thing to be doing with my life.

CHANGE OF TACK

My sister began to get better, and after about two weeks she was allowed to go home. I went back to my life in London, relieved but determined. I decided to take a master's degree in neuropsychology, with the aim of becoming a clinical psychologist. But I did not become a clinical psychologist. I became a scientist instead — by accident. How did this happen?

There are four stages on the road to becoming a scientist, and I remember them all. ►

CANADA

Call for policy reform

The Canadian Association of University Teachers (CAUT) in Ottawa wants the government to provide more federal funds for basic research, restore the role of independent national science officer and reduce restrictions on scientists' interactions with media and the public (see *Nature* 483, 6; 2012). In its Get Science Right campaign, launched on 25 April, the CAUT aims to promote transparency in research and support of basic science through its website and public discussions about federal policy. James Turk, executive director of the CAUT, which represents 68,000 academic faculty members, researchers and staff, argues that the government is focusing on business innovation at the expense of basic research. "Changes must be made," he says.

UNITED STATES

Health-coverage clarity

US lawmakers should clarify how the health-care legislation known as Obamacare applies to adjunct faculty members, says a higher-education union. The law — parts of which are slated for adoption by 2014 — could be a boon to adjuncts, many of whom do not currently have health insurance. Under the rules, anyone working at least 30 hours per week would qualify for coverage. But universities have said that it will be difficult to quantify workloads by the hour. "We're very concerned about transparency," says Craig Smith, director of higher education for the American Federation of Teachers in Washington DC. He adds that the law should require that adjuncts help institutions to calculate their work hours.

EUROPEAN UNION

Mobility initiatives

A university coalition is proposing schemes to expand student mobility. In *International Curricula and Student Mobility*, out on 25 April, the League of European Research Universities in Leuven, Belgium, argues for networked mobility — in which one university sets up student exchanges with others — and embedded mobility, in which several universities create a curriculum and exchange students and teachers. Each would involve more students than Erasmus, the existing European exchange programme, says Bart De Moor, vice-rector of international policy at the Catholic University of Leuven and co-author of the report.

► To begin with, you simply want someone in the know to tell you the truth. You read textbooks and attend lectures, and are overawed by the immensity of it all but struck by how neatly everything fits together. You do a few simple experiments in your lab, and you get exactly the results that are expected. There seem to be answers to all of your questions, and you feel that if you read enough textbooks and attend enough lectures then you will understand all there is to understand. This is the stage I was at when I finished my first undergraduate degree, and what I was expecting to find when I went back to do my master's.

CONFLICTING STORIES

The second stage begins when you realize that scientists frequently disagree with each other about what is true. This stage is disturbing, and is caused by taking the business of writing essays and papers seriously. Typically, you will be given a question along the lines of, "What function does Broca's area of the brain serve?" To answer it, you start by reading a long paper by Professor X, who sets out his theory in convincing detail. You think, "Of course, how obvious. It controls the processing of syntax — how could anyone think otherwise?" Next, you read an equally long and detailed review paper by Professor Y, who takes a contrary view, and you think, "Hmm. Professor Y makes some very good points. Perhaps Professor X doesn't know what he's talking about after all". And then on you go to Professor Z, and utter confusion. One of them must be telling the truth, but which one? So you write your essay, describing the contrasting theories of X, Y and Z and conclude: "Opinion is divided — more research is necessary." This is the stage I was at when I finished my master's degree. I decided that maybe I could do some of that research, so I started a PhD.

The third stage of becoming a scientist begins with the realization that nobody knows the truth. This stage is absolutely terrifying, and is caused by doing research. When I started running real experiments, collecting data and testing my ideas against those data, I came to realize that things were not as clear cut as they had seemed from the papers that I had been reading. Sometimes things did not work out as predicted by any of the theories that I knew about. There was always something that could not be explained. I found this troubling, and began to doubt my work. Luckily, I had a very supportive supervisor.

"If I am lucky, I will spend the rest of my life finding new things that I will never quite be able to explain."

When you start doing science at the PhD level, you begin to work and socialize with real scientists — occasionally the very scientists who wrote the papers that so impressed you during your studies. Once you become a professional scientist, these people are usually happy to let you in on an important trade secret: nobody is really sure of anything. A scientific paper is just one cut and polished facet of a bigger, uglier stone. Behind the beautiful graphs and whip-smart arguments lies a tangled mass of doubts, conjectures and anomalies. Pulling any loose thread is usually enough to make the paper lose its shape. The most important thing my supervisor taught me was that this is not a bad thing.

BETTER AND BETTER

Some scientists are lucky enough to pass through a fourth stage. This is when you realize that science is not about finding the truth at all, but about finding better ways of being wrong. The best scientific theory is not the one that reveals the truth — that is impossible. It is the one that explains what we already know about the world in the simplest way possible, and that makes useful predictions about the future. When I accepted that I would always be wrong, and that my favourite theories are inevitably destined to be replaced by other, better, theories — that is when I really knew that I wanted to be a scientist.

A theory can never be perfect: the best it can be is better than the theory that went before. I want to come up with better theories about how the brain works. If I can do this, then someone else can use my ideas to come up with something even better. As theories improve, we are able to make more useful predictions about how things might work in the real world, and from those predictions we can develop better treatments. I want to be part of this progression. This means that, if I am lucky, I will spend the rest of my life finding new things that I will never quite be able to explain.

So there it is. My interest in the brain is pragmatic, rather than curious. I never really wanted to become a scientist. But I became one eventually, because I had to. ■

Thomas M. Schofield was a postdoctoral fellow in neuroscience at New York University. He died in 2010 in a bus accident in Colombia. Writer Stephen S. Hall helped to edit this essay on his behalf.

CORRECTION

The Careers Feature 'Artistic merit' (*Nature* 496, 537–539; 2013) wrongly named the Scientists/Artists Research Collaborations as an initiative of the Santa Fe Institute instead of the 1st-Mile Institute in Santa Fe.

TURNING POINT

Ben Novak

*Ben Novak has spent his young career endeavouring to resurrect extinct species. Although he has no graduate degree, he has amassed the skills and funding to start a project to bring back the passenger pigeon (*Ectopistes migratorius*), once the United States' most numerous bird, which died out in 1914.*

What is it about the passenger pigeon that motivates you?

I have wanted to work in extinct DNA since I was 13 years old, when I saw press reports about work on the DNA of the Tasmanian tiger. I did a science-fair project about whether we could bring back the dodo, basically a giant extinct pigeon. It didn't take long before I came across the passenger pigeon. I was captivated by the fact that in just a few decades, humans caused a complete system collapse, from billions of birds to extinction.

How did you get the skills to do this work?

After getting a bachelor's degree in ecology, I took time off to do field work, then applied to do a PhD at Pennsylvania State University in University Park, working on passenger-pigeon genetics. Unfortunately, I didn't get accepted.

What did you do next?

I ended up working on a master's degree at McMaster University in Hamilton, Canada, focusing on passenger pigeons. But extinct DNA is hard to come by. Museum curators were getting multiple requests and wanted to see results before handing out samples. After five months, I was losing time to wrap up my thesis, so I abandoned the project to work with mastodon fossils that we had in hand.

How did you return to passenger pigeons?

I travelled to the Field Museum of Natural History in Chicago, Illinois, to sample other mastodon fossils. The bird-fossil curator remembered a request that I had made and let me take samples from three passenger pigeons collected from the same flock, which is pretty rare. It was too late to use them for my thesis and the mastodon work was going too slowly to finish in the master's timeline, so I took a year off.

What happened then?

Once I had passenger-pigeon tissue, I started applying for grants to do a population analysis, but I couldn't secure funding. I got about US\$4,000 from family and friends to sequence the DNA of the samples. When I had data, I contacted George Church, a molecular geneticist



at Harvard Medical School in Boston, Massachusetts, who was working in this area. He and members of the Long Now Foundation in San Francisco, California, which fosters long-term thinking, were planning a meeting on reviving the passenger pigeon. We had a few phone calls and Long Now ended up funding more sequencing. The more we talked, the more they discovered how passionate I was. Eventually, Long Now offered me full-time work so that nothing was standing in my way.

Where are you doing that work?

I have just moved to the University of California, Santa Cruz, to work in the lab of molecular biologist Beth Shapiro. She has her own sample set of passenger pigeons, and we want to do population genetics and the genome. It's a good fit. Long Now pays me, and we do the work in her lab, taking advantage of her team's expertise in genome assemblies and ancient DNA.

Do you worry about your long-term career prospects without a PhD?

That is the major question. I know that I would be taken more seriously with those three letters, and that it helps to have the right credentials. At same time, I'm doing work that a postdoc or full researcher gets to do. So I have mixed emotions. One possibility is doing a PhD in Shapiro's group. I'm definitely interested in that.

Will you see a live passenger pigeon one day?

I'm 100% convinced that I will. That's the reason I have the job. I will definitely be attacked as overly optimistic, but people thought Dolly the sheep and *in vitro* fertilization were impossible. These big leaps get made when someone has a vision and they think through the challenges to realize it. That's the optimism I cling to. ■

INTERVIEW BY VIRGINIA GEWIN

THE FRONT LINE

How to save the Universe.

BY SYLVIA SPRUCK WRIGLEY

First of all, I want you forget every single word that they told you at the recruiting office. No, just stop, I don't need to hear it. It's all lies.

Stand right up here with me and take a look around. This is the front line. No, that is not a euphemism. War's not normally neat with straight lines and easy-to-understand strategies, but here we have a line. It's that trench right there. Don't get too close to the edge.

The Sporians disintegrate about four of our people a day. Your ship came in with 10 crates of supplies and 500 raw recruits. You do the maths. Don't make friends.

Listen. We don't need you to wear uniforms or learn to shoot a gun or do anything but be here and drink cod liver oil and die. That's the reality.

Nah, I'm joking. It's not actually cod liver oil. It's worse. It smells like something the dog shat out and tastes like rancid butter. You'll learn to ignore your gag reflex and force it down, just like the rest of us.

That's one of the few things we know. We don't know how to fight them. We don't even know if they are intelligent. But every time we give up and leave the rock to them, they move in closer. Your job is to stand around like you might want to get infected. Don't get infected. That's it.

You won't know if you get infected. You just zombie off looking for high ground and a few hours later, a stalk grows out of your head and explodes. Neon orange spores scatter everywhere, looking for a new home. See, that's why we like this trench right here. You see one of your mates acting like a zombie, push him in. *Fast*.

Truth is, when we first got the reports from Earth, we just quarantined it off. There was barely anyone left there anyway, right? But then, suddenly, we're getting orange mould patches on Mars. Military went in

that time, bombed the planet with every fungicide known to man. That's when we discovered the

oil. The Sporians don't like it. No, we don't know why. We don't know shit about them other than right here, right now, we're holding them at this trench. And we know that if they have a choice between someone who's been drinking the anti-fungal oil and some

populated 'stroid is only 2 AU from here, a hell of a lot closer than Mars. That settlement's not seen a single patch of mould. And they won't, so long as dumb recruits like you keep coming.

The oil's the only thing we've found that even makes 'em wince. It won't help if you're the last one standing, but for now? Drink the oil. Tell the guy next to you not to bother. Try not to get infected. Push anyone infected down into the deep as fast as you goddamn can.

I'm sorry to be the one to tell you, but that's our war. Stand guard at the top of a trench and try to last more than a week while brighter minds search for a way to fight back.

Right, now get to work. Start unpacking those crates and I'll tell you the good news. Yeah, it's not much, but there is good news.

Number 1. The infected seem like they die happy. I've seen more than my fair share. Hallinan didn't talk or anything but he got this real peaceful look. Patel's last word was: "Finally." Steinberg just stared at the sky and grinned. So, here's my thought: maybe the Sporians are God. Maybe this is the second coming. Maybe you are all about to get saved.

I don't know that it's true, but it helps to get me through the night.

Number 2. Half of those crates you are unloading are full of gin. We don't need to stay sober, we just need to stay here. There's no way off this rock so we might as well have a party. Might even find some cocktail sticks, if you're lucky.

Good News Number 3. See all those stars out there? There's over a centillion people out there, all of them living happy lives. See that muddy trench? That's where the Sporians are and because we're here, that's where they're going to stay. You are saving the Universe. You are a goddamn hero.

Now drink. ■

Sylvia Spruck Wrigley was born in Germany and spent her childhood in Los Angeles. She now splits her time between South Wales and Andalucia, two coastal regions with almost nothing in common. You can find out more about her at www.intrigue.co.uk.



JACEY

fussy idiot who hasn't, they'll infect the fussy kid every time.

Anyway, we gave 'em Mars, too. G Council just said, fine, have a planet. Wrote it off.

And it didn't work. A few weeks later, orange flecks. The Sporians start showing up here in the belt. There're no transports. Not a soul has travelled here from Mars in a hundred years. So how'd they get here in a month? No one knows.

Listen, here's what we do know. Sporian expansion only happens when we stop showing up. They don't want the rock, they want us. And as long as the G Council keeps sending in new blood, they'll stay here. The next